Advanced Microwave Embedded Sensors for Infrastructure Health Monitoring

by

Md Ashraful Islam

B.Sc, M.Sc (Electrical & Electronic Engg.)

A thesis submitted for the degree of
Doctor of Philosophy in Infrastructure Engineering

WESTERN SYDNEY UNIVERSITY

Centre for Infrastructure Engineering
School of Computing, Engineering and Mathematics
Western Sydney University, Australia

March 2017

To

Inspiring Parents
&
Loving Kids and Wife

Acknowledgements

First of all, I would like to acknowledge the blessings of Allah, the almighty, who kept me strong and patience throughout my candidature.

I would like to express my heartiest gratitude and thankfulness to my Principal Supervisor, A/P Sergey Kharkovsky for his sincere guidance, continued encouragement, invaluable support and suggestions throughout my study at Western Sydney University. He has been a great source of motivation for me, continuously providing insightful comments with detailed attention to my arguments and timely advice on my work. He offered comprehensive comments and suggestions in reviewing my writings at the same time respecting my voice. I am greatly indebted to Kharkovsky for his valuable time and efforts throughout this thesis.

I would also like to express my gratitude to my co-supervisor Dr Ranjith Liyanapathirana for his sincere advice, support and recommendation.

I would like to extend my appreciation to all the academic, administrative and technical staff at the Centre for Infrastructure Engineering in Western Sydney University. Special thanks go to Mr Ranjith Ratnayake, technical officer of IHM Sensor Laboratory for his assistance in preparing specimens and conducting measurements. Moreover, I give thanks to my fellow PhD colleagues and friends for being supportive and providing courage and inspiration during the study period.

I gratefully acknowledge Bangladesh Government and Public Works Department for granting me deputation for this PhD research study. I equally acknowledge Western Sydney University for awarding me the UWS Postgraduate Scholarship.

Finally, my sincere and heartfelt gratitude to my respected parents for their silent inspiration. I would especially like to thank my passionate life partner, beloved wife Shamsunnaher Begum, sweet daughter Sadia Sarah Ashraf and loving son Md Shadid Ashraf for their continuous unconditional support and sacrifices to make my study smooth.

Statement of Authentication

I, Md Ashraful Islam, declare that all the materials presented in the PhD thesis entitled '**Advanced Microwave Embedded Sensors for Infrastructure Health Monitoring**' are of my own work, and that any work adopted from other sources is duly cited and referenced as such.

This thesis contains no material that has been submitted previously, in whole or in part, for any award or degree in other university or institution.

………………………………………

Md Ashraful Islam

March 2017

Table of Contents

Chapter 1:   Introduction

Chapter 2:   Literature Review

Chapter 3:   Determination of Dielectric Permittivity of Early-Age Concrete Specimens

Chapter 4:   Dual Waveguide Sensor

Chapter 5:   Dual Waveguide Sensor with Rectangular Dielectric Insertions

Chapter 6:   Dual   Waveguide   Sensor   with   Attached Dielectric Layer

Chapter 8:   Conclusions and Recommendations

List of Tables

List of Figures

Abbreviations

CST	Computer simulation technology
CFST	Concrete-filled steel tube
DC	Direct current
DWS	Dual waveguide sensor
EM	Electromagnetic
EMI	Electromagnetic interference
FBG	Fiber Bragg grating
GPS	Global positioning system
IHM	Infrastructure health monitoring
LVDT	Linear variable differential transformers
MEMS	Micro-electromechanical system
OEW	open-ended waveguide
PEC	Perfect electric conductor
PNA	Performance network analyser
PZT	Lead zirconate titanate
SHM	Structural health monitoring
STD	Standard deviation
SWS	Single waveguide sensor
TDR	Time-domain reflectometry

Symbols

f	Frequency or natural frequency of vibration,
l	Length of the wire
T	Tension in the wire
m	Mass per unit length
d	Displacement
ε	Complex permittivity
μ	Complex permeability
ε'	Real part of complex permittivity
ε''	Imaginary part of complex permittivity
ε_r	Relative complex permittivity
ε_r'	Dielectric constant or real part of the relative complex permittivity
ε_r''	Loss factor or imaginary part of the relative complex permittivity
$\varepsilon_r''_{eff}$	Effective loss factor
ε_0	Permittivity in free space
σ	Conductivity
ω	Angular velocity
$\tan\delta$	Loss tangent
$\overline{E_\iota}$	Incident electric field
E_0	Amplitude of incident electric field
$\overline{H_\iota}$	Incident magnetic field
$\overline{E_r}$	Reflected electric field

$\overline{H_r}$	Reflected magnetic field
$\overline{E_t}$	Transmitted electric field
$\overline{H_t}$	Transmitted magnetic field
E_0	
η_0	Impedance of free-space
η	Intrinsic complex impedance of the lossy medium
Γ	Reflection coefficient of the reflected electric field
T	Transmission coefficient of the transmitted electric field
γ	Propagation constant
$\lvert S \rvert_{\mathrm{s}}$	Simulated magnitude of reflection coefficient
$\lvert S \rvert_{\mathrm{m}}$	Measured magnitude of reflection coefficient
L	Distance between the two waveguide sections
S_{11} or $\lvert S_{11} \rvert$	Magnitude of reflection coefficient
S_{21} or $\lvert S_{21} \rvert$	Magnitude of transmission coefficient
$\lvert S_{11} \rvert_{\mathrm{s}}$	Simulated magnitude of reflection coefficient
$\lvert S_{11} \rvert_{\mathrm{m}}$	Measured magnitude of reflection coefficient
$\lvert S_{21} \rvert_{\mathrm{s}}$	Simulated magnitude of transmission coefficient
$\lvert S_{21} \rvert_{\mathrm{m}}$	Measured magnitude of transmission coefficient

Abstract

Microwave sensor systems have been widely investigated for many applications due to their ability to provide non-destructive, noncontact, one-sided and wireless testing. Among these applications infrastructure health monitoring of bridges, building, and dams using microwave sensors, which are mounted on or embedded in composite structures of infrastructure has been attracting an increasing interest. One of the current needs of infrastructure health monitoring includes the detection and monitoring of disbonding and gaps in concrete-based structures, which are also required for simultaneous characterization of concrete. A recently proposed microwave sensor technique exploiting a relatively simple waveguide sensor embedded in a concrete-metal structure such as a concrete-filled steel tube exhibited great potential. However, it suffers from a few drawbacks that need to be solved. This thesis aims to develop and investigate advanced microwave embedded sensors to solve main problems in the current microwave sensory technique including characterization of concrete in concrete-based structures at different stage of its life, size of the interface under inspection, detection and monitoring of a small gap between concrete and dielectric material surfaces and sensitivity to gaps. To achieve this aim the following five research contributions have been made:

The first contribution is the methodology for the determination of the complex dielectric permittivity of concrete using both measurement data and simulation results at different stages (fresh, early-aged and dry) of its life. Firstly, it is developed and tested for a single flanged open-ended waveguide sensor with a hardened concrete specimen, and then the methodology is modified for the developed sensors embedded in concrete-based composite structures with fresh, early-age and dry concrete. Modern computational tool CST Microwave Studio and a performance network analyser are used for simulation and measurement, respectively, throughout this research work.

The second contribution is a dual waveguide sensor, which is proposed, designed and applied for the detection and monitoring of a small gap in concrete-metal composite structures. It consists of two waveguide sections and a metal plate

and uses the transmission of electromagnetic waves along gap when it occurs between the metal plate and concrete surfaces. It provides more measurement data than the single waveguide sensor for characterising concrete-metal structures such as transmission properties of guided waves along the gap and reflection properties of the metal–concrete interface at two different places at the same stage of concrete. As a result, the proposed sensor increases the size of the interface under inspection and sensitivity to the gap using the magnitude of reflection coefficient and magnitude of transmission coefficient together and/or independently.

The third contribution is the design and application of a dual waveguide sensor with rectangular dielectric insertions that is proposed and tested for the characterisation of concrete–metal structures at different stages of the concrete life including its fresh stage. The dielectric insertions are designed and implanted in the waveguide sections in such a way that they create the resonant response of the sensor and prevent water and concrete entering the sections. The resonant properties of the sensor allow long-term monitoring of the concrete hydration, including the detection of the transition from fresh to hardened concrete on its first day. The proposed sensor along with the modified algorithm provides the determination of the complex dielectric permittivity of fresh concrete.

The fourth contribution is a dual waveguide sensor with tapered dielectric insertions. Each tapered dielectric insertion is designed with a tapered part and rectangular part to reduce wave reflection from the insertions over an entire frequency band. The proposed sensor has improved performance at the resonant responses of a quarter-wavelength resonator formed by an open end at the tapered part and shorted end at the rectangular part of each insertion.

The last contribution is the development of dual waveguide sensors with attached dielectric layer and their application for the detection and monitoring of gap between dielectric materials and concrete in metal-dielectric layer-concrete composites as well as the determination of complex dielectric permittivity of concrete at different stages of its life. One of the most attractive designs is the sensor with empty waveguide sections due to its simplicity and robustness, and capability of

the layer for preventing penetration of the obstacles and water, and for optimization of the sensor. On the other hand, the sensors with dielectric insertions and the layer demonstrate a significantly higher magnitude of transmission coefficient. The proposed DWSs can be applied to characterise fresh concrete in a dielectric mould or on-line, and to investigate the shrinkage of different categories of concrete.

Chapter 1

Introduction

1.1   Introduction

Civil structures are very common in every society around the globe regardless of culture, religion, geographical location and economic development. It is difficult to imagine a modern society without complex infrastructure such as buildings, roads, bridges, tunnels, dams and power plants. With increased demand, the number of complex and innovative structures is also increasing. However, damages and defects in these structures may cause serious consequences in terms of human life, economy, and environment. The process of providing accurate information concerning structural condition and performance of these civil engineering infrastructures, referred to as Infrastructure Health Monitoring (IHM), is very important for their reliable and safe operation.

Composite structures including concrete-based structures have been widely used in infrastructure engineering applications such as high-rise buildings, bridges and offshore marine platforms. A concrete-filled steel tube (CFST) is an example of these structures as shown in Figure 1.1a. CFSTs are very attractive in infrastructure engineering due to their high strength, large stiffness and ductility, corrosion resistance, economy in construction and reduced local buckling provided by infill concrete [1] – [5]. However, since two types of materials are used to fabricate CFST members, it is expected that there may be imperfections originating from both the steel tube and its core concrete in CFST. It has been shown that steel imperfections and/or imperfections of concrete caused by not proper manufacturing process and/or its natural shrinkage may lead to gap between steel and concrete surfaces of CFST which reduces compressive and flexural behaviour of CFST members [3], [5], [6]. Figure 1.1b illustrates schematic of cross-sectional view of circular and rectangular CFSTs with a small gap between steel tube and concrete. The existence of gap should be detected and monitor at different stage of CFST life to avoid the failure of structures. In general, research study related to detection and monitoring small gap is

still required to fill gaps in our knowledge of concrete behaviour including its disbonding and shrinkage in concrete-based composite materials.

Microwave sensors have great advantages and potential for material characterization and quality assessment of concrete-based materials, and monitoring critical parts of infrastructure [10]. However, there are no reliable microwave sensors for fresh and early-age concrete characterization as well as for the detection and monitoring of debonding gaps between concrete and other materials.
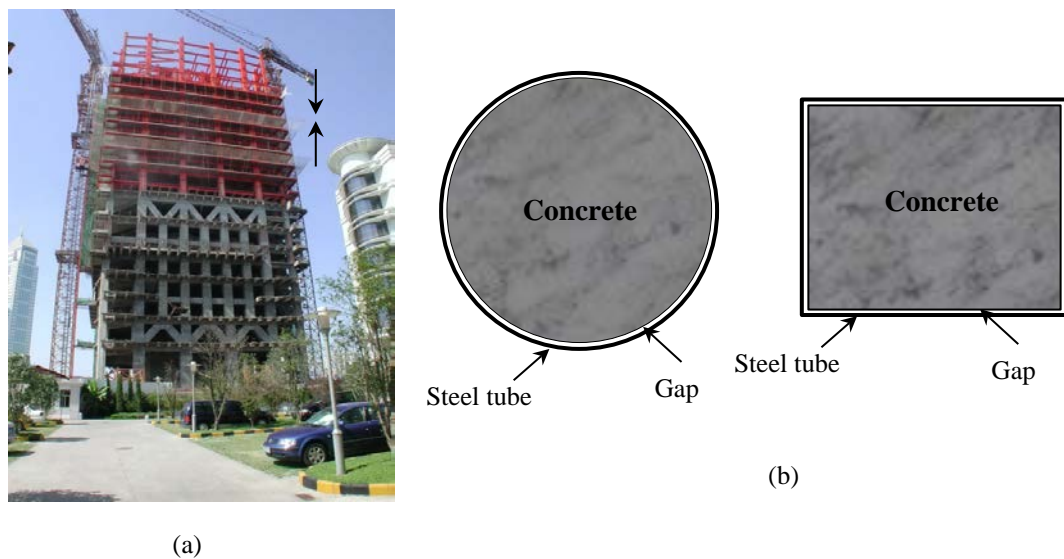
Figure 1.1: (a) Photograph of a high-rise building constructed with CFSTs, and (b) schematic of cross-sectional view of (left) circular and (right) rectangular CFST showing a circumferential gap between steel tube and core concrete (not-to-scale).

Motivated by this situation, it is desirable to develop advanced microwave sensors which can be used to overcome the drawbacks of existing sensors for IHM including microwave ones. In this thesis, advanced microwave sensors will be developed for the characterization of concrete and concrete-metal composites to detect and monitor debonding gaps between concrete and other materials.

1.2   Research Background

A few methods have been applied for detecting the gaps in concrete-based structures. They include conventional acoustic methods (sonic, ultrasonic and acoustic emission technique), guided wave techniques [7] and piezoelectric

technologies using wavelet packet analysis [8], [9]. However, these techniques demonstrated low sensitivity and faced challenges to be applicable especially for CFST, since the real debonding gap between concrete and metal are in the range from ~0 to 3 mm as reported in [6]. To overcome this limitation, the application of microwave sensor technique has been proposed for the first time in [10] which explores a microwave single open-ended waveguide sensor along with a reflectometer. Preliminary investigations into the feasibility of this technique for the detection and monitoring of gap between concrete and steel surfaces have revealed promising results [10]. However, for the application of this technique in practice, several issues should be resolved to use advantages of microwave sensory techniques properly.

Microwave sensory techniques have been used for non-destructive testing and evaluation of concrete based materials for decades [11] – [24]. For example, a microwave reflectometry with an OEW sensor has been applied for the determination of electromagnetic properties of cement-based materials [12] – [15], for the detection and evaluation of disbonds between concrete and CFRP laminates [16], and cracks in concrete [17] – [19]. In addition, microwave sensing of displacement in the presence of reinforced concrete has been experimentally tested for structural health monitoring of concrete structures [20]. Besides, a dual open-ended coaxial sensor system has been studied to determine complex permittivity of liquid specimen from two magnitudes of reflection coefficient [21]. Furthermore, a dual waveguide probe was used for non-destructive characterization of a free-space-backed magnetic material [22].

1.3   Statement of Research Problem

The investigation into the feasibility of measurement sensory approaches with microwave techniques for addressing practical challenges of IHM, includes experimental study and numerical investigation using computational tools such as CST Microwave Studio (CST) [25] which is a very powerful and useful tool for this purpose. However, knowledge of electromagnetic properties of concrete is required for effective and accurate modelling of sensors and the structure under investigation, and numerical study. Another problem related to the characterization of concrete and

its interfaces with other materials using a single waveguide sensor is that the area of interface under inspection, which is covered by one sensor arrangement, is small and part of this area is the interface between air or dielectric insert and concrete [10]. Therefore, there is a demand of advanced sensors for the detection and monitoring of small gaps in concrete-based composite structures, and for determining the electromagnetic properties of concrete at different stages of its life at the place of measurement.

1.4   Research Objectives

The main aim of this research is to design and develop advanced microwave sensors for the detection and monitoring of small gaps in concrete-based composites similar to those that are used in infrastructures such as concrete-filled steel tubes. To achieve the aim, these sensors should be embedded in the structure under test and designed in such a way that they can provide knowledge of electromagnetic properties of concrete in the place of detection and monitoring of disbonding gap at different stages of concrete life. Therefore, the objectives of this thesis are outlined as:

- To propose and apply a methodology for the determination of complex dielectric permittivity of concrete using the measurement data and simulation results obtained with a single open-ended waveguide sensor. To verify this methodology, investigate the sensitivity of the reflection properties of concrete specimen to the changes in waveguide aperture–specimen arrangement.

- To design, develop and validate a microwave dual waveguide sensor for the detection and monitoring of a small gap between concrete and metal surfaces, and characterization of concrete. To use these data in a proper way, a modified algorithm for the determination of complex dielectric permittivity of concrete using the measurement data and simulation results should be developed, and sensitivity of the proposed dual

waveguide sensor to gap and variations in dielectric properties of concrete should be analysed.

- To design, develop and apply microwave dual waveguide sensors for measuring disbonding gap in concrete-based composites at different stages of concrete life including fresh concrete. For this purpose, dielectric insertions implanted in the waveguide sections of the senor should be designed and optimized to prevent penetration of concrete obstacles in the sections, and to extend capability of the sensors using the resonant properties of the insertions. Matching between the insertions and empty parts of the waveguide section should be provided. The modified algorithm for determining the complex dielectric permittivity of concrete in concrete-metal composites at different stages of its life using the proposed sensors should be developed and the sensitivity of the proposed sensors to the variations of dielectric permittivity and geometry of the insertions should be analysed.

- To propose, design and apply dual waveguide sensors with an attached dielectric layer for the detection and monitoring of gap between concrete and dielectric materials interfaces, and for the determination of dielectric properties of concrete in concrete-dielectric composites at different stages of its life. One of the most attractive designs is the sensor with empty waveguide sections due to their simplicity and robustness, and capability of the layer for preventing penetration of the obstacles and water, and for optimization of the sensor. However, the sensors with dielectric insertions and layer may have better performance and new applications.

1.5   Research Methodology

To fulfil the objectives of this study, the research will be conducted into two programs; namely, theoretical program and experimental program. Figure 1.2 shows parts of these programs and links between them.
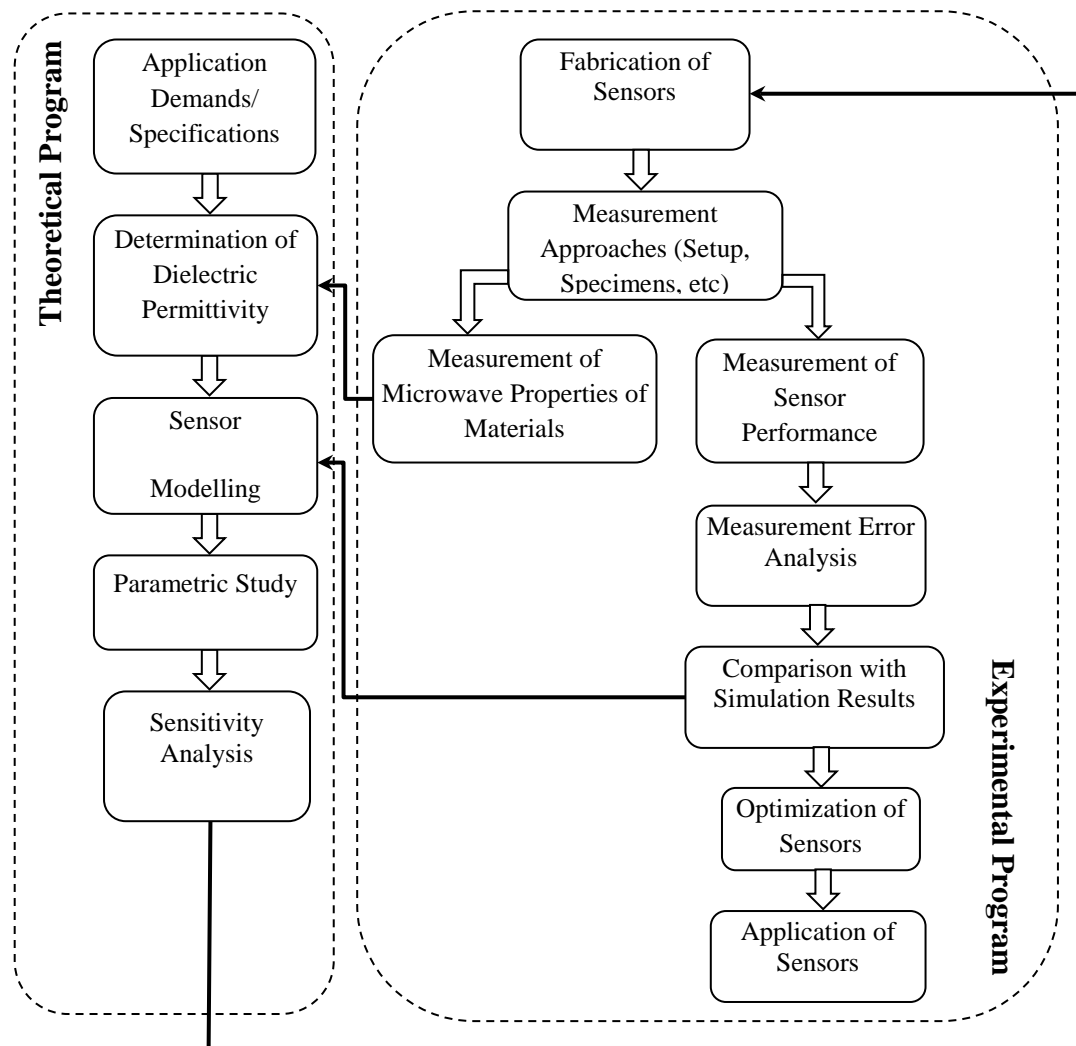
Figure 1.2: Flow chart of research methodology.

1.5.1 Theoretical Program

The theoretical program of this research mainly consists of modelling, simulation and calculation-based post processing studies which include:

- Application (practical) demands
- Determination of dielectric permittivity
- Sensor modelling
- Parametric study
- Sensitivity analysis

Modern electromagnetic computational software CST Microwave Studio module of CST Studio Suite 2014 package has been extensively used in this research study to create models of proposed sensors along with concrete-metal specimens, and to simulate the electromagnetic performance of those sensors at different properties of concrete-metal composite structures. Time domain solver, adaptive mesh setting features and material library of CST Microwave Studio will be used in these studies to achieve desired design parameters. Furthermore, MATLAB software package has been used for post pressing and plotting the exported simulation results and measurement results from CST Microwave Studio environment and performance network analyser, respectively.

1.5.2 Experimental Program

The experimental program of this research study involves fabrication of the proposed sensors, measurement approaches including arrangement of setups and preparation of specimens, measurements, comparison with simulation results and optimization of sensors. Measurement of reflection and transmission coefficients of the sensors embedded in composite structures will be conducted to determine dielectric properties of materials and to determine gaps. All measurement related activities including measurement of sensor performance and measurement error analysis will be conducted using performance network analyser (PNA). Calibration kits, waveguide adapters, cables and associated tools are also used for preparing the experimental setup with the proposed sensors.

The Agilent N5225A PNA shown in Figure 1.3 has been used as the main measurement instrument of this research study. It can generate 10 MHz to 50 GHz microwave signals having two ports with single source. This PNA as shown in has high output power (up to +13 dBm) and a wide power sweep range (up to 38 dB) with best dynamic accuracy of 0.1 dB compression with +12 dBm input power at the test port. In measurement with the proposed sensors, the PNA is used to measure magnitude or/and phase of reflection and transmission coefficients for different specimens. Measurement data are received and stored in PNA for further processing. This basic measurement procedure is followed throughout the research study.
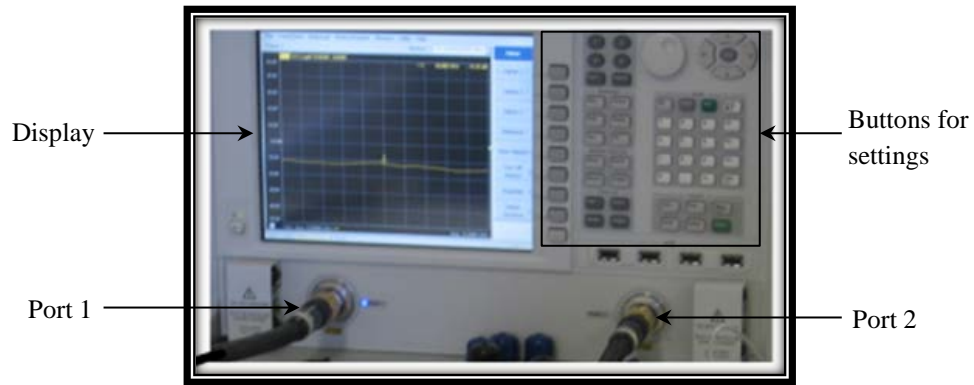
Figure 1.3: Agilent N5225A performance network analyser (PNA).

1.6   Research Contributions

In this thesis, advanced microwave sensors have been developed and employed for infrastructure health monitoring applications. The major contributions of this thesis include:

- A methodology are proposed and applied for the determination of the complex dielectric permittivity of concrete in concrete-based composite structures at different stages of its life using measurement data and simulation results.

- Novel microwave dual waveguide sensor (DWS) with empty rectangular waveguide sections is proposed, designed and applied for the detection and monitoring of small gap in concrete-metal composite structures. This sensor provides more measurement data than the single waveguide sensor for characterisation of concrete-metal structures including transmission properties of wave propagated along the gap between the metal and concrete surfaces, reflection properties of the concrete-metal interface at two different places at the same stage of concrete, and data for a larger area of the interface under inspection.

- Novel DWS with rectangular dielectric insertions is proposed for characterization of fresh concrete in concrete-metal composites including a long-term monitoring of the concrete hydration, the

determination of the complex dielectric permittivity of concrete, and for the detection and monitoring of disbonding gap. The resonant response of insertions in the proposed sensor increases the sensitivity of the sensor, in addition to capability of the insertions to prevent water and concrete entering the waveguides,

- Novel DWS with tapered dielectric insertions is proposed for characterization of concrete at different stages of its life, i.e., from fresh to dry concrete, in concrete-metal composites. Compared to the DWS with rectangular dielectric insertions, a significant improvement of matching between an empty part and a dielectric-filled part is achieved in the proposed DWS with the tapered dielectric inserts. It results in increasing of dynamic range of measurement using the reflection coefficient. In addition, the increase of 1dB - 2 dB in the magnitude of transmission coefficient is also achieved.

- Novel DWSs with attached dielectric layer are proposed for the detection and monitoring of gap between concrete and dielectric material surfaces, and for characterization of fresh concrete. The simple and robust sensor is the DWS with empty waveguide sections and dielectric layer. However, better performances are achieved in DWSs with dielectric insertions and layer. The DWS with tapered dielectric insertions and layer demonstrates the highest magnitude of transmission coefficient over an entire frequency band. The proposed DWSs can be applied to characterise fresh concrete in a mould with a plastic wall or on-line, and to investigate the shrinkage of different categories of concrete.

1.7   Publications

The following papers that are either published or submitted to peer-reviewed journals and conference proceedings are the outcome of this thesis:

1. M. A. Islam and S. Kharkovsky, "Detection and monitoring of gap in concrete-based composite structures using microwave dual waveguide sensor", *IEEE Sensors Journal,* vol. 17, no. 4, pp. 986-993, Feb. 2017.

2. M.A. Islam and S. Kharkovsky, "Determination of dielectric permittivity of concrete using microwave dielectric-loaded dual-waveguide sensor for infrastructure health monitoring", *in Proc. of International Conference on Electromagnetics in Advanced Applications (ICEAA 2016)*, pp. 662-665, Sept. 19-23, 2016, Cairns, Australia.

3. M.A. Islam and S. Kharkovsky, "Microwave dual waveguide sensor system for the measurement of gap between concrete and metal surfaces", *in Proc. IEEE Intern. Instrum. Meas. Techn. Conf. (I2MTC 2016)*, pp. 557-562, May 23-26, 2016, Taipei, Taiwan.

4. M.A. Islam and S. Kharkovsky, "Advanced microwave sensors for the detection of gap in concrete-filled steel tubes," *in Proc. Third International Conference on Smart Monitoring, Assessment and Rehabilitation of Civil Structures (SMAR 2015)*, Sept 9-11, 2015, Antalya, Turkey, 8 pages.

5. M.A. Islam, S. Kharkovsky and K. Chung, "Microwave reflection properties of early-age concrete specimens: Sensitivity analysis," *in Proc. IEEE Intern. Instrum. Meas. Techn. Conf. (I2MTC 2015)*, pp. 920-924, May 11-14, 2015, Pisa, Italy.

6. M. A. Islam and S. Kharkovsky, "Microwave dielectric-loaded dual waveguide sensor for infrastructure health monitoring applications," *IEEE Sensors Journal* (prepared).

1.8   Outline of the Thesis

This thesis is organised in eight chapters including this Chapter 1 and is outlined as follows:

Chapter 2 presents a comprehensive literature review on sensing techniques for infrastructure health monitoring including microwave sensors and their applications. Research studies on CFST with initial concrete imperfection and debonding are also reviewed. Furthermore, few methods of detecting gap between concrete and metal, and various microwave techniques for non-destructive testing and evaluation of concrete using the open-ended waveguide sensor are presented. Finally, summary of the findings from the literature and identification of the research gaps is presented.

Chapter 3 presents the developed methodology for the determination of complex dielectric permittivity of concrete using measurement data and simulation results obtained with the single open-ended waveguide sensor. The sensitivity analyses of the reflection properties of the concrete-metal specimen to the changes in the waveguide aperture–specimen arrangement are also provided in this chapter.

Chapter 4 describes the design and development of microwave dual waveguide sensor. Measurement and simulation results for the detection and monitoring of small gap between a concrete surface and the metal plate using the proposed DWS are presented here in details. The results of numerical investigations for the detection of cracks inside dry concrete specimen using the proposed DWS are also presented in this chapter.

Chapter 5 presents microwave DWS with rectangular dielectric insertions which is proposed to determine the complex dielectric permittivity of fresh concrete in concrete-metal composites and to measure a small gap between concrete and metal plate. The sensitivity of the proposed sensor to the variations of dielectric permittivity and geometry of insertions are analysed.

Chapter 6 presents the design and optimization of empty DWS with attached dielectric layer and dielectric-loaded DWS with attached dielectric layer. Simulation results and experimental verifications for measuring gap between concrete and dielectric layer using the optimized sensors are also presented in this chapter.

Chapter 7 describes the design, modification and results of parametric study of the proposed DWS with tapered dielectric insertions with and without attached dielectric layer. Measurement and simulation results for the detection and monitoring of gap between dry concrete specimens and metal plate are also presented. Furthermore, comparison between DWS with rectangular dielectric insertions and DWS with tapered dielectric insertions is discussed in this chapter.

In chapter 8, the conclusions of this thesis are summarised and finally some recommendations for future research works are presented.

Chapter 2

Literature Review

2.1   Introduction

This chapter reviews publications related to infrastructure health monitoring, focusing on sensing techniques and their applications in concrete and concrete-based composite structures. Publications related to disbond or debonding gaps in a concrete-filled steel tube (CFST), and existing sensory techniques for detecting and monitoring such gaps are also reviewed. Finally, it presents a summary of research gaps in the monitoring of the infrastructure health of concrete–metal structures such as CFSTs.

2.2   Infrastructure health monitoring

Structural health monitoring (SHM) is the process of implementing damage identification strategies for aerospace, civil and mechanical engineering structures at every moment of their lifespan. This process involves the observation of the structure over time using periodical measurements, and the extraction of defect-sensitive features from such measurements, then through analysis, determining the current state of the system's health [28]. For long-term SHM, the output of this process is the updated information regarding the ability of the structure to continue performing its intended function in light of ageing and accumulated damage resulting from the operational environment [29]. At the current stage of sensor, communication and signal-processing technologies, it is now possible to measure structural properties and behaviour to make appreciable assessments of defect levels and predict future courses of structural health [30] and enable the owners, builders, designers and users to make rational decisions about the safe functionality of structures. Various forms of SHM (visual inspection, tap tests) have been employed in different structural sectors for at least half a century [31]; however, SHM has evolved from manual checking to go far beyond data collection procedures and limited processing, to include smart sensors, local data storage and transmission systems, central data management

systems, local (embedded) or central data analysis, reporting and alerting, diagnosis with respect to structural knowledge, and prognosis of future performance [29], [32].

Civil engineering structures are generally the most expensive national investment and asset of any state [33]. In addition, civil engineering structures have a longer service life than other commercial products, and are costly to maintain and replace once they are built. Further, there are few prototypes in civil engineering, and each structure tends to be unique in terms of materials, design and construction [34]. The most important civil infrastructures include high-rise buildings, bridges, towers, tunnels, highways, dams, port facilities and nuclear power plants. Each of these structures deteriorates with time. The deterioration is mostly due to the ageing of constituent materials, continuous use, overloading, environmental exposure conditions, insufficient maintenance, and difficulties encountered in proper inspection methods. All of these factors contribute to material and structural degradation; internal and external damage may result in severe structural failure, causing significant safety and financial concerns. To prevent this circumstance, SHM has been developed [35] for civil engineering applications; it is referred to as infrastructure health monitoring (IHM) hereafter in this document.

Ideally, health monitoring of civil infrastructure consists of determining, by measured parameters, the location and severity of damage in buildings or bridges as they happen [36]. However, current state-of-the-art methods of health monitoring do not provide sufficiently accurate information for determining the extent of the damage [33]. Currently, these methods can only determine whether or not damage is present in the entire structure. Such methods are referred to as 'global health monitoring' methods [28], [36]. They are important because often merely knowing that damage has occurred is enough to initiate further examination of the structure to find the exact location and severity of the damage. Non-destructive evaluation methods are used to find the damage [34], [36]. Methods such as ultrasonic guided waves [37] to measure the state of stress, or eddy current techniques [38] to locate corrosion and cracks can determine the exact location and extent of the damage; these are 'local health monitoring' methods. Therefore, both global and local health monitoring are necessary [36]. However, there is no single IHM method that addresses all requirements.

2.3   Sensors and Sensing Techniques in IHM

Sensors are the first and most important component in any IHM system for civil engineering structures. They not only measure the physical quantities and produce certain information about the state of a structure, but also form a starting point from which to interact with other IHM components. Because of their dissimilar size, geometry, measurement parameters and technology, sensors used in IHM may be categorised in different ways. Figure 2.1 shows the general sensor categories.
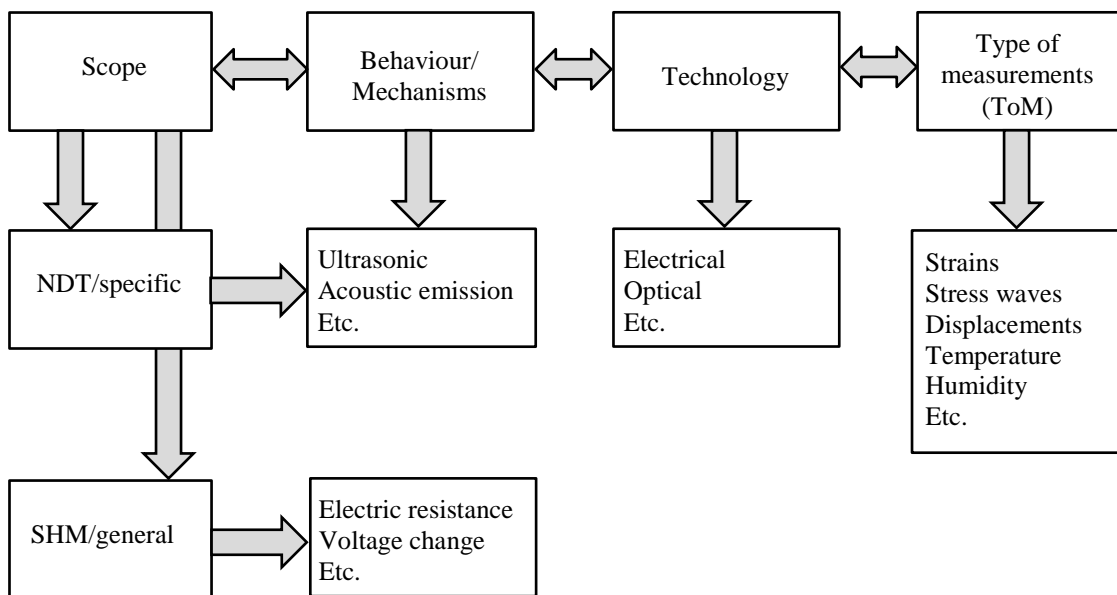
Figure 2.1: Sensor categories [32].

In terms of their technology, sensors are classified as electrical, optical, mechanical and so on, as they transduce physical phenomena into corresponding signals. Electrical sensors use electrical and/or electromechanical phenomena for transduction. Most electrical sensors ultimately rely on the measurement of current. The development of miniature high-impedance circuits has enabled the measurement of a variety of quantities: charge, capacitance, inductance, resistance or voltage, without regard to the details of the measurement circuit. Electrical resistance sensors, resistive strain gauges, resistive temperature gauges, capacitive sensors and piezoelectric sensors are all electrical-quantity-based sensors. The most commonly used mechanical sensors are accelerometers which measure acceleration relative to

an inertial reference frame; tilt meters, wire tension meters, stress meters and pressure gauges may be counted among the other commonly used mechanical transducers. Simplicity and reliability are common characteristics of mechanical sensors. Depending on measurement type, sensors are used to measure strain, stress, temperature, humidity, displacement, motion and so on. Generally, these are operated as point sensors; when connected in a network, they are referred to as distributed sensors. For example, a wireless sensor may be used to measure a physical phenomenon at a node; it is then a point sensor, but is regarded as a distributed sensor when connected in a network. Likewise, optical fibres are used as either point sensors or distributed sensors.

The wide range of sensors developed for civil engineering applications all require access to, or contain, intelligent features to detect problems [39]. It is therefore important to be aware of the existence of the many varieties of sensor and associated technologies for IHM. The following subsections describe the general types of sensors predominantly used in health monitoring systems for civil engineering applications.

Sensors for Displacement and Gap Detection

One of the most common types of sensor used for monitoring bridges, dams and other large civil structures measures relative displacement. Because of the very large scale and geometry changes during the lifecycle of a civil engineering structure, this type of sensor has proved very useful in monitoring them [40]. Traditional displacement measurements typically use linear variable differential transformers (LVDT) or potentiometers connected at two locations on, or at the boundary of, the structure, and measure displacements in structures directly [41]. Figure 2.2 shows a typical LVDT unit and field application of an LVDT for displacement measurement. LVDTs give the position of the object they are mechanically attached to. This is converted into a DC voltage to be read by an appropriate device, and does not require physical connection to the extension in the same way as a potentiometer. The LVDT extension valve shaft (or control rod) moves between primary and secondary windings of a transformer, causing the inductance between the two windings to vary. This is reflected in the output voltage, which is proportional to the position of the valve extension. LVDT-based displacement sensors may be used to measure lateral

and axial deformation when studying the influence of the gap between the steel tube and concrete core of a CFST member on its compressive and flexural behaviour, as shown in Figure 2.3. LVDTs are attractive for measuring displacement for several reasons. They are reliable and robust [32] and are also sensitive to temperature effects [42]. However, the installation of contact-type displacement sensors such as LVDTs requires access to the structure in order to physically connect it to a stationary reference point, which is often difficult or even impossible [43]. Therefore, non-contact displacement sensors have been intensively studied and developed: for example, GPS, laser vibrometer and radar interferometry systems [43]–[50]. GPS sensors are easily installable but have limited measurement accuracy, usually producing errors of 5–10 mm [45], [46]. Non-contact laser vibrometers are generally accurate, but the small measurement range precludes their application for monitoring civil engineering structures, since longer-distance measurement requires a high-intensity laser beam that is dangerous to human health [47], [48]. Interferometric radar systems are capable of high-resolution remote measurement, but require a reflecting surface to be mounted on the structure [49], [50].
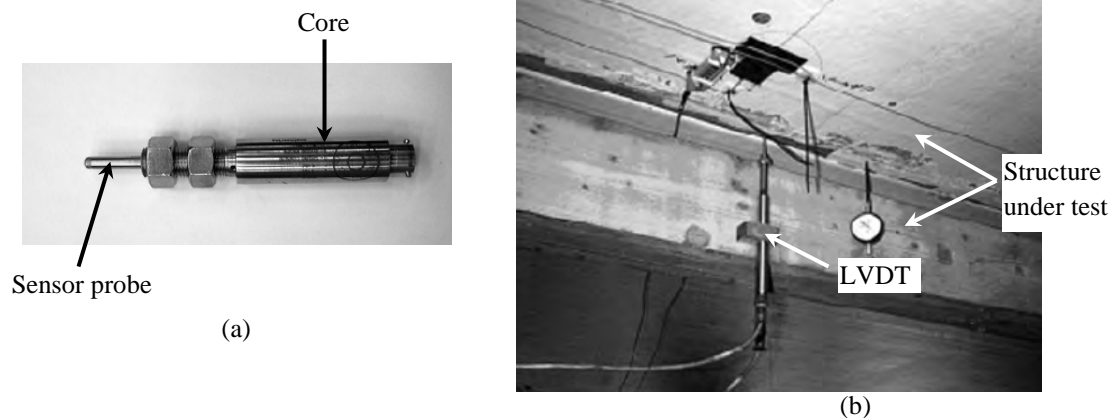
Figure 2.2: (a) Typical LVDT unit; (b) field application for measuring displacement [32].
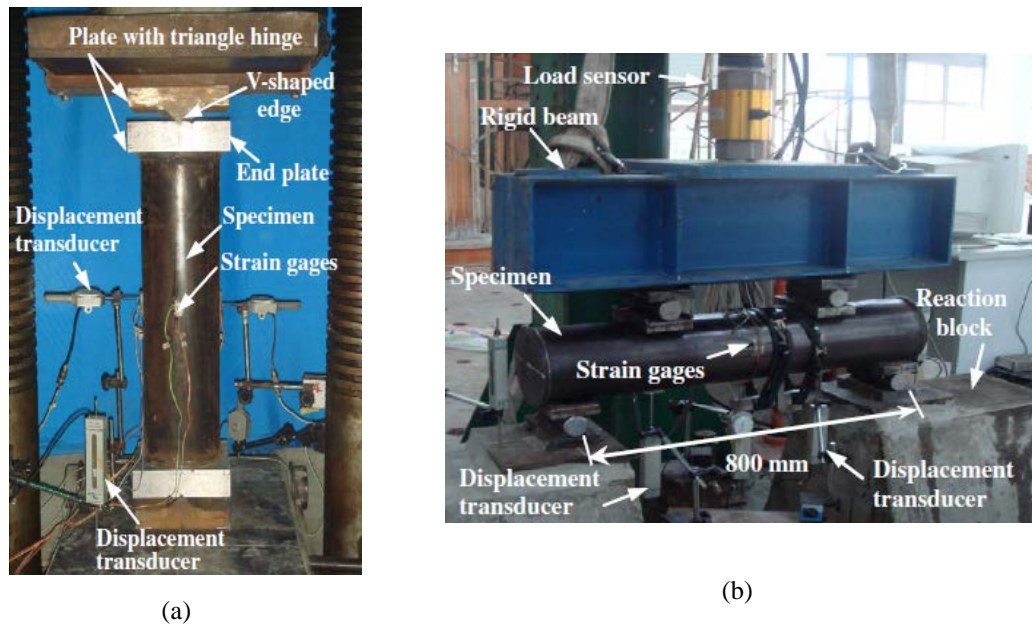
Figure 2.3: Displacement transducers for measuring (a) lateral and axial deformation for short column, and (b) in-plane displacements of a beam [5].

Strain Gauges

Strain gauges are very widely used in civil engineering testing and research to measure structural behaviour under load. Figures 2.4 shows a schematic of a resistive or foil strain gauge and a typical application in measuring the axial and transverse strain for experimental investigation of the effects of debonding in circular CFSTs [6], [51]. These simple sensors are bonded to the structure of interest so that the deformation of the structure also causes the sensor to elongate or contract. Deformations less than approximately 2 per cent cause a change of resistance of the gauge [52], which is typically converted to an absolute voltage using a Wheatstone bridge circuit [53]. Resistive strain gauges are small and consequently have relatively negligible mass loading effects on the structure; therefore, their response is dominated by local effects such as stress concentrations. For large structures this means that strain gauge use should be restricted to monitor 'hot spots' where damage is expected to occur, or on critical components, because large areas require correspondingly large numbers of strain gauges for global monitoring [32], [53]. Resistive strain gauge measurements are also affected by changes in temperature [53], and they may not be suitable for long-term monitoring due to the effect of

electromagnetic interference (EMI) and other problems related to their endurance [54].

(a)

(b)
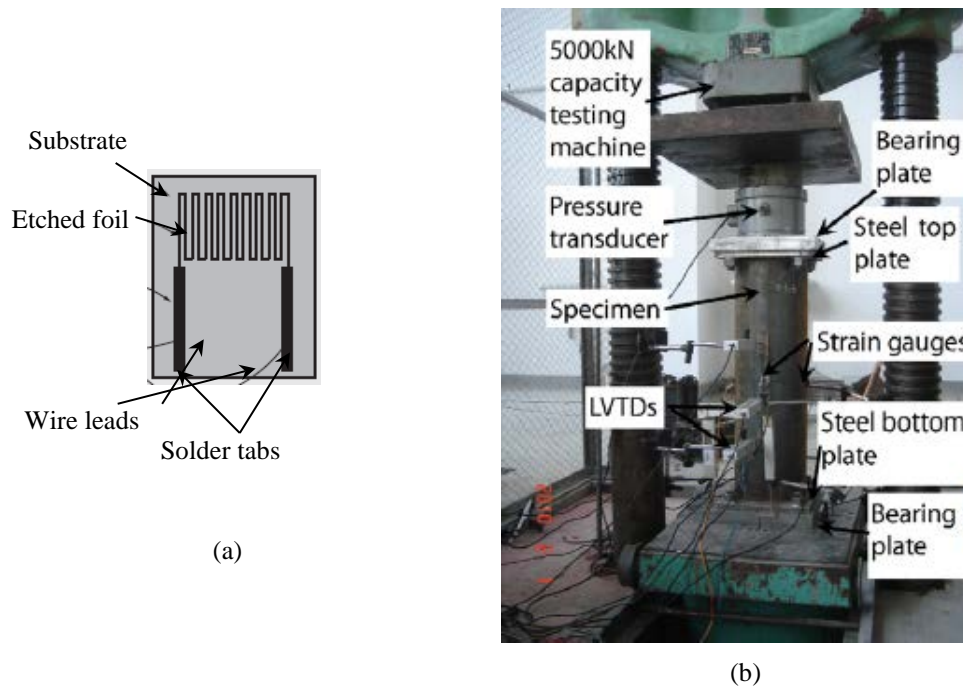
Figure 2.4: (a) Schematic of a foil strain gauge [32]. (b) Strain gauges applied for measuring axial and transverse strains in an axial load test [6].

Vibrating-wire strain gauges are commonly used to measure strains and deformation in large structures, applying the principle that the first mode of natural frequency of vibration, *f*, of a wire fixed at both ends and subjected to tension, is given by

$$f = \frac{1}{2l}\sqrt{\frac{T}{m}},$$ (2.1)

where *l* is the length of the wire; *T* is the tension in the wire; and *m* is its mass per unit length. The fixed ends of the wire are attached at locations of interest on the structure, and the strain along the length of the wire is determined by monitoring changes in its natural frequency [53], [54].

Vibrating-wire strain gauges are generally much larger than resistive strain gauges, typically between 50 and 250 mm long. The gauges themselves may be welded directly to the structure of interest, or they may be embedded in concrete. Their relatively large size is advantageous in that it measures the strain over a

sufficient distance to average out much of the local inhomogeneity inherent in concrete [53]. Figure 2.5 shows typical uses of vibrating-wire strain gauges: on a concrete slab surface, and in a slab prior to pouring concrete.

(a)   (b)
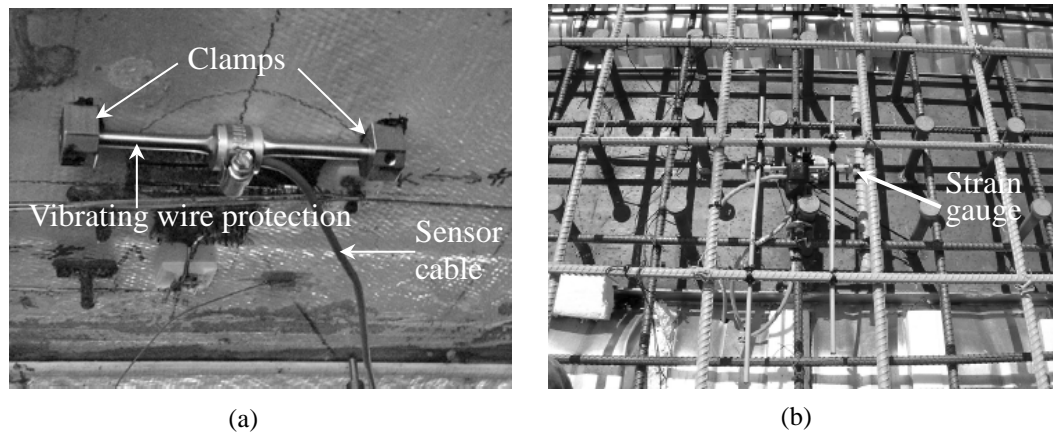
Figure 2.5: Vibrating wire strain gauge: (a) surface mounted, and (b) in slab prior to concrete placement [32].

The development of a vibrating-wire strain gauge for measuring small strains in concrete beams [55] and in a system for monitoring the structural safety of mega-trusses using wireless vibrating wire strain gauges [56] have also been also reported.

Fibre Optic Sensors

Fibre optic sensors use light both for transduction and for signal transmission. They act as transducers by modifying the intensity, fast frequency (wavelength), slow frequency (time-modulated intensity), polarisation, phase and the coherence of the optical signals [30], [57]. Compared to traditional mechanical and electrical sensors, fibre optic sensors have certain distinct advantages: their small size, light weight, immunity to EMI, immunity to corrosion, and embedding capability [57] – [59]; they are employed worldwide for monitoring civil engineering structures. Fibre Bragg grating (FBG)-based fibre optic sensors, intensity-based fibre optic sensors and interference-based fibre optic sensors are among the most commonly used [59]. Figure 2.6 shows the basic cross-section of a fibre optic cable which can be used as a fibre optic sensor. The light passes through a cladded glass or plastic fibre core, which is embedded in an environmentally protective cover.
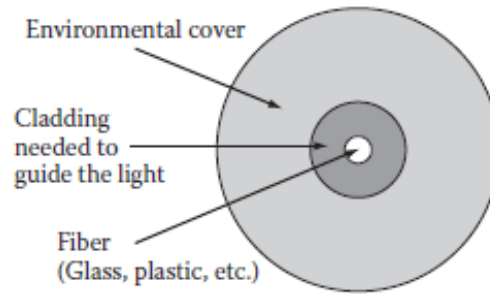
Figure 2.6: Basic cross-section of fibre optic sensor [32].

In the past two decades, a considerable number of investigations have been conducted in reviewing the progress of research and development of fibre optic sensing technology and its applications for the monitoring of various kinds of engineering structures [60]–[64]. López-Higuera et al. [65] summarised the main types of fibre optic techniques suitable for structural monitoring and for various fibre optic sensor-based engineering scenarios. Strain monitoring of concrete structures using fibre optic sensors has been reported in [66], [67]. An FBG-based system with embedded displacement and strain transducers were developed for long-term monitoring of structural performance was applied to a concrete bridge [68]. Barbosa et al. [69] developed a novel weldable FBG sensing system for strain and temperature monitoring of steel bridges and for loading tests and health monitoring of a circular steel pedestrian bridge.
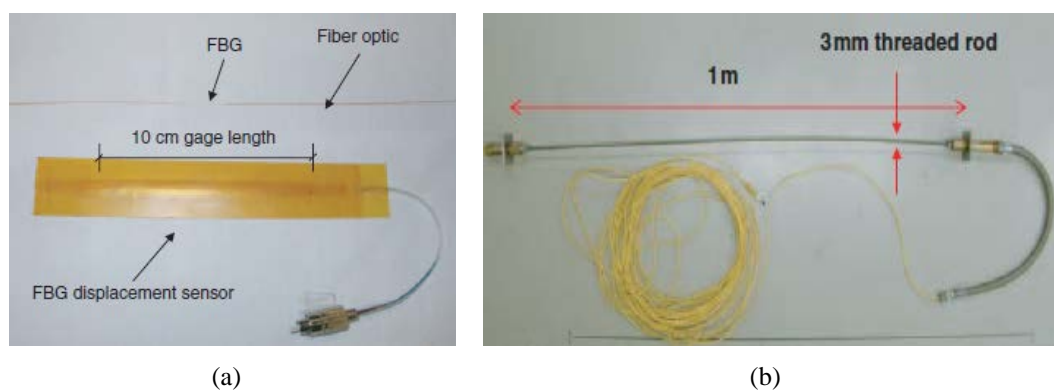
Figure 2.7: (a) Fibre optic displacement sensor, and (b) long gauge sensor for embedment in concrete bridge decks [61].

Bastianini et al. [70] utilised embedded fibre optic Brillouin sensors for strain monitoring and crack detection in a historical building. An investigation was carried out by Li et al. [71] on the feasibility of the FBG-based monitoring instrumentation in an 18-storey building during construction. The sensors were used to monitor the strain and temperature of the building at three stages of construction: before concrete pouring, during pouring and curing of concrete, and during the construction of subsequent upper storeys. A fibre optic sensory system has also been used for assessing the health of pipelines subjected to earthquake-induced ground movement [72], and for safety monitoring during railway tunnel construction [73].

(a)   (b)

Figure 2.8: (a) Two rebars in a first-storey horizontal beam bonded with FBG sensors; (b) the lower parts of two rebars in a vertical underground column bonded with FBG sensors [71].

Smart Aggregates: Multifunctional Sensors

Recently developed smart aggregates are formed by embedding a waterproof piezoelectric patch with lead wires into a small concrete block. The proposed smart aggregates are multi-functional, performing three major tasks: early-age concrete strength monitoring, and impact detection for crack and structural health monitoring [74]. Piezoelectric transducers are very fragile and easily damaged by the vibrator during the pouring of concrete structures. To protect it, the piezoelectric patch is first coated with an insulating material to prevent water and moisture damage then embedded, as shown in Figure 2.9. The proposed smart aggregates can then be embedded at the desired locations in the larger concrete structure before pouring. The smart aggregate-based active sensing system shown in Figure 2.9b was developed for

monitoring the health of large-scale concrete structures [74]; the piezoelectric transducer in one smart aggregate is used as an actuator to send excitation signals. The piezoelectric transducers in the other smart aggregates act as sensors. The crack or damage inside the concrete structure acts as stress relief in the wave propagation path. The amplitude of the wave and the transmission energy decrease when a crack is present. The magnitude of the drop in transmission energy is then correlated with the extent of the internal damage.
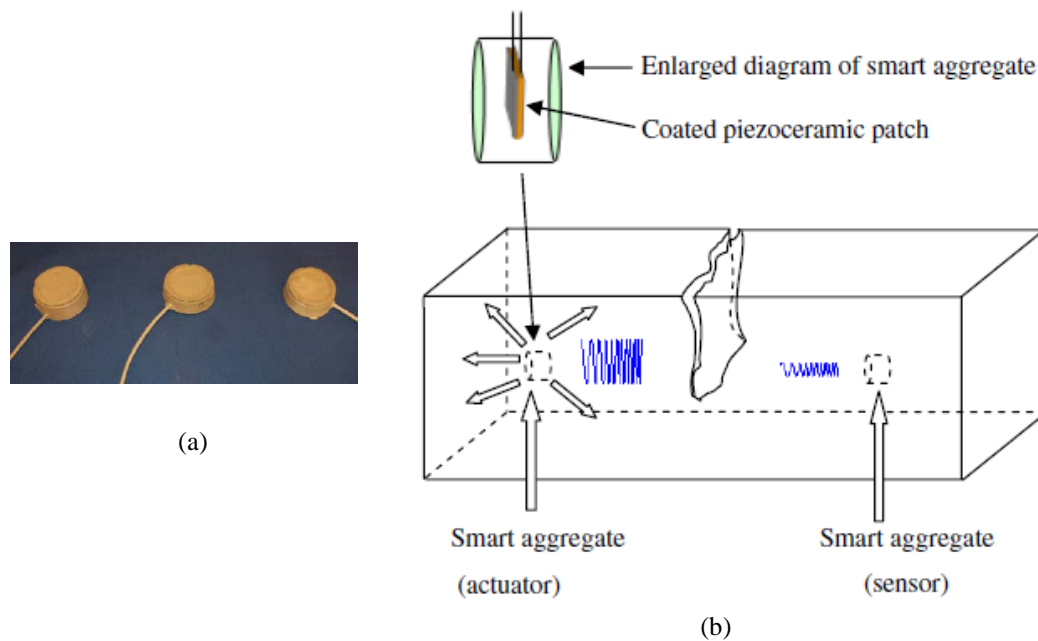
Figure 2.9: (a) Three fabricated smart aggregates, and (b) block diagram of a piezoelectric-based active sensing system [74].

An investigation of water-presence detection in a concrete crack using smart aggregates was conducted by Kong et al. [75]. The use of a piezoceramic-based smart aggregate was successfully applied to the health monitoring of concrete structures under both static loading [76], [77] and seismic excitation [78], [79]. In those studies, a number of smart aggregates were embedded in concrete structures whose health state was evaluated by monitoring the signals recorded by the smart aggregates. Combined smart aggregates and piezoceramic patches for health monitoring of concrete structures have been reported, in which the smart aggregate embedded in a concrete beam acted as actuator (or transmitter) and piezoceramic patches attached to the surface of the concrete beam acted as sensors [80].

MEMS sensors

Micro-electromechanical system (MEMS) sensors are claimed as the smallest functional machines currently engineered by humans [81]. Development of micro machines began as early as the 1970s but, since 1995, there has been significant progress due to the variety of new materials and bulk micromachining processes, which has led to new MEMS applications [82]. A MEMS is a collection of microsensors and actuators which both sense their environment and have the ability to react to changes in that environment by the use of microcircuit control [83]. They include, in addition to the conventional microelectronics packaging, integrating antenna structures for command signals into micro-electromechanical structures for the sensing and actuating functions. MEMS combine the signal processing and computational capability of analogue and digital integrated circuits with a wide variety of non-electrical elements (e.g., pressure, temperature, chemical, stress/strain and acceleration). MEMS sensing technology brings three advantages to its applications to civil infrastructure: miniaturisation, multiple components and microelectronics [83]. A typical MEMS chip is shown in Figure 2.10a; Figure 2.10b shows a packaged MEMS sensor.

MEMS have been developed for many areas, including in the medical and automotive industries [84]. Furthermore, a number of research projects have explored the application of MEMS technology to help enhance structural health monitoring practices in civil engineering (e.g., smart pebbles, a pavement strain-monitoring system, a roadway ice-detection system, etc.) [85]. By incorporating MEMS sensor technology into highway infrastructure, there are potential benefits that include improved system reliability, improved longevity and enhanced system performance, improved safety against natural hazards, and lower lifetime costs in both operation and maintenance [86]. Temperature and moisture monitoring in concrete structures using embedded MEMS sensor have also been reported [83].
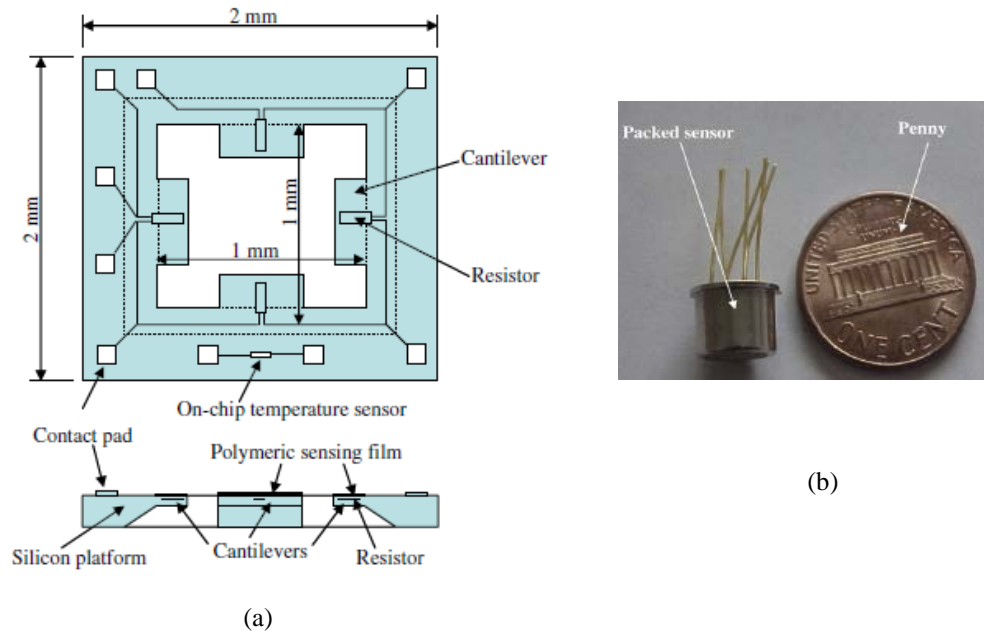
Figure 2.10: (a) MEMS chip; (b) packaged MEMS sensor [83].

2.4 Microwave sensors and their applications

Presently existing standard sensors used in civil infrastructure, such as strain gauges and displacement sensors, may not always be capable of sensing the behaviour of critical parts of the infrastructure. For instance, strain is one of the most important physical parameters that provide information about loading, boundary, fatigue and material conditions. Traditional strain gauges are reliable, practical and inexpensive; however, they require a wired physical connection and this is not suitable for structural health monitoring of large-scale civil infrastructure systems. Instead, microwave sensor technology may provide wireless strain sensor networks. Moreover, microwave sensors and techniques offer advantages such as non-contact, one-sided inspection capability and the ability to penetrate into dielectric materials and interact with their internal structure. In this section, some microwave sensors and the common applications of existing microwave sensors in civil engineering structures will be presented.

2.4.1 Microwave Displacement and Strain Sensors

A quarter-wavelength microwave resonator sensor has been proposed for displacement measurement [92]. The resonator consists of an empty rectangular

waveguide section, a metal plate and a dielectric slab inserted into the waveguide midway along its wall, as shown in Figure 2.11. The resonator is terminated by a movable metal plate with a displacement d (Figure 2.11b) and connected to a measurement device such as a reflectometer through a waveguide-coaxial line connector and an antenna (not shown here). The magnitude and phase of the reflection coefficient is measured and interpreted as the response of the sensor to wall displacement. The dielectric slab, which has specific dimensions and shapes for particular applications, tends to concentrate the electromagnetic fields in it, thereby improving the sensitivity of this approach. It has been shown that the resonant frequency of this type of resonator is some 10 times more sensitive to plate displacement than the resonant frequency of a conventional half-wavelength resonator [93]. For instance, Figure 2.12 shows the resonant response of the proposed and the half-wavelength resonator.
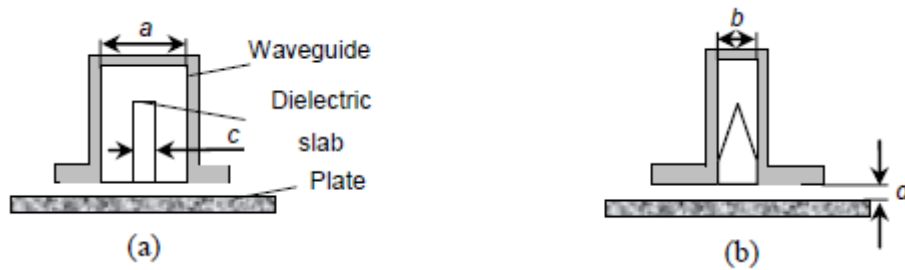
Figure 2.11: Schematic cross-section of the dielectric-slab-loaded waveguide resonator with a movable metal plate: (a) top view; (b) side view (not to scale) [92].
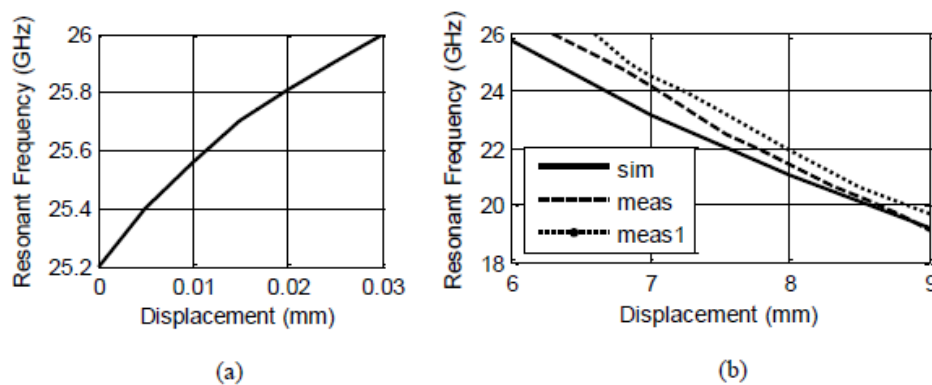
Figure 2.12: Resonant frequency vs. plate displacement for (a) the proposed resonant sensor, and (b) a half-wavelength resonator [92].

The resonant response behaviour of the resonator to wall displacement is different from that due to increasing the length of the half-wavelength resonator, which causes decreasing resonant frequency as shown in Figure 2.12a. In addition, the average sensitivity is estimated from Figure 2.12 to be about 27 GHz/mm for the proposed resonator and about 2.5 GHz/mm for the half-wavelength resonator. The simulated results of this investigation were verified by the measured results. The proposed resonator can be used to construct efficient sensors for non-destructive evaluation of metal surfaces and measurements of their displacements. The development of microwave displacement sensors for hydraulic devices has been also reported [94].

Microwave strain measurement sensors exploit the strain-dependent behaviour of the electromagnetic waves in the microwave components of the sensing mechanism. The basic concept is that when the microwave component (e.g., antenna and resonator) is subjected to strain or deformation, its resonant frequency changes accordingly. For example, a radio frequency cavity sensor using a 25.4 mm diameter copper tube 90 mm long with end plates as the strain or displacement sensing element [95] is shown in Figure 2.13a. A rectangular microwave patch antenna (Figure 2.13b) has been designed, fabricated and validated for strain measurement [96]. Furthermore, Daliri et al. [97] used a circular micro-strip patch antenna (Figure 2.13c) for structural health monitoring.

| (a) | (b) | (c) |
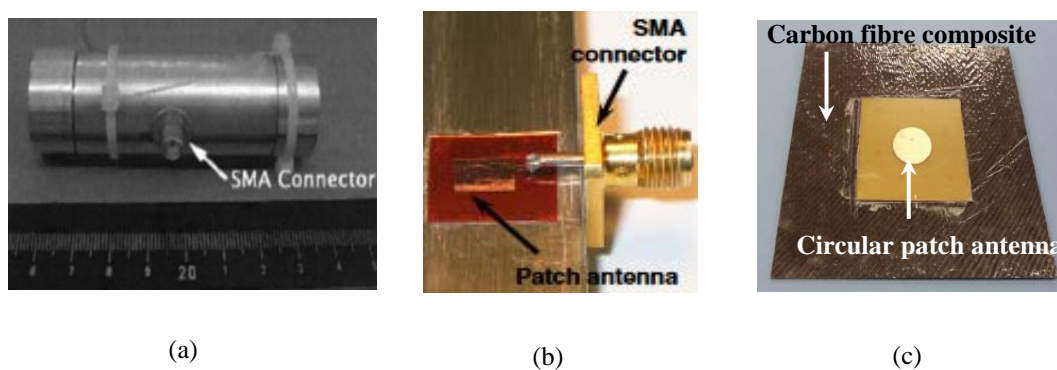
Figure 2.13: Microwave strain measurement sensors: (a) resonant cavity sensor [95]; (b) rectangular patch antenna sensor with width-direction elongation [96]; and (c) a circular micro-strip patch antenna sensor attached to carbon fibre composite material [97].

2.4.2   Monitoring of Cure-State of Concrete

Concrete is one of the most commonly used materials in the construction industry around the world. Being a heterogeneous mixture of cement, water, fine aggregate, coarse aggregate and air, the quality of cement concrete is highly dependent on its composition [98]–[100]. For example, the water/cement ratio (w/c) strongly influences the microstructure of the paste and hence its mechanical properties, including its compressive strength and durability [99]. Therefore, quick and efficient determination of the cure-state and water/cement ratio is an important issue. At present there is no reliable and accurate technique that can perform this task [101], although the piezoelectric-based transducer technique has been used to monitor very early-age concrete hydration [102] and to measure early-age compressive strength [103]. Recently, cure-state monitoring of concrete and mortar specimens using smart aggregates has also been proposed [104]. However, all such techniques require very careful embedding of the piezoelectric patches before casting, which is both difficult and time-consuming.

On the other hand, the microwave near-field sensing technique has been shown to have great potential as a direct and non-invasive approach for concrete cure-state determination [105]–[108]. Open-ended rectangular waveguides have been used as the microwave sensor in conjunction with a performance network analyser (PNA) in monitoring early-age concrete samples. This near-field technique is mainly based on the microwave reflection and transmission properties of cement-based materials [109]. Microwave sensing is easy, quick and applicable for monitoring large-scale in-situ concrete, and is useful for characterising the material composition of cement-based materials [110]–[113] and hence for quality control of the concrete mixture in its early stages of curing. Evaluation of the compressive strength of cement-based materials has also been investigated [114]–[116] using this near-field sensing technique. The use of a microwave coaxial probe as sensor has also been reported for cement-based material characterisation and compressive strength evaluation [117]–[119].

Another important advantage of using microwave techniques for monitoring the concrete cure-state, or for concrete quality assessment in the curing period, for characterising concrete and for compressive strength evaluation is that they are direct

and non-destructive [120]–[123]. For example, in standard methods of determining the strength of concrete, a concrete cylinder of the same material as the structure is loaded to failure in a testing machine. Such methods give only indirect information about the structure or specimen; they are also time-consuming and involve extra budgets. Sometimes several nondestructive methods are combined to ensure reliable results [124], [125]. A free-space, far-field microwave non-destructive technique for cement-based materials has also been reported [126].

2.4.3   Estimation of the Dielectric Permittivity of Concrete

Precise permittivity determination of dielectric materials is a very important task for the ever-increasing numbers of microwave and millimetre-wave applications [127]. For example, knowledge of the dielectric properties of building materials such as concrete, mortar, brick wall, plywood or gypsum is essential for non-destructive investigations of materials and for structural assessment, and also in studies of radio signal propagation in both indoor and outdoor environments [128]. Several experimental methods have been used to measure the dielectric properties of a material: the parallel plate capacitor technique [129], the resonator technique [130], [131], the transmission line technique [11], [132]–[136] and the free-space technique [137]–[141].

In the parallel plate capacitor technique, the dielectric permittivity is measured using a perfect capacitor model, and is thus more applicable for a laboratory study than for in-situ material characterisation [129]. The resonator cavity technique employs closed- and open-cavity configurations in which resonant EM responses are measured from the material as a basis for determining the real and imaginary part of complex permittivity. This method provides more accurate results than the parallel plate capacitor method, but it obtains results for only one frequency at a time [130].

Although there are different approaches in transmission-line techniques, including a large coaxial closed cell for dielectric permittivity measurement of concrete specimens containing aggregates up to 30 mm [142], the open-ended coaxial probe [11], [136], [143] and/or a rectangular waveguide probe [144]–[151] is the simplest, most robust and most promising approach for dielectric characterisation of cement-based materials, especially in construction site conditions. The EM fields

at the end of the probe change depending on the interaction with the material being tested, and its dielectric permittivity is computed from the measured reflection coefficient. The numerical calculation of the reflection coefficient of a rectangular waveguide radiating into a dielectric half-space and determination of the dielectric constant of the half-space from its measured reflection coefficient have been investigated [147], [148]. This method is easy, quick and non-destructive, although inaccurate measurements may occur due to the presence of an air gap between the sensor and the specimen, and due to the size of the specimen [133]. The free-space technique usually uses a horn antenna and radar as the sensor; at higher frequencies, multiple reflections pose potential difficulties in estimating the dielectric permittivity [137].

The combined use of the open-ended rectangular waveguide technique and the embedded modulated scattering technique has been investigated for determining the dielectric properties of sand [149]–[151]. The measurements of the complex permittivity of mortar and materials such as wood and polyvinyl siloxane (PVS) rubber using a coplanar waveguide [152] and a complementary split ring resonator [153], respectively, have also been reported. In addition, the microwave characterisation of layered structures and dielectric sheets using waveguide measurements [154]–[157] and computationally intelligent sensor systems [158], respectively, have been investigated. It was found in the referenced articles that, of the reports on saturated cement-based materials, few used early-aged concrete [11], [100], [136], [142], and only one [11] used wet or fresh concrete. Therefore, there is a lack of available information on the dielectric properties of fresh and early-aged concrete, which is essential for non-destructive assessment of concrete-based structures.

Table 2.1: Cement-based materials reported for determination of complex dielectric permittivity

Materials	Age conditions	References
Cement	Early age	[105]
Cement	Saturated or natural dry	[118], [160]
Concrete	Wet/fresh	[11]

Concrete	Early age	[14], [100] [136], [142]
Concrete	Saturated or natural dry	[11], [18], [128], [129], [138], [140], [141], [160]

2.4.4 Detection of Cracks and Corrosion in Concrete

Detection and characterisation of cracks in cement-based materials is an integral part of damage evaluation for health monitoring of civil structures. Novel coaxial cable sensors that feature high sensitivity and high spatial resolution have been developed for health monitoring of concrete structures using a time-domain reflectometry (TDR) [159]. The new sensor was designed based on the topology change of its outer conductor, which was fabricated as a tightly wrapped commercial tin-plated steel spiral covered with solder. The cracks that developed in concrete structures lead to out-of-contact local steel spirals. This topology change results in a large impedance discontinuity that can be measured by TDR. The utility of open-ended rectangular waveguide probes for detecting surface-breaking cracks in cement-based materials has also been reported [17]. The evaluation of reinforced-bar corrosion in concrete has been explored using microwave coaxial and waveguide transmission-line methods [160]. The detection of rust [160] and corrosion precursor pitting [161] under paint, and shallow flaws in metal using a near-field open-ended waveguide has been reported [162]. A microwave tomographic imaging technique has been developed for the detection of damage inside concrete structures [164]. The formation of cracks in glass particles was monitored by the application of linearly polarised microwaves [165]. The assessment of the structural integrity of fibre-reinforced polymer-strengthened concrete structures has been experimentally investigated using a non-invasive microwave technique [166], [167]. Other non-destructive testing methods for crack assessment and damage detection in concrete structures have also been recorded [168], [169].

2.5   Detection and Monitoring of Debonding and Gaps in Concrete–Metal Structures

Concrete–metal composite structures have been widely used in infrastructure engineering. Steel bar-reinforced concrete and concrete-filled steel tubes used in civil and marine structures are examples. It has been shown that imperfections in concrete from incorrect manufacturing process and/or natural shrinking of the concrete may lead to a debonding gap between the metal and concrete surfaces in CFSTs or in reinforced concrete, which reduces the compressive and flexural behaviour of structural members [170]–[171], [3]–[6]. Therefore, the presence of possible gaps or disbonding should be detected as early as possible to avoid premature failure of structures.

2.5.1   Debonding and Gaps in Concrete–Metal Structures

In CFST structures, two types of gaps have been reported [170], namely circumferential gap and spherical-cap gap, as shown in Figure 2.14. Circumferential gap caused by the concrete shrinkage in the radial direction usually appears in a vertical CFST member. The different expansion of the outer steel tube and the concrete due to temperature difference is another possible cause of circumferential gap formation. On the other hand, spherical-cap gaps are more likely to occur in a horizontal CFST member, as in CFST arch bridges and CFST truss structures. This type of gap mainly originates during the construction process [170], in which the hollow steel tubular arch or truss is usually erected and closed first, and then it is filled with concrete by means of pumping. In this case, the possible presence of residual air combined with the effect of concrete settlement, may lead to the spherical-cap gap existing at the top segment of concrete section, as shown in Figure 2.14b. Figure 2.14c shows an example of an actual circumferential debonding gap in a circular CFST.

Compared with the thickness of the debonding area shown in Figure 2.14a and b, it is obvious that the circumferential gap is small but uniform. It has been reported that a common value of debonding thickness is 0.5–3.0 mm [171]; if the debonding gap exceeds 3.0 mm, retrofitting work needs to be done. It is also pointed out that this kind of debonding is almost impossible to avoid.
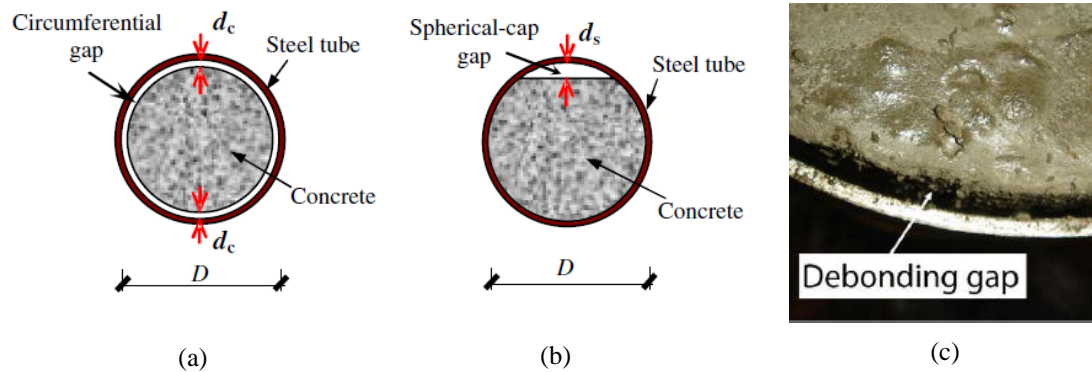
Figure 2.14: Gaps in CFST: schematics of (a) circumferential gap; (b) spherical cap gap; and (c) photograph of a circumferential debonding gap [170], [171].

2.5.2 Sensory Technique for Detecting and Monitoring of Debonding and Gaps

A few nondestructive techniques, including sonic, ultrasonic, acoustic emission and guided wave techniques have been used for inspecting distressed areas and inside voids in concrete-filled steel pipes [172]; however, most of these techniques require access to both ends of the steel pipe or tube, which is not practical for an installed CFST. Relatively new methods, such as piezoelectric techniques using wavelet packet analysis [9], [173]–[174], have also been investigated for detecting and monitoring debonding between the steel and concrete surfaces in CFST. For this purpose, three lead zirconate titanate (PZT)-based smart aggregates were positioned at different heights in a rectangular CFST column (Figure 2.15), and steel/concrete debonding was created artificially by adhering styrofoam plates to the inner surface of the steel tube. Experiments showed that a debonding thickness of 4 mm was detectable using this technique [173]; however, this is larger than the most commonly found width of circumferential debonding gaps. Also, the fragility of PZT requires special handling and treatment to ensure that it survives in the concrete and functions as designed. Therefore, further research is required for measuring debonding gaps in the 0.5–3.0 mm range [173].
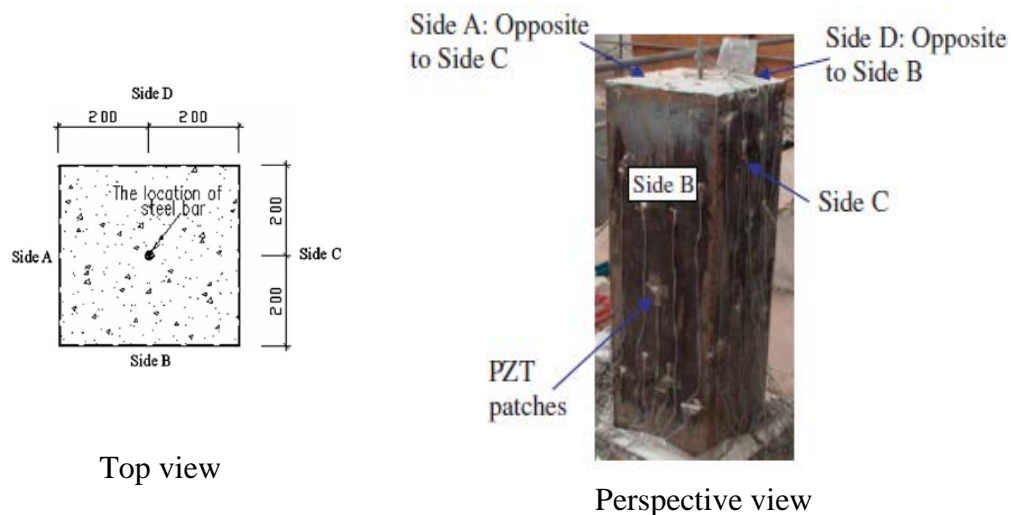
Figure 2.15: CFST specimen with embedded smart aggregates and PZT patches for debonding detection [173].

2.5.3 Microwave Sensors

Microwave techniques have been applied to detect disbonds in dielectric layered materials [175]–[177] using an open-ended rectangular waveguide probe, taking advantage of the properties of microwave signals, such as penetration into dielectric materials and interaction with flaws in the materials [175]–[176]. Microwave near-field detection and characterisation of disbonds in concrete structures using fuzzy logic techniques has also been reported [178]. However, microwave signals do not penetrate metal, posing practical challenges to the use of microwave techniques for detecting gaps between metal and concrete, especially in CFST structures. To overcome this limitation, a novel microwave sensor technique has been proposed for measuring and monitoring gaps in concrete–metal structures [179]. The technique explores a simple microwave single open-ended waveguide sensor embedded in the metal wall of a CFST [179]. Preliminary investigations into the feasibility of this technique for the detection and monitoring of gaps between concrete and steel surfaces have revealed promising results. However, knowledge of the electromagnetic properties of the concrete in the vicinity of the measurement area at different stages of its life, to increase the sensitivity of measurement and expand the area of the interface being inspected, are the main challenges of practical implementation of this technique.

2.6 Summary of Research Gaps

Infrastructure health monitoring is becoming compulsory for all civil structures, mainly for safety and economic reasons; therefore, there are high demands for advanced sensory techniques. This literature review has indicated that microwave sensors have great advantages and potential for material characterisation and quality assessment of cement-based materials, and for monitoring critical parts of infrastructure such as a concrete-filled steel tube. Compared to conventional sensors such as displacement devices, strain gauges and fibre optic sensors, microwave sensors are non-contact, remote, one-sided, wireless, and most of them give easy and quick sensing data for in-situ conditions. Another important advantage of microwave sensor technology is that there are various microwave techniques that can be optimised for particular applications.

However, there are research gaps that should be filled for the application of such sensors in practice. The literature review has shown that there are currently no reliable microwave sensors for fresh and early-age concrete characterisation, which is highly essential for the initial quality assessment of concrete and associated structures, as well as for the detection and monitoring of debonding between concrete and metal surfaces.

The available data for the dielectric properties of concrete at different stages of its life starting from fresh to dry is limited. In particular, the lack of such data in the vicinity of the sensing area is very critical, since it is required for the modelling and simulation to be used for the development and optimisation of microwave sensors. Increasing the sensitivity of the sensors to debonding and small gaps, while decreasing their sensitivity to changes of environmental conditions, including changes in the concrete itself, are also important and challenging tasks. The physical protection of recently proposed microwave sensors from penetration of water and concrete obstacles in the sensing area, as well as increasing the dimensions of this area, require a mechanical solution. These are also electromagnetic problems, since the concrete core of the CFST is itself part of the sensor system.

Overall, the literature review has shown that further advanced sensory techniques and methods for IHM of concrete-metal composites are required.

Chapter 3

Determination of Dielectric Permittivity of Early-Age Concrete Specimens

3.1   Introduction

In this chapter, the dielectric properties of early-age concrete specimens will be determined using measured data and simulation results obtained using a microwave single waveguide sensor (SWS) attached to concrete specimens. Motivation for this research is based on the lack of information on the dielectric properties of early-age concrete in the vicinity of a metal–concrete interface. The sensor is based on an open-ended rectangular waveguide probe which has been widely used for nondestructive testing and evaluation of different materials [121]. This chapter describes, for the first time, the complex dielectric permittivity of early-age concrete specimens determined using a full computational model that includes the open-ended SWS and a concrete specimen as a part of the sensor. For this purpose, an algorithm is developed to determine the dielectric permittivity of concrete material from the measured magnitude of the reflection coefficient and simulated results using CST Microwave Studio software. An analysis of the sensitivity of the reflection properties of the metal–concrete specimen to changes in the waveguide aperture–specimen arrangement is also provided.

3.2   Background: Microwave Properties of Concrete and Open-Ended Waveguide Probe

Every material has a unique set of electromagnetic (EM) properties affecting the way in which it interacts with EM electrical and magnetic fields. A dielectric material can be characterized essentially by two independent electro-magnetic properties: the complex permittivity, ε, and the complex permeability, μ. In general, four independent measurements are necessary to establish the magnitudes of both the real and imaginary parts of ε and μ. However, most of the common dielectric materials, including concrete, are nonmagnetic, making the permeability μ very

similar in magnitude to the permeability of free space. Thus, the focus of this section is on the complex permittivity, ε, defined by [87] as:

$$\varepsilon = \varepsilon' - j\,\varepsilon'',\tag{3.1}$$

where ε' is the real part of the complex permittivity, and ε'' is the imaginary part. Dividing Eq. (3.1) by the permittivity in free space, ε_0, the property becomes dimensionless and relative to the permittivity of free space:

$$\frac{\varepsilon}{\varepsilon_0} = \frac{\varepsilon'}{\varepsilon_0} - j\frac{\varepsilon''}{\varepsilon_0},\tag{3.2}$$

$$\varepsilon_r = \varepsilon_r' - j\varepsilon_r'',\tag{3.3}$$

where ε_r is the relative complex permittivity, ε_r' is the real part of the relative complex permittivity, or dielectric constant; ε_r'' is the imaginary part of the relative complex permittivity, or loss factor; and ε_0 is the permittivity in free space (a lossless medium) = 8.854×10^{-12} F/m. In conductive materials such as fresh and early-age concrete, the loss factor is the effective loss factor $\varepsilon_{r_{eff}}''$ given by [180], [181]

$$\varepsilon_{r_{eff}}'' = \varepsilon_r'' + j\frac{\sigma}{\omega\varepsilon_0},\tag{3.4}$$

where σ is the conductivity; $\omega = 2\pi f$; and f is the frequency.

The dielectric constant, ε_r', is a measure of how much energy from an external electric field is stored in a material; $\varepsilon_r' > 1$ for most solids and liquids. The imaginary part of the relative complex permittivity ε_r'' is a measure of how dissipative or lossy a material is to an external electric field and is referred to as the relative loss factor, or simply the loss factor. The loss factor ε_r'' is always > 0 and is usually much smaller than ε_r' for dielectric materials.

The ratio of the energy lost to the energy stored in a material is known as the loss tangent, $tan\,\delta$, defined as:

$$tan\,\delta = \frac{\varepsilon''}{\varepsilon'} = \frac{\varepsilon_r''}{\varepsilon_r'},\tag{3.5}$$

or

$$tan\,\delta = \frac{\varepsilon''_{r_{eff}}}{\varepsilon'_r}\;. \tag{3.6}$$

3.2.1 Plane Wave Method

Let us consider an incident EM plane wave from free space normal to a half-space of an arbitrary material [87]. The geometry is shown as a schematic in Figure 3.1, in which the material half-space at z > 0 is defined by the complex permittivity ε and the complex permeability μ.

We assume that the incident plane wave has an electric field vector oriented along the x-axis and is propagating along the positive z-axis. The incident fields can then be written, for $z < 0$, as

$$\overline{E_\iota} = \hat{x}E_0 e^{-jk_0 z}, \tag{3.7}$$

$$\overline{H_\iota} = \hat{y}\frac{1}{\eta_0}E_0 e^{-jk_0 z}, \tag{3.8}$$

where η_0 is the impedance of free-space and E_0 is an arbitrary amplitude. Also in the region $z < 0$, a reflected wave may exist with the form

$$\overline{E_r} = \hat{x}\Gamma E_0 e^{+jk_0 z}, \tag{3.9}$$

$$\overline{H_r} = \hat{y}\frac{\Gamma}{\eta_0}E_0 e^{+jk_0 z}, \tag{3.10}$$

where Γ is the unknown reflection coefficient of the reflected electric field. In Equations (3.9) and (3.10), the sign in the exponential terms has been chosen as positive, to represent waves travelling in the $-\hat{z}$ direction of propagation.

Similarly, the transmitted field for $z > 0$ in the lossy medium is written as

$$\overline{E_t} = \hat{x}T E_0 e^{-\gamma z}, \tag{3.11}$$

$$\overline{H_t} = \frac{\hat{y}T E_0}{\eta} e^{-\gamma z}, \tag{3.12}$$

where T is the transmission coefficient of the transmitted electric field, and η is the intrinsic complex impedance of the lossy medium in the region $z > 0$, defined as

$$\eta = \frac{j\omega\mu}{\gamma}, \tag{3.13}$$

and the propagation constant $\gamma = \alpha + j\beta$

$$= j\omega\sqrt{\mu\varepsilon}\sqrt{1 - j\sigma/\omega\varepsilon}. \tag{3.14}$$

The two unknown constants Γ and T are found by applying boundary conditions for E_x and H_y at $z = 0$. Since these tangential components must be continuous at $z = 0$, we arrive at

$$1 + \Gamma = T, \tag{3.15}$$

$$\frac{1 - \Gamma}{\eta_0} = \frac{T}{\eta}. \tag{3.16}$$

Solving Eqs. (15) and (16) for the reflection and transmission coefficients gives

$$\Gamma = \frac{\eta - \eta_0}{\eta + \eta_0}, \tag{3.17}$$

$$T = 1 + \Gamma$$

$$= \frac{2\eta}{\eta + \eta_0}. \tag{3.18}$$

An approximate value of the complex dielectric permittivity of a material under test conditions can be determined using the measured Γ and/or T values; however, application of this method is limited by the requirement for a relatively large specimen with a plane surface, and the sensitivity to reflected EM waves from the edges of the specimen and from components of the parts of measurement setup, walls, etc. must be taken into account.

3.2.2 Open-Ended Waveguide Method

Dielectric property measurement using open-ended rectangular waveguides has received significant attention from both the modelling and experimental points of view. These works have primarily been focused on the inspection of infinite half spaces or multilayered structures [148], [154]. Figure 3.1b is a schematic of a waveguide aperture radiating into a half-space of an arbitrary material. In this case, errors may occur due to higher-order modes, which have been ignored in many published reports which take into account only the influence of the dominant mode. This results in errors when the model is used to determine the complex permittivity

of materials. Another issue is radiation of EM waves in free space when a waveguide with a finite flange is used. Overall, higher-order modes and radiation in free space are critical issues for the analytical determination of the complex dielectric permittivity of material using this method. In this chapter, a modified waveguide method will be developed using measurement of the reflection coefficient as the *S*-parameter and a full formulation computation.
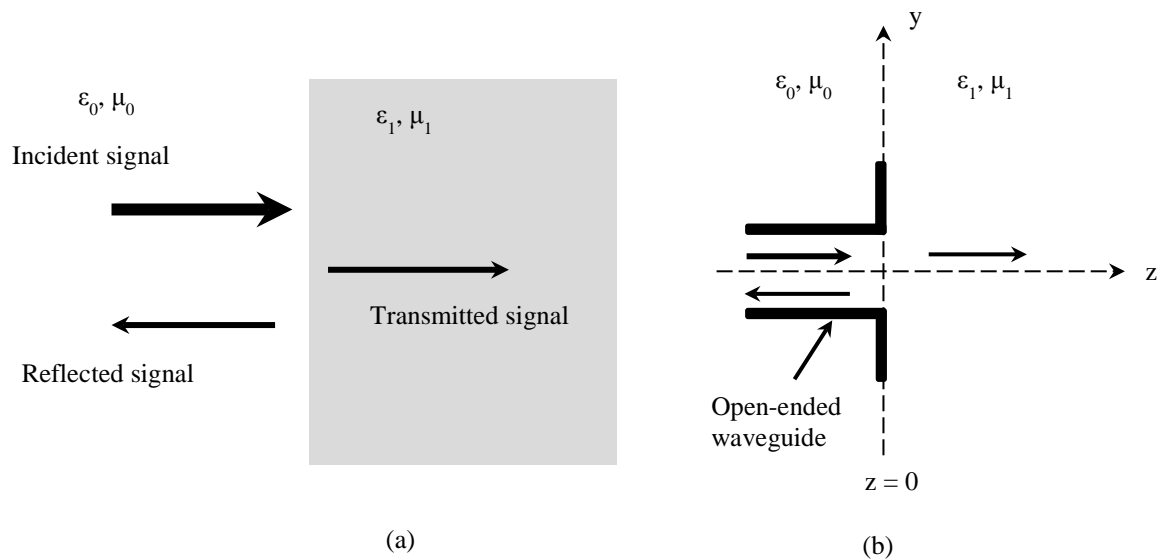
Figure 3.1: Schematic of (a) plane wave reflection from, and transmission in, an arbitrary medium (normal incidence); and (b) an open-ended waveguide aperture radiating microwave signals in a half-space of an arbitrary medium.

3.3 Determination of Dielectric Permittivity of Concrete Specimens

In this investigation, the dielectric permittivity of a concrete specimen was determined using the measured reflection coefficient and an algorithm developed here for an open-ended single waveguide sensor at R-band (1.7 GHz – 2.6 GHz) and X-band (8.2 GHz – 12.4 GHz). A model of the sensor-specimen was created using CST Microwave Studio software. In the model, concrete is characterized by its dielectric constant and loss tangent.

3.3.1   Development of an Algorithm for Determining Dielectric Permittivity

To determine the complex dielectric permittivity of early-age concrete using the measured magnitude of the reflection coefficient, an algorithm was developed as shown in Figure 3.2. First, the magnitudes of reflection coefficient $|S|_m$ of a concrete specimen are measured at different locations on the specimen surface and the results are averaged. Then a model of a single waveguide sensor (R-band or X-band) and concrete specimen is constructed to simulate the magnitude of the reflection coefficient $|S|_S$ with a guessed value of the complex dielectric permittivity, and it is compared with $|S|_m$. If the difference between the simulated and measured reflection coefficient magnitudes is zero (i.e., $|S|_S - |S|_m = 0$), or lies within a predefined accuracy level, then the guessed value is the estimated complex dielectric permittivity of the concrete being tested. If the difference is not within the predefined accuracy level, then another value of the complex dielectric permittivity is guessed and new simulated reflection coefficient is compared with the measured value of $|S|_m$. This process continues until the difference between the measured and simulated magnitudes of the reflection coefficient is within the accuracy level, and the final guessed value is accepted as the determined complex dielectric permittivity of the concrete specimen.
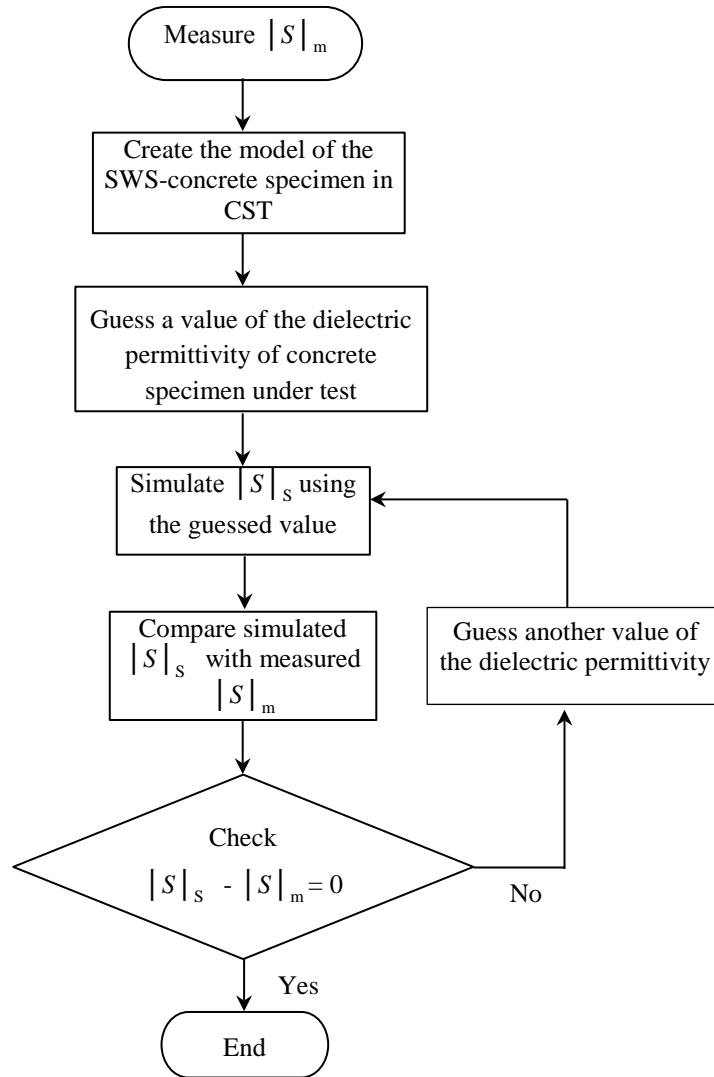
Figure 3.2: Proposed algorithm for determining the complex dielectric permittivity of concrete using measured and simulated magnitudes of the reflection coefficient.

3.3.2   Measurement Setup and Approach

Preparation of specimens

Several concrete specimens of dimensions 250 mm × 250 mm × 250 mm were prepared for this investigation in accordance with American Society for Testing and Materials (ASTM) standard. The proportions of water, gravel, sand and cement in the concrete mix was 0.5 : 2.42 : 1.57 : 1.0. All specimens with moulding cases were covered with plastic sheets after casting and cured naturally in outdoor conditions for

two days, then in a laboratory at a temperature of about 24°C and a humidity of about 55%.

A schematic of the measurement setup is shown in Figure 3.3a. The microwave properties of the early-age concrete specimen were investigated using a performance network analyser (PNA) at R-band (1.7 GHz – 2.6 GHz) and X-band (8.2 GHz – 12.4 GHz) as shown in Figure 3.3a. Standard R-band and X-band waveguide sections (aperture dimensions $109.22 \, \text{mm} \times 54.61 \, \text{mm}$ and $22.86 \, \text{mm} \times 10.16 \, \text{mm}$, respectively) were used as SWSs as shown in Figure 3.3b. The SWSs radiated microwave signals into the specimen and picked up the reflected signals that were then received and computed by the PNA. Calibration of the setup arrangement at the output aperture of the microwave sensors was performed using R-band and X-band rectangular waveguide calibration kits. The measurements of complex reflection coefficient (S_m) commenced on the second day (hereafter '2nd day') after the concrete specimen was prepared, immediately after dismantling the moulding case. Measurements were taken from each of the four side surfaces at 10 different locations during the first nine days of the curing period. Then the average magnitude of the reflection coefficient $\left| S \right|_m$ was calculated for each day from 40 measurements. Here, the averaged measured data for the 2nd and 9th days are presented for the determination of the dielectric permittivity of 2nd and 9th day concrete.

(a)

(b)
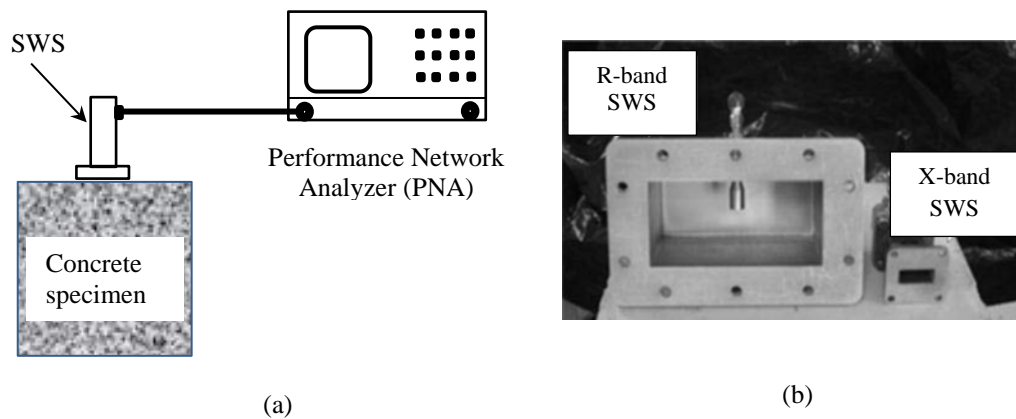
Figure 3.3: (a) Schematic of measurement setup; (b) photograph of two SWSs.

3.3.3   Simulations using Measured Data

Different views of R-band and X-band SWSs along with cubic concrete specimen models in CST are shown in Figure 3.4. First, as per the developed algorithm, the reflection coefficient $|S|_S$ over each R-band and X-band was simulated for different values of the complex dielectric permittivity of the concrete. The simulation results and measurement results at the R-band for 2nd day and 9th day are shown in Figures 3.5 and 3.6, respectively.
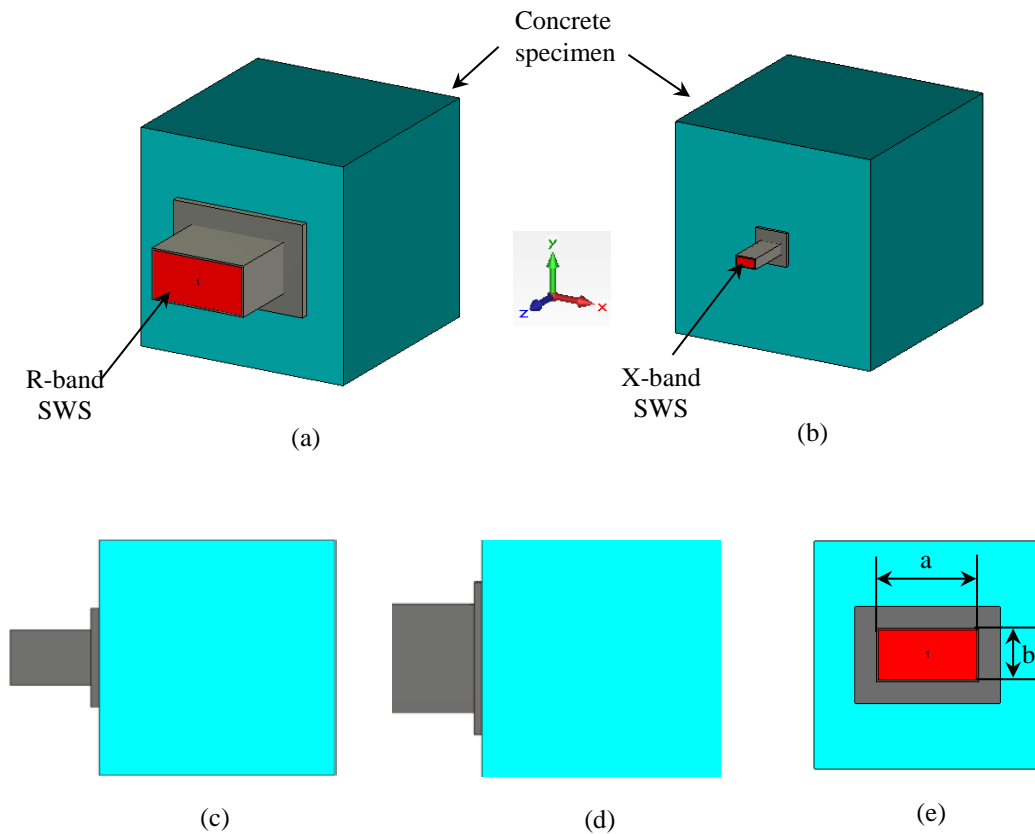
Figure 3.4: Models of SWSs along with concrete cube specimen in CST at (a) R-band, (b) X-band; and different views of the R-band SWS with the specimen: (c) side view, (d) top view and (e) front view.

It can be seen from Figures 3.5 and 3.6 that a good agreement between the simulated and measurement results was achieved; the relative complex dielectric permittivity was determined to be 10.60 – j2.737 at the 2nd day and 5.5 – j1.375 at the 9th day. It should be mentioned that the best agreement is at frequencies ranging from 1.95 GHz to 2.2 GHz at the 2nd day, and from 1.7 GHz to 2.15 GHz at the 9th day.
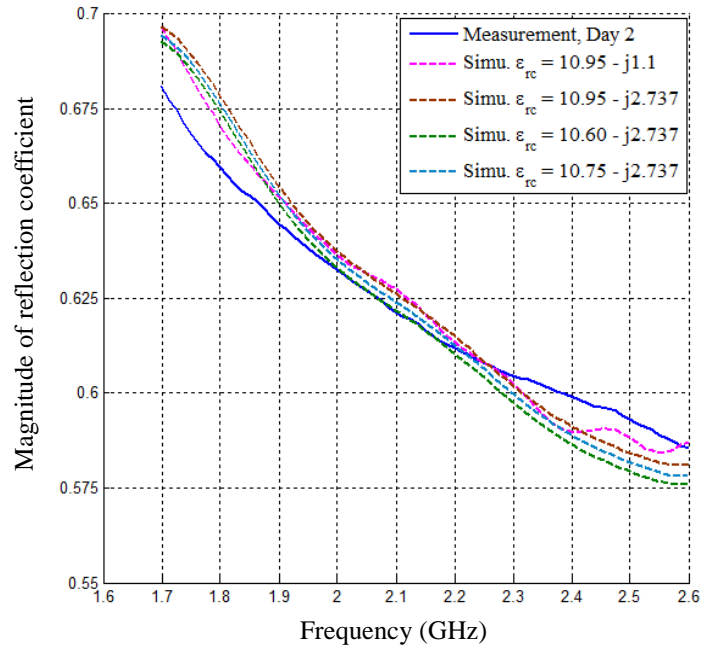
Figure 3.5: Measured and selected simulated magnitude of reflection coefficient vs. frequency for 2nd day concrete at R band.
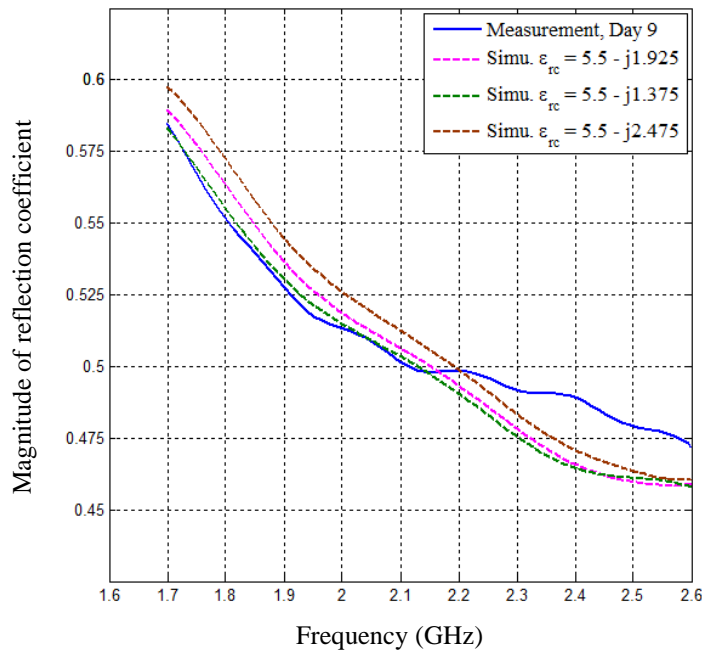
Figure 3.6: Measured and selected simulated magnitude of reflection coefficient vs. frequency for 9th day concrete at R band.

Figures 3.7 and 3.8 present the measured and simulated magnitude of reflection coefficient vs. frequency for 2nd day and 9th day concrete, respectively, at X band.

Consequently, the relative complex dielectric permittivity of the concrete specimen was determined to be $10.15 - j1.537$ at 2nd day and $4.8 - j0.864$ at 9th day.
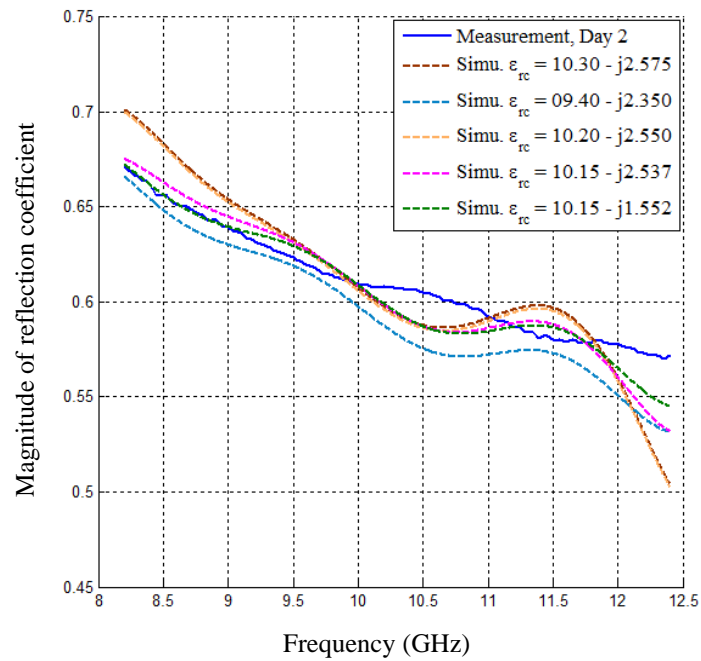
Figure 3.7: Measured and selected simulated magnitude of reflection coefficient vs. frequency for 2nd day concrete at X band.
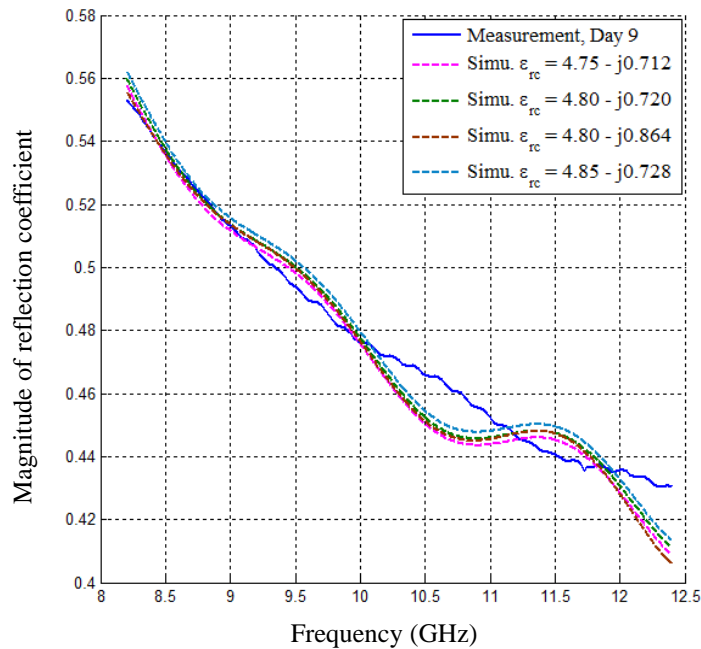
Figure 3.8: Measured and selected simulated magnitude of reflection coefficient vs. frequency for 9th day concrete at X band.

3.4   Sensitivity Analysis

During the measurement of the reflection coefficient, measurement errors may occur due to several sources, including roughness of the surface of the concrete specimen, the heterogeneous nature of the concrete specimen, surface-wave and radiation losses. These affect the accuracy and reliability of the results. Experimental investigations into the influence of such sources are time consuming tasks. The development of advanced computational tools such as CST Microwave Studio [25] for electromagnetic applications significantly facilitates the simulation of microwave techniques for material characterisation and sensitivity analysis. In this section, a numerical investigation into the sensitivity of the reflection coefficient to changes in the sensor–specimen arrangement will be performed. Such changes are selected for their potential effect on measurement accuracy: they include a small gap between the waveguide aperture and the surface of the specimen, a shift of the aperture with respect to the centre of the specimen, and non-uniform dielectric property distribution in the concrete specimen. The sensitivity of the reflection coefficient to changes of specimen size will also be investigated.

3.4.1   Effect of Small Gap between Sensor and Concrete Specimen

The magnitude of the reflection coefficient vs. frequency for concrete at 2nd day for different values of the gap, g (c.f. Figure 3.9a) between the open-ended waveguide aperture and the side surface of the concrete specimen at R-band and X-band are shown in Figures 3.9b and 3.10, respectively. It can be seen from Figure 3.9b that the magnitude slightly decreased over the entire frequency band when g increased from 0.0 mm to 1.4 mm; however, a relatively large drop is observed when g increased from 1.4 mm to 1.5 mm. The average sensitivity of the magnitude of the reflection coefficient to small changes of gap   (0–1.4 mm) was ~ 0.01 mm^{-1}. On the other hand, at X-band the average sensitivity was ~ 0.25 mm^{-1} when the gap increased from 0.0 to 0.3 mm, and a relatively large drop was observed when g decreased from 0.3 mm to 0.4 mm, as shown in Figure 3.10. Overall, the results show that the sensitivity of the magnitude of the reflection coefficient to the size of the gap was greater at X-band than at R-band.
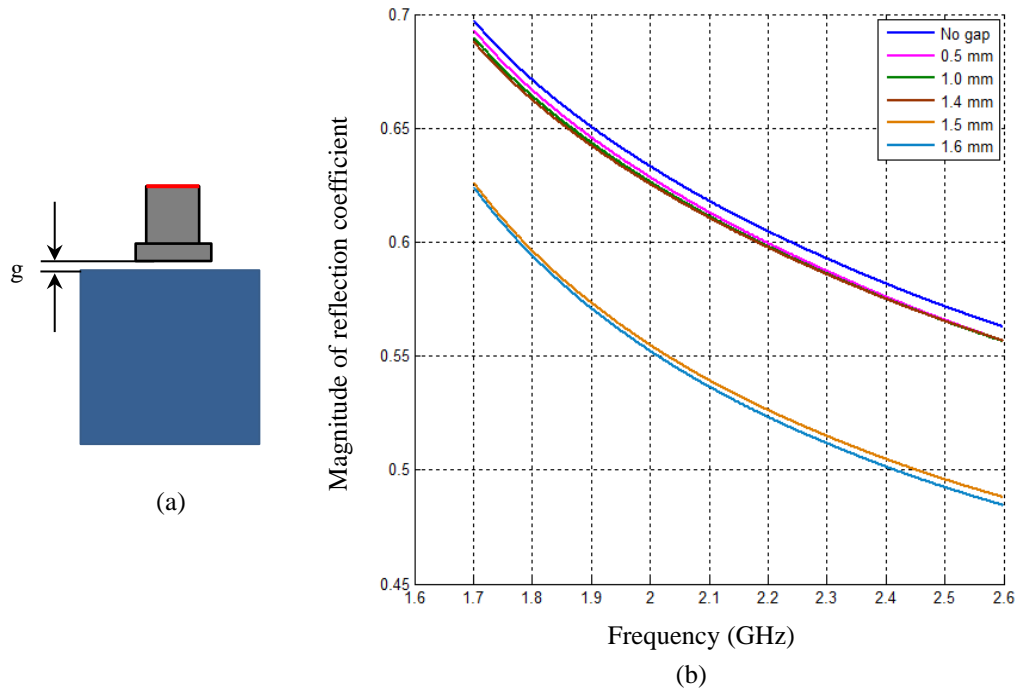
Figure 3.9: (a) Model of SWS with the specimen under test; (b) simulated magnitude of reflection coefficient vs. frequency for 2nd day concrete ($\varepsilon_r = 10.60 - j2.737$) for different values of the gap (g) between the SWS aperture and the side surface of the concrete specimen at R-band.
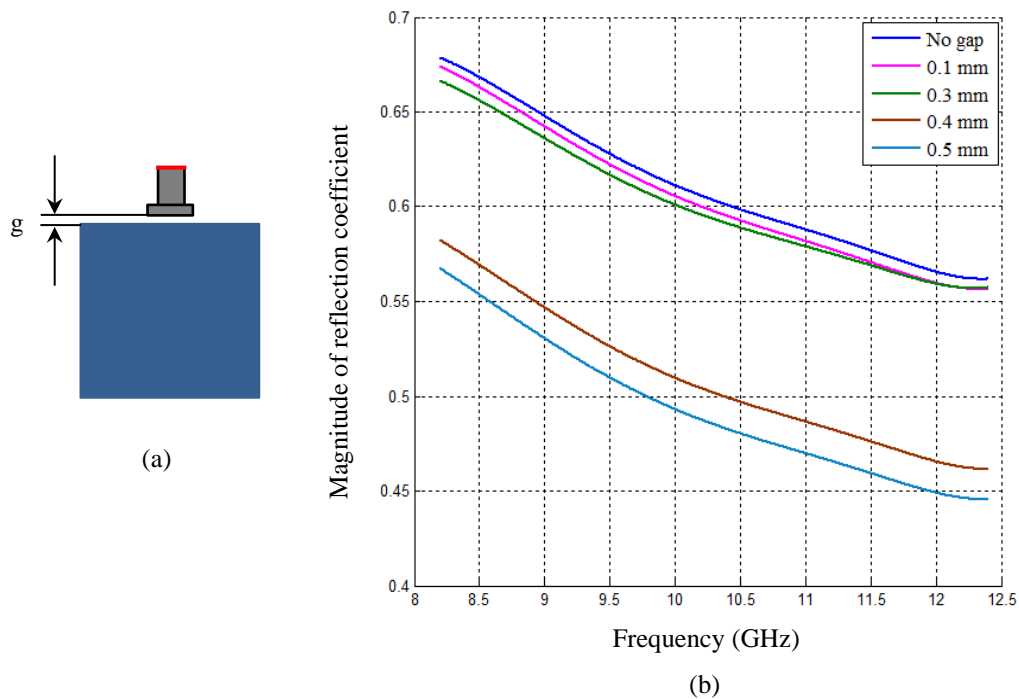
Figure 3.10: (a) Model of SWS with the specimen under test; (b) simulated magnitude of reflection coefficient vs. frequency for 2nd day concrete ($\varepsilon_r = 10.15 -$

j1.522) for different values of the gap (g) between the SWS aperture and the side surface of the concrete specimen at X-band.

The electric field intensity distributions in the sensor–specimen model were simulated in order to clarify these observations; the results for the top and side cross-sectional views of the system are shown in Figures 3.11 and 3.12 (at R-band, $g = 0$ and 1.5 mm) and Figures 3.13 and 3.14 (at X-band, $g = 0$ and 0.3 mm). Overall, the following features are indicated by Figures 3.9 – 3.14:

1) The influence of the small gap is negligible.
2) When there is no gap only the influence of the interface changes the distributions, and this change is very similar at both R-band and X-band.
3) Significant changes of the magnitude of reflection coefficient and electric field distributions occur at a relatively large critical value of gap. This value is frequency-dependent and increases at lower frequencies.
4) These changes can be attributed to the influence of higher-order modes whose indications can be clearly seen at the edges of the apertures in Figures 3.12b and 3.14b as a result of the influence of gap.
5) Reflection and radiation in free space can be clearly seen in all cases at both R-band and X-band.
6) Free-space radiation patterns change when a gap occurs.
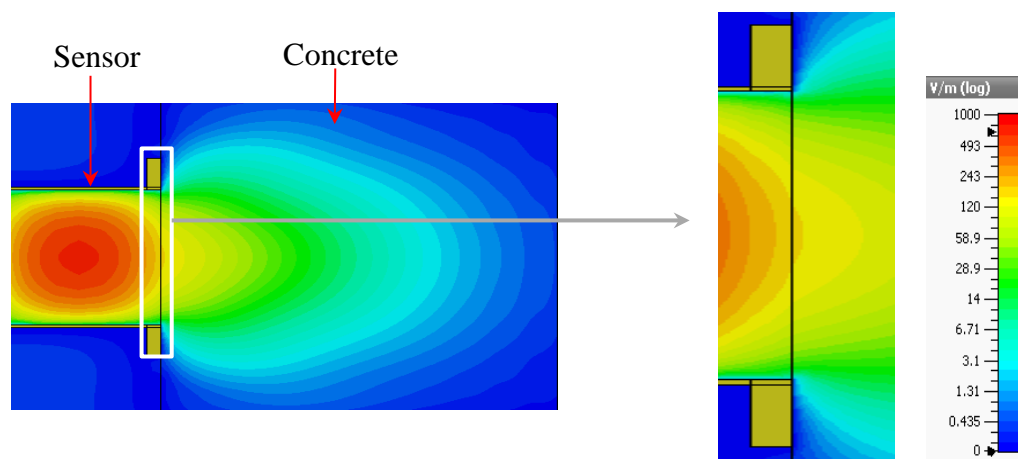
(a) No gap between waveguide and concrete specimen
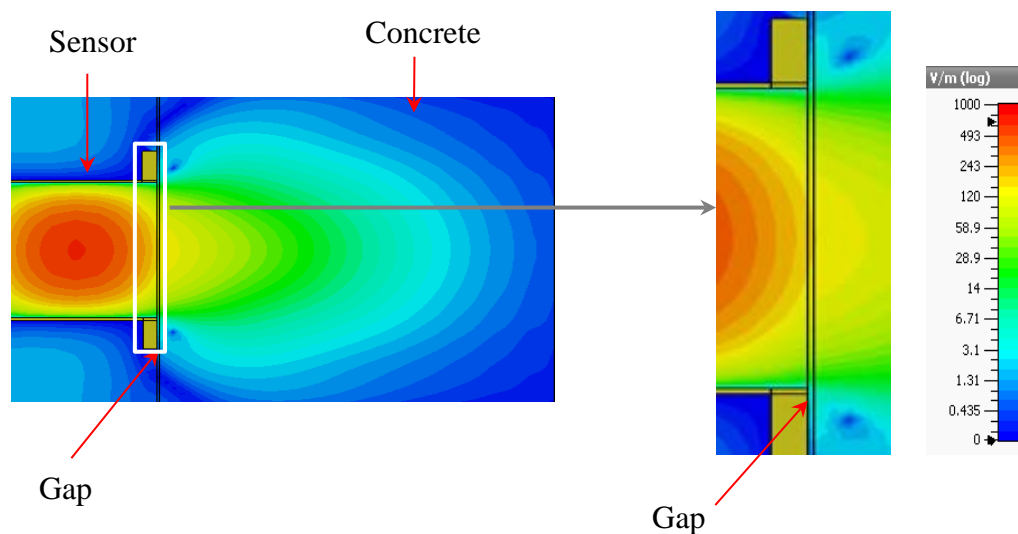
(b) A gap of 1.5 mm between waveguide and concrete specimen

Figure 3.11: Cross-sectional top view of electric field intensity distribution inside the R-band sensor and concrete specimen at 2.0 GHz with 2nd day concrete ($\varepsilon_r = 10.60 - j2.737$): (a) no gap; and (b) 1.5 mm gap between sensor and concrete surface.
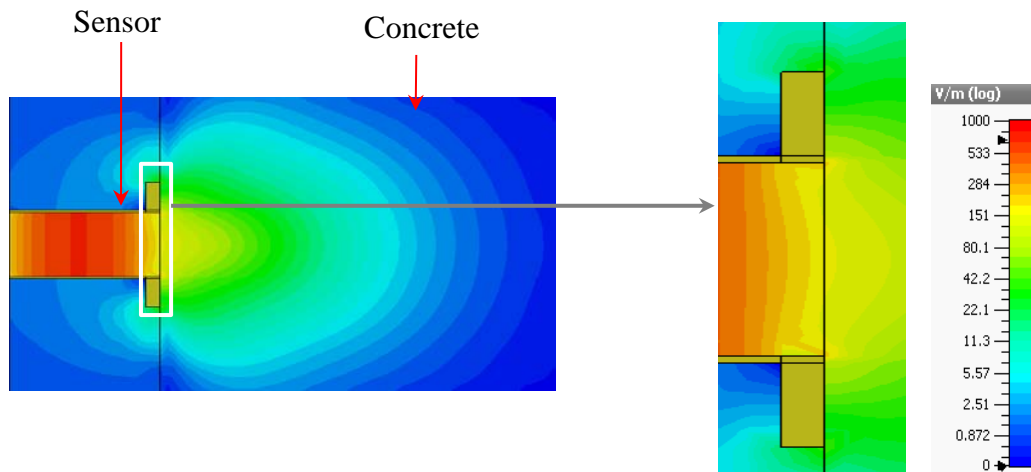
(a) No gap between waveguide and concrete specimen
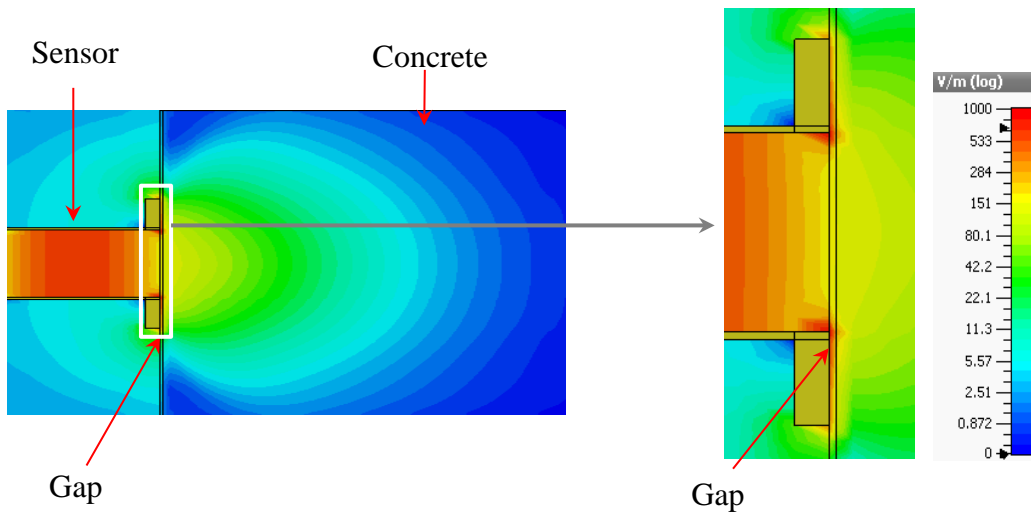
(b) A gap of 1.5 mm between waveguide and concrete specimen

Figure 3.12: Cross-sectional side view of electric field intensity distribution inside the R-band sensor and concrete specimen at 2.0 GHz with 2nd day concrete (ε_r = 10.60 – j2.737): (a) no gap; and (b) 1.5 mm gap between sensor and concrete surface.
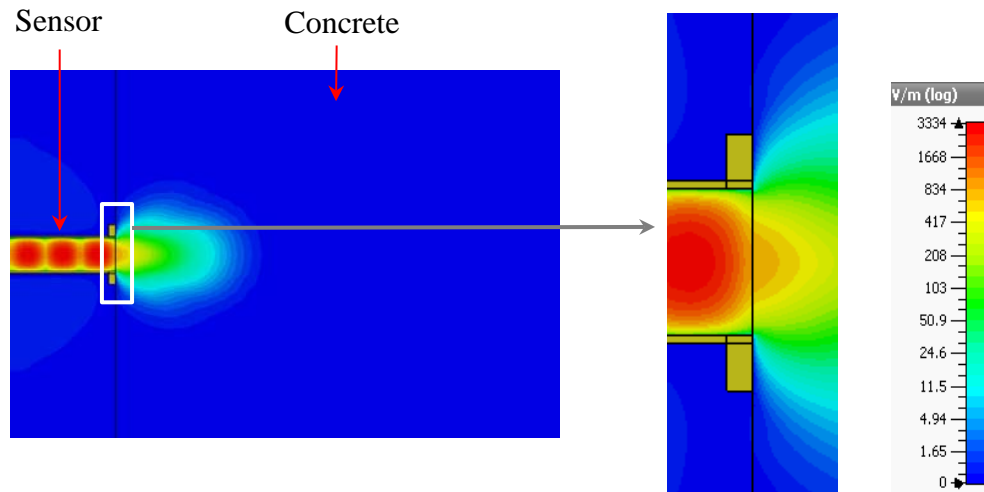
(a) No gap between waveguide and concrete specimen
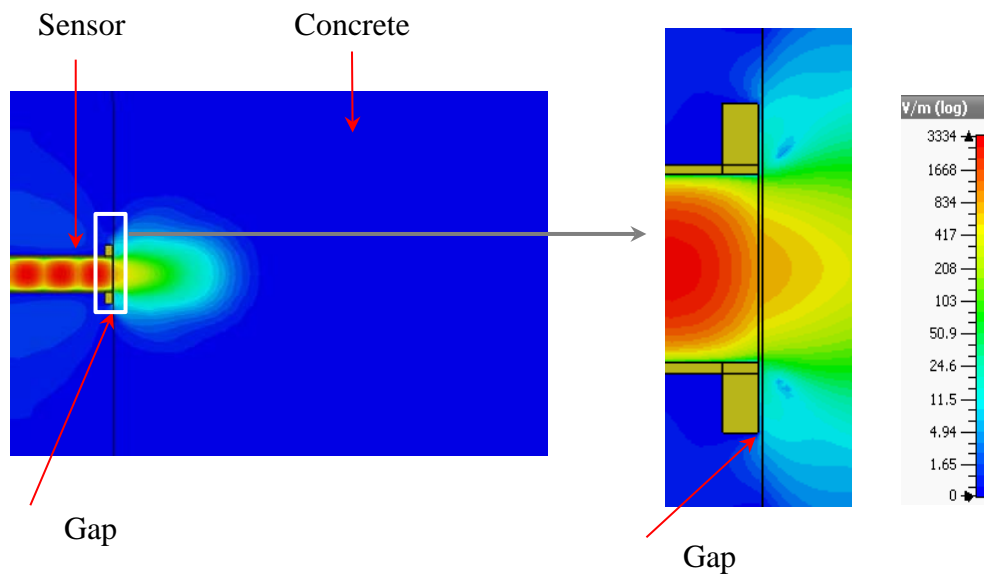
(b) A gap of 0.5 mm between waveguide and concrete specimen

Figure 3.13: Cross-sectional top view of electric field intensity distribution inside the X-band sensor and concrete specimen at 10.0 GHz with 2nd day concrete ($\varepsilon_r = 10.15 - j1.522$): (a) no gap; and (b) 0.5 mm gap between sensor and concrete surface.
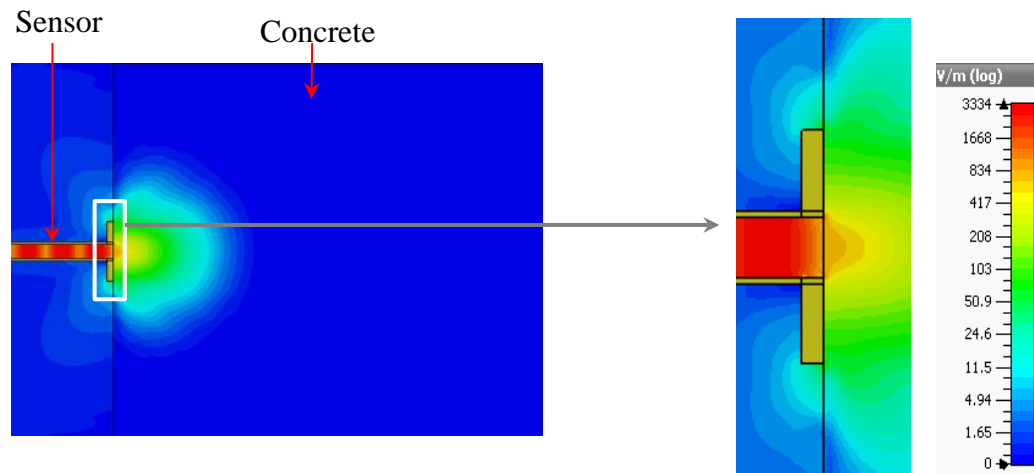
(a) No gap between waveguide and concrete specimen
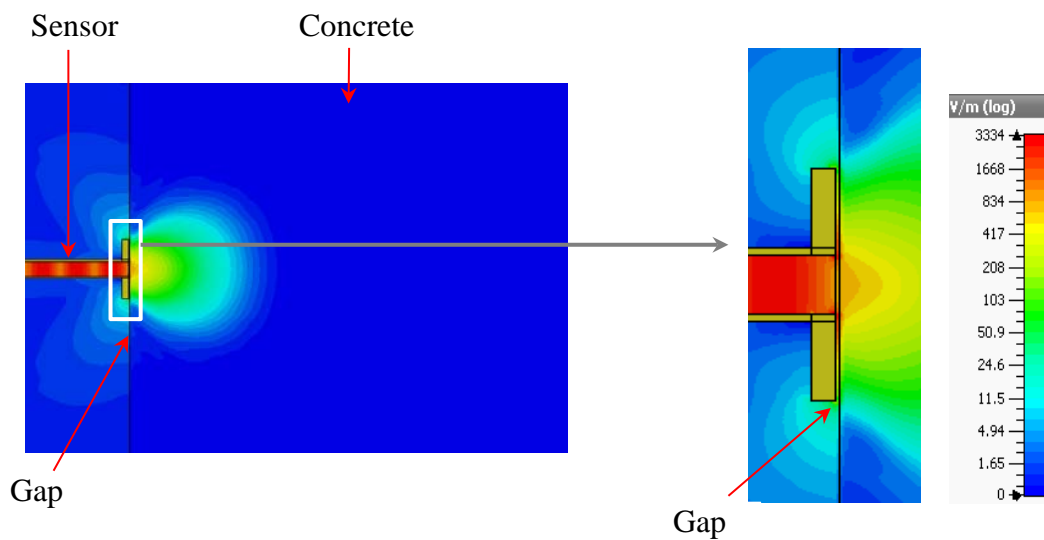
(b) A gap of 0.5 mm between waveguide and concrete specimen

Figure 3.14: Cross-sectional side view of electric field intensity distribution inside the X-band sensor and concrete specimen at 10.0 GHz with 2nd day concrete (ε_r = 10.15 – j1.522): (a) no gap; and (b) 0.5 mm gap between the sensor and concrete surface.

3.4.2 Effect of Changing Sensor Location on the Specimen Surface

The location and position of the waveguide sensor aperture on the surface of the specimen is another potential cause of measurement error. In particular, it is critical at R-band since the dimensions of the R-band waveguide sensor aperture are relatively large. Simulations were performed for changes of the location of the centre of the aperture along the x- or y-axis with no gap between sensor and concrete specimen. Figure 3.15 shows eight locations on the specimen surface; the simulated magnitudes of the reflection coefficient at these locations are shown in Figures 3.16–3.19.
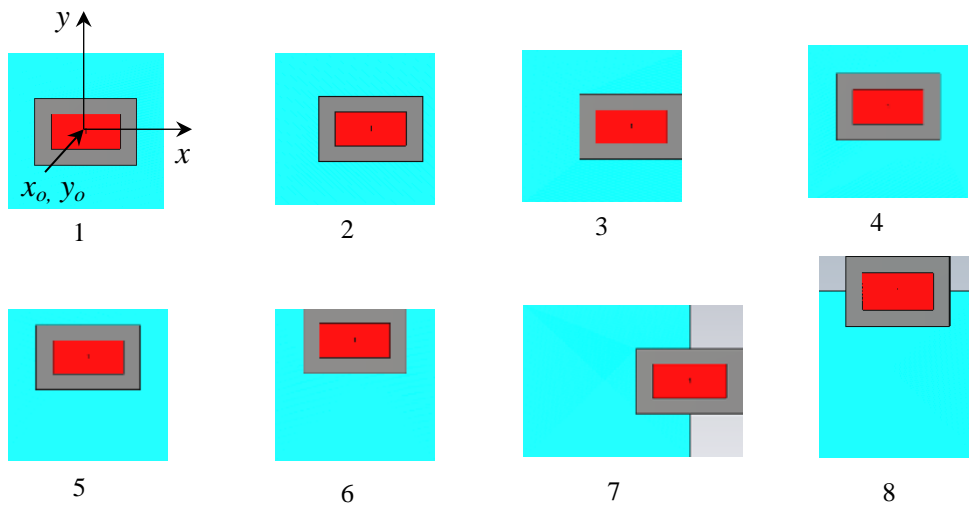
Figure 3.15: Positions of the centre of the open-ended waveguide aperture (x_0, y_0) with respect to the centre of the concrete specimen: (1) 0, 0; (2) 25 mm, 0; (3) 45 mm, 0; (4) 0, 25 mm; (5) 0, 45 mm; (6) 0, 72.5 mm; (7) 125 mm, 0; (8) 0, 125 mm.

It can be seen from Figure 3.16 that when the R-band sensor aperture is located within the boundaries of the specimen surface, changes of reflection coefficient magnitude (~ 0.01–0.02) are observed at lower and higher frequencies for cases (2) and (4), corresponding to a relatively small shift (25 mm) of the aperture, whereas they are negligible for cases (3) (45 mm shift in the x-direction), (5) (45 mm shift in the y-direction), and (6) (72.5 mm shift in the y-direction). However, when the sensor aperture moves past the edge of the specimen surface in either the x- or y-direction (i.e., cases (7) and (8)), significant changes are observed in the magnitude of the reflection coefficient, as shown in Figure 3.17.
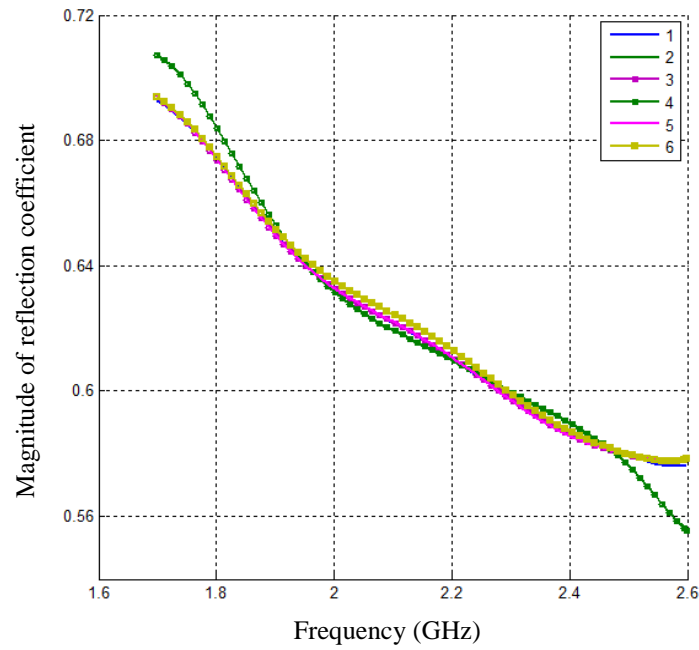
Figure 3.16: Simulated magnitude of reflection coefficient vs. frequency for 2nd day concrete, with sensor-concrete specimen arrangements (1)–(6) in Figure 3.15 using the R-band SWS.
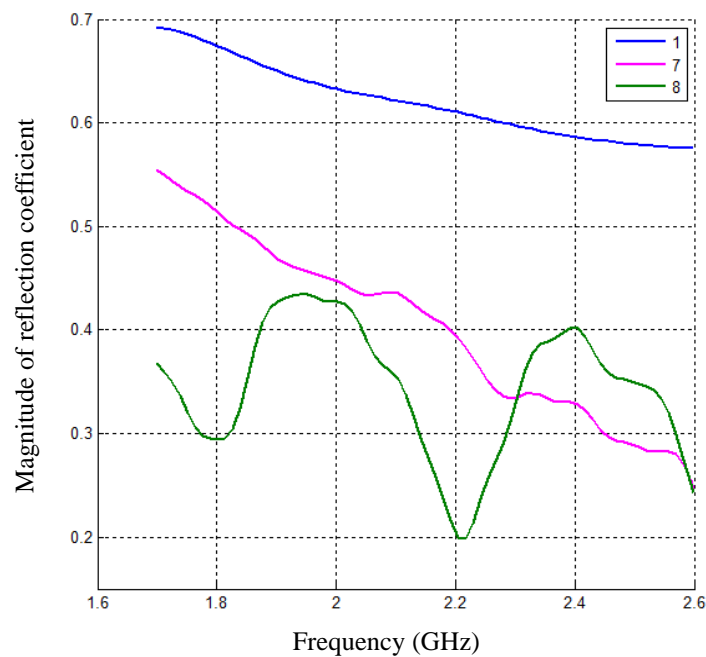
Figure 3.17: Simulated magnitude of reflection coefficient vs. frequency for 2nd day concrete, with sensor-concrete specimen arrangements (1), (7), (8) in Figure 3.15 using the R-band SWS.

The sensitivity of the magnitude of the reflection coefficient at the X-band due to the sensor aperture shifting in the *x*- and *y*-directions of the concrete specimen surface are seen in Figures 3.18 and 3.19, respectively. In these cases it was found that when the sensor aperture was located wholly within the surface of specimen, the sensitivity is extremely low (~ 0.002 mm^{-1}); however, as for the R-band, when the sensor aperture overlapped one of the edges of the specimen in either the *x*- or *y*-direction, significant changes were observed in the magnitude of the reflection coefficient.
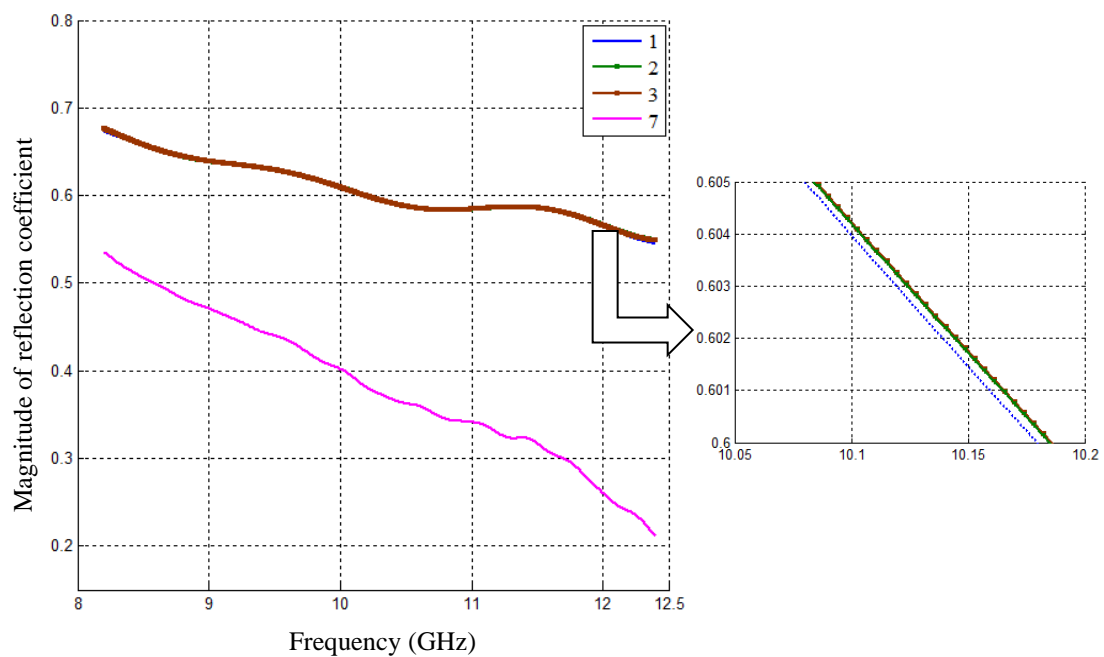
Figure 3.18: Simulated magnitude of reflection coefficient vs. frequency for 2nd day concrete, with four different sensor-concrete specimen arrangements (1)–(3), (7) in Figure 3.15 using the X-band SWS.
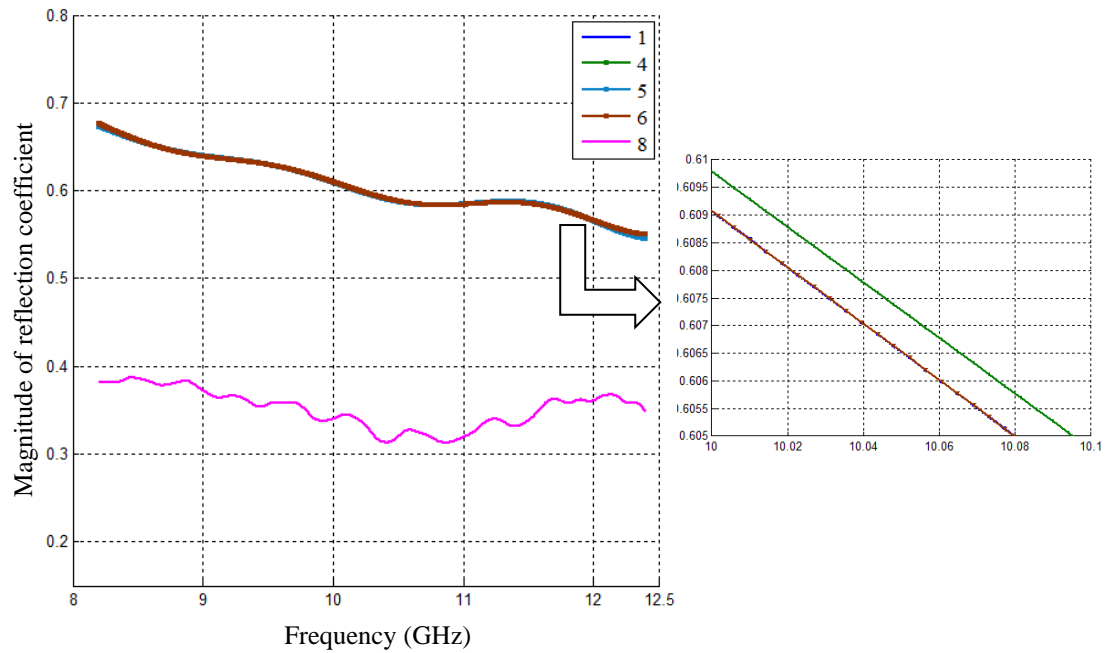
Figure 3.19: Simulated magnitude of reflection coefficient vs. frequency for 2nd day concrete, with five different sensor-concrete specimen arrangement (1), (4)–(6), (8) in Figure 3.15 using the X-band SWS.

3.4.3 Effect of Non-uniform Dielectric Permittivity Distribution in Concrete Specimen

In determining the dielectric permittivity of 2nd day concrete, it was assumed that the dielectric permittivity of the concrete was uniform over the cubic specimen. In practice, however, concrete is a heterogeneous mixture of cement, sand, water and coarse aggregates, and hence the dielectric property distribution is not uniform. The non-uniform distribution of water/moisture is one of the main reasons, of non-uniform dielectric property distribution. In this section, the effect of the non-uniform dielectric constant on the magnitude of the reflection coefficient in 2nd day concrete is investigated numerically for both the R-band and the X-band sensors. For this purpose, a concrete specimen was modelled in CST as a combination of 10 layers, each 25.0 mm thick, and 25 layers, each 10.0 mm thick, with dissimilar dielectric constants. Figure 3.20 shows the model of the 10-layer specimen tested for the R-band sensor. For simplicity, variations of dielectric constant were considered only in the z-direction; $tan\ \delta = 0.2582$ for each layer. The layers closest to the surface of the

2nd day specimen had a dielectric constant of $\varepsilon_r' = 10.60$, incrementally increasing to $\varepsilon_r' = 14.0$ towards the centre of the specimen from 10.6 to 11, 12, 13 and 14 for the 10-layer specimen, and from 10.6 to 11.0, 11.25, 11.50, 11.75, 12.00, 12.25, 12.50, 12.75, 13.00, 13.25, 13.50 and 14 for the 25-layer specimen.

(a)   (b)
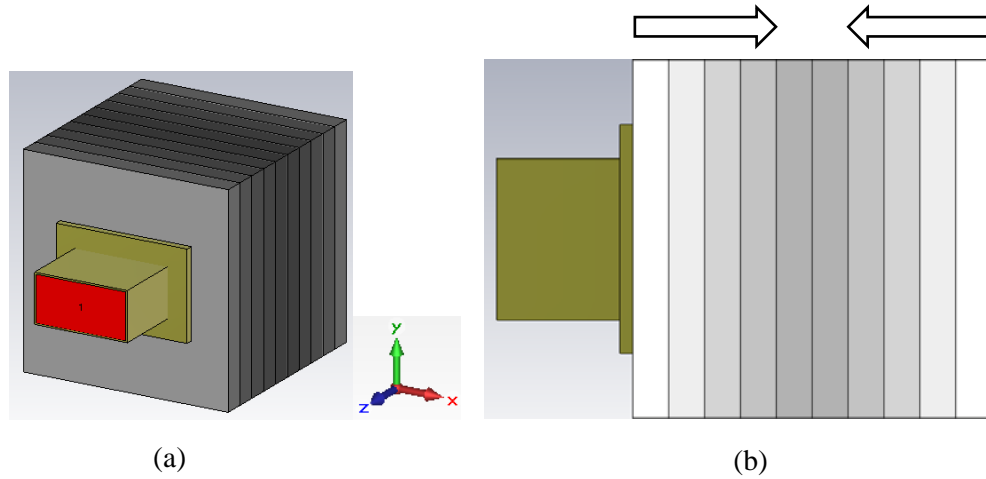
Figure 3.20: A model of 10-layer concrete specimen with non-uniform distribution of dielectric constant with the R-band waveguide sensor in CST: (a) perspective view; (b) side view.

Figures 3.21 and 3.22 show the magnitude of reflection coefficient at R band for 2nd and 9th day, respectively, for the homogeneous and layered specimens. It can be seen in Figure 3.21 that the results for 10-layer specimen and the uniform specimen are very similar. Increasing the number of layers to 25 slightly decreases the magnitude of reflection coefficient. For 9th day specimens the results are very close for all specimens. Figures 3.23 and 3.24 show the magnitude of the reflection coefficient at X band for the uniform and the layered specimens. These figures demonstrate that the results for 10 layers and 25 layers are very similar, and resemble the average results for the uniform specimens of both 2nd day and 9th day concrete.

The electric field intensity distributions inside the sensors and concrete specimens at R- and X-bands for 2nd day concrete are shown in Figures 3.25 and 3.26, respectively. It can be seen from these figures that the difference in the distributions for the uniform and non-uniform layered specimens is negligible. On the other hand, it can be clearly seen that the microwave signal at the R-band

penetrated more deeply into the concrete specimen than at X-band, as expected. Another observation is that reflection/radiation of EM waves in free space is higher at X-band than at R-band, attributed to the fact that the X-band sensor is smaller than the R-band sensor in size.

Overall, the results show that most of the microwave signals are reflected in the thin near-interface region of the metal–concrete composite.
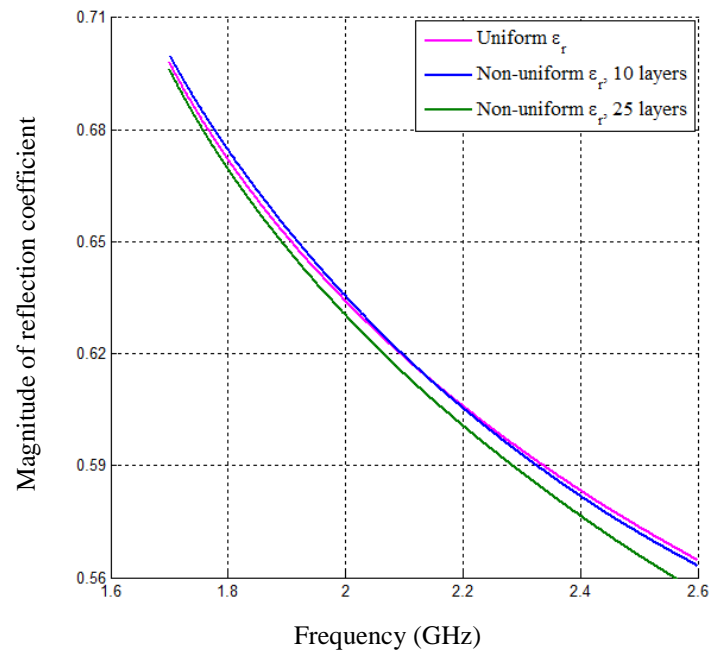
Figure 3.21: Simulated magnitude of reflection coefficient vs. frequency using R-band waveguide sensor for uniform and layered 2nd day concrete specimens.
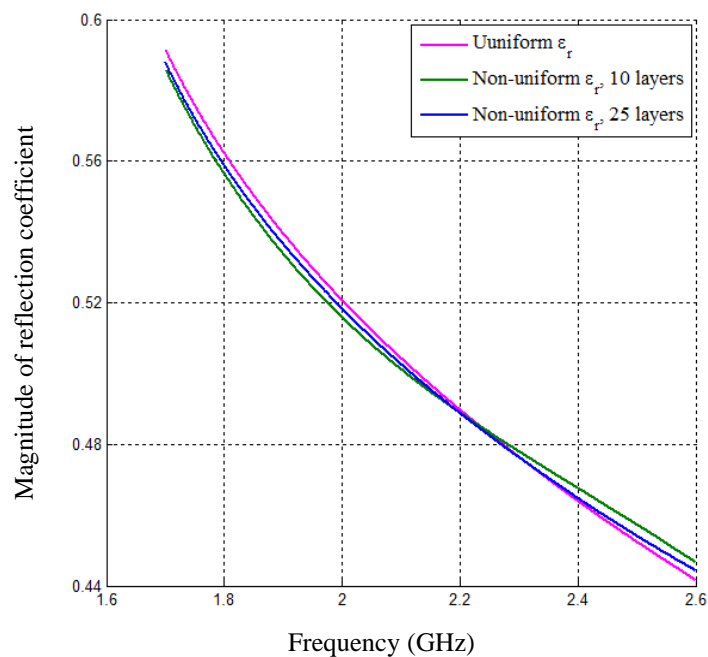
Figure 3.22: Simulated magnitude of reflection coefficient vs. frequency using R-band waveguide sensor for uniform and layered 9th day concrete specimens.
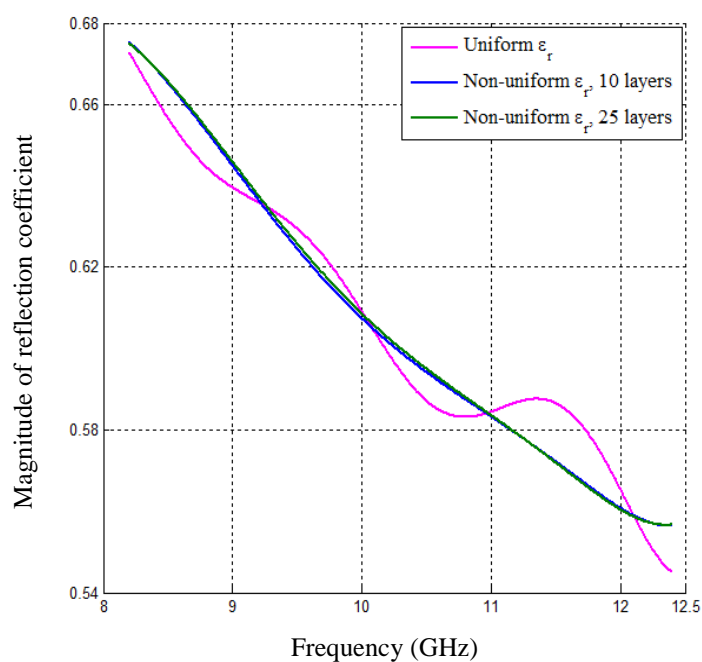
Figure 3.23: Simulated magnitude of reflection coefficient vs. frequency using X-band waveguide sensor for uniform and layered 2nd day concrete specimens.
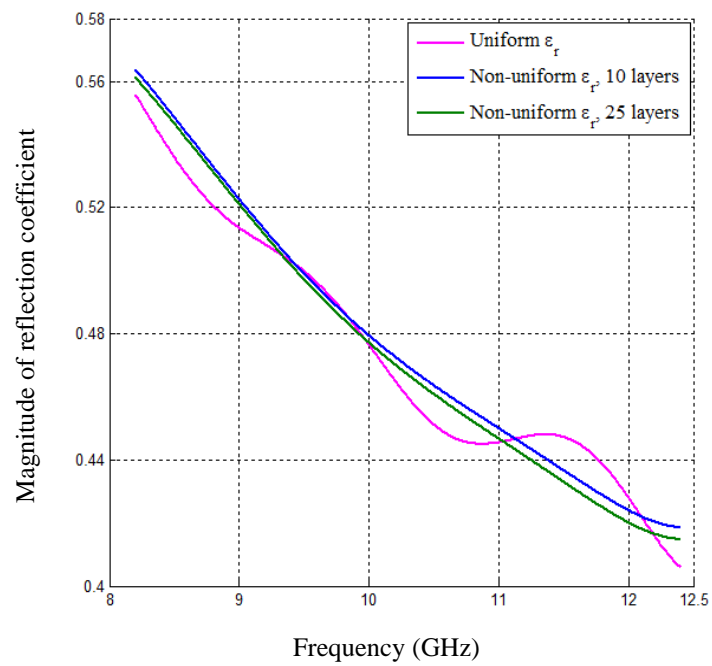
Figure 3.24: Simulated magnitude of reflection coefficient vs. frequency using X-band waveguide sensor for uniform and layered 9th day concrete specimens.
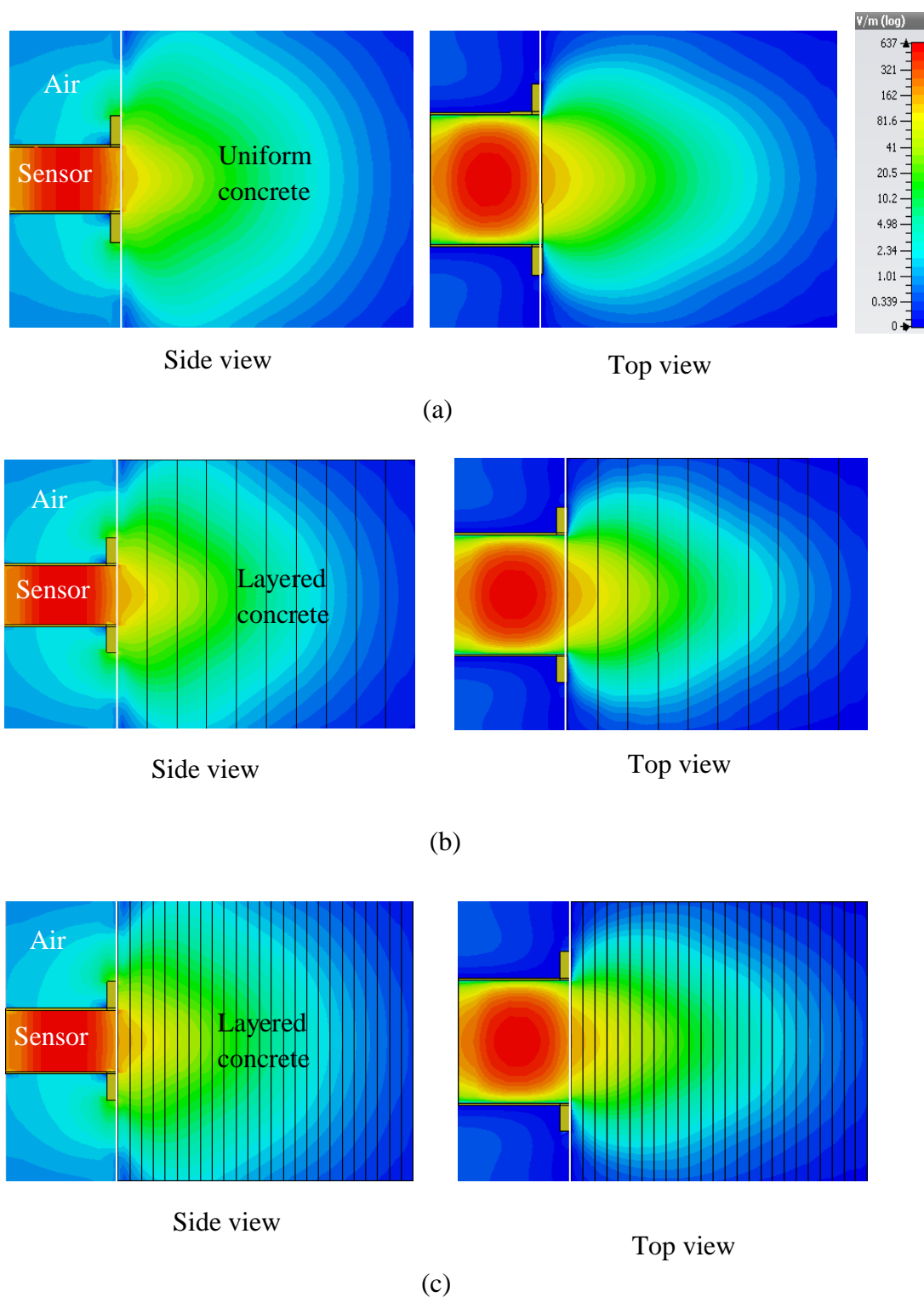
Figure 3.25: Simulated electric field intensity distribution inside the R-band sensor and 2nd day concrete specimen at 2.15 GHz for (a) uniform specimen with $\varepsilon_r = 10.6 - j2.737$; (b) non-uniform 10-layer specimen; and (c) non-uniform 25-layer specimen.
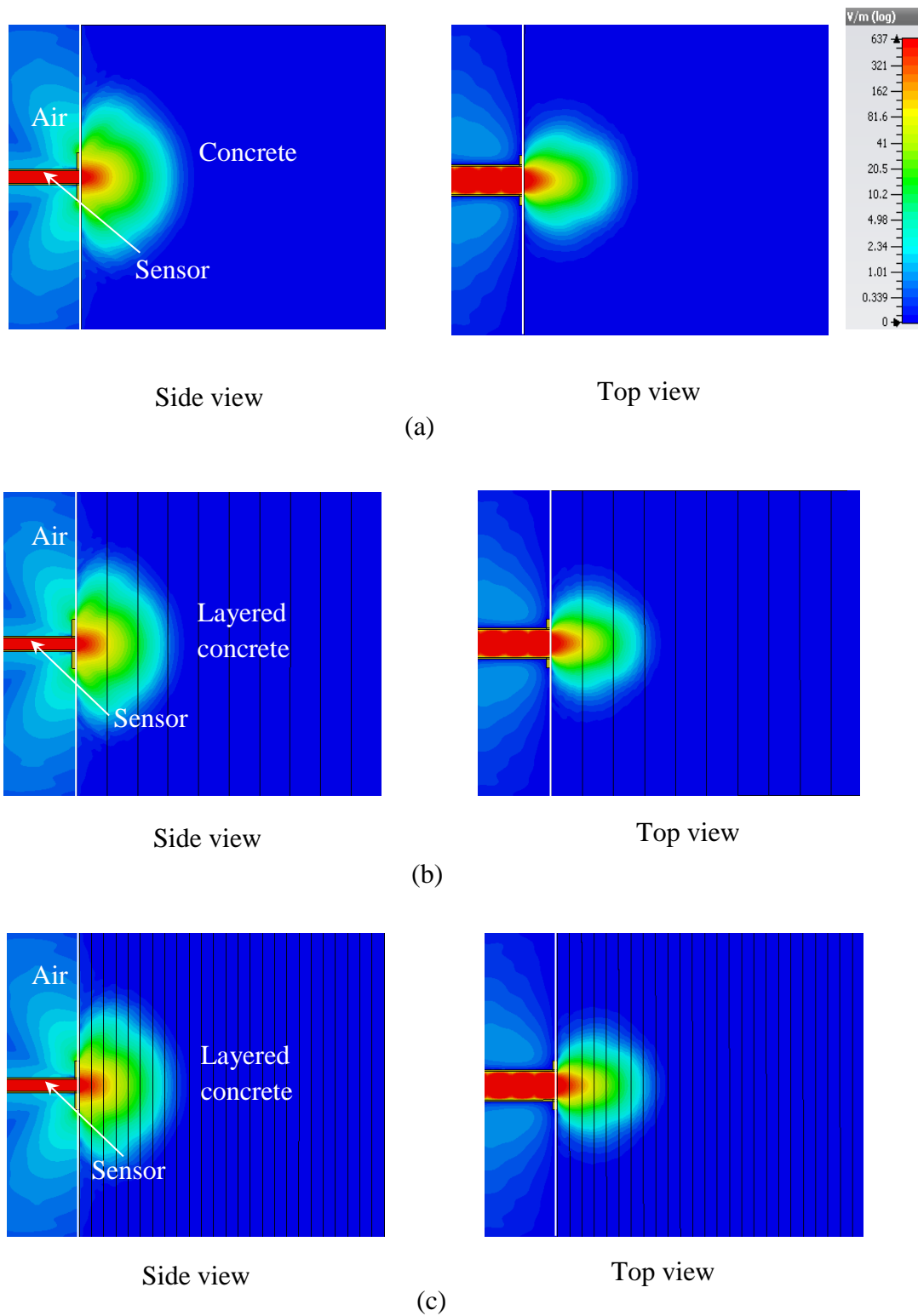
Figure 3.26: Simulated electric field intensity distribution inside the X-band sensor and 2nd day concrete specimen at 10.3 GHz for (a) uniform specimen with $\varepsilon_r = 10.15 - j1.552$; (b) non-uniform 10-layer specimen; and (c) non-uniform 25-layer specimen.

3.4.4   Effect of Different Sizes of Concrete Specimen

The change of size of cubic specimens, *L,* (c.f. Figures 3.27a and 3.28a) may also affect the reflection properties and cause measurement error. The results for magnitude of reflection coefficient vs. frequency for different sizes of 2nd day concrete specimens with no gap between the open-ended waveguide aperture and the concrete surface at R-band and X-band are shown in Figures 3.27 and 3.28, respectively. Using the determined value of the complex dielectric permittivity of 2nd day concrete, simulations were performed for concrete specimens of different size. It can be seen from Figures 3.27b and 3.28b that the simulated magnitudes of the reflection coefficient are very similar for all specimens. A negligible change in $|S|_S$ is seen at the lowest and highest frequencies, attributable to simulation error at limited frequencies.
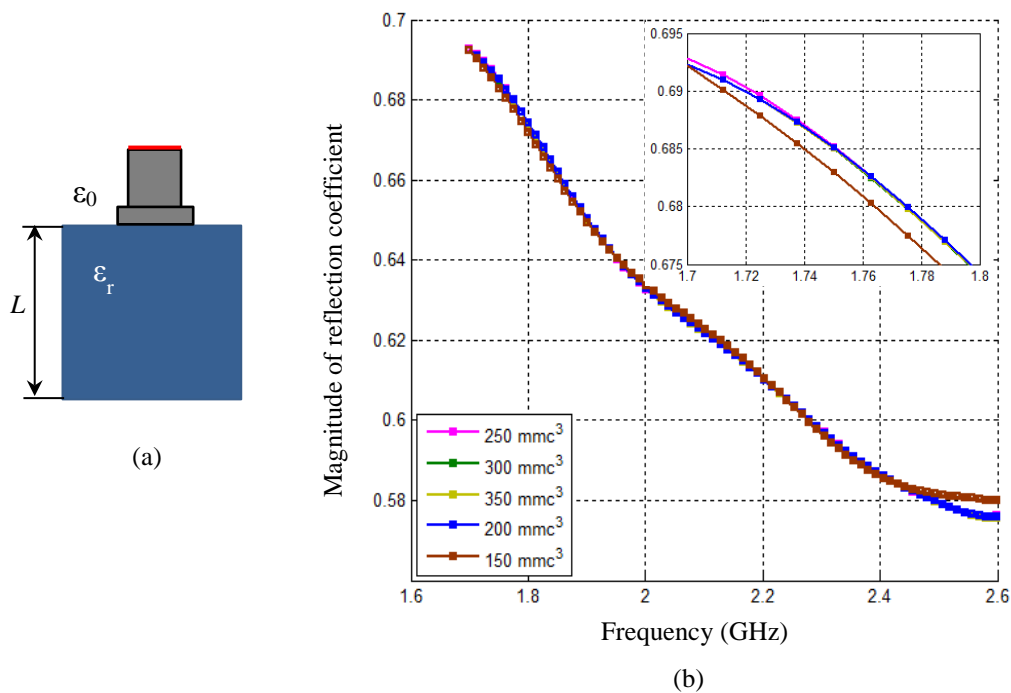
Figure 3.27: (a) Model of the SWS and cubic specimen; (b) simulated magnitude of reflection coefficient vs. frequency at R-band for different sizes of 2nd day concrete specimens.
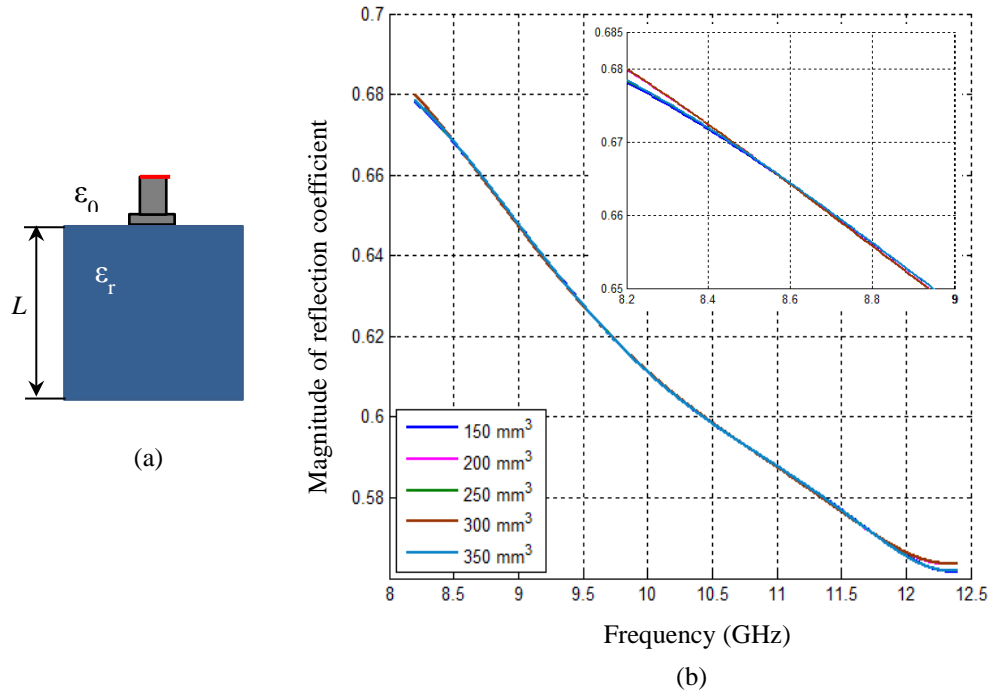
Figure 3.28: (a) Model of the SWS and cubic specimen; (b) simulated magnitude of reflection coefficient vs. frequency at X-band for different sizes of 2nd day concrete specimens.

3.5 Summary

In this chapter, an algorithm to determine the complex dielectric permittivity of concrete specimens from the measured and simulated magnitude of reflection coefficients has been developed. The developed algorithm was applied for a single waveguide sensor to characterise early-age (2–9 day) concrete specimens in response to the demand for such data for this study and, in general, in practice. The determined complex dielectric permittivity of 2nd day and 9th day concrete specimens in R-band (X-band) was 10.15 – j1.552 (10.60 – j2.737) and 4.8 – j0.864 (5.5 – j1.375), respectively.

The sensitivity of the magnitude of the reflection coefficient to the variations of a small gap between the sensor aperture and the specimen, changes in the sensor aperture position on the specimen surface, non-uniform dielectric permittivity distribution, and the effect of the size of the concrete specimen were numerically

investigated. It is shown that small gaps between sensor and specimen up to 1.5 mm for R-band and 0.3 mm for X-band SWS do not have significant effects on the measured magnitude of the reflection coefficients. However, significant changes were observed for gaps larger than those, attributable to the influence of higher-order modes at the aperture. It was also found that the magnitude of the reflection coefficient varies significantly when the sensor aperture locations approached and passed the edge of the concrete specimen. It is also shown that the influence of a selection of non-uniform dielectric permittivity distributions in early-age concrete specimens is negligible. On the other hand, it was clearly seen that the R-band microwave signal penetrated more deeply than at X-band into both the uniform and the non-uniform concrete specimens. This is attributed to higher losses in concrete at higher frequencies. Finally, it was found that changing the dimension of the cubic specimens from 150 mm to 350 mm had a negligible effect on the magnitude of the reflection coefficient at both the R band and the X band when the sensor aperture was located at the centre of specimen surface.

Chapter 4

Dual Waveguide Sensor

4.1   Introduction

The design, development and applications of a microwave dual waveguide sensor (DWS), comprising two waveguide sections and a metal plate/wall attached to a concrete specimen, are described in this chapter. Firstly, the proposed sensor is modelled along with the concrete specimen as a part of the sensor. Secondly, extensive simulation of this model operating as DWS and SWS is performed and compared with the results obtained with these sensors. Then, a DWS is fabricated and applied to measure a small gap between the metal plate and cement-based fresh concrete and dry concrete materials. The simulated electric field intensity distribution inside the waveguide sections of the DWS, and the gap between the specimen and the metal plate are illustrated to give a clear explanation of the 'guided wave' phenomenon. The DWS is further used to measure the small distance from a steel plate; comparative results of reflection and transmission properties of the steel plate, the fresh concrete and the dry concrete specimens in X-band frequencies are presented. The numerical investigations for the detection of cracks in dry concrete specimens using the proposed DWS, and the effect of the size and position of the crack on the reflection and transmission coefficients are also included in this chapter. Finally, an analysis of the sensitivity of the proposed dual waveguide sensor to variations in the concrete dielectric constant, loss factor and surface roughness is presented. CST Microwave Studio software was used to model the DWS with different specimens for simulation purposes. Extensive simulations were performed to determine the complex dielectric permittivity of the concrete in the measurement zone from the measured data, and to carry out the parametric studies.

4.2   Sensor Design

A schematic of the proposed microwave DWS is shown in Figure 4.1. The sensor consists of two hollow rectangular waveguide sections with broad and narrow dimensions a and b, respectively, installed in the metal wall of the structure under

inspection, with flanges for connection to the measurement system (Figure 4.1a). The distance between the two waveguide sections is L. A cross-sectional side view of the sensor for detecting the gap between the metal wall and the concrete specimen is shown in Figure 4.1b.
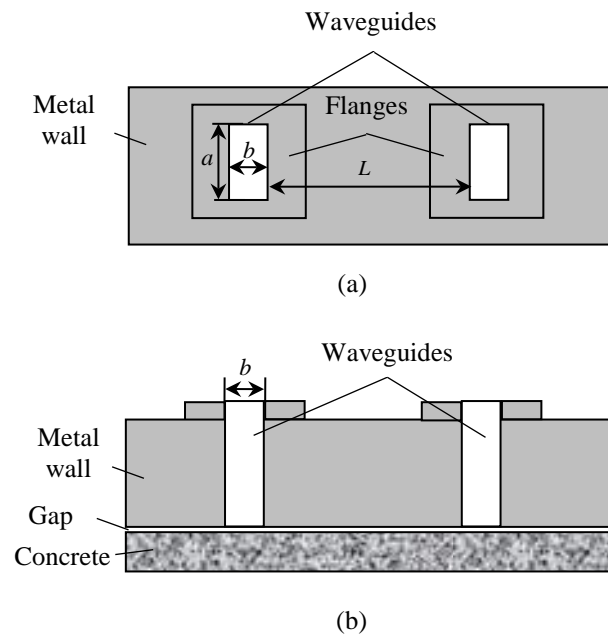
Figure 4.1: Schematic of the dual waveguide sensor: (a) top view, (b) cross-sectional view of the sensor with concrete structure under test in the E-plane of the waveguides.

4.2.1   Modelling the Sensor

For the numerical investigation of the cement-based composite specimen using the proposed sensor, a model of the microwave DWS and specimen was constructed using the time domain solver in CST Microwave Studio software. In the simulations, a Gaussian excitation signal and format X-band (8.2–12.4 GHz) were used.
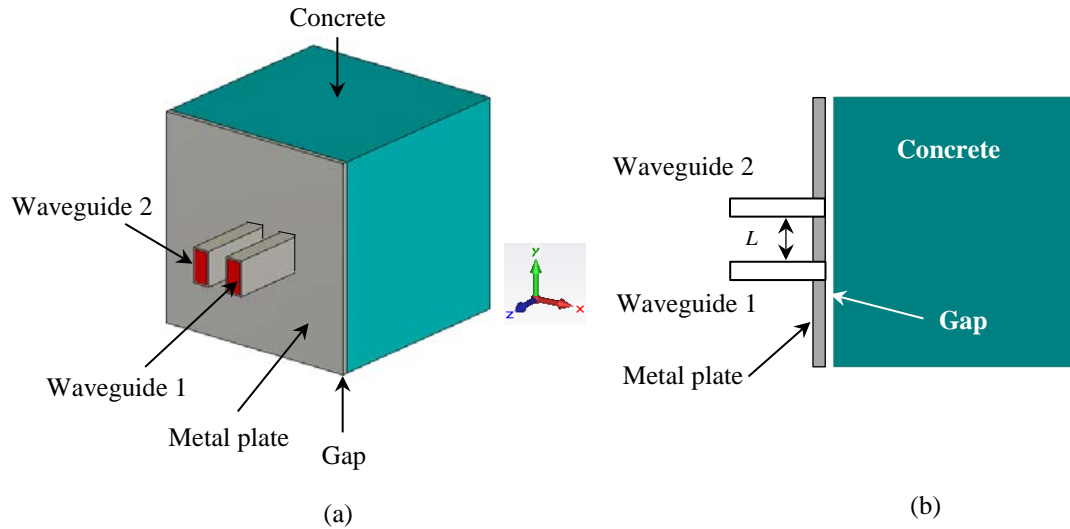
Figure 4.2: Model of DWS with concrete specimen and gap between surfaces of metal plate and concrete specimen: (a) perspective; and (b) cross-sectional top view.

Figure 4.2a is a perspective view of the model of a 250 mm cubic concrete specimen with DWS, including two standard X-band microwave rectangular waveguide sections (dimensions of the aperture of each section is 22.86 mm × 10.16 mm). The thickness of the metal plate is 4 mm. The distance between the waveguide sections is denoted by *L* as shown in Figure 4.2b. This model was used for a parametric study of the DWS with a concrete specimen.

4.2.2   DWS vs. SWS

Figure 4.3 shows the simulated magnitude of the reflection coefficient (in dB) vs. frequency for three different values of the gap between the metal and concrete surfaces, for different values of the dielectric constant of the concrete specimen (tan δ = 0.105) using SWS. It can be clearly seen that the magnitude of the reflection coefficient decreases with the increase of gap between the metal plate and the concrete specimen. Furthermore, the magnitude of the reflection coefficient decreases with decreasing dielectric constant of the concrete at each gap size. This is seen in Figure 4.4 platted at a frequency of 10.0 GHz; for example, the magnitude of the reflection coefficient for a dielectric constant of 14.0 with no gap is –3.64 dB, whereas with gaps of 1.0 and 2.0 mm they are –6.79 and –10.15 dB, respectively. Also, for the no-gap condition, the magnitude of the reflection coefficient dropped from –3.64 to –4.29 dB due to the decrease in dielectric constant from 14.0 to 8.0.

It is important to note that the change in magnitude of the reflection coefficient due to the change of dielectric constant of the concrete is less than that due to the change of gap between metal plate and specimen surface. The investigation into electric field intensity distributions in the model (shown and analysed below) indicated that this is one of the effects of electromagnetic wave propagation between the metal plate and the specimen (termed 'guided wave') when a gap occurs. This effect leads to greater losses in the electromagnetic energy of the waves reflected from, and penetrating into, the concrete. Furthermore, in this study this effect became a physical background of the proposed DWS, which is able to create, collect and measure the guided wave for the purpose of characterising the metal–concrete composite, including detecting and monitoring the gap between the metal plate and the concrete.
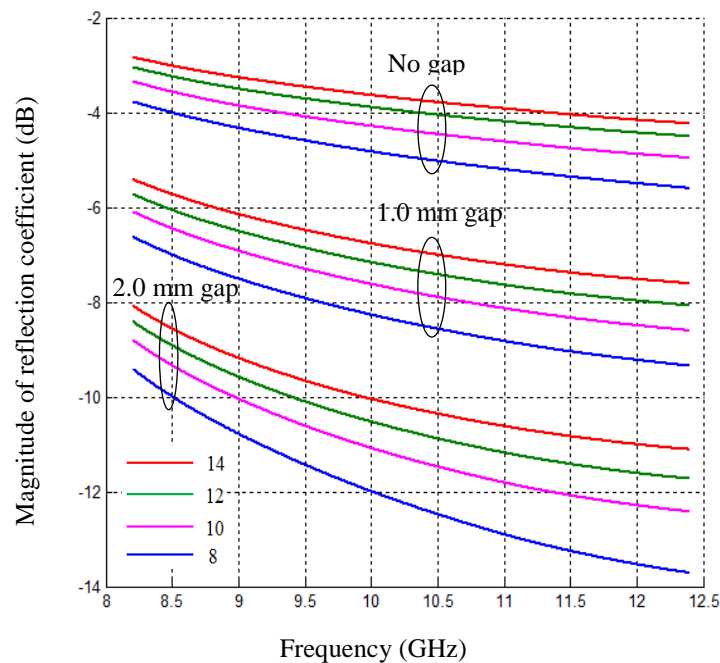
Figure 4.3: Simulated magnitude of reflection coefficient vs. frequency, for gaps of different magnitude between the metal plate and the concrete specimen and for different values of dielectric constant the single waveguide sensor.
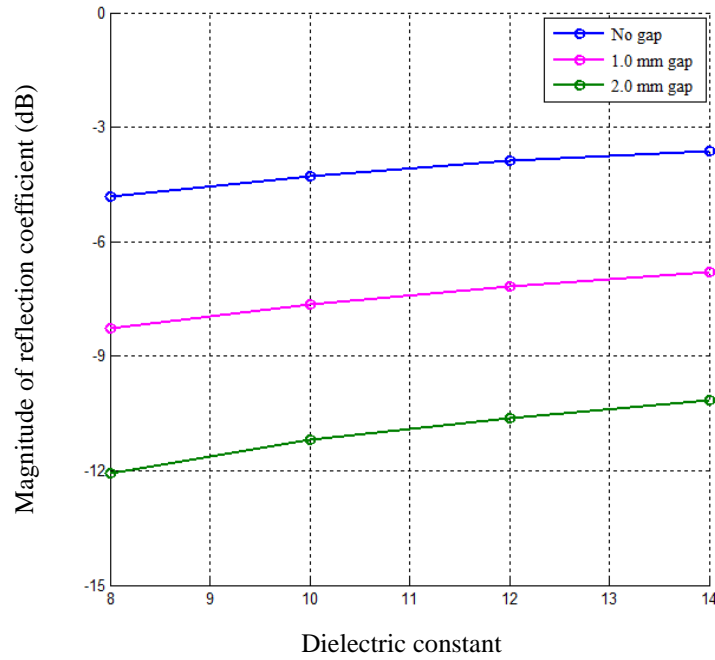
Figure 4.4: Simulated magnitude of reflection coefficient vs. dielectric constant of the concrete specimen for different gaps between the metal plate and the concrete specimen, using the single waveguide sensor at a frequency of 10.0 GHz.

Figure 4.5 shows the simulated magnitude of the reflection coefficient S_{11} vs. frequency with SWS and DWS, for different values of gap between metal plate and fresh concrete ($\varepsilon_r = 14.8 - j1.8$). Four values of the distance between the waveguide sections, L, were considered for the DWS study. The solid line represents S_{11} determined by DWS; the dotted line represents the S_{11} determined by SWS. It can be seen from the figure that, for $L = 5$ mm and 10 mm, S_{11} at gaps of 0.0 and 0.5 mm are almost the same for both SWS and DWS, but at gaps of 1.0, 1.5 and 2.0 mm, S_{11} is different for SWS and DWS. The differences tend to decrease as L increases to 20 mm. Larger L implies that larger areas of the concrete specimen are under inspection; however, it may result in a lower transmission coefficient. Considering both practical aspects, L has been chosen to be 15 mm for fabricating the DWS. For these reasons, $L = 15$ mm is assumed in all the following DWS simulations and measurements.

Figure 4.6 shows the magnitude of the transmission coefficient of an empty dual waveguide sensor vs. frequency for three metal–concrete gaps and four values of dielectric constant for each gap. It is clearly seen that the magnitude of the

transmission coefficient (in dB) is low at the no-gap condition and increases with increasing gap. Additionally, the magnitude of the transmission coefficient decreases with decreasing dielectric constant of the concrete specimen when there is a gap between the metal plate and the specimen, and for the no-gap condition the opposite is true. For instance, Figure 4.7 shows that at a frequency of 10.0 GHz, the magnitude of the transmission coefficient for a dielectric constant of 14.0 at no gap is –50.38 dB, and increases to –35.60 and –24.57 dB at 1.0 and 2.0 mm gap, respectively. For a gap of 1.0 mm, the transmission coefficient decreases from –35.60 to –37.61 dB when the dielectric constant of the concrete drops from 14 to 8, but for the no-gap condition it increases from –50.38 to –45.95 dB for the same reduction in dielectric constant.

Another important issue is the influence of the configuration of the waveguide sections in DWS. Figure 4.8 shows the electric field intensity distribution in amplitude and phase for E-plane and H-plane configurations at the plane of the DWS apertures for the no-gap condition, at 10.3 GHz. It clearly indicates that microwaves propagate mostly in the E-plane of the DWS apertures, providing stronger E-plane mutual coupling between them than in the H-plane configuration. This result is also consistent with coupling between two open-ended apertures on a common-ground plane radiated in free space, where the coupling coefficient of the E-plane exceeds that of the H-plane [182]-[183]. Therefore, to ensure higher mutual coupling between the waveguide apertures, the E-plane configuration between waveguide sections has been chosen.

The results show that the proposed DWS may have the following additional advantages over SWS for characterising metal–concrete structures: (1) data for transmission coefficient, (2) data for reflection coefficients at two different places on the metal–concrete interface at the same stage of concrete, and (3) a larger interface area under inspection.
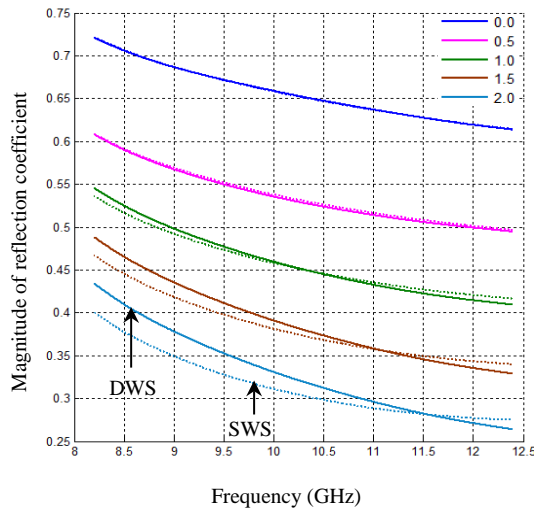
(a) L = 5 mm
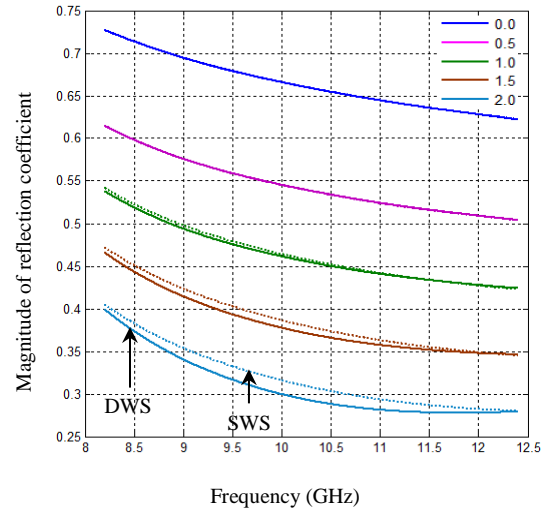
(b) L = 10 mm
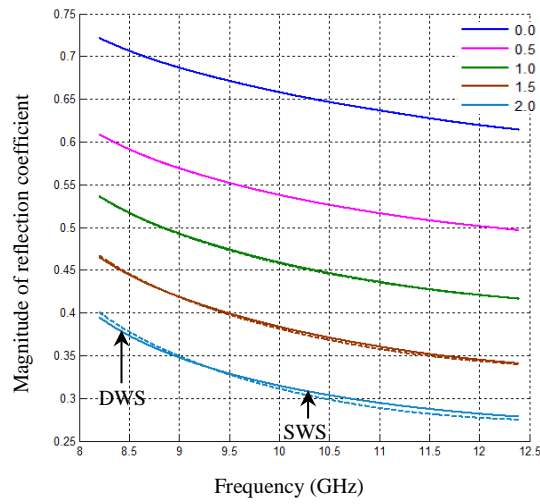
(c) L = 15 mm
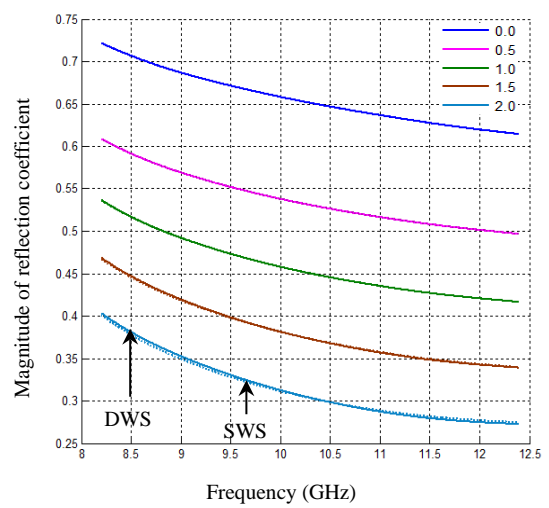
(d) L = 20 mm

Figure 4.5: Simulated magnitude of reflection coefficient vs. frequency at different gap values (mm) between the surfaces of the metal plate and concrete specimen (ε_r = 14.8 – j1.8) using SWS, and DWS with different distances between its waveguide sections.
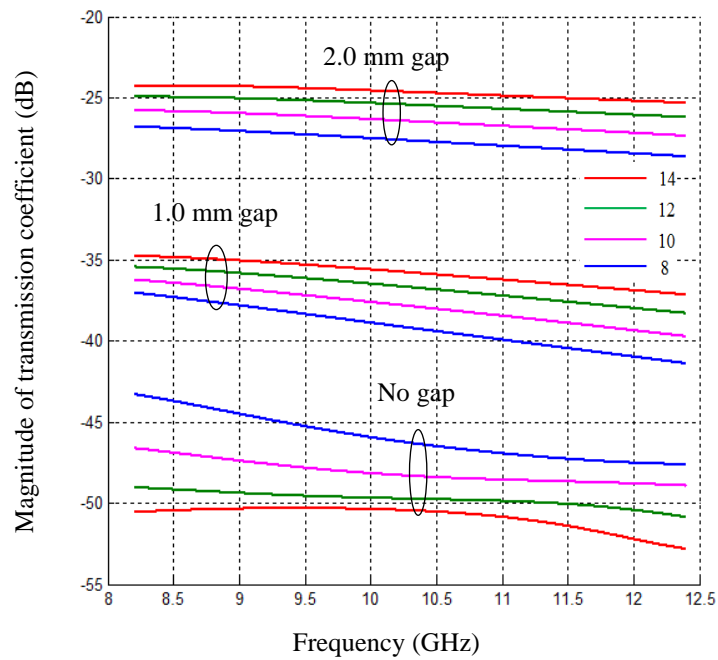
Figure 4.6: Simulated magnitude of transmission coefficient vs. frequency for different gap values between metal plate and concrete and for different dielectric constants, using the DWS.
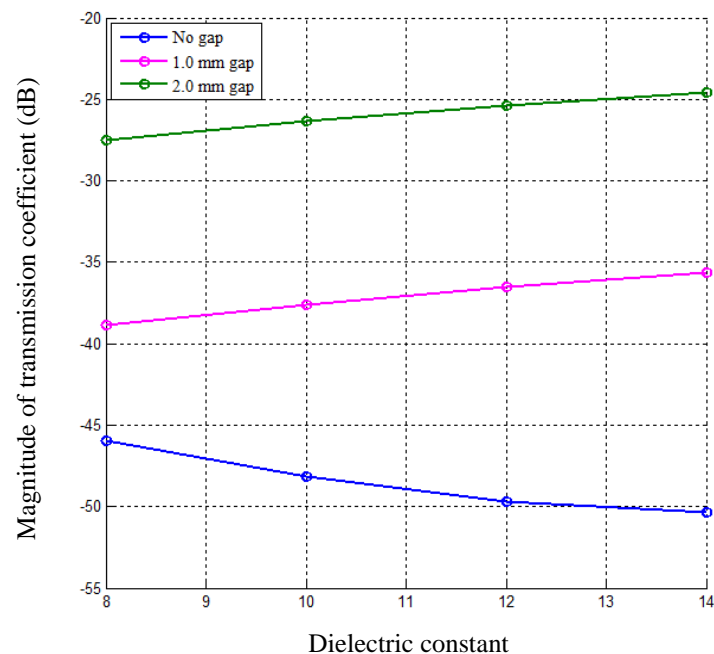
Figure 4.7: Simulated magnitude of transmission coefficient vs. dielectric constant of concrete specimen for three gaps between metal plate and concrete specimen using DWS at 10.0 GHz.
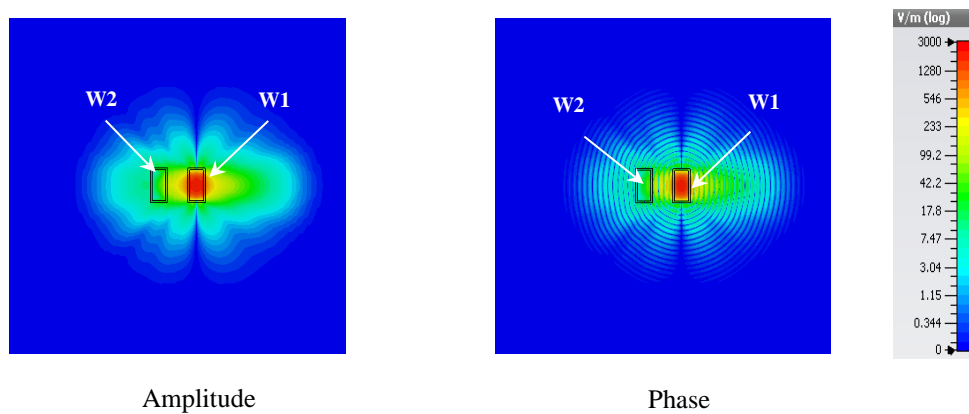
Amplitude   Phase

(a) E-plane configuration
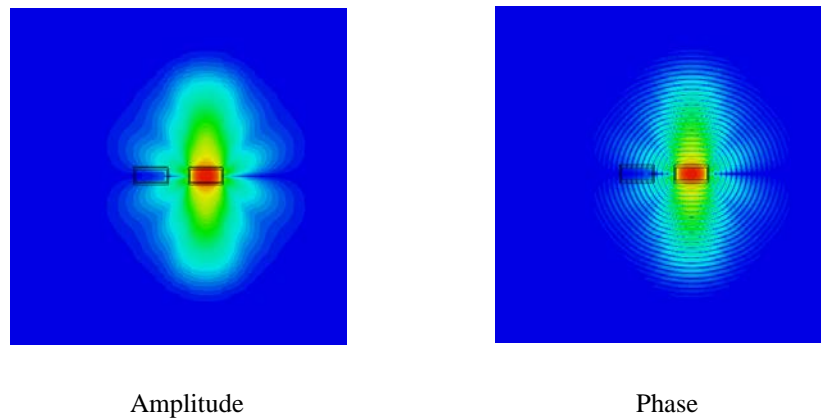
Amplitude   Phase

(b) H-plane configuration

Figure 4.8: Cross-sectional views of electric field intensity distribution (amplitude and phase) at the plane of DWS apertures, with no gap between surfaces of metal and concrete specimen (ε_r = 14.8 – j1.8) for (a) E-plane; and (b) H-plane configuration at 10.3 GHz.

4.2.3 Fabricated Sensor

In accordance with the model of the DWS developed and optimised in CST, the sensor was fabricated with two standard X-band rectangular waveguide sections and a 4 mm-thick metal plate with dimensions 250 mm × 250 mm, as shown in Figure 4.9. Dissimilar lengths of waveguide sections were chosen (97 mm and 45 mm) for

convenient connection with the measurement device. Two rectangular openings, each 25.4 mm $\times$ 12.7 mm (the external dimensions of the X-band rectangular waveguide) were cut in the central area of the metal plate. These were separated 27.70 mm centre-to-centre, producing a distance of 15 mm between the walls of the two waveguides. Then the waveguide sections were embedded and soldered into the openings as shown in Figure 4.9. The other flanged, open end of each waveguide section was fitted with a waveguide-coaxial adapter to allow for a cable connection to a performance network analyser (PNA).
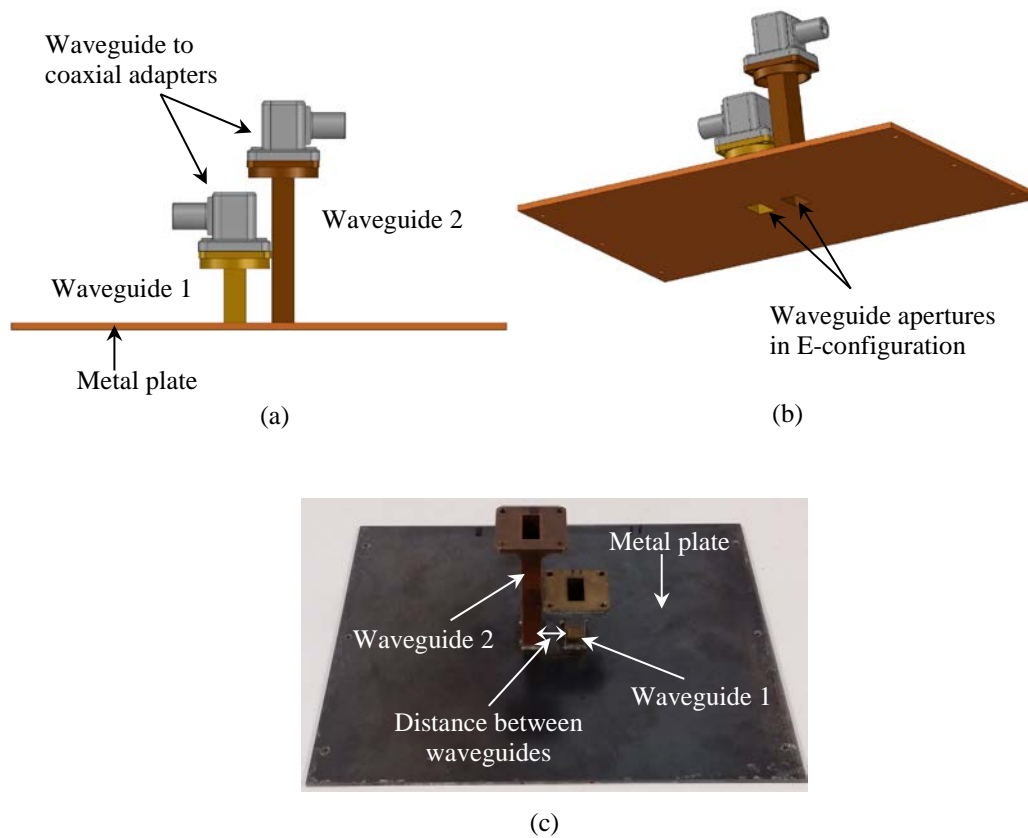
Figure 4.9: X-band dual waveguide sensor: (a) side view; (b) perspective view of the sensor design showing waveguide-coaxial adapters; and (c) photograph of fabricated sensor without adapters.

4.3   Measurement with Fresh Mortar Specimens

This section describes the measurement approach and gives the results for the DWS. The magnitudes of the reflection coefficients and transmission coefficients for

different metal plate–concrete gaps were measured during first four days after preparing mortar.

4.3.1 Measurement System

A schematic of a relatively simple microwave system for measuring the gap in a cement-based composite structure using DWS is shown in Figure 4.10. For simplicity, a cross-sectional side view of a part of a concrete–metal structure (a concrete-filled steel tube) is shown. The system consists of the DWS, a microwave transceiver, a measurement unit and an indicator. One section of the proposed DWS is used to illuminate the interface between the metal wall and the concrete and to receive the signal reflected from the structure, while another waveguide is used to receive the signal transmitted through the part of the structure between the sections, including the interface. The transceiver generates the microwave signal and transmits it to the DWS. The measurement unit and the indicator produce information about the magnitude of the reflection and transmission coefficients.
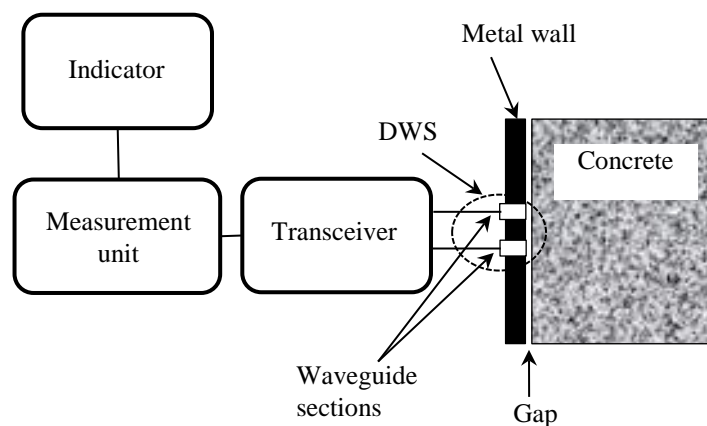
Figure 4.10: Schematic of the microwave measurement system with a cross-sectional side view of the DWS and the structure being tested.

4.3.2 Specimens and Measurement Setup

For simplicity, in this investigation fresh mortar (i.e., concrete without coarse aggregates such as gravel) was used. An open-topped 250 mm cubic wooden mould was used to prepare the mortar specimen, as shown in Figure 4.11a. The mortar was prepared by mixing cement, sand and water in an approximately 1:3:1 ratio and placed on the coarse aggregate/sand mixture. The thickness of the fresh mortar

specimen was 50 mm. A very thin, transparent polythene film was then used to cover the fresh mortar specimen to prevent the entry of water or sand–cement paste into the hollow DWS during measurement and affecting the measurements.

(a)

(b)
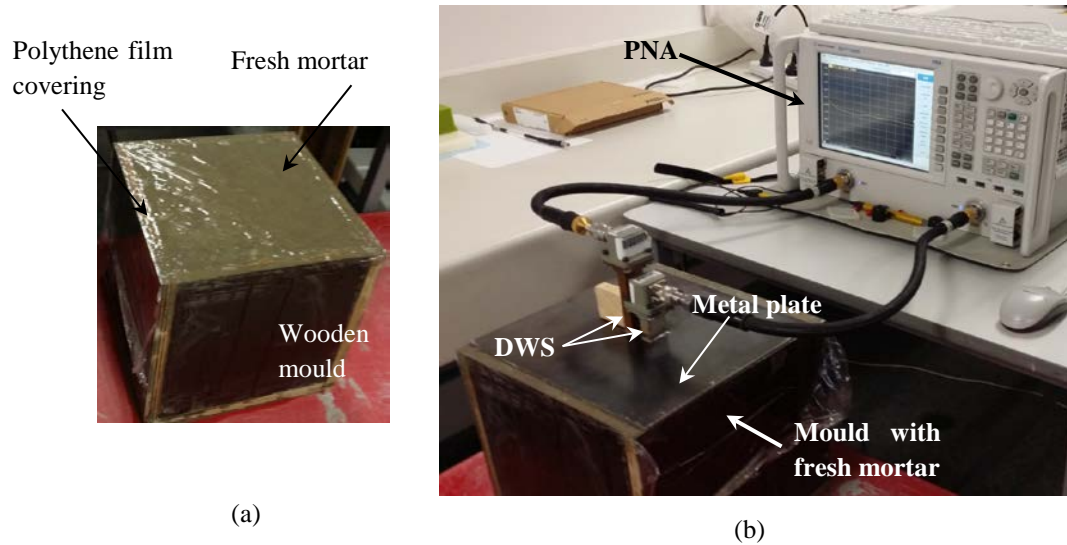
Figure 4.11: Photographs of (a) fresh mortar specimen in the mould, and (b) the measurement arrangement for detecting and monitoring the gap between the surfaces of the metal plate and the fresh mortar specimen using the DWS.

Figure 4.11b shows the experimental setup used in this investigation to measure the gap between the surfaces of the fresh mortar specimen and the metal plate, using the proposed DWS. An Agilent N5225A PNA was used as a combined unit of transceiver, measurement unit and indicator. Two waveguide sections were connected to the PNA via the waveguide coaxial adapters and joining cables. The desired gap (spacing) was created using thin paper sheets. The microwave sensor radiated microwave signals into the specimen and picked up the reflected and transmitted signals that were then processed by the PNA. The arrangement at the output apertures of the waveguide–coaxial adapters was calibrated using an X-band rectangular waveguide calibration kit. The reflection coefficient, S_{11} and the transmission coefficient S_{21} for the five gap values 0, 0.5, 1.0, 1.5 and 2.0 mm were measured on the first six hours of Day 1 (the day on which the fresh mortar specimen was prepared). Measurement data was stored in the PNA as a function of frequency, then processed and plotted using MATLAB software. S_{11} and S_{21} data for each gap

value was taken three times on each of Day 2, Day 3 and Day 4, and averaged. The hourly S_{11} and S_{21} values for each gap for the first six hours on Day 1 were also averaged.

4.3.3   Measurement Results and Discussion

Figure 4.12 shows the measured magnitude of the reflection coefficient, S_{11} (in dB) vs. frequency for different gap widths between the fresh mortar surface and metal plate in the first six hours after the specimen was prepared. It is seen that S_{11} decreased with the increase of gap widths over the entire frequency band in each hour. The differences of S_{11} between adjacent curves are almost constant, with the exception of the 0–0.5 mm gap curve. This comparatively small difference in the magnitude of S_{11} for the 0–0.5 mm gap was probably an artefact of the presence of the thin polythene film on top of the fresh, wet specimen during measurement. This is also seen clearly in Figure 4.13, which illustrates the magnitude of reflection coefficient vs. gap value in first six hours after preparing the mortar specimen at a frequency of 10.0 GHz that S_{11} started to decrease with the hourly ageing of the fresh mortar specimen. The figure indicates that at gap values less than 1.0 mm the magnitude of S_{11} decreased only marginally in the first six hours.

The measured magnitude of the transmission coefficient S_{21} vs. frequency for the different gap values between fresh mortar surface and metal plate in the first six hours after preparing the specimen are presented in Figure 4.14. It was found that S_{21} increased with the increase of gap value over the entire X-band frequency range in each hour. Although in some hours (e.g., hours 1, 3 and 4) the differences between adjacent S_{21} curves are not equal, the curves do not overlap and the gaps are distinguishable for each value of S_{21}.

Figure 4.15 shows another way in which S_{21} varied as a function of gap width in the first six hours after preparing the fresh mortar specimen, in this case at the single frequency of 10.0 GHz. It is clearly seen that the wider gaps correlate to an increase in S_{21}, but the ageing of the mortar specimen in its first six hours had little effect on the value when gaps were more than 0.5 mm wide.
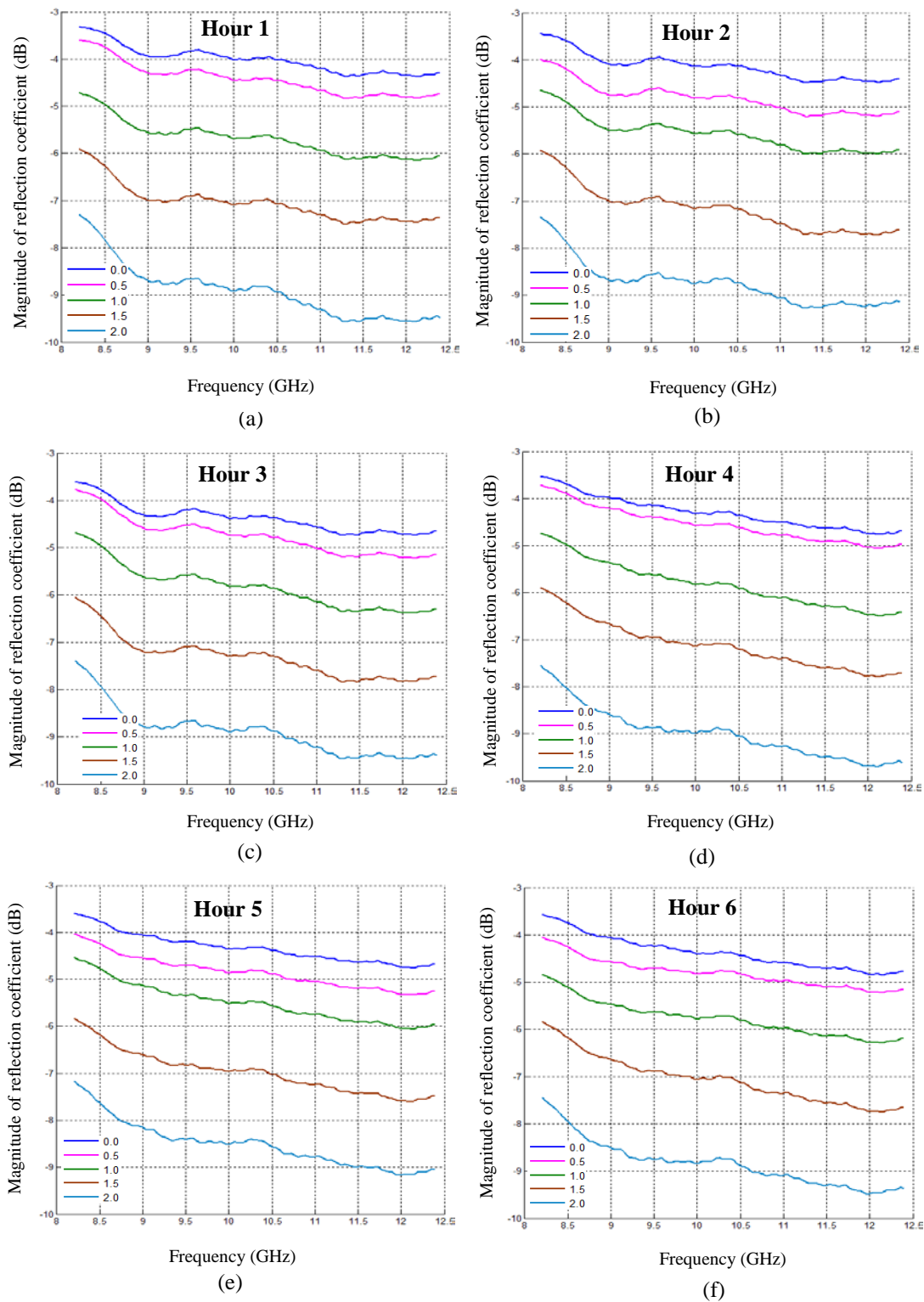
Figure 4.12: Measured magnitude of reflection coefficient vs. frequency at different gap values (mm) between the surfaces of the fresh mortar specimen and the metal plate at hour: (a) 1, (b) 2, (c) 3, (d) 4, (e) 5 and (f) 6.
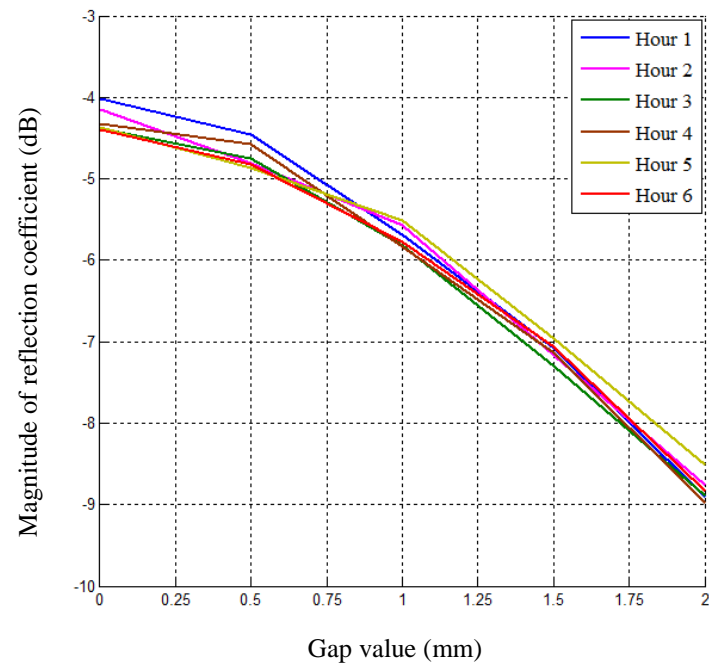
Figure 4.13: Measured magnitude of reflection coefficient vs. gap value between the surfaces of the fresh mortar specimen and metal plate in the first six hours, at a frequency of 10.0 GHz.
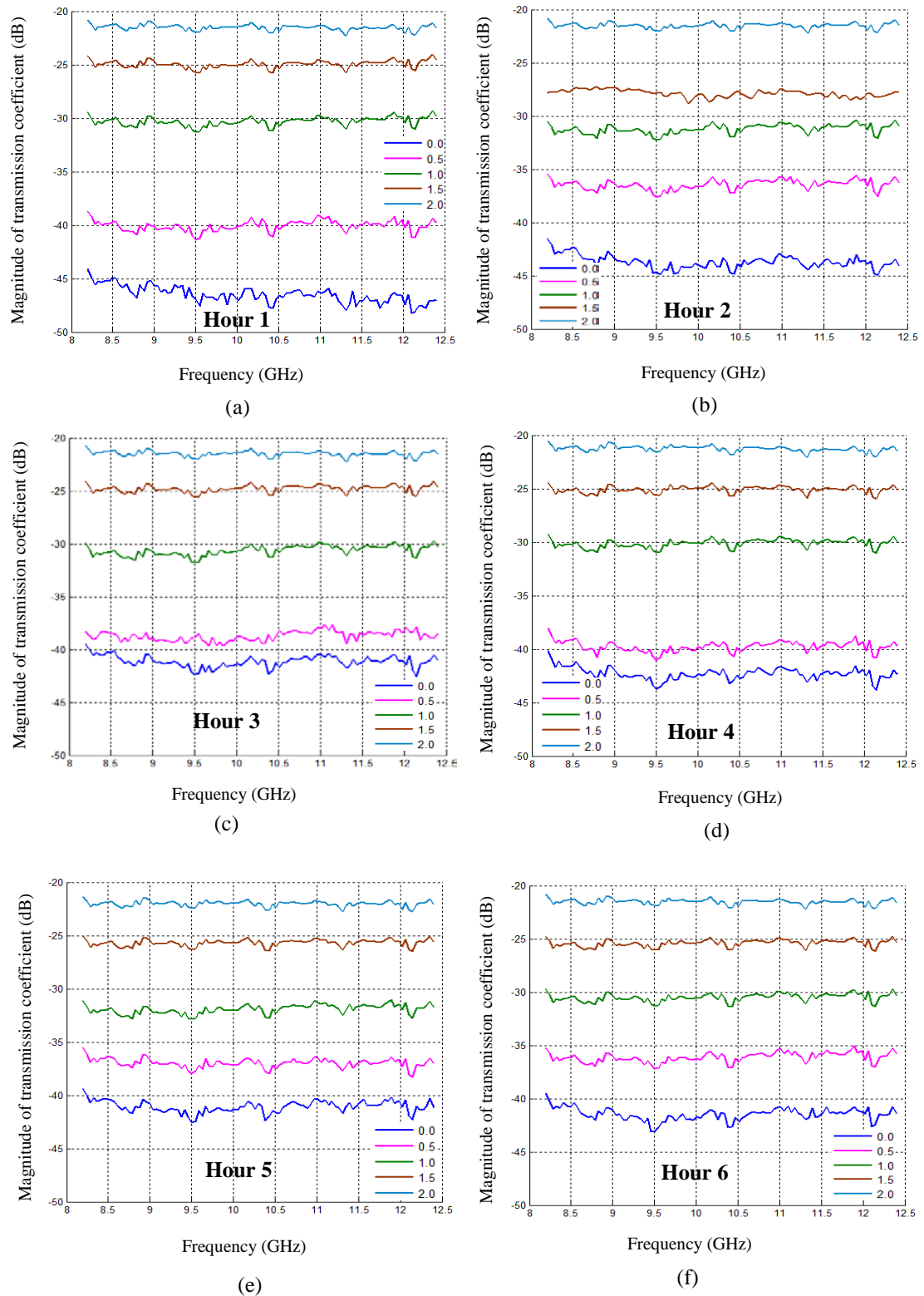
Figure 4.14: Measured magnitude of transmission coefficient vs. frequency for different gap values (mm) between the surfaces of the fresh mortar specimen and the metal plate at hour: (a) 1, (b) 2, (c) 3, (d) 4, (e) 5 and (f) 6.
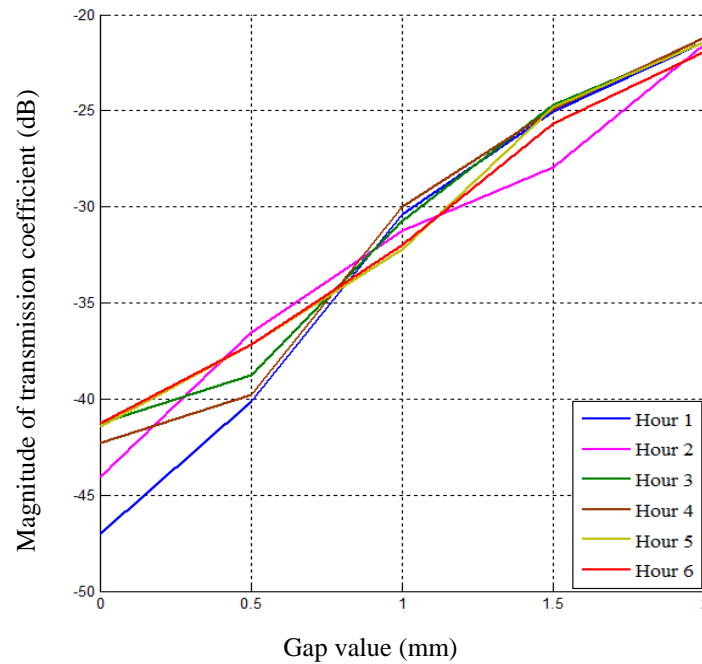
Figure 4.15: Measured magnitude of transmission coefficient vs. gap between fresh mortar specimen and metal plate in the first six hours, at a frequency of 10.0 GHz.

The average measured magnitude of the reflection coefficient, S_{11} in the first six hours after sample preparation is shown in Figure 4.16a as the Day 1 average S_{11} vs. frequency. For Days 2, 3 and 4, the average S_{11} was calculated from three measured reflection coefficient values taken on each day for each gap condition; these are shown in Figure 4.16b–d. The plots also show one standard deviation (STD) as $\pm \sigma$ on either side of the averaged curves at each frequency point of S_{11} for each gap value.

Several observations can be made from Figure 4.16. The average S_{11} decreases with increasing gap value over the entire frequency band. When the average S_{11} for any gap value (including the standard deviation) does not overlap that of adjacent gap values, the measured magnitude of the reflection coefficient clearly indicates a particular gap between the metal and fresh mortar surface. With this knowledge, the measurement data at the 0 and 0.5 mm gaps on Days 1 and 2 has a little uncertainty, and at the 0.5, 1.0 and 1.5 mm gaps for Day 4 the data has greater uncertainty; Day 3 shows the best measurement results. Figure 4.17 shows the average measured magnitude of the reflection coefficient as a function of gap value for different ages of mortar specimen in days after preparation. It indicates that S_{11} tended to decrease

with the age of the fresh mortar specimen, but the decrease is minor compared to the decrease in S_{11} related to the gap between metal and specimen surface.
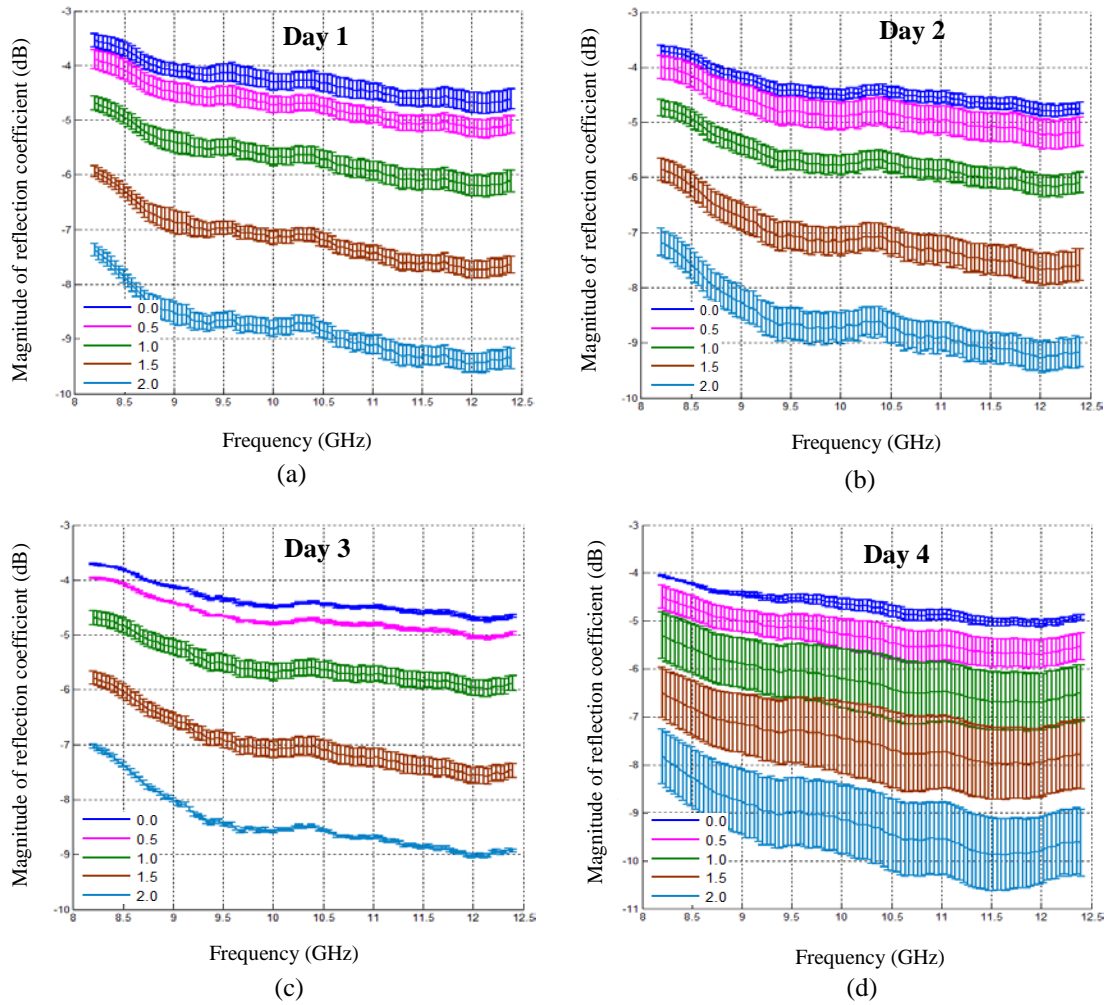
Figure 4.16: Average measured magnitudes of reflection coefficient vs. frequency, showing the standard deviation at different values of gap (mm) between the surfaces of fresh mortar and metal plate on the first four days: (a) Day 1, (b) Day 2, (c) Day 3 and (d) Day 4.
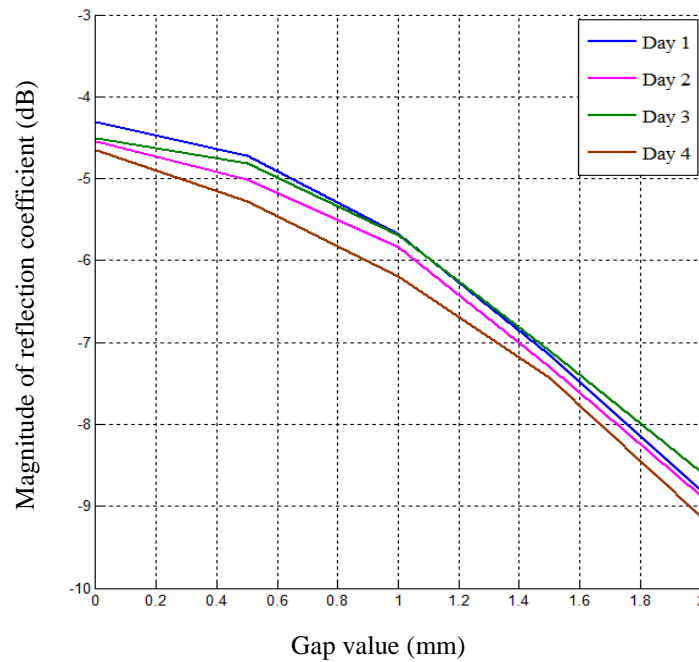
Figure 4.17: Average measured magnitude of reflection coefficient vs. gap value between fresh mortar specimens and metal plate on first four days at a frequency of 10 GHz.

Figure 4.18 shows the average measured magnitude of transmission coefficient S_{21} vs. frequency for different gap values on the first four days after preparing the fresh mortar specimen. Standard deviations of S_{21} for different gap values are also shown. It is clear that average S_{21} increases with increasing gap value. Similarly to the average S_{11}, when the average S_{21} with standard deviation does not overlap adjacent values, the measured magnitude of the transmission coefficient clearly indicates a particular value of the gap between metal and fresh mortar surface. Figure 4.18 shows that the measured S_{21} at 0 and 0.5 mm gap has a little uncertainty on Days 1 and 2, and at 0, 0.5, 1.0 and 1.5 mm gap on Day 4 it has higher uncertainty; Day 3 shows the best measurement results.

Figure 4.19 shows the average measured transmission coefficient in dB as a function of gap value for different ages of mortar specimen in days after preparation. It indicates that S_{21} starts to decrease with increasing age of the specimen, but this decrease is minor compared to that related to the size of the gap between the metal and specimen surfaces.
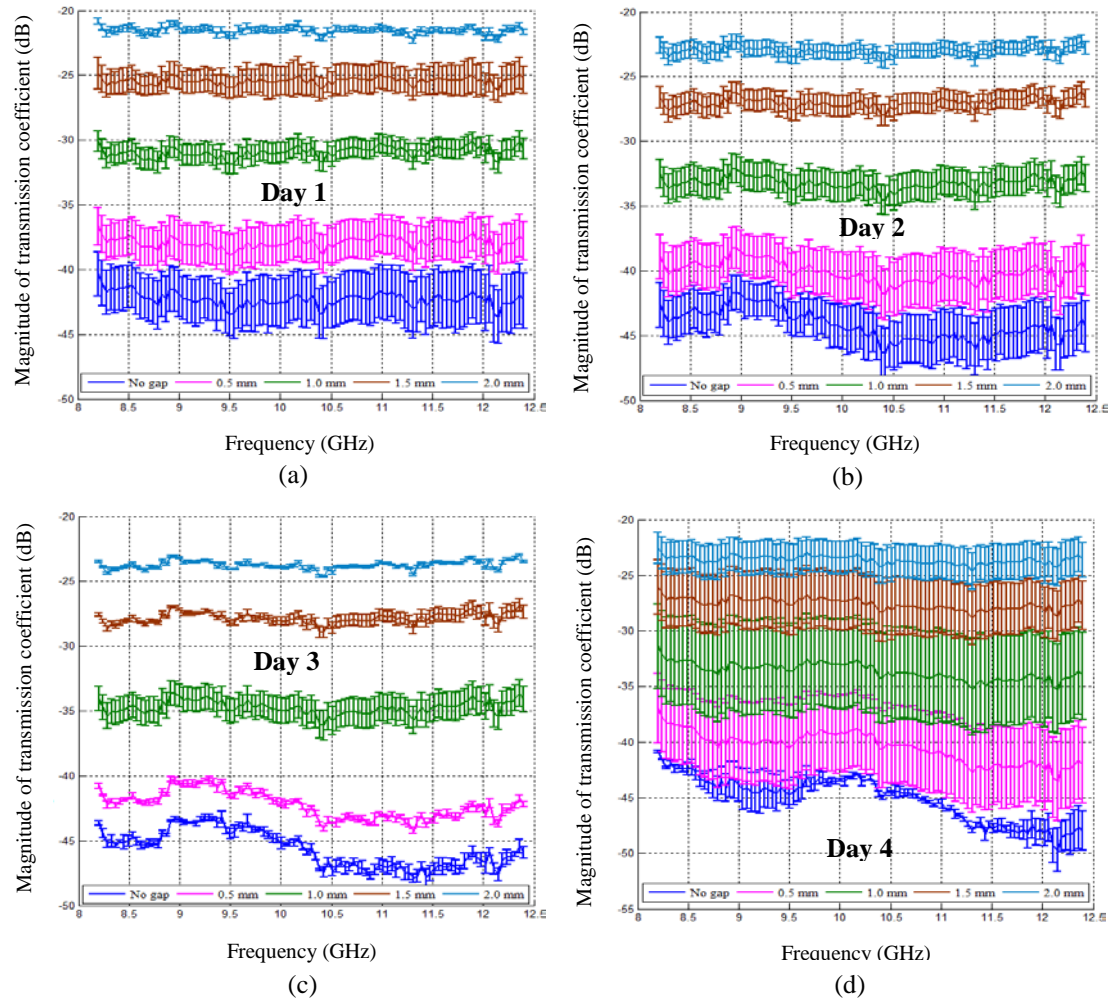
Figure 4.18: Average measured magnitude of transmission coefficient vs. frequency, showing standard deviations at different values of the gap between the surfaces of the fresh mortar specimen and the metal plate on the first four days after preparing the specimen: (a) Day 1, (b) Day 2, (c) Day 3 and (d) Day 4.
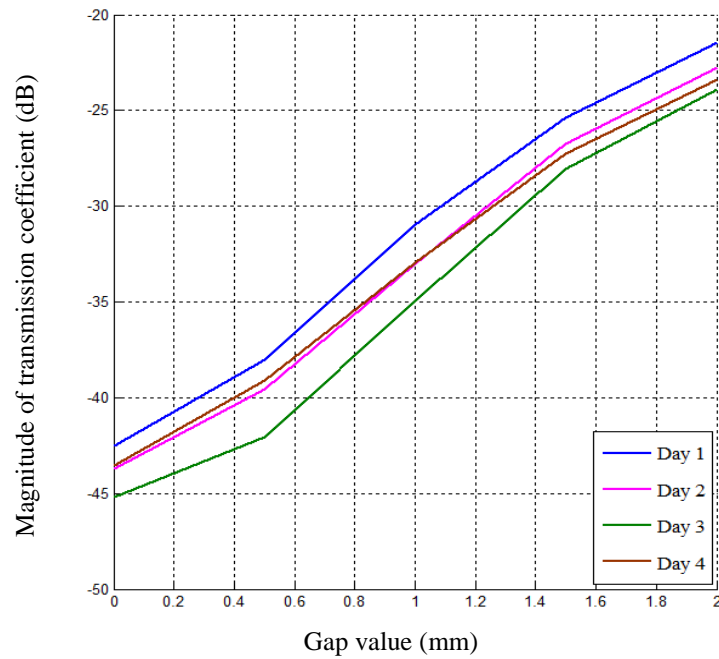
Figure 4.19: Average measured magnitude of transmission coefficient vs. gap value between fresh mortar specimen and metal plate on the first four days after mortar preparation, at a frequency of 10.0 GHz.

4.3.4   Comparison between Measurement and Simulation Results
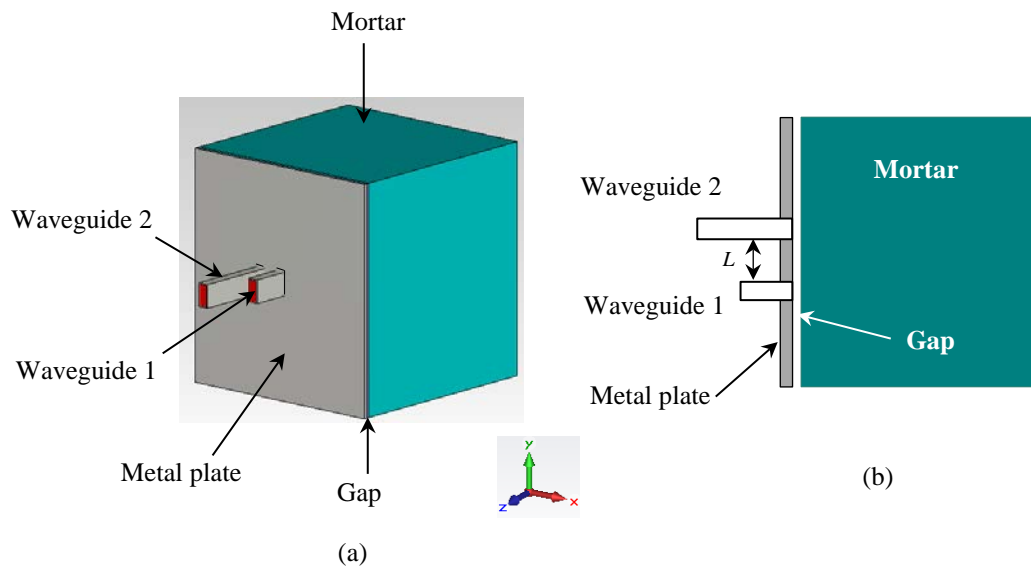
Figure 4.20: A model of DWS with fresh mortar specimen and gap between specimen and metal plate surfaces in CST: (a) perspective view, and (b) cross-sectional top view.

The model of the proposed dual waveguide sensor with mortar specimen is shown in Figure 4.20. The lengths of the waveguide sections are chosen as 97 mm

and 45 mm consistent with the measurement arrangement for the fresh mortar specimen. In the simulation, the dielectric permittivity of the fresh mortar was initially selected as 14.8 – j0.18, and subsequently varied for comparison with the measured results.

Figure 4.21 shows the average Day 1 measured magnitudes of the reflection coefficient with standard deviation, and the simulated reflection coefficient vs. frequency for different values of the gap between the fresh mortar specimen and the metal plate. It is seen that S_{11} decreased with increasing gap value and with frequency, both for the measured and the simulated results, which are similar and comparable for all gap values except 0 and 0.5 mm. The differences between adjacent S_{11} curves are equal in the simulations but not in the measured results, especially for gaps of 0 to 0.5 mm and from 0.5 to 1.0 mm. The differences in magnitude of the reflection coefficient at 0 and 0.5 mm gap are probably due to the presence of the thin polythene film placed over the fresh specimen during measurement, whose thickness and dielectric properties were not taken into account in the simulation.

Similar types of observations are found for the transmission coefficient S_{21} in Figure 4.22, which shows both the average measured and simulated S_{21} vs. frequency for Day 1 at different gap values. The simulated magnitudes of the transmission coefficients gaps wider than 0.5 mm agree well with the measured values. These findings are readily explained by Figures 4.23 and 4.24. Figure 4.23 shows the magnitude of the reflection coefficient vs. gap width for the average of the first four days' measurements for the fresh mortar and the simulations with variable dielectric constants at a fixed loss tangent of 0.105 and at the single frequency of 10.0 GHz. It is seen that at $\varepsilon_r' = 17$, the simulation curve is very similar to the average Day 4 curve. Likewise, the magnitude of the transmission coefficient for the first four days' average measurements and simulations with variable dielectric constants at a fixed loss tangent of 0.105 and a single frequency of 10.0 GHz is illustrated in Figure 4.24. It is clearly seen that at $\varepsilon_r' = 17$, the simulation curve agrees very closely with the measured results. The roughness of the top surface of the mortar specimen together with the thickness of the polythene film is possible reasons for the small differences between the measured and simulated results. Therefore, it is obvious that the

microwave dual waveguide sensor can be used to measure the gap between the fresh mortar specimen and the metal plate, provided that the dielectric properties of the specimen are known.
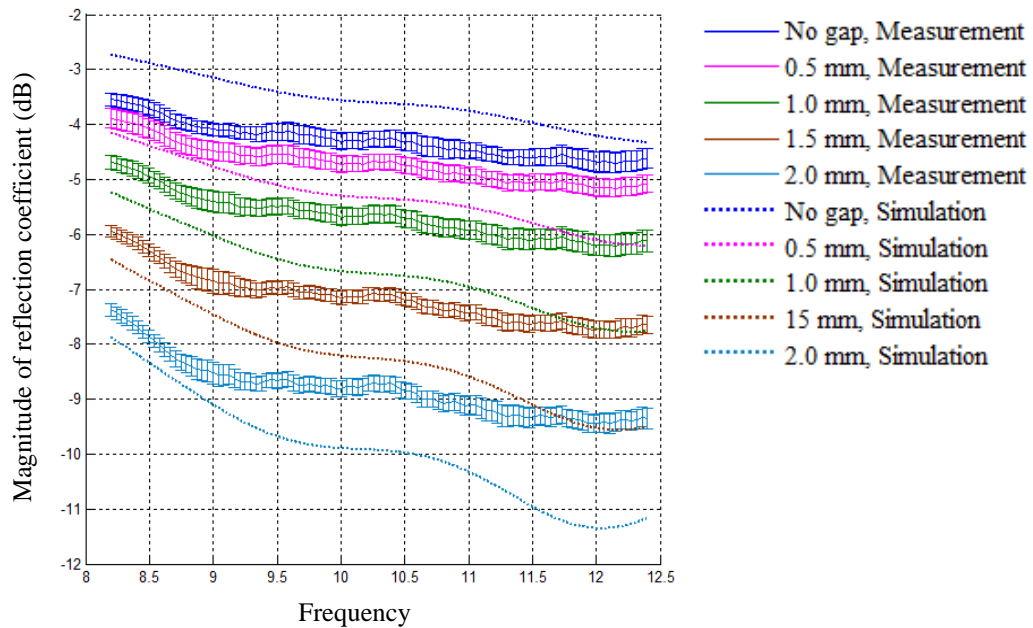
Figure 4.21: Comparison of measured and simulated magnitude of reflection coefficient vs. frequency for different values of the gap between the surfaces of metal plate and mortar specimen on Day 1 ($\varepsilon_r = 14.8 - j1.8$) using DWS.
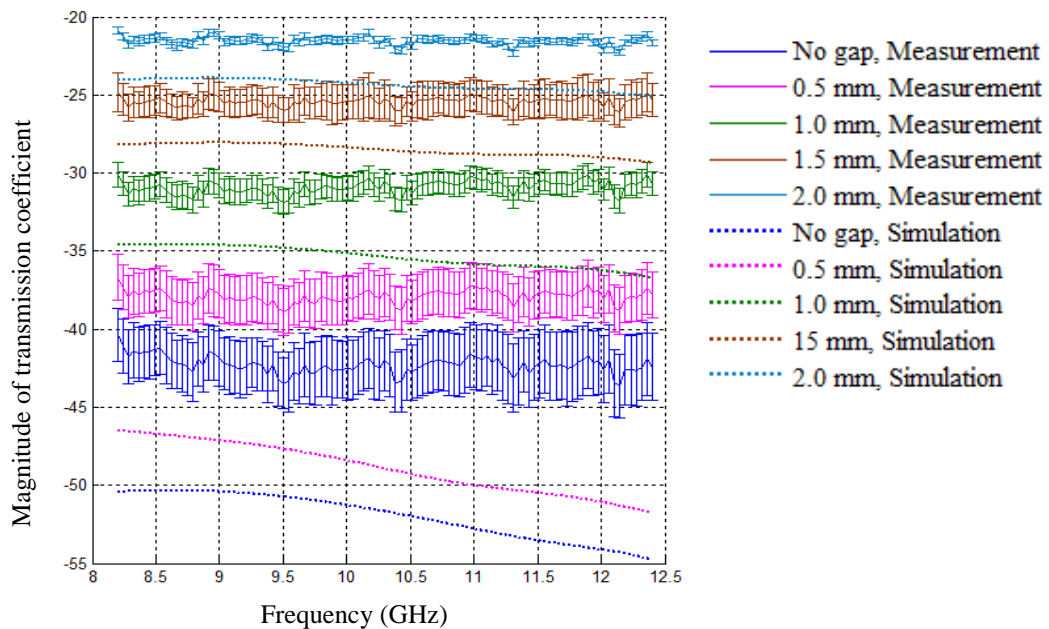
Figure 4.22: Comparison of measured and simulated magnitude of transmission coefficient vs. frequency for different values of the gap between the surfaces of metal plate and mortar specimen on Day 1 ($\varepsilon_r = 14.8 - j1.8$) using DWS.
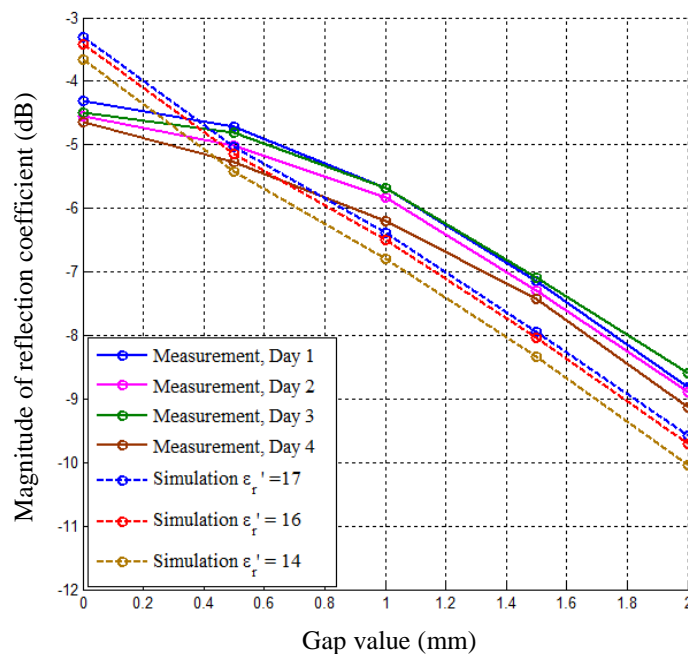
Figure 4.23: Comparison of measured and simulated magnitude of reflection coefficient vs. gap value at a frequency of 10.0 GHz using DWS.
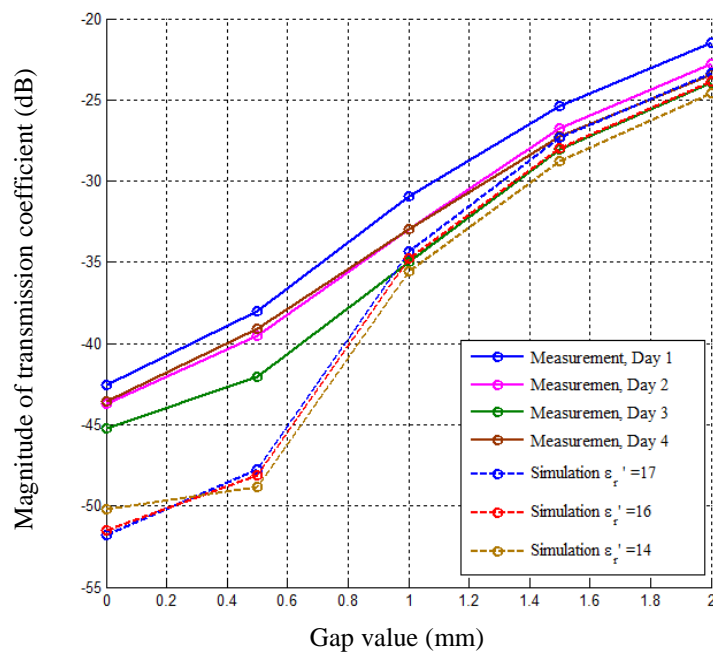
Figure 4.24: Comparison of measured and simulated magnitude of transmission coefficient vs. gap value at the frequency of 10.0 GHz using DWS.

Figure 4.25 is a cross-sectional side view of the simulated electric field intensity

distribution (amplitude and phase) inside a DWS, both in the interface area and in the fresh mortar ($\varepsilon_r = 17.0 - j3.4$) for the three gap values 0, 1 and 2 mm, at 10.3 GHz. Figure 4.25a shows that waveguide 1 (W1) radiated microwaves into the fresh mortar specimen and that a small proportion of these waves penetrated into the other waveguide (W2) for the no-gap condition. Figure 4.25b, c clearly show changes in the electric field intensity distribution at the interface of the mortar and metal surfaces due to differences in the gap. An animated phase version of these distributions (not included here) shows the propagation of electromagnetic waves between the metal and mortar surfaces (referred as guided waves) at the 1.0 and 2.0 mm gaps. These guided waves lead to losses in the electromagnetic energy of both the incident and reflected waves. Another important observation from Figures 4.25b, c is that a part of the guided wave and a part of the wave radiated by W1 in fresh mortar penetrated into W2, causing interference there. It was also found that for the no-gap condition, the microwave signals are more focused inside the mortar specimen; but, with an increase of the gap between metal and specimen they tend to scatter vertically within the mortar. The guided-wave phenomenon is clearly illustrated in Figures 4.26–4.28, described in the following.

Figure 4.26 shows a cross-sectional top view of the simulated electric field intensity distribution (amplitude and phase) inside W2 and the mortar specimen at 10.3 GHz. It is seen that when there is no gap, a very small amount of the transmitted signal is present in W2 (Figure 4.26a), but it increases significantly at gaps of 1.0 and 2.0 mm (Figure 4.26b, c).

Figure 4.27 illustrates the amplitude and phase of the electric field intensity distribution in a 3D cutting plane at 10.3 GHz. It is seen in Figure 4.27a that, in the no-gap condition at $x = 0$ in the yz cutting plane, microwave signals radiating from W1 penetrate only into the mortar specimen in a focused way, and very little of the signal enters W2; however, for 1.0 and 2.0 mm gaps, the microwave signals pass through the gaps between the metal and the fresh mortar specimen as guided waves, and establish a strong mutual coupling between the waveguides. Therefore, a significant amount of the signal is present in W2 (Figure 4.27b, c).

Figure 4.28 illustrates the amplitude and phase of the electric field distribution in

the *zx* cutting plane at $y = 27.7$ mm (i.e., in the middle of W2) for 0, 1.0 and 2.0 mm gap conditions at 10.3 GHz frequency. It is clearly seen that the gap between the metal plate and the mortar specimen contributed guided wave signals to W2.
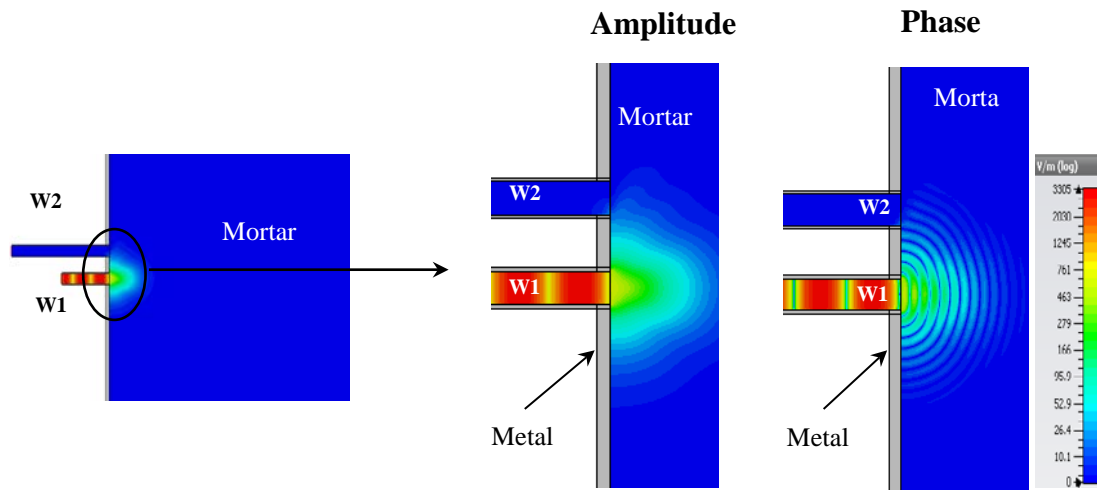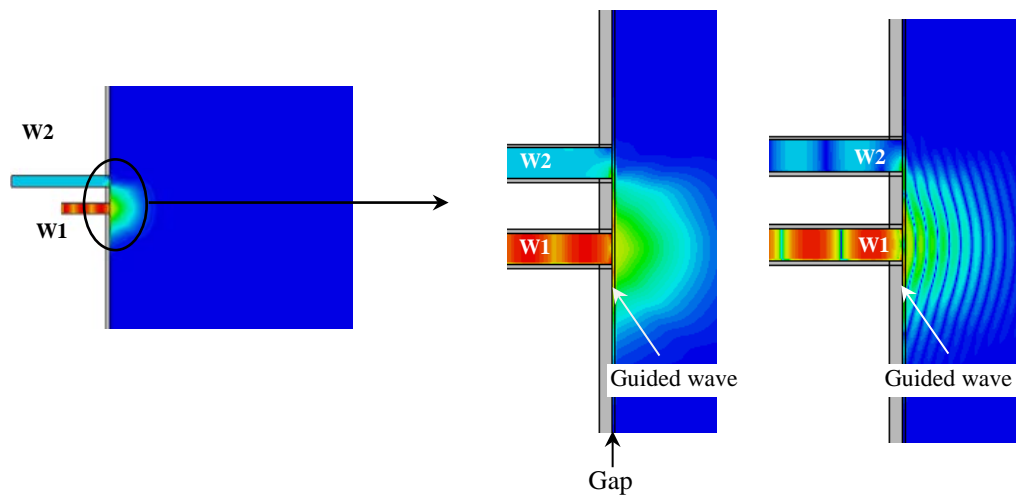
Amplitude   **Phase**

(a) No gap between metal and fresh mortar

(b) 1.0 mm gap between metal and fresh mortar
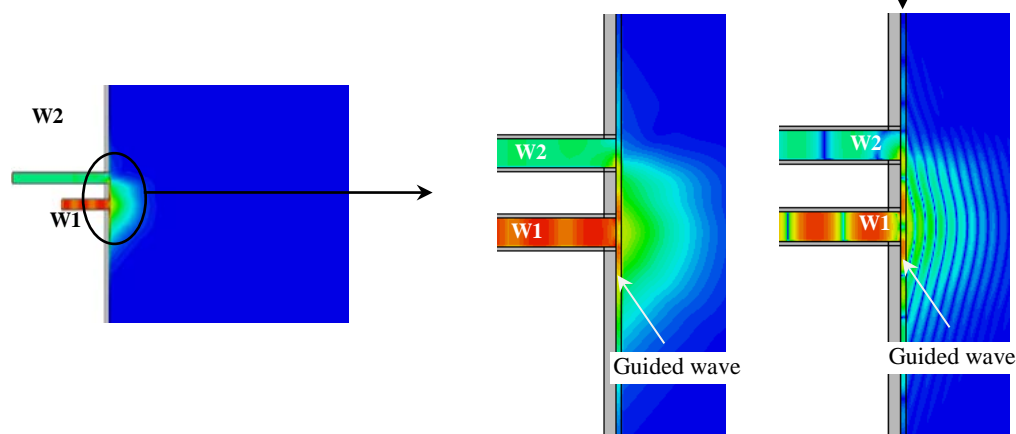
(c) 2.0 mm gap between metal and fresh mortar

Figure 4.25: Cross-sectional side view of electric field intensity distribution inside waveguides of DWS and fresh mortar specimen ($\varepsilon_r = 17.0 - j3.4$) for different values of the gap between the metal and specimen surfaces at 10.3 GHz.

Amplitude   **Phase**
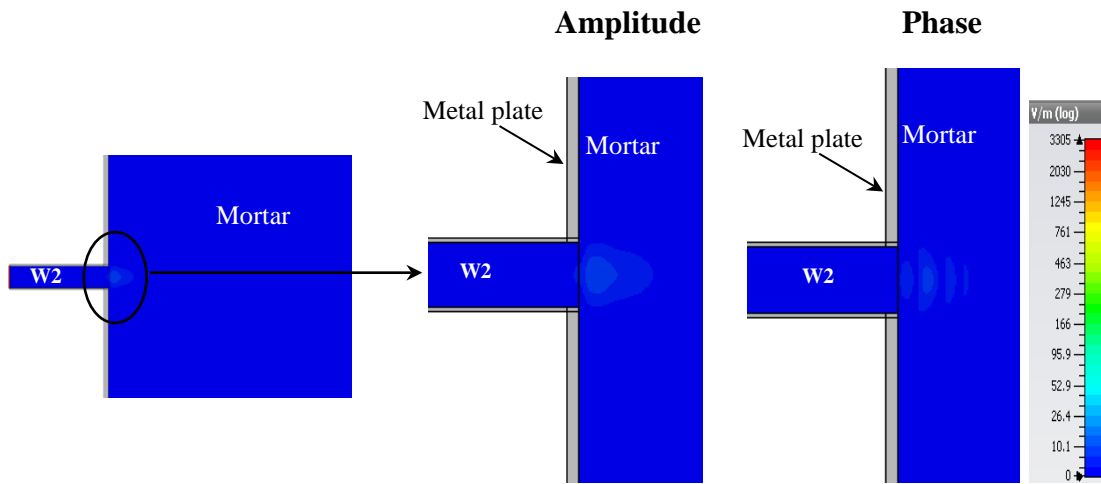
(a) No gap between metal and fresh mortar
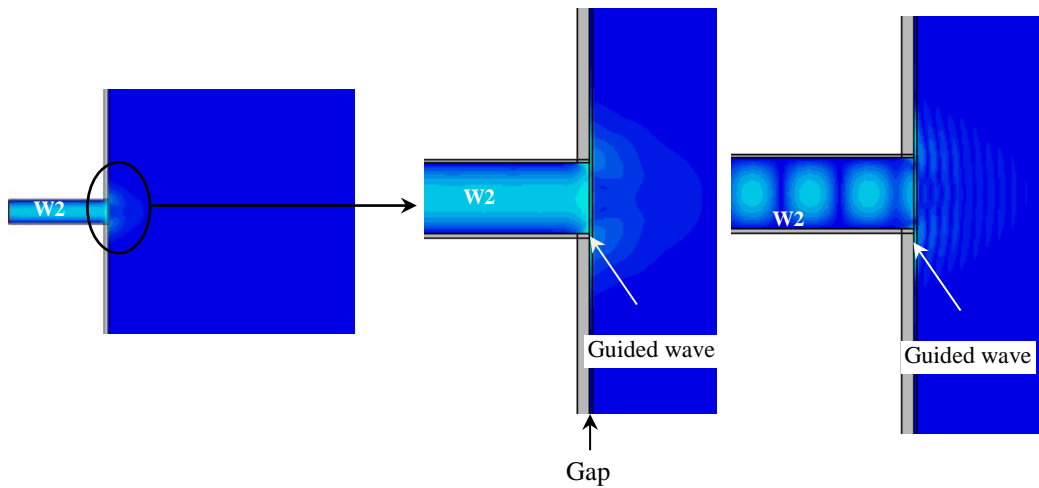
(b) 1.0 mm gap between metal and fresh mortar
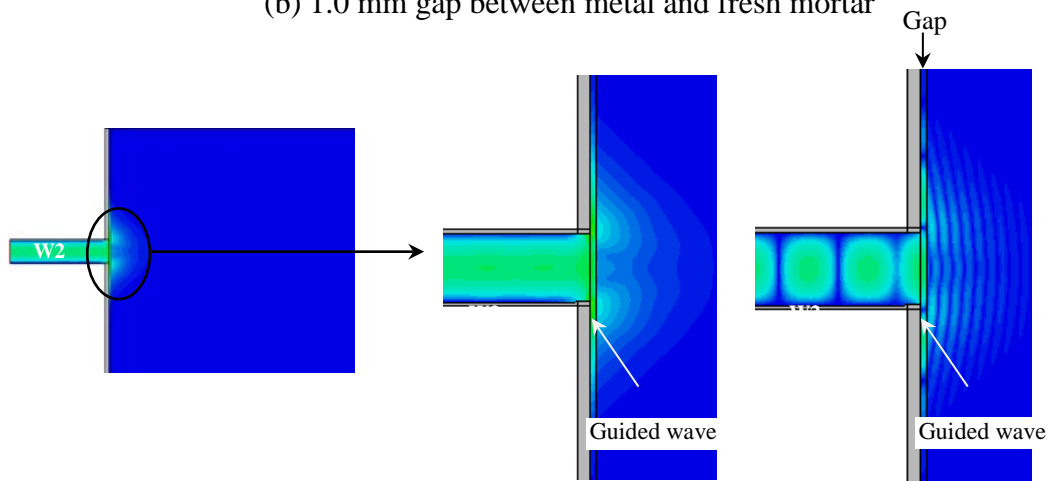
(c) 2.0 mm gap between metal and fresh mortar

Figure 4.26: Cross-sectional top view of electric field intensity distribution inside waveguide 2 of DWS and fresh mortar specimen (ε_r = 17.0 – j3.4) for different values of gap between surfaces of metal and specimen at 10.3 GHz.

Amplitude

Phase

(a) No gap between metal and fresh mortar

(b) 1.0 mm gap between metal and fresh mortar

(c) 2.0 mm gap between metal and fresh mortar
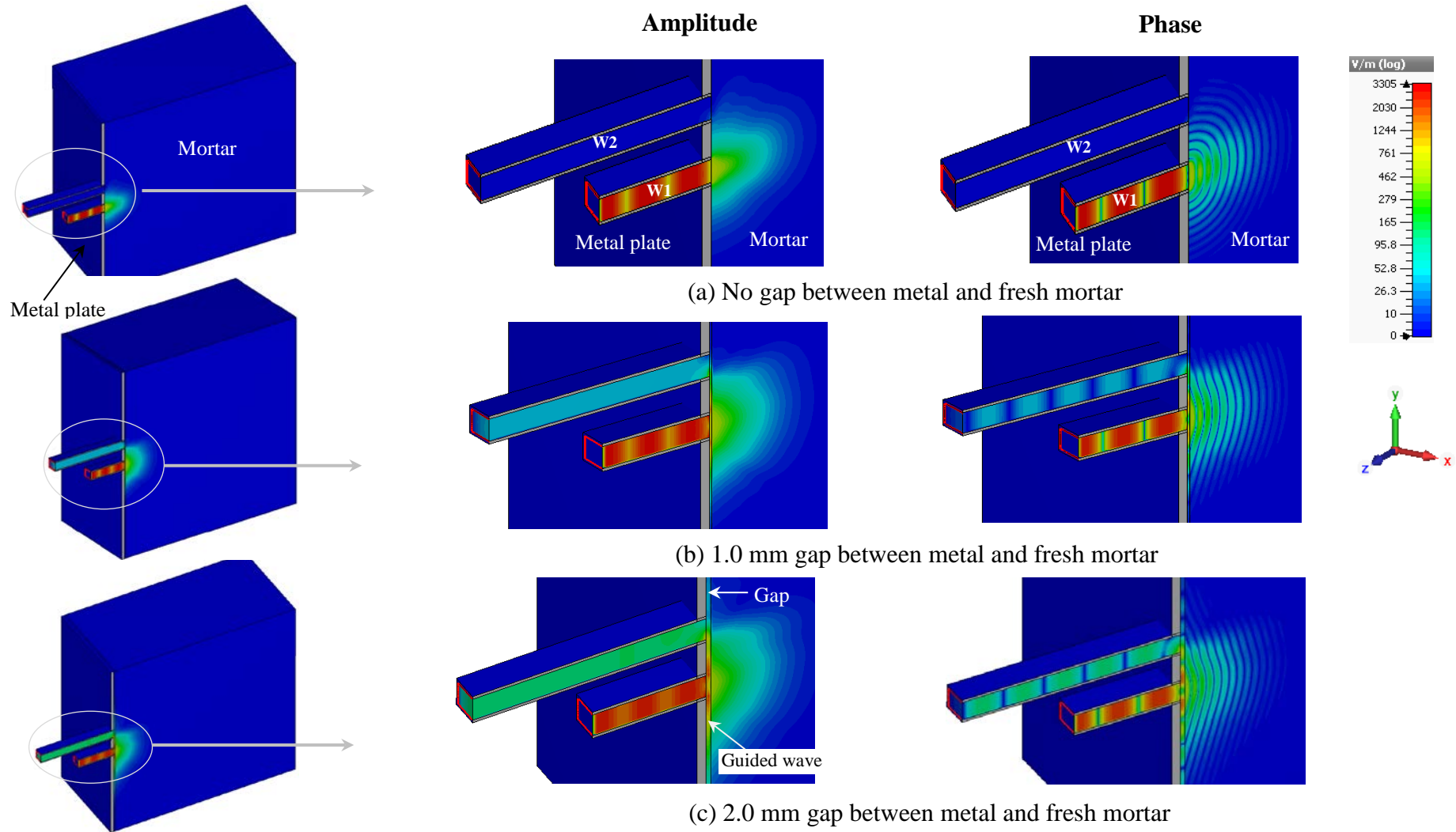
Figure 4.27: Electric field intensity distribution inside waveguides of DWS and fresh mortar specimen (ε_r = 17.0 – j3.4) for different values of the gap between the metal and specimen surfaces at $x = 0$ of the yz cutting plane at 10.3 GHz.

(a) No gap between metal and fresh mortar

(b) 1.0 mm gap between metal and fresh mortar

(c) 2.0 mm gap between metal and fresh mortar
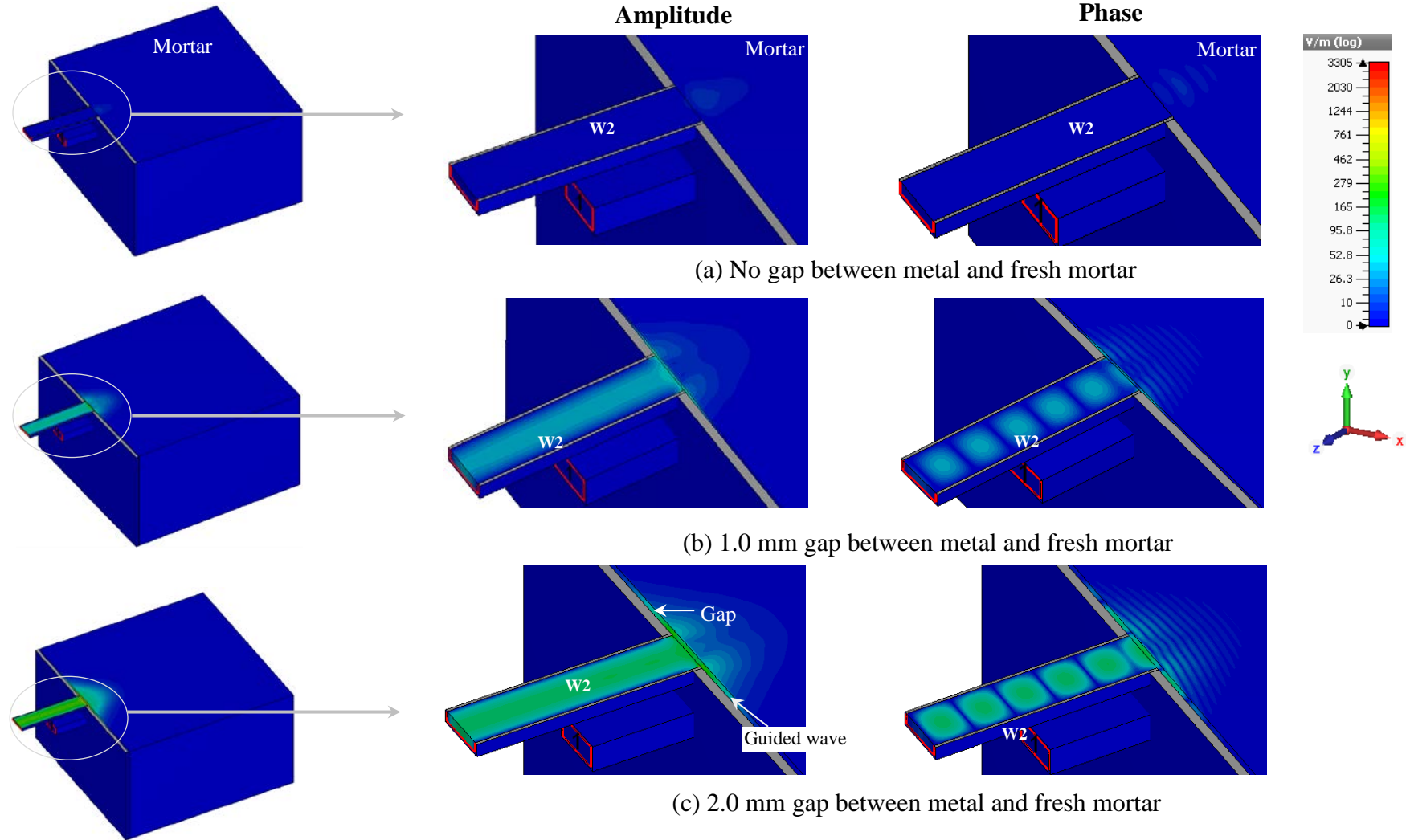
Figure 4.28: Electric field intensity distribution inside waveguide 2 of the DWS and the fresh mortar specimen ($\varepsilon_r = 17.0 - j3.4$) for different values of the gap between the metal and specimen surfaces at $y = 27.7$ (i.e., middle of waveguide 2) of the zx cutting plane at 10.3 GHz.

4.4   Measurement with Fresh Concrete Specimens

This section presents the measurement approach and measurement results for fresh concrete specimens using the DWS. The magnitudes of the reflection coefficients and transmission coefficients at different values of the gap between fresh and early-age concrete specimens and the metal plate were measured. Firstly, the measurements were taken at hour 1 and hour 6 of Day 1 of the fresh concrete specimen. Then S_{11} and S_{21} were also measured at different gap values on Days 2 and 3 of the concrete specimen.

4.4.1   Specimens and Measurement Setup
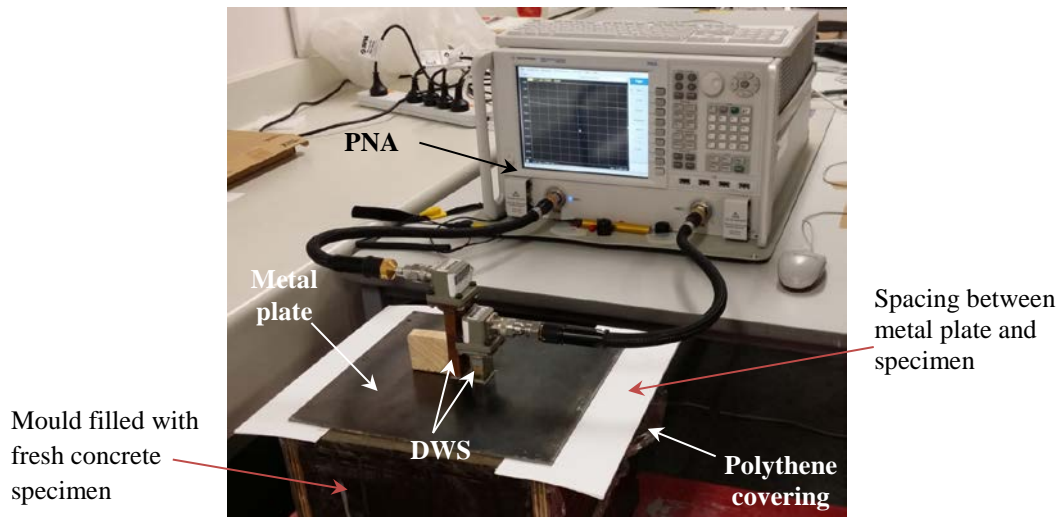
Figure 4.29: Experimental setup for measuring the gap between the fresh concrete specimen and metal plate surfaces using the microwave DWS.

A fresh concrete specimen was prepared by mixing cement, sand, coarse aggregate and water in roughly 2:4:4:1 ratio, and the mould was filled with the fresh concrete mix as shown in Figure 4.29. A very thin, transparent polythene film was used to cover the fresh concrete specimen during measurement to prevent the entry of water or sand-cement paste into the empty dual waveguide sections and affecting the measurement results. The measurement approach was similar to that described in subsection 4.3.2.

The magnitude of the reflection coefficient S_{11} and the transmission coefficient S_{21} were measured for five different gap values (i.e., 0, 0.5, 1.0, 1.5, 2.0 mm) at hours 1

and 6 of Day 1 of preparing the fresh concrete specimen. S_{11} and S_{21} were measured on Days 2 and 3 for each gap value three times on each day and were averaged.

4.4.2 Measurement Results and Discussion

Figure 4.30 shows the measured magnitude of the reflection coefficient vs. frequency for five values of the gap between the metal and fresh concrete surfaces, taken at hours 1 and 6 on Days 2 and 3 after preparing the specimen. It is seen that at hour 1, S_{11} decreases with increasing gap value; however, the differences between S_{11} at the different gap values are not equal over the full frequency band; rather, the differences decrease at frequencies above 10.5 GHz. It is observed that with increasing concrete age, S_{11} decreases at all gap values: for instance, for the no-gap condition at 10.0 GHz and at the concrete ages of hours 1 and 6 on Days 2 and 3, S_{11} is respectively –7.10, –12.80, –14.40 and –14.60 dB.

Figure 4.31 illustrates the measured transmission coefficient vs. frequency at different values of the gap between the surfaces of the metal plate and the fresh concrete at hours 1 and 6 on Days 2 and 3. It is clearly seen that S_{21} increases with increasing gap value, and that the differences of S_{21} between adjacent gap values decreases with increasing gap value. It is also observed that S_{21} decreases with increasing concrete age for all gap conditions: for example, the value of S_{21} for a 1.0 mm gap between the hour 1 concrete and the metal plate at 10.0 GHz frequency is –14.6 dB, decreasing to –16.1, –18.5 and –18.7 dB for concrete of hour 6, on Days 2 and 3, respectively, for the same gap value and at the same frequency.

In Figure 4.32 shows the magnitudes of both the reflection coefficient and the transmission coefficient vs. gap value between the metal plate and the fresh concrete specimen at different ages and at a frequency of 10.6 GHz. It is seen that for hour 1 concrete, S_{11} decreases sharply with gap value non-monotonically; however, for hour 6, on Days 2 and 3, S_{11} decreases monotonically with gap value at a slower rate (Figure 4.32a). Conversely, it is observed in Figure 4.32b that S_{21} increases with increase in gap value; at gap values greater than 0.5 mm, the value of S_{21} for hour 1 concrete is seen to drop significantly to the Day 2 and Day 3 values. During specimen preparation for this laboratory investigation, it was found that the sand to be used in the concrete mix was wet: because of this, the fresh concrete specimen contained more

moisture in the first few hours than the standard fresh concrete specimen.
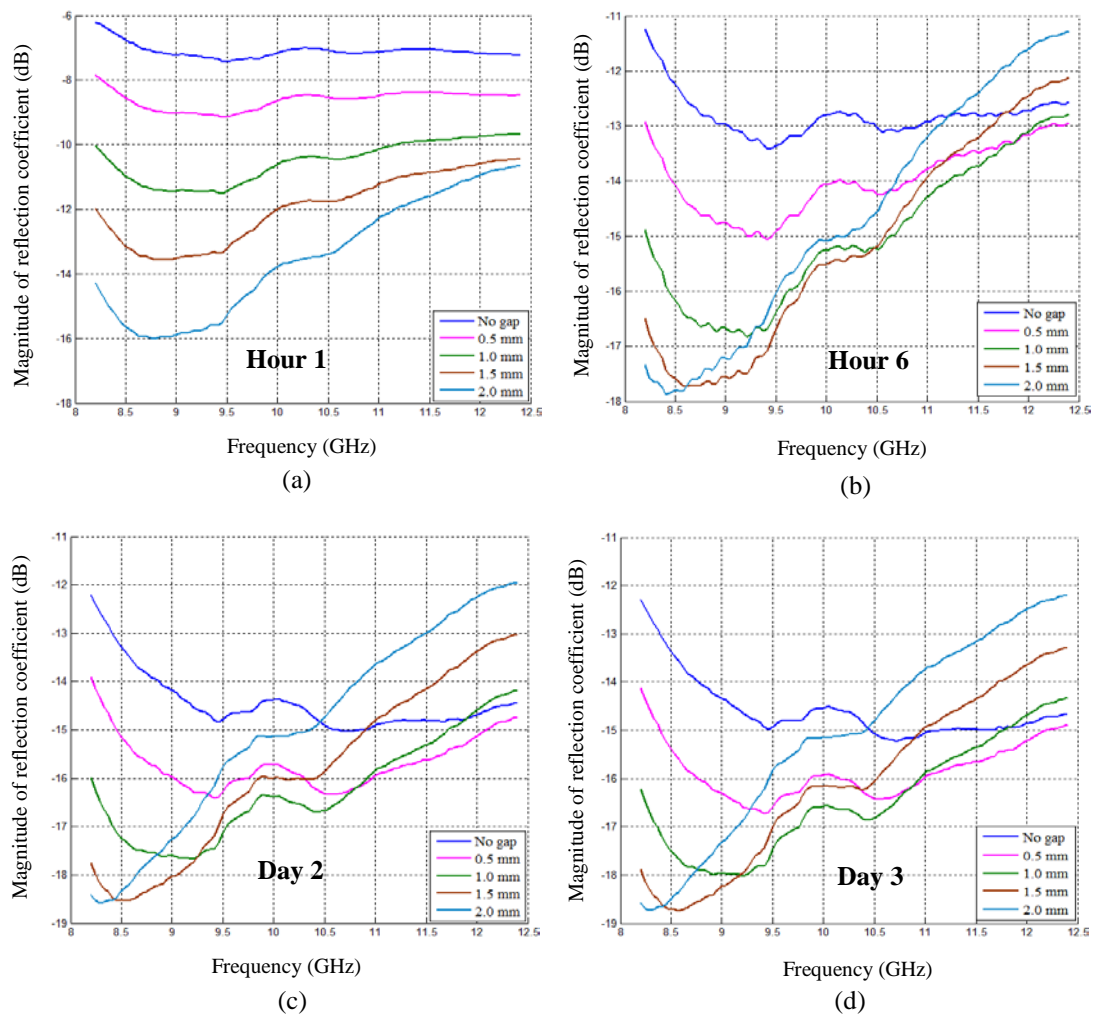
Figure 4.30: Measured magnitude of reflection coefficient vs. frequency at different values of gap between the metal and fresh concrete surfaces at four different times after preparing the specimen.
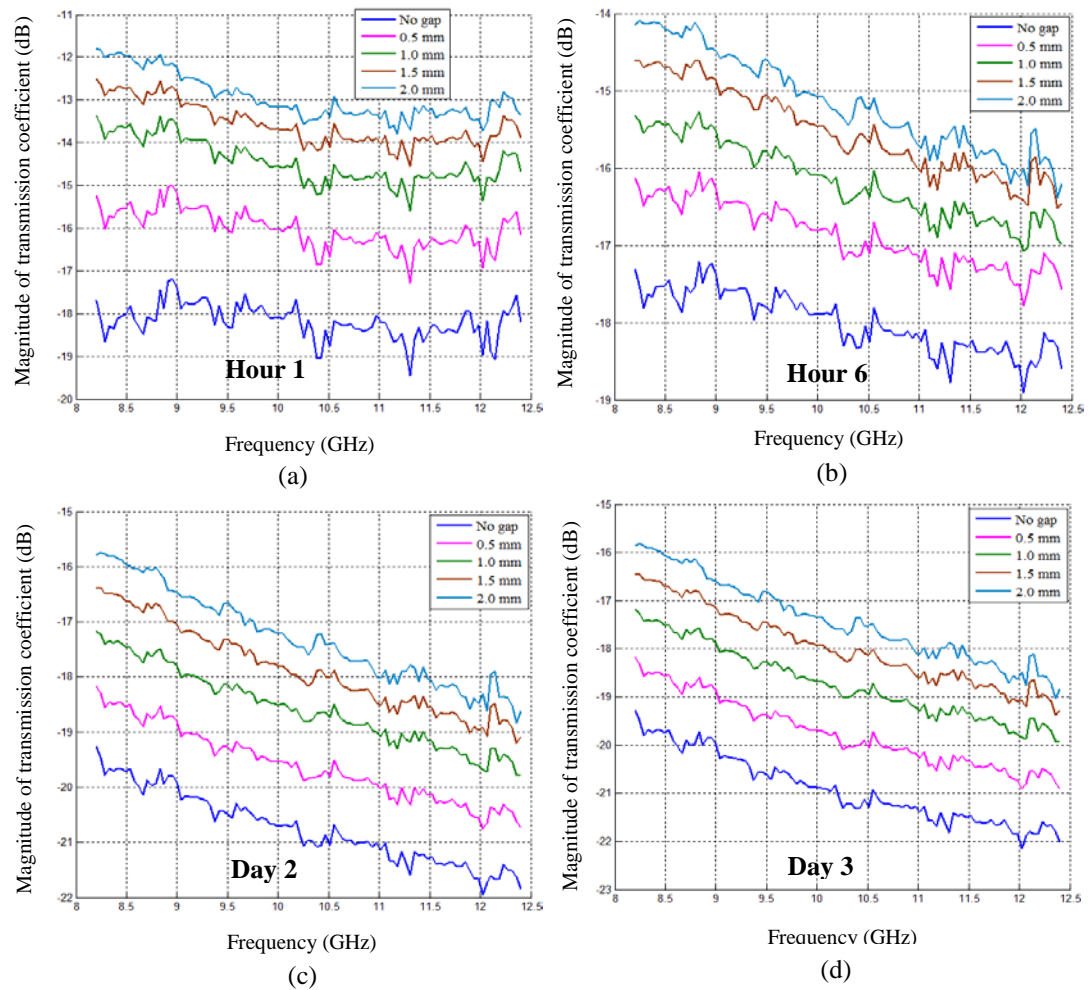
Figure 4.31: Measured magnitude of transmission coefficient vs. frequency at different values of gap between the metal and fresh concrete surfaces at four different times after preparing the specimen.
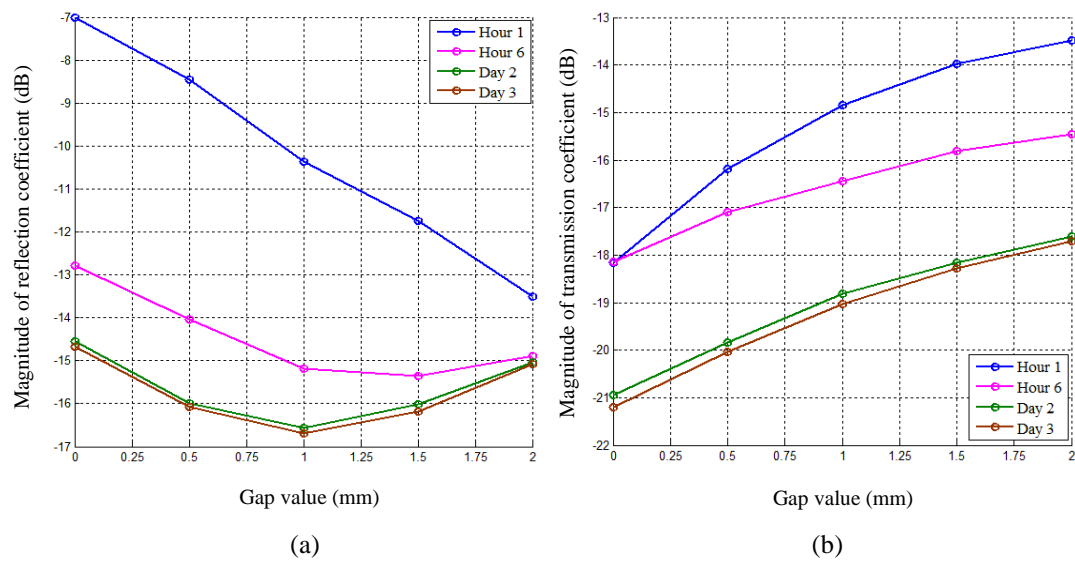
Figure 4.32: Measured magnitude of (a) reflection coefficient, and (b) transmission coefficient vs. gap values between the metal plate and fresh concrete surfaces at 10.6

GHz using DWS.

4.5   Measurement with Dry Concrete Specimens

This section describes the measurement procedure and results for different gap values between the dry concrete specimen and the metal plate of the DWS, as a function of the reflection coefficient and transmission coefficient. The age of the dry concrete specimen used in this investigation was about two years.

4.5.1   Specimens and Measurement Setup
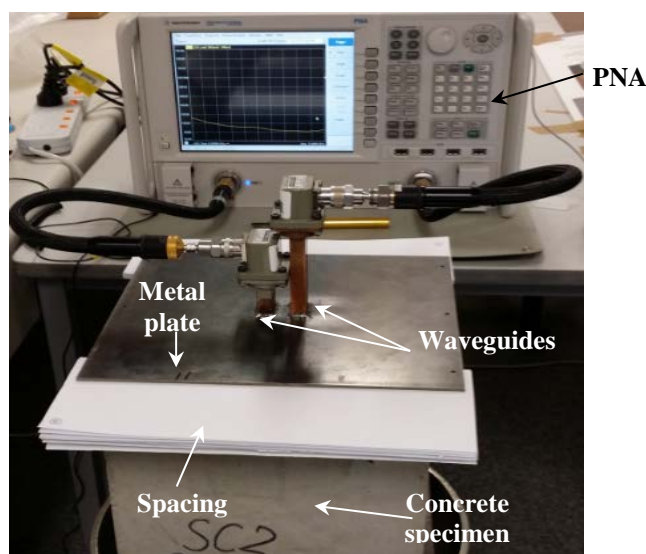
Figure 4.33: Experimental setup for measurement of the gap between the surfaces of the concrete specimen and metal plate using the microwave dual rectangular waveguide sensor.

The photograph in Figure 4.33 shows the experimental arrangement for measuring the gap between the dry concrete and metal plate using the proposed dual waveguide sensor. A dry concrete cube with side dimension 250 mm and initial water : cement ratio of 1 : 2 was used in this investigation. Thin sheets of paper were used to create the desired gap (spacing), as shown in the figure. Ten measurements of the reflection and transmission coefficients were taken for each gap value (0.0, 0.5, 1.0, 1.5, 2.0 mm), then averaged and presented together with the standard deviation.

4.5.2   Measurement Results and Discussion

Figure 4.34a, b show the measured average magnitudes of the reflection coefficient and transmission coefficients, respectively, at different gap values over the operating frequency band. The vertical bars in Figure 4.34 represent one standard deviation (s.d., ± σ) of the average value at each measurement frequency. It is seen in Figure 4.34a that the magnitude of the reflection coefficient decrease with increasing gap from 0 to 2 mm over the operating frequency range. The differences between the magnitudes for different gap values at each frequency were measurable and, taken together with the STD, they demonstrate that the gap was measured to an accuracy in the order of ~0.2 mm. The magnitude of the transmission coefficient increases with increasing gap values between 0.5 and 2 mm, as shown in Figure 4.34b. It is also seen in Figure 4.34b that it is not possible to distinguish gaps between 0 and 0.5 mm at most frequencies. The relatively low transmission coefficient and high standard deviations in this range may suggest that the low probability of evaluating these small gap values is the result of measurement error due to surface roughness, and inaccuracies in sensor fabrication and gap arrangement.

The results also indicate that the standard deviation of the measured data differs between frequencies and for different gap values. For the reflection coefficient measurement, the STD is low at the lowest frequencies (8.4–9.2 GHz) and at the highest frequencies (> 12 GHz), as shown in Figure 4.34a. It should be noted that the smallest STD for all gap values was obtained at a frequency of ~ 9 GHz. The smallest STD was found for the 0 and 0.5 mm gap values. For the transmission coefficient measurement, the STD at gap values of 0 and 0.5 mm is much higher than those at wider gap values at high frequencies (> 9.7 GHz). This behaviour also changes with frequency change, however; at lower frequencies the STD for the different gap values are comparable.

Figure 4.35 shows the measured magnitude of the reflection coefficient and transmission coefficient vs. size of gap between the dry concrete and metal plate surfaces at 10.6 GHz. It is seen that the magnitude of the reflection coefficient decreases monotonically with increase of gap value, but the transmission coefficient changes non-monotonically, initially decreasing as the gap value first increases from zero, then gradually increasing as the gap increases from 0.5 to 2.0 mm.
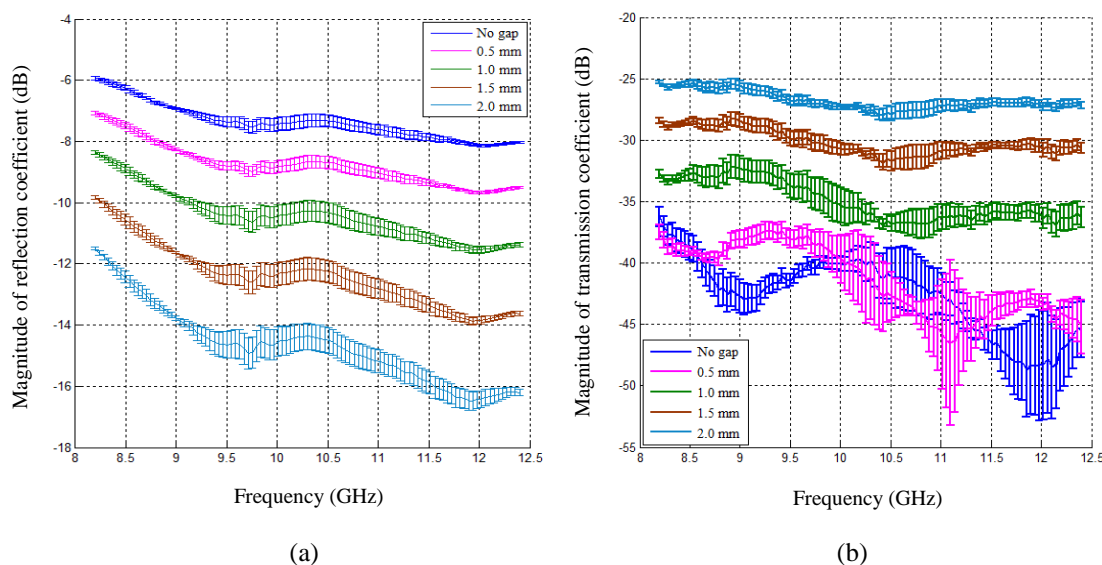
Figure 4.34: Measured average magnitude of (a) reflection coefficient, and (b) transmission coefficient vs. frequency, showing standard deviation, for different values of gap between concrete and metal plate surfaces.
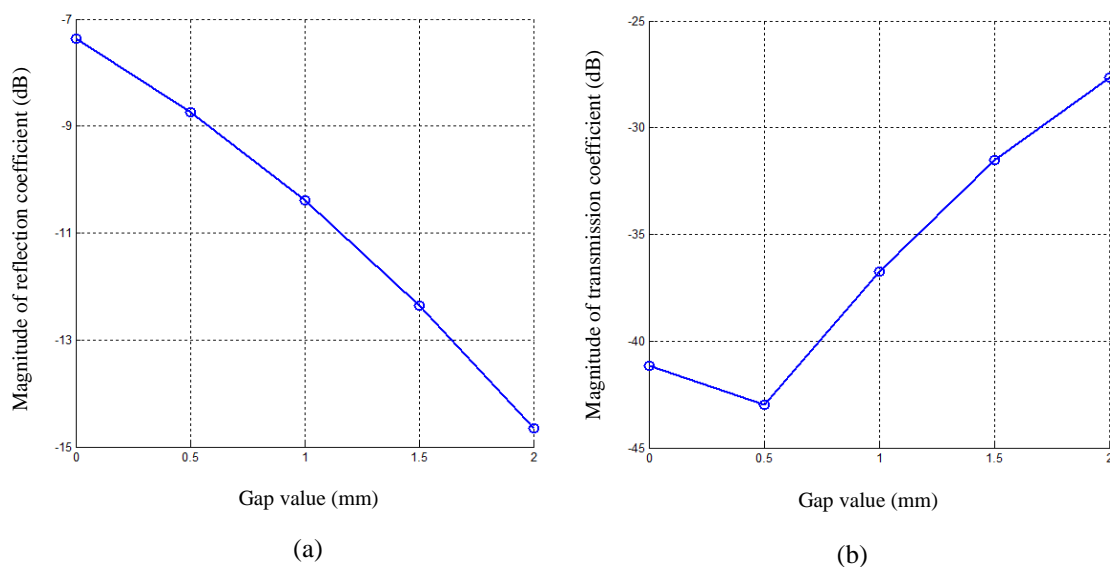
Figure 4.35: Measured average magnitude of (a) reflection coefficient, and (b) transmission coefficient vs. values of gap between concrete and metal plate surfaces at 10.6 GHz.

4.5.3   Simulation Results and Discussion

The model of DWS and fresh mortar specimen (cf. Figure 4.20) was also used in the simulations of DWS with dry concrete; all simulation settings (frequency range, boundary conditions, background properties, excitation signals) were identical. The model differed only in the dielectric properties of the specimen. In the fresh mortar/DWS simulations, the dielectric properties of the specimen were chosen from reports of previous study [11], and subsequently adjusted on the basis of measured values. In this case, however, to avoid this uncertainty in the simulations, the dielectric properties of the dry concrete specimen were determined from the measured reflection and transmission coefficients using the procedure and algorithm described in Chapter 3, section 3.3.

Figure 4.36a shows the measured average magnitude of reflection coefficient vs. frequency, including standard deviation, for the no-gap condition. Selected simulation results of the magnitude of reflection coefficient for different values of the dielectric properties are also plotted. Figure 4.36b shows the measured average magnitude of the transmission coefficient (complete with standard deviation) vs. frequency, and selected simulated magnitudes of the transmission coefficient vs. frequency. It is seen that no single combination of the complex dielectric properties matches both the reflection coefficient and transmission coefficient with the same accuracy. Therefore, considering the frequency range of 10.0–11.0 GHz and focusing on the DWS guided wave, the complex dielectric permittivity determined for dry concrete was chosen as $4.1 – j0.82$; this value was then used in simulations for the dry concrete specimen.

Figure 4.37 shows the magnitude and phase of the simulated reflection coefficient vs. frequency for different values of the gap between surfaces of concrete ($\varepsilon_r = 4.1 – j0.82$) and metal plate. It can be seen from Figure 4.37a that increasing the gap results in a lower reflection coefficient; relatively large decreases are seen in the reflection coefficient for 0–0.5 mm gaps over the entire frequency band. The values of the magnitude of reflection coefficient and its behaviour agree very closely with the measured results (cf. Figure 4.34a). The behaviour of the phase differ as the gap value increases: the change of phase gradually increases with frequency increase, and

at each frequency the difference between the phases in adjacent curves (i.e., the gap values) also increases, as shown in Figure 4.37b.

Figure 4.38 shows the simulated magnitude and phase of the simulated reflection coefficient vs. gap between the surfaces of the dry concrete ($\varepsilon_r = 4.1 - j0.82$) and the metal plate at a frequency of 10.6 GHz. It is seen in Figure 4.38a that themagnitude of reflection coefficient decreases with increase in gap from –7.15 dB at no gap to –16.03 dB at 2.0 mm gap. Similarly, at 10.6 GHz the phase of the reflection coefficient decreases from –81.70° at no gap to –98.37° at 2.0 mm gap (Figure 4.38b).

Figure 4.39 shows the magnitude and phase of the simulated transmission coefficient vs. frequency at different values of the gap between surfaces of dry concrete ($\varepsilon_r = 4.1 - j0.82$) and metal plate. Figure 4.39a shows an initial marginal decrease in S_{21} with the increasing gap value from no gap to 0.5 mm gap, followed by an increase with increase of gap value from 0.5 mm to 2.0 mm. This is clearly shown in the plot of transmission coefficient vs. gap value at 10.6 GHz frequency in Figure 4.40a. In Figure 4.39b it is seen that the phase of S_{21} shifts as the gap value increases. The amount of shift changes as frequency increases; however, at any given frequency (e.g. 10.6 GHz, Figure 4.40b), the phase of the transmission coefficient increases monotonically with increasing gap values. These variations in the phase and magnitude of the transmission coefficient (and reflection coefficient) with changes in gap values between dry concrete and metal plate can be best understood by analysing the electric field intensity distribution near the concrete–dual waveguide sensor interface, as shown in Figures 4.41 to 4.44.
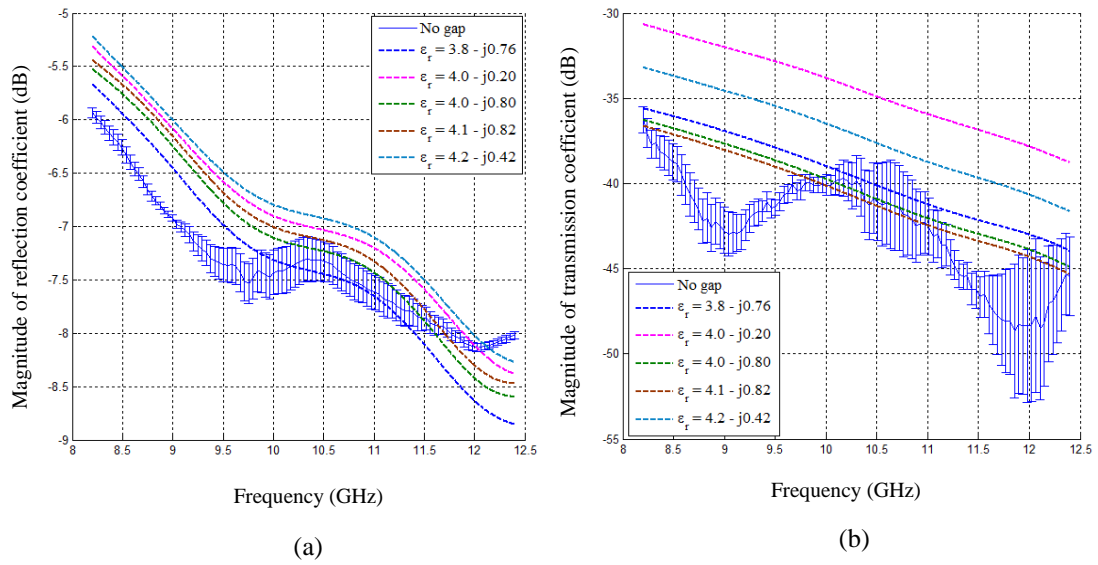
Figure 4.36: Measured and simulated magnitude of (a) reflection coefficient, and (b) transmission coefficient vs. frequency with no gap between concrete and metal plate surfaces using DWS.
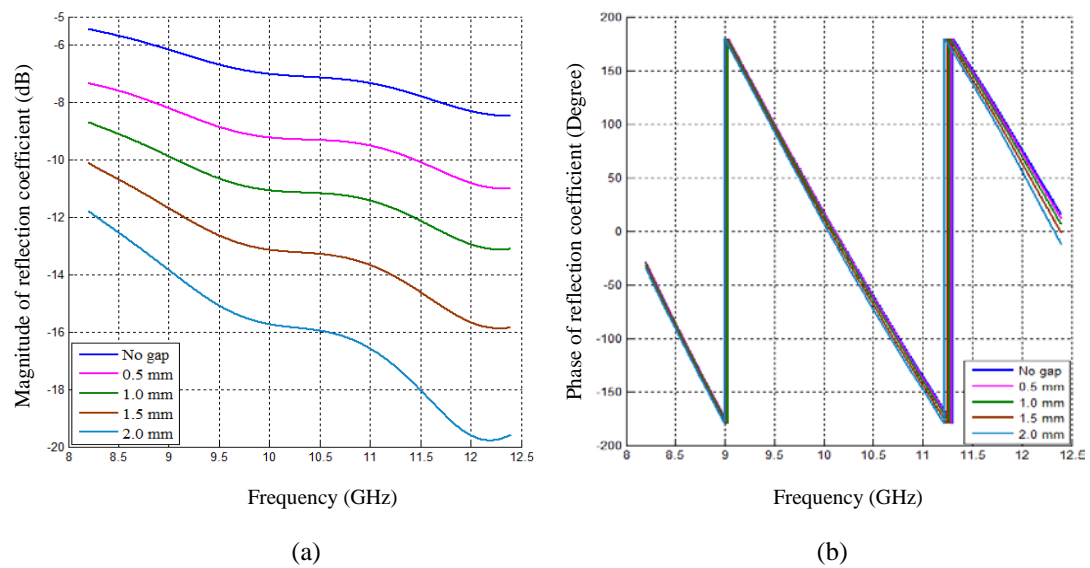
Figure 4.37: Simulated reflection coefficient vs. frequency at different gap values between dry concrete ($\varepsilon_r = 4.1 - j0.82$) and metal plate surfaces: (a) magnitude, (b) phase.
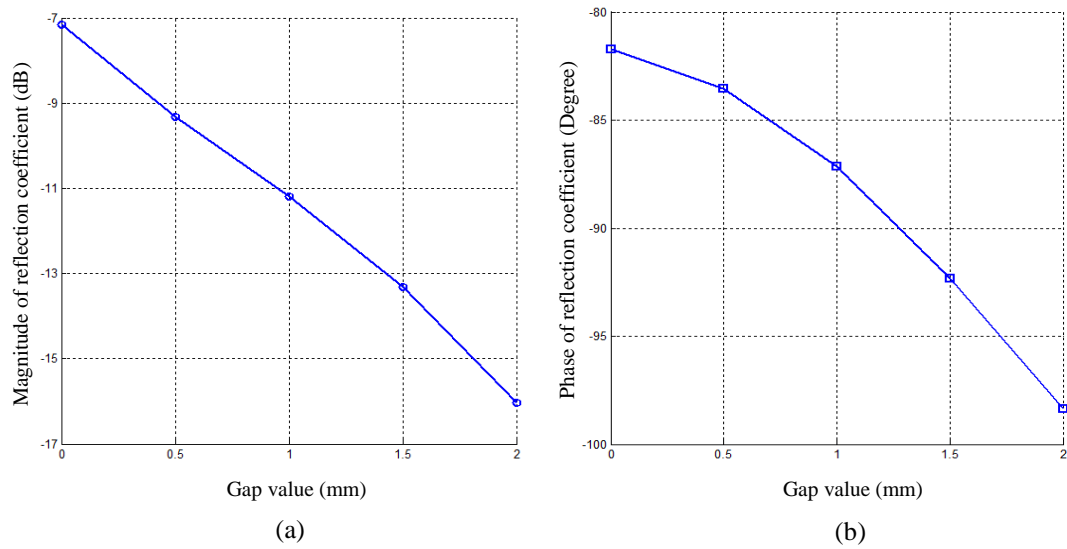
Figure 4.38: (a) Magnitude and (b) phase of reflection coefficient vs. gap between surfaces of dry concrete $\varepsilon_r = 4.1 - j0.82$) and metal plate, simulated at 10.6 GHz.
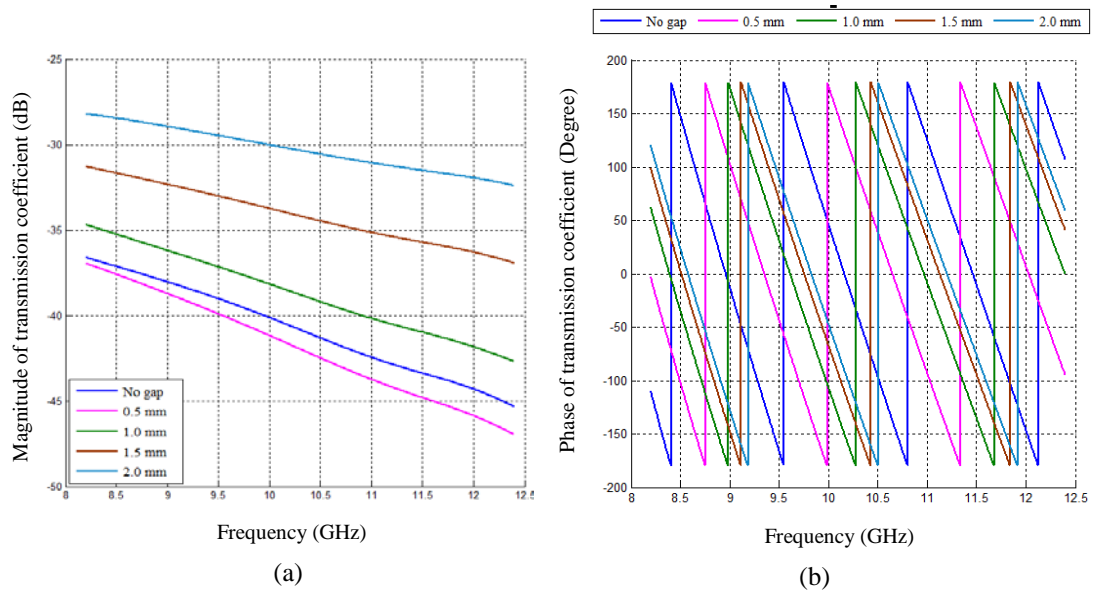
Figure 4.39: (a) Magnitude, and (b) phase of simulated transmission coefficient vs. frequency for different gaps between surfaces of dry concrete ($\varepsilon_r = 4.1 - j0.82$) and metal plate.
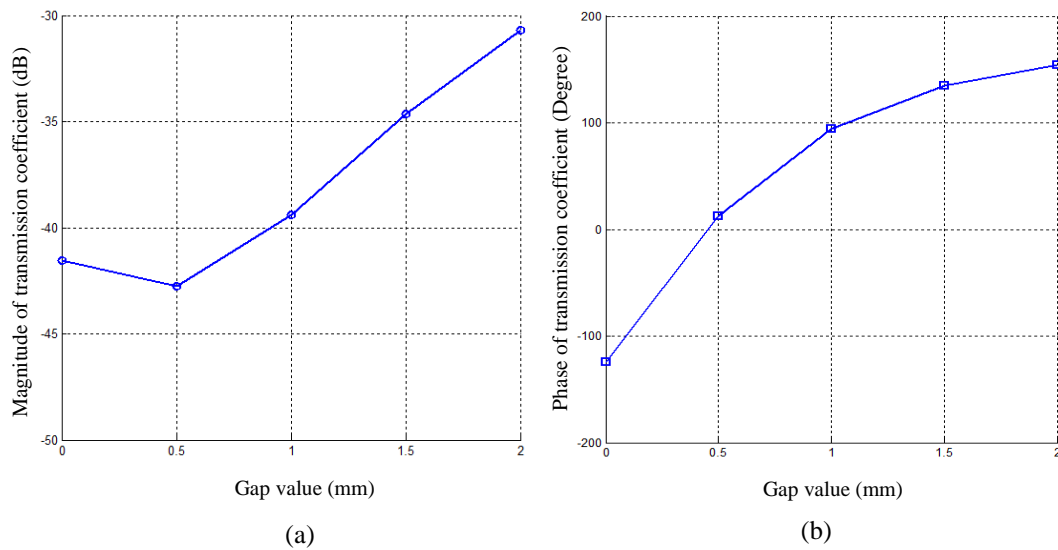
Figure 4.40: (a) Magnitude and (b) phase of transmission coefficient vs. gap between concrete and metal plate surfaces, simulated at 10.6 GHz.

Figures 4.41a–c is a cross-sectional side view of the simulated electric field intensity distribution in the DWS and concrete for 0, 1 and 2 mm gaps at 10.6 GHz. Figure 4.41a shows that W1 radiated microwaves into the dry concrete, with a small proportion penetrating into W2 at the no-gap condition. Several observations may be made from Figure 4.41b and c. They clearly show changes in the electric field intensity distribution at the interface between the concrete and metal surfaces when a gap is present. An animated-phase version of these distributions (not shown here) show electromagnetic waves propagating between the metal and concrete surfaces (guided waves) at the 1.0 and 2.0 mm gap. Such guided waves cause losses in electromagnetic energy both of the incident wave and the reflected wave. Another important observation from the figure is that a part of the guided wave and a part of the wave radiated by W1 into the concrete penetrate into W2 and cause interference there. As a result, due to the change of interference conditions as the gap increases from zero, the magnitude of the transmission coefficient changes non-monotonically as the gap increases from 0 to 1.0 mm, then increases when the value of the gap exceeds 1.0 mm.

Figure 4.42 is a cross-sectional top view of the simulated electric field intensity distribution (amplitude and phase) inside both W2 and the dry concrete ($\varepsilon_r = 4.1$ –

j0.82) at 10.6 GHz. A small change is observed in the electric field intensity distribution in W2 from 0.0 gap (Figure 4.42a) to 1.0 mm gap (Figure 4.42b) and 2.0 mm gap, consistent with the results presented in Figure 4.39a. For comparison with the electric field distribution in the fresh mortar specimen (ε_r = 17.0 – j3.4; Figure 4.26), S_{21} = –52.32, –34.8 and –23.62 dB at 0.0, 1.0 and 2.0 mm gap, respectively; for the dry concrete specimen S_{21} = –41.56, –39.4 and –30.67 dB at 0.0, 1.0 and 2.0 mm gaps, respectively.

Figure 4.43 illustrates the amplitude and phase of the electric field intensity distribution in 3D cutting plane at 10.6 GHz. It is seen in Figure 4.43a that, for the no-gap condition at $x = 0$ of the yz cutting plane, microwave signals radiated from W1 penetrated a larger zone of the dry concrete specimen than the mortar specimen, and more signals entered W2. The reason for this is that the fresh mortar contained more moisture, preventing microwave signal penetration. At 1.0 and 2.0 mm gap conditions, microwave signals passed through the gaps between the metal and dry concrete specimen as guided waves; this also occurred in the dry concrete specimen, but to a lesser extent.

Figure 4.44 illustrates the amplitude and phase of the electric field distribution in the zx cutting plane at $y = 27.7$ mm (i.e., the middle of W2) for 0, 1.0 and 2.0 mm gap conditions at 10.6 GHz frequency. It is clearly seen that the gap between the metal plate and the dry concrete specimen contributed guided wave signals to W2.
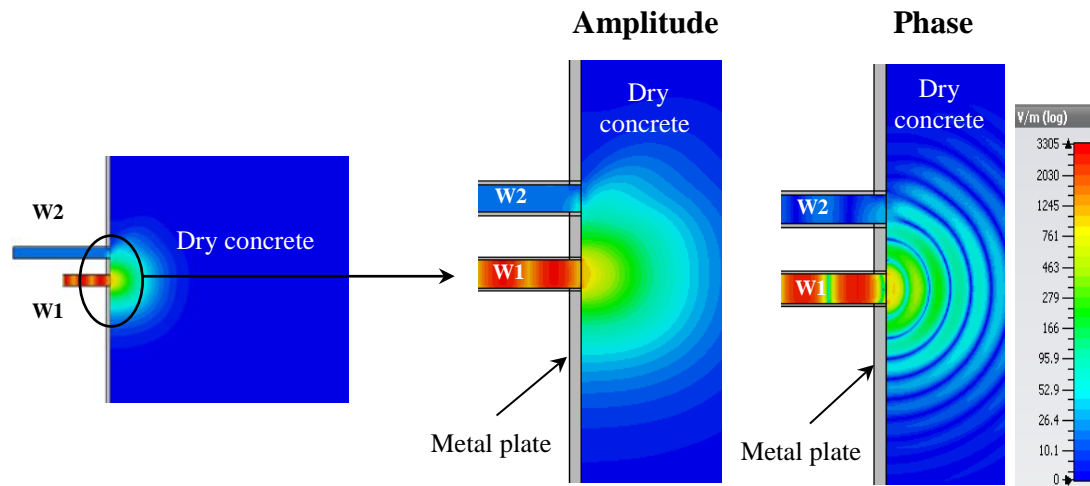
Amplitude   **Phase**

(a) No gap between metal and dry concrete
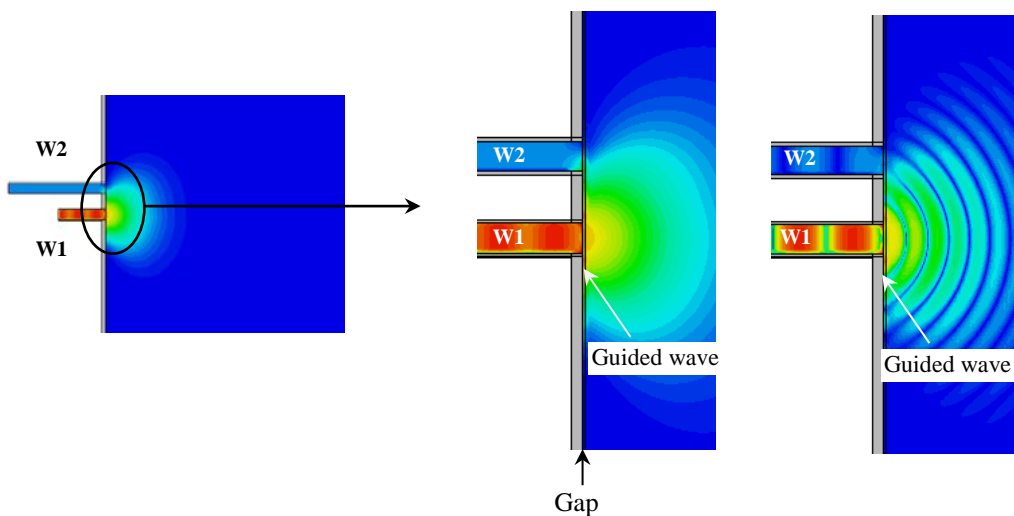
(b) 1.0 mm gap between metal dry concrete
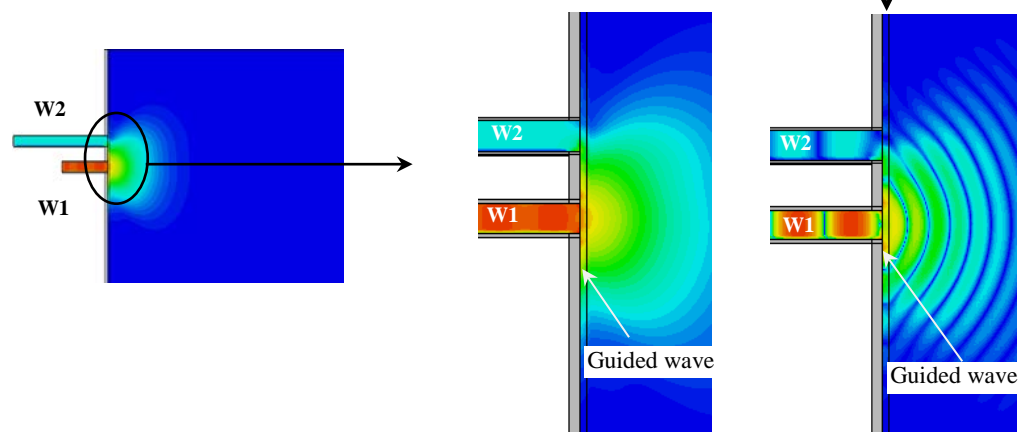
(c) 2.0 mm gap between metal and dry concrete

Figure 4.41: Cross-sectional side view of electric field intensity distribution inside waveguides of DWS and dry concrete specimen ($\varepsilon_r = 4.1 - j0.82$) for different gap values between metal and specimen at 10.6 GHz.

Amplitude   **Phase**

(a) No gap between metal and dry concrete

(b) 1.0 mm gap between metal and dry concrete

(c) 2.0 mm gap between metal and dry concrete
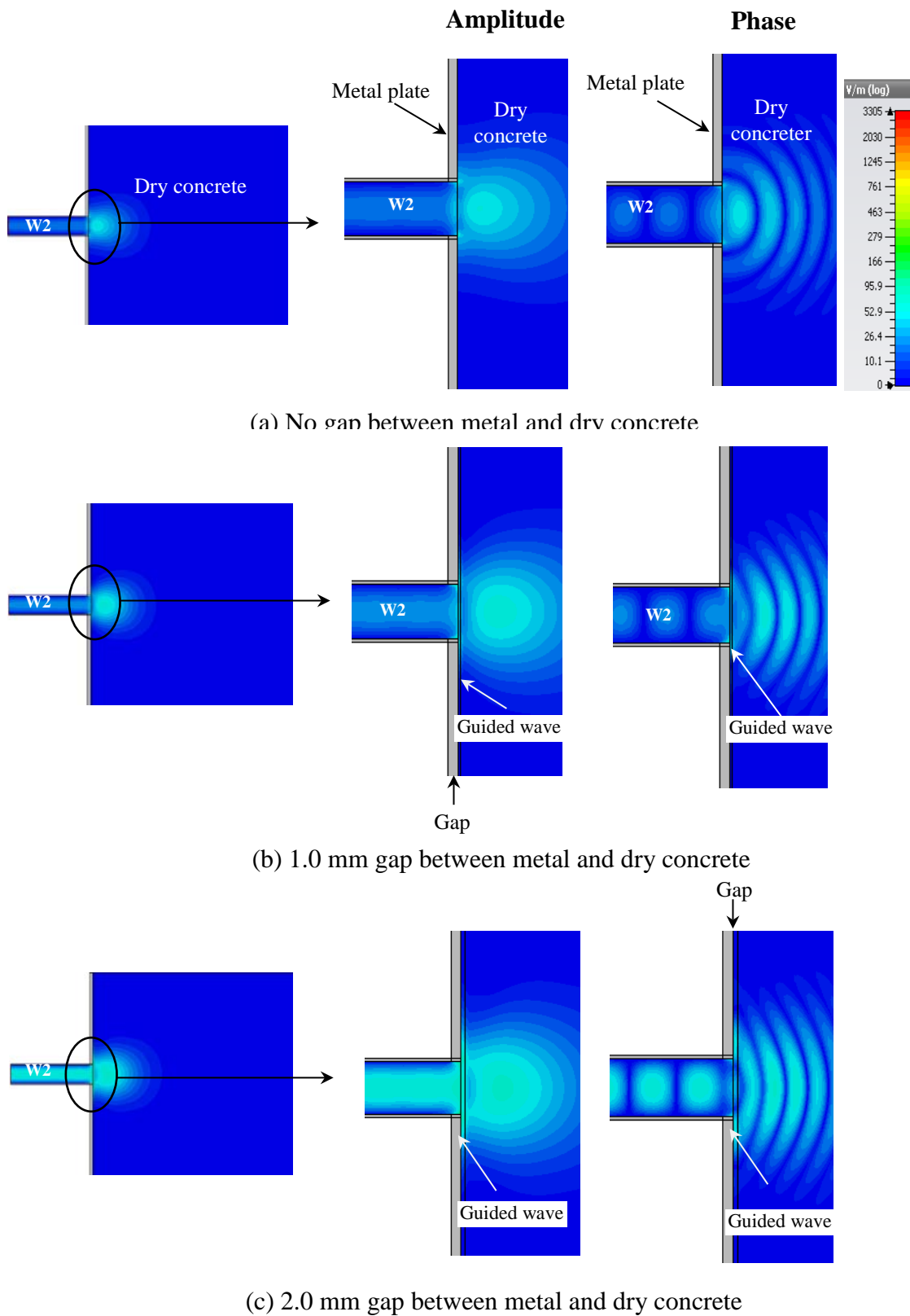
Figure 4.42: Cross-sectional top view of electric field intensity distribution inside waveguide 2 of DWS and dry concrete specimen ($\varepsilon_r = 4.1 - j0.82$) for different gap values between metal and specimen at 10.6 GHz.
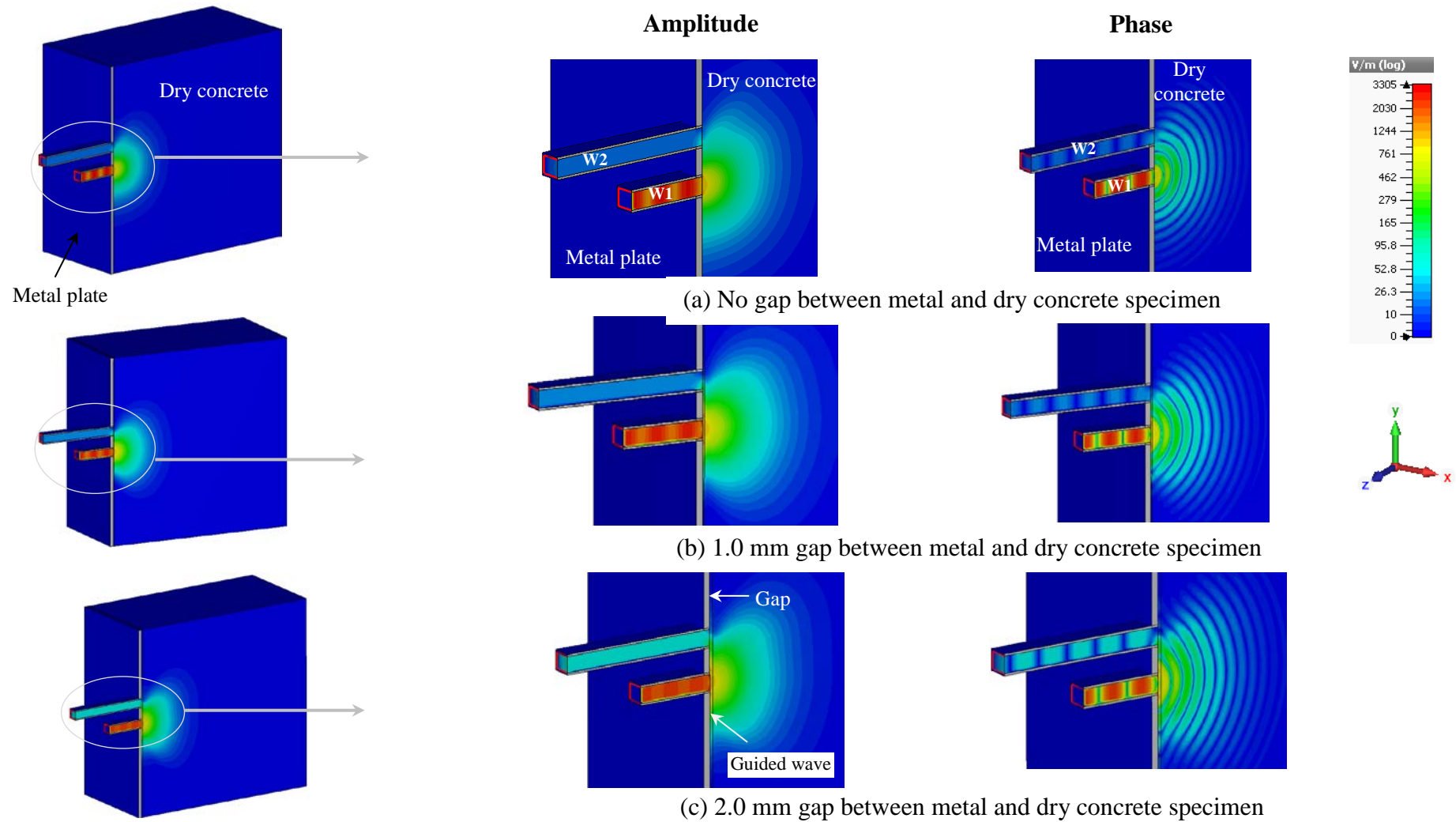
Figure 4.43: Electric field intensity distribution inside waveguides of DWS and dry concrete specimen for different gaps between surfaces of metal and specimen ($\varepsilon_r = 4.1 - j0.82$) at $x = 0$ of yz cutting plane at 10.6 GHz.

(a) No gap between metal and dry concrete specimen

(b) 1.0 mm gap between metal and dry concrete specimen

(c) 2.0 mm gap between metal and dry concrete specimen
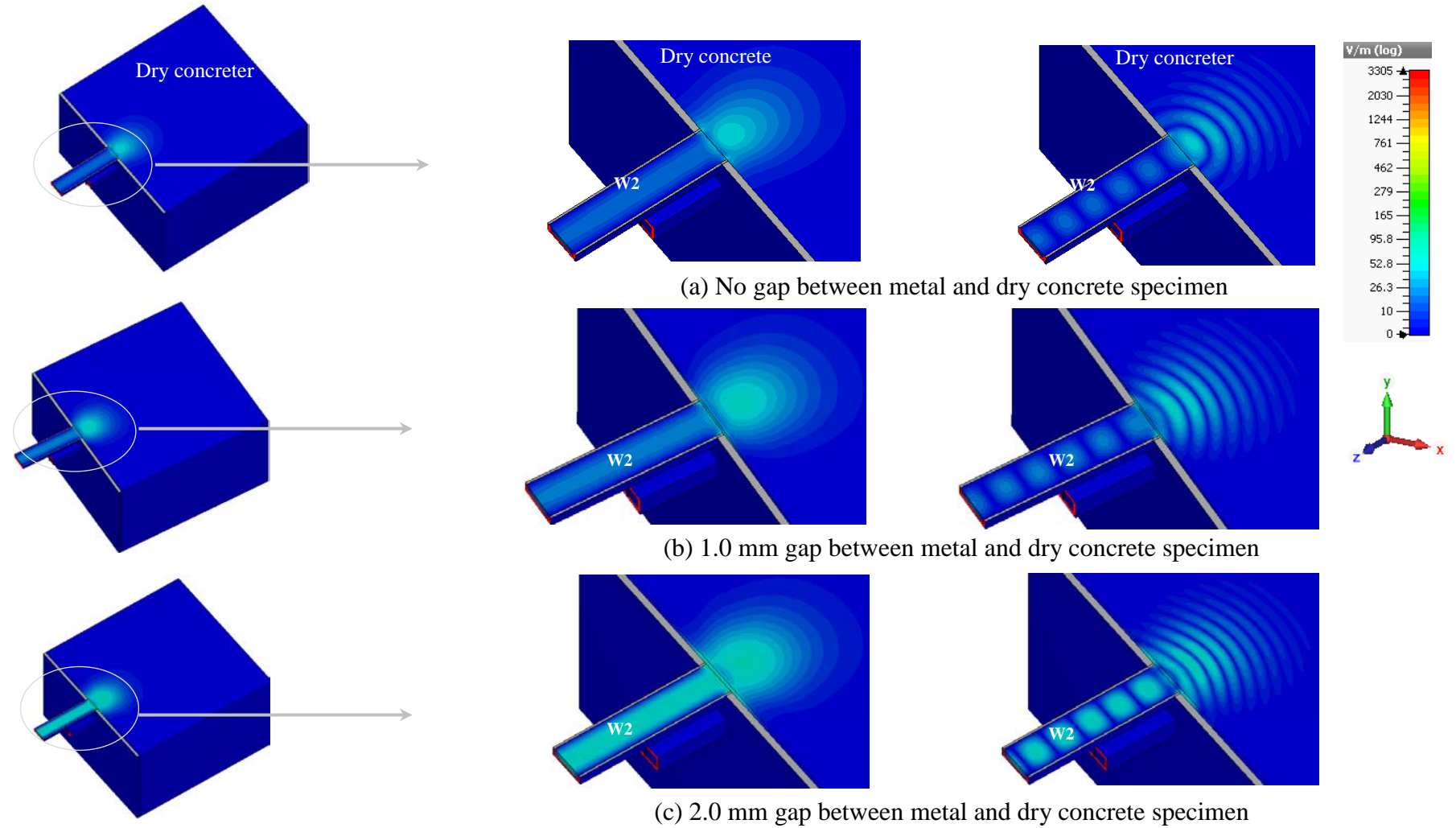
Figure 4.44: Electric field intensity distribution inside waveguide 2 of DWS and dry concrete specimen for different gaps between surfaces of metal and specimen ($\varepsilon_r = 4.1 - j0.82$) at $y = 27.7$ (i.e., middle of waveguide 2) of zx cutting plane at 10.3 GHz.

4.5.4 Comparison of Measurement and Simulation Results
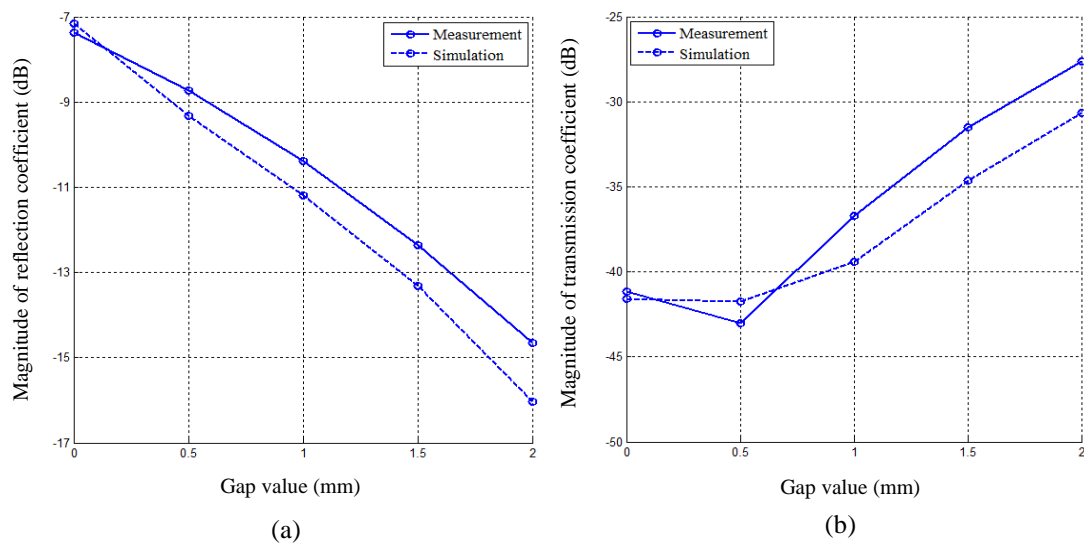
Figure 4.45: Simulated and measured results for (a) reflection coefficient, (b) transmission coefficient vs. gaps between concrete and metal plate surfaces at 10.6 GHz.

Figure 4.45 shows the measured and simulated magnitude of reflection coefficient and transmission coefficient vs. gap value at 10.6 GHz. Figure 4.45a clearly shows good agreement between the measured and simulated reflection coefficient. Figure 4.45b shows some discrepancy between the measured and simulated transmission coefficient, attributable to sensor fabrication error and gap arrangement error due to roughness of the concrete specimen surface. This error is very critical at small gap values. Therefore, the dual waveguide sensor is capable of detecting and measuring small gaps, using the magnitude reflection coefficient and transmission coefficient separately.

4.6 Measurement and Simulation with Metal Plate Specimens

Sections 4.1–4.5 have described the design and development of the microwave dual waveguide sensor and its application for detecting and monitoring the size of the gap between different cement-based specimens and a metal plate. This section compares these with the results obtained when a steel plate specimen replaces the concrete specimen.

4.6.1 Measurement Setup
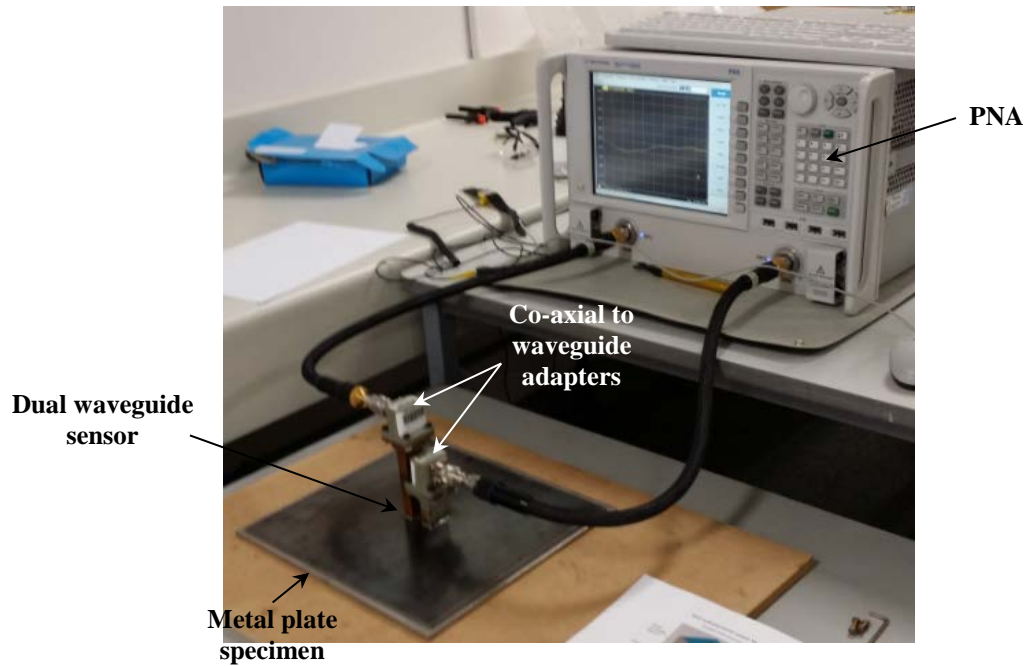
Figure 4.46: Experimental setup for measuring the air gap between a steel plate specimen and the metal plate of the dual waveguide sensor.

Figure 4.46 shows the experimental setup for measuring the reflection and transmission coefficients for various air gaps between a steel plate and the proposed DWS. A performance network analyser was the measuring tool, with a coaxial cable connection to the DWS, using coaxial-waveguide adapters as shown in the figure.

The dimensions of the steel plate was 260 mm × 260 mm × 5 mm; thin paper sheets were used as before to create the desired gap between the plate specimen and the DWS. The arrangement was calibrated at the output apertures of the coaxial-waveguide adapters using an X-band rectangular waveguide calibration kit. Eight measurements of the reflection and transmission coefficients were made for each gap value (0.0, 0.5, 1.0, 1.5 and 2.0 mm), then averaged.

4.6.2 Measurement Results and Discussion
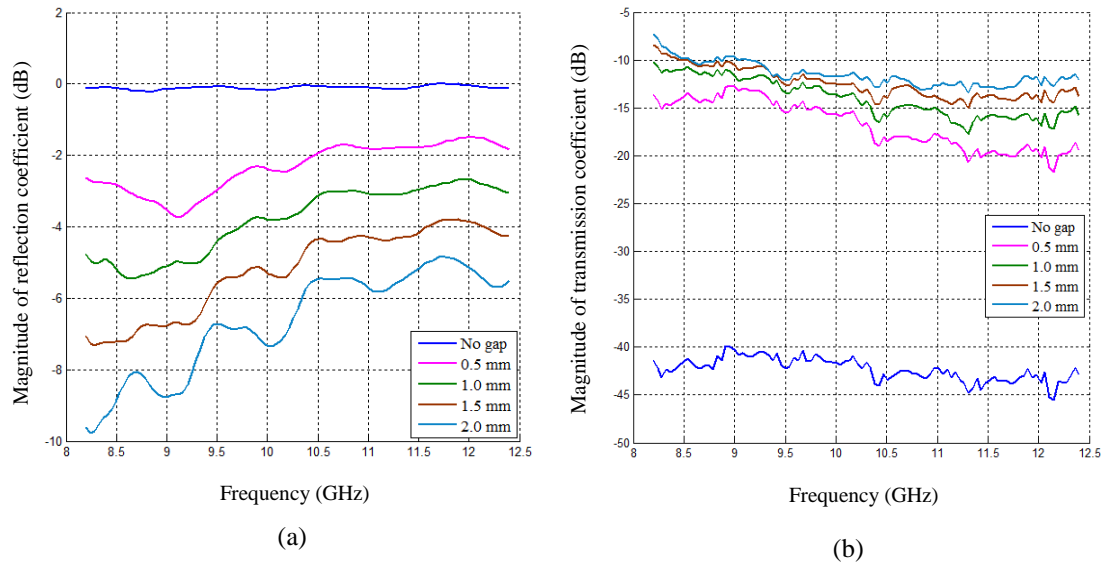
Figure 4.47: Average measured magnitude of (a) reflection coefficient, and (b) transmission coefficient vs. frequency for different values of the gap between the surfaces of the steel plate specimen and the metal plate of dual waveguide sensor.

Figure 4.47 shows the average measured magnitudes of the reflection and transmission coefficients vs. frequency for different values of the gap between the steel plate specimen and the DWS. It is seen in Figure 4.47a that with no gap, the reflection coefficient is very close to 0.0 dB over the entire frequency band. The reason is that the steel is a very good conductor, and almost all signals radiated from the DWS aperture are reflected back to it. The reflection coefficient decreases with increasing gap value, with a greater decrease occurring at low frequency than at high frequency. It is seen in Figure 4.47b that the magnitude of the transmission coefficient at zero gap ranges from –40 to –45 dB, increasing with greater gap value; however, small differences of S_{21} are seen for other gap values, the difference decreasing with increasing gap value. It is also observed that, for all gaps, S_{21} is slightly higher at the lower frequencies.

4.6.3 Simulation Results and Discussion

For these simulations, the same dual waveguide sensor model created in CST Microwave Studio was used, but with the steel plate specimen as shown in Figure 4.48. For the simulation purposes of the model, the steel specimen was regarded as a

pure electric conductor (PEC). All other simulation settings (frequency range, boundary conditions, background properties, excitation signals) were identical to those for the concrete specimens.
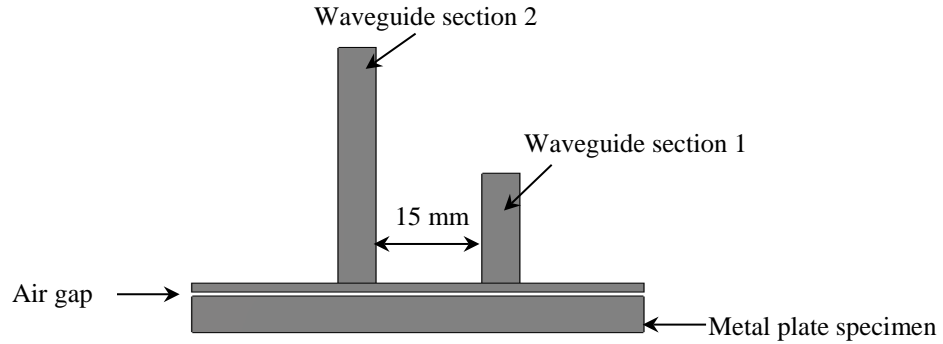
Figure 4.48: A model of the DWS created in CST, with a steel plate specimen and gap between specimen and DWS surfaces.

Figure 4.49 shows the simulated magnitude of reflection and transmission coefficients vs. frequency for different gaps between the steel plate specimen and the DWS. It is seen in Figure 4.49a that the trend of the simulated magnitude of reflection coefficient is very similar to the measured value (cf. Figure 4.47a). The value of S_{11} at the no-gap condition is very close to 0 dB. For other gaps, S_{11} decreases with increasing gap value. It is observed that S_{11} is greater at higher frequencies. The magnitude of the simulated transmission coefficient shown in Figure 4.52b is negligible (–200 dB) at no gap, and increases as gap value increases. The differences in S_{21} at different gap values are relatively small, except from 0 to 0.5 mm, and decrease with rise in gap value.

Figure 4.50 shows the simulated magnitude of reflection coefficient and transmission coefficient vs. gap value at a frequency of 10.3 GHz for three dissimilar specimens, namely steel, fresh concrete and dry concrete. In these simulations the complex dielectric permittivity of the fresh and dry concrete were chosen as $15 – j4.5$ and $4.1 – j0.82$, respectively. It is clear in Figure 4.50a that S_{11} decreases with gap value for all specimen types, but at any given gap value the steel has the highest reflection coefficient, and dry concrete has the lowest. It is also observed in Figure 4.50b that S_{21} increases with gap value; again, the steel specimen produces the highest transmission coefficient at gaps more than 0.25 mm.
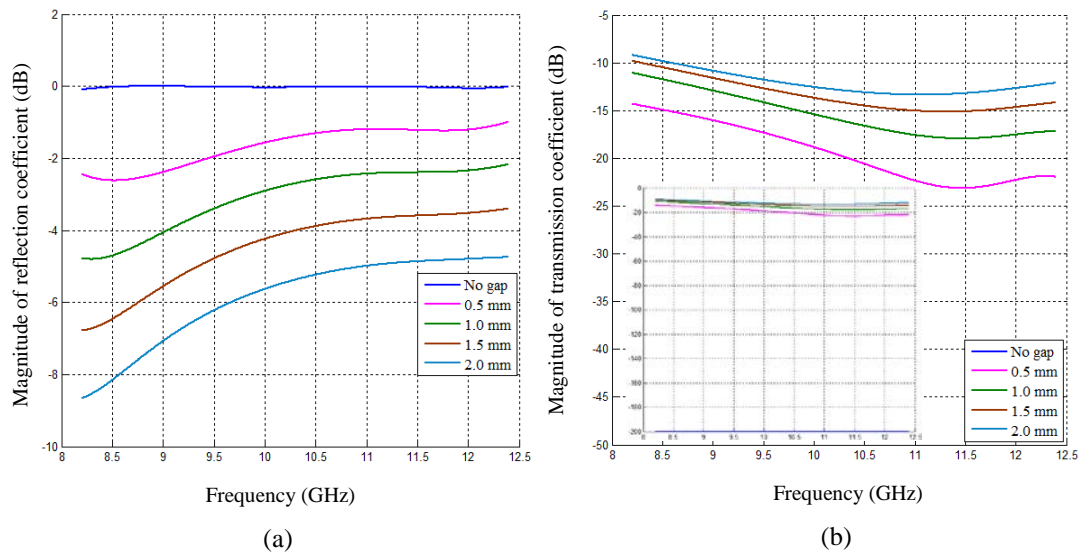
Figure 4.49: Simulated magnitude of (a) reflection coefficient, and (b) transmission coefficient vs. frequency for different gaps between the steel plate specimen and the metal plate of the DWS.
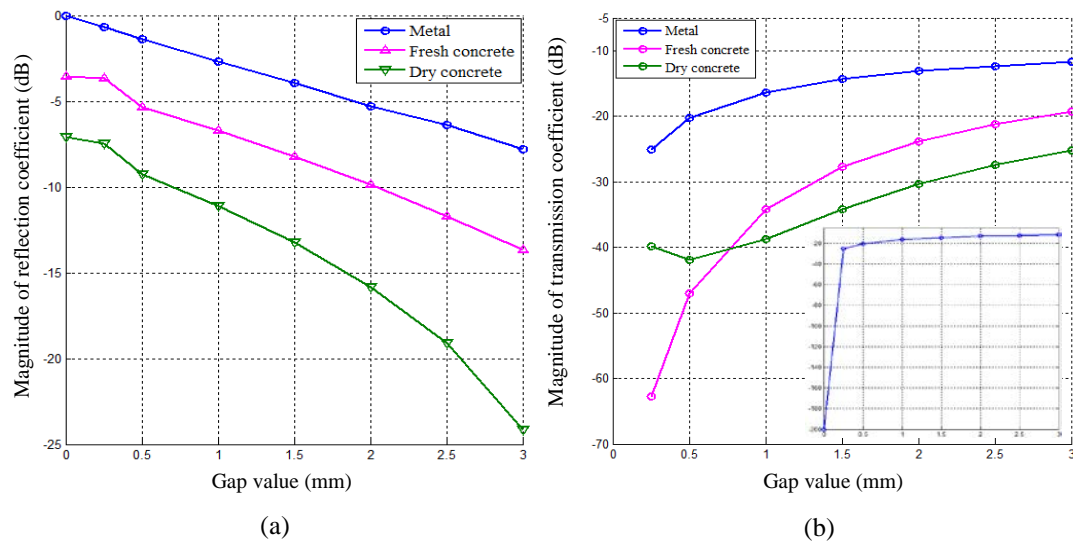
Figure 4.50: Simulated magnitude of (a) reflection coefficient, and (b) transmission coefficient vs. gap between metal wall of DWS and steel metal, fresh concrete (15 – j4.5) and dry concrete (4.1 – j0.82) specimens at a frequency of 10.3 GHz.

4.6.4 Comparison of Measurement and Simulation Results

Figure 4.51 illustrates the measured and simulated magnitude of the reflection and transmission coefficients vs. gap value at the three frequencies 8.5, 10.0 and 12.0

GHz. In Figure 4.51a it is clear that the measured and simulated S_{11} are comparable; however, they are in closer agreement at 8.5 and 12.0 GHz than at 10.0 GHz. In Figure 4.51b it is seen that the measured and simulated transmission coefficients are very close at all gap values at all three frequencies, except at zero gap, since in practice it is not possible to ensure precisely zero gap between the steel plate specimen and the DWS (surface scratches, roughness of the metal etc.); once there is any gap, however small, the S_{21} signal passes through the two conducting materials.

Figure 4.52 shows the measured and simulated magnitude of the transmission coefficient vs. gap at 10.3 GHz between the metal plate of DWS and the steel, fresh concrete and dry concrete specimens. It is seen that the steel specimen provides the highest transmission coefficient. Measurements and simulations agree well in all cases. To consider the 0.5 mm measurement error in a practical scenario such as surface roughness, or a tiny scratch on the steel specimen, or the thickness of polythene film for fresh concrete, or surface roughness for the dry concrete specimen, Figure 4.53 illustrates very good agreement between simulated and measured results.
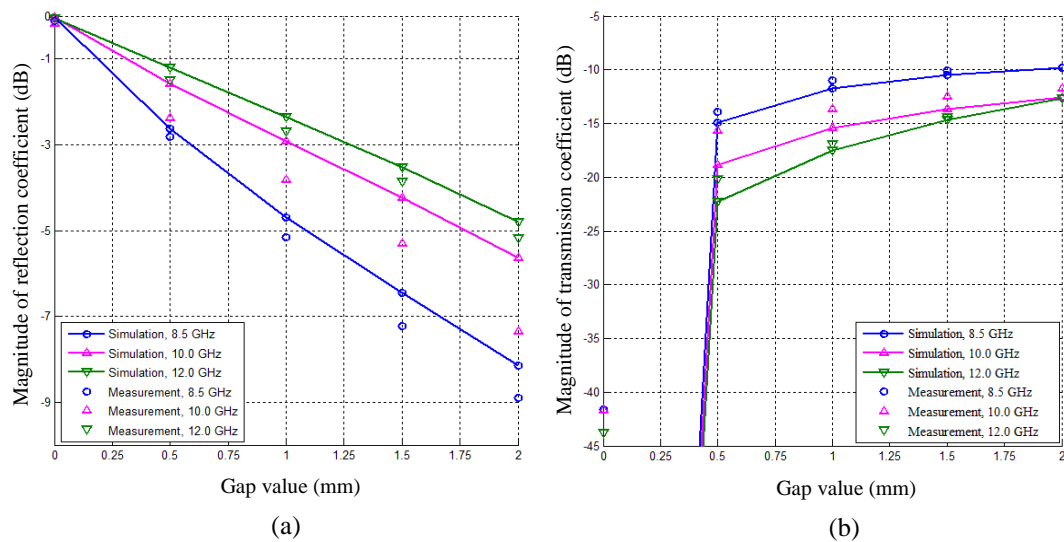
Figure 4.51: Measured and simulated magnitudes of (a) reflection coefficient, and (b) transmission coefficient vs. gap between the steel plate specimen and DWS at three different frequencies.
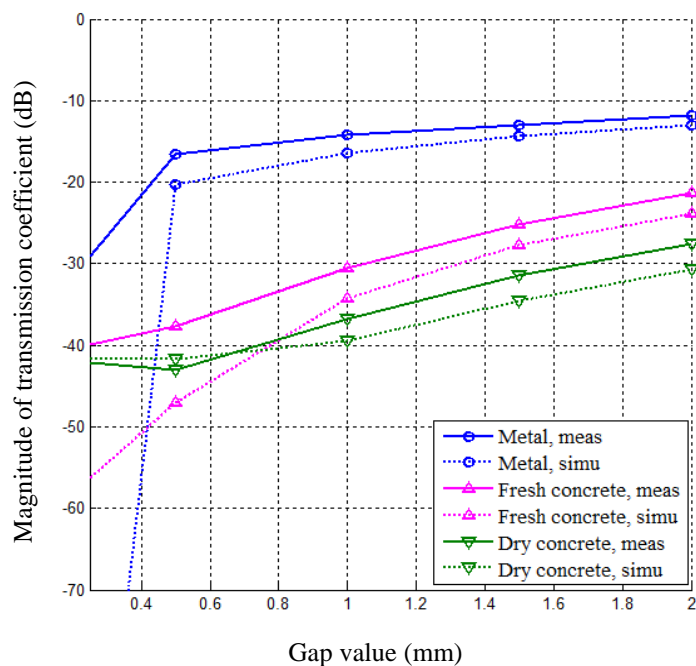
Figure 4.52: Measured and simulated magnitude of transmission coefficient vs. gap value between metal plate of DWS and three different specimens at a frequency of 10.3 GHz.
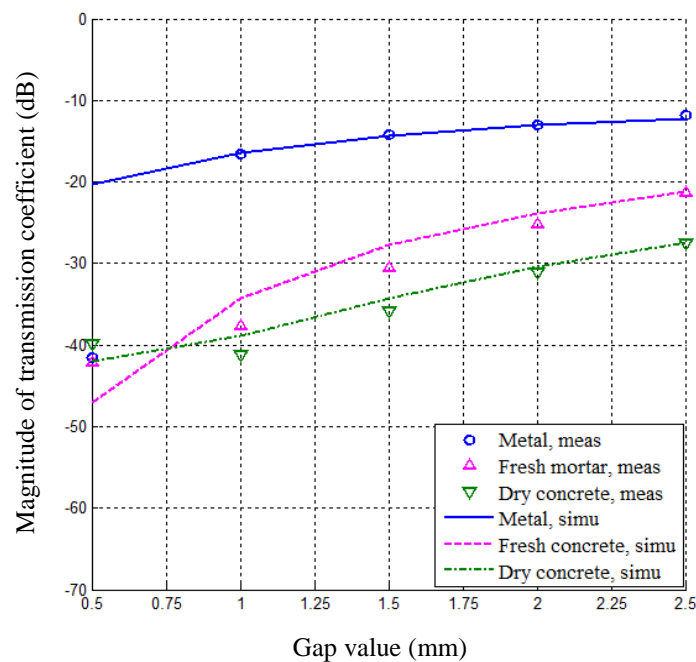
Figure 4.53: Measured and simulated magnitude of transmission coefficient vs. gap value between metal plate of DWS and three different specimens at a frequency of 10.3 GHz after measurement data for 0.5 mm are adjusted.

4.7 Numerical Investigation of Crack Detection inside Dry Concrete Specimens

Cracks develop in concrete under different environmental, structural and manufacturing conditions. They may be in different sizes and shapes, but need to be detected and evaluated before causing any damage to structure. In this section, the effect of the location, dimensions and shape of cracks in a dry concrete specimen ($\varepsilon_r' = 4.1 - j0.82$) on the magnitude of the reflection and transmission properties of that specimen will be investigated numerically using the developed DWS. Figure 4.54a shows a model of dry concrete specimen with a through crack in the *zx* plane; Figure 4.54b shows the DWS with the cracked specimen: in this model, the lengths of waveguide sections were equal and 30 mm apart. Figure 4.54c–d shows models containing a crack in each (rectangular or triangular, as shown) and its location with respect to the DWS.
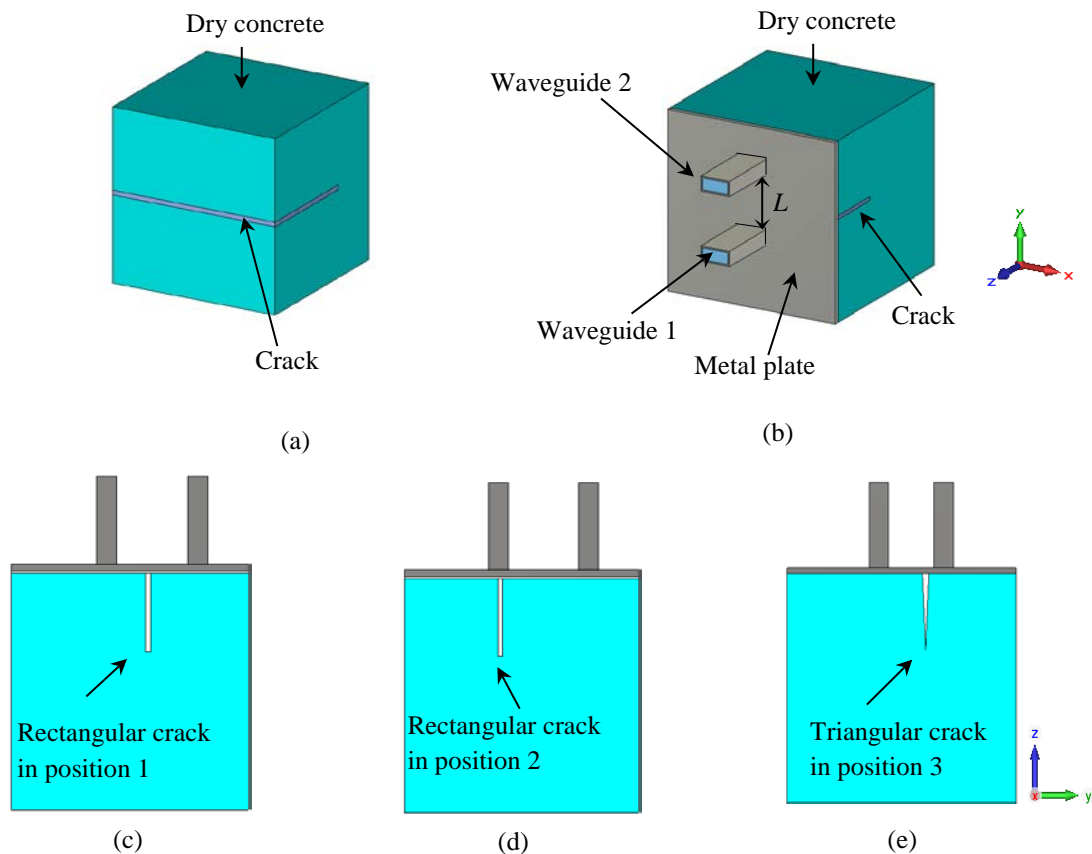
Figure 4.54: A model of DWS and dry concrete specimen with cracks in CST: (a) perspective view; (b) with metal plate of DWS; (c) rectangular crack in position 1; (d) rectangular crack in position 2; and (d) triangular crack in position 3.

Figure 4.55 shows the magnitudes of the reflection and transmission coefficients vs. frequency at different gap values, for the DWS and dry concrete ($\varepsilon_r' = 4.1 - j0.82$) without cracks. In Figures 4.56 to 4.59 the magnitudes of the reflection and transmission coefficients vs. frequency are presented for different values of the gap between the DWS and dry concrete specimens containing rectangular cracks 1, 2, 3 and 4 mm wide, respectively, located at position 1 (shown in Figure 4.54c). In all cases, the cracks are 50 mm deep. It is seen that S_{11} decreases with increasing gap value for all cases. The values of S_{11} are almost identical for the different gap values, with small fluctuations in the periodic frequencies when cracks are present. Although these fluctuations are minor, they are indicative of the presence of small cracks; the fluctuations increase with the increasing crack width. However, the magnitude of the reflection coefficients for different gaps between the DWS and the dry concrete specimen with/without cracks are somewhat irregular. The S_{21} values in the uncracked specimen are irregular but linear at different gaps; only the 1.0 mm gap curve generates resonance at 10.5 GHz. For specimens with cracks, S_{21} values at zero gap are almost linear, with higher values; the S_{21} at other gap values creates either oscillation or resonance at different frequencies.

Figure 4.60 shows the magnitude of the reflection and transmission coefficients vs. frequency for dry concrete specimens ($\varepsilon_r' = 4.1 - j0.82$) with no crack and with cracks of different width at zero gap between DWS and specimen. It is seen in Figure 4.60a that the magnitude of the reflection coefficient for specimens with cracks fluctuates around the linear S_{11} value for the uncracked specimen. Thus, S_{11} measurement can be used for detecting cracking in dry concrete. Figure 4.60b shows that the magnitude of the transmission coefficient decreases with increase of frequency for uncracked and cracked specimens, and with increasing crack width. It is also observed that within the lower frequency range of 8.4–9.3 GHz, S_{21} decreases with increasing crack width, and the differences are comparable. This implies that the width of cracks can be monitored by analysing the measurements of magnitude of transmission coefficient.
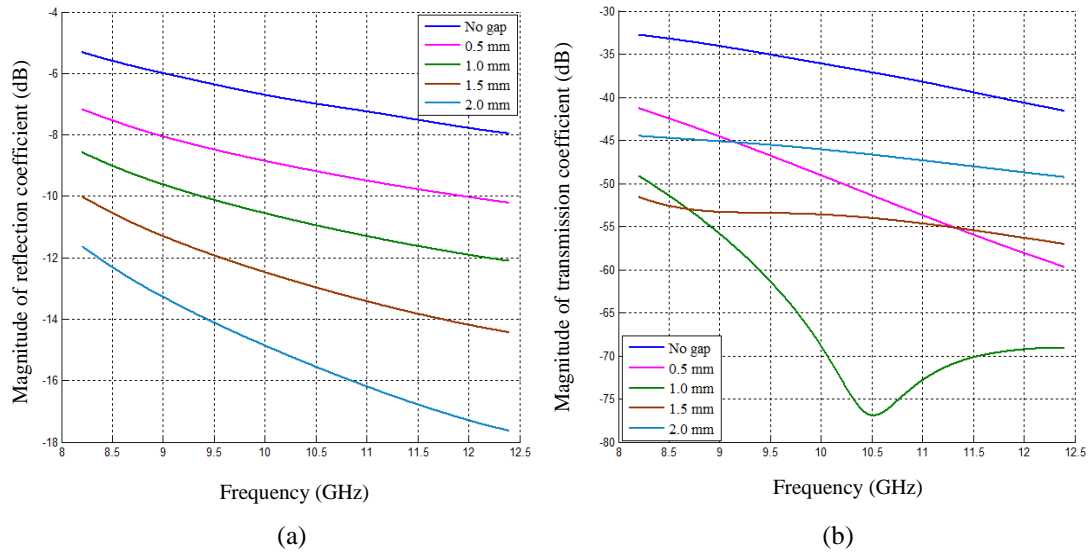
Figure 4.55: Simulated magnitude of (a) reflection coefficient, and (b) transmission coefficient vs. frequency for different values of the gap between the metal plate of the DWS and the dry, uncracked concrete specimen ($\varepsilon_r' = 4.1 - j0.82$).
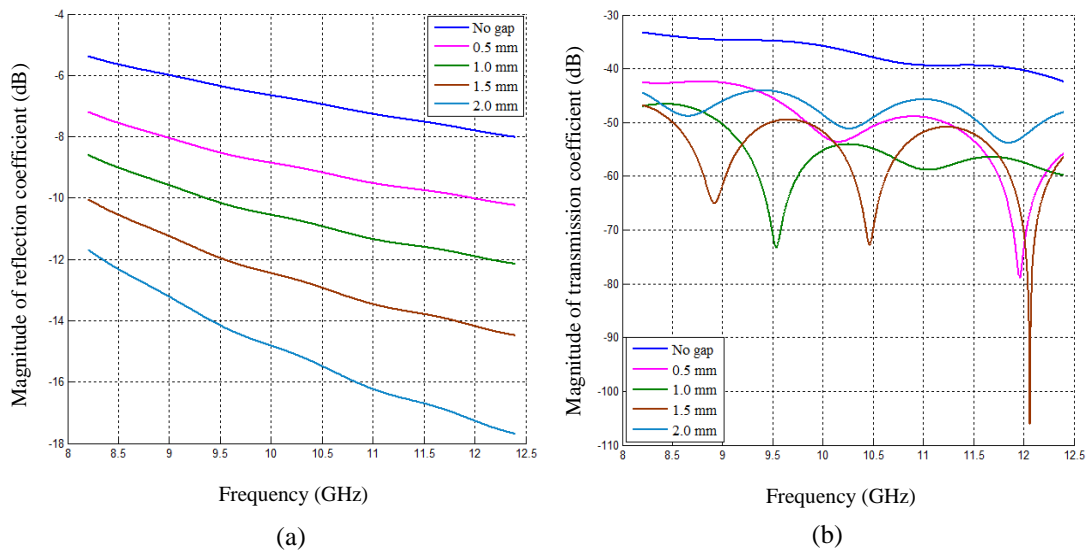
Figure 4.56: Simulated magnitude of (a) reflection coefficient, and (b) transmission coefficient vs. frequency for different values of the gap between the metal plate of the DWS and dry concrete specimen ($\varepsilon_r' = 4.1 - j0.82$) with a rectangular crack 1 mm wide and 50 mm deep at position 1 shown in Figure 4.54c.
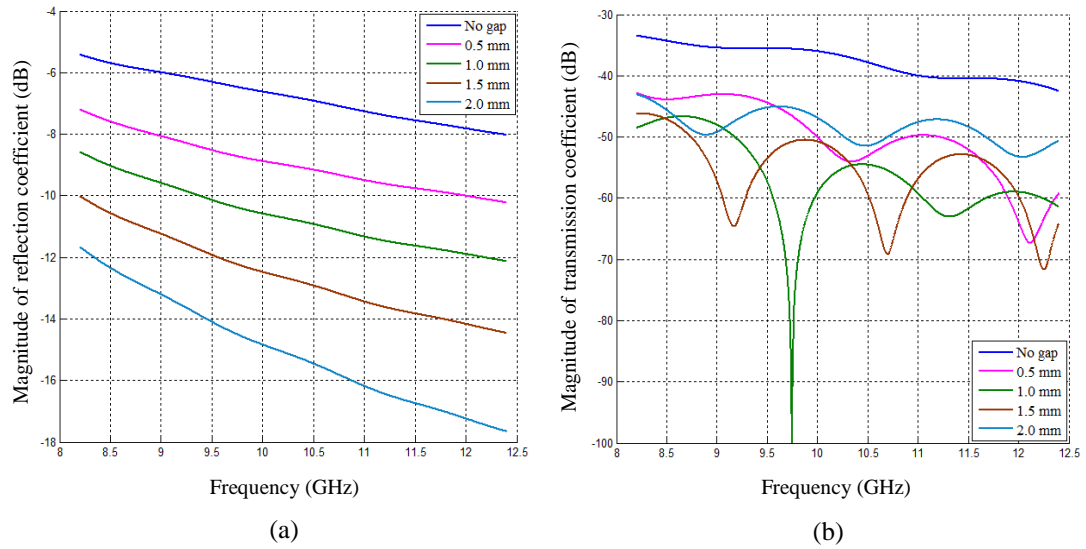
Figure 4.57: Simulated magnitude of (a) reflection coefficient, and (b) transmission coefficient vs. frequency for different values of the gap between the metal plate of the DWS and dry concrete specimen ($\varepsilon_r' = 4.1 - j0.82$) with a rectangular crack 2 mm wide and 50 mm deep at position 1 shown in Figure 4.54c.
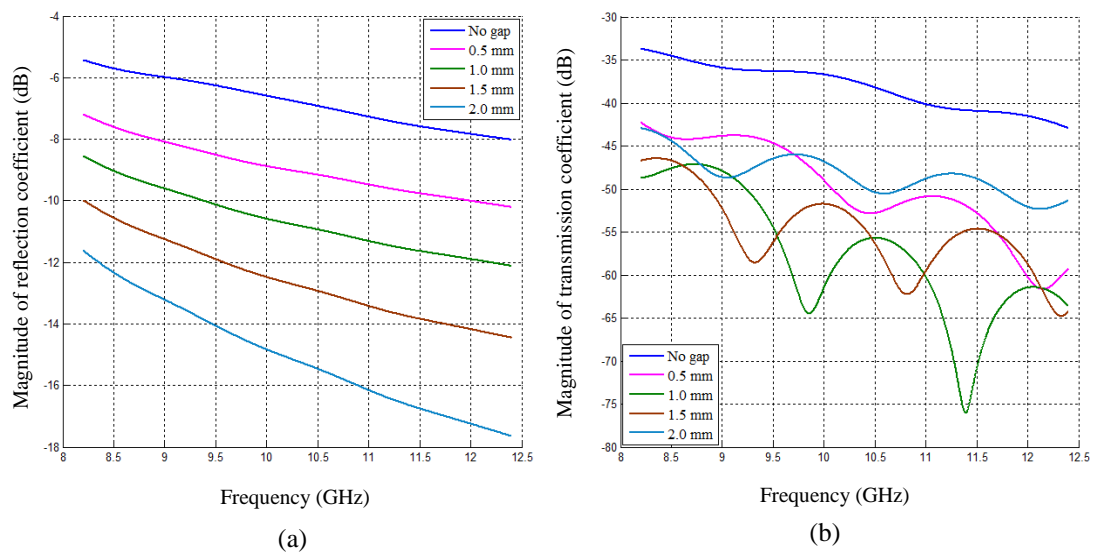
Figure 4.58: Simulated magnitude of (a) reflection coefficient, and (b) transmission coefficient vs. frequency for different values of the gap between the metal plate of the DWS and dry concrete specimen ($\varepsilon_r' = 4.1 - j0.82$) with a rectangular crack 3 mm wide and 50 mm deep at position 1 shown in Figure 4.54c.
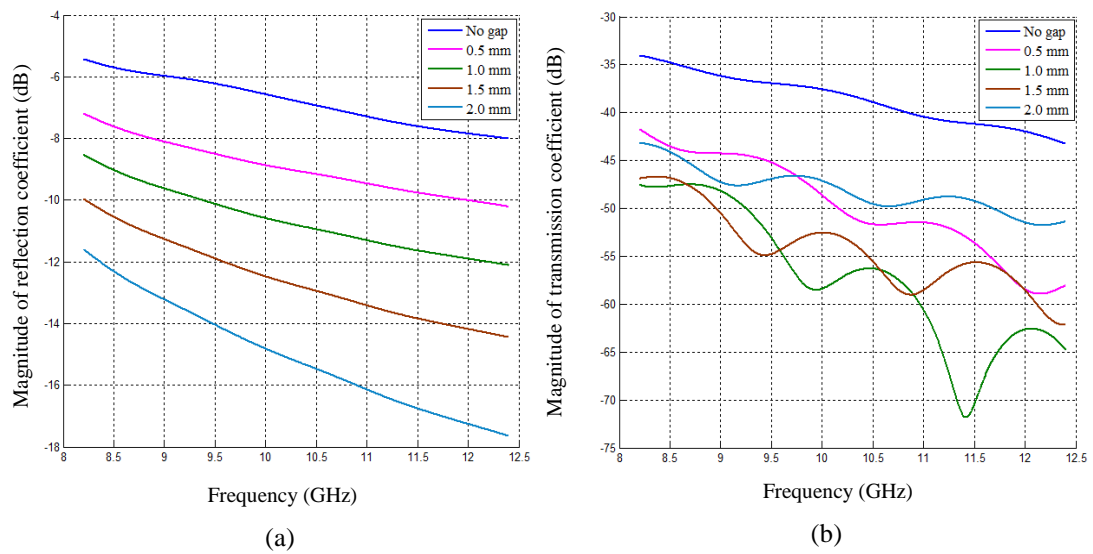
Figure 4.59: Simulated magnitude of (a) reflection coefficient, and (b) transmission coefficient vs. frequency for different values of the gap between the metal plate of the DWS and dry concrete specimen ($\varepsilon_r' = 4.1 - j0.82$) with a rectangular crack 4 mm wide and 50 mm deep at position 1 shown in Figure 4.54c.
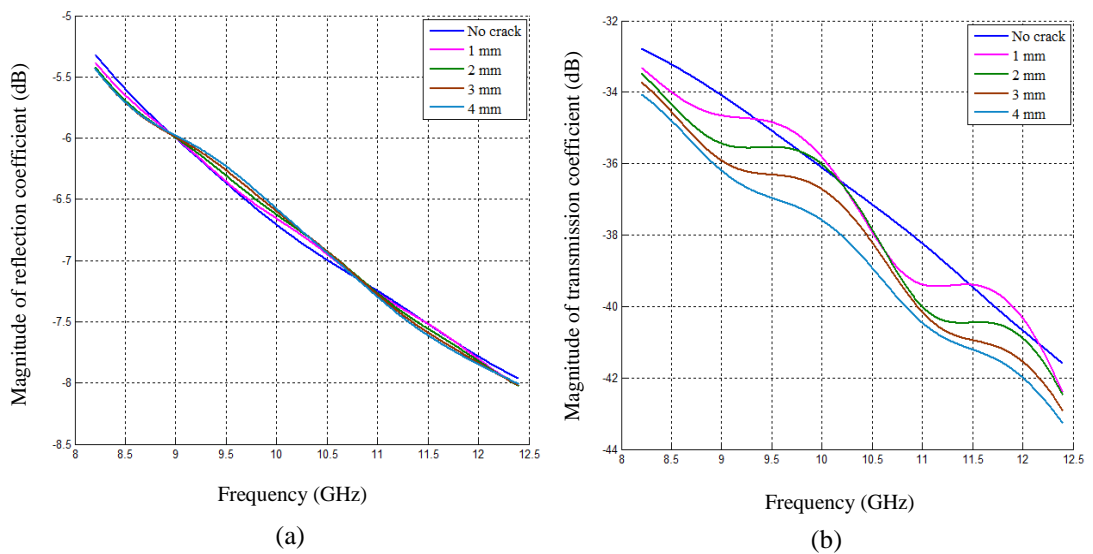
Figure 4.60: Simulated magnitude of (a) reflection coefficient, and (b) transmission coefficient vs. frequency for different widths of crack 50 mm deep at position 1 in Figure 4.54c, with no gap between the metal plate of the DWS and the dry concrete specimen ($\varepsilon_r' = 4.1 - j0.82$).

Figures 4.61 and 4.62 show the magnitudes of the reflection and transmission coefficients vs. frequency for different gap values between the DWS and dry concrete ($\varepsilon_r' = 4.1 - j0.82$) with rectangular cracks 1 mm and 3 mm wide, respectively at position 2 shown in Figure 4.54d. It is seen that because the crack is immediately beneath waveguide section 1, the magnitude of the reflection coefficient decreases significantly for all gap conditions compared to specimens with either no crack or with a crack in position 1. For instance, at the no-gap condition and 10.3 GHz, for the no-crack specimen, S_{11} is –6.88 dB (cf. Figure 4.57a); for the specimen with a crack 1 mm wide at position 1, the value of S_{11} is –6.82 dB, whereas when the crack is at position 2, the value of S_{11} is –7.68 dB. It is also found that an increase in crack width reduces the magnitude of reflection coefficient. At the no-gap condition and 10.3 GHz, S_{11} decreases from –7.68 dB for the 1 mm-wide crack to –9.18 dB for the 3 mm-wide crack (Figure 4.62a). It is observed that for cracks in position 2, the magnitude of the transmission coefficient at the no-gap condition increases with crack width. For example, at the no-gap condition, S_{21} increases from –35.41 dB to –32.71 dB at 10.3 GHz frequency.

Figures 4.63 and 4.64 show the magnitudes of the reflection and transmission coefficients vs. frequency for different gap values between the DWS and dry concrete ($\varepsilon_r' = 4.1 - j0.82$) with triangular cracks with a 4 mm base and with heights of 50 mm and 100 mm, respectively, at position 3 shown in Figure 4.54e. It is seen that the magnitudes of the reflection and transmission coefficients at no-gap fluctuate slightly more when the crack is 50 mm deep than when it is 100 mm deep possibly because the microwave signal strongly penetrates a dry concrete specimen ($\varepsilon_r' = 4.1 - j0.82$) up to 40 or 50 mm, but beyond that the signal strength is very low. Therefore, a triangular crack 100 mm depth has less effect than a crack 50 mm depth. This and other crack phenomena can best be understood by analysing the electric field intensity distribution inside the cracked concrete specimens.

Figure 4.65 illustrates the electric field intensity distributions inside the waveguides and concrete specimens ($\varepsilon_r' = 4.1 - j0.82$) with cracks of different width and height at 10.3 GHz frequency for the no-gap condition. Furthermore, in Figures 4.66 and 4.67, the electric field intensity distribution inside the waveguides and concrete specimens ($\varepsilon_r' = 4.1 - j0.82$) with cracks of different widths and 50 mm

height at different frequencies are presented for the cases where the gap between the DWS and the top surface of the specimen is 0.5 mm and 1.5 mm, respectively.

(a)   (b)
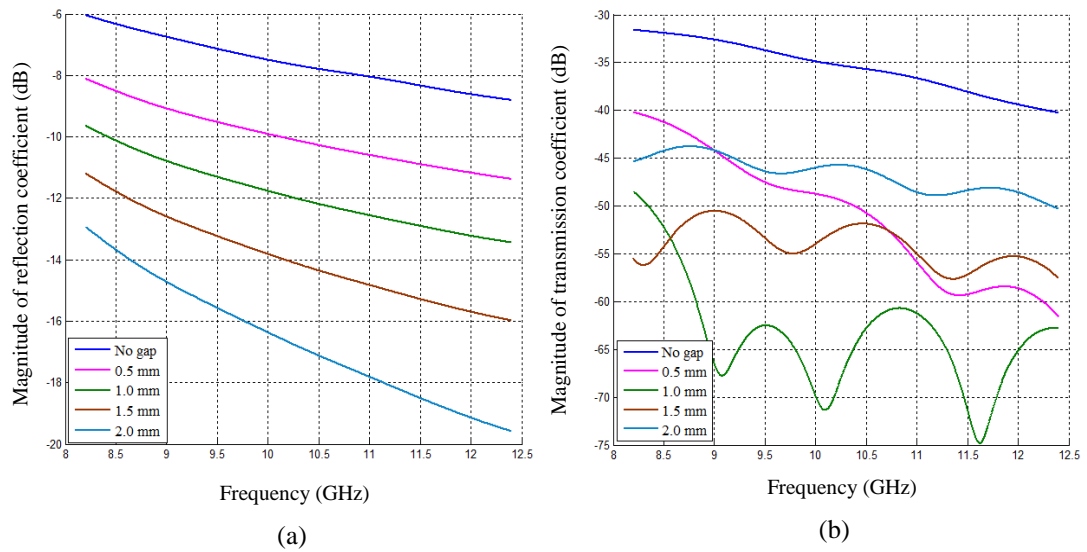
Figure 4.61: Simulated magnitude of (a) reflection coefficient, and (b) transmission coefficient vs. frequency for different values of the gap between the metal plate of the DWS and dry concrete specimen ($\varepsilon_r' = 4.1 - j0.82$) with a rectangular crack 1 mm wide and 50 mm deep at position 2 shown in Figure 4.54d.

(a)   (b)
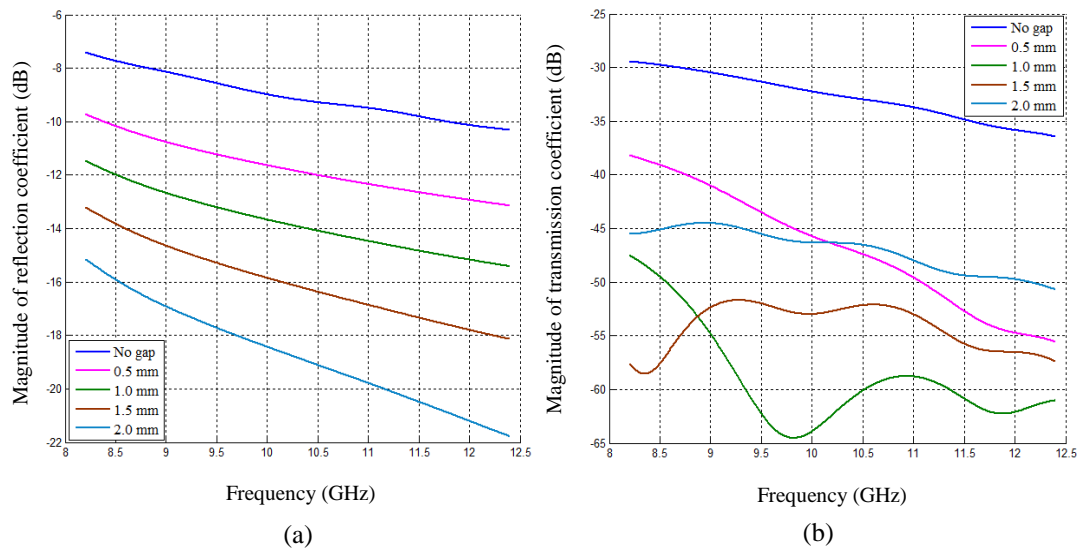
Figure 4.62: Simulated magnitude of (a) reflection coefficient, and (b) transmission coefficient vs. frequency for different values of the gap between the metal plate of

the DWS and dry concrete specimen ($\varepsilon_r' = 4.1 – j0.82$) with a rectangular crack 3 mm wide and 50 mm deep at position 2 shown in Figure 4.54d.

(a) (b)
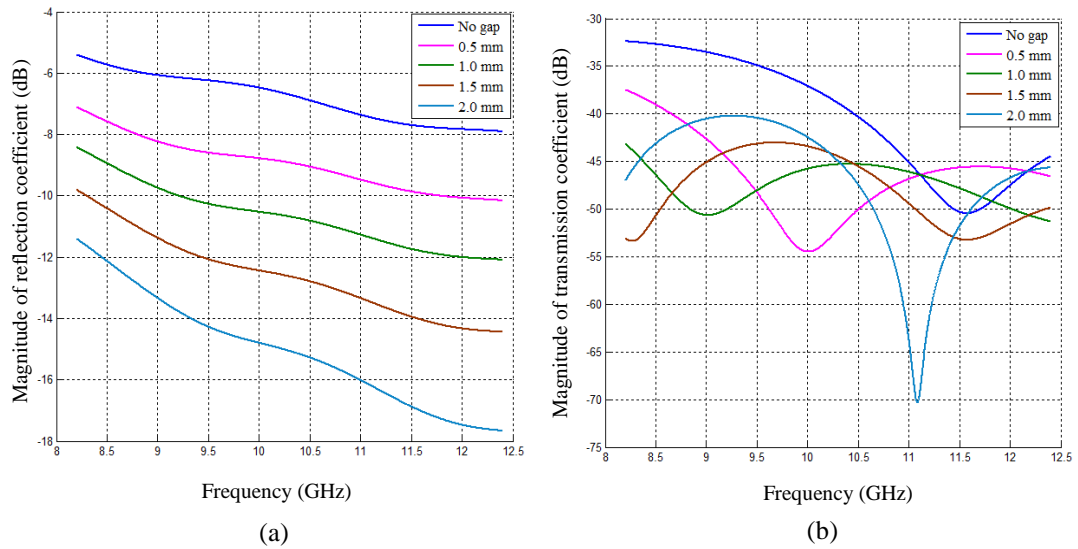
Figure 4.63: Simulated magnitude of (a) reflection coefficient, and (b) transmission coefficient vs. frequency for different values of the gap between the metal plate of the DWS and dry concrete specimen ($\varepsilon_r' = 4.1 – j0.82$) with a triangular crack of 4 mm base and 50 mm depth at position 3 shown in Figure 4.54e.

(a) (b)
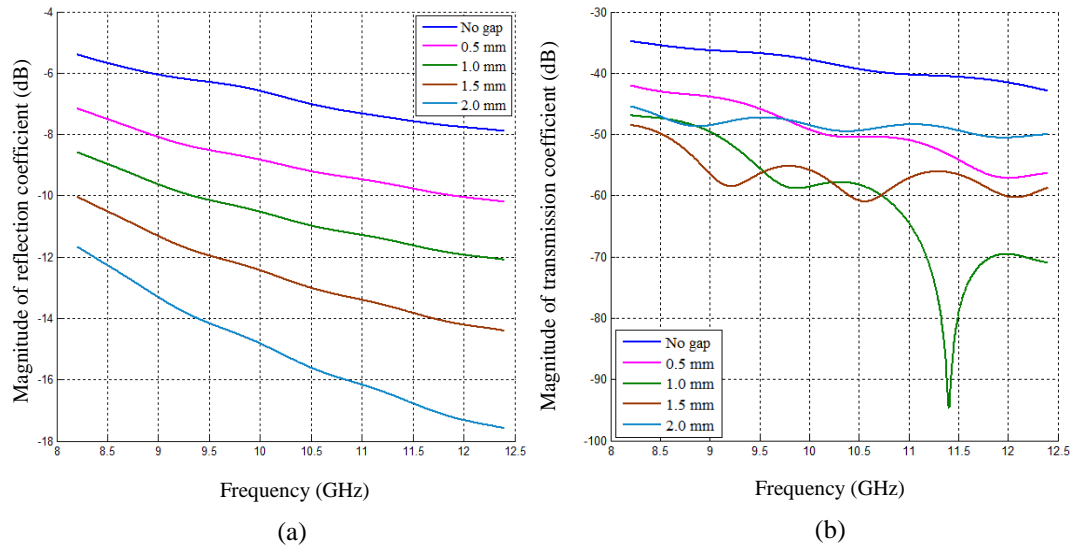
Figure 4.64: Simulated magnitude of (a) reflection coefficient, and (b) transmission coefficient vs. frequency for different values of the gap between the metal plate of the DWS and dry concrete specimen ($\varepsilon_r' = 4.1 – j0.82$) with a triangular crack of 4 mm base and 100 mm depth at position 3 shown in Figure 4.54e.
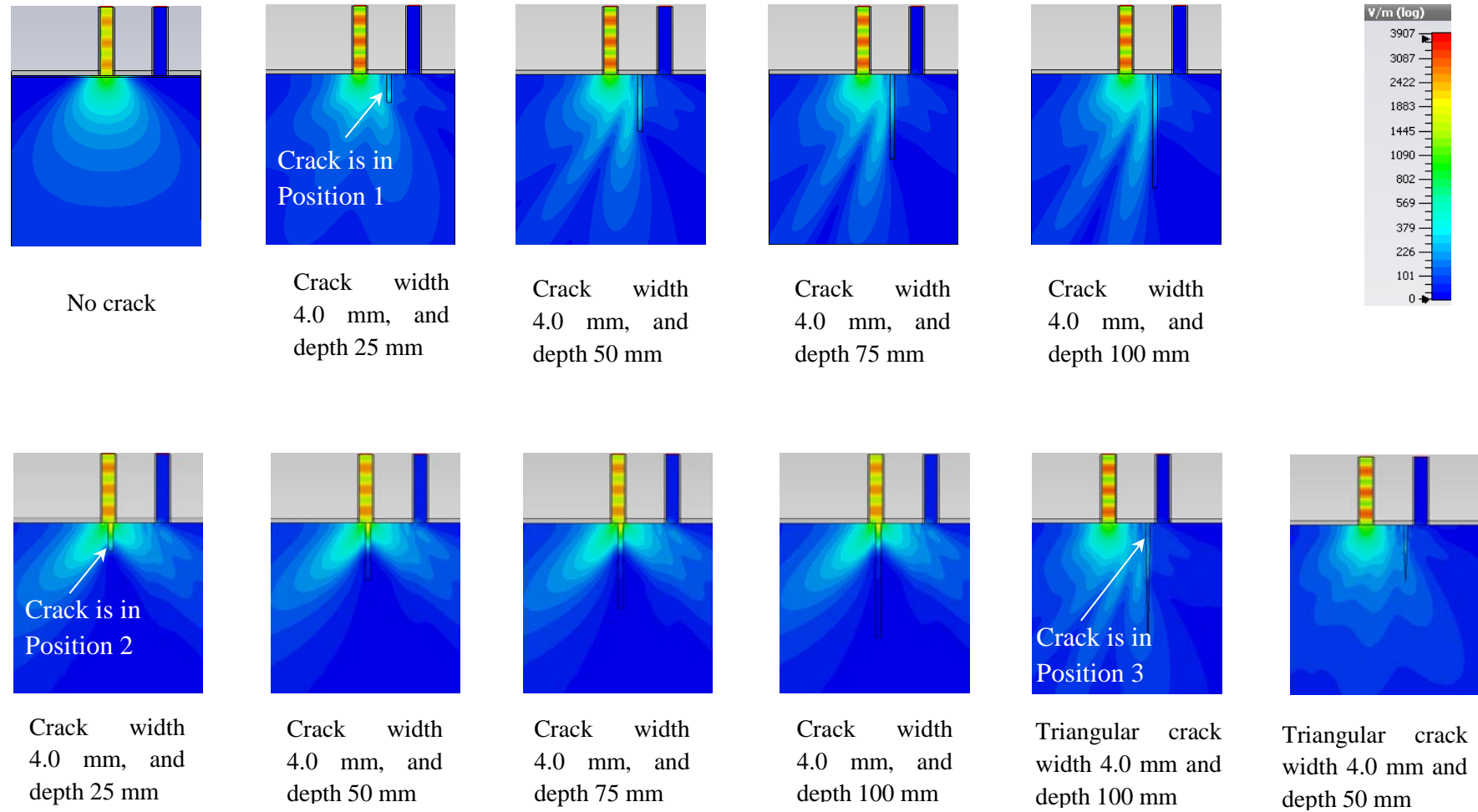
Figure 4.65: Electric field intensity distribution inside waveguides and concrete specimen ($\varepsilon_r' = 4.1 - j0.82$) with cracks of different width and height at 10.3 GHz frequency when there is no gap between the DWS and the top surface of the specimen.
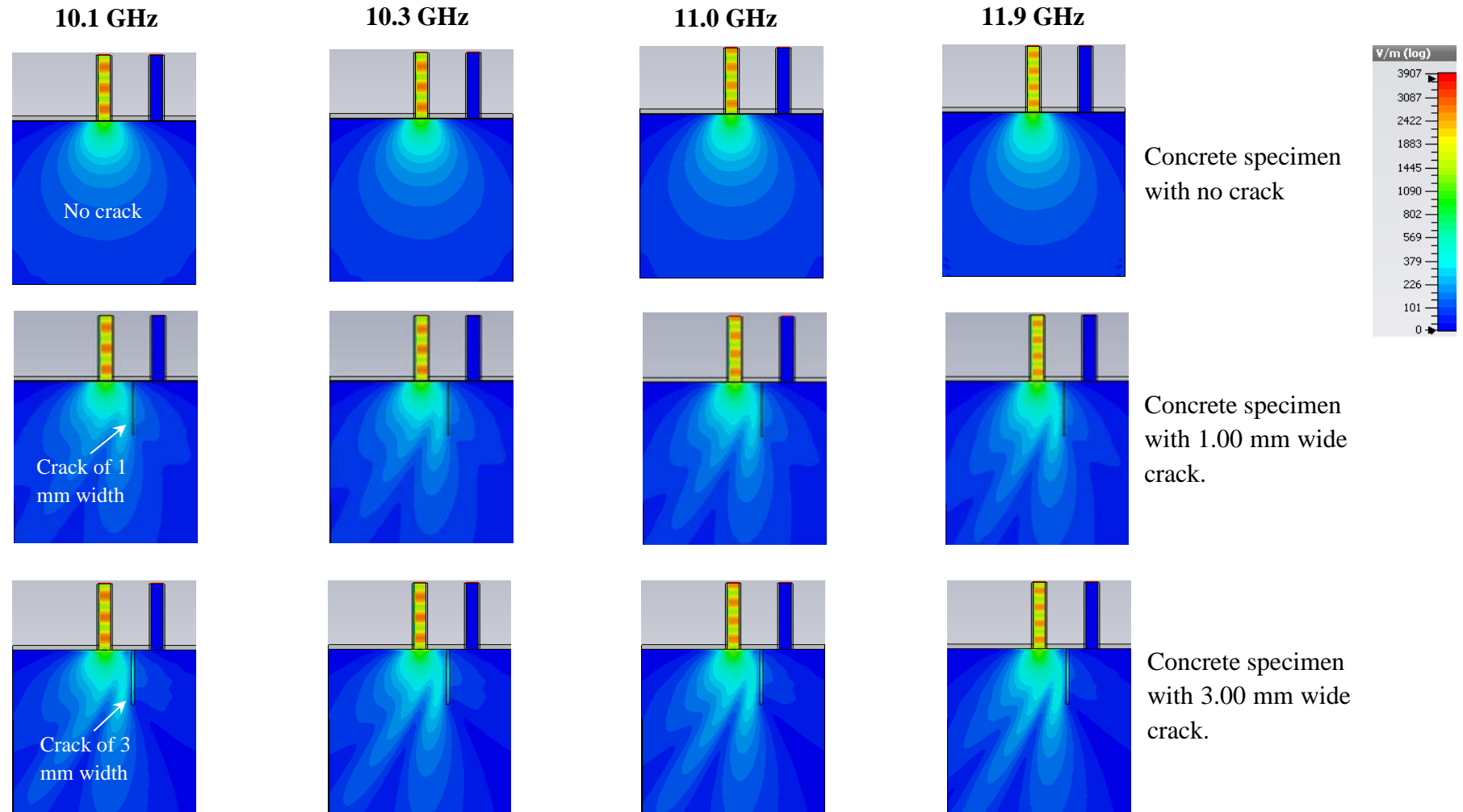
Figure 4.66: Electric field intensity distribution inside waveguides and concrete specimen ($\varepsilon_r' = 4.1 - j0.82$) with cracks of different width and 50 mm height at different frequencies, when there is a 0.5 mm gap between the DWS and the top surface of the specimen.

10.3 GHz **10.4 GHz** **11.25 GHz** **12.1 GHz**

No crack

Crack of 1 mm width

Crack of 3 mm width

Concrete specimen with no crack

Concrete specimen with 1.00 mm wide crack.

Concrete specimen with 3.00 mm wide crack.
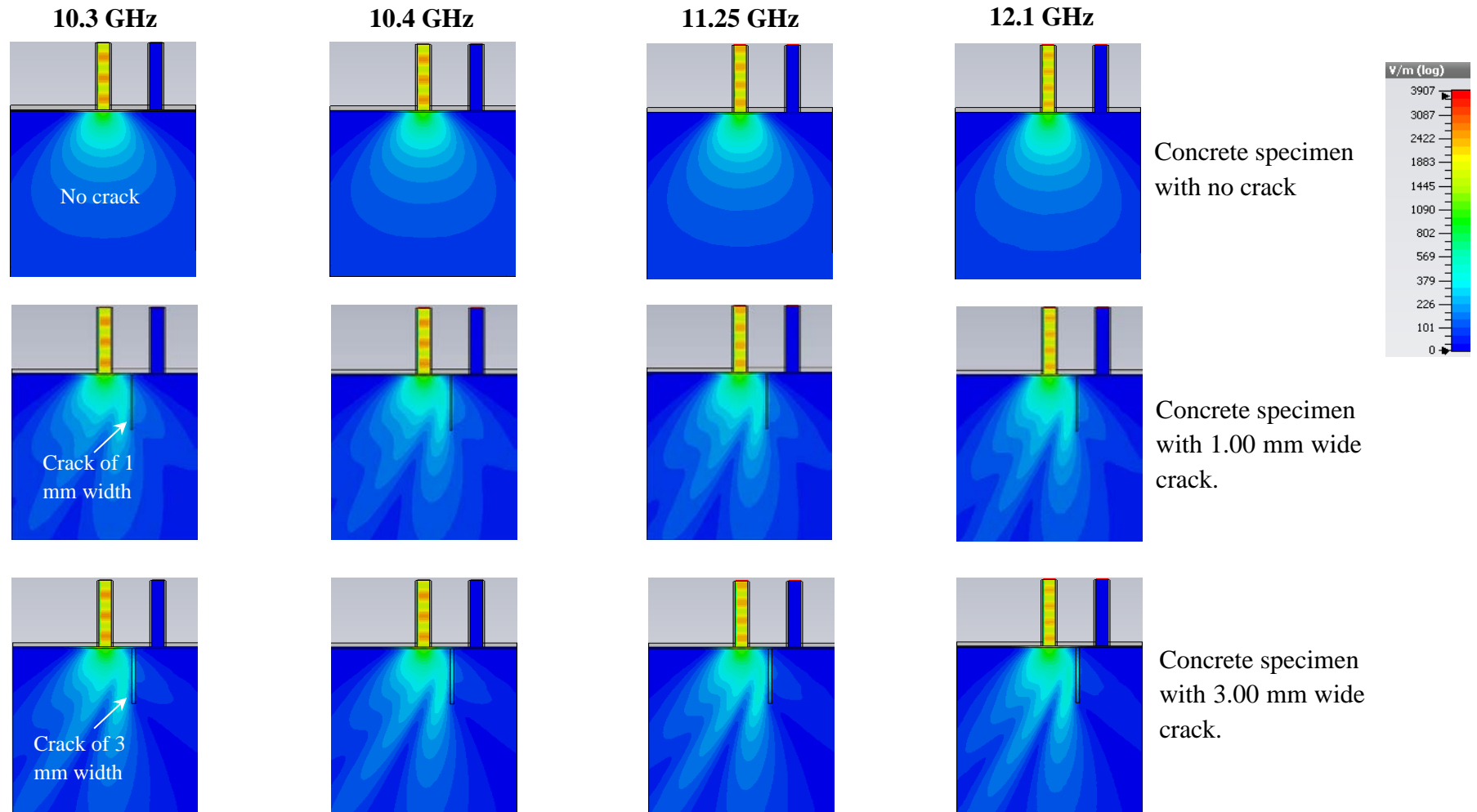
Figure 4.67: Electric field intensity distribution inside waveguides and concrete specimen ($\varepsilon_r' = 4.1 - j0.82$) with cracks of different width and 50 mm height at different frequencies, when there is a 1.5 mm gap between the DWS and the top surface of the specimen.

4.8   Sensitivity Analysis

During the measurement with cement-based specimen using DWS, it has been found that there are some situations that may affect the accuracy of the measured parameter. For instance, the fresh mortar specimen lost moisture by natural dehydration as it aged, thus varying its dielectric properties. This section contains numerical analyses of events that might change the measured magnitude of the reflection coefficient, S_{11}, and the transmission coefficient S_{21}.

Figure 4.68 shows the simulated magnitude of the reflection and transmission coefficient vs. frequency for different dielectric constant values of the fresh mortar specimen for no gap between the specimen and the metal plate of the DWS. The loss tangent of the specimen was set as 0.105. It is seen that the magnitude of the reflection coefficient decreases with the decrease of dielectric constant over the entire X-band frequency, and also decreases with increasing frequency, with equal differences in S_{11} between adjacent dielectric constant curves. On the other hand, the magnitude of the transmission coefficient decreases with increase of dielectric constant and the differences in S_{21} between adjacent dielectric constant curves are not equal, but increase with decreasing dielectric constant of the specimen.

In Figure 4.69, the simulated magnitudes of the reflection coefficient and transmission coefficient vs. frequency for different loss tangents for the fresh mortar at no gap between specimen and DWS metal plate are presented. The dielectric constant of the specimen under test was fixed at 17.0. It is clearly seen in Figure 4.69a that variations in the loss tangent of the specimen have negligible effect on the magnitude of the reflection coefficient. However, the magnitude of the transmission coefficient is significantly affected by variations in loss tangent, decreasing with increasing loss tangent (Figure 4.69b).

Figure 4.70 shows the simulated magnitudes of reflection coefficient and transmission coefficient vs. frequency for very small values of the gap between specimen and DWS. These may be attributable to the thickness of the polythene film covering the specimen, or the surface roughness of the specimen, operator error, and so on. It is clearly seen that small gaps up to 0.3 mm have a minor effect on both S_{11}

and S_{21} but, once the gap exceeds 0.3 mm, large jumps are seen in the magnitude of both the reflection and transmission coefficients.
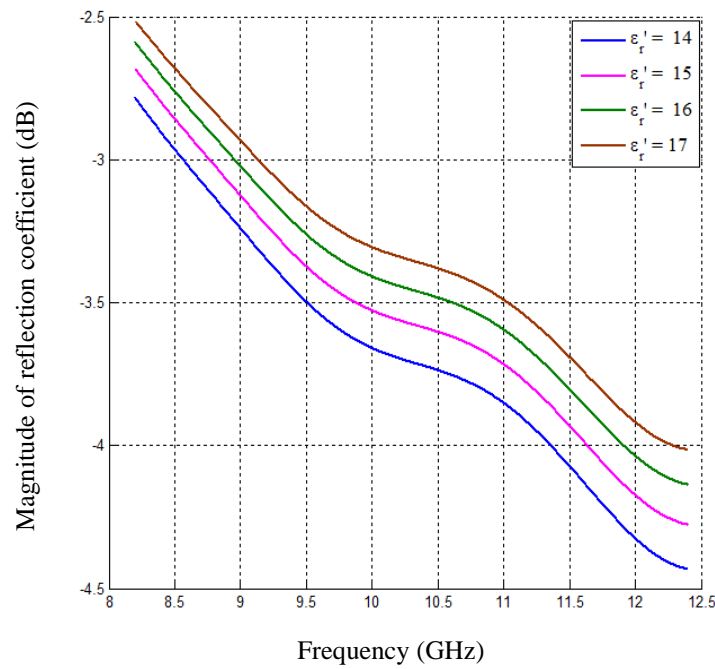
(a)
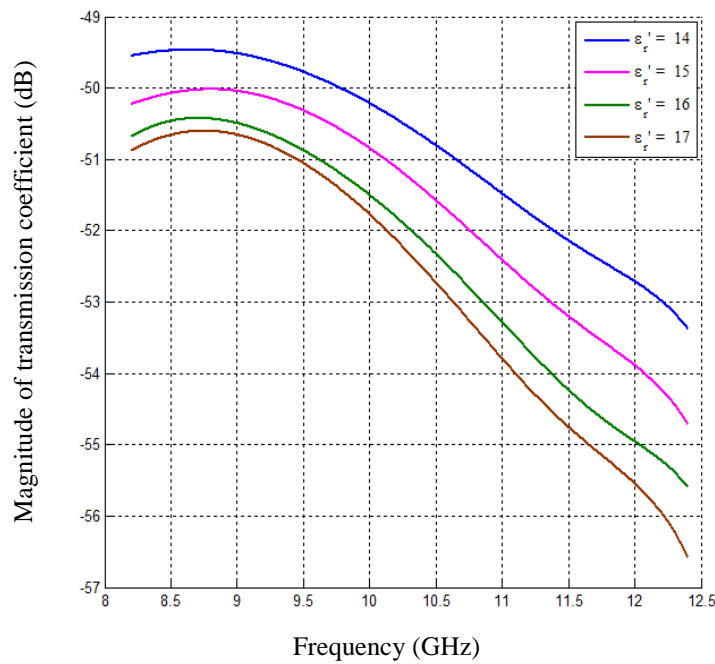
(b)

Figure 4.68: Simulated magnitude of (a) reflection coefficient and (b) transmission coefficient vs. frequency for different values of dielectric constant of fresh mortar with no gap between specimen and DWS metal plate.

(a)

(b)
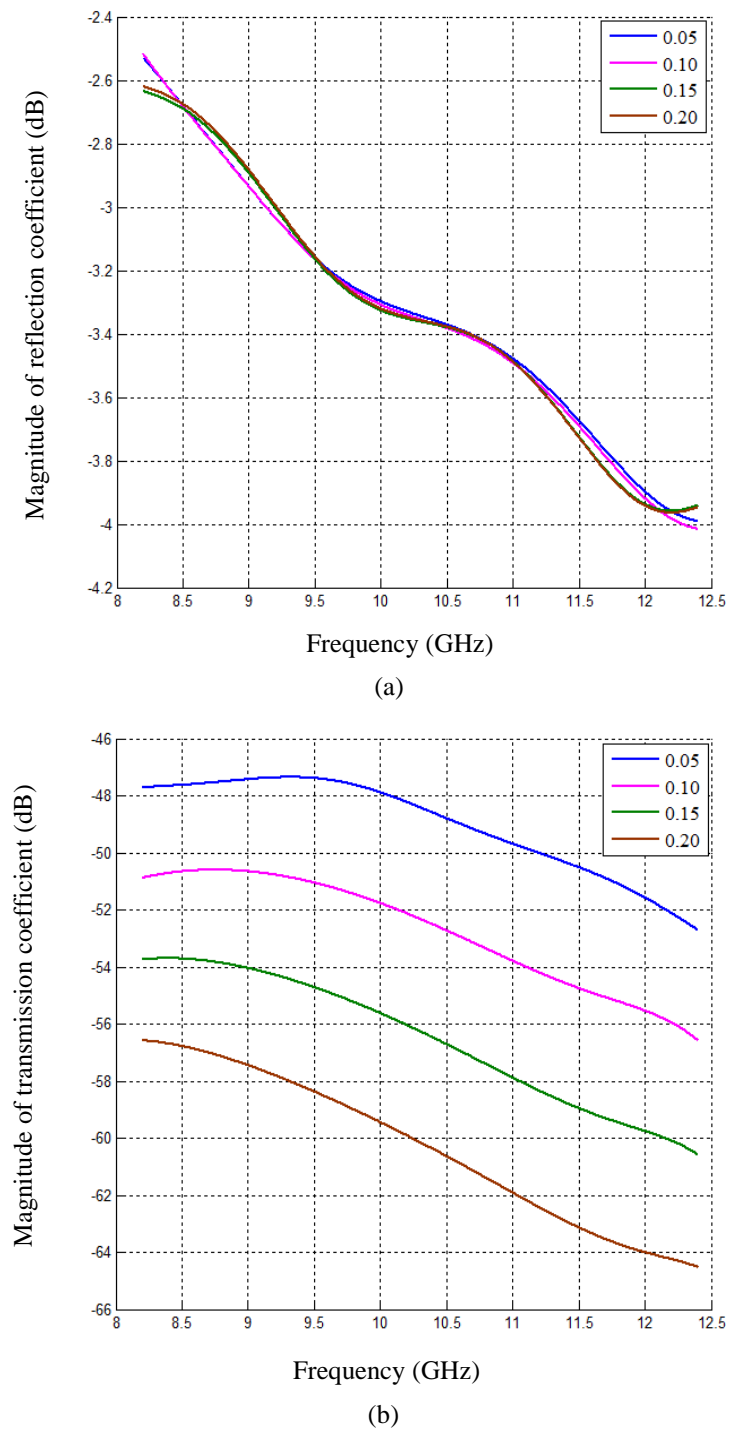
Figure 4.69: Simulated magnitude of (a) reflection coefficient and (b) transmission coefficient vs. frequency for different values of loss tangent of mortar specimen with no gap between specimen and DWS metal plate.
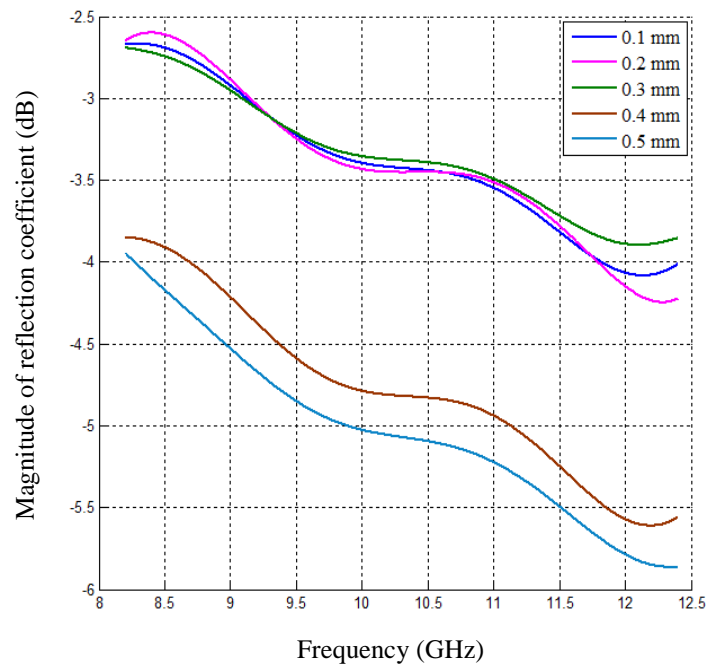
(a)
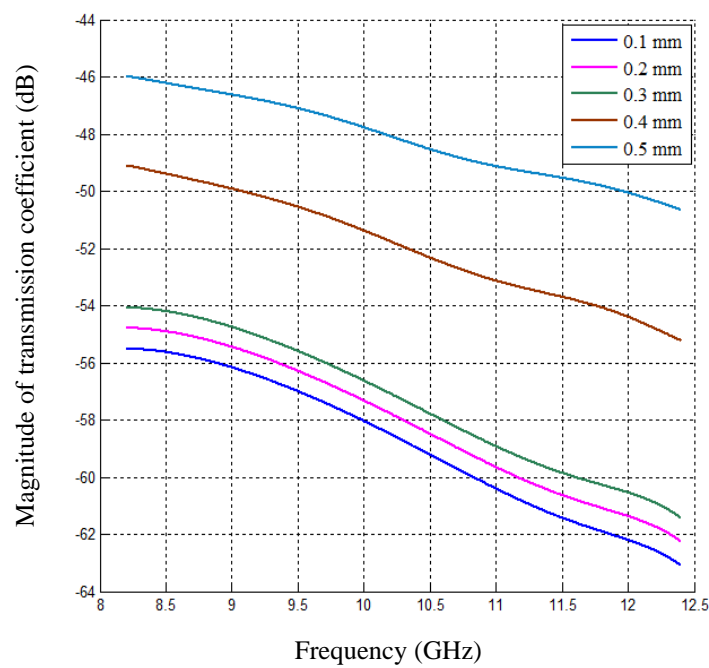
(b)

Figure 4.70: Simulated magnitude of (a) reflection coefficient and (b) transmission coefficient vs. frequency for different values of small gap (0.1–0.5 mm) between the mortar specimen ($\varepsilon_r = 17.0 – j\ 3.4$) and the DWS metal plate.

4.9   Summary

The design and development of a novel microwave dual waveguide sensor for cement-based composite structures are presented in this chapter. The proposed sensor mainly consists of two standard X-band waveguide sections having each end embedded in a metal plate. A parametric study of the proposed DWS with fresh concrete specimens performed in single waveguide mode (described in Chapter 3) and in dual waveguide mode showed that the dual waveguide mode of the proposed DWS may provide more measurement data than the single waveguide mode for characterising metal–concrete structures, such as: (1) transmission properties of wave propagated along the gap between the metal and concrete surfaces (i.e., guided wave); (2) reflection properties of the metal–concrete interface at two different places at the same stage of concrete; and (3) data for a larger area of the interface under inspection. These measurements may provide advanced characterisation of the metal–concrete structures, including the detection of gaps and cracks, and the dielectric/physical properties of concrete.

The DWS was fabricated and applied to measure small gaps (0.0–2.0 mm) between fresh and dry concrete specimens and a steel plate specimen. For this purpose, the reflection and transmission coefficients were measured with no gap to determine the dielectric permittivity of the fresh concrete specimen in the area of measurement, using the algorithm developed in Chapter 3. Ultimately, it was found that the fabricated DWS was capable of measuring small gap between the metal plate of the DWS and fresh (or dry) concrete specimens. Comparisons between measured and simulated results clearly indicated that the highest accuracy was attained in the range 1.0–2.0 mm for fresh concrete, and 0.5 –2.0 mm gaps for dry concrete. The relatively large measurement error at small gaps are attributed to sensor fabricated error as well as the arrangement of the gap (mainly for fresh concrete) and surface roughness of concrete (mainly for dry concrete).

The proposed DWS was tested by measuring small distances between its metal plate and a steel plate specimen. It was shown that the DWS measured small distances from the steel plate specimen using the reflection coefficient and the transmission coefficient. Additionally, a comparison of the reflection and

transmission properties at different gap values for the steel plate and the concrete specimens showed that the steel plate specimen had higher S_{11} and S_{21} magnitudes than the concrete specimens at all gap values.

The detection of cracks inside dry concrete specimens, and the influence of the size, position and shape of the crack were also numerically investigated using the proposed dual waveguide sensor. It was shown that variations in the reflection coefficient and transmission coefficient were the indicators of crack depth and location.

Finally, the sensitivity of the magnitude of the reflection coefficient and transmission coefficient of the proposed DWS to variations in dielectric constant and loss tangent of concrete specimens, and the effects of surface roughness or polythene film thickness were studied numerically. It was found that the magnitude of the reflection coefficient was most sensitive to changes of dielectric constant, while the transmission coefficient was most sensitive to changes of loss tangent in the concrete specimens. These results showed that the measurement and analysis of both the reflection coefficient and the transmission coefficient can distinguish the effect of changes of gap size and dielectric properties of concrete.

Chapter 5

Dual Waveguide Sensor with Rectangular Dielectric Insertions

5.1   Introduction

In the previous chapter it was shown that the proposed dual waveguide sensor comprising empty waveguide sections was capable of measuring a small gap (e.g., a debonding gap) between the concrete and a metal plate. However, for measurement with fresh and early-age concrete specimens there is always a risk of cement paste and/or water entering the waveguide sections and significantly affecting the results. The main aim of the work included in this chapter was to overcome this problem in the proposed rectangular dielectric insertions implanted in the dual waveguide sensor (referred to as the dielectric-loaded DWS) such that their component parts prevent the penetration of undesired substances and thus improve sensor performance. The design and fabrication of the proposed dielectric-loaded DWS is described. Next, the reflection, transmission and resonant properties of the sensor with a concrete–metal structure with no gap are investigated, and the complex dielectric permittivities of specimens of fresh and dry concrete are determined using measured data and extensive simulations combined with an improved algorithm. Measurement and simulation are then performed to detect and monitor the gap between the metal plate and concrete specimens of different age, and the results are compared. Finally, the sensitivity of the dielectric-loaded DWS to variations of dielectric and geometrical properties of the insertions is analysed.

5.2   Design of Sensor

Figure 5.1 is a schematic of the proposed microwave dielectric-loaded DWS. The sensor consists of two dielectric-loaded rectangular waveguide sections installed in a metal plate complete with flanges for connection to the measurement system (Figure 5.1a). The distance between the waveguide sections is L. The cross-sectional side view of the sensor for detecting the gap between a metal plate and concrete is

shown in Figure 5.1b. Figure 5.1c is a perspective-view schematic of one of the dielectric insertions with dimensions $a \times b$, which are equal to the aperture dimensions of the rectangular sections, and of variable length.

Figures 5.2a, b are two views of the fabricated X-band dielectric-loaded DWS, showing the waveguide sections and a metal plate similar to those described in Chapter 4. Two rectangular acrylic dielectric insertions measuring $22.75 \times 22.5 \times 10.0$ mm are shown in Figure 5.2c. The length was selected to provide a resonant response within the X-band.
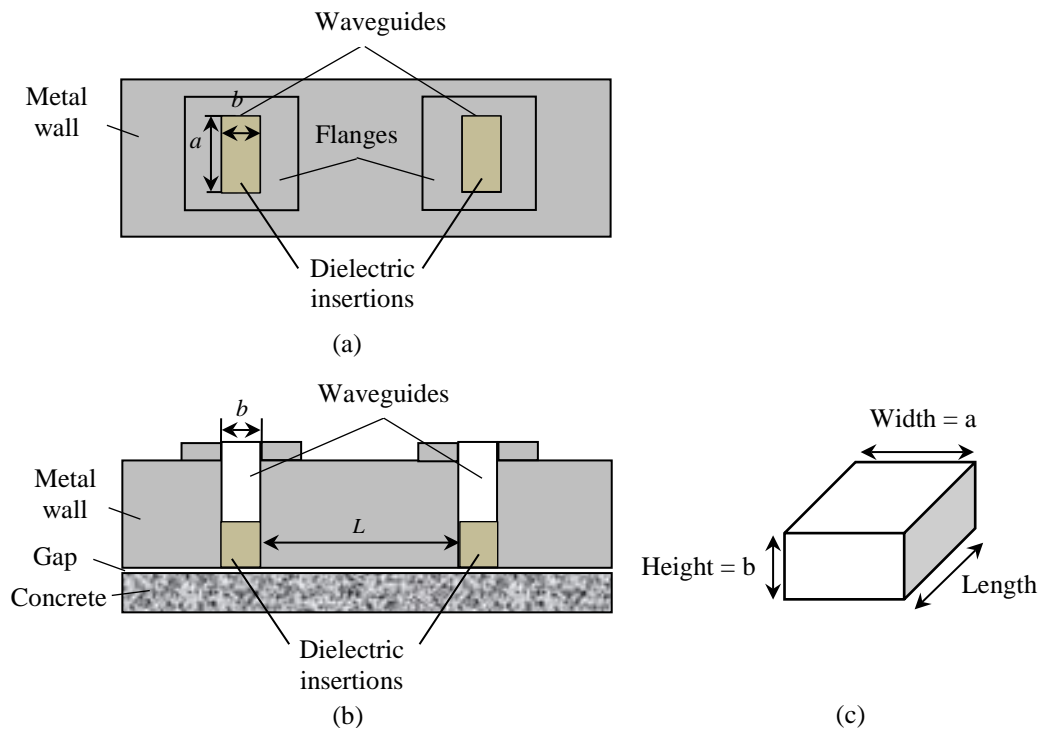
Figure 5.1: Schematic of the proposed dielectric-loaded dual waveguide sensor: (a) top view; (b) cross-sectional side view with concrete structure; and (c) perspective-view schematic of the dielectric insertion.
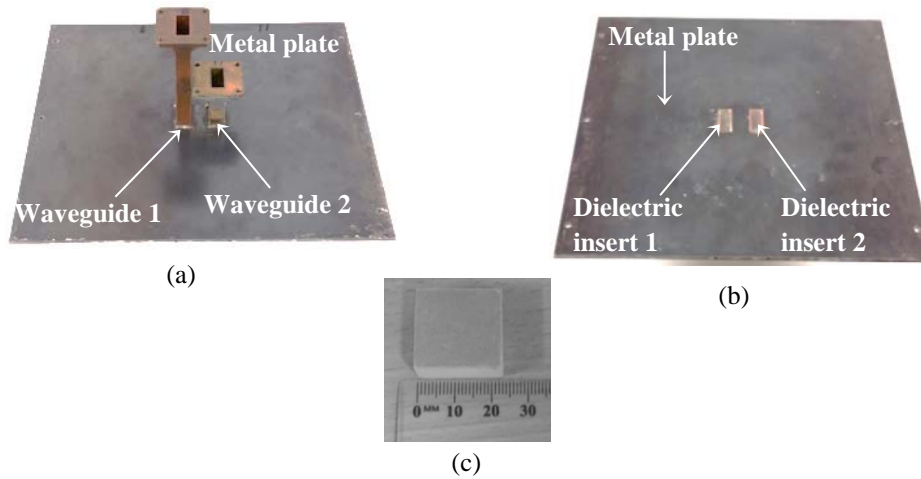
Figure 5.2: Photographs of (a) top of DWS and (b) its rear view, showing dielectric inserts, and (c) the rectangular dielectric insert made of acrylic material.

5.3 Measurement with Fresh and Early-Age Concrete Specimens

This section describes the measurement approach and results with concrete specimens using the proposed dielectric-loaded DWS. First, the reflection coefficient, S_{11}, and transmission coefficient, S_{21}, were measured with no gap between the concrete specimen and the metal plate. Second, S_{11} and S_{21} were measured for different gaps with early-age concrete specimens of variable ages.

5.3.1 Specimens and Measurement Setups

In this study, a standard specimen of fresh concrete with maximum aggregate size of 10 mm, 18 mm slump and 40 MPa 28-day compressive strength was prepared. A cubic wooden mould measuring $250 \times 250 \times 250$ mm was used to hold the fresh concrete specimen; the fabricated dielectric-loaded DWS replaced one side of the mould to ensure a no-gap condition between the fresh concrete and metal plate, as shown in Figure 5.3a, b.
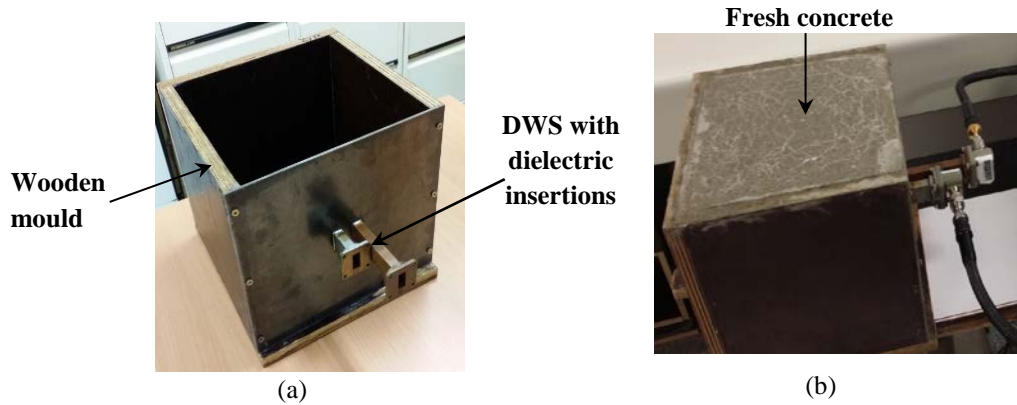
Figure 5.3: Cubic wooden mould with one side replaced by the dielectric-loaded DWS: (a) empty mould, and (b) with fresh concrete, adapters and cables.

Two measurement arrangements were used in this investigation for measuring the magnitude and phase of the reflection and transmission coefficients of fresh and early-age concrete with the microwave dielectric-loaded DWS, using a performance network analyser (PNA). Figure 5.4a shows measurement setup 1, where one side of fresh specimen holding mould is replaced by the fabricated sensor, thereby ensuring that no gap would be present between the specimen and the metal plate of the DWS. In measurement setup 2, the early-age concrete specimen with the mould removed was used as shown in Figure 5.4b, to provide air gaps of values (0, 0.5, 1.0, 1.5 and 2.0 mm between the specimen and metal plate, using thin paper sheets. Suitable adapters and cables were used to connecting the sensor to the PNA. The dielectric-loaded DWS radiated microwave signals from the PNA into the specimen through the dielectric insertions and picked up the reflected and transmitted signals again through insertions. The calibration of the setup at the output apertures of the waveguide-coaxial adapters was performed using an X-band rectangular waveguide calibration kit.

(a)

(b)
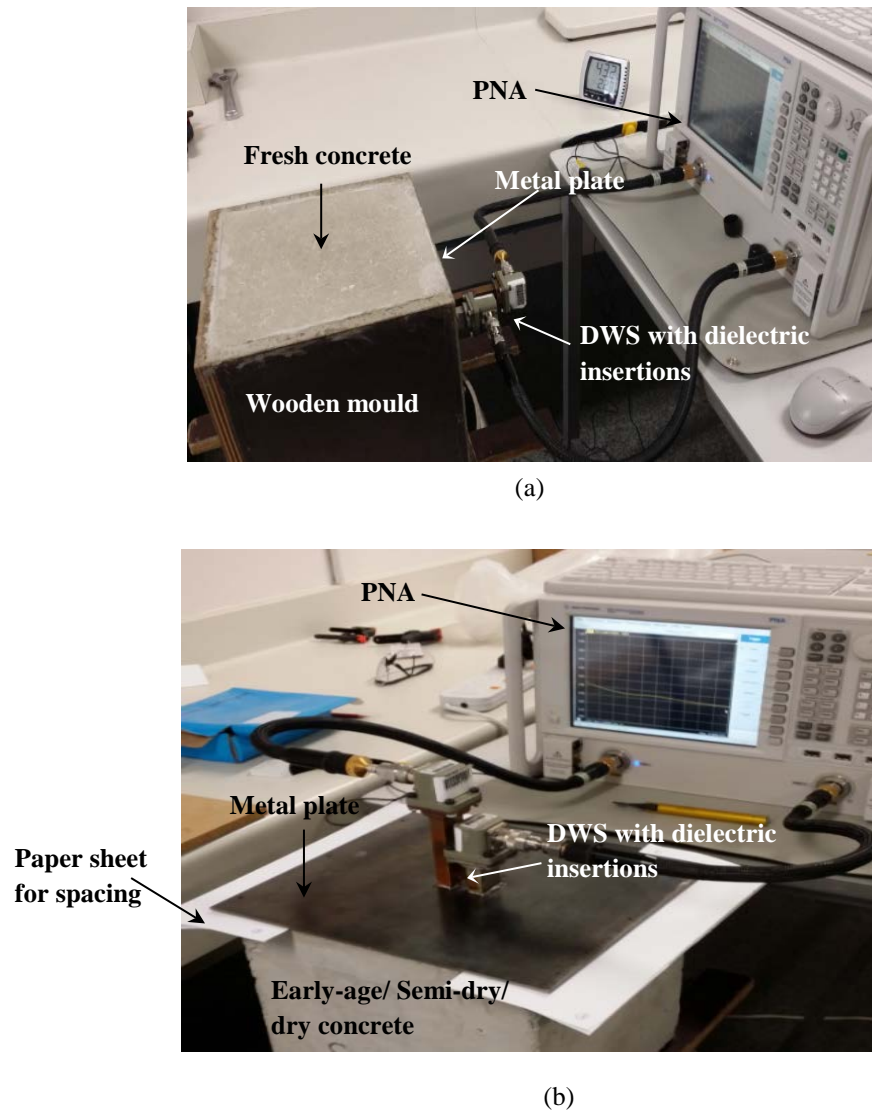
Figure 5.4: Measurement setup, including PNA and dielectric-loaded DWS: (a) for fresh concrete at no-gap condition, and (b) for early-age / semi-dry / dry concrete specimens with different gaps between metal and specimen.

5.3.2 Measurement Results and Discussion

No gap between metal plate and specimens

The reflection and transmission coefficients were measured at each of first six hours after casting the fresh concrete specimen. Measurements were also conducted for five times in each day from the second to the eighth day using identical settings, and averaged for each day.

Figure 5.5 shows the measured magnitude and phase of the reflection coefficient vs. frequency at the first six hours after casting the fresh concrete specimens obtained with the dielectric-loaded DWS at the no-gap condition. The reflection coefficient showed a resonant response which decreased over time at all frequencies; the most noticeable decrease takes place at the resonant frequency at approximately 10.9 GHz. It should be emphasised that the resonant frequency did not change in this case. Also, it was observed that the phase of the reflection coefficient showed no significant change in the first six hours. During the first six hours, changes of loss factor of the concrete were the main contributor to changes in the reflection coefficient.

For illustrative purposes, Figure 5.6 presents the average measured magnitude and phases of the reflection coefficient along with and standard deviation vs. frequency for the first day after casting the concrete using the dielectric-loaded DWS in the no-gap condition. The average of the first six hours' measurements is shown; the standard deviation is a measure of the changes of measured magnitude and phase at these measurement times. It is clearly seen that the change in magnitude exceeds the phase change for the reflection coefficient in the first-day fresh concrete.

Figure 5.7 shows the measured magnitude and phase of the transmission coefficient vs. frequency for the first six hours after casting the concrete specimen, using the dielectric-loaded DWS at the no-gap condition. It is seen that the magnitude of the transmission coefficient has no resonant response, but S_{21} fluctuates over the frequency band. It is also noted that S_{21} (dB) increases over time for the entire frequency band. Furthermore, it is observed that the phase of S_{21} shifts significantly towards higher frequencies with increasing time in the first six hours of the fresh concrete.

The average measured magnitude and phase of the transmission coefficient, along with the standard deviations vs. frequency of first-day fresh concrete using dielectric-loaded DWS in the no-gap condition are shown in Figure 5.8. It is clearly seen that both the magnitude and the phase of the transmission coefficient change over time at each frequency. The two sets of measurement results shown in Figures 5.6 and 5.8 were used to determine the complex dielectric permittivity of first-day fresh concrete specimen as described in section 5.5.2.

Figure 5.9 shows the average measured magnitude and phase of the reflection coefficient vs. frequency for the first eight days for the no-gap condition. It is seen that S_{11} decreases significantly from the first to second day over the entire operating frequency range, attributed to the transition from fresh to hardened concrete on the first day [13], [14]. Changes of the magnitude are negligible over the next six days. The phase of the reflection coefficient demonstrates similar behaviour, as Figure 5.9b shows; however, it is notable that the change of phase occurs only in the vicinity of the resonant frequency (10.9 GHz). These results show that the changes in the dielectric constant of concrete contribute most to the changes of the reflection properties during the transition from fresh to hardened concrete.

Figure 5.10 shows the average measured magnitude and phase of transmission coefficient vs. frequency in first eight days for the no-gap condition. It is seen that S_{21} increases significantly from the first to second day, and by a small amount from the second to fourth day over the entire operating frequency range, then barely changes. It is also found that the phase of the transmission coefficient shifts towards the higher frequencies by a reasonable amount from the first to second day, then continues to shift but by a lesser amount.
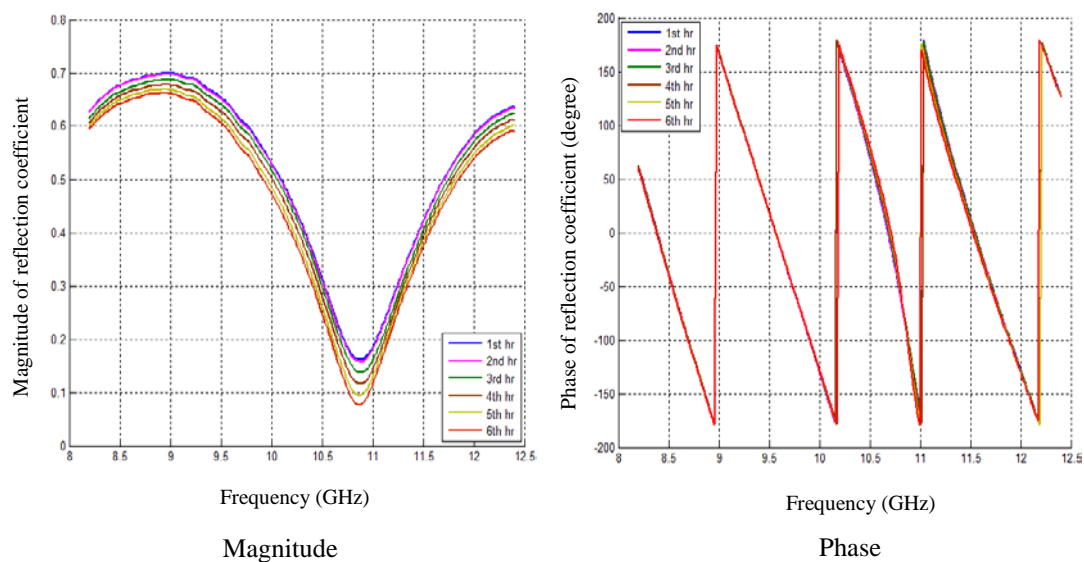
Figure 5.5: Measured magnitude and phase of reflection coefficient vs. frequency for the first six hours after casting the concrete specimens, using the dielectric-loaded DWS with no gap between specimen and metal plate.
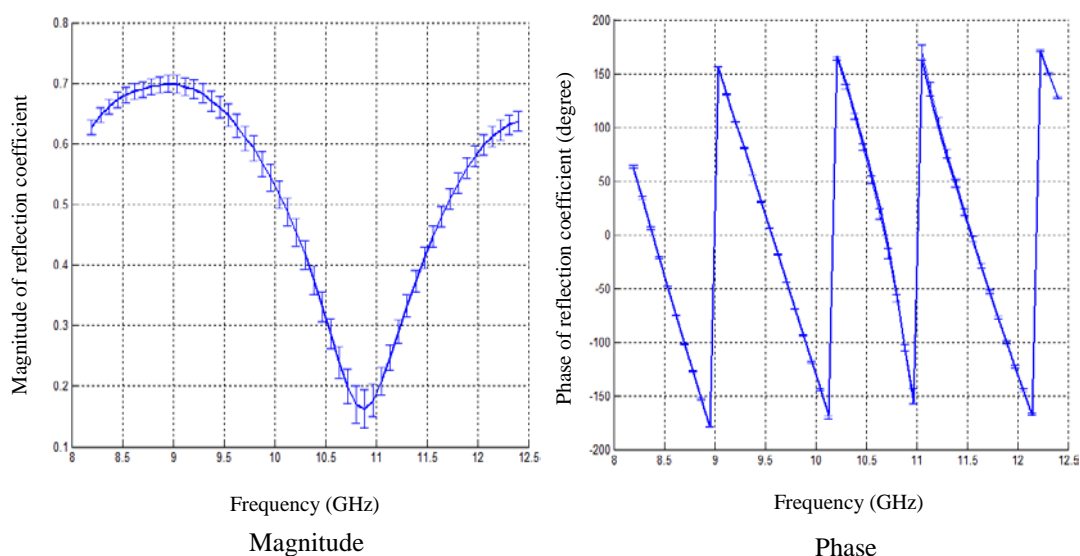
Figure 5.6: Average measured magnitude and phase of reflection coefficient vs. frequency along with standard deviations for first-day concrete using the dielectric-loaded DWS with no gap between specimen and metal plate.
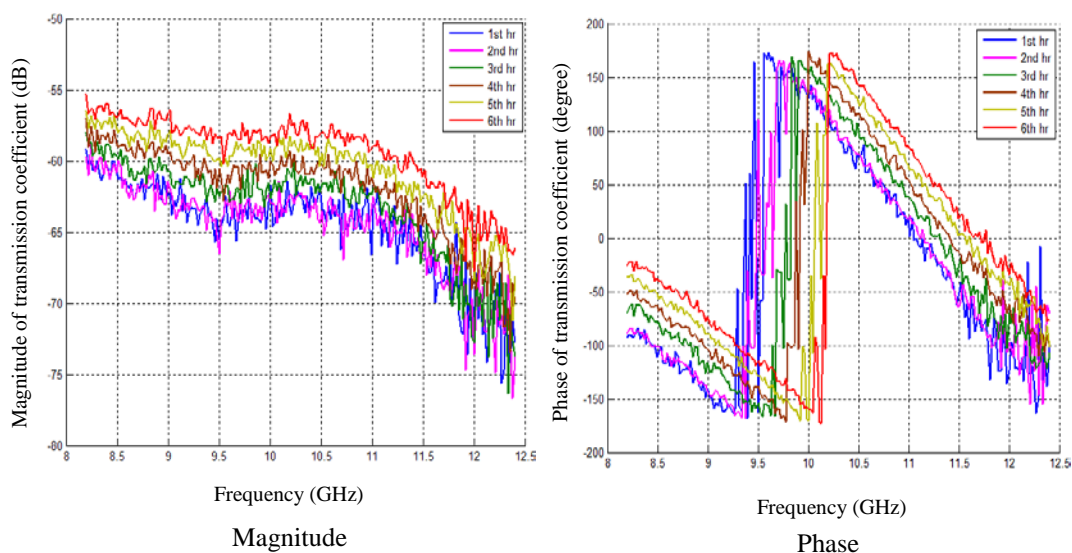
Figure 5.7: Measured magnitude and phase of transmission coefficient vs. frequency for first six hours of first-day concrete using the dielectric-loaded DWS with no gap between specimen and metal plate.
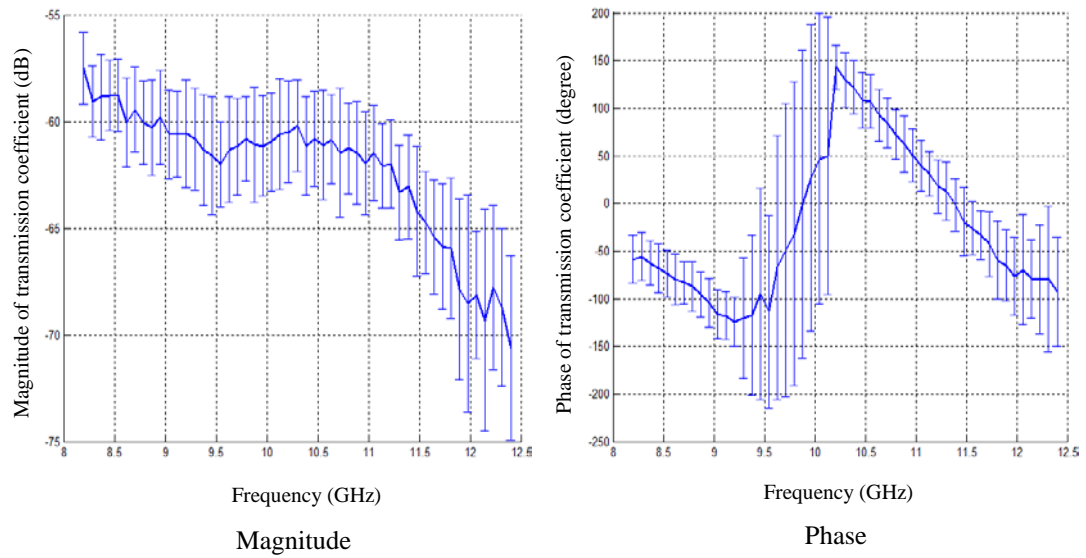
Figure 5.8: Average measured magnitude and phase of transmission coefficient vs. frequency along with standard deviations for first-day concrete using the dielectric-loaded DWS with no gap between specimen and metal plate.
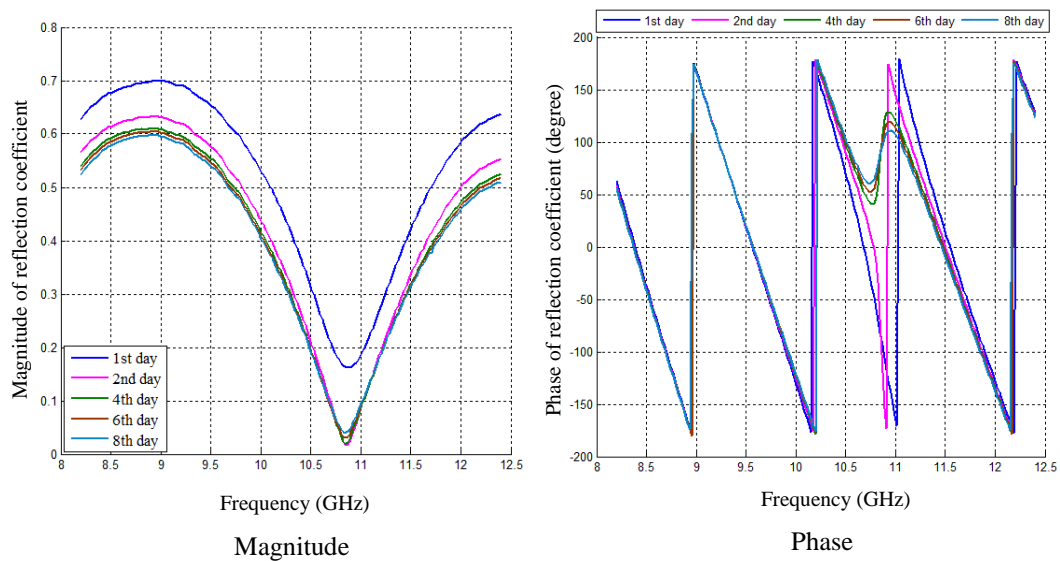
Figure 5.9: Average measured magnitude and phase of reflection coefficient vs. frequency at selected days in the first eight days of the concrete specimen using dielectric-loaded DWS with no gap between specimen and metal plate.
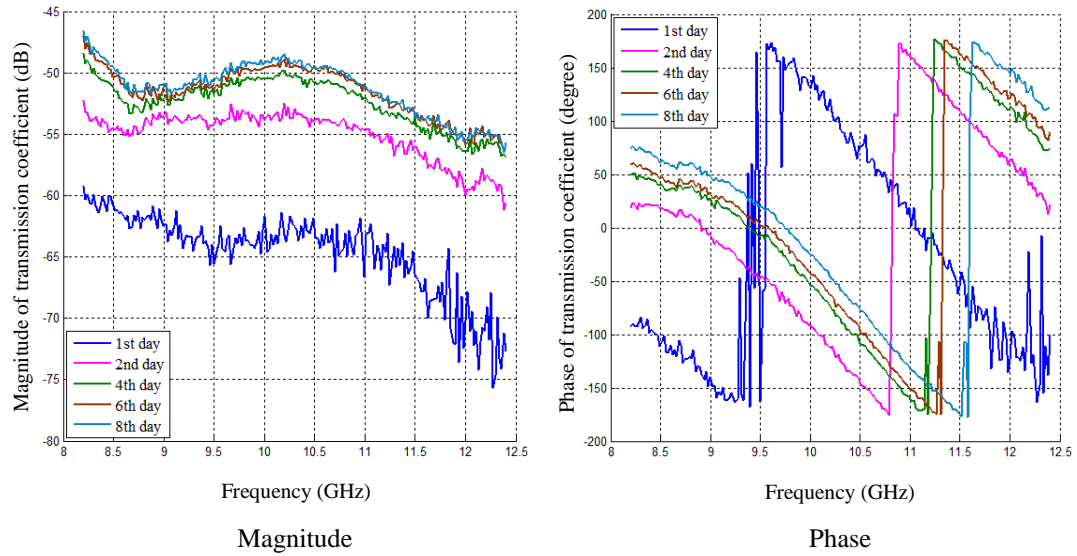
Figure 5.10: Average measured magnitude and phase of transmission coefficient vs. frequency at selected days in the first eight days of the concrete specimen using dielectric-loaded DWS with no gap between specimen and metal plate.

Different gaps between metal plate and specimens

The magnitudes and phases of the reflection and transmission coefficients were measured for five selected gaps between the early-age concrete specimens and the metal plate (0.0, 0.5, 1.0, 1.5, 2.0 mm). Measurements were conducted five times a day for each gap from the ninth to the 17th day with identical settings, then averaged for each day. Selected results are presented here.

Figure 5.11 shows the average measured magnitude of the reflection coefficient vs. frequency at all five values of the gap between the metal plate and concrete specimens of different age (days 9, 12, 15 and 17). It is clearly seen that for concrete specimens of all ages, resonance takes place in all S_{11} curves for all gap values. It is seen that the resonant frequency changes with different gap values, but not appreciably with the age of the concrete. Furthermore, S_{11} changes at the resonant frequencies for different gap values.

Figure 5.12 shows the average measured phase of the reflection coefficient vs. frequency for all five values of the gap between the metal plate and concrete specimens of different age (days 9, 12, 15 and 17). Phase shifts are seen for S_{11} in the

frequency scale with increasing gap, and the shift changes at corresponding resonant frequencies.

Figure 5.13 shows the average measured magnitude of transmission coefficient vs. frequency for all five values of the gap between the metal plate and concrete specimens of different age (days 9, 12, 15 and 17). It is clearly seen that S_{21} increases with the increase of gap value over the entire frequency band for concrete specimens of all ages. It is also found that concrete age does not affect S_{21} at gap values of 1.0, 1.5 and 2.0 mm, but S_{21} is seen to change at gap values of 0.0 and 0.5 mm.

Figure 5.14 shows the average measured phase of transmission coefficient vs. frequency for all five values of the gap between the metal plate and concrete specimens of different age (days 9, 12, 15 and 17). It is seen that phase of S_{21} increases with increase in gap from 0.5 to 2.0 mm over almost the entire frequency band, the exception being at the lowest and highest frequencies, significantly decreasing from no gap to 0.5 mm gap over the same frequency band.
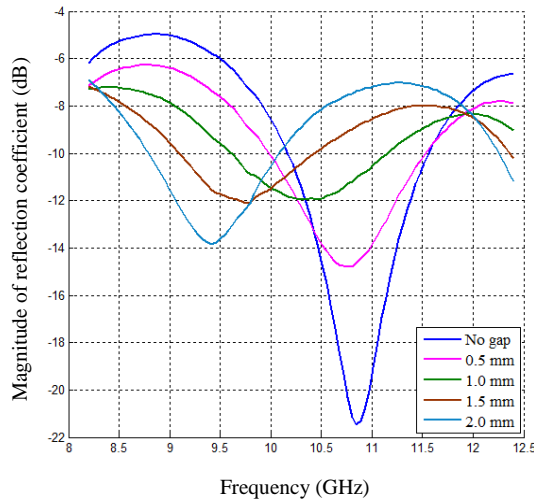
9th Day
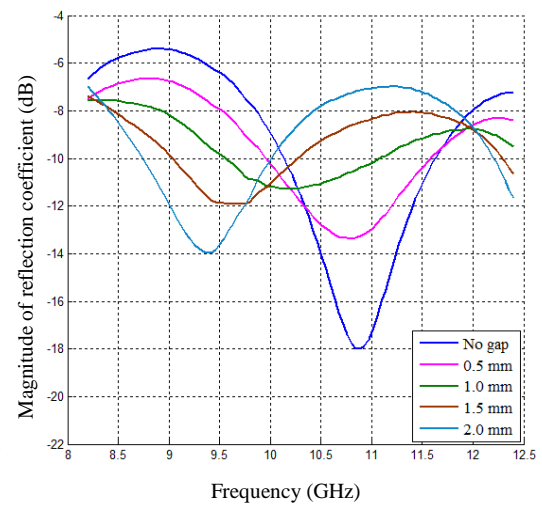
12th Day
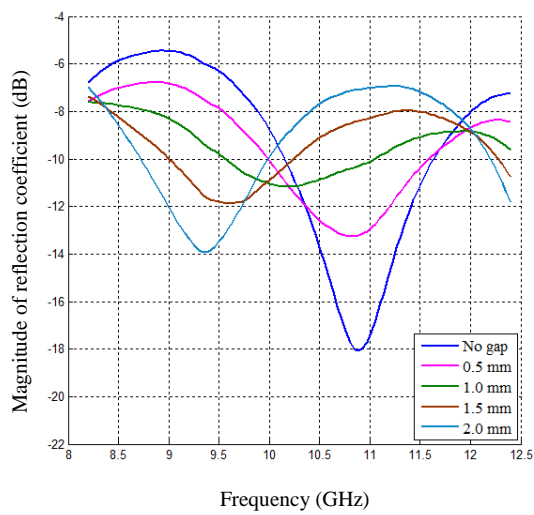
15th Day
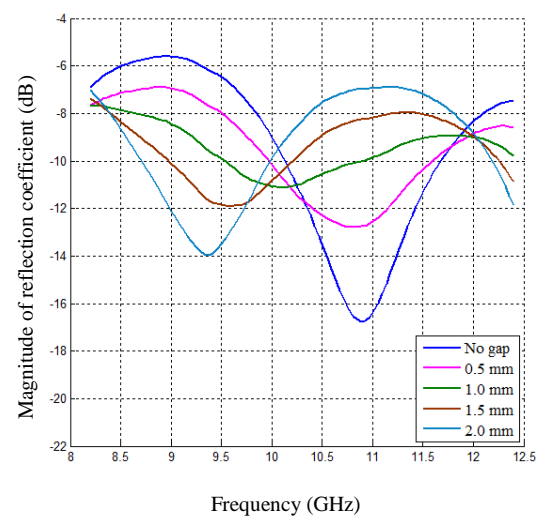
17th Day

Figure 5.11: Average measured magnitude of reflection coefficient vs. frequency for different gaps between concrete specimens of different age and metal plate using the dielectric-loaded DWS.

9th Day

12th Day

15th Day

17th Day
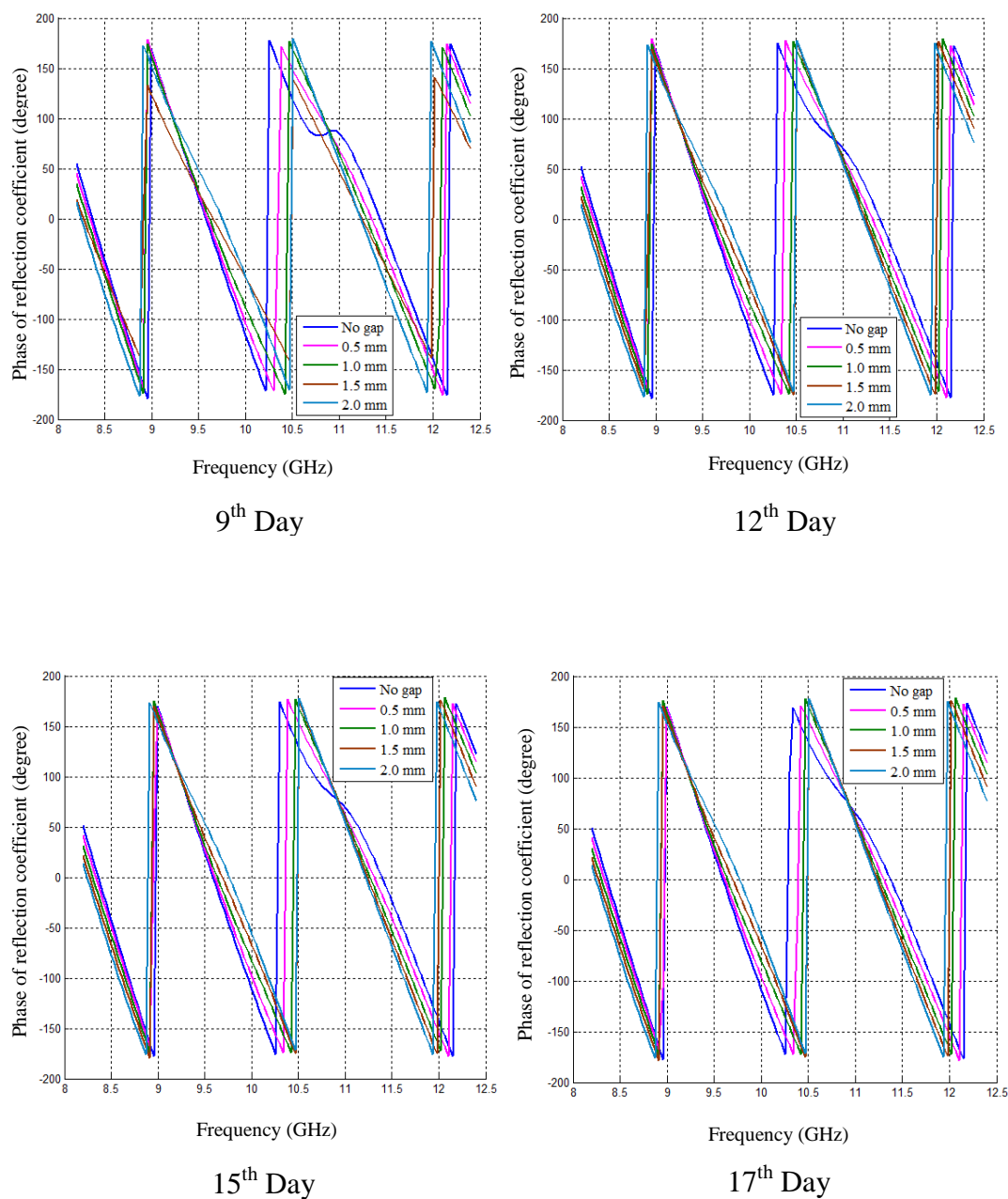
Figure 5.12: Average measured phase of reflection coefficient vs. frequency for different gaps between concrete specimens of different age and metal plate using dielectric-loaded DWS.

9th Day

12th Day

15th Day

17th Day
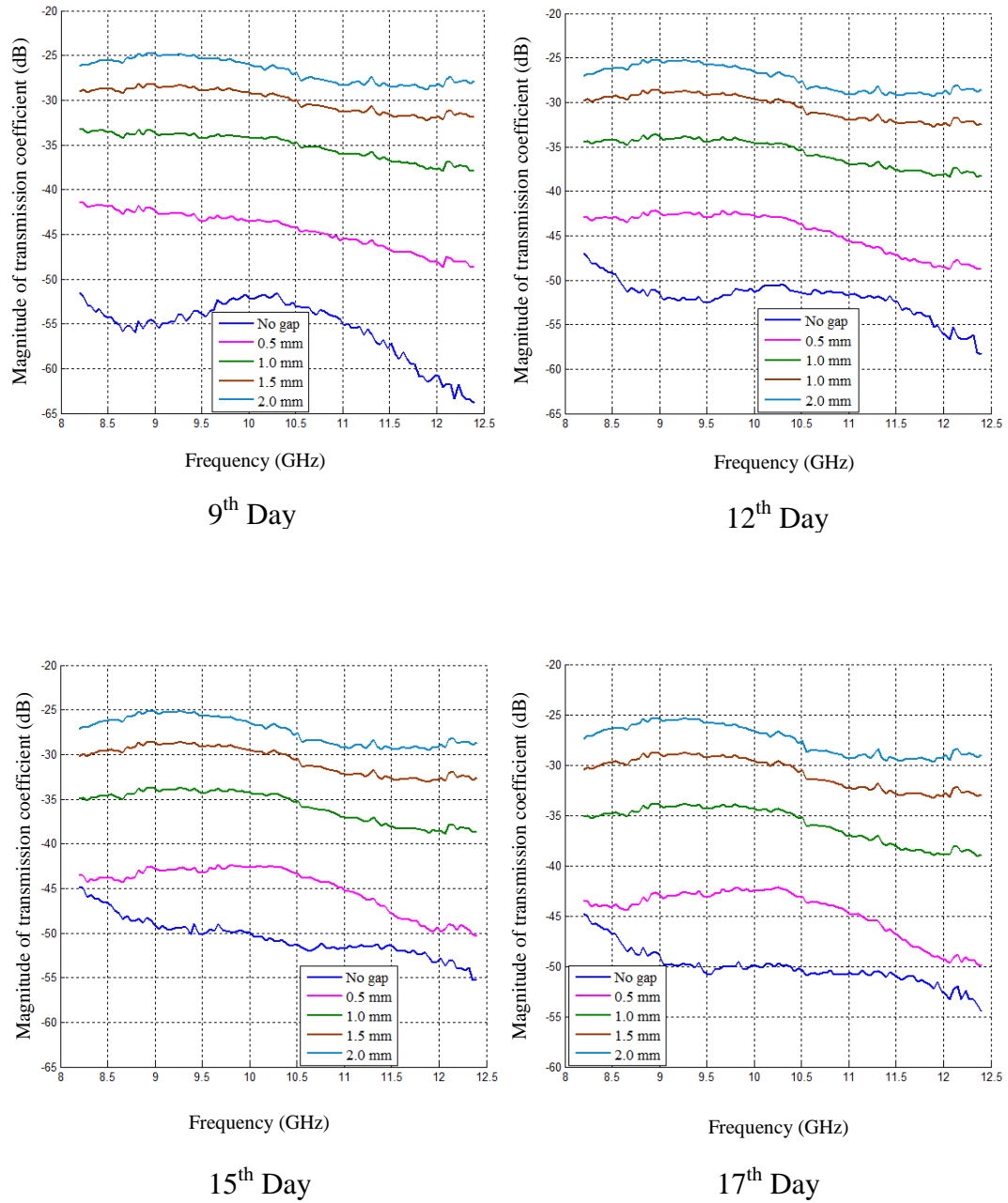
Figure 5.13: Average measured magnitude of transmission coefficient vs. frequency for different gaps between concrete specimens of different age and metal plate using the dielectric-loaded DWS.

9th Day

12th Day

15th Day

17th Day
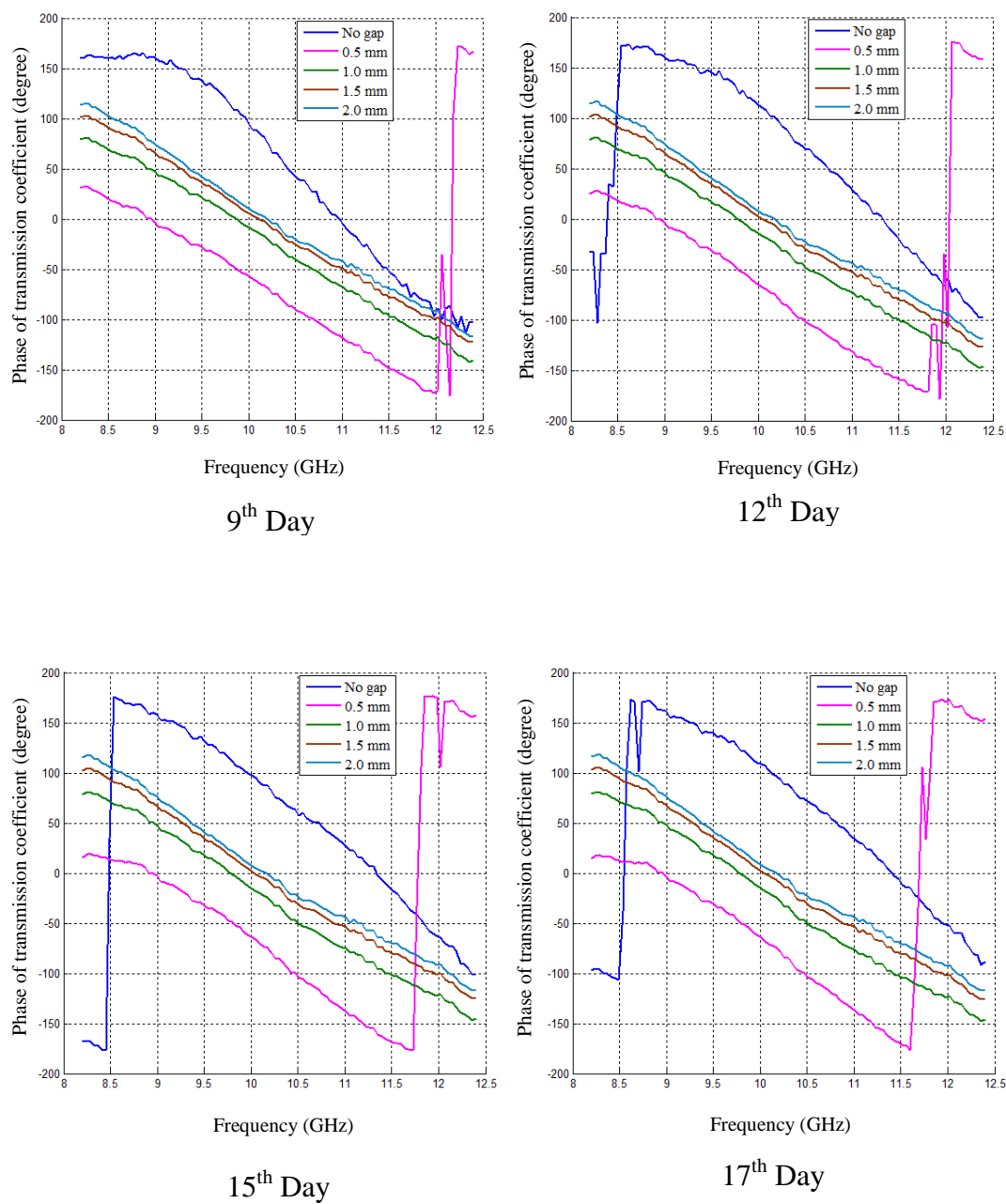
Figure 5.14: Average measured phase of transmission coefficient vs. frequency for different gaps between concrete specimens of different age and metal plate using dielectric-loaded DWS.

5.4 Measurement with Semi-Dry and Dry Concrete Specimens

This section discusses the measurement results for semi-dry and dry concrete specimens using the dielectric-loaded DWS. For this investigation, the ages of the concrete specimens were 50 days (semi-dry) and two years (dry). The measurement setup shown in Figure 5.4b was adopted to measure S_{11} and S_{21} for the same five gap values as above (0.0, 0.5, 1.0, 1.5 and 2.0 mm) between the specimens and the metal plate of the proposed dielectric-loaded DWS. Five measurements were conducted and averaged for each gap value as for the early-age concrete specimens.

Semi-Dry Concrete Specimens

Figure 5.15 shows the average measured magnitude and phase of the reflection coefficient vs. frequency for different gaps between the semi-dry concrete specimens and the metal plate. It is clearly seen that resonance occurred in all S_{11} curves for each gap value, but the resonant frequencies differ for all gap values. It is also found that the resonant frequencies for different gaps for semi-dry concrete are very similar to those for early-age concrete. The phase of the reflection coefficient shifts in frequency scale with increasing gaps and there are changes in shifts at corresponding resonant frequencies.

Figure 5.16 shows the average measured magnitude and phase of the transmission coefficient vs. frequency for different gaps between the semi-dry concrete specimens and metal plate. It is seen that S_{21} increases with the increasing gap value over the entire operating frequency as for the early-age concrete case. It is also observed that the phase of S_{21} increases with increase of gap value from 0.5 to 2.0 mm in the frequency range 9.0–11.5 GHz. However, the phase of S_{21} decreases from no gap to 0.5 mm gap in the same frequency range.
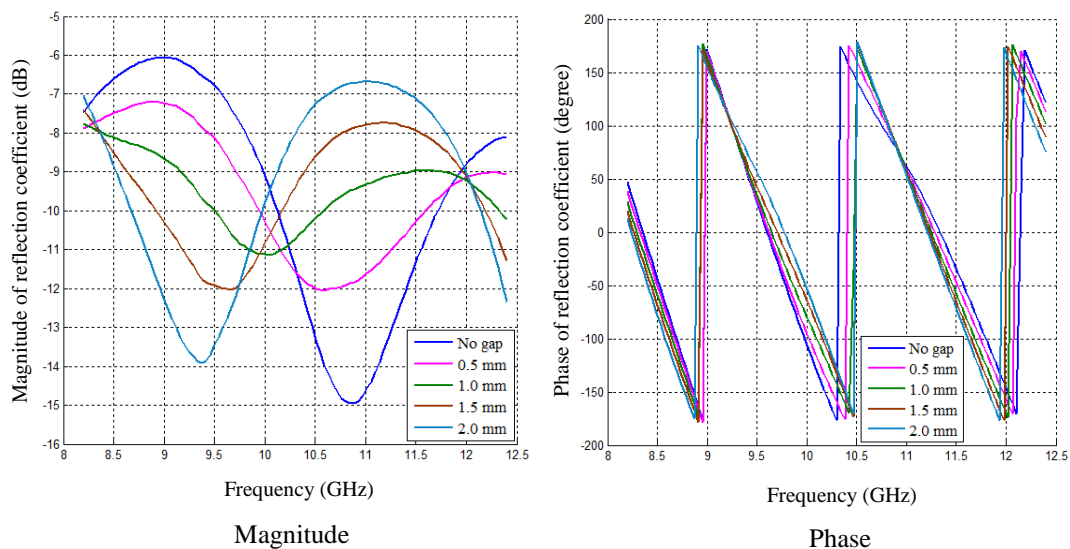
Figure 5.15: Average measured magnitude and phase of reflection coefficient vs. frequency at different values of gap between semi-dry concrete specimens and metal plate at day 50.
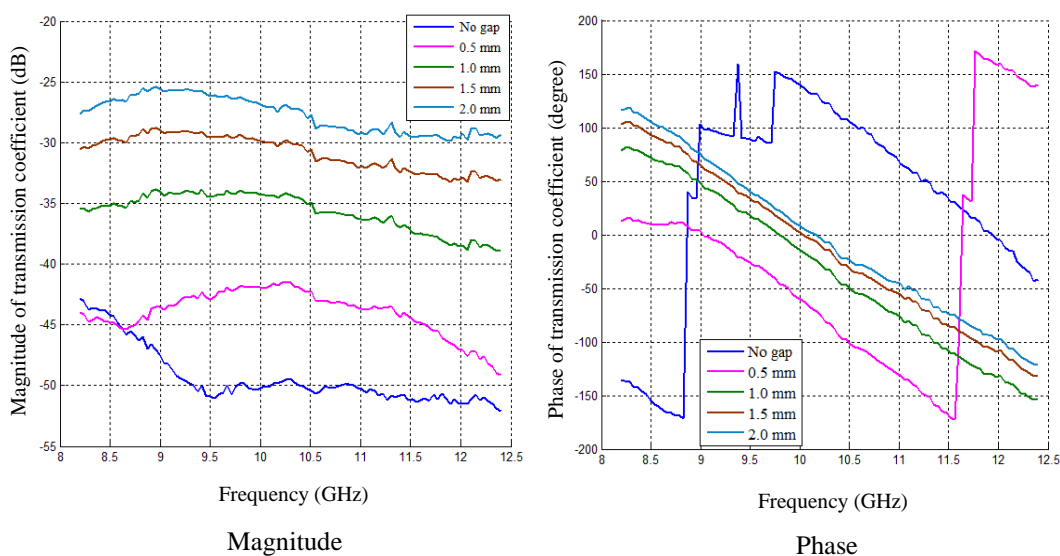
Figure 5.16: Average measured magnitude and phase of transmission coefficient vs. frequency at different values of gap between semi-dry concrete specimens and metal plate at day 50.

Dry Concrete Specimens

Figure 5.17 shows the average measured magnitude and phase of the reflection coefficient vs. frequency and standard deviations for dry concrete with no gap between specimen and metal plate. The average and standard deviation were calculated from five measurements. It is clearly seen that the variation in magnitude measurements is higher at resonant frequency than at other frequencies. However, variations in measurement for phase are negligible.

Figure 5.18 shows the average measured magnitude and phase of transmission coefficient vs. frequency and standard deviations for dry concrete with no gap between specimen and metal plate. The average and standard deviation were calculated from five measurements. It is clearly seen that the variations in magnitude measurements is highest at the higher frequencies; however, variations in phase measurement are lower by comparison, except around 10.0 GHz. The measurement results in Figures 5.17 and 5.18 were used to determine the complex dielectric permittivity of dry concrete specimen as described in section 5.5.2.

Figure 5.19 shows the average measured magnitude and phase of the reflection coefficient vs. frequency for different gap values between dry concrete specimen and metal plate. It is seen that the resonant frequency in the S_{11} curve changes with the change of gap value. Another important observation is that although S_{11} changes at resonant frequencies (cf. early-age and semi-dry concrete specimen), the resonant frequencies do not change very much with change of concrete type. The phase of the reflection coefficient curves shift with frequency scale as the gap increases, accompanied by shift changes at corresponding resonant frequencies.

Figure 5.20 shows the average measured magnitude and phase of transmission coefficient vs. frequency at different values of the gap between the dry concrete specimen and the metal plate. It is seen that the magnitude of S_{21} increases with the increasing gap value from 0.5 to 2.0 mm over the entire frequency band. The difference between adjacent curves decreases as the gap increases. S_{21} at no gap changes with frequency non-monotonically over the entire frequency band and intersects the 0.5 mm gap curve in several places. It is also observed that the phase of

the transmission coefficient increases with larger gap value at frequencies below 10 GHz.

Figure 5.21 shows the resonant frequency in the average measured magnitude of the reflection coefficient vs. gap between concrete specimen of different ages and metal plate. It is clear that the resonant frequency decreases with increase of the gap between concrete specimens of all ages and the metal plate of the proposed dielectric-loaded DWS. The resonant frequency at different gap values does not vary excessively for early-age and semi-dry concrete, but the resonant frequency for dry concrete is slightly less than the other concrete specimens for gaps greater than 0.5 mm.

Figure 5.22 shows the average measured magnitude of transmission coefficient vs. gap between concrete specimens of different age and metal plate at 10.3 GHz. The transmission coefficient increases monotonically with increasing gap value for early-age and semi-dry concrete. For dry concrete, S_{21} initially decreases from 0.0 to 0.5 mm gap, then increases with the increasing gap value. It is also observed that values of S_{21} at different gap values for early-age and semi-dry concrete specimens are very close, and for dry concrete they are a little less than for early-age and semi-dry concrete.
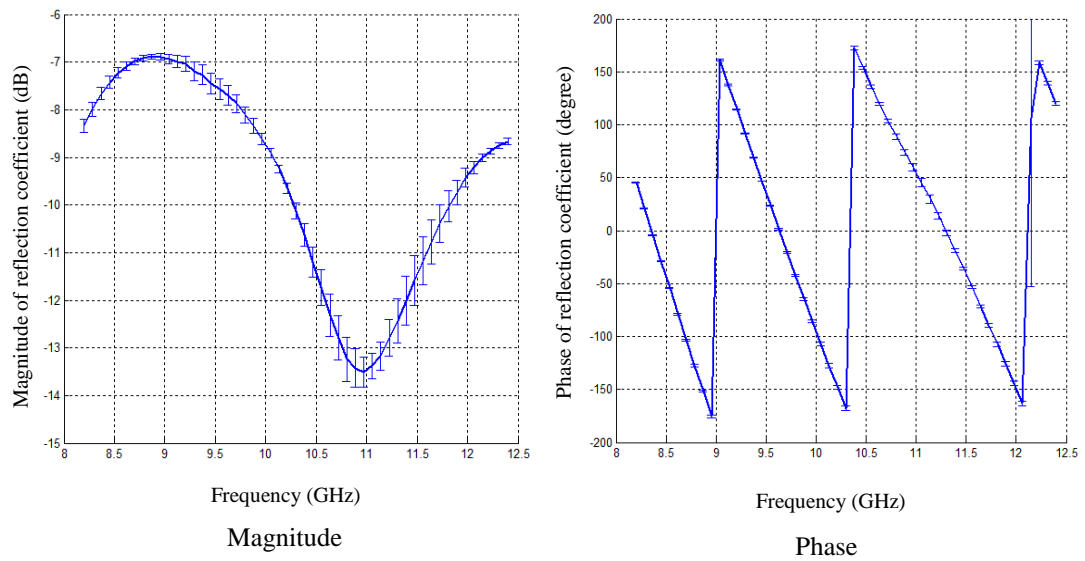
Figure 5.17: Average measured magnitude and phase of reflection coefficient vs. frequency with standard deviations for dry concrete with no gap between specimen and metal plate.
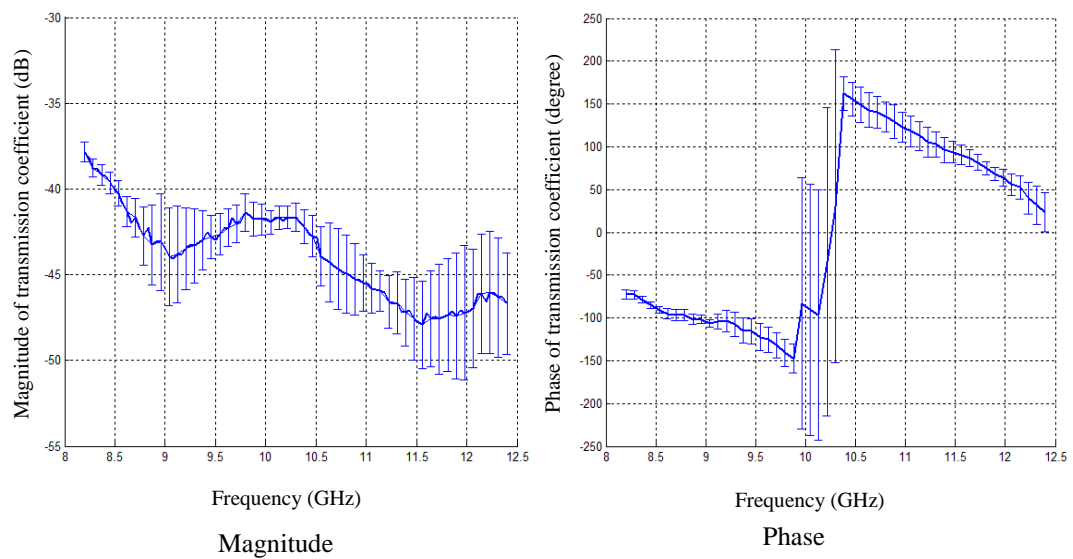
Figure 5.18: Average measured magnitude and phase of transmission coefficient vs. frequency with standard deviations for dry concrete with no gap between specimen and metal plate.
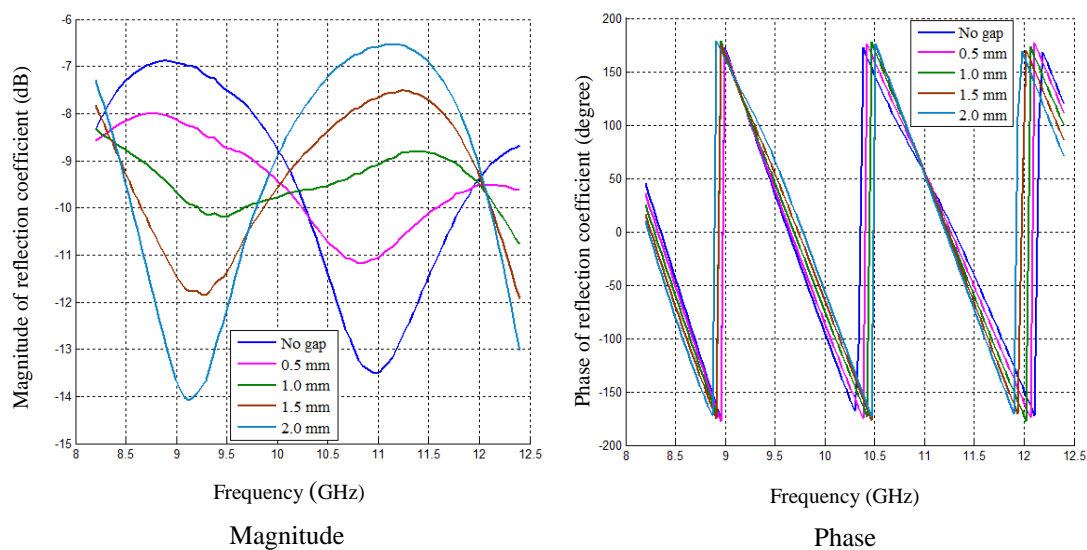
Figure 5.19: Average measured magnitude and phase of reflection coefficient vs. frequency for different gaps between dry concrete and metal plate.
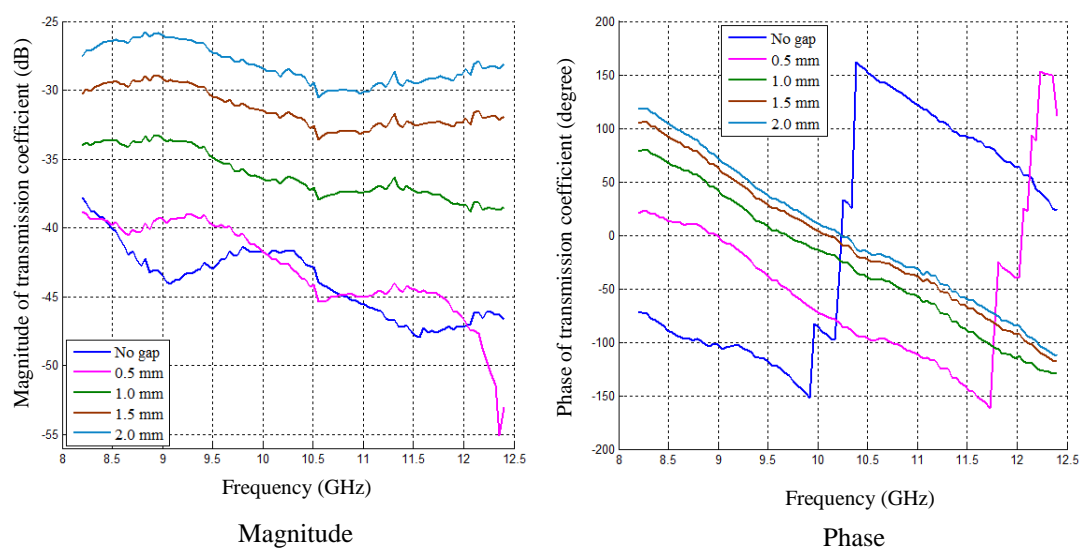
Figure 5.20: Average measured magnitude and phase of transmission coefficient vs. frequency for different gaps between dry concrete and metal plate.
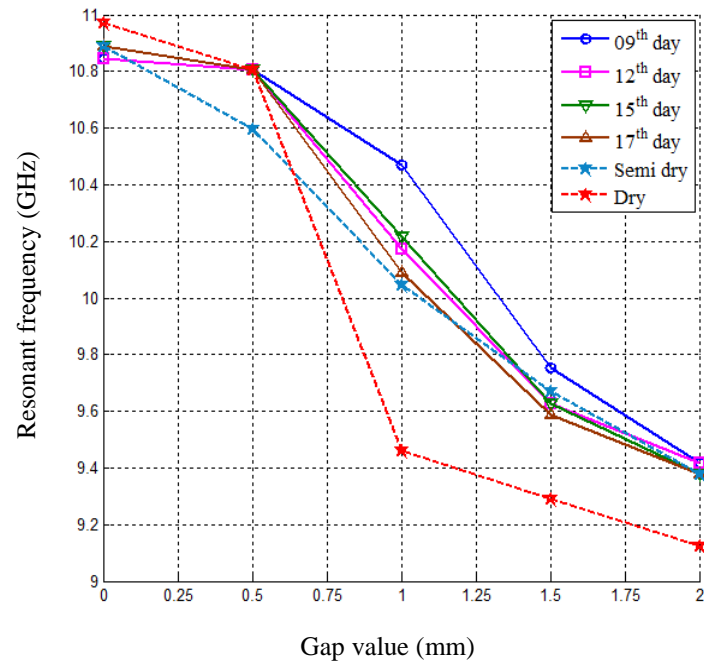
Figure 5.21: Resonant frequency in measured magnitude of reflection coefficient vs. gap between concrete specimens of different age and metal plate.
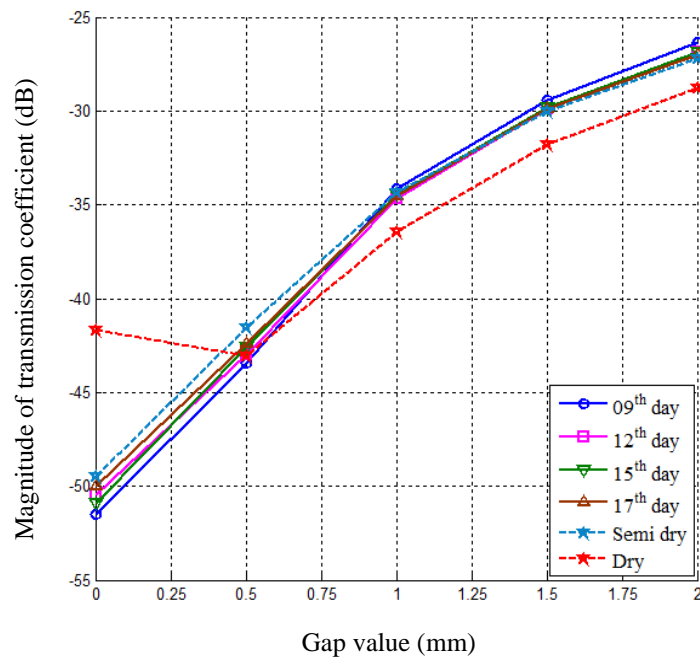
Figure 5.22: Measured magnitude of transmission coefficient vs. gap between concrete specimens of different age and metal plate at a frequency of 10.3 GHz.

5.5 Numerical Investigation into the Concrete Specimens

In the previous sections, measurement procedure and results for concrete specimens of different ages have been presented. Reflection coefficients and transmission coefficients at no gap and for different gap values between concrete specimens and metal plate were measured. In this section, the proposed dielectric-loaded DWS along with concrete specimen will be modelled and extensive simulations will be performed to determine the complex dielectric permittivity of the fresh and dry concrete specimens using measured S_{11} and S_{21} and the developed algorithm. Then, a parametric study of the different concrete specimens at different gap values will be conducted using the determined dielectric properties of concrete specimens.

5.5.1 Modelling of Sensor

A model of the microwave dielectric-loaded DWS and concrete specimen was created (Figure 5.23). In the model, all previously listed dimensions of the fabricated model (waveguide section length, aperture dimensions, distance between waveguides, thickness of metal plate and cubic concrete specimen) are used. The dielectric permittivity of acrylic dielectric insertions is considered as 2.6 – j0.01 [154]. The model provided simulated magnitude of reflection coefficient, $\left| S_{11} \right|_s$ and magnitude of transmission coefficient, $\left| S_{12} \right|_s$ with a setting value of concrete dielectric constant (real part), ε_r' and loss tangent, $\tan \delta$ (ratio of imaginary part to real part of complex dielectric permittivity).
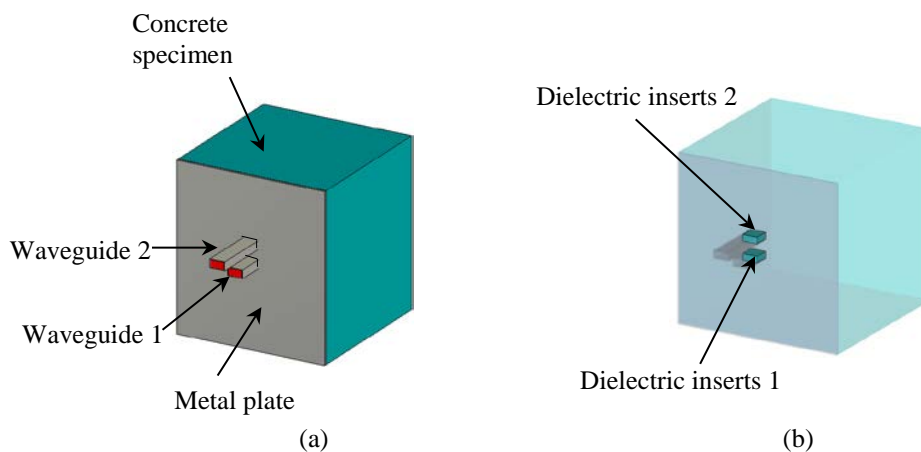
Figure 5.23: A model of dielectric-loaded DWS and concrete specimen in CST: (a) perspective general view and (b) perspective transparent view showing the dielectric inserts.

5.5.2 Determination of Complex Dielectric Permittivity of Concrete Specimen using Improved Algorithm

Figure 5.24 is a flow chart developed and used for the determination of the complex dielectric permittivity of concrete using measured magnitude of reflection coefficient and transmission coefficient. In Chapter 3, a similar algorithm was used to determine the complex dielectric permittivity of early-age concrete using open-ended SWS, and hence only the measured magnitude of reflection coefficient was taken into account. Here, that algorithm has been updated for used with the dielectric-loaded DWS, where the measured magnitude of reflection coefficient and transmission coefficient are both taken into consideration. The $|S_{11}|_s$ and $|S_{21}|_s$ were calculated with a guessed value of the dielectric permittivity of concrete and compared with $|S_{11}|_m$ and $|S_{21}|_m$. The initial guessed values for fresh and dry concrete were chosen as in [11], [18]. If the difference between the simulated and measured magnitudes of the coefficients is zero or within a predefined accuracy level, then the guessed value is the estimated dielectric permittivity of the concrete. If the difference is not within the predefined accuracy level, then another value is guessed and the reflection and transmission coefficient is again compared with the measurement value of $|S_{11}|_m$ and $|S_{21}|_m$.

Figures 5.25 and 5.26 show the average measured magnitude of the reflection and transmission coefficients for day 1 fresh concrete along with selected simulation results after applying the developed algorithm. Figure 5.25a shows $|S_{11}|_m$ and $|S_{11}|_s$ vs. frequency for different values of dielectric constant and a loss tangent of 0.3. Figure 5.25b shows $|S_{11}|_m$ and $|S_{11}|_s$ vs. frequency for a dielectric constant of 15 and at different values of loss tangent. It is clearly seen that the simulation results with $\varepsilon_r' = 15$ and $\tan \delta = 0.3$ match the measurement results very well. Similar observations may be made from Figure 5.26a, b for the transmission coefficient. Therefore, the determined complex dielectric permittivity of day 1 fresh concrete is 15.0 – j4.5. In addition, the results show that magnitude of reflection coefficient is more sensitive to changes of dielectric constant than to changes of loss tangent value and magnitude of transmission coefficient is more sensitive to changes of loss tangent than to changes of dielectric constant.

Likewise, Figures 5.27 and 5.28 show the average measured magnitude of the reflection and transmission coefficient with selected simulation results after applying the developed and updated flow chart for dry concrete. Figure 5.27a shows $|S_{11}|_m$ and $|S_{11}|_s$ vs. frequency at different values of dielectric constant and at loss tangent of 0.2. Figure 5.27b shows $|S_{11}|_m$ and $|S_{11}|_s$ vs. frequency for a dielectric constant of 4.1 and for different values of loss tangent. It is clearly seen that the simulations with $\varepsilon_r' = 4.1$ and $\tan \delta = 0.2$ match the measured results very closely. Figure 5.28a, b shows similar results. Therefore, the complex dielectric permittivity of dry concrete specimen is determined as $4.1 - j0.82$.
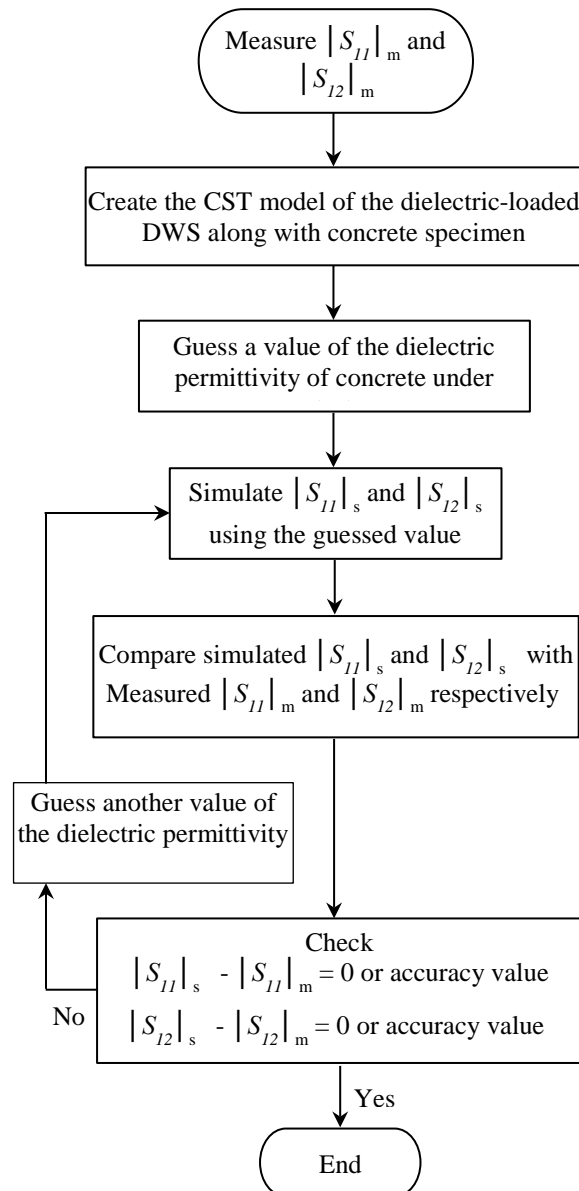
Figure 5.24: An improved algorithm for determining complex dielectric permittivity of concrete specimens from the measured magnitude of reflection and transmission coefficients.
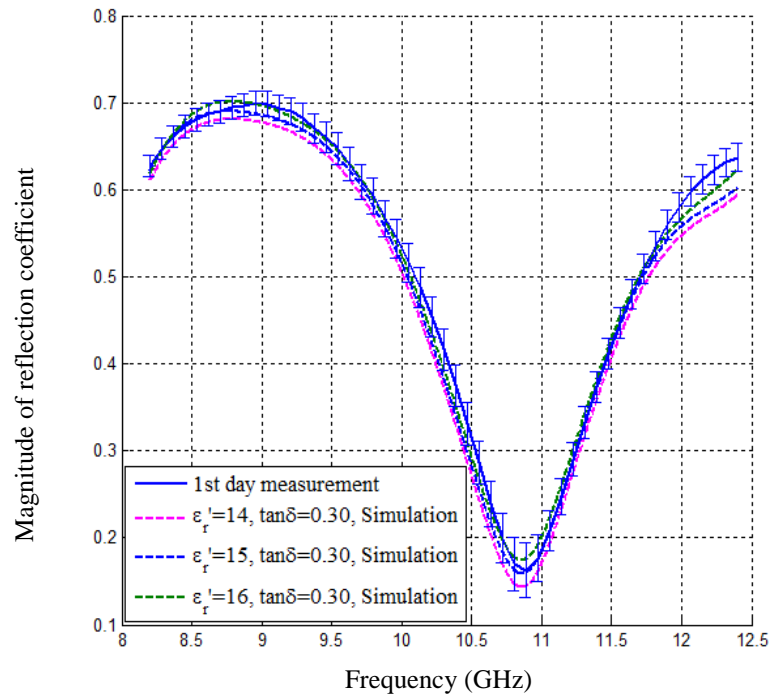
(a) At different values of dielectric constant
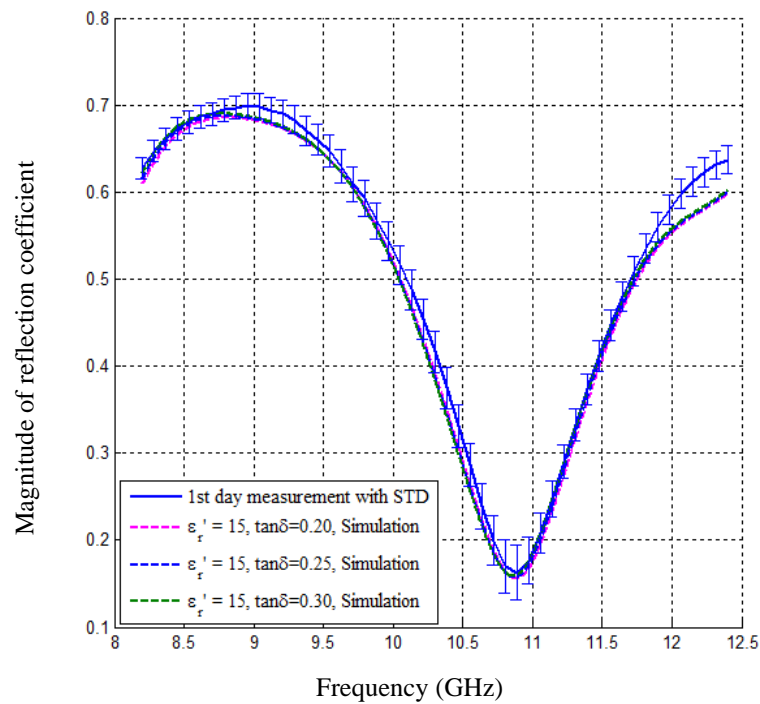
(b) At different values of loss tangent

Figure 5.25: Average measured (with STD) and simulated magnitude of reflection coefficient vs. frequency at selected values of (a) dielectric constant and (b) loss tangent for day 1 concrete at no gap condition.
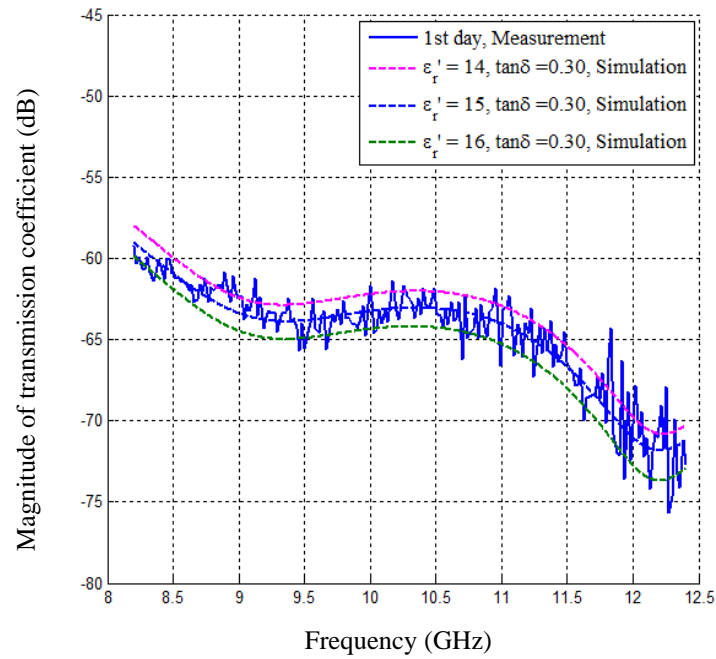
(a) At different values of dielectric constant
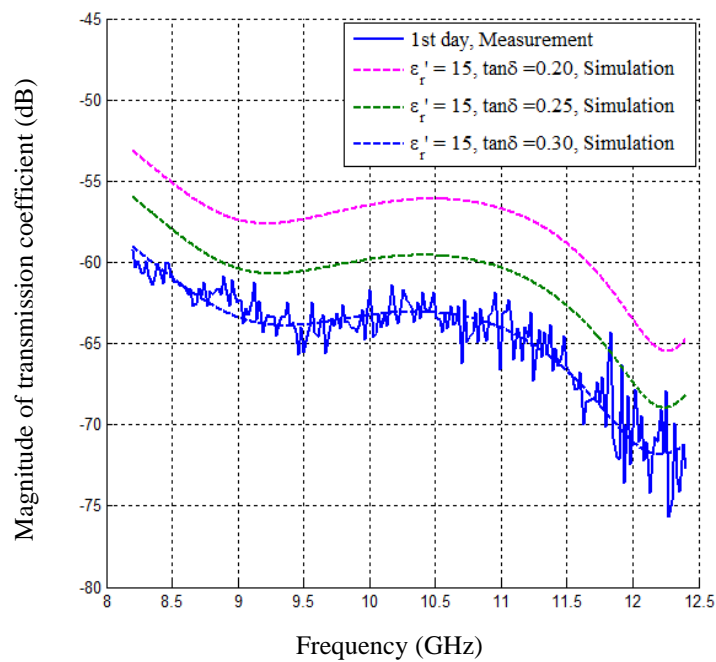
(b) At different values of loss tangent

Figure 5.26: Average measured (with STD) and simulated magnitude of transmission coefficient vs. frequency at different selected values of (a) dielectric constant and (b) loss tangent for day 1 concrete at no gap condition.
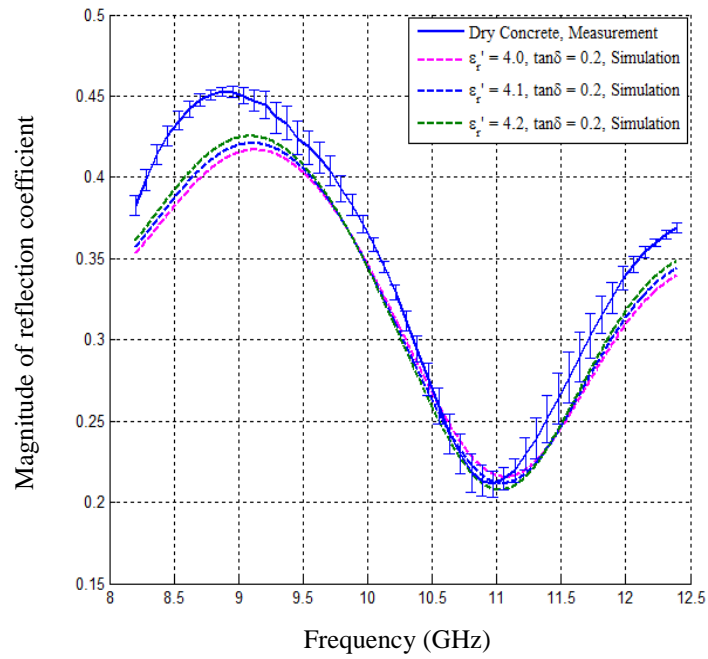
(a) At different values of dielectric constant
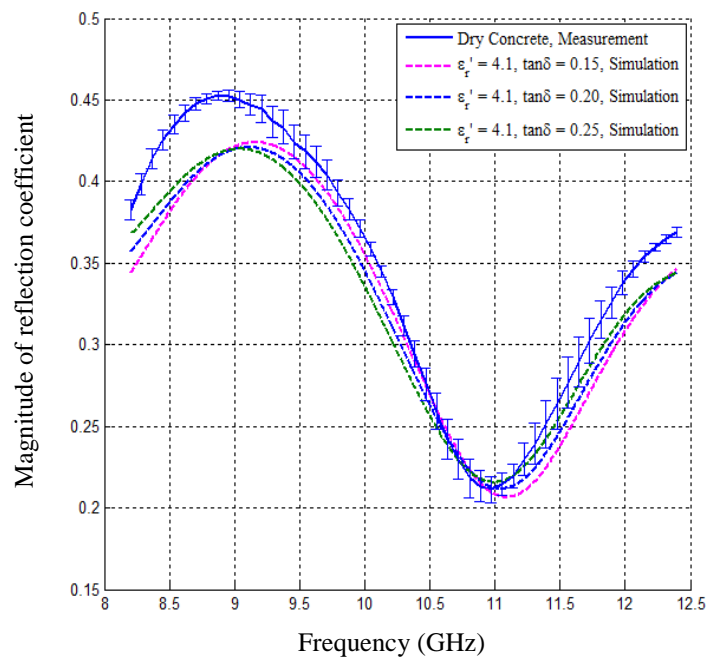
(b) At different values of loss tangent

Figure 5.27: Average measured (with STD) and simulated magnitude of reflection coefficient vs. frequency at different selected values of (a) dielectric constant and (b) loss tangent for dry concrete at no gap condition.
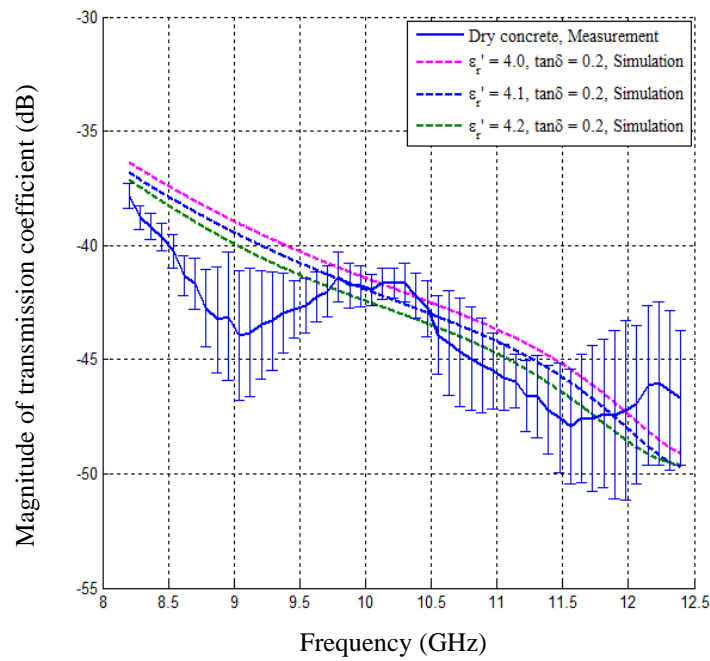
(a) At different values of dielectric constant
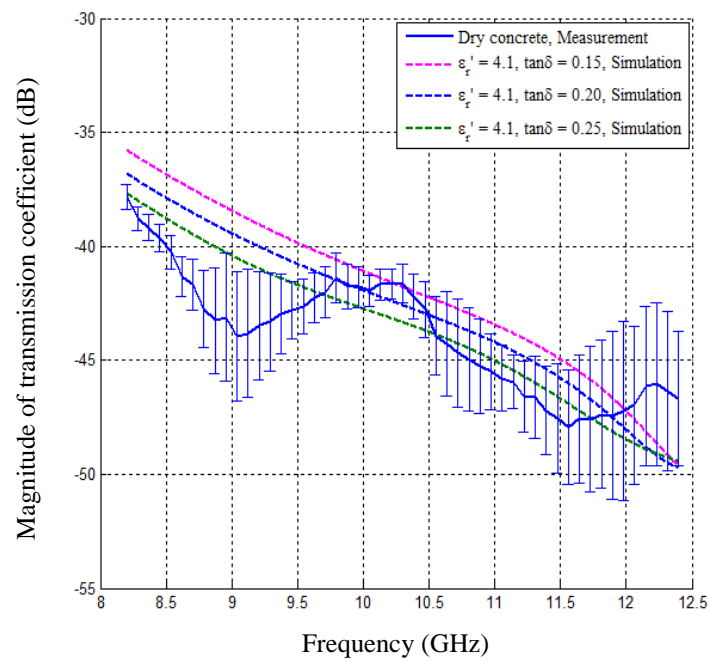
(b) At different values of loss tangent

Figure 5.28: Average measured (with STD) and simulated magnitude of transmission coefficient vs. frequency at different selected values of (a) dielectric constant and (b) loss tangent for dry concrete at no gap condition.

5.5.3 Simulation Results for Measurement of Gap between Metal Plate and Concrete Specimen

The determined complex dielectric permittivity of day 1 fresh concrete and dry concrete in the previous section are $15.0 - j4.5$ and $4.1 - j0.82$ respectively, and these values will be used in a parametric analysis of the gap values between the concrete specimen and metal plate of dielectric-loaded dual waveguide sensor.

Figure 5.29 shows the simulated magnitude of the reflection coefficient and the transmission coefficient vs. frequency for different gaps between the metal plate and fresh concrete ($\varepsilon_r = 15.0 - j\,4.5$). It is clearly seen that resonance takes place at all S_{11} curves for each gap value, and the resonant frequency changes with the change of gap value. It is found in Figure 5.29b that the magnitude of transmission coefficient increases with gap increase over the entire frequency band. Furthermore, the difference between adjacent curves decreases with increase of gap value.

Figure 5.30 illustrates the simulated magnitude of the reflection coefficient and transmission coefficient vs. frequency at different gap values between metal plate and dry concrete ($\varepsilon_r = 4.1 - j\,0.82$). It is observed in Figure 5.30a that resonance takes place at all S_{11} curves for each gap value and the resonant frequency changes with the change of gap value, although values of S_{11} are different from the fresh concrete, as expected. Additionally, Figure 5.30b shows that the magnitude of the transmission coefficient decreases with increasing frequency for all gap values, and S_{21} increases with gap value from 0.5 to 2.0 mm.

Figure 5.31 shows the simulated resonant frequency in S_{11} vs. gap value between the metal plate and the concrete with different dielectric constants and loss factors. The blue line represents the resonant frequency for fresh concrete; the pink line represents dry concrete. Simulations were also executed for concretes with two other values of complex dielectric permittivity. It is seen that the resonant frequency decreases with the increase of gap values for all concrete types, and increases with the decreasing dielectric constants for all gap values up to 0.5 mm, after which the resonant frequency increases with the increase of concrete dielectric constant.

Figure 5.32 presents the simulated magnitude of transmission coefficient vs. gap value between metal plate and concrete specimens with different dielectric constant

and loss factor at a frequency of 10.3 GHz. The blue line represents the magnitude of transmission coefficient for fresh concrete; the pink line represents dry concrete. Simulations were also executed for concretes with two other values of complex dielectric permittivity. It is clearly seen that fresh concrete S_{21} increases monotonically when gap value increases. However, as the concrete starts to dry (i.e., when the dielectric constants tend to decrease), S_{21} changes non-monotonically, initially decreasing with increasing gap value up to 0.5 mm, then it increases with gap value. For gaps more than 0.5 mm, a higher dielectric constant of concrete raises its transmission coefficient.

These results clearly show that gaps of 0.5–2.0 mm between the concrete and the metal plate can be effectively and independently monitored by measuring the resonant frequency and magnitude of the transmission coefficient. The variations in reflection and transmission coefficients caused by the gap between the concrete and the metal plate can be better understood by analysing the electrical field intensity distribution inside the dielectric-loaded DWS, and in the interface area of the sensor-specimen as well as in the concrete specimen. These are shown in Figures 5.33 to 5.36.
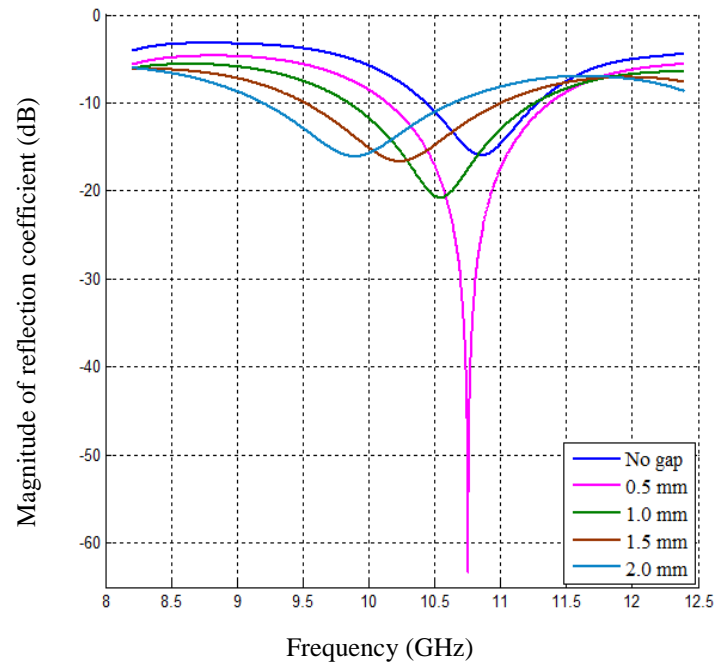
(a)
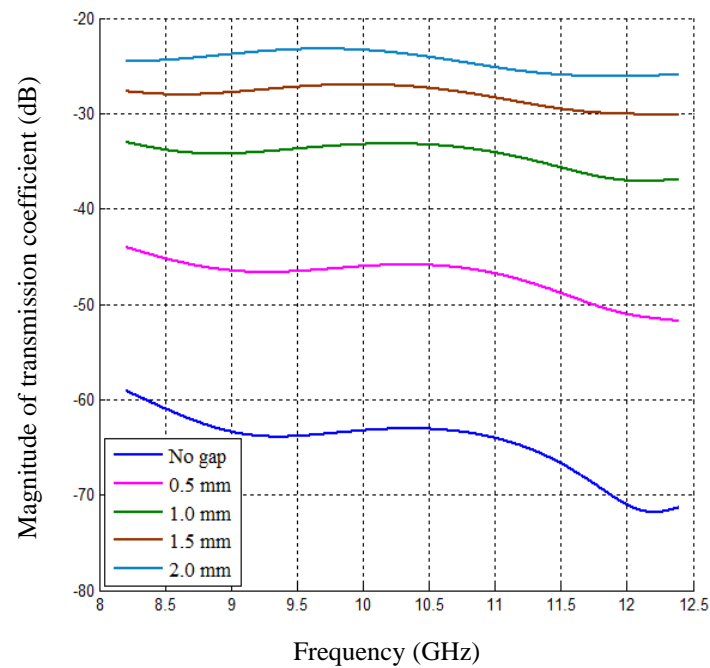
(b)

Figure 5.29: Simulated magnitude of (a) reflection coefficient, and (b) transmission coefficient vs. frequency for different gaps between metal plate and fresh concrete ($\varepsilon_r = 15.0 - j4.5$).
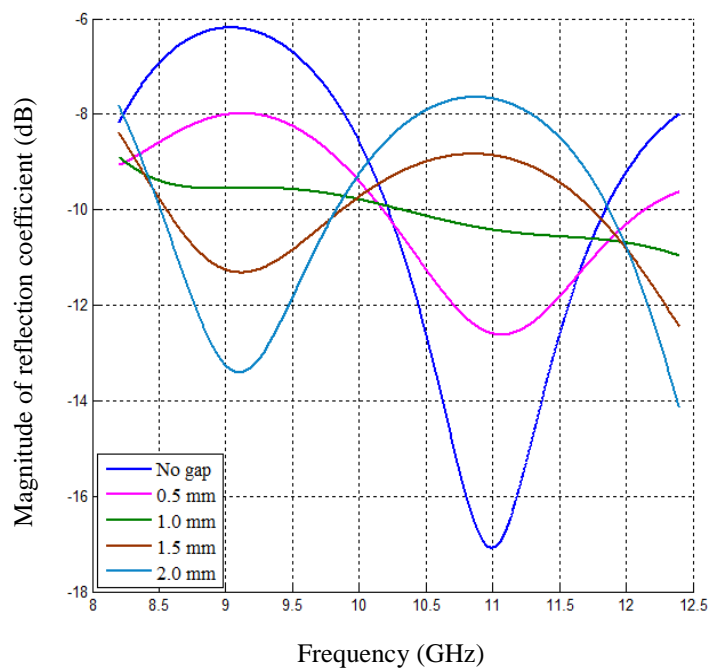
(a)
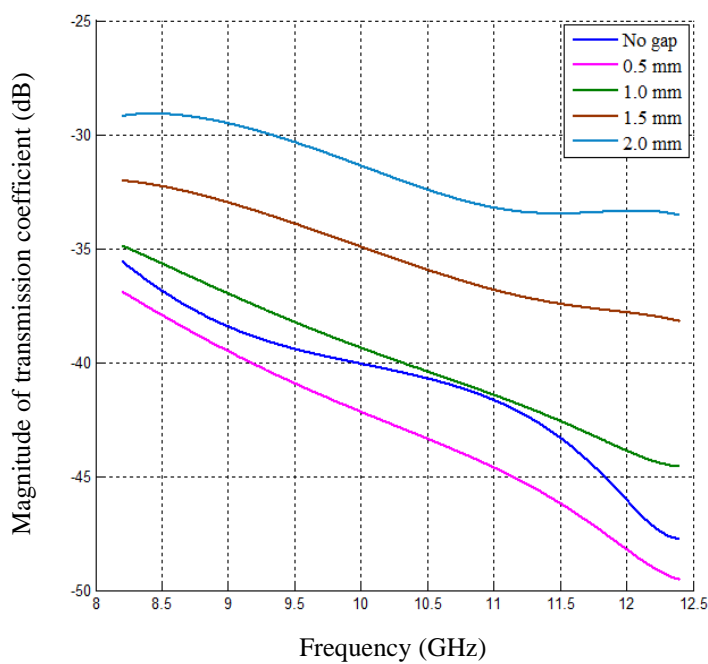
(b)

Figure 5.30: Simulated magnitude of (a) reflection coefficient, and (b) transmission coefficient vs. frequency for different gaps between metal plate and dry concrete ($\varepsilon_r = 4.1 - j0.82$).
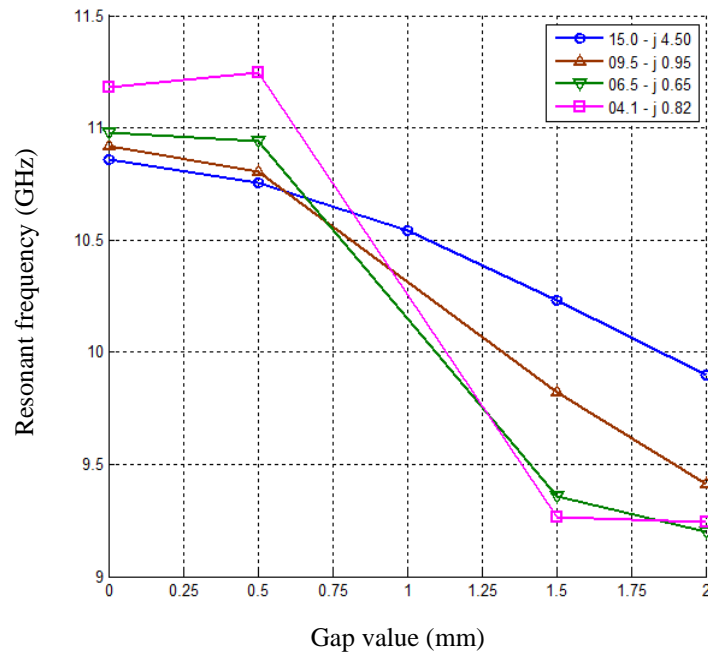
Figure 5.31: Simulated resonant frequency in S_{11} vs. gap value between metal plate and concrete specimens with different dielectric constants and loss factors.
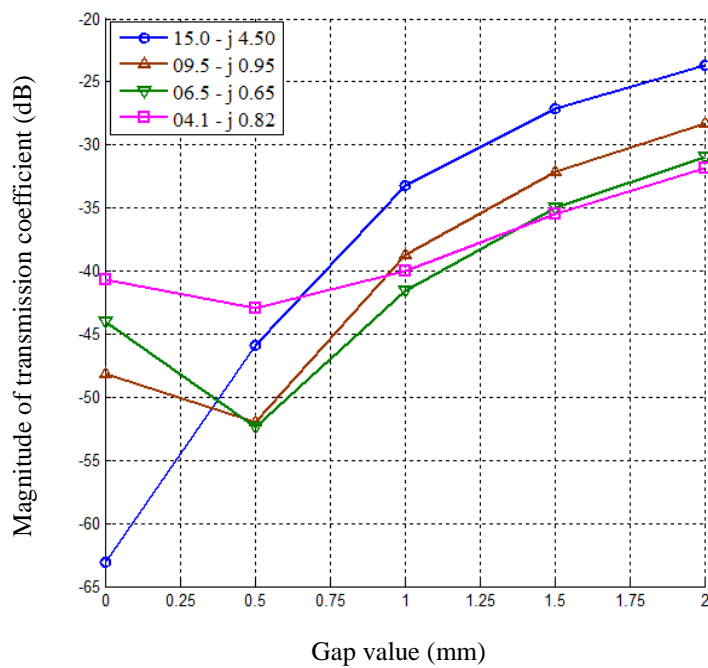
Figure 5.32: Simulated magnitude of transmission coefficient vs. gap value between metal plate and concrete specimens with different dielectric constants and loss factors at a frequency of 10.3 GHz.

Figure 5.33 is a cross-sectional side view of the simulated electric field intensity distribution inside the dielectric-loaded DWS, in the interface area and in fresh concrete specimens ($\varepsilon_r = 15.0 - j4.5$) for gaps of 0.0, 1.0 and 2 mm at 10.3 GHz. Figure 5.33a shows that waveguide 1 (W1) radiates microwaves through the dielectric insertion in the fresh concrete specimen, some of which penetrate into waveguide 2 (W2) through the dielectric insertion in the no-gap condition. Figure 5.33b, c clearly show changes in the electric field intensity distribution at the interface of concrete and metal surface due to the gap. An animated phase version of these distributions (not shown here) demonstrates the propagation of electromagnetic waves between metal and concrete surfaces (guided waves) at 1.0 and 2.0 mm gap. These guided waves lead to losses in electromagnetic energy of the incident wave as well as the reflected wave. Another important observation from Figure 5.33b, c is that part of the guided wave and part of the wave radiated by W1 in fresh concrete penetrate into W2 and interfere there. It is also found that at the no-gap condition, microwave signals are more focused inside the mortar specimen. However, with increasing gap between metal and specimen they tend to scatter vertically within concrete specimen.

Figure 5.34 is a cross-sectional top view of the simulated electric field intensity (amplitude and phase) inside waveguide 2 and fresh concrete ($\varepsilon_r = 15.0 - j4.5$) at 10.3 GHz for three gap values between specimens and metal plate. It is seen that at the no-gap condition, only a very small amount of the transmitted signal (no guided waves, only minor penetration through fresh concrete) is present in W2 (Figure 5.34a), but the amount of the transmitted signal increases significantly inside W2 (Figure 5.34b, c) when the gap value increases to 1.0 and 2.0 mm.

Figures 5.35 is a cross-sectional side view of the simulated electric field intensity distribution in the dielectric-loaded DWS and dry concrete ($\varepsilon_r = 4.1 - j0.82$) for the three gap values 0.0, 1.0 and 2.0 mm at 10.3 GHz. Figure 5.35a shows that W1 radiates microwaves in dry concrete, part of which penetrates into W2 at the no-gap condition. However, microwave signals penetrate further with increased concrete dryness at the no-gap condition. Figure 5.35b, c shows clear changes in the electric field intensity distribution at the interface of concrete and metal with changes in gap. An animated phase version of these distributions (not shown here) demonstrated the propagation of guided waves for gaps of 1.0 and 2.0 mm. The guided waves lead to

losses in electromagnetic energy both of the incident wave and the reflected wave. Another important observation from Figures 5.35b, c is that some of the guided wave and some of the wave radiated by W1 penetrate and cause interference in W2. The change of interference when a gap occurs and then increases from 0.0 to 1.0 mm causes the magnitude of the transmission coefficient to change non-monotonically, whereas the transmission coefficient increases when the value of the gap is equal to or greater than 1.0 mm.

Figure 5.36 is a cross-sectional top view of the simulated electric field intensity distribution (amplitude and phase) inside W2 and dry concrete ($\varepsilon_r = 4.1 - j0.82$) at 10.3 GHz. Small changes in electric field intensity distribution are observed in W2 from no gap (Figure 5.36a) to 1.0 mm gap (Figure 5.36b); but significant changes are observed for a 2.0 mm gap (Figure 5.36c), which is consistent with Figure 5.32.
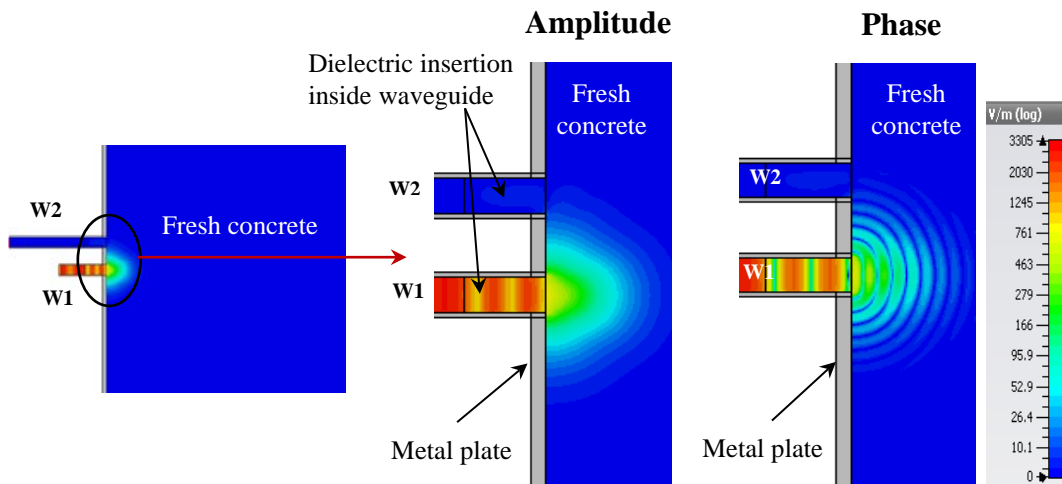
Amplitude **Phase**

(a) No gap between metal and fresh mortar
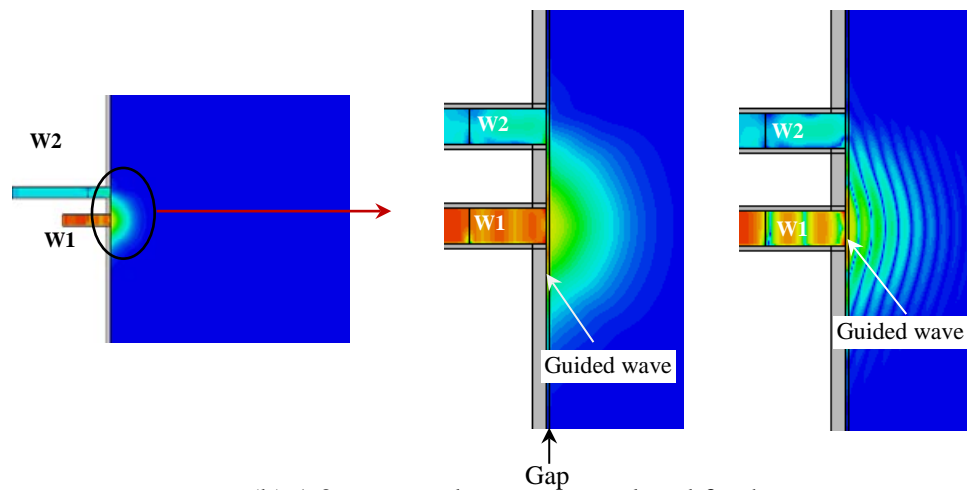
(b) 1.0 mm gap between metal and fresh mortar
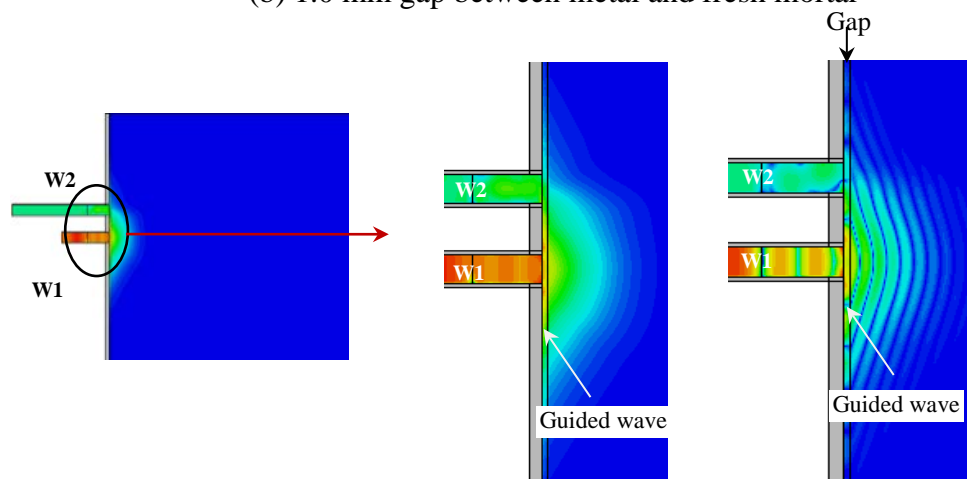
(c) 2.0 mm gap between metal and fresh mortar

Figure 5.33: Cross-sectional side view of electric field intensity distribution inside waveguides of dielectric-loaded DWS and fresh concrete specimen ($\varepsilon_r = 15.0 - j4.5$) for different gaps between metal and specimen surfaces at 10.3 GHz.

Amplitude   **Phase**

(a) No gap between metal and dry concrete

(b) 1.0 mm gap between metal and dry concrete

(c) 2.0 mm gap between metal and dry concrete
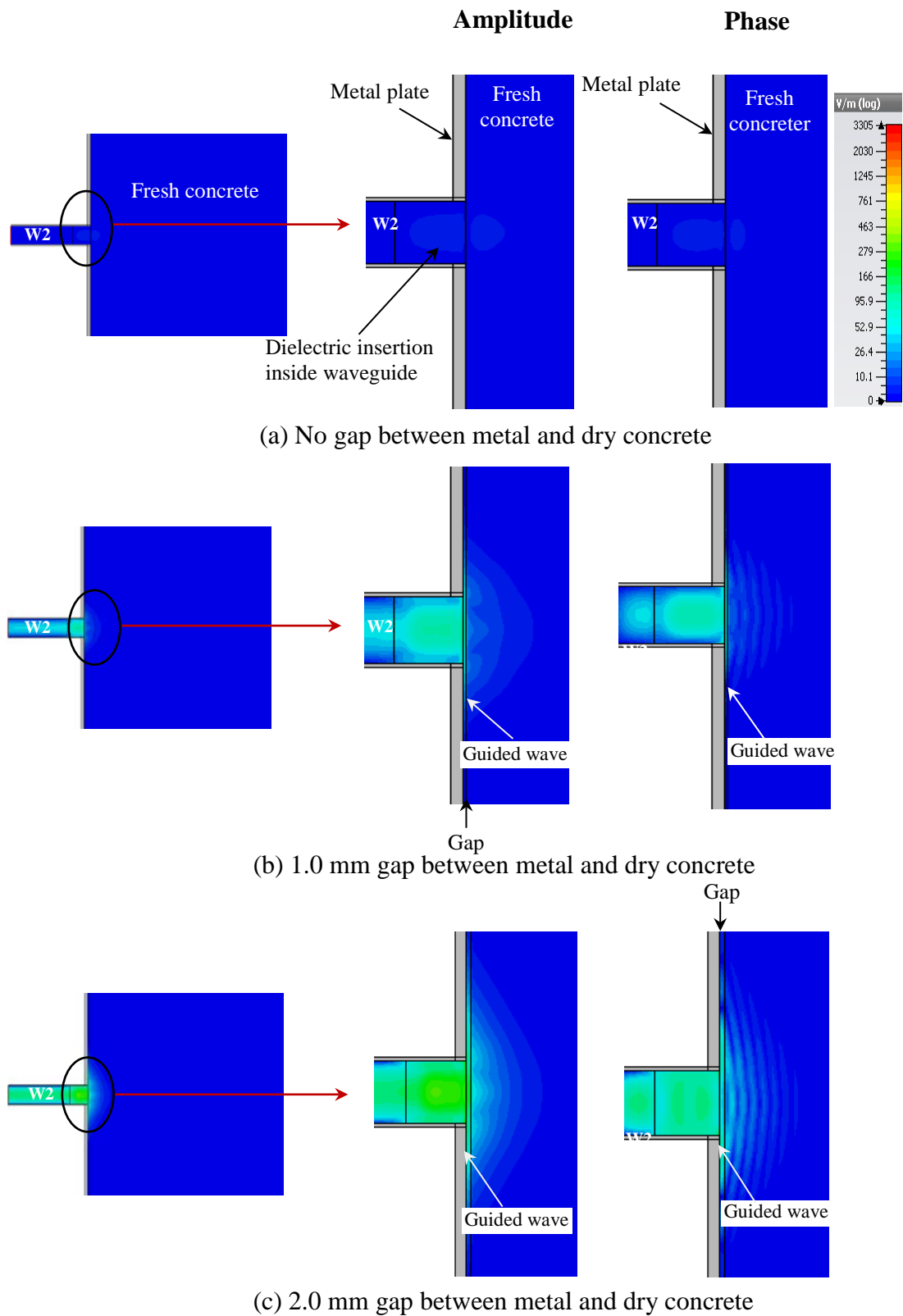
Figure 5.34: Cross-sectional top view of electric field intensity distribution inside waveguide 2 of dielectric-loaded DWS and fresh concrete specimen ($\varepsilon_r = 15.0 - j4.5$) for gaps between metal and specimen surfaces at 10.3 GHz.
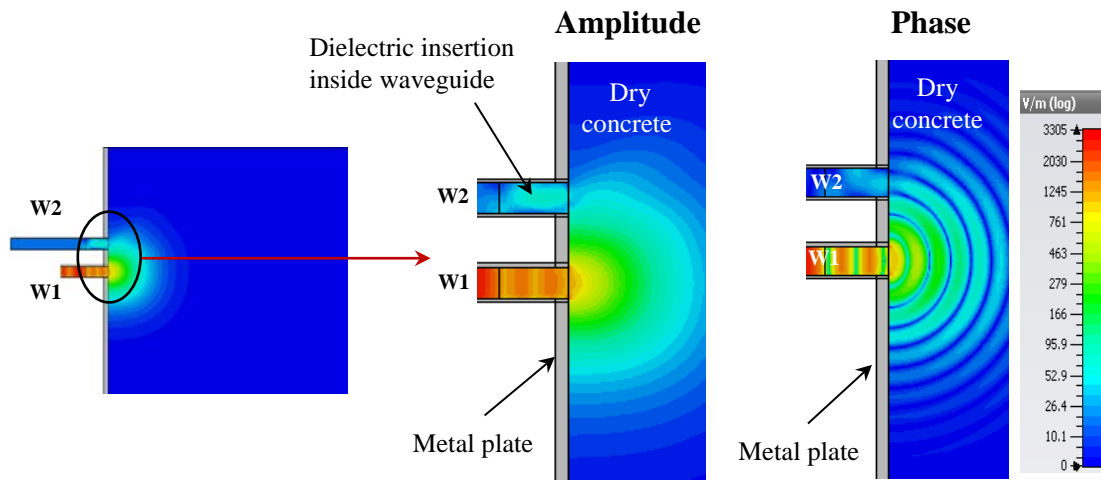
(a) No gap between metal and dry concrete
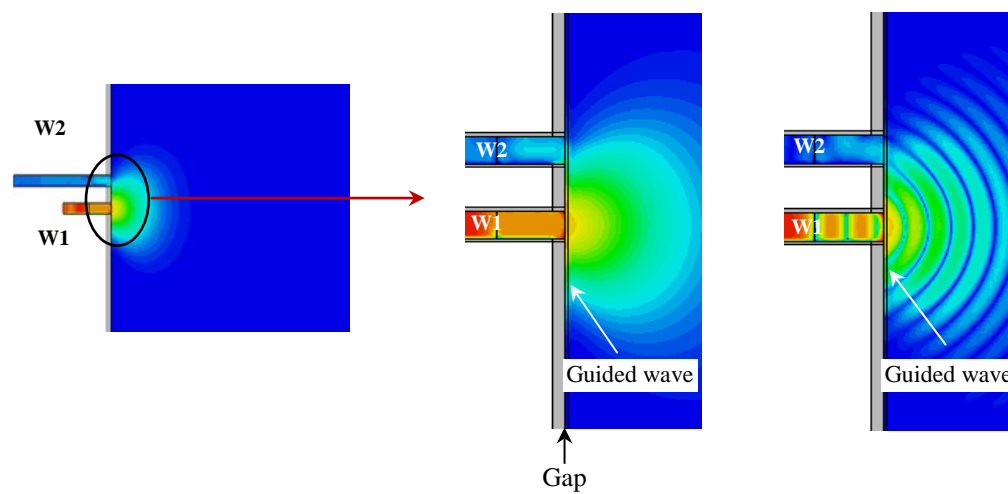
(b) 1.0 mm gap between metal dry concrete
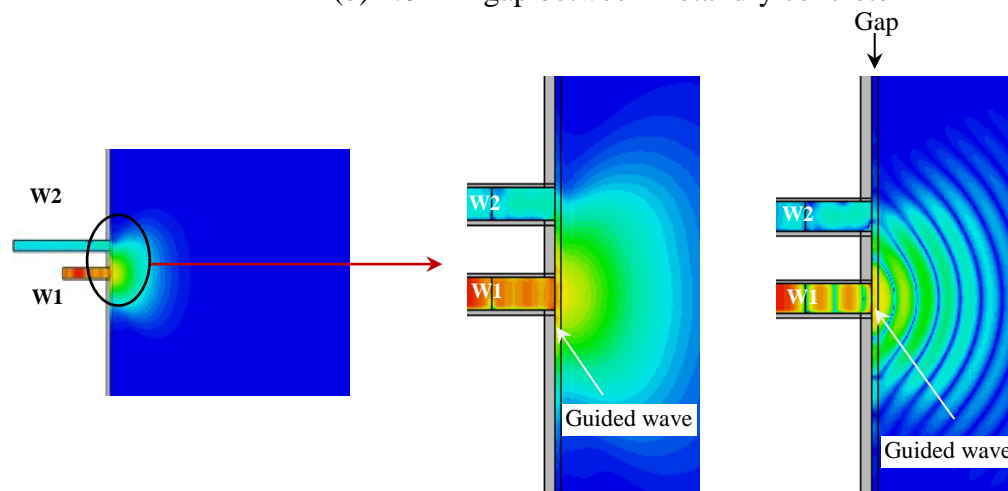
(c) 2.0 mm gap between metal and dry concrete

Figure 5.35: Cross-sectional side view of electric field intensity distribution inside waveguides of dielectric-loaded DWS and dry concrete specimen ($\varepsilon_r = 4.1 - j0.82$) for different gaps between metal and specimen surfaces at 10.3 GHz.
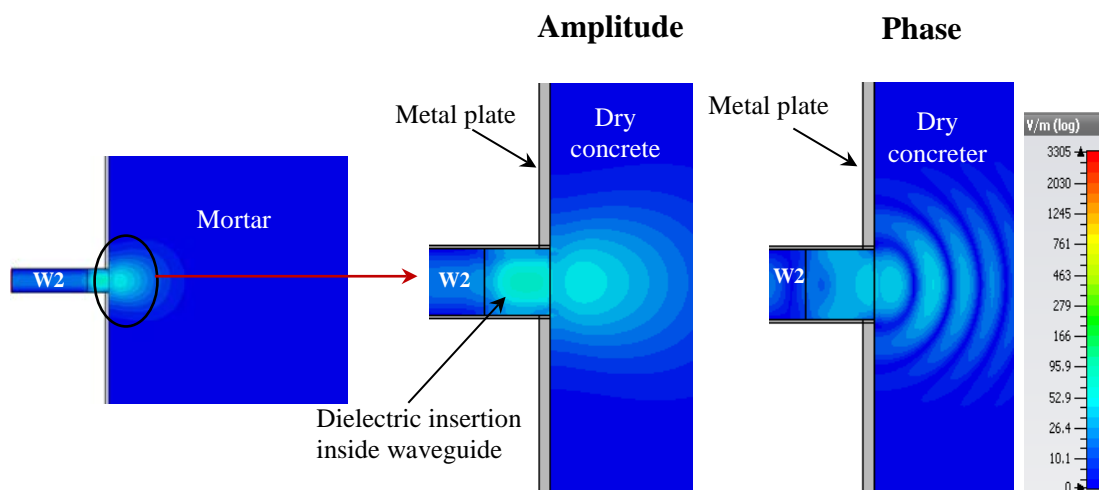
(a) No gap between metal and dry concrete
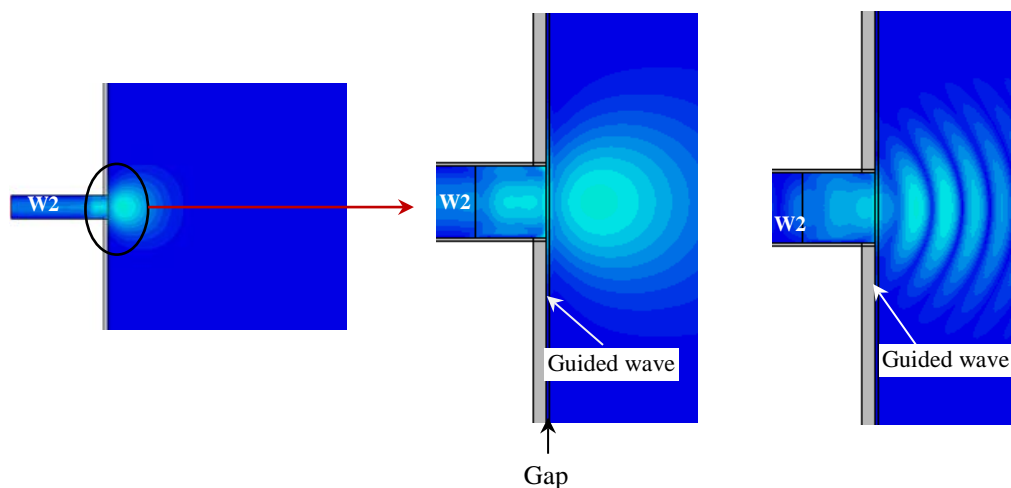
(b) 1.0 mm gap between metal and dry concrete
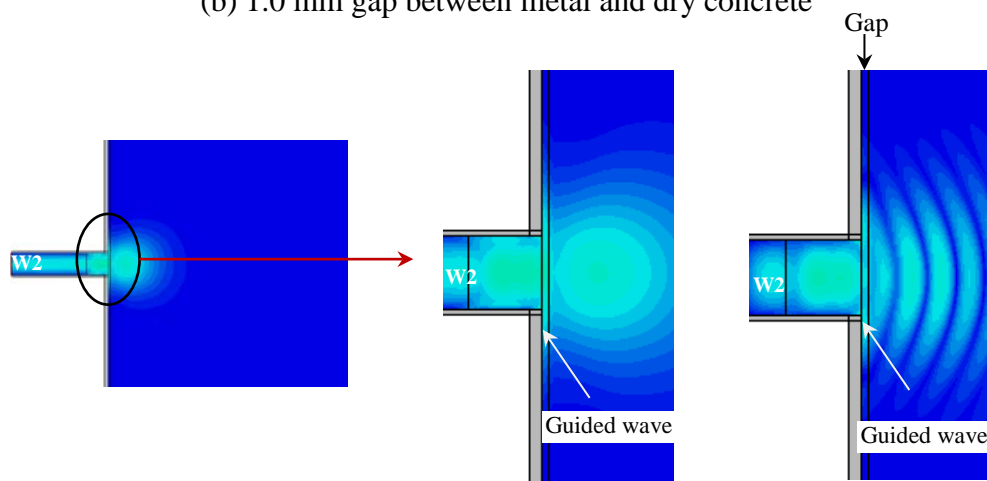
(c) 2.0 mm gap between metal and dry concrete

Figure 5.36: Cross-sectional top view of electric field intensity distribution inside waveguide 2 of dielectric-loaded DWS and dry concrete specimen ($\varepsilon_r = 4.1 - j0.82$) for different gaps between metal and specimen surfaces at 10.3 GHz.

The variations in resonant frequency due to the gap between concrete specimen and metal plate can be better understood by analysing the electric field intensity distribution inside an empty DWS and a dielectric-loaded DWS, in the sensor–specimen interface area and in a concrete specimen, as shown in Figures 5.37–5.40.

Figure 5.37 is a cross-sectional side view of the simulated electric field intensity distribution (amplitude) in empty waveguide sections and in dielectric-loaded DWS waveguide sections and in concrete specimen $\varepsilon_r = 4.1 - j0.82$ for no-gap conditions at non-resonant (9.0 GHz) and resonant (11.0 GHz) frequencies. It is seen that the intensity and wavelength of the incident microwave signal decreases in the dielectric insertions in W1 compared to the empty waveguide. It is also observed that intensity and wavelength further decrease at resonant frequency; however, the signal strength in W2 increases in the dry concrete specimen at the no-gap condition.

Figure 5.38 is a cross-sectional top view of the simulated electric field intensity distribution (amplitude) inside the empty waveguide section W1 and in dielectric-loaded waveguide section W1 with concrete specimen for the no-gap condition at two frequencies. It is clearly seen that the intensity and wavelength of the microwave signal decreases more in the dielectric insertions of the dielectric-loaded DWS both at resonant and non-resonant frequencies.

Figure 5.39 is a cross-sectional side view of schematic and simulated electric field intensity distribution (amplitude) inside the empty waveguide sections and the dielectric-loaded waveguide DWS sections, with part of the concrete specimen, for a 2.0 mm gap at non-resonant (9.0 GHz) and resonant (11.0 GHz) frequencies. The signal intensity decreases in the dielectric insertion, and some of the incident signal passes through the gap to reach W2 when there is a 2.0 mm gap; thus more signals are present in W2 than at the no-gap condition.

Figure 5.40 is a cross-sectional top view of simulated electric field intensity distribution (amplitude) inside W1 of an empty waveguide section and a dielectric-loaded waveguide section, along with the concrete specimen, for a 2.0 mm gap at different frequencies. As in the previous case, it shows a reduction of signal intensity and wavelength. The dielectric insertions and a gap between the metal plate and the concrete specimen both contribute to this change. Therefore, an insertion with suitable dielectric properties provides options for optimising dielectric-loaded DWS.
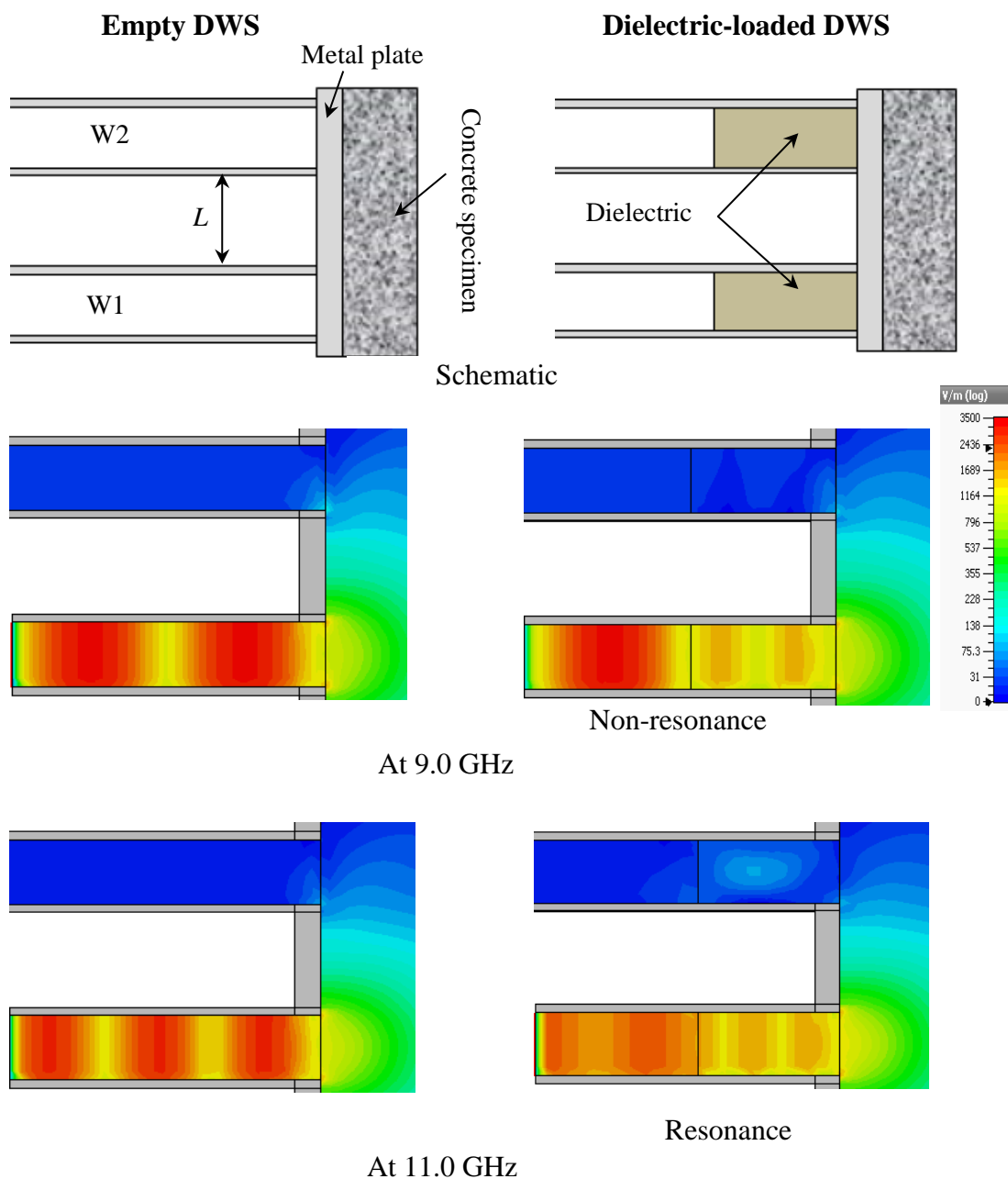
Figure 5.37: Cross-sectional side view of schematic and simulated electric field intensity distribution (amplitude) inside empty waveguide sections and dielectric-loaded waveguide sections of DWS along with concrete specimen ($\varepsilon_r = 4.1 - j0.82$) for no-gap condition at different frequencies.

**Empty Waveguide
Section W1**

**Dielectric-loaded
Waveguide Section W1**

Non-resonance

At 9.0 GHz

Resonance

At 11.0 GHz
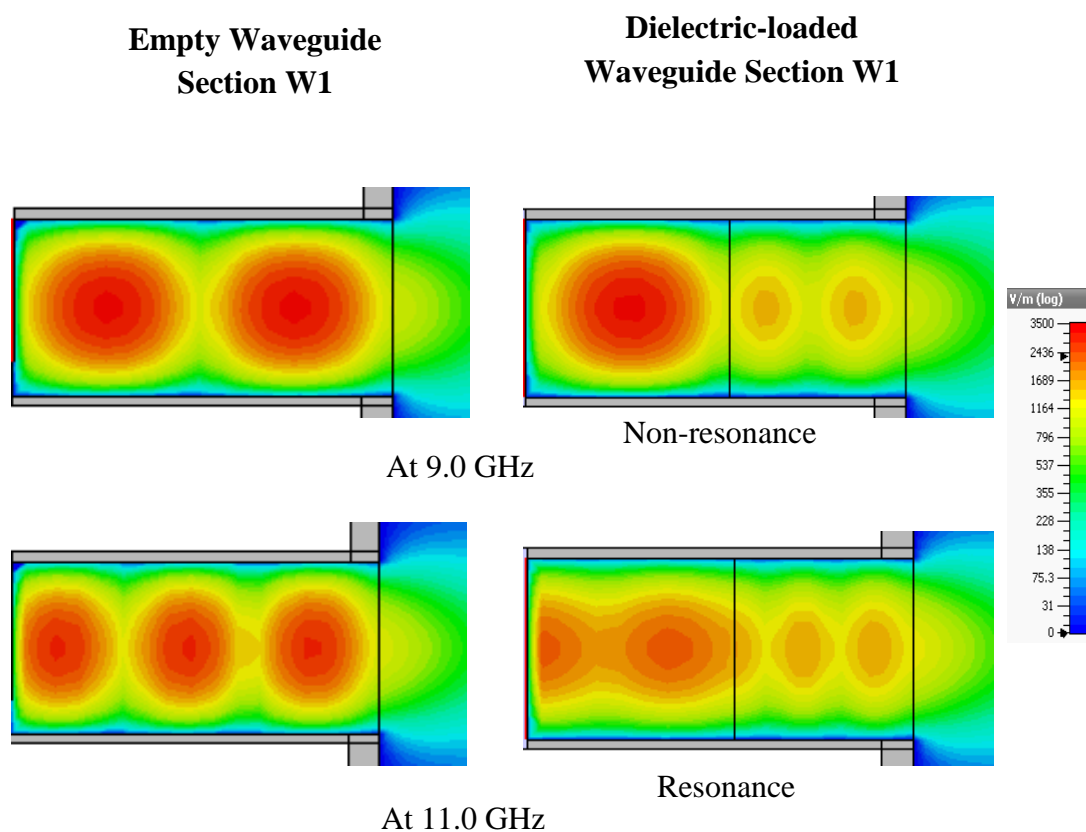
Figure 5.38: Cross-sectional top view of simulated electric field intensity distribution (amplitude) inside empty waveguide section W1 and dielectric-loaded waveguide section W1 with concrete specimen for no-gap condition at different frequencies.

Empty DWS   **Dielectric-loaded DWS**

Schematic

Resonance

At 9.0 GHz

Non-resonance

At 11.0 GHz
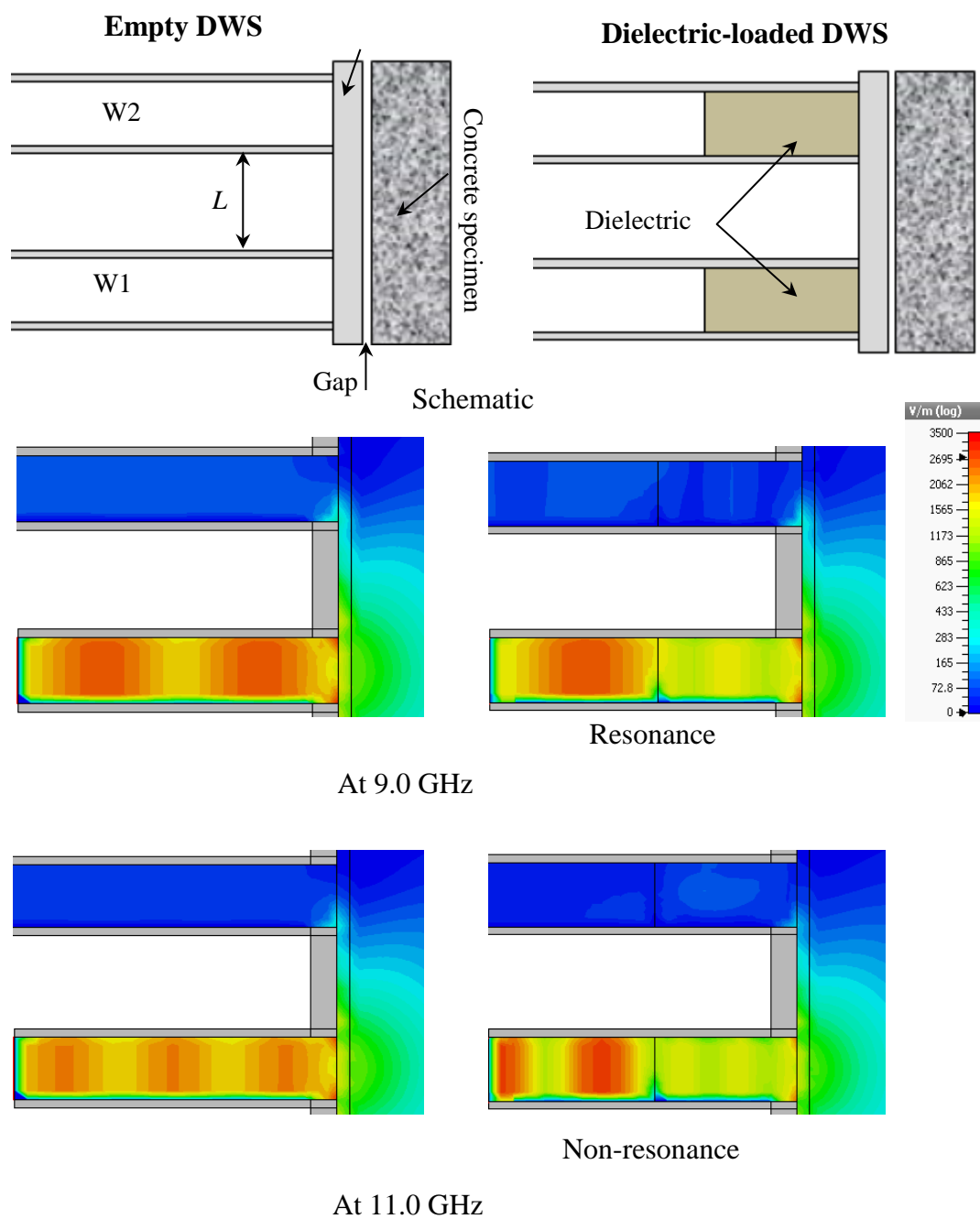
Figure 5.39: Cross-sectional side view of schematic and simulated electric field intensity distribution (amplitude) inside empty waveguide sections and dielectric-loaded waveguide sections of DWS, with part of concrete specimen for 2.0 mm gap condition at different frequencies.

**Empty Waveguide
Section W1**

**Dielectric-loaded
Waveguide Section W1**

Resonance

At 9.0 GHz

Non-resonance

At 11.0 GHz
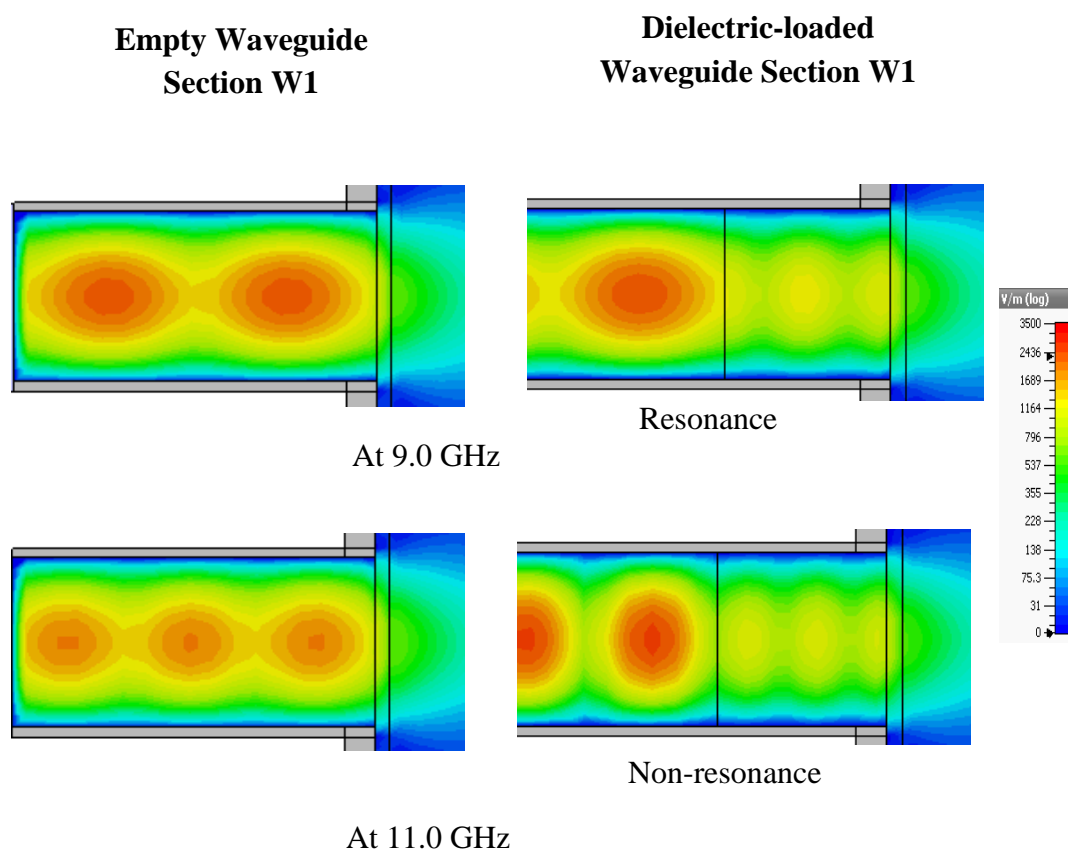
Figure 5.40: Cross-sectional top view of simulated electric field intensity distribution (amplitude) inside empty waveguide section W1 and dielectric-loaded waveguide section W1 with concrete specimen for 2.0 mm gap at different frequencies.

5.6   Comparison between Measurement and Simulation Results

Figure 5.41 shows measured and simulated resonant frequency of the reflection coefficient vs. gap between different concrete specimens and metal plate using the dielectric-loaded DWS for concrete at days 9 and 17, and for two-year dry concrete. The simulated results are presented for day 1 concrete ($\varepsilon_r = 15.0 - j4.5$) and two-year concrete ($\varepsilon_r = 4.1 - j0.82$). It is clear that both the measured and simulated resonant frequencies of the different specimens decrease with increasing gap value, and also that the measured resonant frequency of day 9 concrete and the simulated resonant frequency concrete ($\varepsilon_r = 15.0 - j4.5$) are similar. Differences between the measured and simulated resonant frequencies increase a little with the age of the concrete.

Figure 5.42 illustrates the measured and simulated transmission coefficient vs. gap value for different concrete specimens using the dielectric-loaded DWS. As in the previous case, the measurement results are for concrete at days 9 and 17, and for two-year dry concrete, and the simulated results are presented for day 1 concrete ($\varepsilon_r = 15.0 - j4.5$) and two-year concrete ($\varepsilon_r = 4.1 - j0.82$). It is obvious from Figure 5.42 that the measured and simulated S_{21} both increase monotonically with larger gaps for fresh and early-age concrete; however, for dry concrete, the measured and simulated S_{21} initially decrease for gaps up to 0.5 mm, then increase for gaps up to 2.0 mm. In general, the measured and simulated results are in good agreement. Small differences may be attributed to sensor fabrication error, gap arrangement error due to surface roughness on both the concrete specimen and the metal plate, variations in dielectric permittivity of the insertions and variations in their geometry, and so on. Some of the situations that may affect measurement using the dielectric-loaded DWS are discussed in the next section.
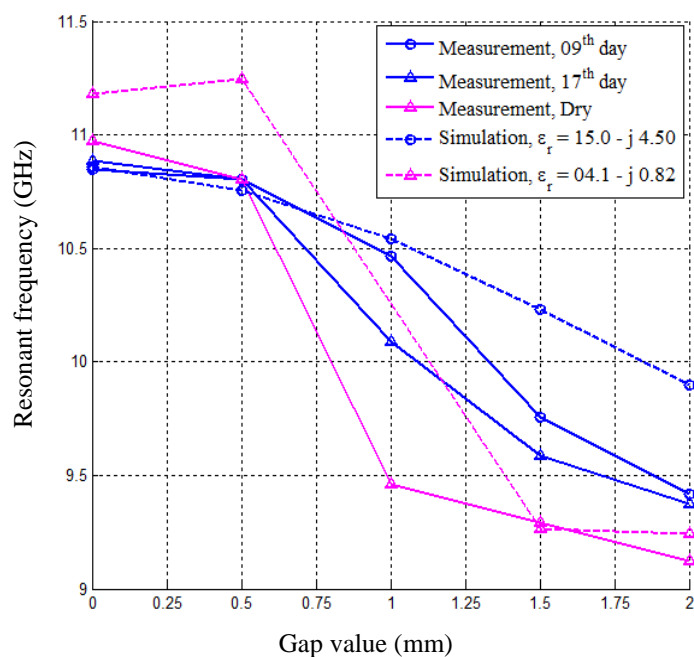
Figure 5.41: Comparison between measured and simulated resonant frequency in S_{11} vs. gap between metal plate and different concrete specimens of different dielectric constants and loss tangents using the dielectric-loaded DWS.
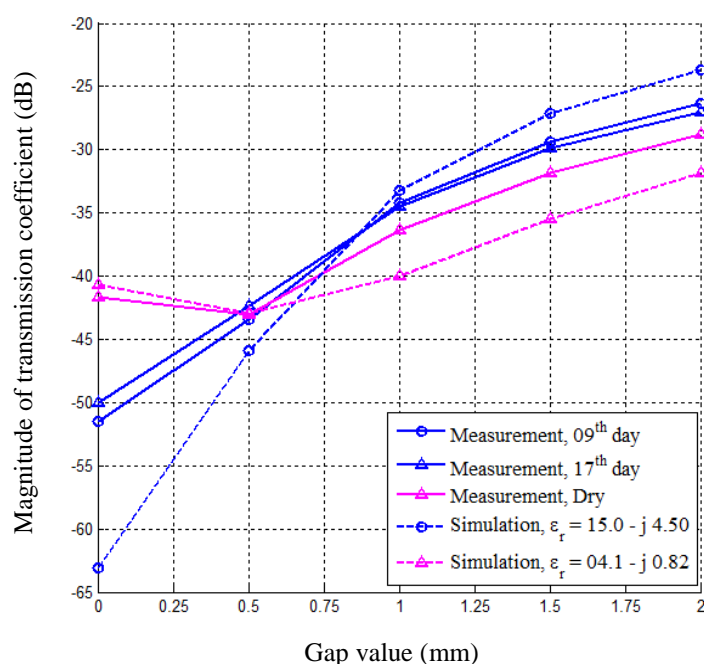
Figure 5.42: Comparison between measured and simulated transmission coefficient vs. gap between metal plate and concrete specimens of different dielectric constants and loss tangents using dielectric-loaded DWS at a frequency of 10.3 GHz.

5.7   Sensitivity Analysis

A numerical investigation into the sensitivity of the reflection and transmission properties of the dielectric-loaded DWS to a relatively wide range of changes of geometrical and electric properties of the rectangular dielectric insertions was also performed. Variations in their dielectric constant (i.e., electrical length) and the effect of changing their physical dimensions (length, height and width) was studied for the case where there was no gap between the DWS metal plate and the dry concrete specimen ($\varepsilon_r = 4.1 - j0.82$).

Figure 5.43a shows the simulated reflection coefficient vs. frequency for different dielectric constants of the insertions. In this case, the loss factor of the insertions was taken to be 0.01. It is clear from the figure that the magnitude of S_{11} at the resonant frequency, and the resonant frequency, both decrease with increase of dielectric constant. Conversely, Figure 5.43b illustrates that S_{21} does not change significantly with the same change of dielectric constant of the insertions.

Figure 5.44 shows the simulated magnitude of reflection and transmission coefficients vs. frequency for different values of loss factor of the dielectric insertions. The dielectric constant of the insertions was considered to be 2.6 in this case. Figure 5.44a shows that the change in loss factor creates small changes in S_{11} only at resonant frequency, and the resonant frequency does not change with loss factor variation. However, Figure 5.44b shows only small changes of S_{21} over the entire frequency range.

Figures 5.45 and 5.46 show the simulated magnitude of reflection and transmission coefficients vs. frequency for different dielectric insert dimensions. It is seen in Figures 5.45a and 5.46a that the resonant frequency and the magnitude of S_{11} change significantly with increasing lengths and heights of the insertions. It is also seen that variations in height have more effect on the value of S_{11} at resonant frequencies than variation in length. Furthermore, Figures 5.45b and 5.46b show that for all changes in length and height of the insertions, the corresponding changes in the transmission coefficient are relatively small.

Figure 5.47 shows the simulated reflection and transmission coefficients vs. frequency for different widths of the dielectric insertions. Figure 5.47a clearly shows that the magnitude of reflection coefficient at resonant frequency changes significantly when the width of the insertion is reduced from 22.5 mm (the width of the waveguide aperture) to 22.0 mm, whereas no change is seen when the width is reduced from 22.0 to 21.0 mm. Negligible change of transmission coefficient is seen in Figure 5.47b. Overall, the transmission coefficient is less sensitive to changes of geometrical and dielectric properties of the dielectric insertions than the reflection coefficient.

(a)

(b)
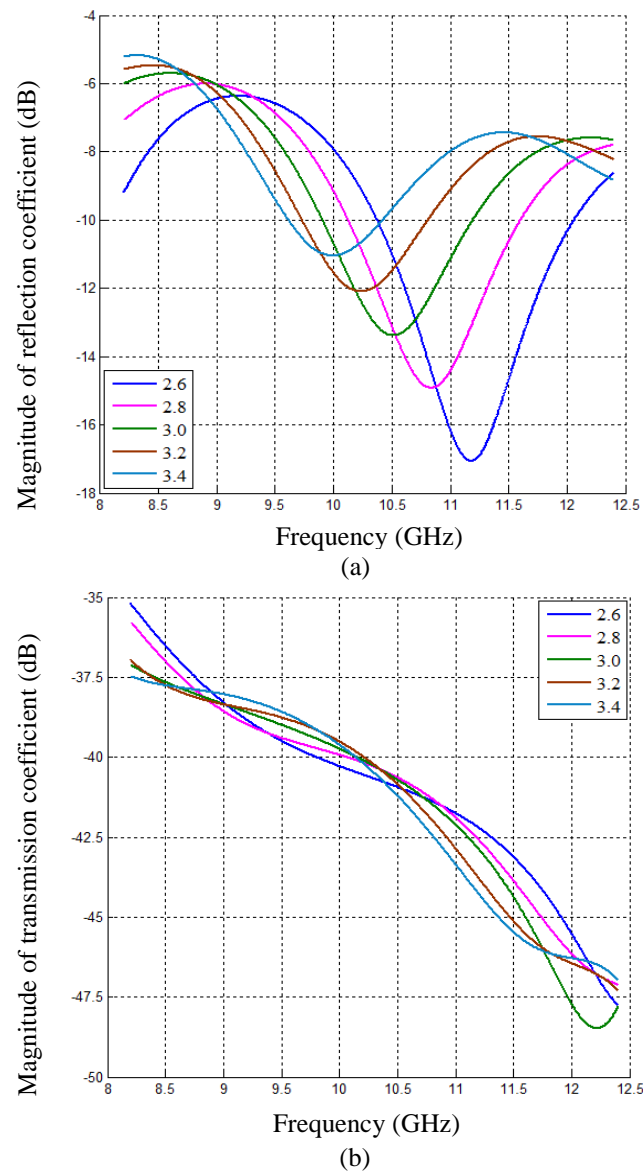
Figure 5.43: Simulated magnitude of (a) reflection coefficient, and (b) transmission coefficient vs. frequency for different dielectric constant of the insertions inside the DWS waveguides for dry concrete ($\varepsilon_r = 4.1 - j0.82$) at no-gap condition.
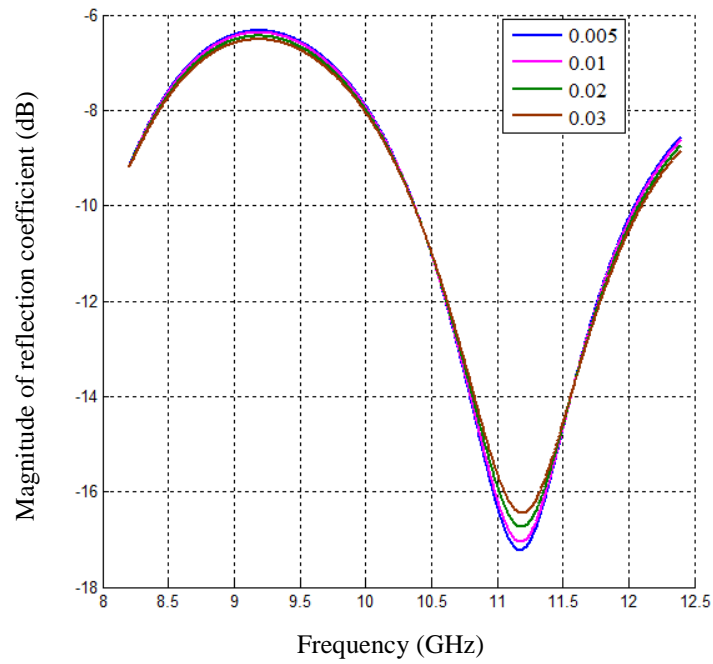
(a)
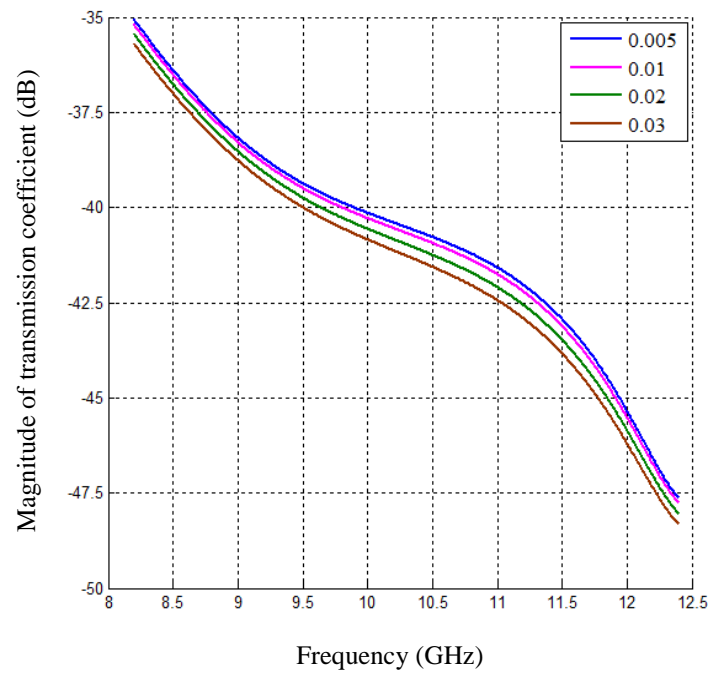
(b)

Figure 5.44: Simulated magnitude of (a) reflection coefficient, and (b) transmission coefficient vs. frequency for different loss factors of the dielectric insertions inside the DWS waveguides for dry concrete specimen ($\varepsilon_r = 4.1 - j0.82$) at no-gap condition.
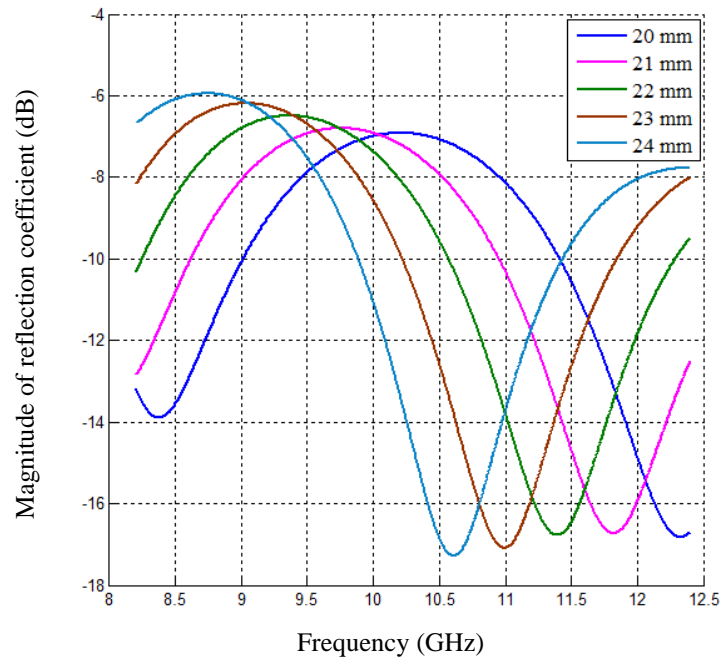
(a)
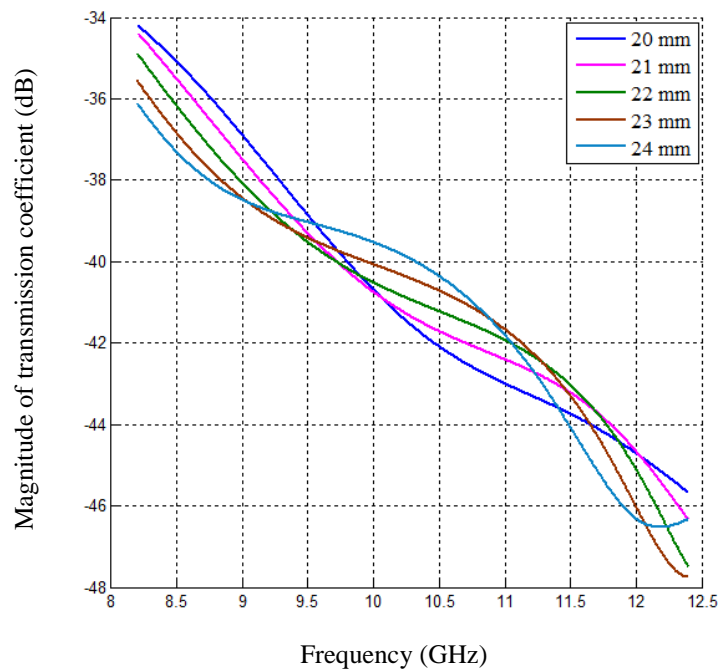
(b)

Figure 5.45: Simulated magnitude of (a) reflection coefficient, and (b) transmission coefficient vs. frequency for different lengths of dielectric inserts inside waveguides of DWS for dry concrete specimen ($\varepsilon_r = 4.1 - j\,0.82$) at no gap condition.
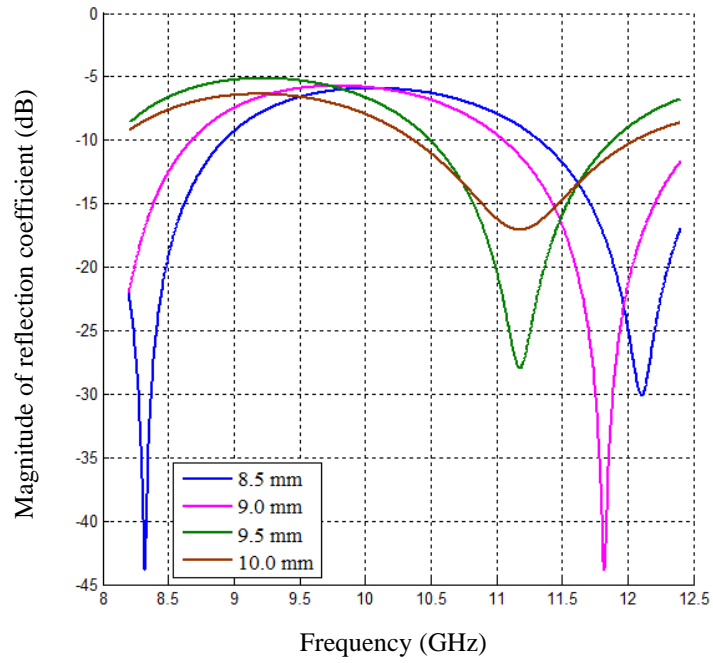
(a)
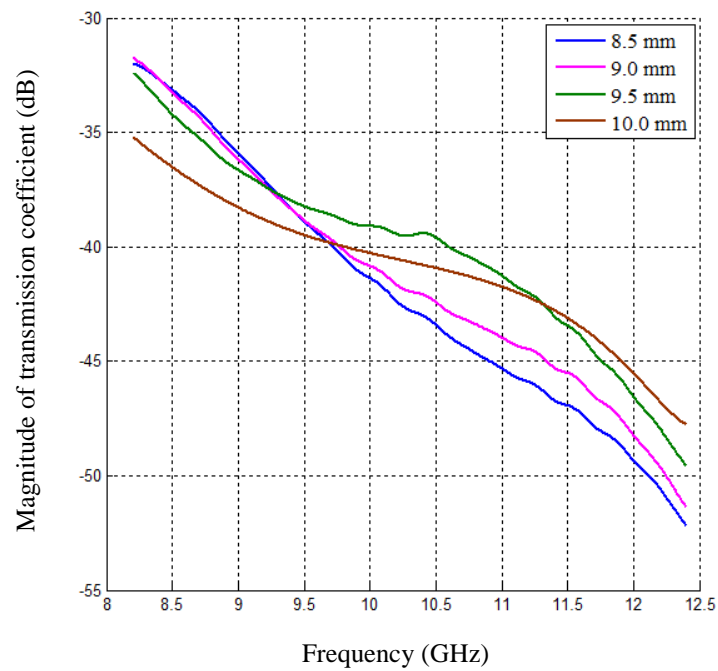
(b)

Figure 5.46: Simulated magnitude of (a) reflection coefficient, and (b) transmission coefficient vs. frequency for different heights of dielectric inserts inside waveguides of DWS for dry concrete specimen ($\varepsilon_r = 4.1 - j0.82$) at no-gap condition.

(a)

(b)
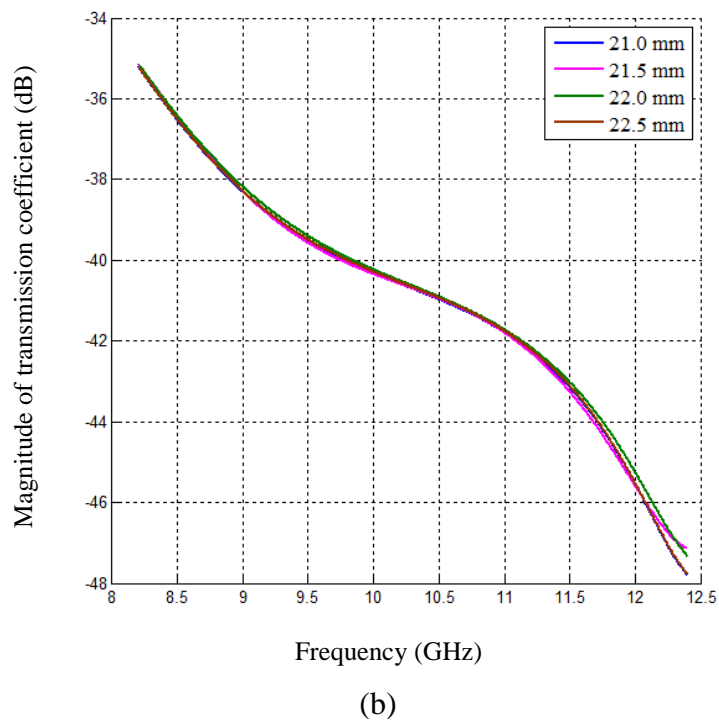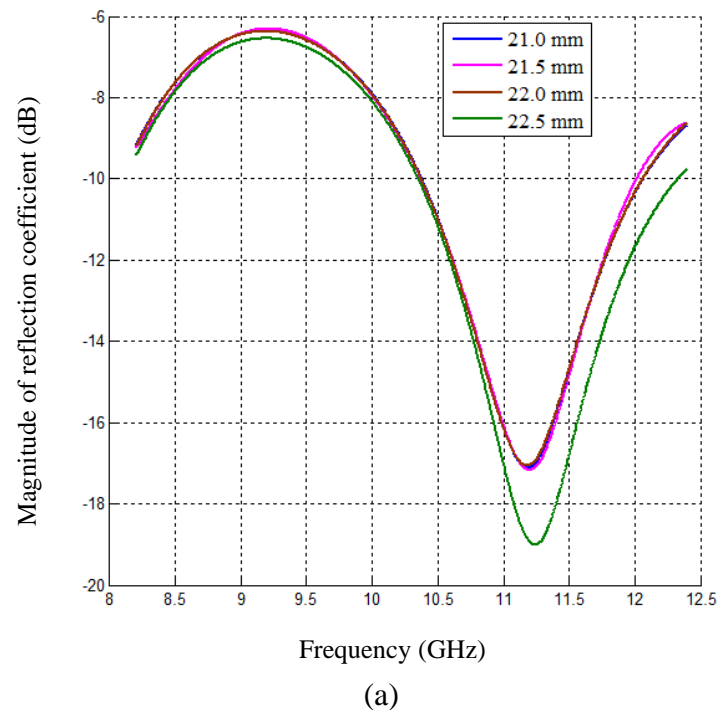
Figure 5.47: Simulated magnitude of (a) reflection coefficient, and (b) transmission coefficient vs. frequency for different widths of dielectric inserts inside waveguides of DWS for dry concrete specimen ($\varepsilon_r = 4.1 - j0.82$) at no gap condition.

5.8   Summary

The design and application of the proposed dual waveguide sensor incorporating rectangular dielectric insertions have been presented in this chapter. The main goal of this work was to improve the dual waveguide sensor for characterisation of concrete–metal structures at different stages of the concrete life, including its fresh stage. The sensor was fabricated to operate at X-band and was applied for three interdependent cases. The first case included the investigation of the reflection, transmission and resonant properties of the sensor with a concrete–metal structure without any gap between the concrete and metal surfaces. It was shown that the dielectric insertions in the sensor–concrete system prevents water and concrete entering the waveguides and allows long-term monitoring of the concrete hydration, including the detection of the transition from fresh to hardened concrete (settling of concrete) on its first day. In particular, the magnitude and phase of the reflection coefficient at the resonant frequency are sensitive changes experienced by the concrete as it hydrates. The second case included the determination of the complex dielectric permittivity of fresh and dry concrete specimens using measured data and extensive simulations with an improved algorithm. The determined complex dielectric permittivity of day 1 fresh concrete and year 2 dry concrete were $15.0 - j4.5$ and $4.1 - j0.82$, respectively. The third case was the measurement and simulation of the reflection and transmission properties of the sensor system for different gaps between concrete and metal plate.

It was clearly shown that the DWS measured 0.5 to 2.0 mm gaps. Comparison of measured and simulated results clearly showed that they were in good agreement. Small differences may be attributed to sensor fabrication error, gap arrangement error due to surface roughness of the concrete specimen and metal plate. Finally, numerical investigation into the sensitivity of the reflection and transmission properties of the dielectric-loaded DWS to changes in the geometry and dielectric properties of the rectangular insertions showed that the magnitude of reflection coefficient at the resonant frequency and the resonant frequency itself are sensitive to changes in physical (geometrical) and electrical length of the insertions as expected, whereas changes of magnitude of the transmission coefficient are relatively small and are attributed to the influence of guided-wave interference; however, loss factor changes in the insertions make only small changes to the magnitude of both the reflection and transmission coefficients.

Chapter 6

Dual Waveguide Sensor with Attached Dielectric Layer

6.1   Introduction

In the previous two chapters, the design, development and applications of empty and dielectric-loaded dual waveguide sensors have been presented. In this chapter a modified DWS with a dielectric layer attached to the metal plate of DWS (referred to as a dual waveguide sensor with attached dielectric layer) is presented and applied. It is expected that the dielectric layer as a part of the sensor will lead to new features and hence new application of DWSs. One potential application is the characterisation of fresh concrete in a mould with a plastic wall or on-line, which are in demand because of the low accuracy of the widely used slump test. Another potential application is the investigation of the shrinkage of different concretes types (cement concrete, geopolymer concrete, etc.) which are still at the research stage and require novel sensory and measurement approaches.

Firstly, an empty DWS with attached dielectric layer is modelled together with fresh and dry concrete specimens, and parametric studies are performed with different thicknesses of dielectric layers for both types of concrete. Then, the proposed DWS is fabricated and applied for the determination of complex dielectric permittivity of fresh concrete, and for the detection of small gaps between concrete specimens of different ages and the dielectric layer.

Secondly, the dielectric-loaded DWS with attached dielectric layer with concrete specimen is modelled. Simulations are performed and measurements are conducted for the detection of small gaps between concrete specimens and attached dielectric layers using the proposed DWS with attached dielectric layer.

Finally, the measurement and simulation results for both sensors are compared. The electric field intensity distributions inside the waveguide sections of the proposed sensors, dielectric layers and concrete specimens are also simulated and presented to confirm some observations made from parametric studies and measurements.

6.2   Design of Sensors

Schematic cross-sectional side views of the proposed dual waveguide sensors with attached dielectric layer are shown in Figure 6.1. As described in the previous chapters, both the empty DWS and dielectric-loaded DWS consist of two X-band rectangular waveguide sections with broad and narrow dimensions *a* and *b*, respectively, installed in the metal wall of the structure under inspection. The distance between the two waveguide sections is *L*. In the new sensor a dielectric layer is placed between the metal plate and the concrete as shown in Figure 6.1.
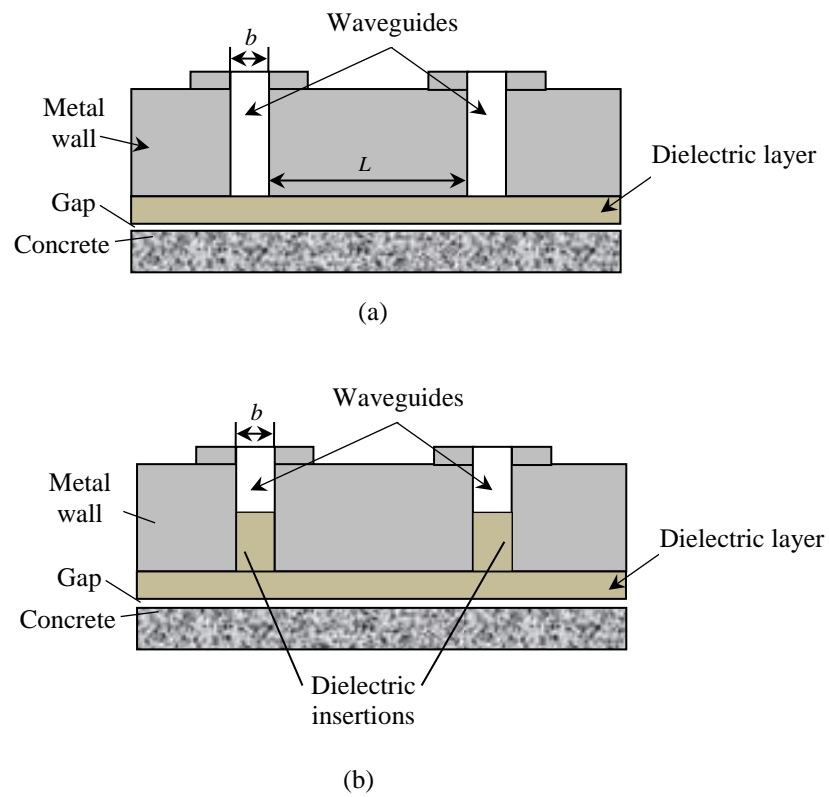
Figure 6.1: Schematic cross-sectional side view of the proposed (a) empty DWS, and (b) dielectric-loaded DWS with attached dielectric layer and concrete.

In this section, an empty DWS with attached dielectric layer is modelled along with a concrete specimen. Simulations will be performed for magnitude of the reflection and transmission coefficients at different gap values between fresh, early-age

and dry concrete specimens and the attached dielectric layers. The simulated results for different thicknesses of attached dielectric layers will be presented and discussed.

6.3 Modelling and Simulation using the Empty DWS with Attached Dielectric Layer

6.3.1 Modelling of Sensor

A model of the microwave empty DWS with attached dielectric layer along with a concrete specimen was created as shown in Figure 6.2. Two X-band microwave rectangular waveguide sections with standard aperture dimensions 22.86×10.16 mm were used. The lengths of waveguide sections are 45.0 mm and 97 mm and the distance between waveguide sections is 15.0 mm. The thickness of the metal plate is 4 mm and the attached dielectric layer ($\varepsilon_r = 2.6 - j0.01$) measuring 250×250 mm is of variable thickness. The dimensions of the concrete specimen is $250 \times 250 \times 250$ mm.
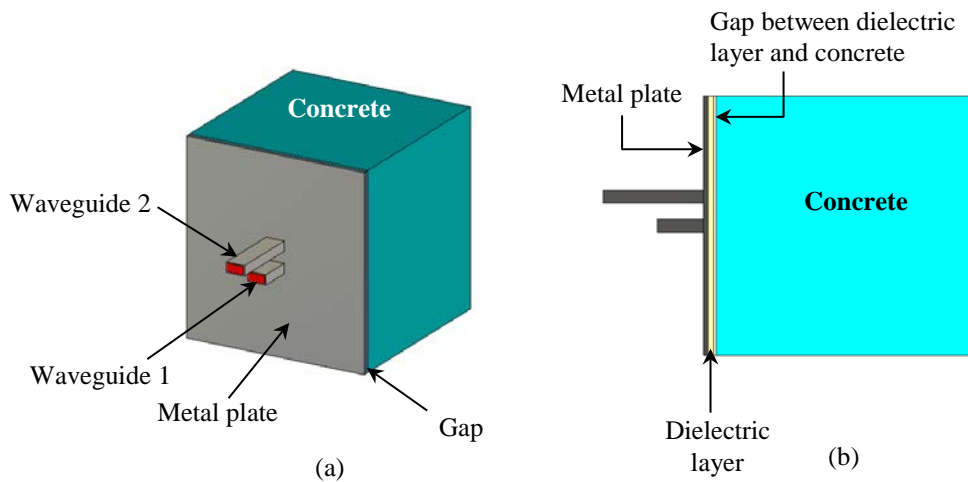
Figure 6.2: Model of empty DWS with attached dielectric layer together with concrete specimen: (a) perspective and (b) cross-sectional side view showing attached dielectric layer and the gap between concrete and dielectric layer.

6.3.2 Parametric Study with Fresh Concrete Specimens

The sensor model will be used in a parametric study to simulate the X-band reflection and transmission coefficients of fresh concrete. The complex dielectric permittivity of fresh concrete is set as $\varepsilon_r = 15.0 - j4.5$, which is the determined permittivity of day 1 fresh concrete. Simulations are further performed for different thicknesses of the attached dielectric layer.

Figures 6.3–6.7 show the simulated magnitude of reflection and transmission coefficients vs. frequency at 2, 3, 6, 8 and 10 mm thick dielectric layers for different gaps between the fresh concrete specimen and the dielectric layer. It is seen from Figures 6.3a and 6.7a that the magnitude of the reflection coefficient in the system without gap decreases (increases) at 2 mm, 3 mm and 10 mm (6 mm and 8 mm) layers with increase of frequency At these thicknesses the changes of gap values result in a decrease (increase) of the magnitude. Regarding the magnitude of the transmission coefficient, Figures 6.3b–6.7b show that the magnitude of transmission coefficients do not change notably with increase of frequency for the 2 mm and 3 mm layers, but change significantly for the 6 mm, 8 mm and 10 mm thick layers. However, a significant change of magnitude can be observed for the 2 mm and 3 mm layers in particular when the gap value changes from 0.0 to 0.5 mm. This result shows that the optimum thickness of layer and operating frequency can be selected for certain applications.

For instance, the 8 mm layer can be used to determine the dielectric property of fresh concrete, because the effect of the changes of gap on the changes in magnitude both of the reflection and transmission coefficients at 9.8 GHz is the smallest suitable at these values. A dielectric layer 2–3 mm thick can be used to detect a gap between the concrete and the dielectric layer. This is clear in Figure 6.8, which shows the magnitude of transmission coefficient vs. gap between fresh concrete and dielectric layers 2 mm and 3 mm thick (Figure 6.8a, b) at 10.3 GHz. In both cases, S_{21} increases with increasing gap, but the magnitude of the transmission coefficient is higher at for a 3 mm layer than a 2 mm layer for all gap values.
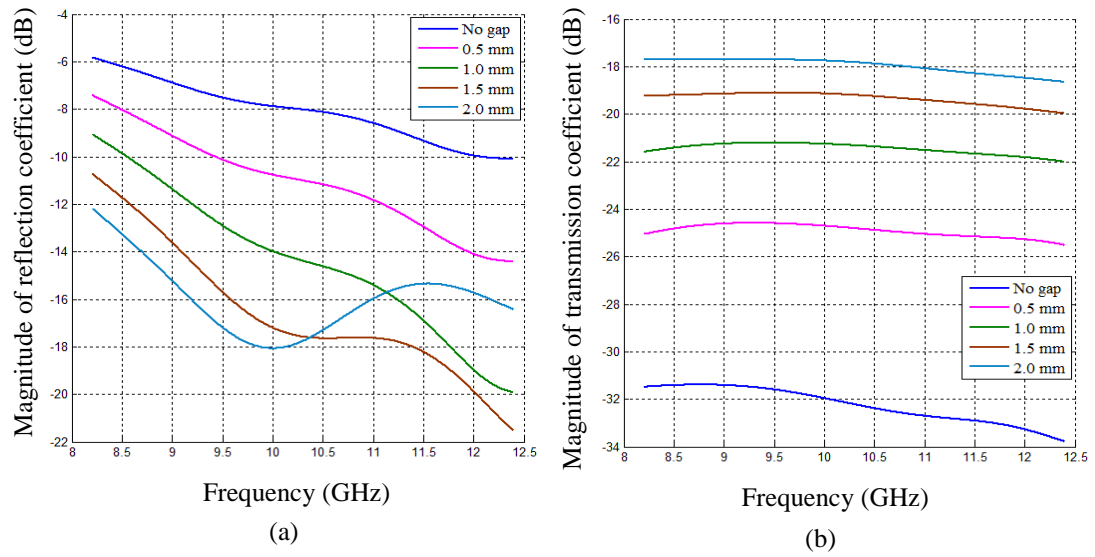
Figure 6.3: Simulated magnitude of (a) reflection coefficient, and (b) transmission coefficient vs. frequency for different gaps between the concrete ($\varepsilon_{rc} = 15.0 - j4.5$) specimen and a 2 mm-thick dielectric layer ($\varepsilon_{rd} = 2.6 - j0.01$).
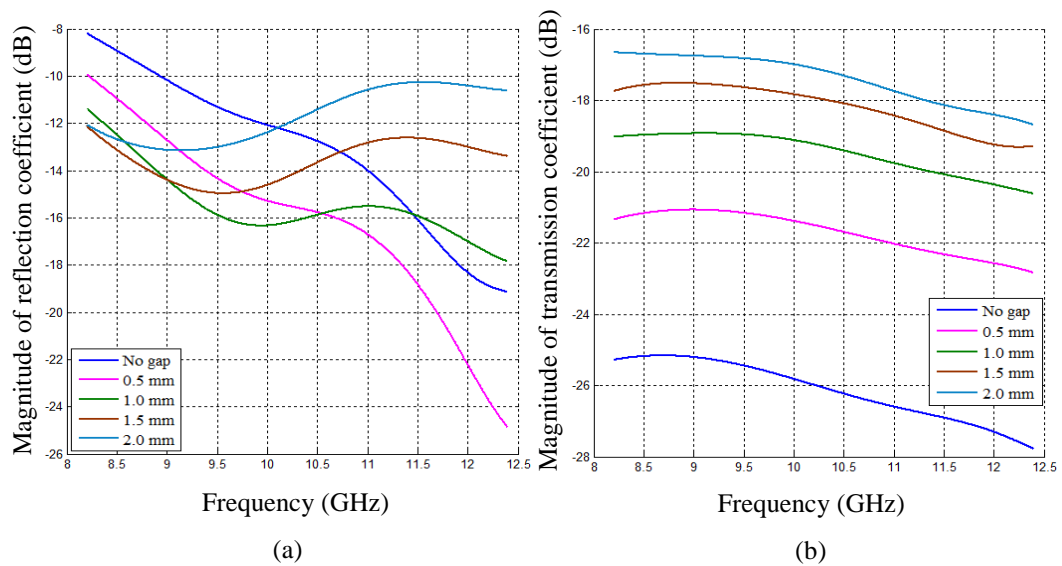
Figure 6.4: Simulated magnitude of (a) reflection coefficient, and (b) transmission coefficient vs. frequency for different gaps between the concrete ($\varepsilon_{rc} = 15.0 - j4.5$) specimen and a 3 mm-thick dielectric layer ($\varepsilon_{rd} = 2.6 - j0.01$).
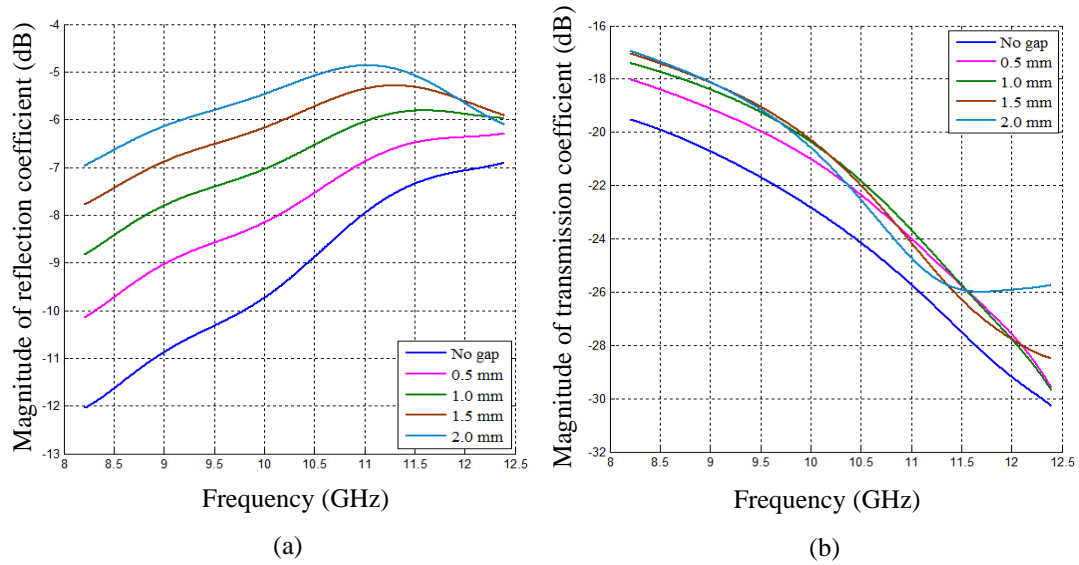
Figure 6.5: Simulated magnitude of (a) reflection coefficient, and (b) transmission coefficient vs. frequency for different gaps between the concrete ($\varepsilon_{rc} = 15.0 - j4.5$) specimen and a 6 mm-thick dielectric layer ($\varepsilon_{rd} = 2.6 - j0.01$).
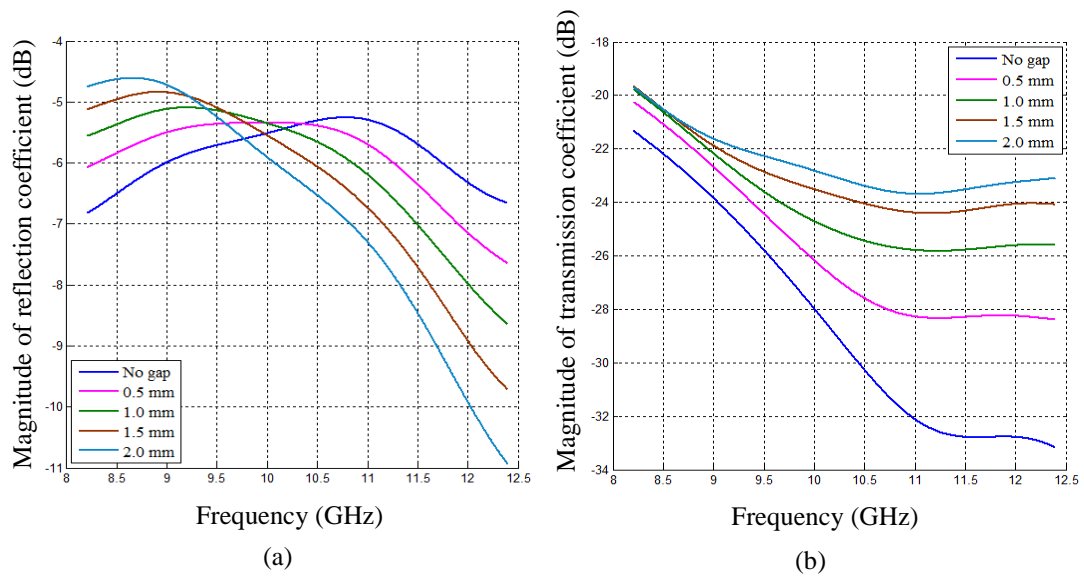
Figure 6.6: Simulated magnitude of (a) reflection coefficient, and (b) transmission coefficient vs. frequency for different gaps between the concrete ($\varepsilon_{rc} = 15.0 - j4.5$) specimen and an 8 mm-thick dielectric layer ($\varepsilon_{rd} = 2.6 - j0.01$).
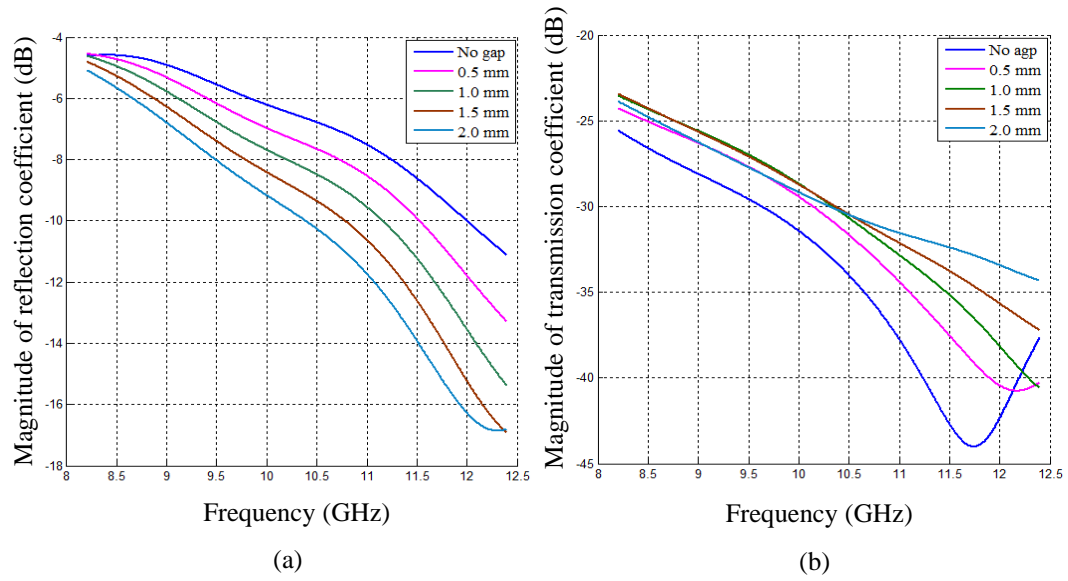
Figure 6.7: Simulated magnitude of (a) reflection coefficient, and (b) transmission coefficient vs. frequency for different gaps between the concrete ($\varepsilon_{rc} = 15.0 - j4.5$) specimen and a 10 mm-thick dielectric layer ($\varepsilon_{rd} = 2.6 - j0.01$).
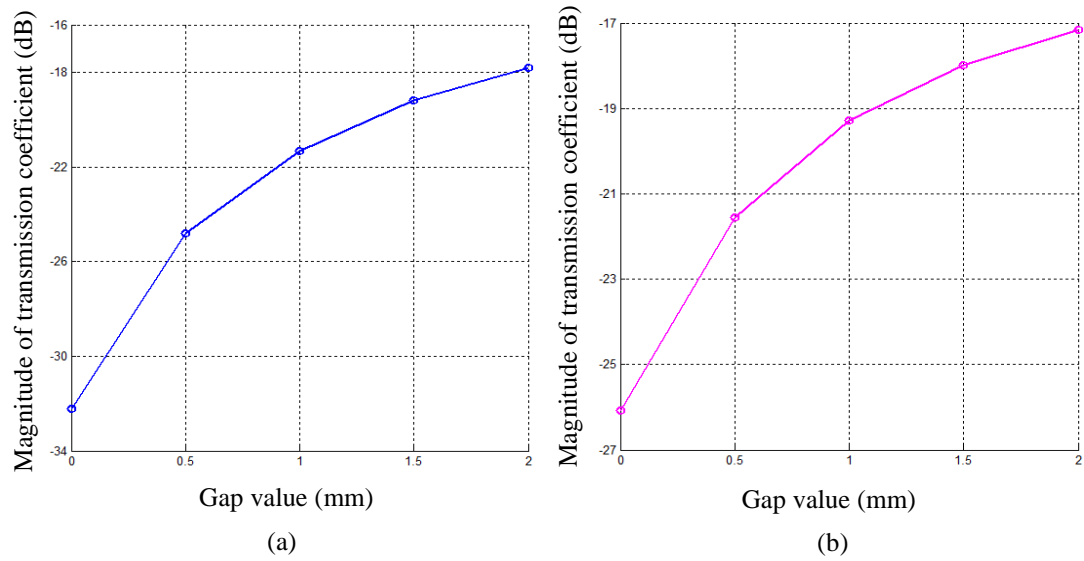
Figure 6.8: Simulated magnitude of transmission coefficient vs. gap at 10.3 GHz between concrete ($\varepsilon_{rc} = 15.0 - j4.5$) and dielectric layer using the empty DWS with attached (a) 2 mm-thick, and (b) 3 mm-thick dielectric layer ($\varepsilon_{rd} = 2.6 - j0.01$).

6.3.3   Parametric Study with Dry Concrete Specimens

The following parametric study with dry concrete uses the complex dielectric permittivity of dry concrete as $\varepsilon_r = 4.1 - j0.82$, which is the permittivity determined for dry concrete about two years old. Simulations are performed for attached dielectric layers variously 2, 3, 6, 8 and 10 mm thick.

Figure 6.9 shows the simulated magnitude of reflection and transmission coefficients vs. frequency for different gaps between the dry concrete specimen and a dielectric layer 2 mm thick, using the empty DWS with attached dielectric layer. It is seen from Figure 6.9a that the magnitude of the reflection coefficient decreases with increase of frequency and gap value, for no gap and 0.5 mm gap value. At other gap values the changes in S_{11} are non-monotonic with frequency and gap values. In Figure 6.9b it is clear that S_{11} decreases slowly with frequency, but S_{21} increases with increase of gap values over the entire operating frequency range. The differences between adjacent gap values in S_{21} decrease as gap value increases.

Figure 6.10 illustrates the simulated magnitude of reflection and transmission coefficients vs. frequency for different gaps between the dry concrete specimen and the dielectric layer of 3 mm thickness using empty DWS with attached dielectric layer. It is seen in Figure 6.10a that the magnitude of the reflection coefficient increases with increasing gap within the frequency range 10.5–12.4 GHz; however, the magnitude of the transmission coefficients increases with the increasing gap over the entire frequency range (Figure 6.10b). Comparing Figures 6.9b and 6.10b, it is seen that, although the differences between adjacent gap values decrease in S_{21} with increased gap value for both cases, the 3 mm dielectric layer results in a higher value of S_{21} for all gap conditions.

Figure 6.11 shows the simulated magnitude of the reflection and transmission coefficient vs. frequency for different gaps between the dry concrete specimen and the 6 mm-thick dielectric layer using the empty DWS with attached dielectric layer. It is clearly seen in Figure 6.11a that the increase of gap increases the magnitude of the reflection coefficient, and there are relatively large increases in the magnitude of the reflection coefficient from 0.0 to 0.5 mm gap conditions over the entire frequency band. It is also noted that the differences between adjacent curves (i.e., gap values)

decrease with the increasing gap. In Figure 6.11b (simulated transmission coefficient vs. frequency for different gaps), it is observed that the magnitude of transmission coefficient increases with increasing gap over the entire frequency range, with a significant increase from 0.0 to 0.5 mm gap conditions.

Figure 6.12 shows the simulated magnitude of reflection and transmission coefficients vs. frequency for different values of the gap between dry concrete specimen and an 8 mm-thick dielectric layer using the empty DWS with attached dielectric layer. It is seen in Figure 6.12a that increasing the gap increases the reflection coefficient at low frequencies, but at frequencies above 11.0 GHz, an increase in gap decreases the reflection coefficient. In Figure 6.12b it is observed that the transmission coefficient increases with increasing gap, but the differences between adjacent curves decrease with increasing gap up to the mid-frequency range, then increase at higher frequencies.

Figure 6.13 shows the simulated magnitude of reflection and transmission coefficients vs. frequency for different values of the gap between dry concrete specimen and a 10 mm-thick dielectric layer using the empty DWS with attached dielectric layer. It is found in Figure 6.13a that increasing the gap decreases the magnitude of reflection coefficient, but the differences in S_{11} at different gap values are not equal in the lower and higher frequencies. However, Figure 6.13b shows that the increase of gap increases the magnitude of transmission coefficient, and again the differences in S_{21} between the gap values at low and high frequencies are not equal.

From the above simulation results, it is found that for the dry concrete specimen, the empty DWS with 6 mm-thick attached dielectric layer (2.6 – j0.01) produces the highest magnitude of transmission coefficients and, in this case, the results for both the reflection coefficient and transmission coefficient can be used to detect a gap between the specimen and the dielectric layer, as further explained by Figure 6.14.

Figure 6.14a, b respectively show the simulated magnitude of reflection and transmission coefficient vs. gap between dry concrete and dielectric layer ($\varepsilon_{rd} = 2.6 -$ j0.01) using empty DWS with a 6 mm-thick dielectric sheet attached to the metal plate at 10.6 GHz frequency. It is seen that both coefficients increase with the increase of gap.

Figure 6.9: Simulated magnitude of (a) reflection coefficient, and (b) transmission coefficient vs. frequency for different gap values between concrete ($\varepsilon_{rc} = 4.1 - j0.82$) specimen and 2 mm-thick dielectric layer ($\varepsilon_{rd} = 2.6 - j0.01$).
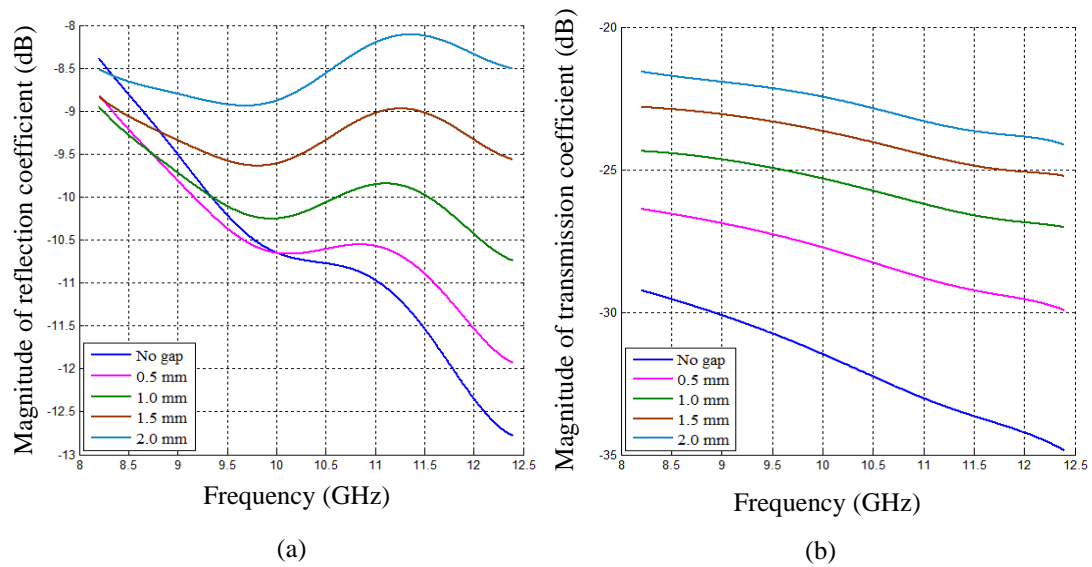
Figure 6.10: Simulated magnitude of (a) reflection coefficient, and (b) transmission coefficient vs. frequency for different gap values between concrete ($\varepsilon_{rc} = 4.1 - j0.82$) specimen and 3 mm-thick dielectric layer ($\varepsilon_{rd} = 2.6 - j0.01$).
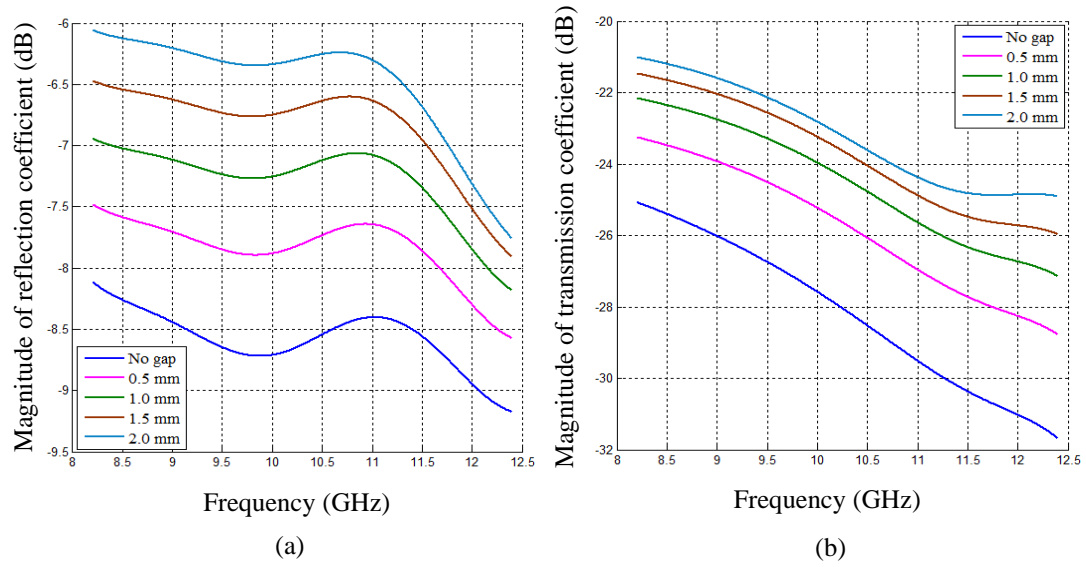
Figure 6.11: Simulated magnitude of (a) reflection coefficient, and (b) transmission coefficient vs. frequency for different gap values between concrete (ε_{rc} = 4.1 – j0.82) specimen and 6 mm-thick dielectric layer (ε_{rd} = 2.6 – j0.01).
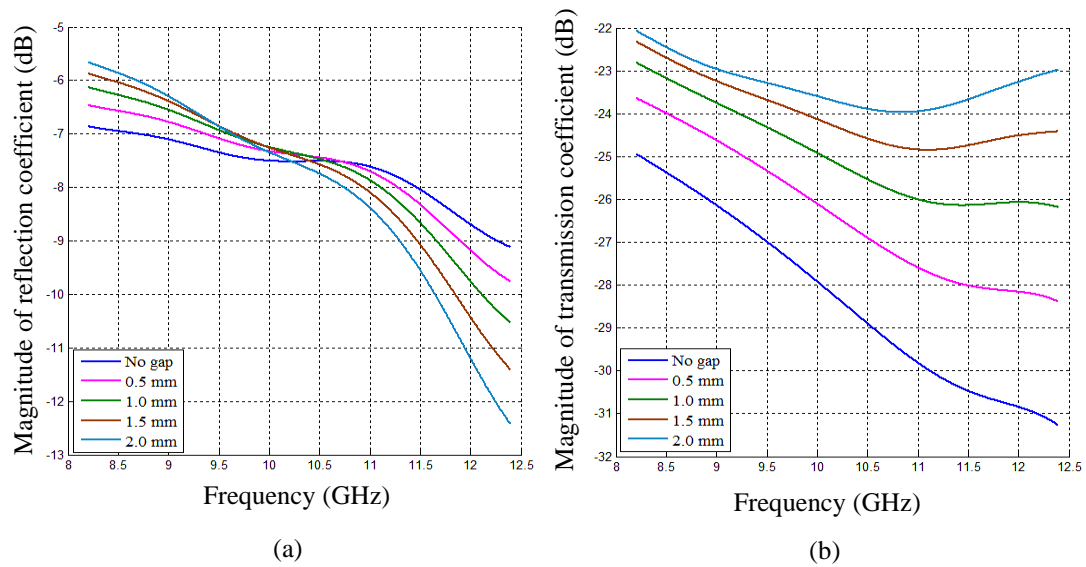
Figure 6.12: Simulated magnitude of (a) reflection coefficient, and (b) transmission coefficient vs. frequency for different gap values between concrete (ε_{rc} = 4.1 – j0.82) specimen and 8 mm-thick dielectric layer (ε_{rd} = 2.6 – j0.01).

(a)

(b)
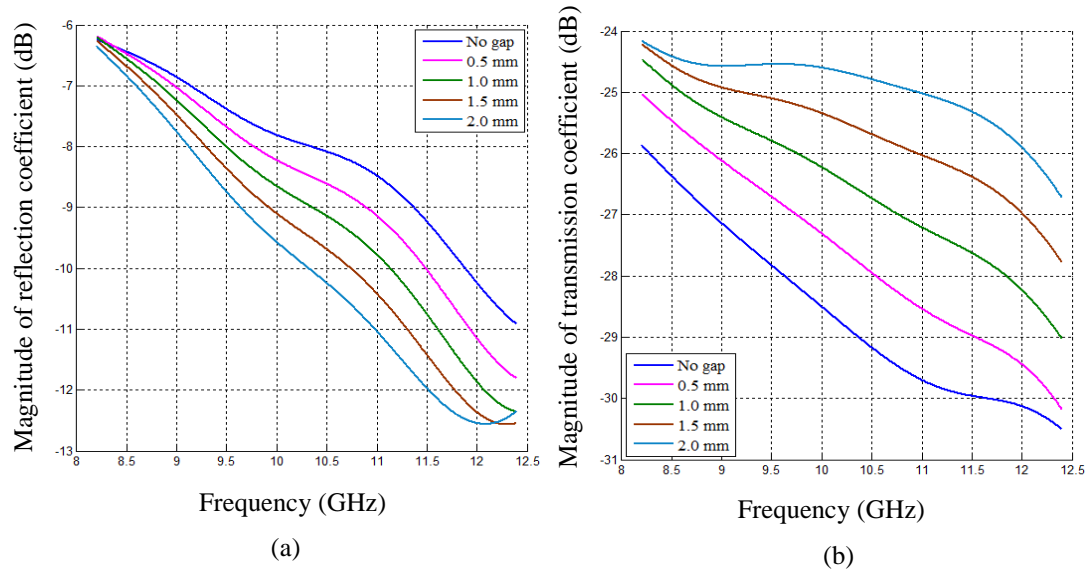
Figure 6.13: Simulated magnitude of (a) reflection coefficient, and (b) transmission coefficient vs. frequency for different gap values between concrete ($\varepsilon_{rc} = 4.1 - j0.82$) specimen and 10 mm-thick dielectric layer ($\varepsilon_{rd} = 2.6 - j0.01$).

(a)

(b)
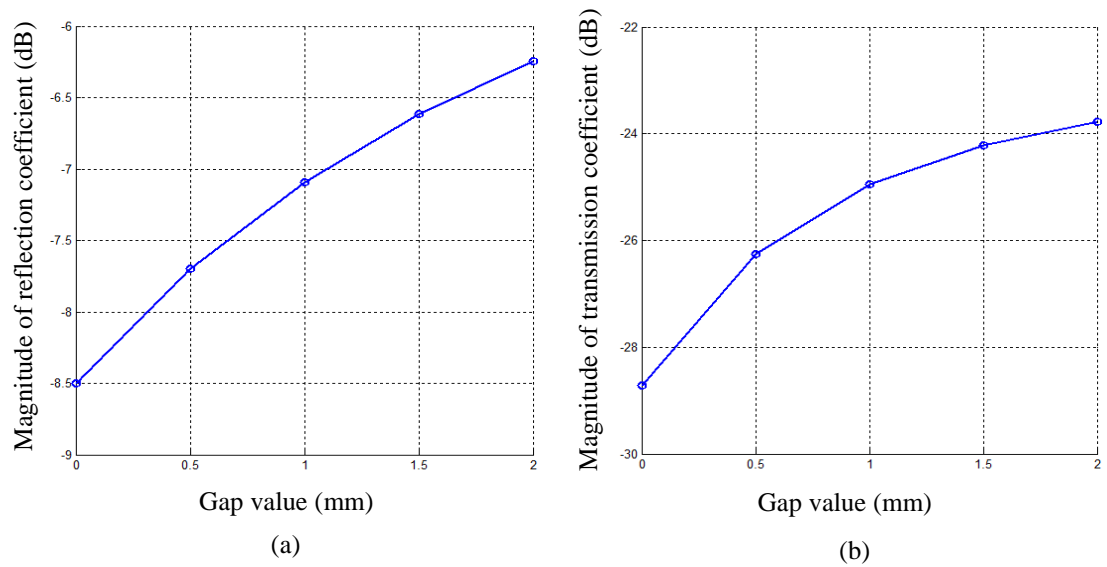
Figure 6.14: Simulated magnitude of (a) reflection coefficient and (b) transmission coefficient vs. gap value between concrete ($\varepsilon_{rc} = 4.1 - j0.82$) and dielectric layer ($\varepsilon_{rd} = 2.6 - j0.01$) using the empty DWS with 6 mm-thick dielectric layer at 10.6 GHz.

6.4 Measurement using Empty DWS with Attached Dielectric Layer

The measurement approach and measurement results for fresh concrete specimen using empty DWS with attached dielectric layer is described in this section. First, the measurement of the reflection coefficient, S_{11} and the transmission coefficient, S_{21} is conducted with no gap between the concrete specimen and 3 mm-thick dielectric layer attached to the empty DWS. Then, S_{11} and S_{21} are also measured for different gaps between 2 mm-thick and 3 mm-thick layers of dielectric acrylic sheet and the dry concrete specimens. Each measurement approach has a separate measurement arrangement which is described in the following.

6.4.1 Specimens and Measurement Setup

Figure 6.15a is a schematic of the experimental setup for measuring the magnitude of reflection and transmission coefficients with no gap between the fresh concrete and dielectric layer using empty DWS with attached dielectric layer. It is seen that one side of an open-top 250 mm cubic wooden mould is replaced by the proposed empty DWS with attached dielectric layer. In the previous section, it is numerically shown that a 3 mm-thick dielectric acrylic sheet with complex permittivity $\varepsilon_{rd} = 2.6 - j0.01$ results in a higher transmission coefficient for fresh concrete than other thicknesses. Therefore, a 3 mm-thick acrylic sheet was used as the attached dielectric layer with empty DWS. Suitable waveguide-to-coaxial adapters and coaxial cables are used to connect the proposed sensor to the PNA. Fresh concrete was prepared by mixing cement, sand, coarse aggregates and water roughly in a ratio of 2:4:4:1 and the mould was filled with this fresh concrete mix. The measurements of S_{11} and S_{21} were recorded at each of the first eight hours after preparing the fresh concrete.

In the second experimental setup (Figure 6.15b), the magnitudes of reflection and transmission coefficients were measured for different gaps between the early-age concrete and dielectric layers at the top of the cubic concrete-filled wooden mould. A separate fresh concrete specimen was prepared by mixing cement, sand, coarse aggregates and water in a roughly 2:4:4:1 ratio; and the top of the fresh concrete in the mould was then covered by a transparent polythene film. Thin paper sheets were

used to create 0.5, 1.0, 1.5 and 2.0 mm air gaps between the specimen and the empty DWS with the attached layer. Suitable waveguide-to-coaxial adapters and coaxial cables connected the sensor to the PNA. In this setup, both 2 and 3 mm-thick acrylic sheet was used as the dielectric layers attached to the empty DWS. Five measurements were conducted on each of the first three days after preparing the specimen.
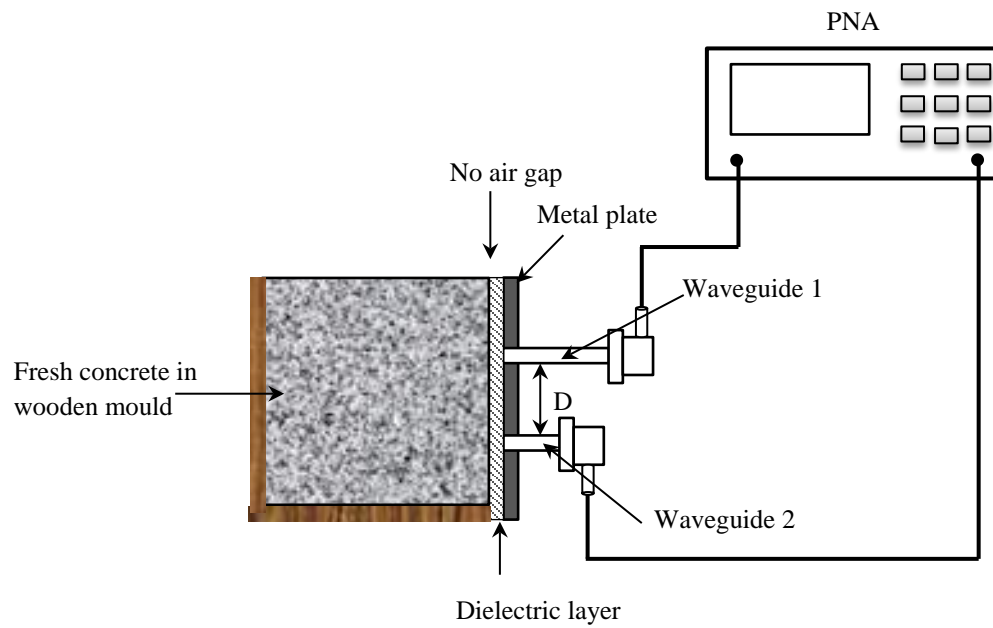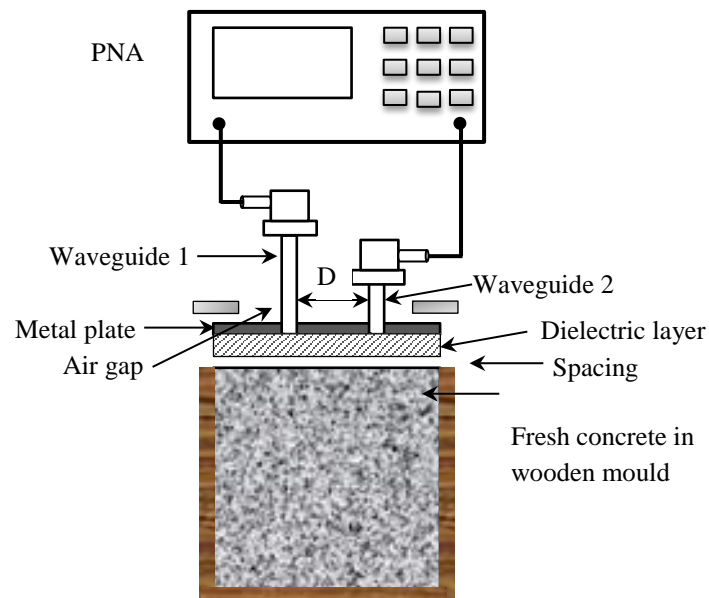
Figure 6.15: Schematic of experimental setup for measuring S_{11} and S_{21} of concrete specimen using the proposed empty DWS with dielectric layer: (a) with no air gap, and (b) with different air gaps between specimen and dielectric layer.

6.4.2   Measurement Results with Fresh and Early-Age Concrete Specimens

Figure 6.16 shows the measured reflection and transmission coefficients vs. frequency for fresh concrete specimen at different hours after preparation for the no-gap condition using empty DWS with attached 3 mm-thick dielectric sheet. It is seen in Figure 6.16a that the reflection coefficient decreases with frequency over the entire frequency range and that S_{11} decreases slightly with the hourly age of the fresh concrete, with a significant decrease between hours 5 and 7. Figure 6.16b shows that the magnitude of the transmission coefficient also decreases with the increase of hourly age of fresh concrete specimen.

The measured magnitudes of the reflection and transmission coefficients vs. frequency for hour 1 fresh concrete are presented in Figure 6.17a, b, together with selected simulated results for S_{11} and S_{21} for concrete specimens of different complex dielectric permittivities which were selected after applying the improved algorithm for determining complex dielectric permittivity of concrete specimen described in section 5.5.2. Therefore, the complex dielectric permittivity of hour 1 fresh concrete for that composition and environment is 21.5 – j4.3.

Figures 6.18 to 6.20 show the measured magnitudes of the reflection coefficient and transmission coefficient vs. frequency for different gap values between a 2 mm-thick dielectric sheet attached with empty DWS and fresh concrete specimen for days 1, 2 and 3 respectively. It is seen in Figures 6.18a, 6.19a and 6.20a that, for concrete specimens 1, 2 and 3 days old, the reflection coefficients increase with the increase of frequency, and also the increase in gap increases the magnitude of the reflection coefficient mainly from 9.5 to 12.4 GHz. Similarly, it is observed in Figures 6.18b, 6.19b and 6.20b that the magnitudes of the transmission coefficients decrease with increase of frequency. In addition, the increase in gap increases the transmission coefficient over the entire frequency band. However, the differences in S_{21} between adjacent gap values decrease with the increase of gap values, and these differences increase with the age of concrete specimens.

Figures 6.21 to 6.23 show the measured magnitudes of the reflection and transmission coefficient vs. frequency for different gap values between a 3 mm-thick dielectric sheet attached with empty DWS and fresh concrete specimen of days 1, 2

and 3 respectively. It is seen in Figures 6.21a, 6.22a and 6.23a that, for concrete specimens 1, 2 and 3 days old, the magnitude of the reflection coefficients increase with increasing frequency, and also the increase in gap value increases the magnitude of reflection coefficient, mainly from 8.8 to 12.4 GHz. Similarly, it is observed in Figures 6.21b, 6.22b and 6.23b that the magnitudes of the transmission coefficients decrease with increasing frequency. In addition, the increase in gap value changes (increases and decreases) the transmission coefficient over the entire frequency band. However, these changes and differences in S_{21} between adjacent gap values are either uneven or very small.

Figure 6.24 summarises the changes in the transmission coefficients for different gap values between dielectric layers and days 1, 2 and 3 early-age concrete specimens at a single frequency of 10.3 GHz. It is seen in Figure 6.24a that S_{21} increases with increase of gap value between a 2 mm-thick dielectric sheet attached to an empty DWS, and day 1 concrete. The same is true for the days 2 and 3 concrete specimen, but at lower values of S_{21}. However, the magnitude of transmission coefficient increases to a peak value, then decreases with increasing gap between the 3 mm-thick dielectric sheet attached to an empty DWS, and the fresh day 1 concrete specimen (Figure 6.24b). Again, the same is true for the days 2 and 3 concrete specimens but at lower values of S_{21}. Therefore, the empty DWS with 2 mm-thick attached dielectric layer is preferred for detecting and monitoring the gap between the fresh concrete and the dielectric layer.
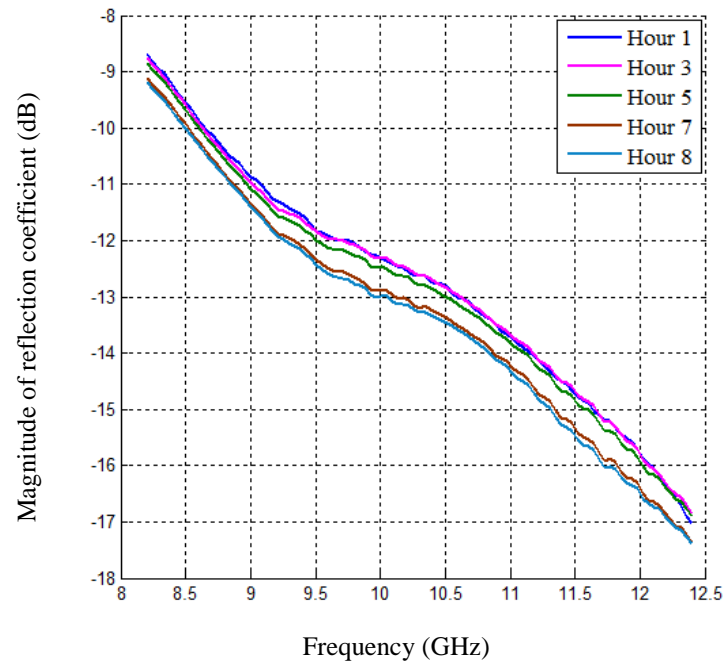
(a)
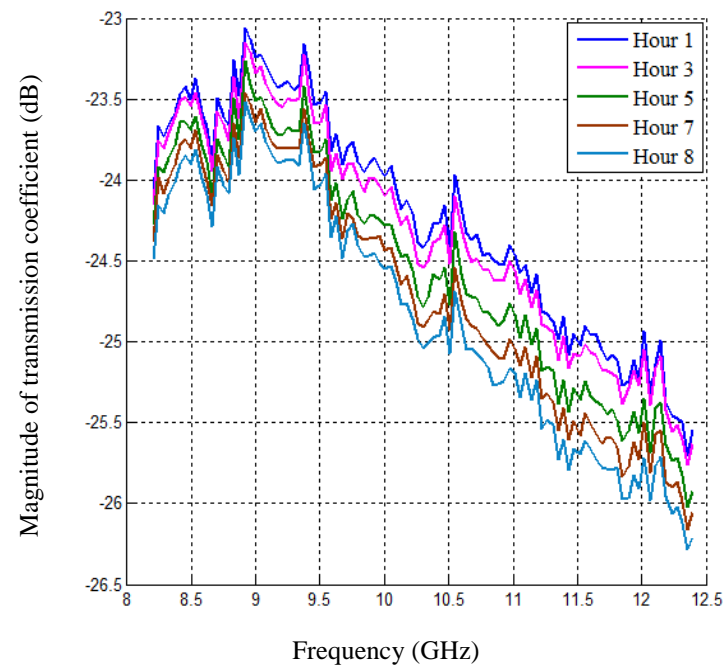
(b)

Figure 6.16: Measured magnitude of (a) reflection coefficient, and (b) transmission coefficient vs. frequency for fresh concrete at different hours after preparation for no-gap condition using empty DWS with 3 mm-thick dielectric sheet ($\varepsilon_{rd} = 2.6 - j0.01$) attached to the metal plate.
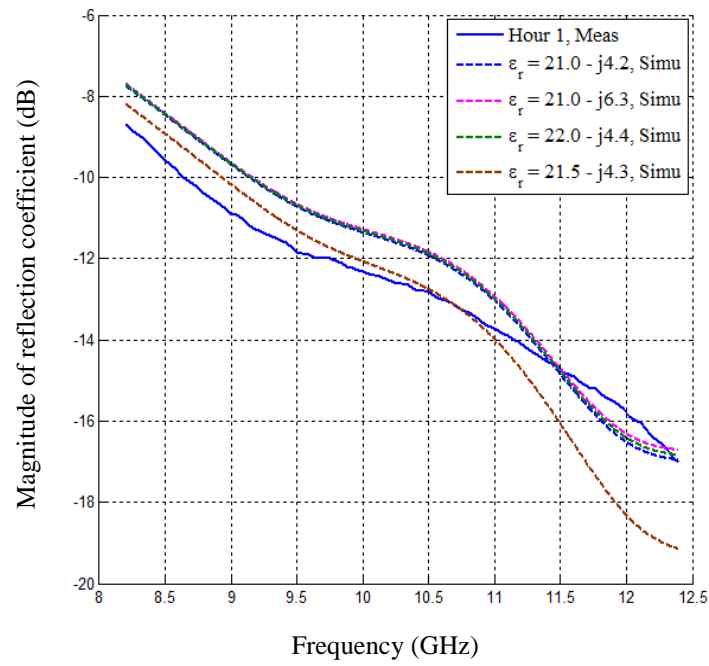
(a)
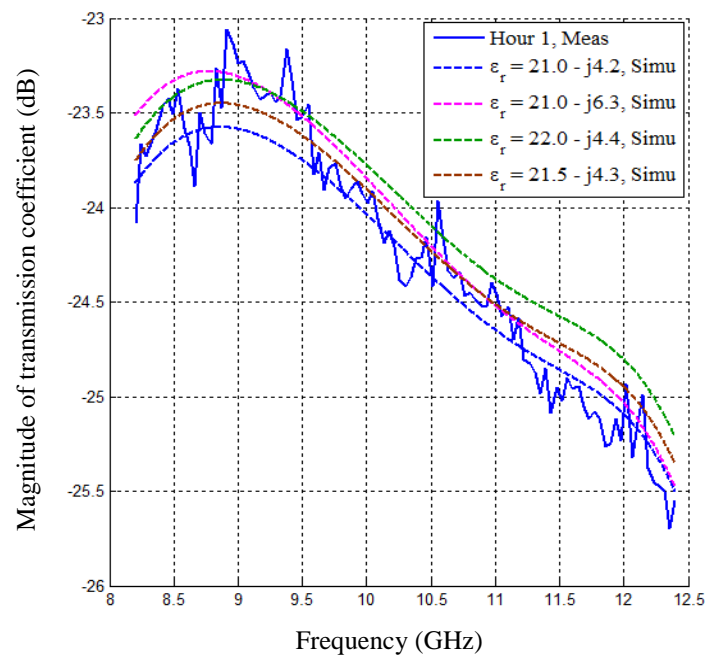
(b)

Figure 6.17: Measured and simulated magnitude of (a) reflection coefficient, and (b) transmission coefficient vs. frequency for fresh concrete at first hour for no-gap condition using empty DWS with 3 mm-thick dielectric sheet ($\varepsilon_{rd} = 2.6 - j0.01$) attached to the metal plate.

Figure 6.18: Measured magnitude of (a) reflection coefficient, and (b) transmission coefficient vs. frequency for different gap values between day 1 fresh concrete and dielectric layer ($\varepsilon_{rd} = 2.6 - j0.01$) using empty DWS with 2 mm-thick dielectric sheet attached to the metal plate.

Figure 6.19: Measured magnitude of (a) reflection coefficient, and (b) transmission coefficient vs. frequency for different gap values between day 2 fresh concrete and dielectric layer ($\varepsilon_{rd} = 2.6 - j0.01$) using empty DWS with 2 mm-thick dielectric sheet attached with the metal plate.
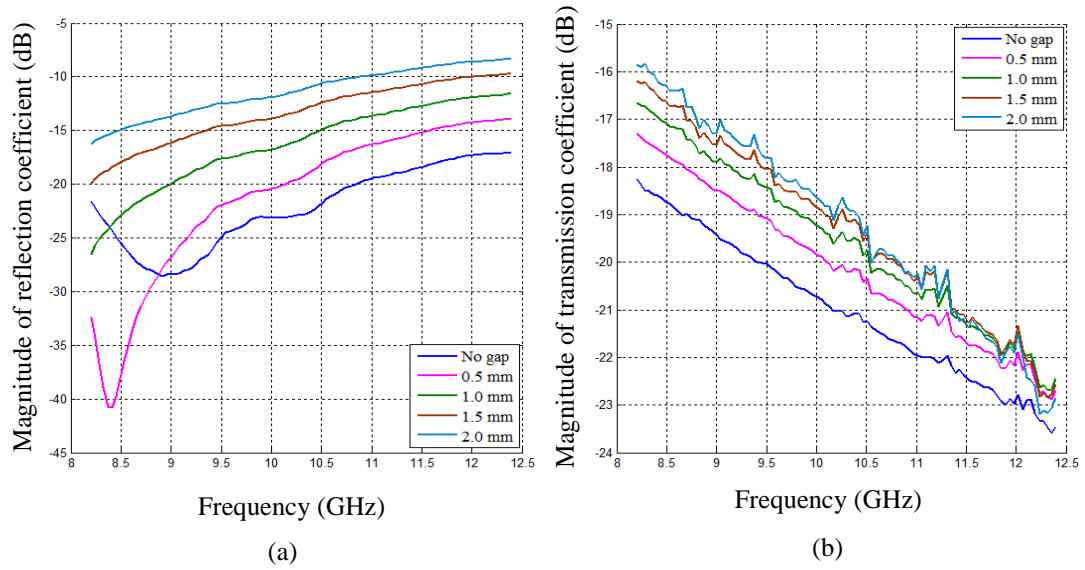
Figure 6.20: Measured magnitude of (a) reflection coefficient, and (b) transmission coefficient vs. frequency for different gap values between day 3 fresh concrete and dielectric layer ($\varepsilon_{rd} = 2.6 - j0.01$) using empty DWS with 2 mm-thick dielectric sheet attached to the metal plate.
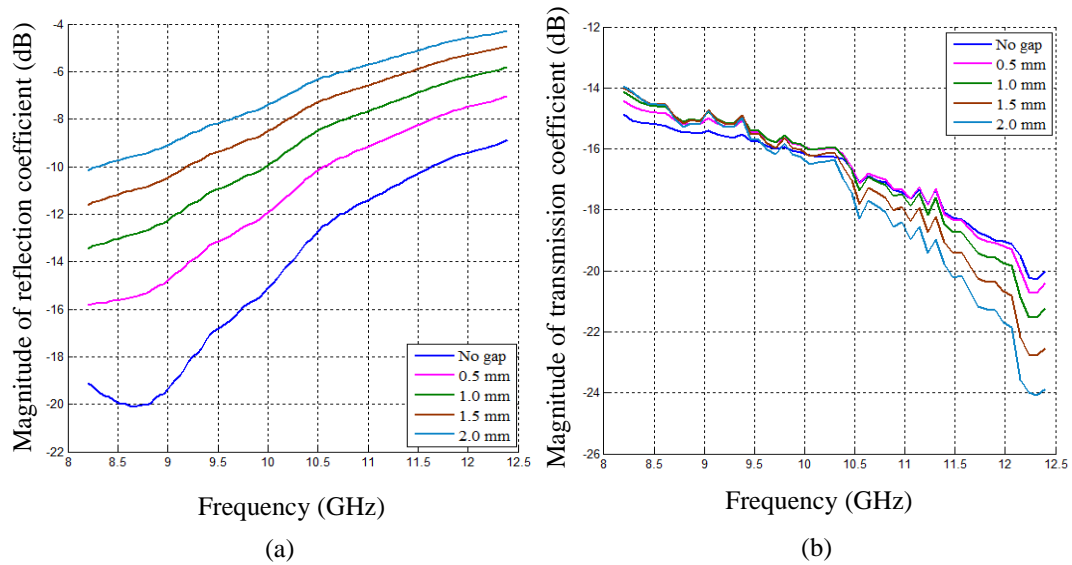
Figure 6.21: Measured magnitude of (a) reflection coefficient, and (b) transmission coefficient vs. frequency for different gap values between day 1 fresh concrete and dielectric layer ($\varepsilon_{rd} = 2.6 - j0.01$) using empty DWS with 3 mm-thick dielectric sheet attached to the metal plate.
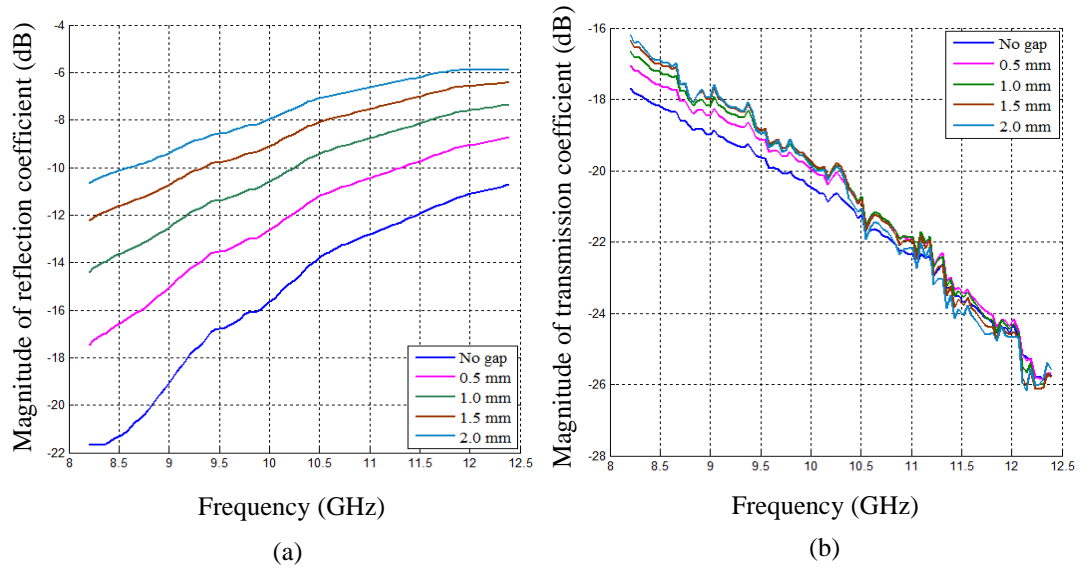
Figure 6.22: Measured magnitude of (a) reflection coefficient, and (b) transmission coefficient vs. frequency for different gap values between day 2 fresh concrete and dielectric layer ($\varepsilon_{rd} = 2.6 - j0.01$) using empty DWS with 3 mm-thick dielectric sheet attached to the metal plate.
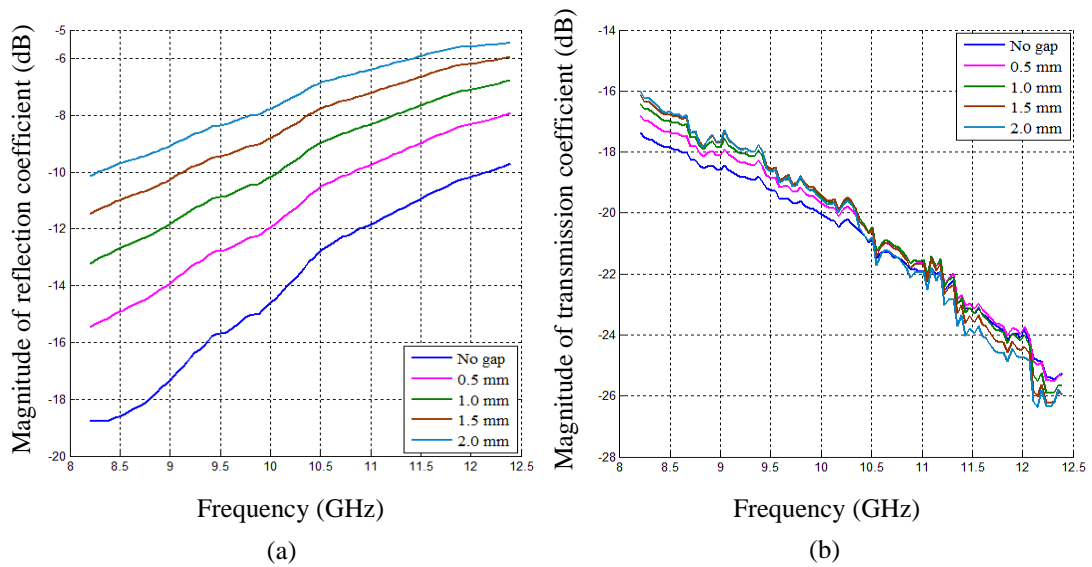
Figure 6.23: Measured magnitude of (a) reflection coefficient, and (b) transmission coefficient vs. frequency for different gap values between day 3 fresh concrete and dielectric layer ($\varepsilon_{rd} = 2.6 - j0.01$) using empty DWS with 3 mm-thick dielectric sheet attached to the metal plate.
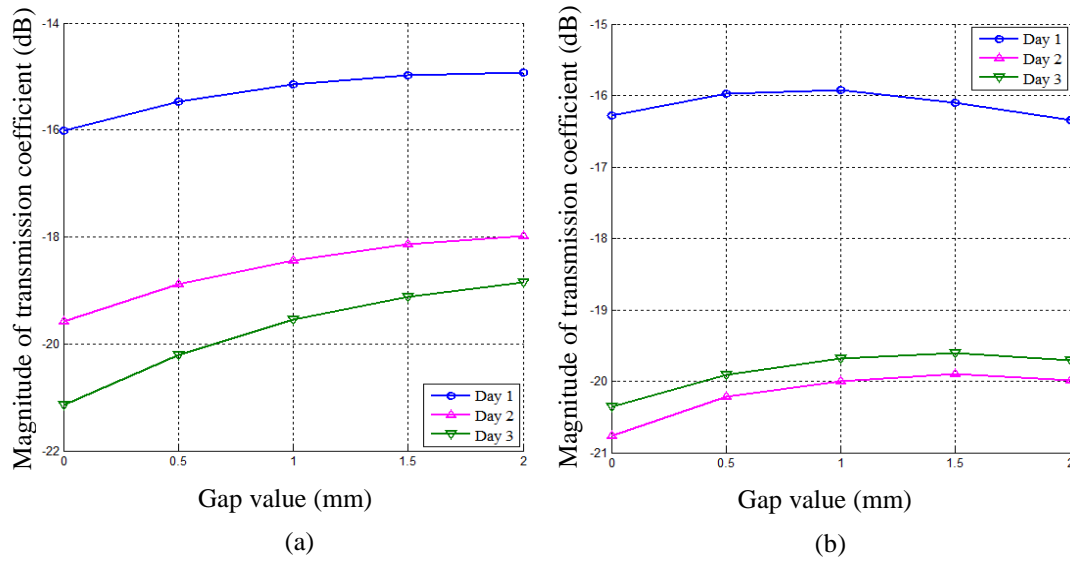
Figure 6.24: Measured magnitude of transmission coefficient vs. gap value between early-age concrete and dielectric layer (ε_{rd} = 2.6 – j0.01) using the empty DWS with (a) 2 mm- and (b) 3 mm-thick dielectric sheet attached to metal plate at 10.3 GHz .

6.4.3   Measurement Results with Dry Concrete Specimens

The experimental setup in Figure 6.15b was used to measure the magnitude of reflection and transmission coefficients for different gaps between the dielectric layer and dry concrete specimens using the proposed empty DWS with attached dielectric layer. The only difference was that the drier concrete specimen was removed from the wooden mould. The acrylic sheet with dielectric permittivity ε_{rd} = 2.6 – j0.01, and 2, 3, 6, 8 and 10 mm thick were used as the dielectric layer. The dimensions of dielectric layers were 250 mm × 250 mm. Five coefficient measurements were conducted for each gap value of 0.0, 0.5, 1.0, 1.5 and 2.0 mm and for each dielectric layer.

Figure 6.25 shows the measured average magnitude of reflection and transmission coefficient vs. frequency for different gaps between the dry concrete and dielectric layer using the empty DWS with a 2 mm-thick dielectric sheet attached to the metal plate. It is seen in Figure 6.25a that the increase of gap lowers the S_{11} from 0.0 to 1.0 mm gap at 8.2–11.0 GHz. With further increase in gap, S_{11} decreases at low frequencies and increases at high frequencies. It is also observed in Figure

6.25b that the increase in gap increases the magnitude of transmission coefficient over the entire frequency range and the differences between adjacent gap values for S_{21} decrease with increasing gap value.

Figure 6.26 illustrates the average measured magnitude of the reflection and transmission coefficient vs. frequency at different gap values between dry concrete specimen and dielectric layer using the empty DWS with a 3 mm-thick dielectric sheet attached to the metal plate. It is seen in Figure 6.26a that increasing gap increases the reflection coefficient at higher frequencies (11.0–12.4 GHz), but increases the magnitude of transmission coefficient over the entire frequency range (Figure 6.26b). The difference in S_{21} between adjacent gap values decreases with increase in gap. One important observation is that S_{21} values are higher for all gap values with 3 mm-thick dielectric layer than with a 2 mm-thick dielectric layer.

Figure 6.27 shows the average measured magnitude of reflection and transmission coefficient vs. frequency at different gap values between dry concrete and dielectric layer using the empty DWS with a 6 mm-thick dielectric sheet attached to the metal plate. It can be seen in Figure 6.27a that increasing the gap increases the reflection coefficient, with relatively large increases in S_{11} from 0.0 to 0.5 mm gap over the entire frequency band. It is also noted that the difference between adjacent gap curves in Figure 6.27a decreases with increasing gap value. The transmission coefficient (Figure 6.27b) increases with increasing gap value over the entire frequency range, showing a significant increase from 0.0 to 0.5 mm. The differences in S_{21} between adjacent curves at higher gap values are relatively small; therefore, gaps smaller than 0.5 mm are easily detected using the transmission measurement. This was not possible for small gap detection in the concrete–metal structure.

Figure 6.28 shows the average measured reflection and transmission coefficient vs. frequency at different gap values between dry concrete and dielectric layer using the empty DWS with an 8 mm-thick dielectric sheet attached to the metal plate. It can be seen in Figure 6.28a that increasing the gap increases the reflection coefficient within the lower half of the frequency range, but at higher frequencies it decreases with increasing gap. It is also noted in Figure 6.28b that the magnitude of

transmission coefficient increases with increasing gap, although the differences between adjacent curves in S_{21} are relatively small at higher gap values.

Figure 6.29 shows the average measured magnitude of reflection and transmission coefficient vs. frequency at different gap values between dry concrete and dielectric layer using empty DWS with a 10 mm-thick dielectric sheet attached to the metal plate. It is observed in Figure 6.29a that the reflection coefficient decreases with increasing gap values in frequency range 9.0–12.0 GHz. Figure 6.29b shows that the magnitude of the transmission coefficient increases with increasing gap. At lower frequencies, differences in S_{21} at higher gap values are very small, but from 10.0 to 12.0 GHz gaps up to 2.0 mm are detectable.

From the measurement results shown in Figures 6.25–6.29 it is clear that, for dry concrete, the empty DWS with 6 mm-thick attached dielectric layer (ε_{rd} = 2.6 – j0.01) to the metal plate produces the highest magnitude of transmission coefficient. The measured magnitude of both the reflection coefficient and the transmission coefficient can be used to detect gaps between a dry concrete surface and the dielectric layer; see Figure 6.30.

Figure 6.30a, b shows the measured magnitude of reflection and transmission coefficient vs. gap between dry concrete and dielectric layer using the empty DWS with 6 mm-thick dielectric sheet attached to the metal plate at 10.6 GHz. It is clearly seen that both coefficients increase with increasing of gap value.

Figure 6.25: Average measured magnitude of (a) reflection coefficient, and (b) transmission coefficient vs. frequency for different gaps between dry concrete and

dielectric layer (ε_{rd} = 2.6 – j0.01) using the empty DWS with 2 mm-thick dielectric sheet attached to the metal plate.
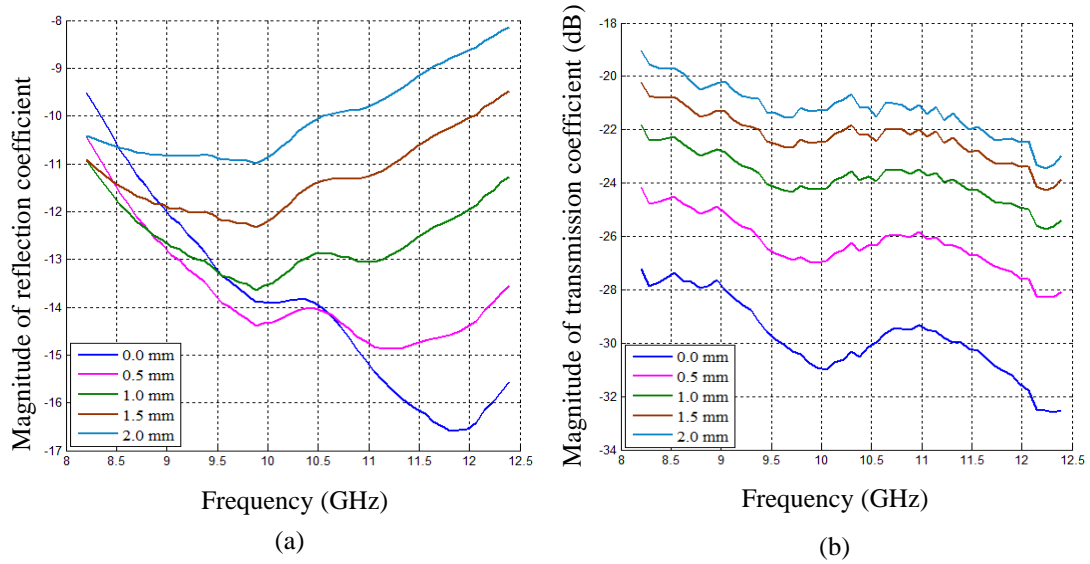
Figure 6.26: Average measured magnitude of (a) reflection coefficient, and (b) transmission coefficient vs. frequency for different gaps between dry concrete and dielectric layer (ε_{rd} = 2.6 – j0.01) using the empty DWS with 3 mm-thick dielectric sheet attached to the metal plate.
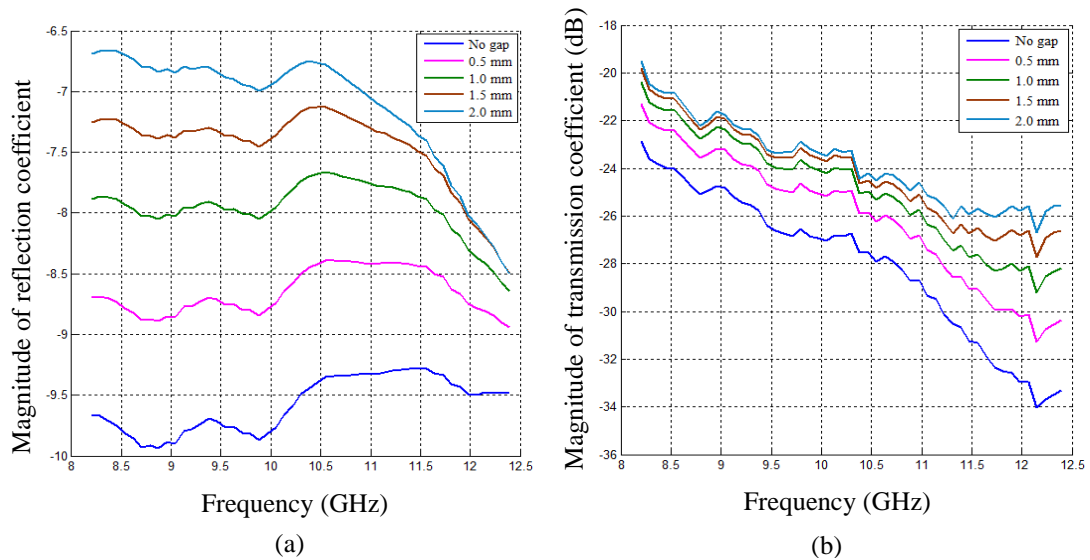
Figure 6.27: Average measured magnitude of (a) reflection coefficient, and (b) transmission coefficient vs. frequency for different gaps between dry concrete and dielectric layer (ε_{rd} = 2.6 – j0.01) using the empty DWS with 6 mm-thick dielectric sheet attached to the metal plate.
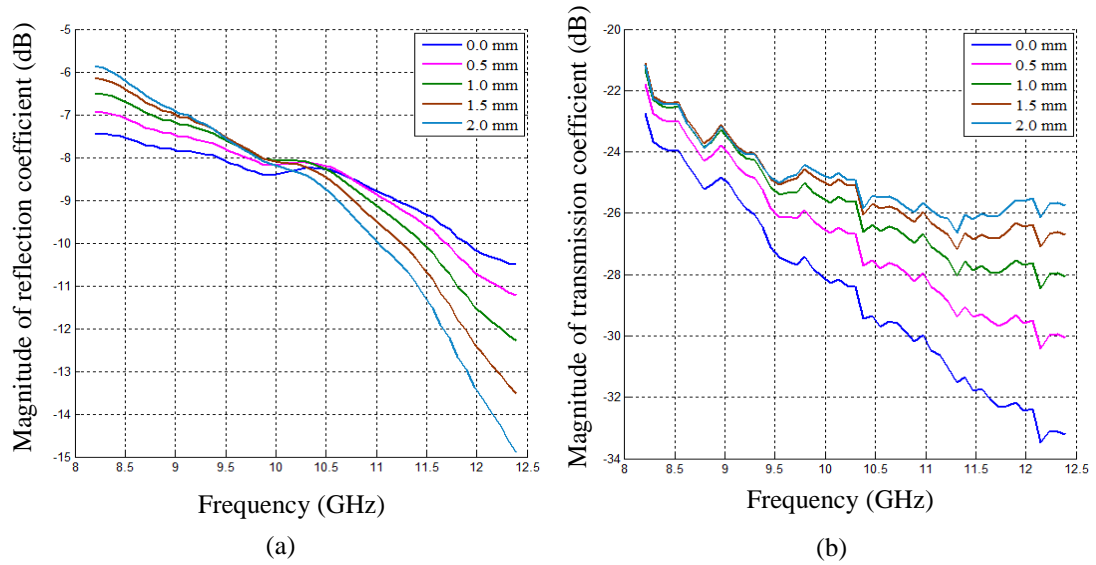
Figure 6.28: Average measured magnitude of (a) reflection coefficient, and (b) transmission coefficient vs. frequency for different gaps between dry concrete and dielectric layer (ε_{rd} = 2.6 – j0.01) using the empty DWS with 8 mm-thick dielectric sheet attached to the metal plate.

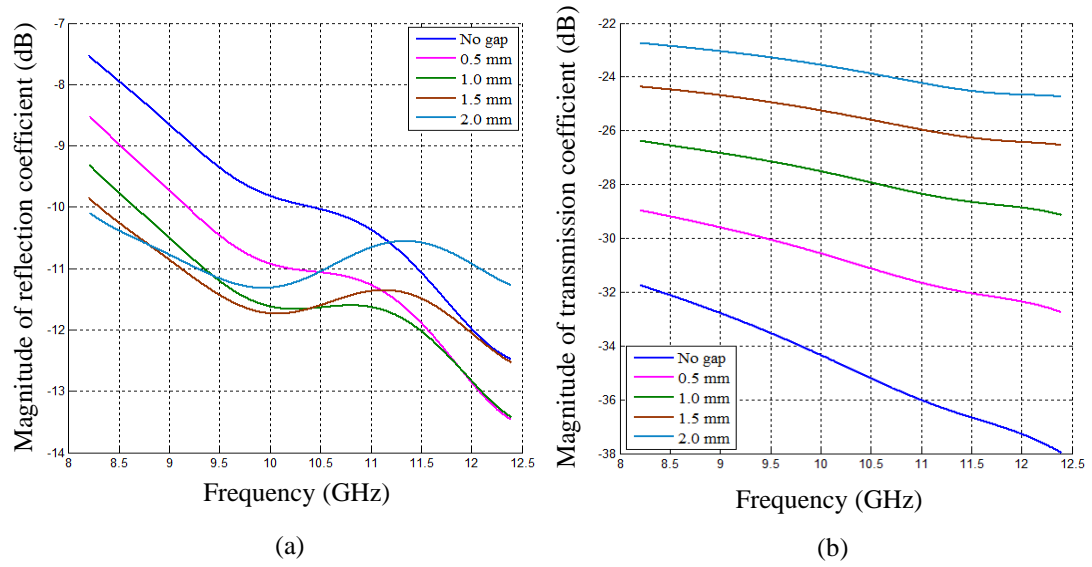Figure 6.29: Average measured magnitude of (a) reflection coefficient, and (b) transmission coefficient vs. frequency for different gaps between dry concrete and dielectric layer (ε_{rd} = 2.6 – j0.01) using the empty DWS with 10 mm-thick dielectric sheet attached to the metal plate.

Figure 6.30: Magnitude of (a) reflection coefficient, and (b) transmission coefficient at 10.6 GHz vs. gap between dry concrete and dielectric layer ($\varepsilon_{rd} = 2.6 - j0.01$) for empty DWS with a 6 mm-thick dielectric sheet attached to the metal plate.

6.5   Numerical Investigation using the Dielectric-loaded DWS with Attached Dielectric Layer

In this section, the dielectric-loaded DWS with attached dielectric layer is modelled along with the concrete specimens. Simulations are performed for the magnitude of the reflection coefficient and the transmission coefficient for different gaps between the dry concrete specimens and the dielectric layers. The simulated results for different dielectric layer thicknesses are presented and discussed.

6.5.1   Modelling of Sensor

A model of the rectangular dielectric-loaded DWS with attached dielectric layer, together with the concrete specimen, was created as shown schematically in Figure 6.31. For this purpose, a model of the dielectric-loaded DWS was first created as in Chapter 5. A sheet of acrylic material ($\varepsilon_{rd} = 2.6 - j0.01$) 250 mm × 250 mm forms the dielectric layer attached to the metal plate of the DWS.
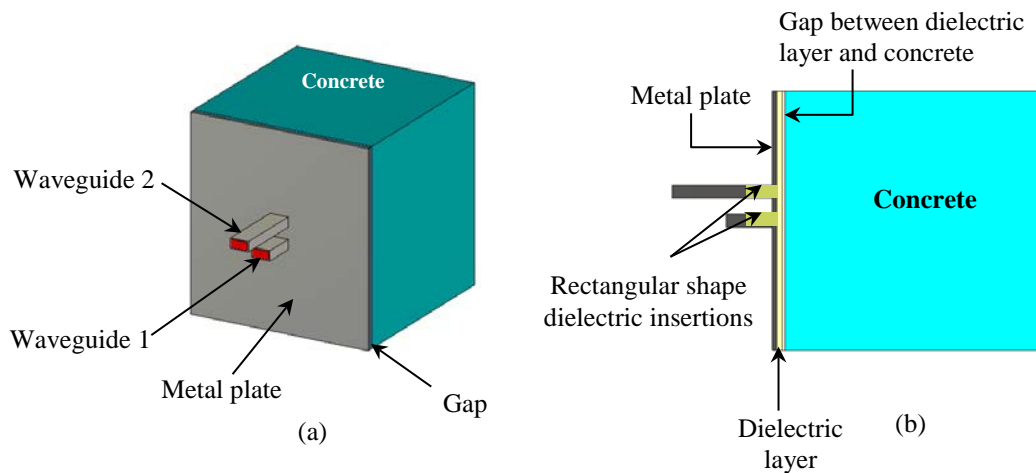
Figure 6.31: Model of rectangular dielectric-loaded DWS with attached dielectric layer and concrete specimen created in CST: (a) perspective view, and (b) cross-sectional side view showing attached dielectric layer and gap between concrete and dielectric layer.

6.5.2   Parametric Study with Dry Concrete Specimens

The model will be used to simulate the magnitude of reflection and transmission coefficients for five values of the gap between the dry concrete specimen and the dielectric layers attached to the sensor (gap 0.0, 0.5, 1.0, 1.5 and 2.0 mm). In this case the complex dielectric permittivity of the dry concrete was taken to be $\varepsilon_r = 4.1 - j0.82$, which is the permittivity that was earlier determined for concrete about two years old. Simulations were performed for dielectric layers variously 2, 3, 6, 8 and 10 mm thick.

Figure 6.32 shows the simulated magnitude of the reflection and transmission coefficient vs. frequency for different gaps between the dry concrete specimen and a dielectric layer 2 mm thick. Figure 6.32a shows resonances in the reflection coefficient curves for different gap values. The resonant frequency is approximately 9.5 GHz, changing slightly with different gap values. It is also noted that S_{11} decreases at the resonant frequency with larger gap values. It is observed in Figure 6.32b that the magnitude of transmission coefficient increases with increase in gap value at all frequencies; differences in S_{21} between adjacent gap curves decreases with increasing gap value.

Figure 6.33 shows the simulated magnitude of the reflection and transmission coefficient vs. frequency for different gaps between the dry concrete specimen and a dielectric layer 3 mm thick. Figure 6.33a shows resonance in the reflection coefficient curves for different gap values. The resonant frequency is approximately 9.3 GHz (i.e., less than the 9.5 GHz for the 2 mm-thick attached dielectric sheet) and changes slightly with gap values. A decrease in S_{11} at resonant frequency also occurs with increasing gap values. It is observed in Figure 6.33b that the magnitude of the transmission coefficient increases with the increase in gap value over the entire frequency range; the difference in S_{21} between adjacent gap curves decreases with increase of gap value. However, with the 3 mm dielectric sheet, the values of S_{21} at all gap values are higher than those for the attached 2 mm dielectric sheet.

Figure 6.34 shows the simulated magnitude of the reflection and transmission coefficient vs. frequency for different gaps between the dry concrete and a dielectric layer 6 mm thick. Figure 6.34a shows resonance in the reflection coefficient curves for different gap values at a frequency of about 9.0 GHz (i.e., less than the 9.3 GHz for the 3 mm-thick attached dielectric sheet) and changes slightly with gap values. It is also noted that S_{11} decreases at resonant frequency with increasing gap values. It is observed in Figure 6.34b that the magnitude of the transmission coefficient increases with increasing gap value at all frequencies; however, at low and high frequencies S_{21} changes non-monotonically. In the middle of the frequency range 9.0–11.0 GHz, the differences in S_{21} between adjacent gap curves decrease with increasing gap.

Figure 6.35 shows the simulated magnitude of the reflection and transmission coefficient vs. frequency for different gaps between the dry concrete and a dielectric layer 8 mm thick. Figure 6.35a shows resonance in the reflection coefficient curves for different gap values at a frequency of about 9.0 GHz, and decreases slightly as gap values increase. It is also noted that S_{11} increases at resonant frequency with increasing gap. It is observed in Figure 6.35b that the magnitude of the transmission coefficient increases with increasing gap value at all frequencies; however, at low and high frequencies S_{21} changes non-monotonically. In the middle of the frequency range 9.0–10.5 GHz, the differences in S_{21} between adjacent gap curves decrease with increasing gap.

Figure 6.36 shows the simulated magnitude of the reflection and transmission coefficient vs. frequency for different gaps between the dry concrete and a dielectric layer 10 mm thick. Figure 6.36a shows resonance in the reflection coefficient curves for different gap values at a frequency of about 8.8 GHz and decreases slightly with increase in gap values. It is also noted that S_{11} increases at resonant frequency with increasing gap values. It is observed in Figure 6.36b that the transmission coefficient increases with increasing gap value at all frequencies; however, at low and high frequencies S_{21} changes non-monotonically. In the middle of the frequency range 9.5–11.0 GHz, the differences in S_{21} between adjacent gap curves decrease with increasing gap value

From the simulation results in Figures 6.32–6.36, it is clear that for dry concrete, the rectangular dielectric-loaded DWS with attached dielectric layer ($\varepsilon_{rd} = 2.6 - j0.01$) 2 or 3 mm thick produce the most uniform value of the transmission coefficient for detecting gaps between the concrete and the dielectric layer, clearly demonstrated in Figure 6.37.

Figures 6.37a, b illustrate the simulated magnitude of transmission coefficient vs. gap between the dry concrete and the dielectric layer using the rectangular dielectric-loaded DWS with attached dielectric layer ($\varepsilon_{rd} = 2.6 - j0.01$) 2 mm and 3 mm thick at 10.3 GHz. In both cases, S_{21} increases as gap increases; however the 3 mm thickness results in a higher magnitude of transmission coefficient for all gap conditions.
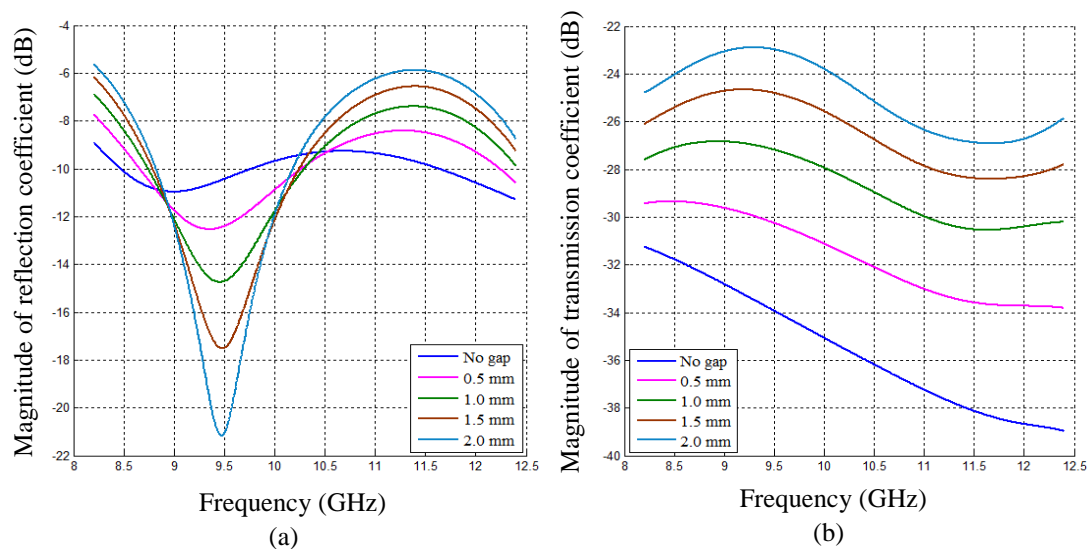
Figure 6.32: Simulated magnitude of (a) reflection, and (b) transmission coefficient vs. frequency for different gaps between concrete ($\varepsilon_{rc} = 4.1 - j0.82$) and dielectric

layer (ε_{rd} = 2.6 – j0.01) using the rectangular dielectric-loaded DWS with a 2 mm-thick dielectric sheet attached to the metal plate.

(a)   (b)
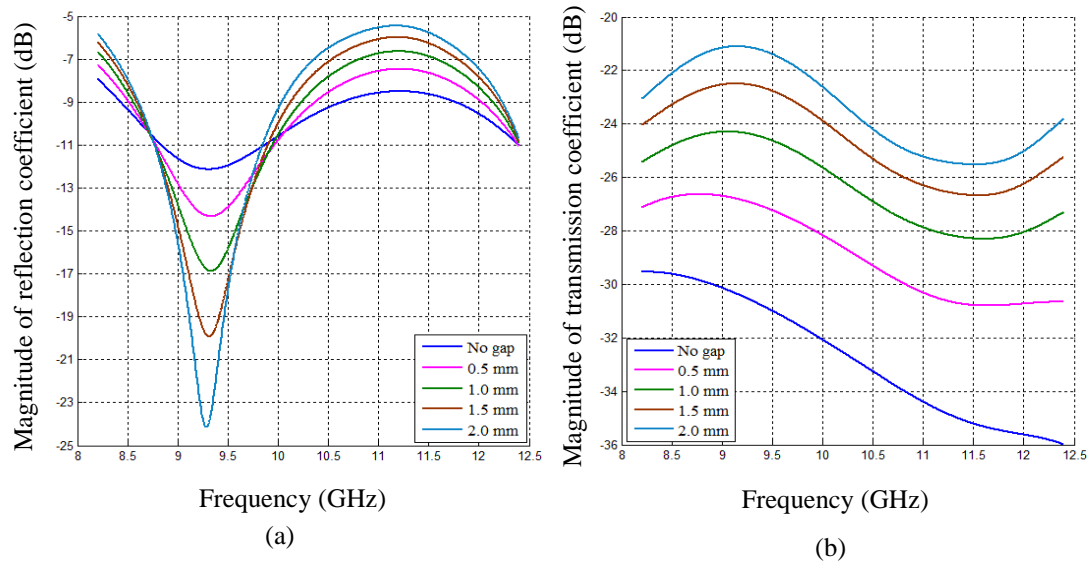
Figure 6.33: Simulated magnitude of (a) reflection, and (b) transmission coefficient vs. frequency for different gaps between concrete (ε_{rc} = 4.1 – j0.82) and dielectric layer (ε_{rd} = 2.6 – j0.01) using the rectangular dielectric-loaded DWS with a 3 mm-thick dielectric sheet attached to the metal plate.

(a)   (b)
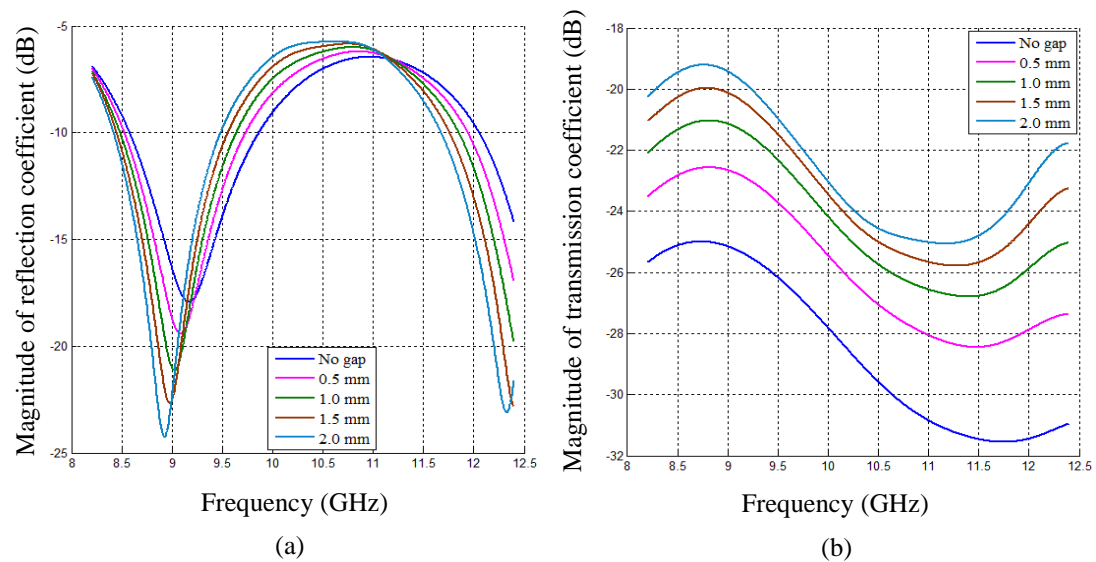
Figure 6.34: Simulated magnitude of (a) reflection, and (b) transmission coefficient vs. frequency for different gaps between concrete (ε_{rc} = 4.1 – j0.82) and dielectric layer (ε_{rd} = 2.6 – j0.01) using the rectangular dielectric-loaded DWS with a 6 mm-thick dielectric sheet attached to the metal plate.
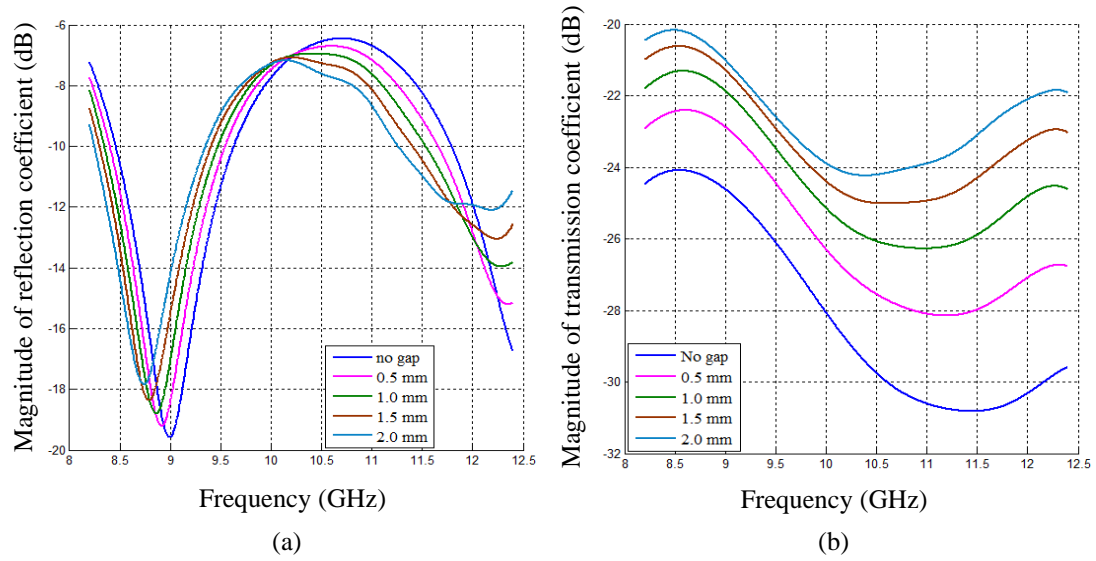
Figure 6.35: Simulated magnitude of (a) reflection, and (b) transmission coefficient vs. frequency for different gaps between concrete (ε_{rc} = 4.1 – j0.82) and dielectric layer (ε_{rd} = 2.6 – j0.01) using the rectangular dielectric-loaded DWS with an 8 mm-thick dielectric sheet attached to the metal plate.
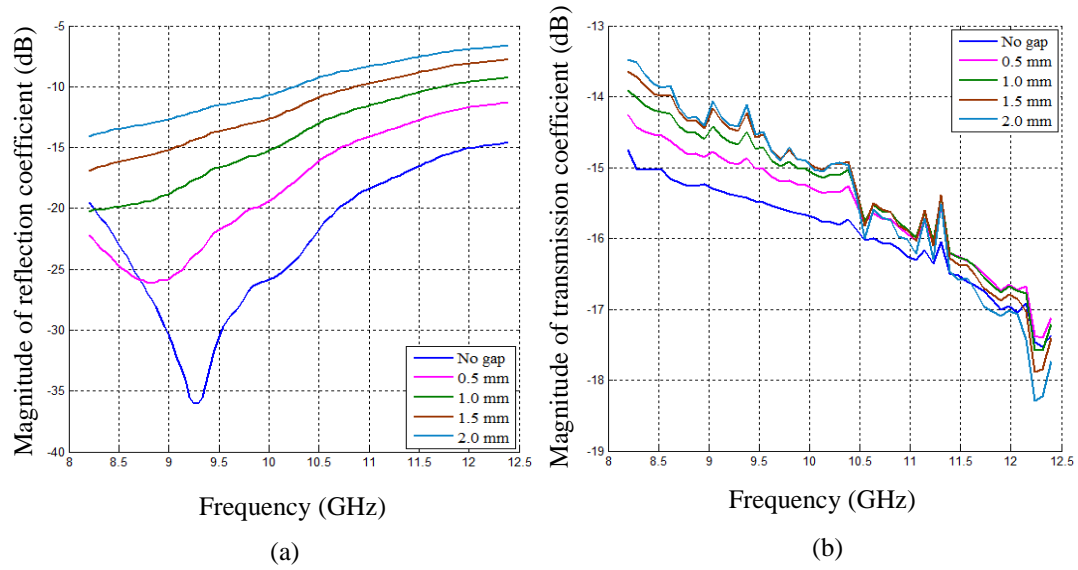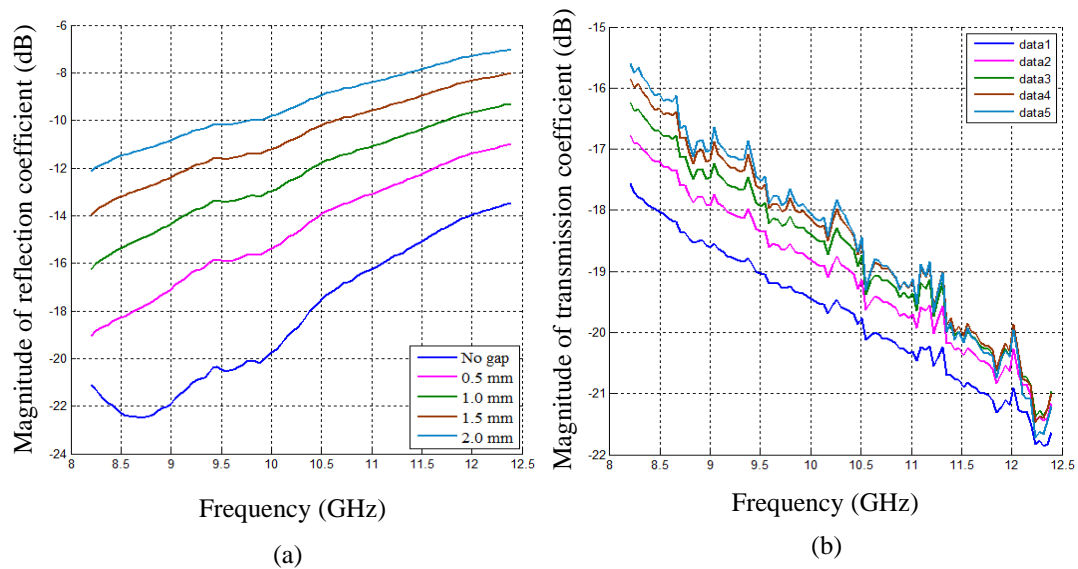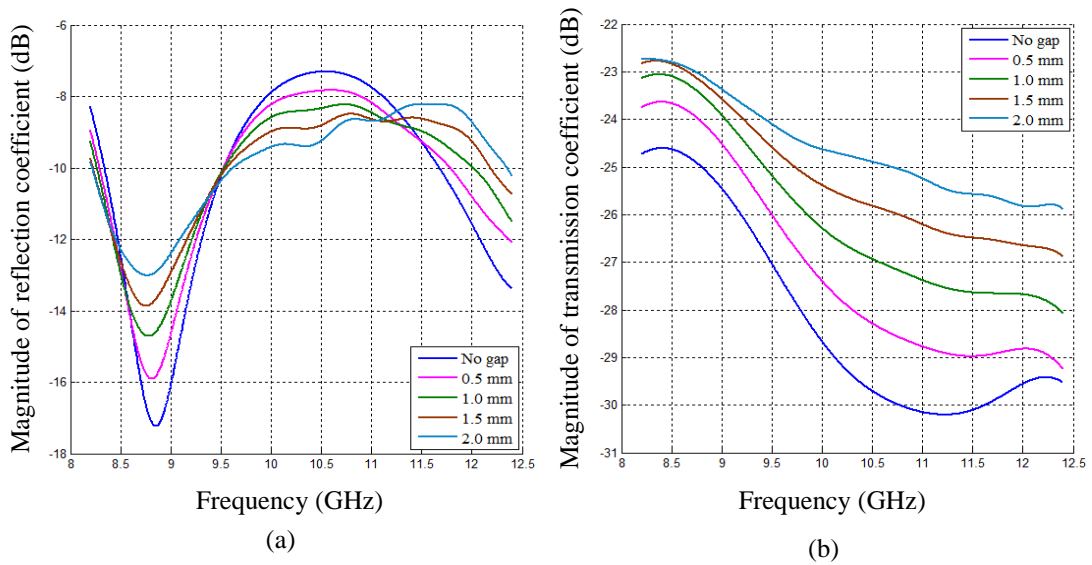

Figure 6.36: Simulated magnitude of (a) reflection, and (b) transmission coefficient vs. frequency for different gaps between concrete (ε_{rc} = 4.1 – j0.82) and dielectric layer (ε_{rd} = 2.6 – j0.01) using the rectangular dielectric-loaded DWS with a 10 mm-thick dielectric sheet attached to the metal plate.
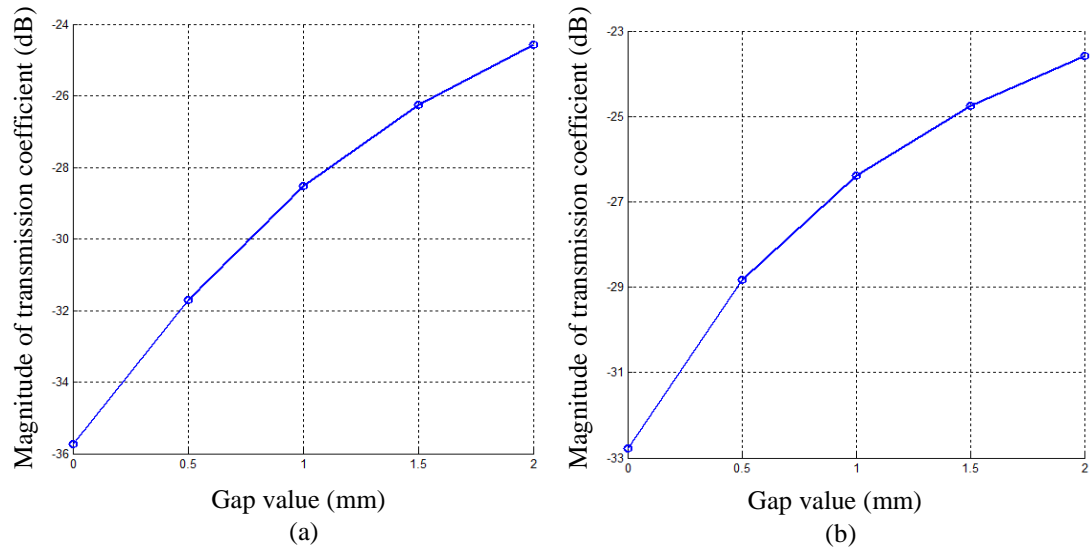
Figure 6.37: Simulated magnitude of transmission coefficient vs. gap between concrete ($\varepsilon_{rc} = 4.1 – j0.82$) and dielectric layer ($\varepsilon_{rd} = 2.6 – j0.0$) using the rectangular dielectric-loaded DWS with (a) 2 mm- and (b) 3 mm-thick dielectric sheet attached to the metal plate at 10.3 GHz frequency.

6.6 Measurement using the Dielectric-loaded DWS with Attached Dielectric Layer

The measurement approach and results using the rectangular dielectric-loaded DWS with attached dielectric layer is described in this section. In this experimental investigation, only the dry concrete is considered as the specimen. The measurement of the reflection and transmission coefficient for different gaps between the concrete and the dielectric layer attached to the proposed sensor will be conducted.

6.6.1 Specimens and Measurement Setup

A cube of dry concrete (age about 2 years) with side dimension 250 mm and initial water: cement ratio 1:2 was used as the specimen in this investigation. The experimental setup for measuring the gap between the dry concrete and the dielectric layer using the rectangular dielectric-loaded DWS with attached dielectric layer is shown in Figure 6.38. An Agilent N5225A PNA acted as transceiver, measurement unit and indicator. The sensor was connected to the PNA by waveguide-to-coaxial adapters and coaxial cables. The gaps between the specimen and the sensor were made by inserting thin paper sheets to the desired gap values (0.0, 0.5, 1.0, 1.5 and 2.0 mm). Acrylic sheet was used as the dielectric layer ($\varepsilon_{rd} = 2.6 – j0.01$).
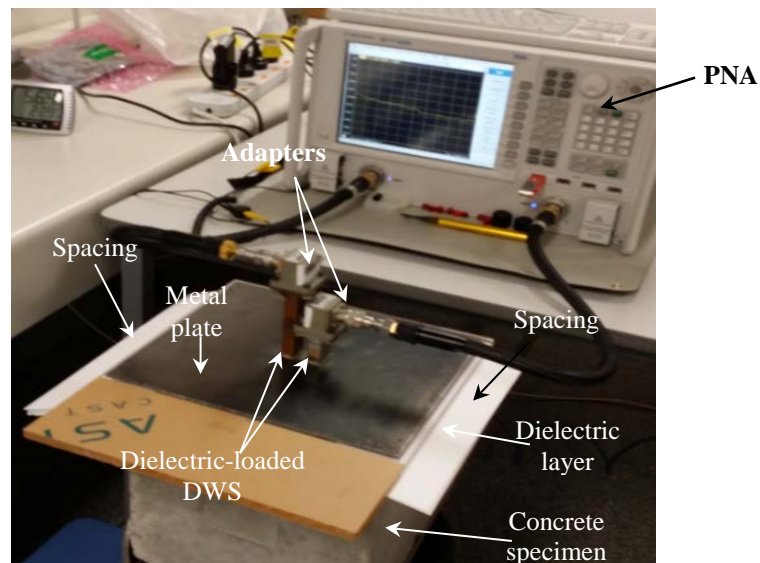
Figure 6.38: Experimental setup for measuring the gap in cement-based composites using the microwave dual rectangular waveguide sensor.

6.6.2 Measurement Results with Dry Concrete Specimens

Dielectric layers 2, 3, 6, 8 and 10 mm thick, were attached to the rectangular dielectric-loaded DWS. In each case, S_{11} and S_{21} were measured, recorded and averaged five times for each gap value (0.0, 0.5, 1.0, 1.5 and 2.0 mm).

Figures 6.39–6.41 show average measured magnitude of reflection and transmission coefficient vs. frequency for different gaps between the dry concrete and the dielectric layer using the rectangular dielectric-loaded DWS with 2-, 3- and 6 mm-thick dielectric sheets attached to the metal plate. Figures 6.39a, 6.40a and 6.41a show resonance at frequencies of approximately 8.8, 8.6 and 8.4 GHz, respectively, in the reflection coefficient curves for different gap values, changing slightly with gap changes. It is also noted that S_{11} decreases at the resonant frequencies with increasing gap values. It is observed in Figures 6.39b, 6.40b and 6.41b that the transmission coefficient increases with increasing gap value at all frequencies. The differences in S_{21} between adjacent gap curves decrease with increasing gap value.

Figures 6.42 and 6.43 show the average measured magnitude of reflection and transmission coefficient vs. frequency for different gaps between dry concrete and dielectric layer using the rectangular dielectric-loaded DWS with 8- and 10 mm-thick

dielectric sheets attached to the metal plate. Figures 6.42a and 6.43a show resonance at frequencies of about 11.1 and 10.9 GHz in the reflection coefficient curves for different gap values, changing slightly with gap changes. It is also noted that S_{11} increases at the resonant frequencies with increasing gap values. It is observed in Figures 6.42b and 6.43b that the magnitude of transmission coefficient increases with increasing gap value at higher frequencies in the X-band; at lower frequencies, S_{21} differences between adjacent gap curves are either very small, or they overlap.

Therefore, from the results in Figures 6.39–6.43 it is obvious that the rectangular dielectric-loaded DWS with attached dielectric layers of acrylic sheet (ε_{rd} = 2.6 – j0.01) of 2- and 3 mm thick offer uniform transmission coefficients for detecting gaps between dry concrete and the dielectric layer, as is clearly shown in Figure 6.44.

Figure 6.44a, b show the measured magnitude of transmission coefficient vs. gap between dry concrete and dielectric layer using the rectangular dielectric-loaded DWS with attached dielectric (ε_{rd} = 2.6 – j0.01) layer 2- and 3 mm thick at 10.3 GHz. It is seen that in both cases, S_{21} increases with the increasing gap value, but the 3 mm dielectric layer results in higher transmission coefficients for all gap conditions.
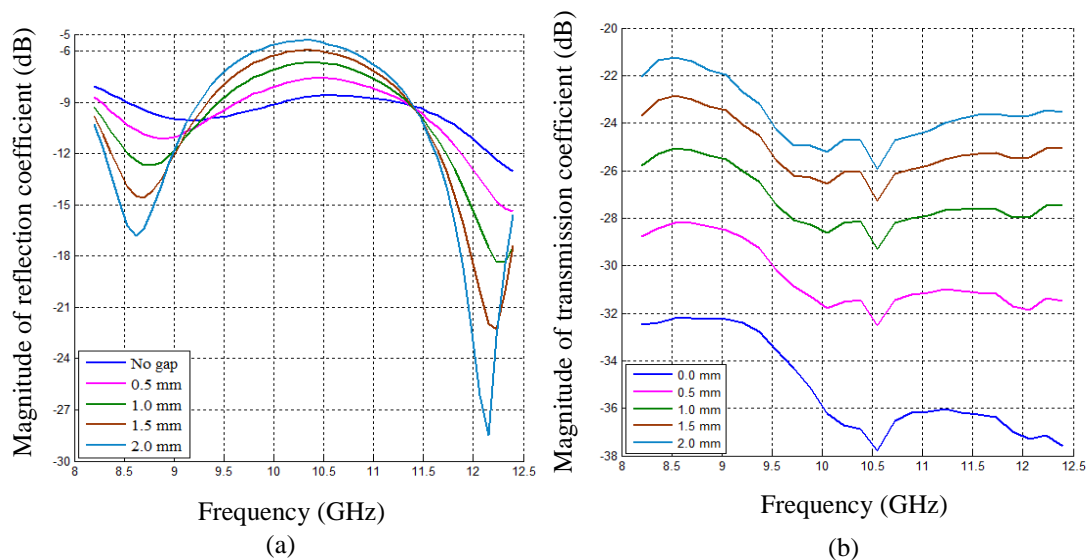
Figure 6.39: Average measured magnitude of (a) reflection, and (b) transmission coefficient vs. frequency for different gaps between the dry concrete specimen and the dielectric layer (ε_{rd} = 2.6 – j0.01) using the rectangular dielectric-loaded DWS with 2 mm-thick dielectric sheet attached to the metal plate.
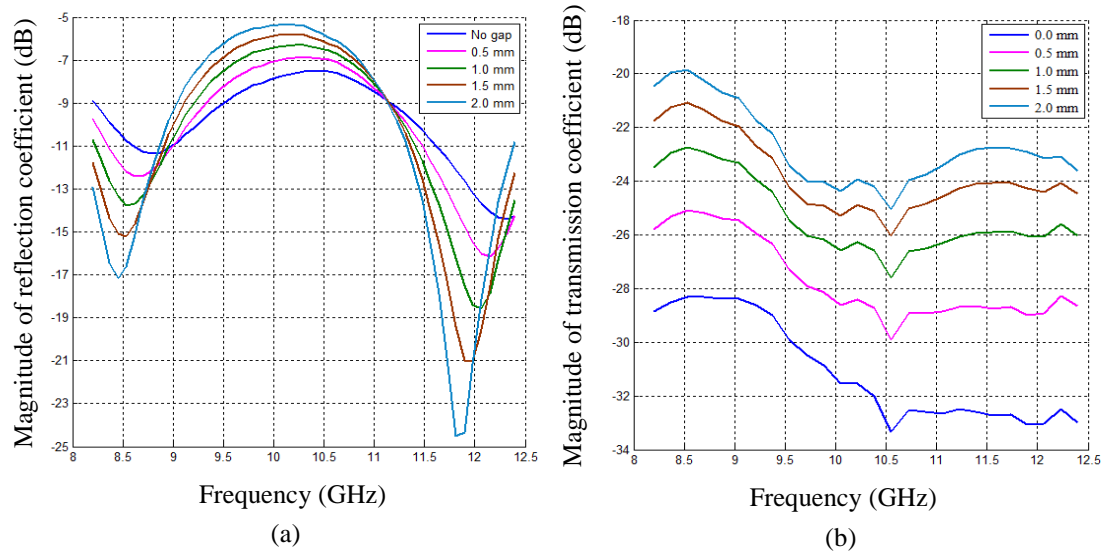
Figure 6.40: Average measured magnitude of (a) reflection, and (b) transmission coefficient vs. frequency for different gaps between the dry concrete specimen and the dielectric layer ($\varepsilon_{rd} = 2.6 - j0.01$) using the rectangular dielectric-loaded DWS with 3 mm-thick dielectric sheet attached to the metal plate.
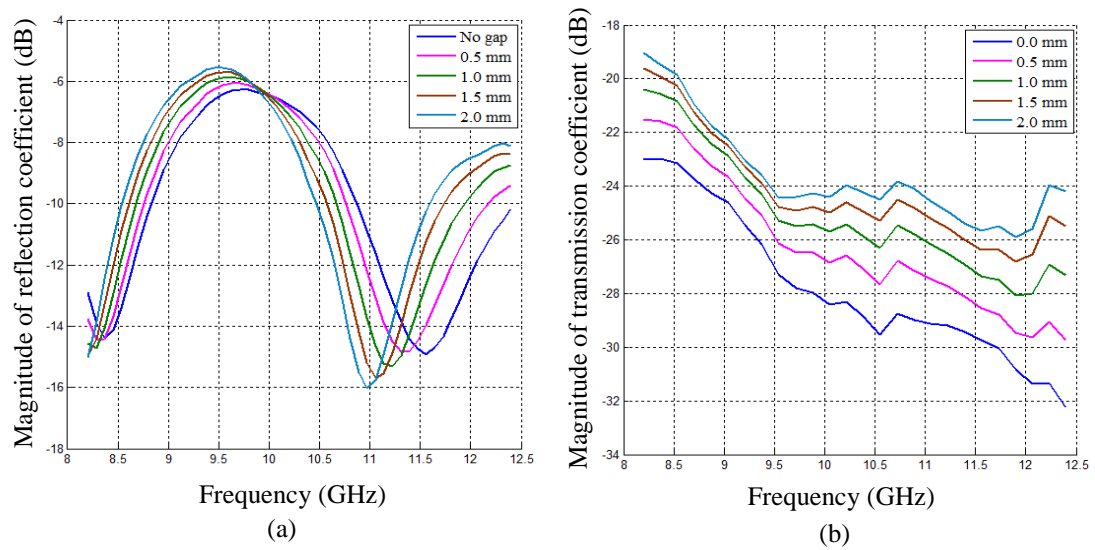
Figure 6.41: Average measured magnitude of (a) reflection, and (b) transmission coefficient vs. frequency for different gaps between the dry concrete specimen and the dielectric layer ($\varepsilon_{rd} = 2.6 - j0.01$) using the rectangular dielectric-loaded DWS with 6 mm-thick dielectric sheet attached to the metal plate.
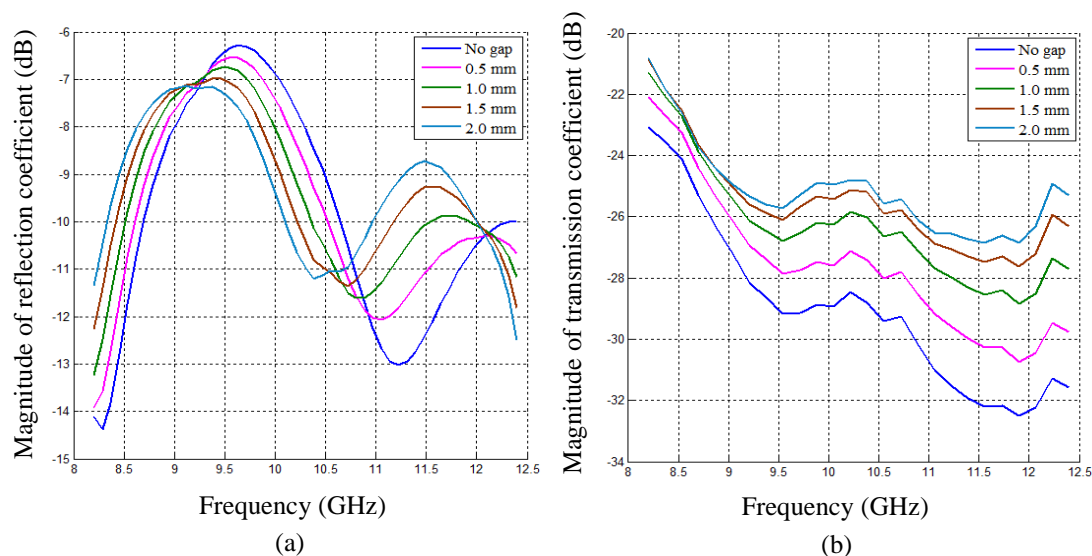
Figure 6.42: Average measured magnitude of (a) reflection, and (b) transmission coefficient vs. frequency for different gaps between the dry concrete specimen and the dielectric layer ($\varepsilon_{rd} = 2.6 - j0.01$) using the rectangular dielectric-loaded DWS with 8 mm-thick dielectric sheet attached to the metal plate.
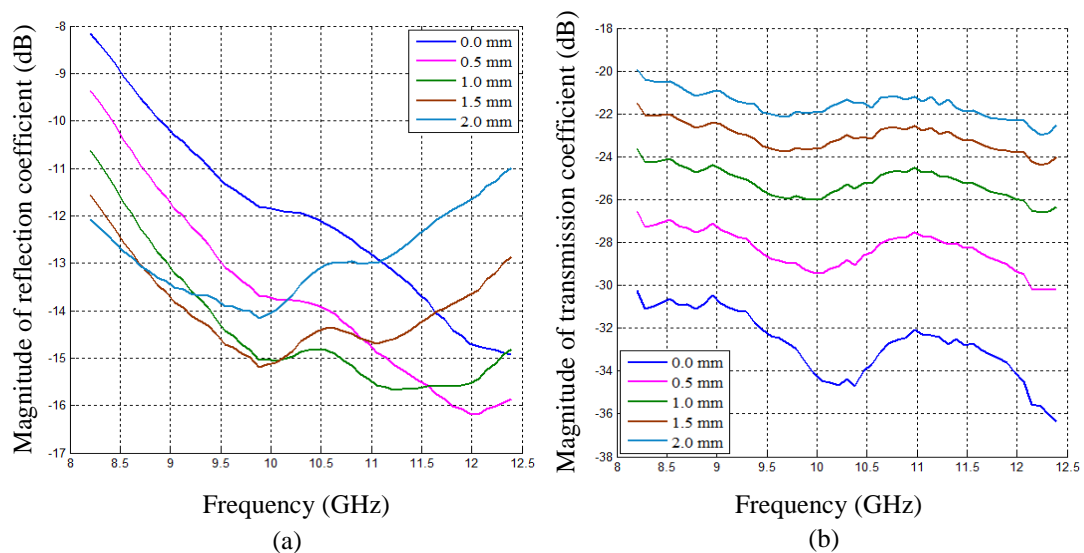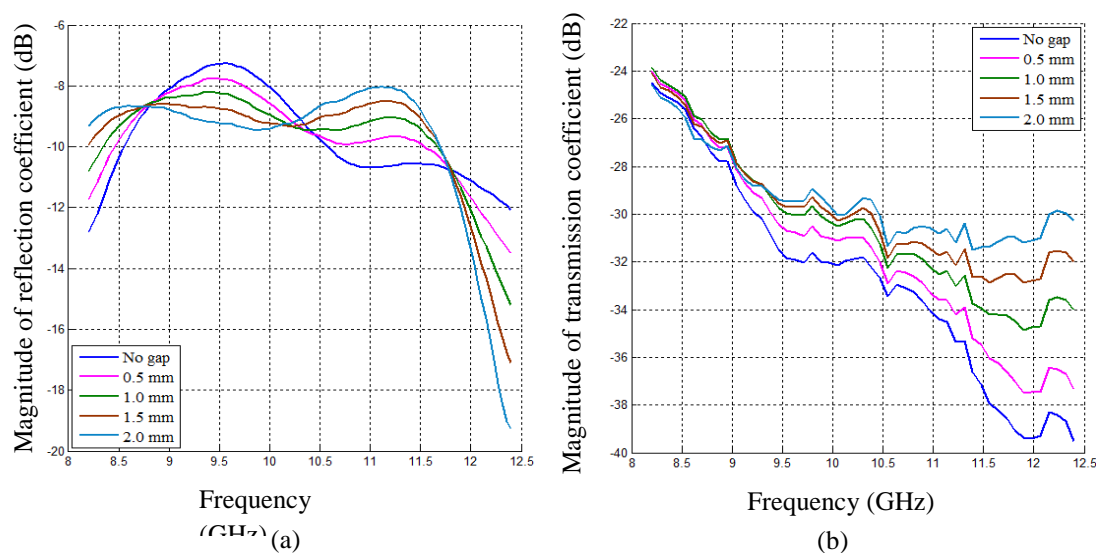

Figure 6.43: Average measured magnitude of (a) reflection, and (b) transmission coefficient vs. frequency for different gaps between the dry concrete specimen and the dielectric layer ($\varepsilon_{rd} = 2.6 - j0.01$) using the rectangular dielectric-loaded DWS with 10 mm-thick dielectric sheet attached to the metal plate.
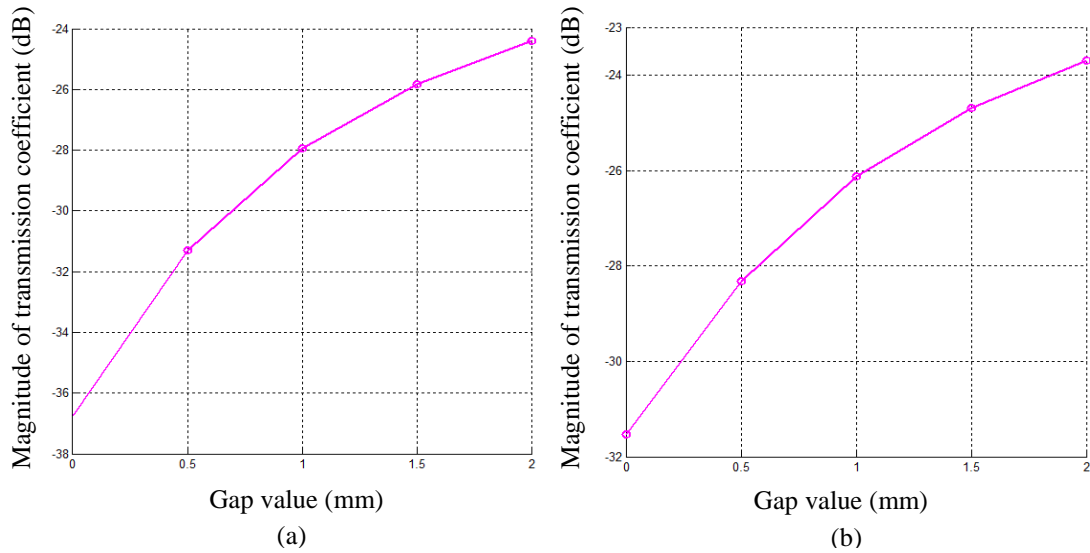
Figure 6.44: Measured magnitude of transmission coefficient vs. gap between dry concrete and dielectric layer ($\varepsilon_{rd} = 2.6 - j0.01$) using the rectangular dielectric-loaded DWS with (a) 2 mm and (b) 3 mm-thick dielectric sheet attached to the metal plate at 10.3 GHz.

6.7   Comparison of Measurement and Simulation Results

The measurement and simulation results for different dual waveguide sensors with attached dielectric layer discussed in previous sections are compared here. In the simulations, the dielectric permittivities adopted for fresh, early and dry concrete are $(22.0 - j6.6)$, $(15.0 - j4.5)$ and $(4.1 - j0.82)$ respectively.

Figure 6.45 shows the measured and simulated magnitude of transmission coefficient vs. gap between fresh/early-age concrete and the dielectric layer ($\varepsilon_{rd} = 2.6 - j0.01$) using the empty DWS with attached 2 mm and 3 mm-thick dielectric layers respectively at 10.3 GHz. In both cases, the S_{21} values measured on days 1, 2 and 3 of concrete curing are compared with two simulation results. It is seen on both graphs that the trends and behaviours of the measurement and simulated results are similar; and that the values of S_{21} agree reasonably well for gaps larger than 0.5 mm and 1.0 mm using 3 mm and 2 mm-thick dielectric layers, respectively.

Figure 6.46 illustrates the measured and simulated reflection and transmission coefficient vs. gap between dry concrete and dielectric layer ($\varepsilon_{rd} = 2.6 - j0.01$) at 10.6 GHz using the empty DWS with a 6 mm-thick dielectric sheet attached to the metal plate. It is observed that, in the reflection coefficient measurement case, the

difference between the measurement and simulation is less than 1 dB for all gaps. The results agree even more closely for the transmission coefficient.

Figure 6.47 shows the measured and simulated magnitude of transmission coefficient vs. gap between the dry concrete and dielectric layer ($\varepsilon_{rd} = 2.6 - j0.01$) at 10.3 GHz using the rectangular dielectric-loaded DWS with 2- and 3 mm-thick dielectric layers attached to the metal plate. It is clearly seen in Figure 6.47a, b that, with the dielectric layers of both thicknesses, the rectangular dielectric-loaded DWS gives excellent agreement between measurement and simulation results.

Therefore, except for the fresh concrete specimen in the smaller gap range (0.0–0.5 mm), the measured and simulated results using the proposed sensors with dry concrete exhibit good agreement; small differences are attributable to errors in sensor fabrication, gap arrangement error due to roughness of the concrete surface and metal plate surface, variations in dielectric permittivity of insertions, variations in geometry of insertions and so on. It is also noted that 3 mm is the preferred thickness of the attached dielectric layer for dielectric-loaded DWS. In the numerical investigation with the fresh concrete, the thickness and dielectric properties of the transparent polythene film covering the freshly cast concrete during measurement has not been considered. Furthermore, the fresh concrete requires very precise handling due to its sensitivity to environment and age.
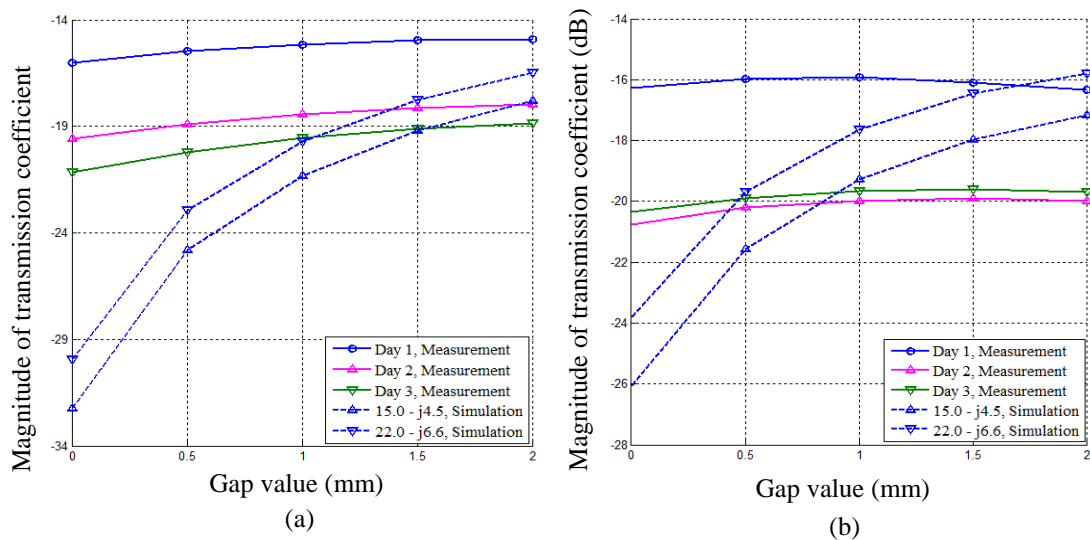
Figure 6.45: Measured and simulated magnitude of transmission coefficient vs. gap between fresh/early-age concrete and dielectric layer ($\varepsilon_{rd} = 2.6 - j0.01$) at 10.3 GHz using the empty DWS with (a) 2 mm and (b) 3 mm-thick dielectric sheet attached to the metal plate.
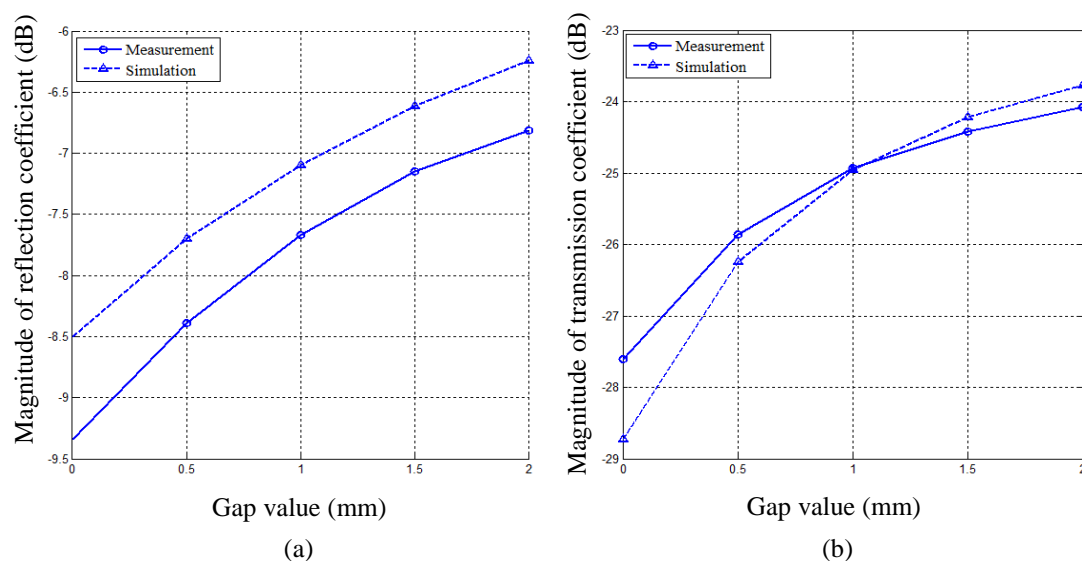
Figure 6.46: Measured and simulated magnitude of (a) reflection coefficient, and (b) transmission coefficient vs. gap at 10.6 GHz between the dry concrete and dielectric layer ($\varepsilon_{rd} = 2.6 - j0.01$) using empty DWS with 6 mm-thick dielectric sheet attached to the metal plate.
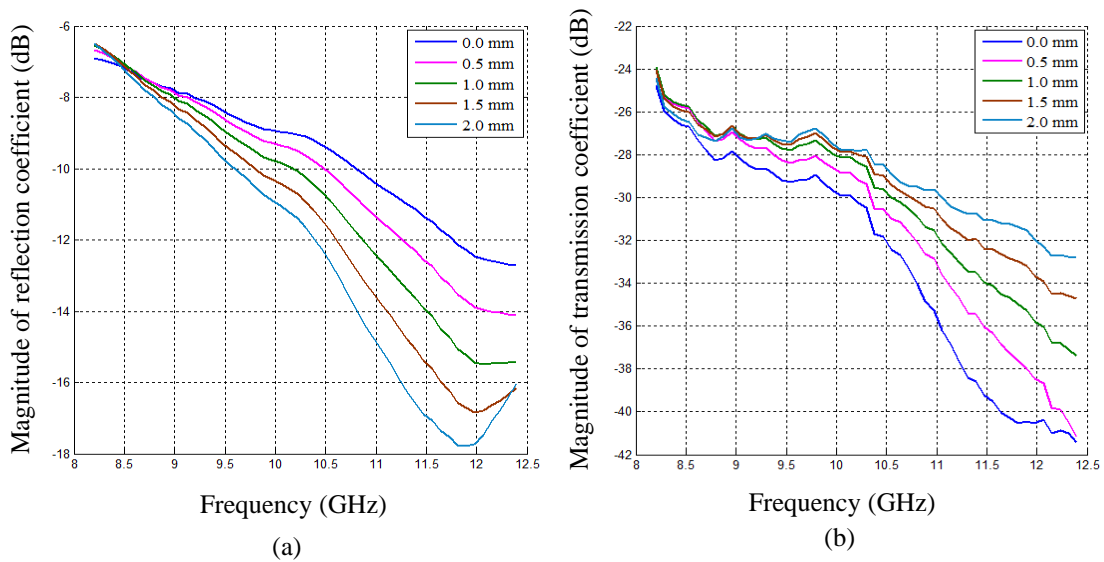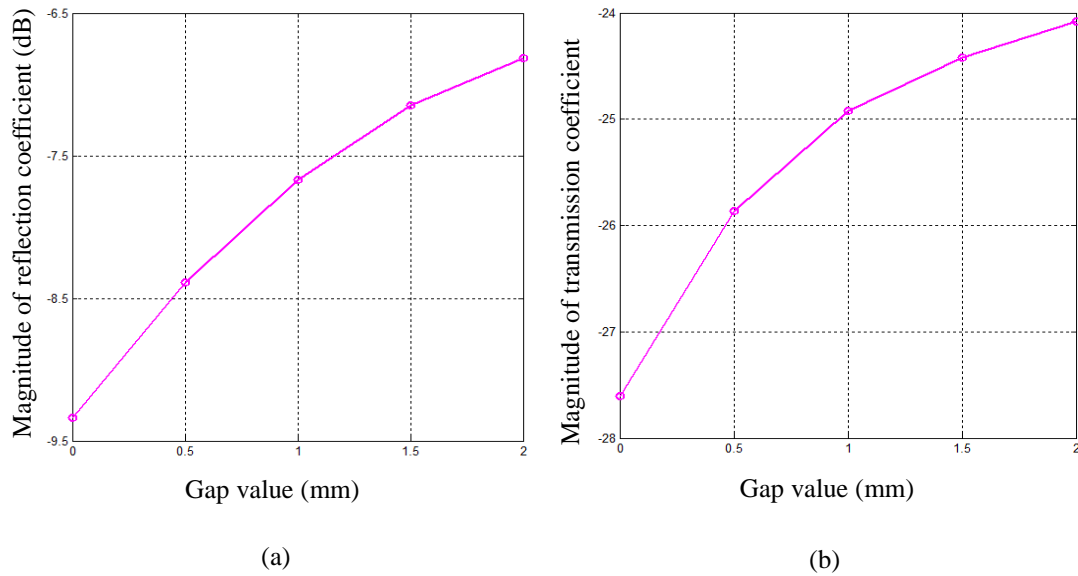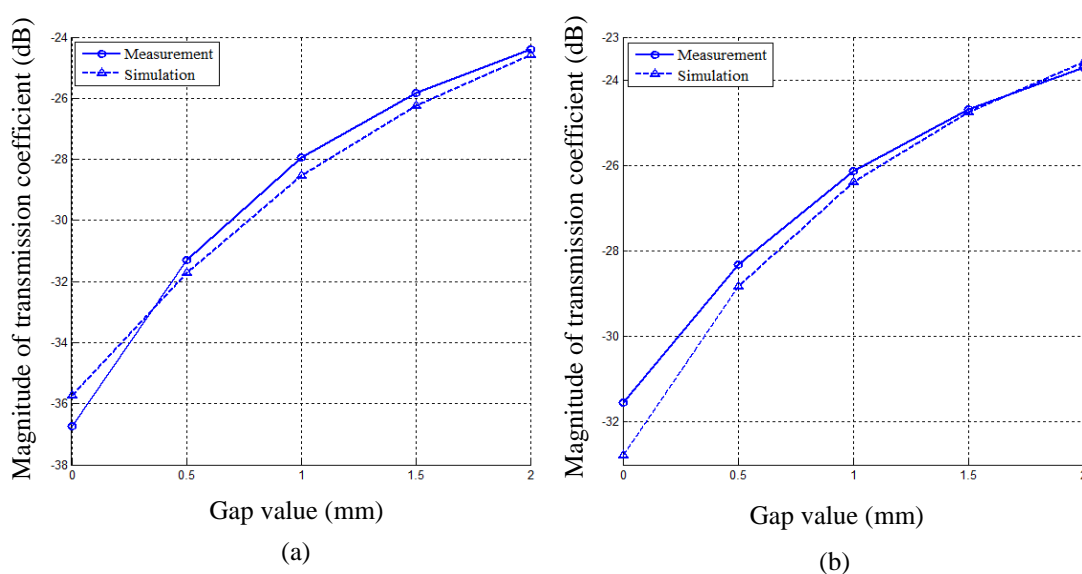

Figure 6.47: Measured and simulated magnitude of transmission coefficient vs. gap between dry concrete and dielectric layer ($\varepsilon_{rd} = 2.6 - j0.01$) at 10.3 GHz using the dielectric-loaded DWS with (a) 2 mm and (b) 3 mm-thick dielectric sheet attached to the metal plate.

6.8   Electric Field Intensity Distributions

The electric field distribution inside the waveguide sections of the proposed DWS, in the attached dielectric layers and in the concrete will be presented and analysed in this section.

Figure 6.48 shows a cross-sectional side view of the electric field intensity distributions (amplitude and phase) inside the waveguide sections W1 and W2, the 3 mm-thick dielectric layer attached to the empty DWS, and in the fresh concrete (ε_r = 15.0 – j4.3) at 10.3 GHz for gaps of 0.0, 1.0 and 2.0 mm between the attached dielectric layer and the concrete. It can be seen from the figure that W1 radiates electromagnetic waves in fresh concrete across the dielectric layer, and a small part of this wave penetrates into W2 through the dielectric layer at the no-gap condition due to minor penetration in the presence of more water particles. Figure 6.48 clearly show changes in the electric field intensity distribution inside the dielectric layer and W2 when there is a gap. It should be noted that a comparison between the field distribution in this arrangement and in the arrangement without a dielectric layer (cf. Figure 4.25, Chapter 4) demonstrates that the dielectric layer enhances the electric field intensity in W2. It also shows the lesser influence of increasing the gap.

Figure 6.49 shows a cross-sectional side view of the electric field intensity distributions (amplitude and phase) inside W1 and W2 and inside the 6 mm-thick dielectric layer attached to the empty DWS and the dry concrete (ε_r = 4.1 – j0.82) at 10.6 GHz for gaps of 0.0, 1.0 and 2.0 mm between the attached dielectric layer and the concrete. It can be seen from the figure that W1 radiates electromagnetic waves in the dry concrete across the dielectric layer, and that a part of this penetrates into W2 through the dielectric layer in the no-gap condition. Figure 6.49 clearly shows changes in the electric field intensity distribution inside the dielectric layer and W2 when a gap exists. It should be noted that a comparison between the field distribution in this arrangement and the arrangement without a dielectric layer (cf. Figure 4.41, Chapter 4) demonstrates that the dielectric layer enhances the electric field intensity in W2. It also shows the lesser influence of increasing the gap.

Figures 6.50 shows a cross-sectional side view of the electric field intensity distributions (amplitude and phase) inside W1 and W2 and inside the 3 mm-thick

dielectric layer attached to the rectangular dielectric-loaded DWS and dry concrete ($\varepsilon_r = 4.1 - j0.82$) at 10.3 GHz for gaps of 0.0, 1.0 and 2.0 mm between the attached dielectric layer and the concrete. It can be seen from the figure that W1 radiates electromagnetic waves in the dry concrete across the dielectric insertion and layer, and that a part of this penetrates into W2 through the dielectric layer in the no-gap condition. Moreover, Figure 6.50 clearly show changes in the electric field intensity distribution inside the dielectric layer and W2 when a gap exists. It should be noted that a comparison between the field distribution in this arrangement and the arrangement without a dielectric layer (cf. Figure 5.35, Chapter 5) demonstrates that the dielectric layer enhances the electric field intensity in W2. It also shows the lesser influence of increasing the gap.
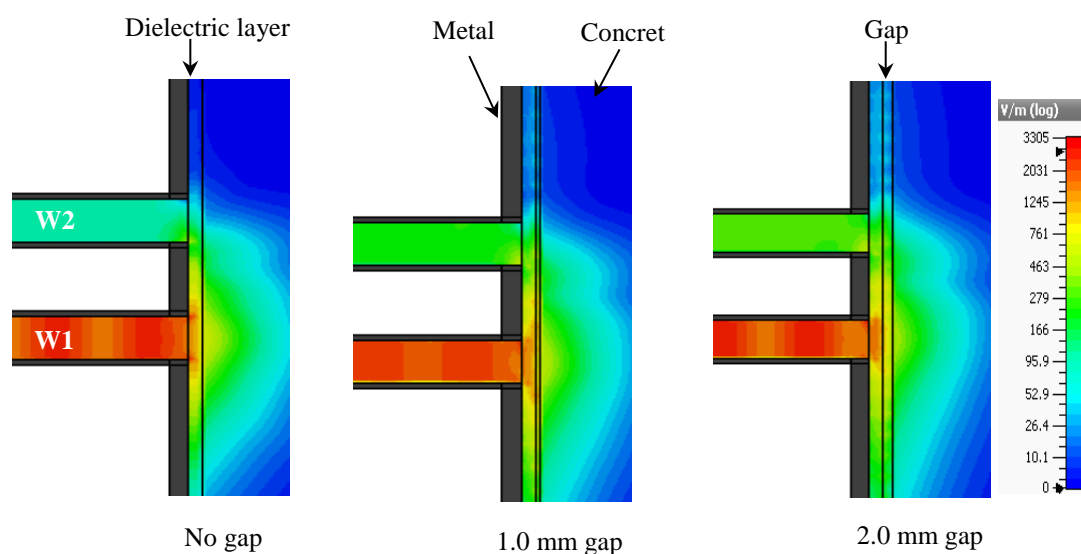
Amplitude of electric field intensity distribution
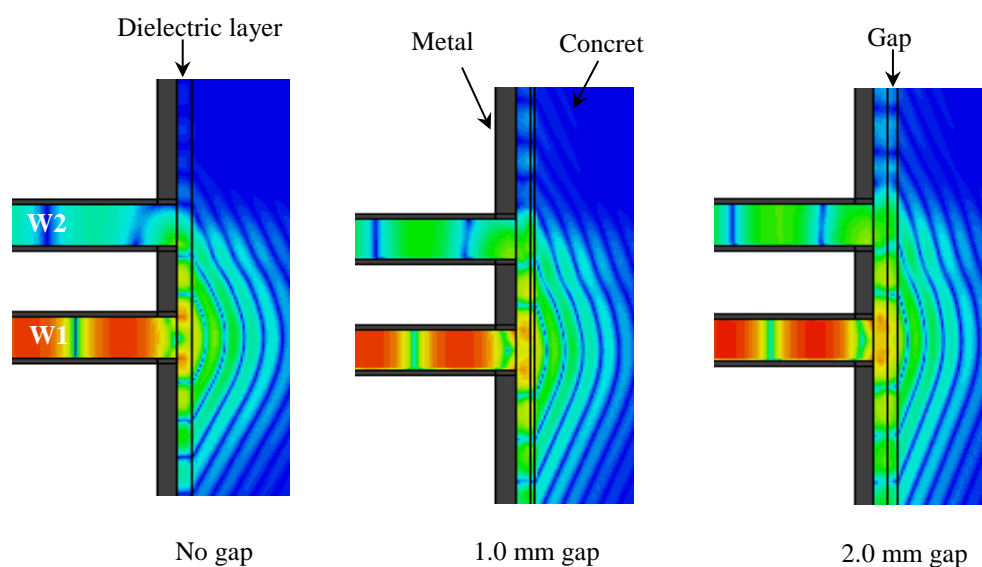
Phase of electric field intensity distribution

Figure 6.48: Cross-sectional side view of electric field intensity distribution inside the waveguide sections W1 and W2, in the 3 mm-thick dielectric layer attached to the empty DWS, and in the fresh concrete ($\varepsilon_r = 15.0 - j4.5$) for three gap values at a frequency of 10.3 GHz.
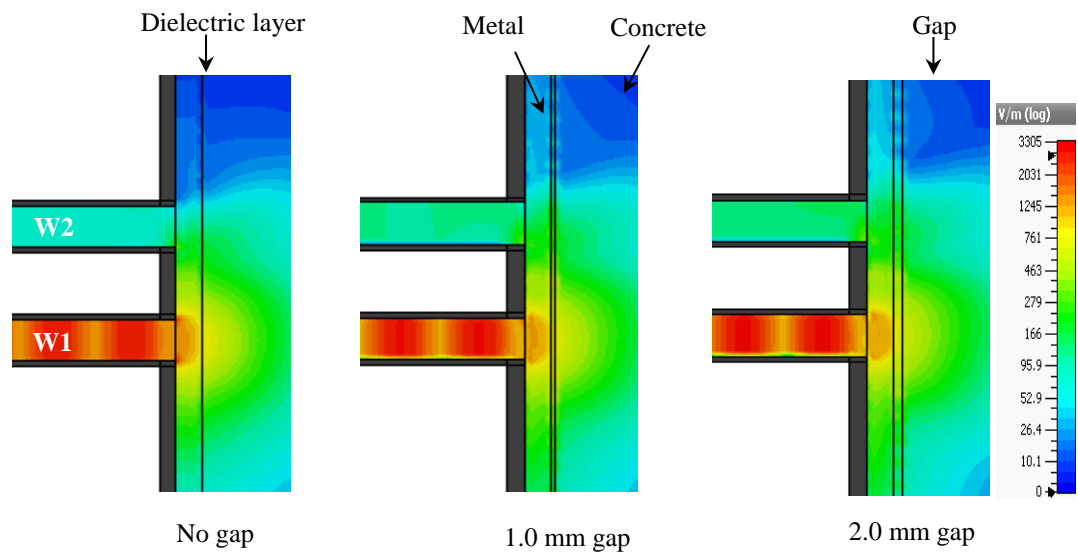
Amplitude of electric field intensity distribution
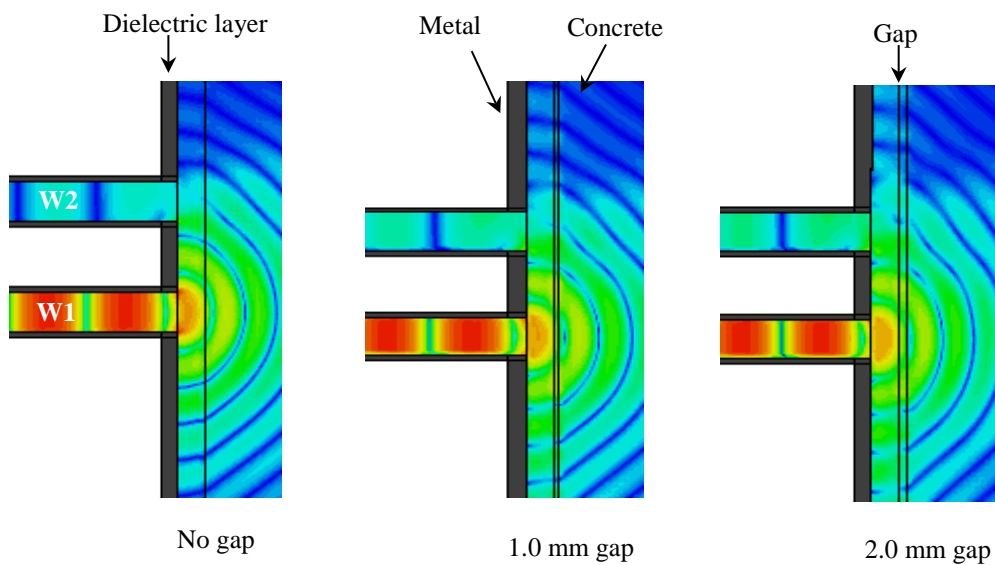
Phase of electric field intensity distribution

Figure 6.49: Cross-sectional side view of electric field intensity distribution inside waveguide sections W1 and W2, in the 6 mm-thick dielectric layer attached to the empty DWS, and in the dry concrete (ε_r = 4.1 – j0.82) for three gap values at a frequency of 10.6 GHz.
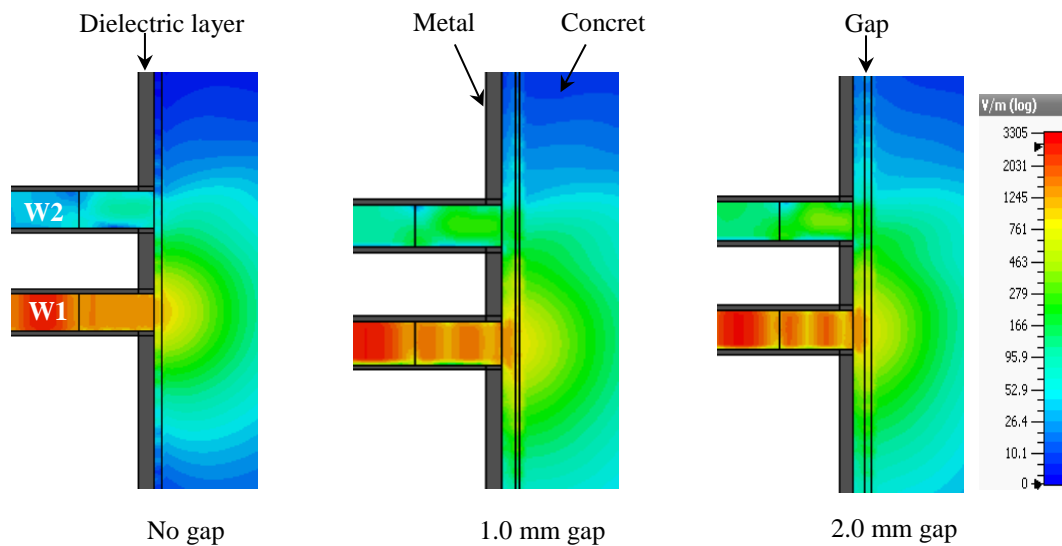
Amplitude of electric field intensity distribution
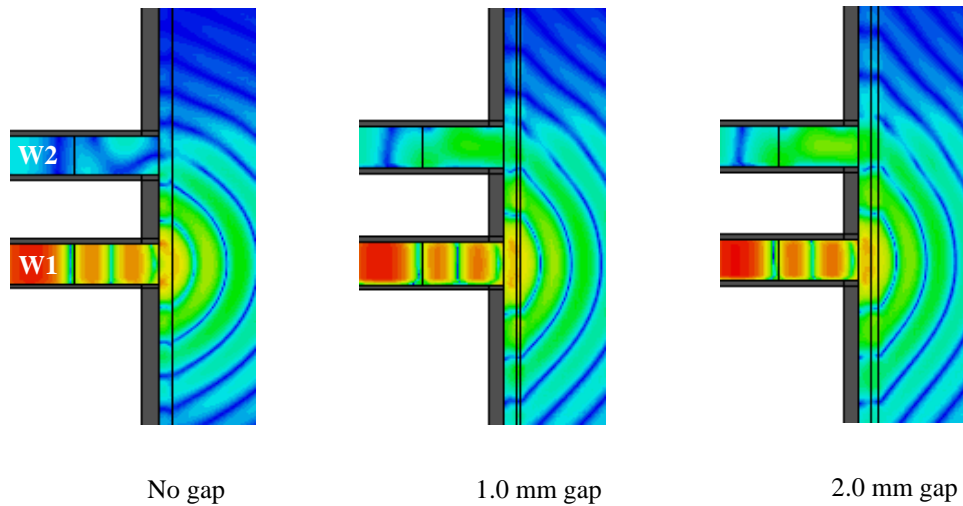
Phase of electric field intensity distribution

Figure 6.50: Cross-sectional side view of electric field intensity distribution inside the waveguide sections W1 and W2, in the 3 mm-thick dielectric layer attached to the rectangular dielectric-loaded DWS, and in the dry concrete ($\varepsilon_{rc} = 4.1 - j0.82$) for three gap values at a frequency of 10.3 GHz.

6.9   Summary

In this chapter, the modified DWSs were presented. They consisted of empty DWS and dielectric-loaded DWS with the attached dielectric layers. The proposed empty DWS with attached dielectric layer was built and tested for the determination of the complex dielectric permittivity of fresh concrete as well as for the detection and monitoring of gaps in concrete-based composite structures of different ages. The dielectric-loaded DWS with attached dielectric layer was used to measure debonding gaps between the dry concrete and the attached layer.

The empty DWS with an attached dielectric layer was modelled together with the various concrete specimens; then an extensive parametric analysis was performed for different thicknesses of the attached layer (2, 3, 6, 8 and 10 mm) with fresh, early-age and dry concrete. The numerical investigation into fresh concrete showed that the 3 mm-thick acrylic layer provided the highest transmission coefficient whereas the 6 mm-thick acrylic layer provided the highest transmission coefficient with dry concrete. Therefore, an empty DWS with attached 3 mm-thick acrylic sheet was constructed, and measurements were conducted to determine the complex dielectric permittivity of hour 1 fresh concrete using the measured and simulated data and the developed algorithm. The dielectric permittivity of the hour 1 concrete was determined as $21.5 - j4.3$.

This fabricated sensor was further used to detect small gaps between early-age concrete and the attached dielectric layer. It was found that it can detect and measure the gap using the reflection and transmission coefficient data independently in the range of 0.5–2.0 mm with moderate accuracy. To detect gaps between dry concrete and the dielectric layer, the proposed empty DWS with a 6 mm-thick dielectric layer produced the best results, especially for gap values in the range of 0.0–0.5 mm over the entire X-band frequency range.

A model of the dielectric-loaded DWS with attached dielectric layer and a dry concrete specimen was developed for a parametric study of the effect of different thicknesses of the attached layer and different gaps between the dry concrete and the dielectric sheet. The study revealed that 2 mm and 3 mm-thick acrylic layers give the most useful results for gap detection between concrete and dielectric layer, using the

magnitude of the transmission coefficient. It was also shown that resonant responses occurred in the magnitude of reflection coefficient curves due to the presence of dielectric insertions inside the waveguide sections; however, the changes of the resonant frequencies were not consistent with the changes of gap values. Consequently, reflection coefficient measurement was not suitable for gap detection; rather, measurement of the magnitude of the transmission coefficient can readily detect and measure the gap.

The measurements with the dielectric-loaded DWS with attached dielectric layer were conducted using dielectric layers in five thicknesses (2, 3, 6, 8 and 10 mm). It was shown that the measurement of the transmission coefficient using the proposed sensor with 2 mm or 3 mm-thick attached dielectric layer detect and monitor gaps between the dielectric layer and dry concrete very effectively, with good agreement of simulated and measured results. The presented electric field intensity distribution demonstrates the propagation of guided waves in the attached dielectric layer, and between the layer and concrete; this is the physical background of most observations relating to the magnitude of the transmission coefficient.

The modified DWSs can be applied to characterise fresh concrete in a mould with a plastic wall or on-line, and to investigate the shrinkage of different categories of concrete.

Chapter 7

Dual Waveguide Sensor with Tapered Dielectric Insertions

7.1   Introduction

In chapter 5, a microwave dual waveguide sensor with rectangular dielectric insertions was proposed to determine the complex dielectric permittivity of concrete specimens of different ages and to measure the gap in concrete-based composite structures. The dielectric insertions were inserted in the waveguide sections of DWS to prevent the penetration of water and concrete obstacles inside the waveguide sections in the case of fresh concrete. It was shown that the dielectric insertions could add new features of sensors such as resonant responses. However, an impedance matching between the empty and the dielectric-filled sections of the waveguide was not considered which led to relatively high wave reflection from an insertion in waveguide 1 and, as a result, lower wave transmission to the waveguide 2. In this chapter, a DWS with tapered dielectric insertions (referred to as a DWS with tapered dielectric insertions) is proposed to reduce the wave reflection from the insertions and create opportunity to optimise the sensor by changing the dimensions of their tapered and regular parts. Therefore, parametric study is performed with different lengths of tapered and rectangular parts of the insertions for the purpose of achieving good impedance matching between the empty and the dielectric-filled sections of the waveguide to increase the wave transmission. Then, the DWS with tapered dielectric insertions is further modified by adding a dielectric layer between the metal plate and concrete (referred to as a DWS with tapered dielectric insertions and attached dielectric layer). Simulations are performed and measurements are conducted for the detection of small gaps between dry concrete specimens and attached dielectric layers using the proposed sensor. The comparison between measurement and simulation results for both sensors is also performed. The electric field intensity distributions inside the waveguide sections of the proposed sensors, dielectric layers and concrete specimens are studied to verify observations made from the simulation and measurement results.

7.2   Design of Sensor with Tapered Dielectric Insertions

The schematic of the proposed microwave dual waveguide sensors with tapered dielectric insertions is shown in Figure 7.1. It consists of two rectangular waveguide sections with broad and narrow dimensions of *a* and *b*, respectively, installed in metal wall of the structure under inspection, and flanges for connection with the measuring system as shown in Figure 7.1a. A tapered dielectric insert is installed inside each waveguide section of the DWS as shown in Figures 7.1b and 7.1c. The insert is tapered along the E-plane of the dominant mode of the waveguide at one end, providing good impedance match between the empty and the dielectric-filled sections of the waveguide. The other end of the insert is ended at the aperture of waveguide that is attached to the concrete surface. The lengths of rectangular and taper parts of dielectric insertions are designated by d_1 and d_2, respectively.
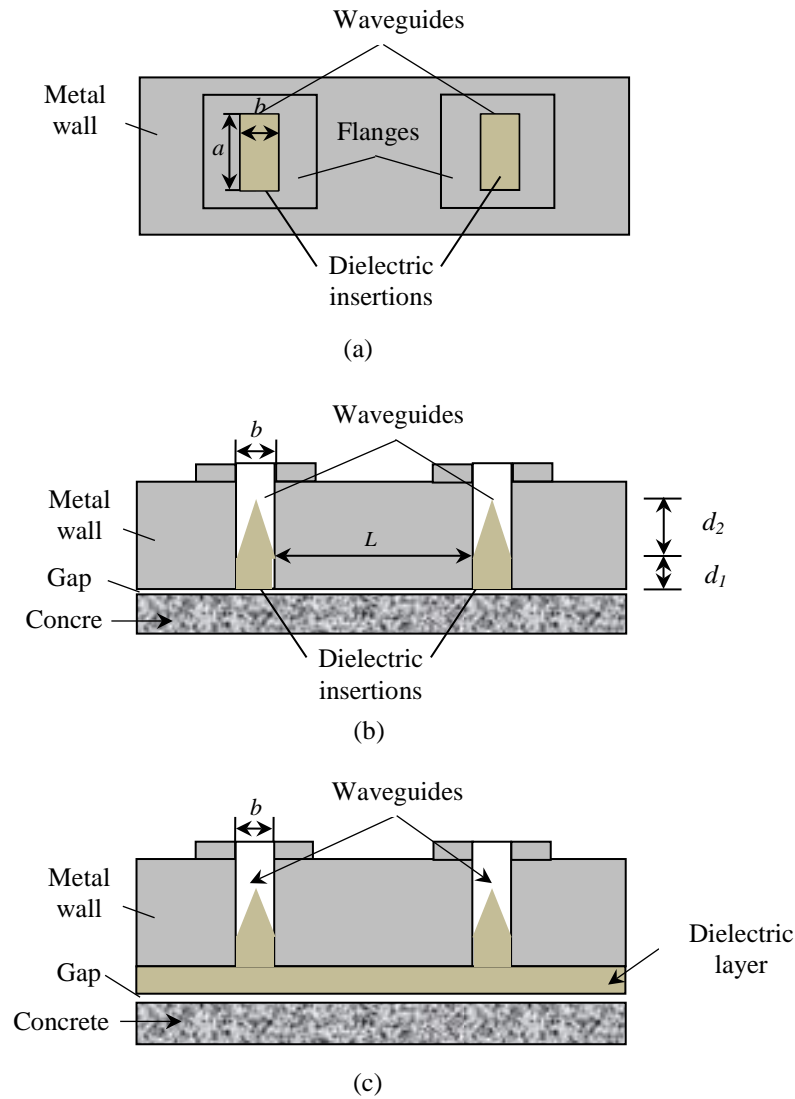
Figure 7.1: Schematic of a dual waveguide sensor with tapered dielectric insertions: (a) top view and cross-sectional side view (b) without and (c) with attached dielectric layer.

7.3 Numerical Investigation using The DWS with Tapered Dielectric Insertions

In this section, the proposed DWS with tapered dielectric insertions is modelled along with the concrete specimen. Simulations are performed for the magnitude of reflection coefficients and transmission coefficients at different gap values between dry concrete specimens and metal plate. The results of parametric study with different combinations of d_1 and d_2 values are presented and discussed.

7.3.1   Model of the Sensor

Figure 7.2a shows a perspective view of the model of DWS with tapered dielectric insertions along with concrete specimen. In this investigation two X-band microwave rectangular waveguide sections with standard aperture dimensions of 22.86 mm $\times$ 10.16 mm, the lengths of waveguide sections of 45.0 mm and 97 mm and the distance between waveguide sections of 15.0 mm are used. The tapered dielectric insert with complex dielectric permittivity of $\varepsilon_d = 2.6 - j0.01$ is inserted in each waveguide section as shown in Figure 7.2b (schematic of the insert is shown in Figure 7.2c). In the simulation, excitation signal of Gaussian type and frequency range from 8.2 GHz to12.4 GHz were used. The time domain solver of CST has been used in this investigation. The complex dielectric permittivity of dry concrete specimen was chosen as, $\varepsilon_c = 4.1 - j0.82$.
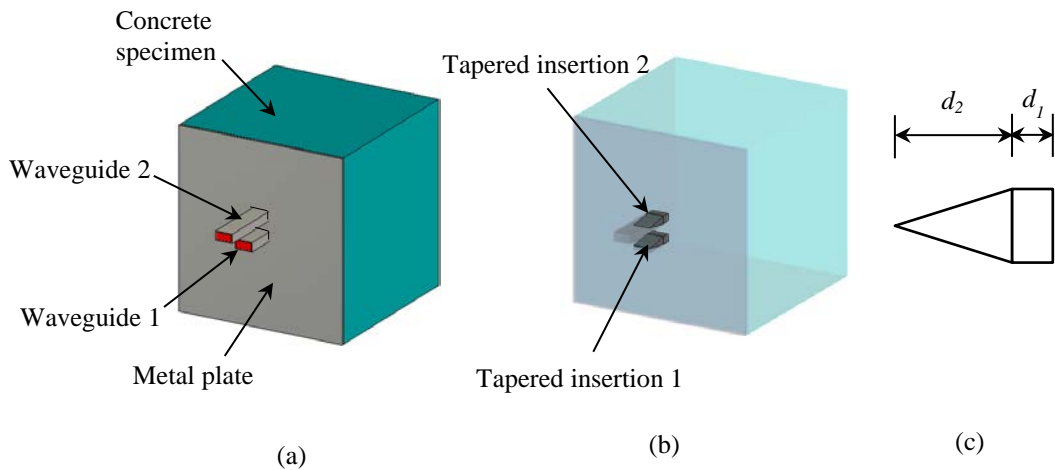
Figure 7.2: A model of DWS with tapered dielectric insertions and concrete specimen in CST: (a) perspective general view, (b) perspective transparent view showing the tapered dielectric insertions and (c) schematic of side view of the tapered dielectric insertion.

7.3.2   Parametric Study with Dry Concrete Specimens

The extensive simulation with the proposed DWS was performed at different lengths of rectangular part ($d_2 = 25$, 30 and 35 mm) and tapered part ($d_1 = 5$ mm and

10 mm), and at five different gap values (0, 0.5, 1.0, 1.5, and 2.0 mm) between the dry concrete specimen and the metal plate of the proposed sensor.

Figures 7.3 - 7.5 show the simulated magnitudes of reflection and transmission coefficients vs. frequency at different gap values between concrete ($\varepsilon_{rc} = 4.1 - j0.82$) and metal plate using the DWS with tapered dielectric insertion at $d_1 = 5$ mm and different d_2. It is clearly seen in Figures 7.3a, 7.4a and 7.5a that the resonant responses occurs at the magnitude of reflection coefficient curves and they moved towards to lower frequencies at all gap values. These resonant responses can be attributed to quarter-wavelength resonator conditions formed in the dielectric-filled area of the waveguide when the resonator has an open end at the tapered part and shorted part at the interface between the aperture and concrete. It is observed that the changes of gap value change the values of magnitude of S_{11} as well as the resonant frequencies. In general, magnitude of reflection coefficient is < -10 dB that is significantly lower than in the DWS with rectangular dielectric insertions (c.f., Figure 5.30a), i.e., a good matching between an empty part and a dielectric-filled part of the DWS with the tapered dielectric inserts is achieved. Furthermore, it can be seen from Figures 7.3b, 7.4b and 7.5b that there are no resonant responses in the magnitude of transmission coefficient curves at all gap values and S_{21} does not change when d_2 changes from 25 mm to 35 mm. However, the magnitude of transmission coefficient non-monotonically increases when gap value increases from 0.5 mm to 2.0 mm over the entire operating frequency band. It is noted that compared to the results of the DWS with rectangular dielectric insertions (c.f., Figure 5.30b) the increase of the magnitude of transmission coefficient of 1dB - 2 dB is observed in the DWS with the tapered dielectric inserts. This increase is less than expected from the increase of the magnitude of reflection coefficient. These results and comparison show that efficiency of transmission of waves from waveguide 1 to waveguide 2 mostly depends of the transformation of waveguide waves (the guided wave) into the guided wave (waveguide waves).

Similar simulation was performed at $d_1 = 10$ mm and the results are shown in Figures 7.6 - 7.8. Again, there is low level of reflection from the inserts (i.e., a good matching) at all d_2. It can be seen from Figures 7.6a, 7.7a and 7.8a that two resonant

responses occur at each gap values at d_2 = 25 mm but only one prominent resonant response exist at no gap condition at d_2 = 30 and 35 mm. The magnitude of this resonant response is very sensitive to a small gap between the metal plate and concrete, e.g., at d_2 = 30 mm (35 mm) it changes from -40 dB to -23 dB (-32 dB to -18 dB) when 0.5-mm gap occurs as shown in Figures 7.7a and 7.8a. Then, the magnitude gradually increases when gap value increases. There are no resonant responses in the magnitude of transmission coefficient curves at all gap values and S_{21} does not change when d_2 changes from 25 mm to 35 mm. The magnitude of transmission coefficient non-monotonically increases when gap value increases from 0.5 mm to 2.0 mm over the entire operating frequency band as shown in Figures 7.6b, 7.7b and 7.8b, and its values are equal to those obtained at d_2 = 5 mm (c.f. Figures 7.3b, 7.4b and 7.5b). These results confirmed observations made from the results d_1 = 5 mm together with them indicate that the transmission of waves from waveguide 1 to waveguide 2 does not depend on d_1 and d_2.

(a) (b)

Figure 7.3: Simulated magnitude of (a) reflection and (b) transmission coefficient vs. frequency at different gap values between concrete (ε_{rc} = 4.1 – j0.82) and metal plate using the DWS with tapered dielectric insertion at d_1 = 5 mm and d_2 = 25 mm.
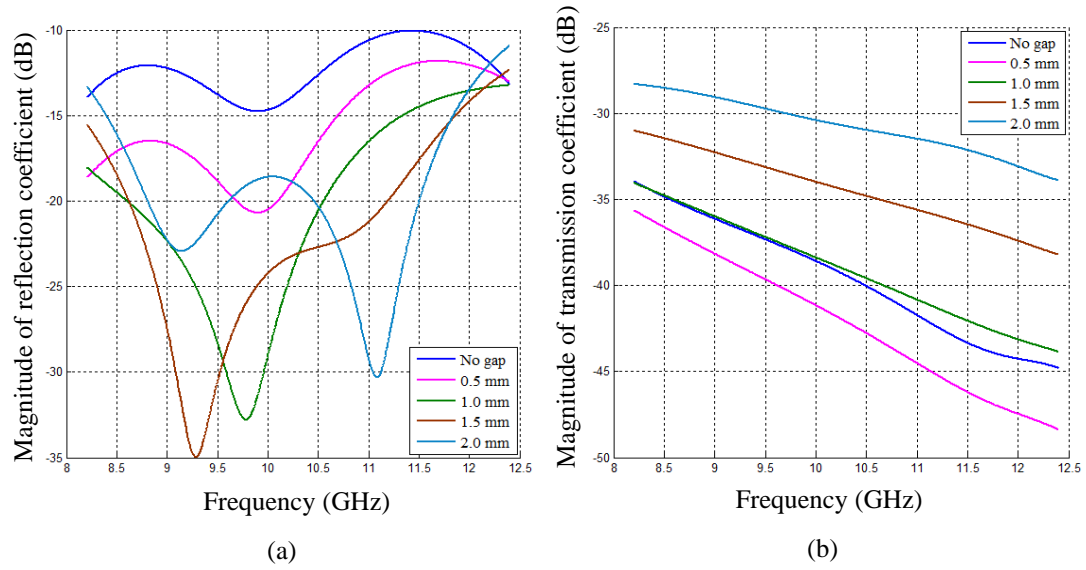
Figure 7.4: Simulated magnitude of (a) reflection and (b) transmission coefficient vs. frequency at different gap values between concrete ($\varepsilon_{rc} = 4.1 - j0.82$) and metal plate using the DWS with tapered dielectric insertion at $d_1 = 5$ mm and $d_2 = 30$ mm.
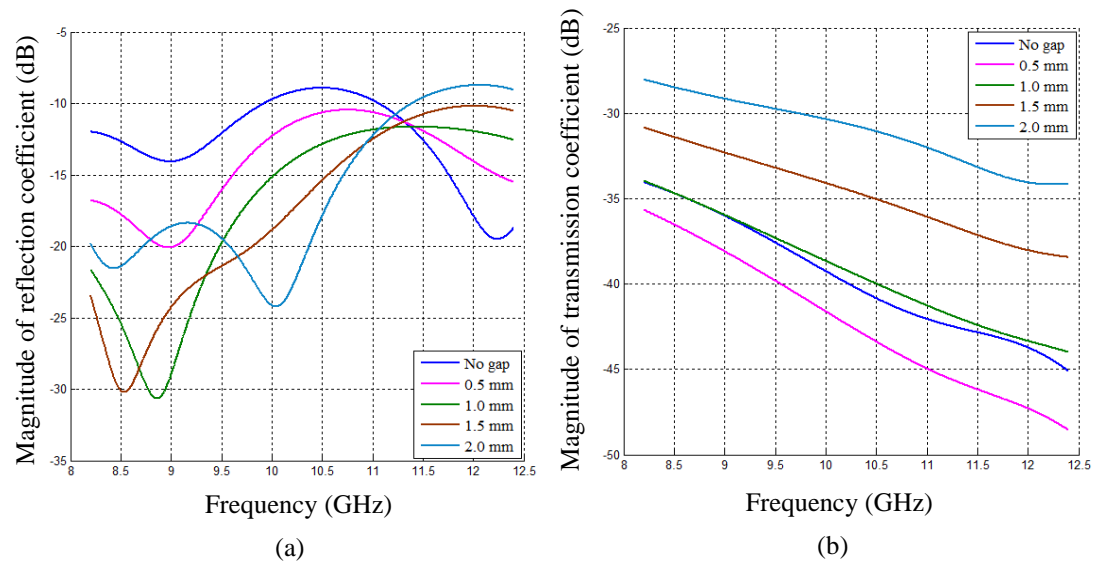
Figure 7.5: Simulated magnitude of (a) reflection and (b) transmission coefficient vs. frequency at different gap values between concrete ($\varepsilon_{rc} = 4.1 - j0.82$) and metal plate using the DWS with tapered dielectric insertion at $d_1 = 5$ mm and $d_2 = 35$ mm.
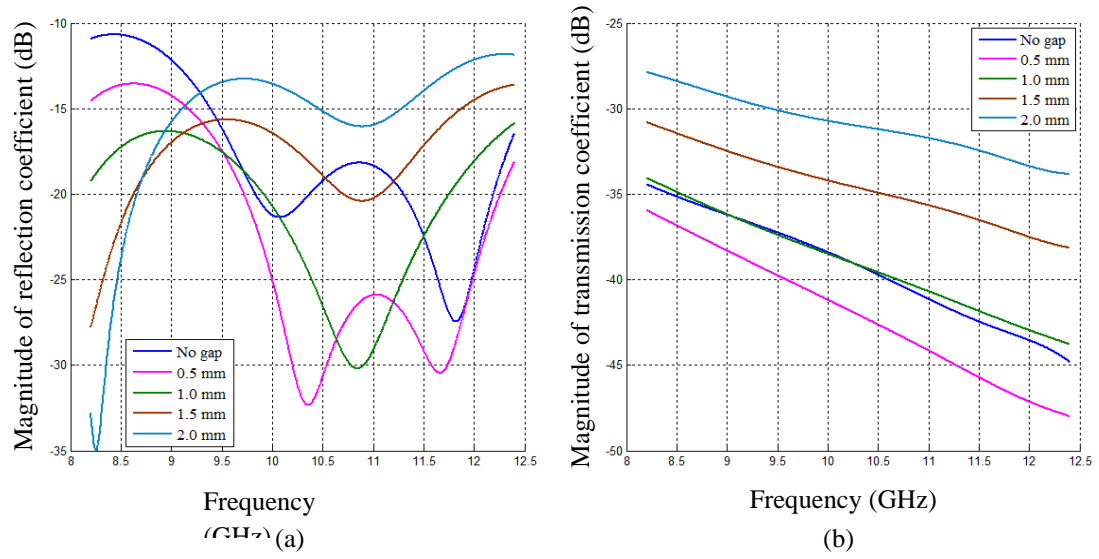
Figure 7.6: Simulated magnitude of (a) reflection and (b) transmission coefficient vs. frequency at different gap values between concrete ($\varepsilon_{rc} = 4.1 – j0.82$) and metal plate using the DWS with tapered dielectric insertion at $d_1 = 10$ mm and $d_2 = 25$ mm.
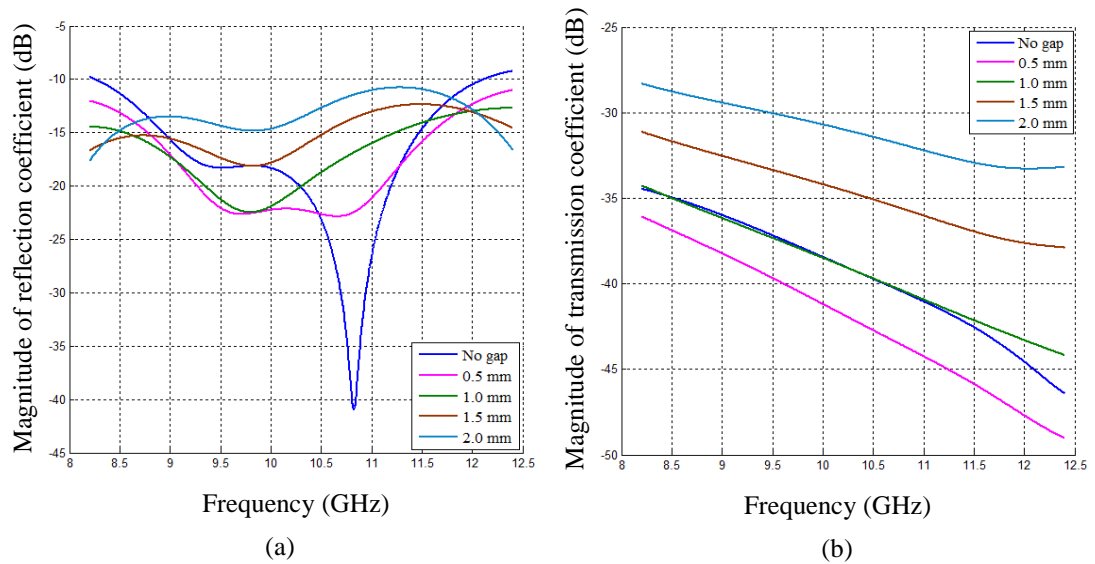
Figure 7.7: Simulated magnitude of (a) reflection and (b) transmission coefficient vs. frequency at different gap values between concrete ($\varepsilon_{rc} = 4.1 – j0.82$) and metal plate using the DWS with tapered dielectric insertion at $d_1 = 10$ mm and $d_2 = 30$ mm.
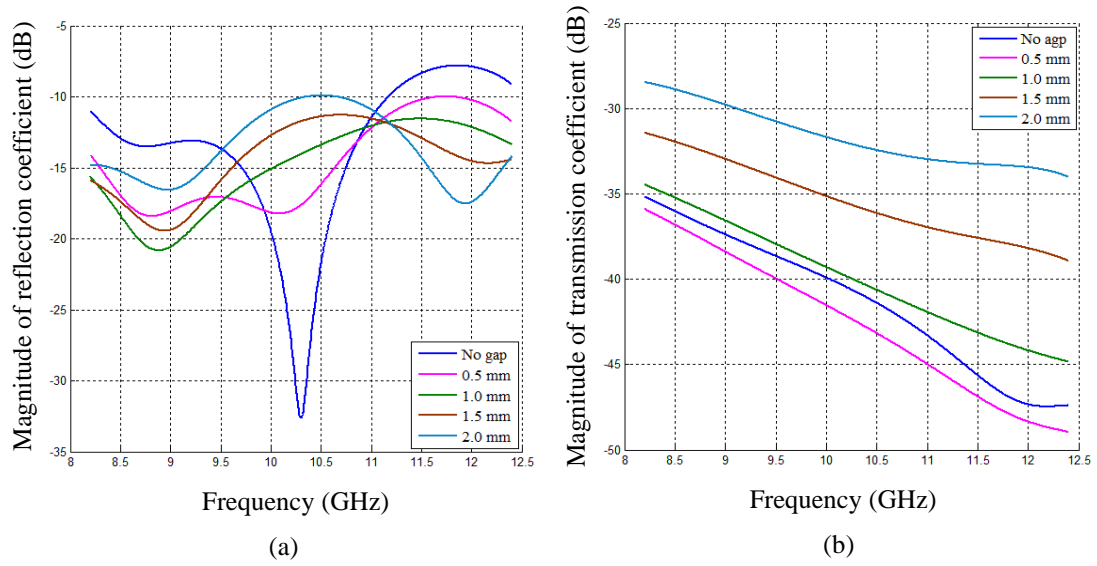
Figure 7.8: Simulated magnitude of (a) reflection and (b) transmission coefficient vs. frequency at different gap values between concrete (ε_{rc} = 4.1 – j0.82) and metal plate using the DWS with tapered dielectric insertion at d_1 = 10 mm and d_2 = 35 mm.

7.4 Measurement using the DWS with Tapered Dielectric Insertions

The measurement approach and measurement results for dry concrete specimen using the DWS with tapered dielectric insertions is described in this section. First, the measurement of magnitude of reflection coefficient, $S_{11,}$ and transmission coefficient, $S_{21,}$ is conducted at no gap condition between the dry concrete specimen and the metal plate of DWS with tapered dielectric insertions. Then, S_{11} and S_{21} at different gap values (0.5, 1.0, 1.5 and 2.0 mm) between specimen and the metal plate are also measured. These procedures are repeated for 5 times at no gap and other gap values and then average values are calculated at each gap condition.

7.4.1 Specimens and Measurement Setup

A 250-mm concrete cube (age of about 2 years) initial water-to cement ratio of 0.5 was used as the specimen in this investigation. Two tapered insertions made of 10-mm thick Acrylic sheet with ε_r = 2.6 – j0.01, d_1 = 10 mm and d_2 = 20 mm are

fabricated and inserted inside the waveguide sections of the DWS. The experimental setup is shown in Figure 7.9. Thin paper sheets were used to create desired (0.5, 1.0, 1.5 and 2.0 mm) air gap values between specimen and the sensor.
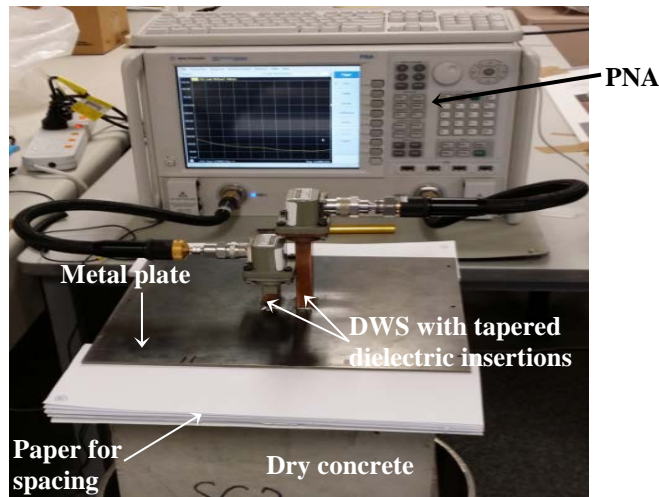
Figure 7.9: Measurement setup including a performance network analyser (PNA), the dry concrete specimen and the DWS with tapered dielectric insertions.

7.4.2   Measurement Results with Dry Concrete Specimens

Figure 7.10 shows the average measured magnitude of reflection and transmission coefficient vs. frequency at different gap values between dry concrete specimen and metal plate of the DWS with tapered dielectric insertions. It can be clearly seen from Figure 7.10a that two resonant responses occur in the magnitude of reflection coefficient curves over the X-band frequency for all gap values. It is found that S_{11} significantly decreases when gap of 0.5 mm occurs and then it non-monotonically increases with the increase of gap values. It is also noted that the resonant frequency decreases slightly with the increase of gap value from 0.5 mm to 2.0 mm. Furthermore, it is observed from Figure 7.10b the increase of gap values from 0.5 mm to 2.0 mm increases the magnitude of transmission coefficient over the entire frequency band. Overall, the behaviour and trends of measurement results are similar to the simulation results (with some differences which can be attributed to measured and fabrication errors) and the results obtained with the DWS with rectangular insertions (c.f. Figure 5.20a).
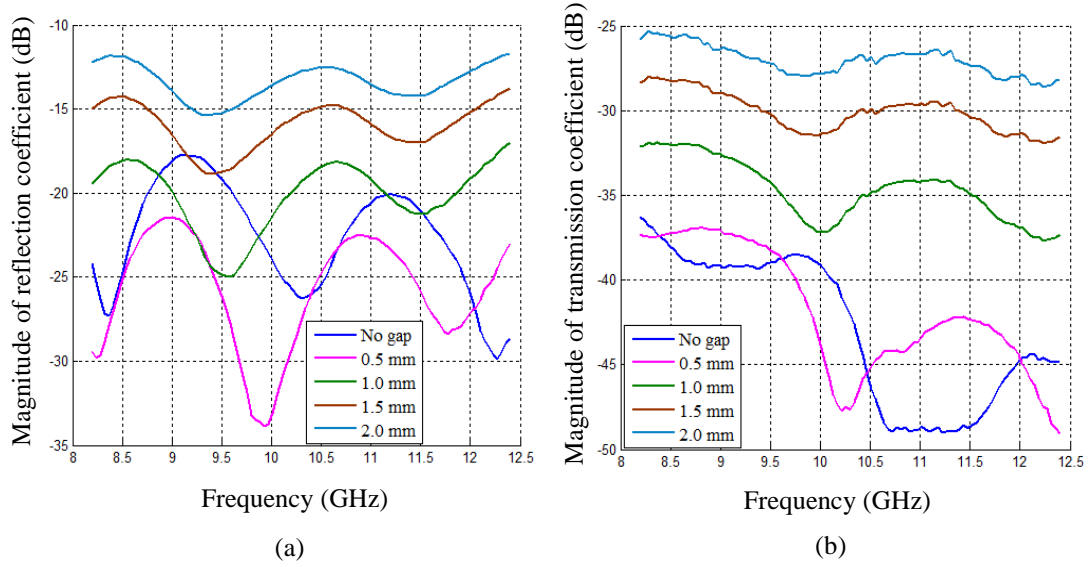
Figure 7.10: Average measured magnitude of (a) reflection and (b) transmission coefficient vs. frequency at different gap values between dry concrete specimen and metal plate of DWS with tapered dielectric insertions having $d_1 = 10$ mm and $d_2 = 35$ mm.

7.5   Numerical Investigation using The Tapered Dielectric-loaded DWS with Attached Dielectric Layer

In this section, a DWS with tapered dielectric insertions and attached dielectric layer is modelled along with the concrete specimen. Parametric studies are performed for the magnitude of reflection and transmission coefficients at different gap values between dry concrete specimens and attached dielectric layers, and different thicknesses of the attached dielectric layers. The main aim of these studies is to increase wave transmission (i.e., coupling) between waveguide 1 and waveguide 2 of the DWS.

7.5.1   Modelling of Sensor

A model of the proposed DWS with a dielectric layer along with concrete specimen is shown in Figure 7.11. The tapered insertions and dielectric layer are made of acrylic with dielectric permittivity of 2.6 – j0.01 and dimensions of $d_1 = 10$ mm and $d_2 = 35$ mm, and 250 mm × 250 mm, respectively.
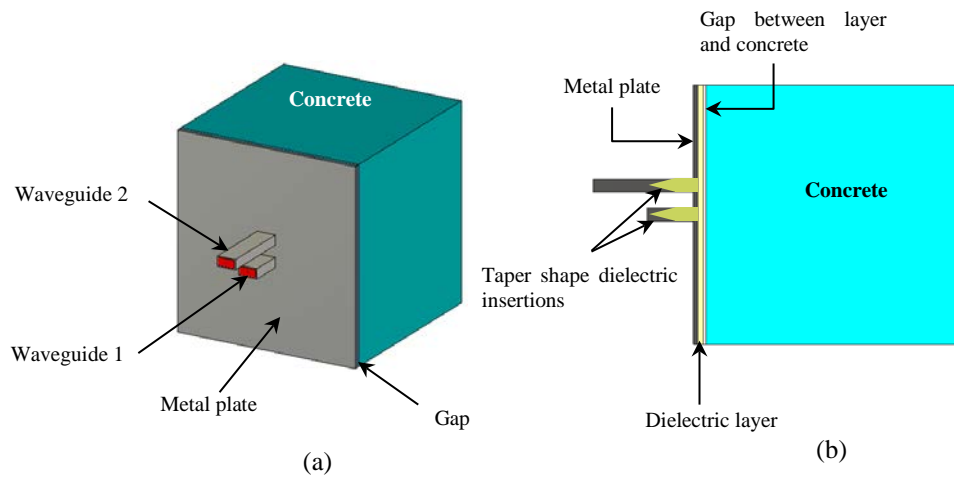
Figure 7.11: A model of the DWS with the tapered dielectric insertions and the attached dielectric layer along with concrete specimen: (a) perspective and (b) cross-sectional side view showing the attached dielectric layer and the gap between concrete and dielectric layer.

7.5.2 Parametric Study with Dry Concrete Specimens

The parametric studies of the proposed DWS with attached dielectric layer were performed at five different gap values (0, 0.5, 1.0, 1.5, and 2.0 mm) between and the dielectric layer and the concrete specimen ($\varepsilon_r = 4.1 - j0.82$) for different thicknesses of the dielectric layer; namely, 2, 3, 6, 8 and 10-mm.

Figures 7.12 - 7.16 show the simulated magnitude of reflection and transmission coefficient vs. frequency at different gap values between dry concrete specimen and dielectric layer using the tapered dielectric-loaded DWS with 2-, 3-, 6-, 8- and 10-mm thick dielectric layer, respectively. It can be seen from Figures 7.12a - 7.16a that reflection (matching) at non-resonant frequencies is slightly higher (lower) than it was without layer (c.f. Figure 7.8a). However, for example, with 2-mm and –mm thick layer it monotonically decreases (increases) when gap value increases from 0 to 2 mm at frequency range from 8.2 GHz – 10.7 GHz and from 12.2 GHz – 12.4 GHz (c.f. Figures 7.12a and 7.13a). Moreover, there is a resonant response area between these two ranges where the magnitude of reflection coefficient at the resonant frequency of 11.1 GHz decreases monotonically from -13 dB to -36 dB (Figure

7.12a) and from -15dB to -33 dB (Figure 7.13a) when gap value increases from 0 to 2 mm. These results show that the DWS with a dielectric layer can be used for the evaluation of gap value between the dielectric layer and concrete. It should be noted that in DWS with the thicker layer, i.e., >6 mm, behaviour of the magnitude of reflection coefficient vs gap value is complex as shown in Figures 7.14a – 7.16a.

However, behaviour of the magnitude of transmission coefficient is straightforward, i.e., the magnitude increases with the increase of gap value over the entire frequency range at all thicknesses of the layer as shown in Figures 7.12b – 7.16b. Comparison between the results with 2-mm layer (Figure 7.12b) and without layer (Figure 7.8b) shows that the layer increases magnitude of transmission coefficient at all gaps and over entire frequency band. Moreover, the further increase of this magnitude can be achieved by the increasing of layer thickness. To emphasise these observations Figure 7.17 shows the magnitude of transmission coefficient without layer and with layer of different thicknesses at single frequency of 10.3 GHz. At least two important observations can be made from Figure 7.17.

1) The magnitude monotonically increases when gap value increases at all thicknesses of layer and 2) the highest magnitude is achieved at thickness of 6 mm.

(a)

(b)
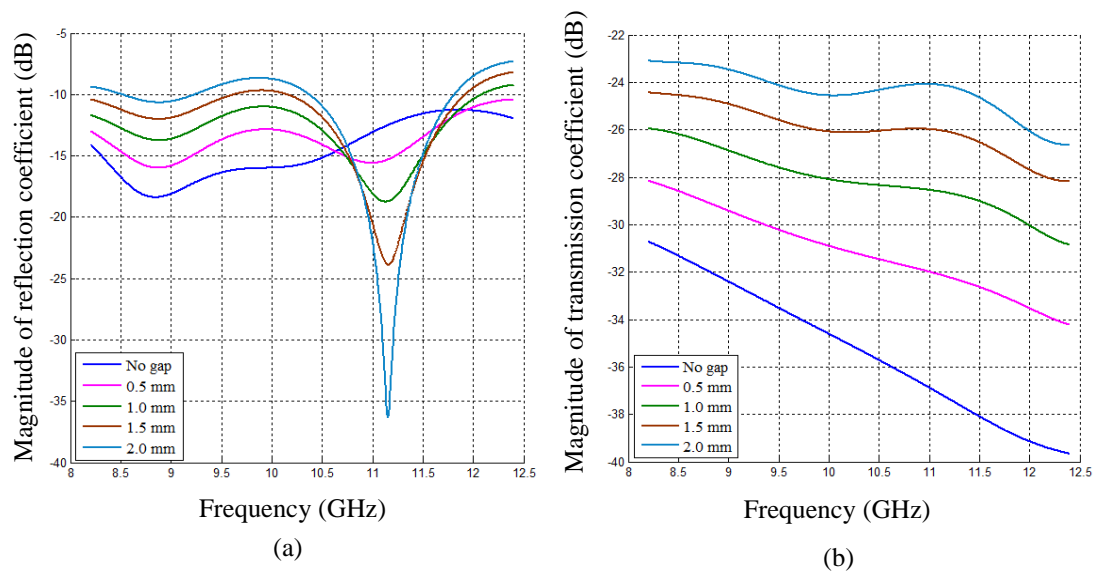
Figure 7.12: Simulated magnitude of (a) reflection and (b) transmission coefficient vs. frequency at different gap values between dry concrete ($\varepsilon_{rc} = 4.1 - j0.82$) and 2-mm thick dielectric layer ($\varepsilon_{rd} = 2.6 - j0.01$).
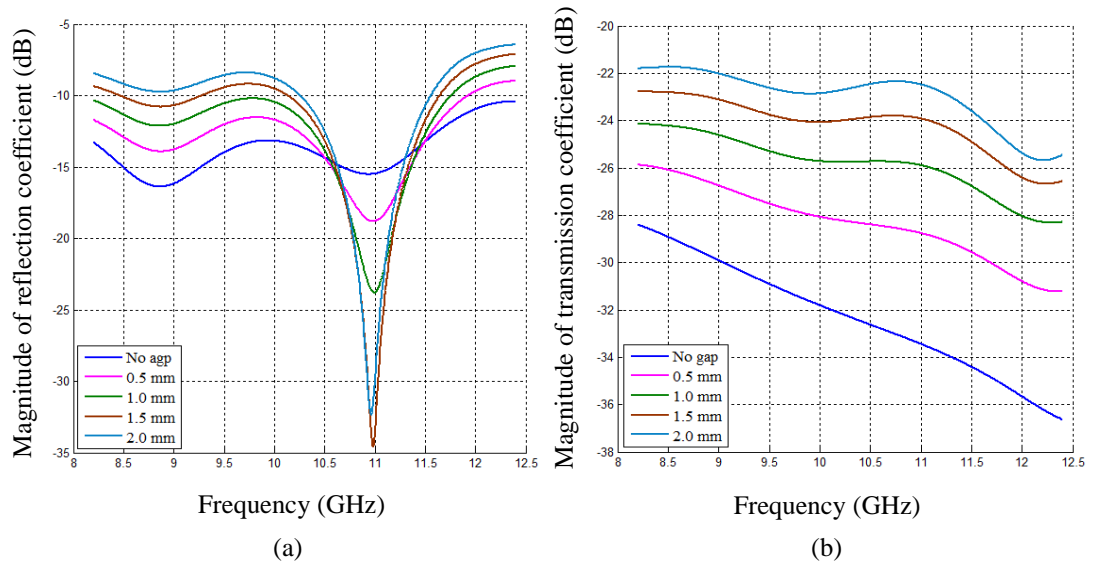
Figure 7.13: Simulated magnitude of (a) reflection and (b) transmission coefficient vs. frequency at different gap values between dry concrete ($\varepsilon_{rc} = 4.1 - j0.82$) and 3-mm thick dielectric layer ($\varepsilon_{rd} = 2.6 - j0.01$).
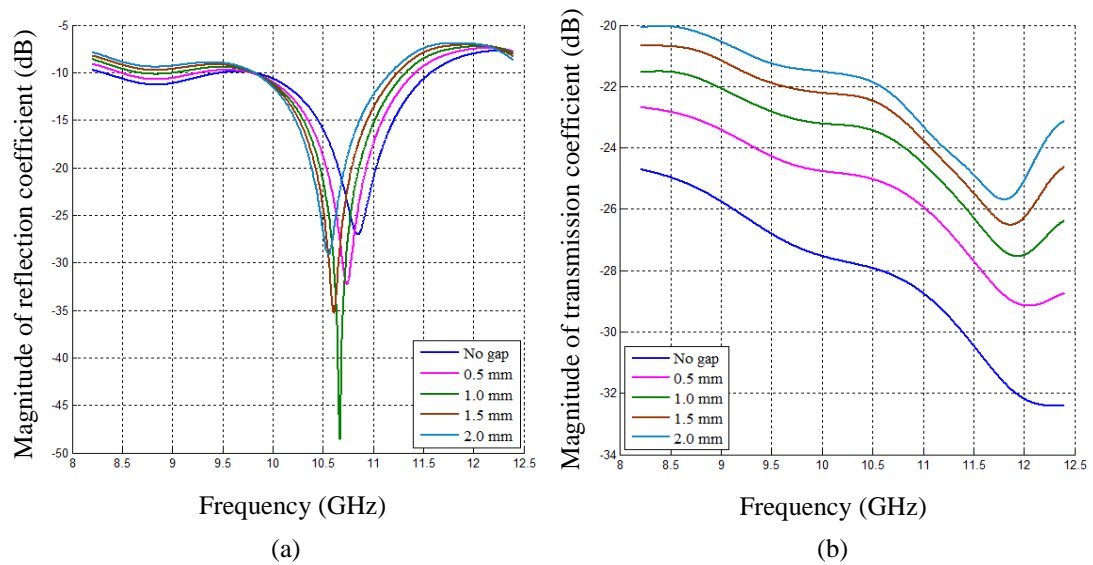
Figure 7.14: Simulated magnitude of (a) reflection and (b) transmission coefficient vs. frequency at different gap values between dry concrete ($\varepsilon_{rc} = 4.1 - j0.82$) and 6-mm thick dielectric layer ($\varepsilon_{rd} = 2.6 - j0.01$).
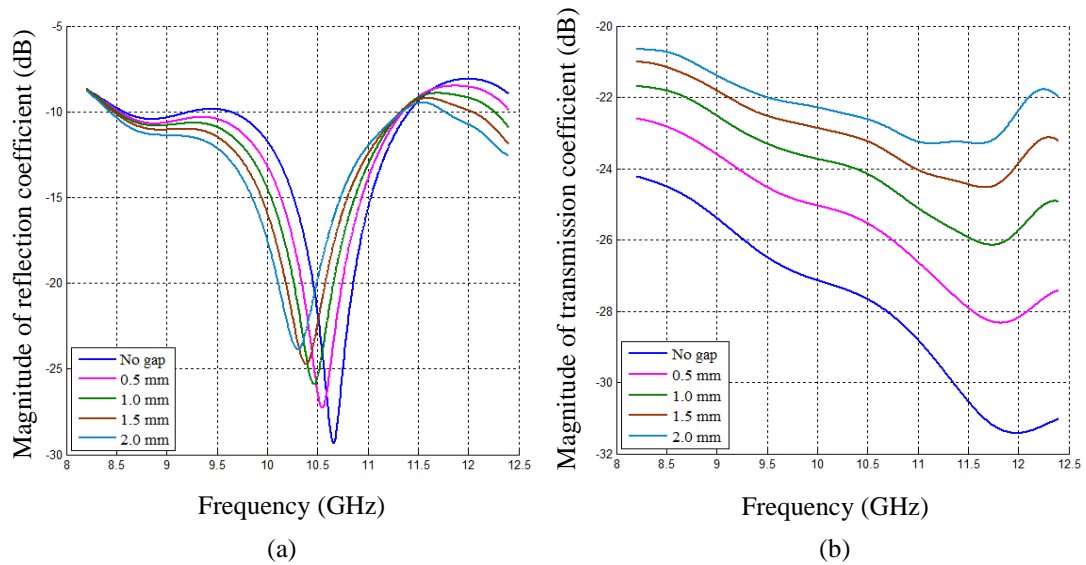
Figure 7.15: Simulated magnitude of (a) reflection and (b) transmission coefficient vs. frequency at different gap values between dry concrete (ε_{rc} = 4.1 – j0.82) and 8-mm thick dielectric layer (ε_{rd} = 2.6 – j0.01).
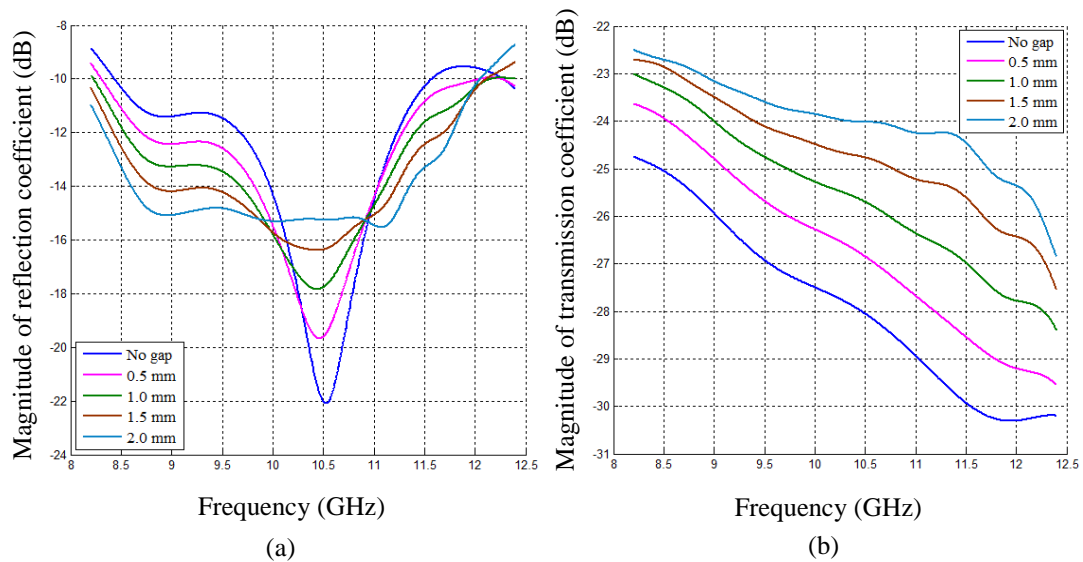
Figure 7.16: Simulated magnitude of (a) reflection and (b) transmission coefficient vs. frequency at different gap values between dry concrete (ε_{rc} = 4.1 – j0.82) and 10-mm thick dielectric layer (ε_{rd} = 2.6 – j0.01).
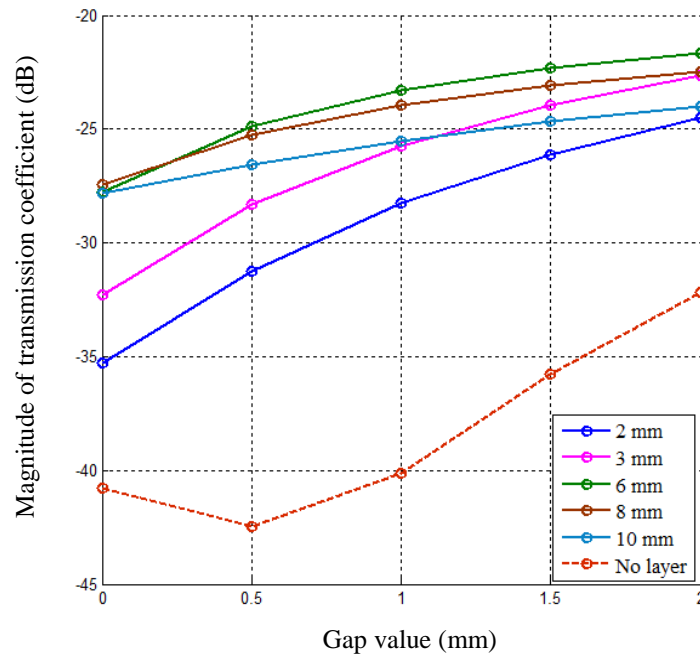
Figure 7.17: Simulated magnitude of transmission coefficient vs. gap value between dry concrete and dielectric layer with different thicknesses at 10.3 GHz ("No layer" curve is shown for comparison).

7.6   Measurement using DWS with the Tapered Insertions and Dielectric Layer

7.6.1   Specimens and Measurement Setup

The DWS with the tapered insertions and dielectric layer along with a 250-mm dry concrete cube were used in this investigation. Five acrylic layers (each of them had dimensions of 250 mm × 250 mm) with different thicknesses (i.e., 2, 3, 6, 8 and 10 mm) were made and used with the measurement setup similar to that shown in Figure 7.9 to verify the simulations results.

7.6.2   Measurement Results with Dry Concrete Specimens

For each acrylic layer, five measurements of S_{11} and S_{21} at each gap value (0, 0.5, 1.0, 1.5 and 2.0 mm) were conducted and then averaged.

Figures 7.18 - 7.22 show the measured average magnitude of reflection and transmission coefficient vs. frequency at different gap values between the concrete

specimen and 2-, 3-, 6-, 8- and 10-mm thick acrylic layer, respectively. The comparison of simulated and measured magnitudes of reflection coefficient shows the measured magnitude have two resonant responses while as mentioned the simulated magnitude had one resonant response. However, that they have similar similar behaviour and trends which have been discussed for the simulations results. The magnitudes of transmission coefficient also have similar behaviour and trends. These observations can also be seen from Figure 7.23 showing the magnitude of transmission coefficient vs gap value at different thicknesses of the layer, and following subsection 7.7 (Comparison of Measurement and Simulation Results).

(a)   (b)
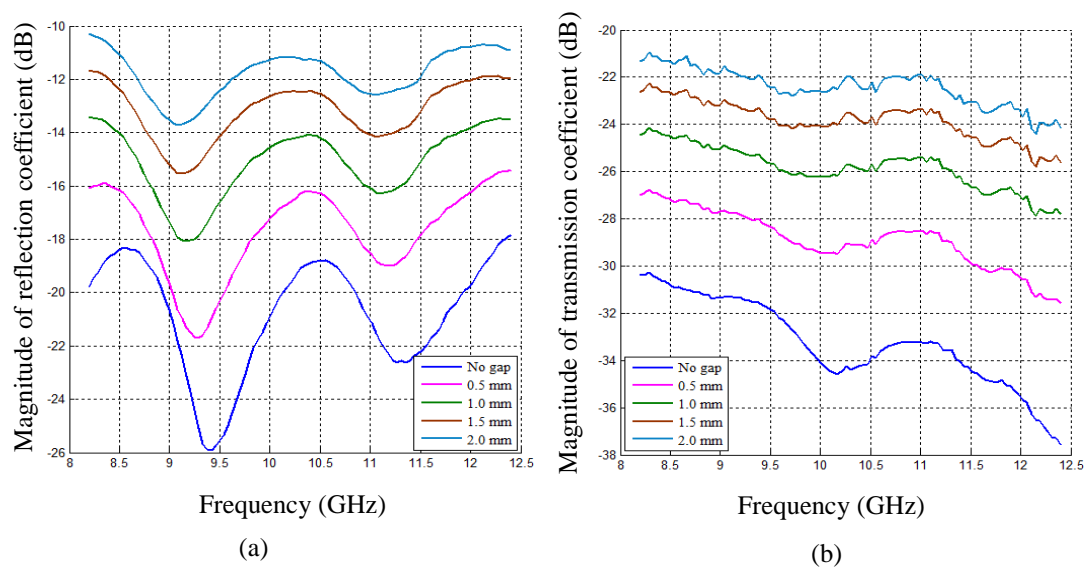
Figure 7.18: Measured average magnitude of (a) reflection and (b) transmission coefficient vs. frequency at different gap values between dry concrete specimen and 2-mm thick acrylic layer.
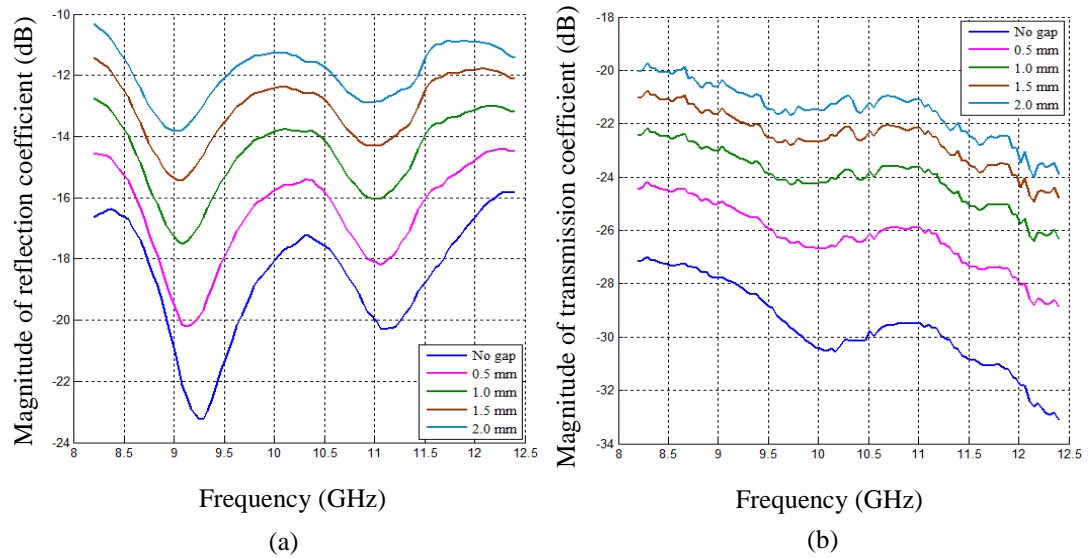
Figure 7.19: Measured average magnitude of (a) reflection and (b) transmission coefficient vs. frequency at different gap values between dry concrete specimen and 3-mm thick acrylic layer.
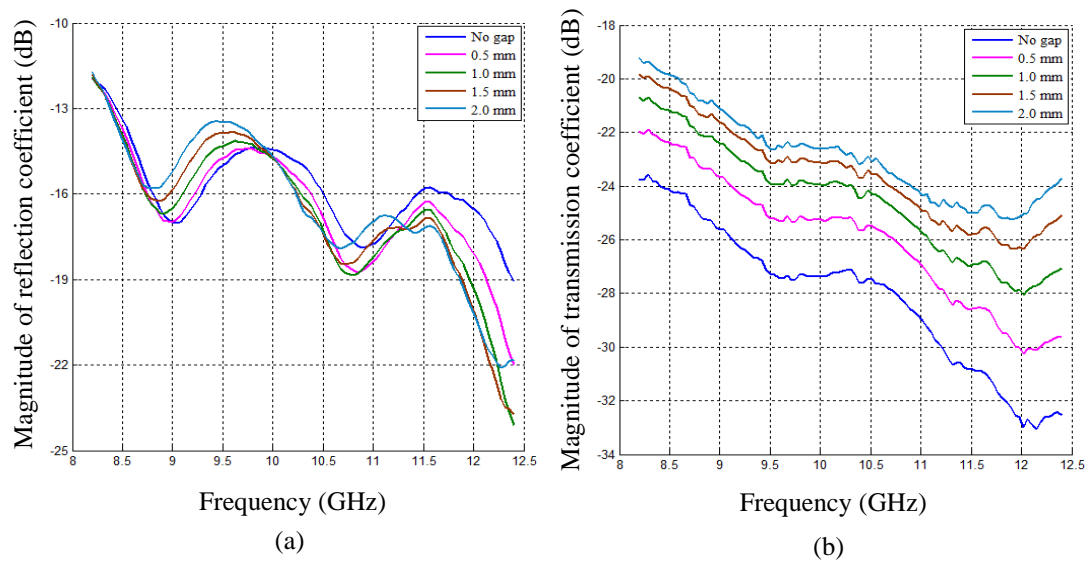
Figure 7.20: Measured average magnitude of (a) reflection and (b) transmission coefficient vs. frequency at different gap values between dry concrete specimen and 6-mm thick acrylic layer.

.
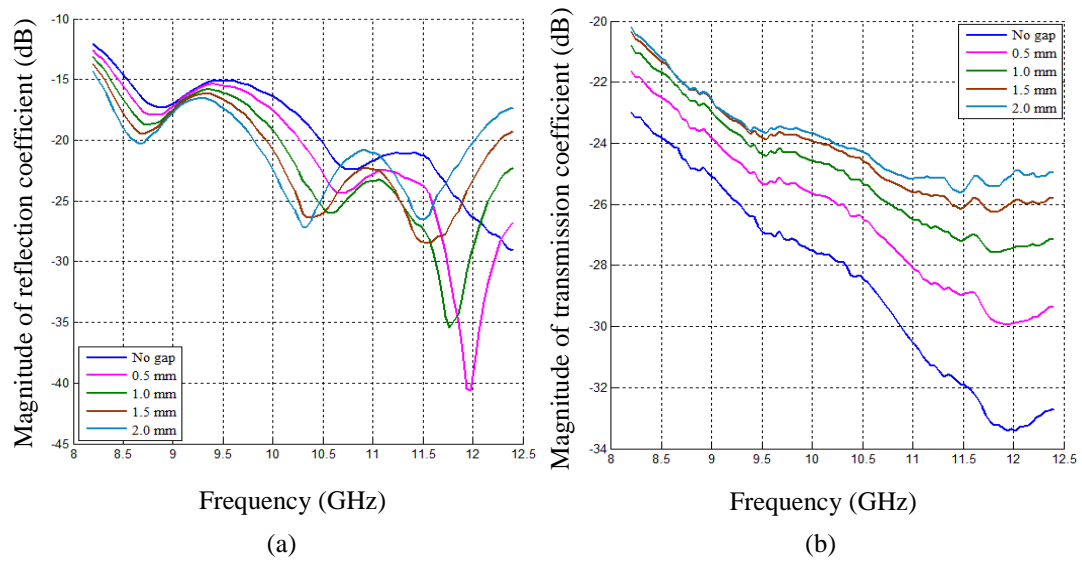
Figure 7.21: Measured average magnitude of (a) reflection and (b) transmission coefficient vs. frequency at different gap values between dry concrete specimen and 8-mm thick acrylic layer.

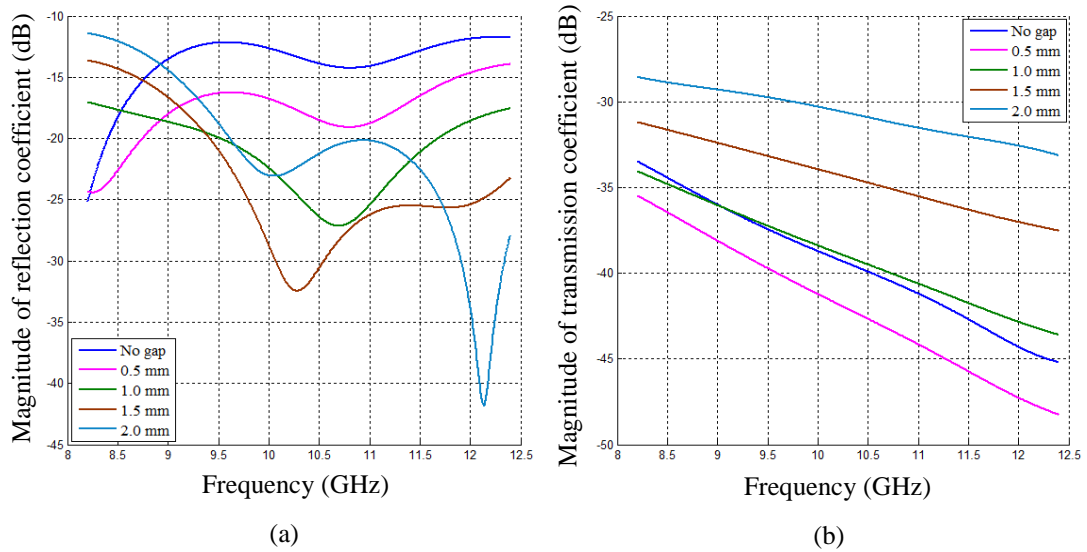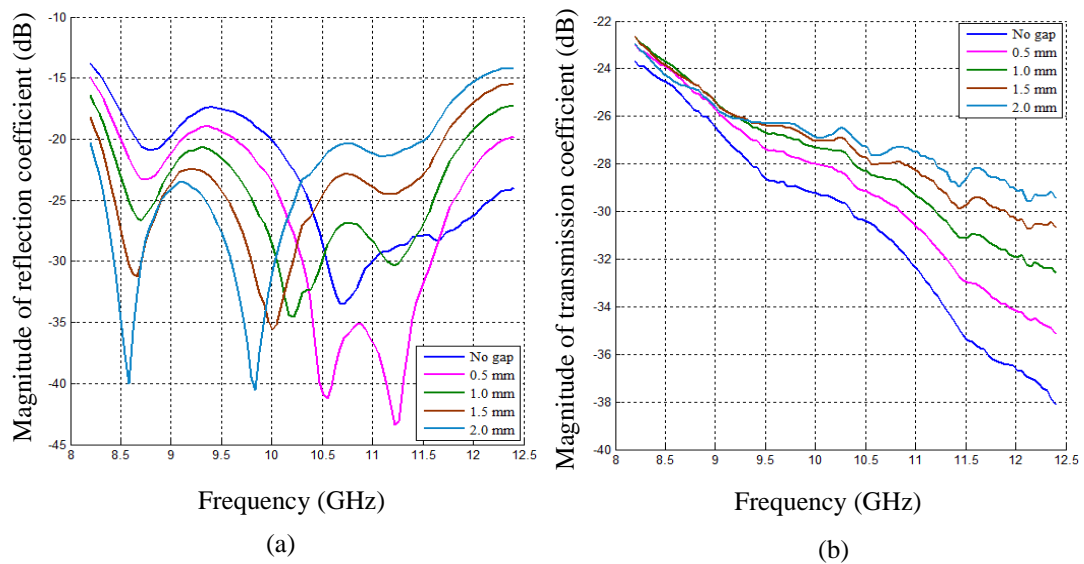Figure 7.22: Measured average magnitude of (a) reflection and (b) transmission coefficient vs. frequency at different gap values between dry concrete specimen and 10-mm thick acrylic layer.
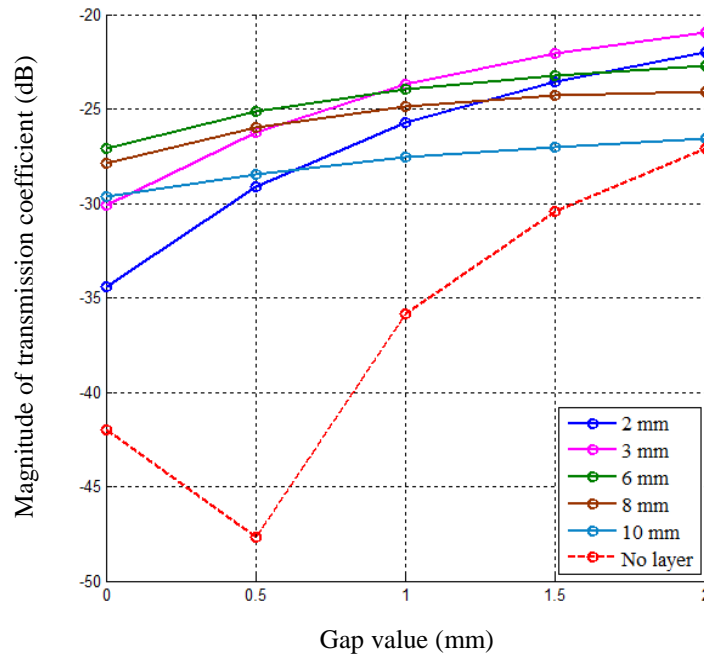
Figure 7.23: Average measured magnitude of transmission coefficient vs. gap value between dry concrete and dielectric layer with different thicknesses at 10.3 GHz ("No layer" curve is shown for comparison).

7.7   Comparison of Measurement and Simulation Results

The results of comparison between measurement and simulation transmission coefficients obtained in previous sections 7.4 – 7.6 using the DWS with tapered dielectric insertions with and without dielectric layer at 10.3 GHz are presented here. The measurement results were obtained with insertion dimensions of $d_1 = 10$ mm and $d_2 = 35$ mm, while simulations are performed at different values of d_1 and d_2.

Figure 7.24 shows the measured and simulated magnitude of transmission coefficient vs. gap value between dry concrete specimen and metal plate using the proposed DWS with tapered dielectric insertion at a frequency of 10.3 GHz. It is clearly seen that the behaviour of both the measured and simulated magnitudes of transmission coefficient is similar; however, there are about differences between their values, which can be attributed to measurement errors.

Figure 7.25 illustrates the measured and simulated magnitude of transmission coefficient vs. gap value between the concrete specimen and dielectric layer of the

DWS with 2-mm and 3-mm thick dielectric layer at 10.3 GHz. It is seen from Figure 7.25 that again the measured and simulated results demonstrate similar behaviour and trends. However, there is a difference between their values which is constant (~2 dB) at 3-mm thickness while it increases from 1 dB to 2.25 dB at 2-mm thickness when gap value increases from 0 to 2 mm.

Overall, measured and simulated results demonstrated similar behaviour and trends when gap value changes. Differences between their values can be attributed to error of fabrication of dielectric insertions and measurement errors as well as a difference between the complex dielectric permittivity of acrylic provided in its specification, which was used in the simulation and the complex dielectric permittivity of acrylic used in the measurement.
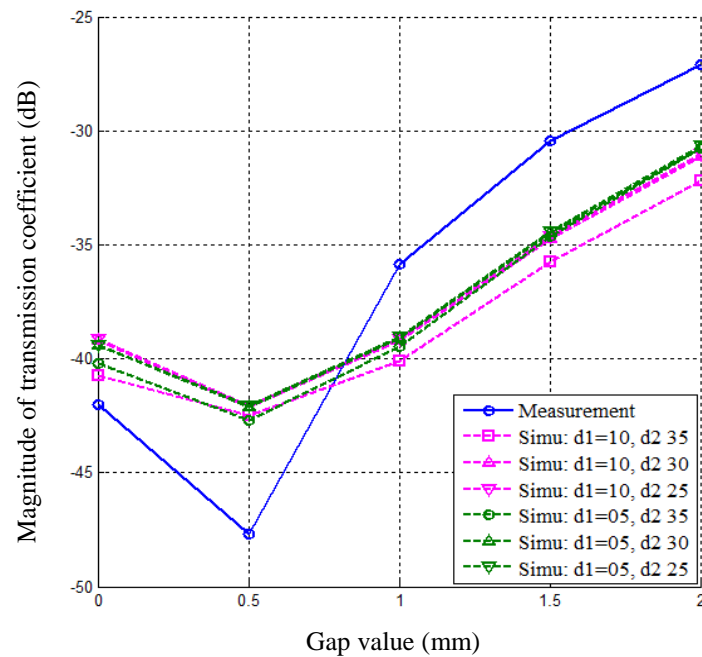
Figure 7.24: Measured and simulated magnitude of transmission coefficient vs. gap value between the concrete specimen and metal plate using the proposed DWS with tapered dielectric insertions and without dielectric layer at 10.3 GHz.
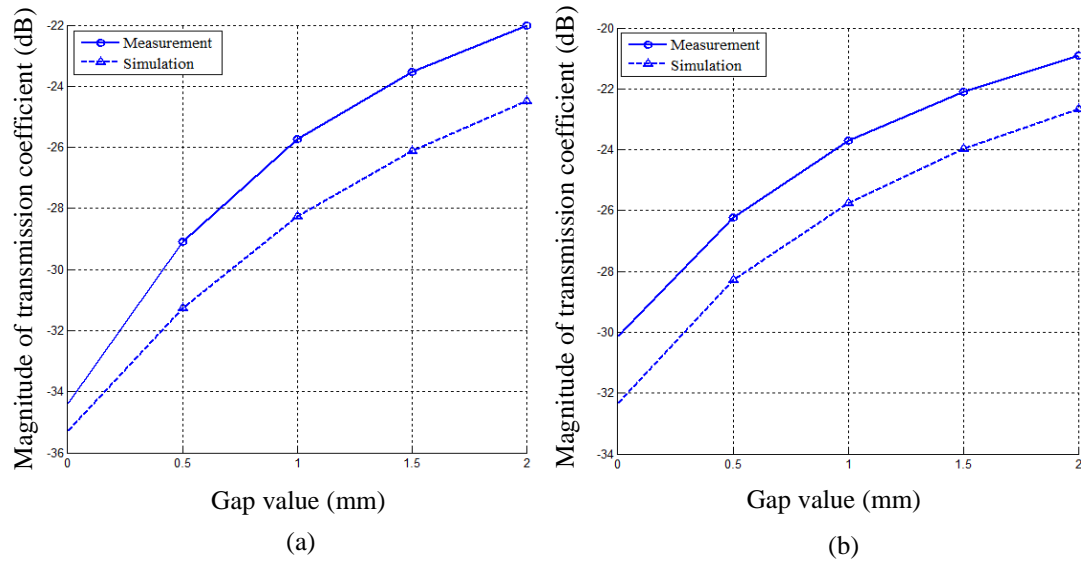
Figure 7.25: Measured and simulated magnitude of transmission coefficient vs. gap value between the concrete specimen and the dielectric layer using the proposed DWS with tapered dielectric insertion (d_1 = 10 mm and d_2 = 35 mm) and (a) 2-mm and (b) 3-mm thick dielectric layer at 10.3 GHz.

7.8   Electric Field Intensity Distributions

The electric field distribution inside the waveguide sections of the proposed DWSs, and concrete specimens at different gap conditions will be presented and analysed in this section.

Figures 7.26 and 7.27 show the cross-sectional views of simulated electric field intensity distribution (amplitude and phase) inside waveguides of DWS with tapered dielectric insertion, in the interface area and in dry concrete specimens for three values of gap; namely, 0 mm, 1 mm and 2 mm at a frequency of 10.3 GHz. Figures 7.26a and 7.27a show that waveguide 1 (W1) radiates microwaves through tapered dielectric insertions in dry concrete specimen and a part of these waves penetrates into another waveguide 2 (W2) through concrete at "no gap" condition. Figures 7.26b-c and 7.27b-c clearly show changes in the electric field intensity distribution at the interface between concrete and metal surfaces due to the gap, and in W2. Animated phase version of these distributions (not shown here) demonstrated the propagation of electromagnetic waves between metal and concrete surfaces (referred

to as guided waves) at 1.0 and 2.0 mm gap. These guided waves lead to losses in electromagnetic energy of the incident wave as well as the reflected wave. Another important observation from Figures 7.26b-c 7.27b-c is that a part of the guided wave and a part of the wave radiated by W1 in dry concrete penetrate into W2 and interfere there. It is also found that at 'no gap' condition, microwave signals are more focused inside the concrete specimen.

Figures 7.28 and 7.29 show the cross-sectional views of electric field intensity distributions (amplitude and phase) inside the waveguide sections (W1 and W2), 3-mm thick dielectric layer and dry concrete specimen at three gap values; namely 0, 1.0 and 2.0 mm between the dielectric layer and concrete specimen at 10.3 GHz. It can be seen from Figure 7.28a and 7.29a that waveguide 1 (W1) radiates electromagnetic wave in the dielectric layer and concrete specimen and a part of this wave penetrates into another waveguide 2 (W2) through the dielectric layer at "no gap" condition. Moreover, Figure 7.28b-c clearly show changes of the electric field intensity distribution inside the dielectric layer and W2 when the gap exists. The comparison of the electric field intensity distribution with and without dielectric layer (c.f. Figures 7.28, 7.29 and 7.26, 7.27) shows that the dielectric layer enhances the electric field intensity in W2 at all considered gaps. These results confirm observation made from the measured and simulated results related to the magnitude of transmission coefficients.

Amplitude　　　　**Phase**

(a) No gap between metal and dry concrete

(b) 1.0-mm gap between metal and dry concrete

(c) 2.0-mm gap between metal and dry concrete
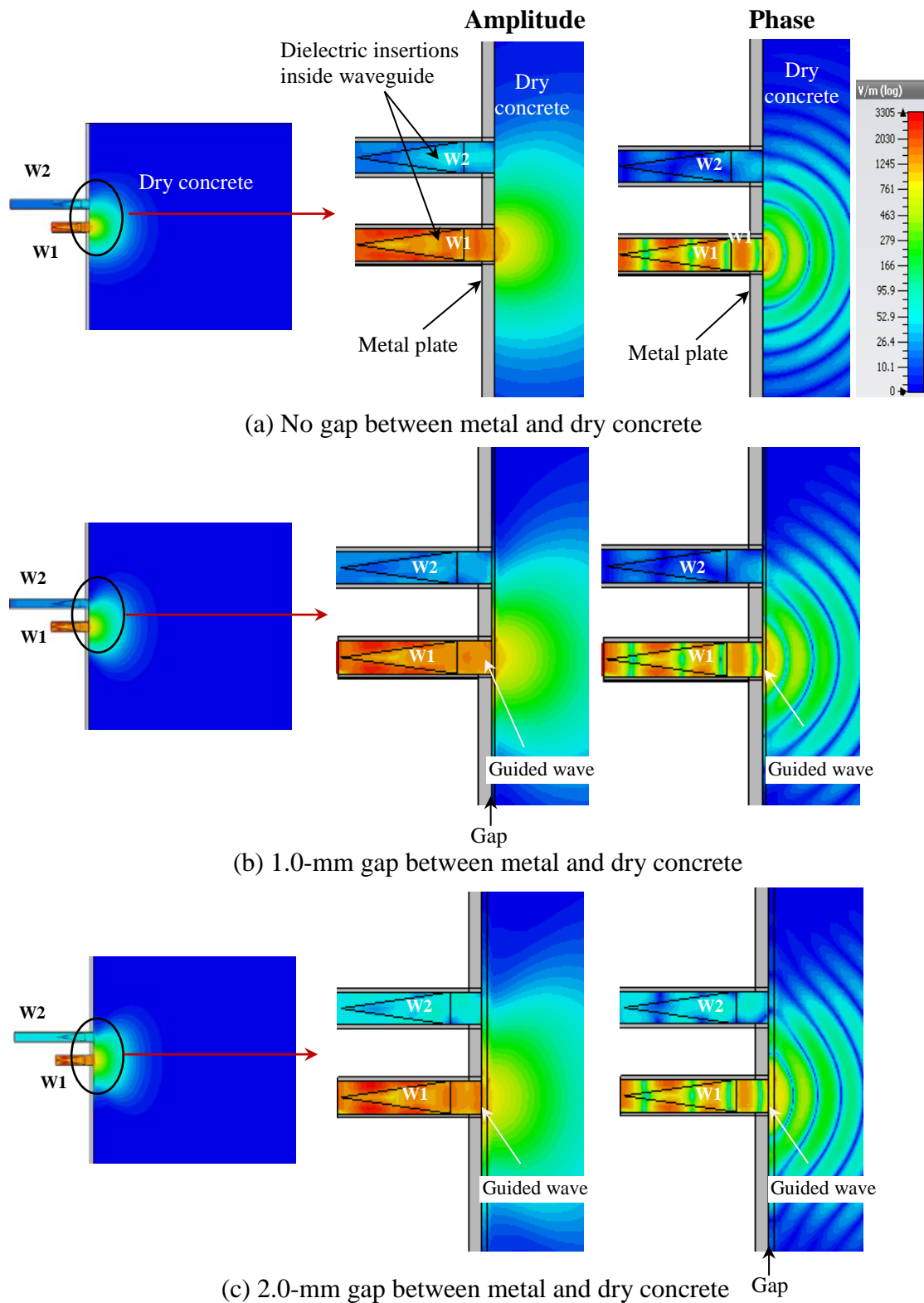
Figure 7.26: Cross-sectional side view of electric field intensity distribution inside waveguides of DWS with tapered dielectric insertion having $d_1 = 10$ mm and $d_2 = 35$ mm and dry concrete specimen ($\varepsilon_r = 4.1 - j\, 0.82$) for different gap conditions between surfaces of metal and specimen at 10.3 GHz (without dielectric layer).

Amplitude **Phase**

(a) No gap between metal and dry concrete

(b) 1.0-mm gap between metal and dry concrete

(c) 2.0-mm gap between metal and dry concrete
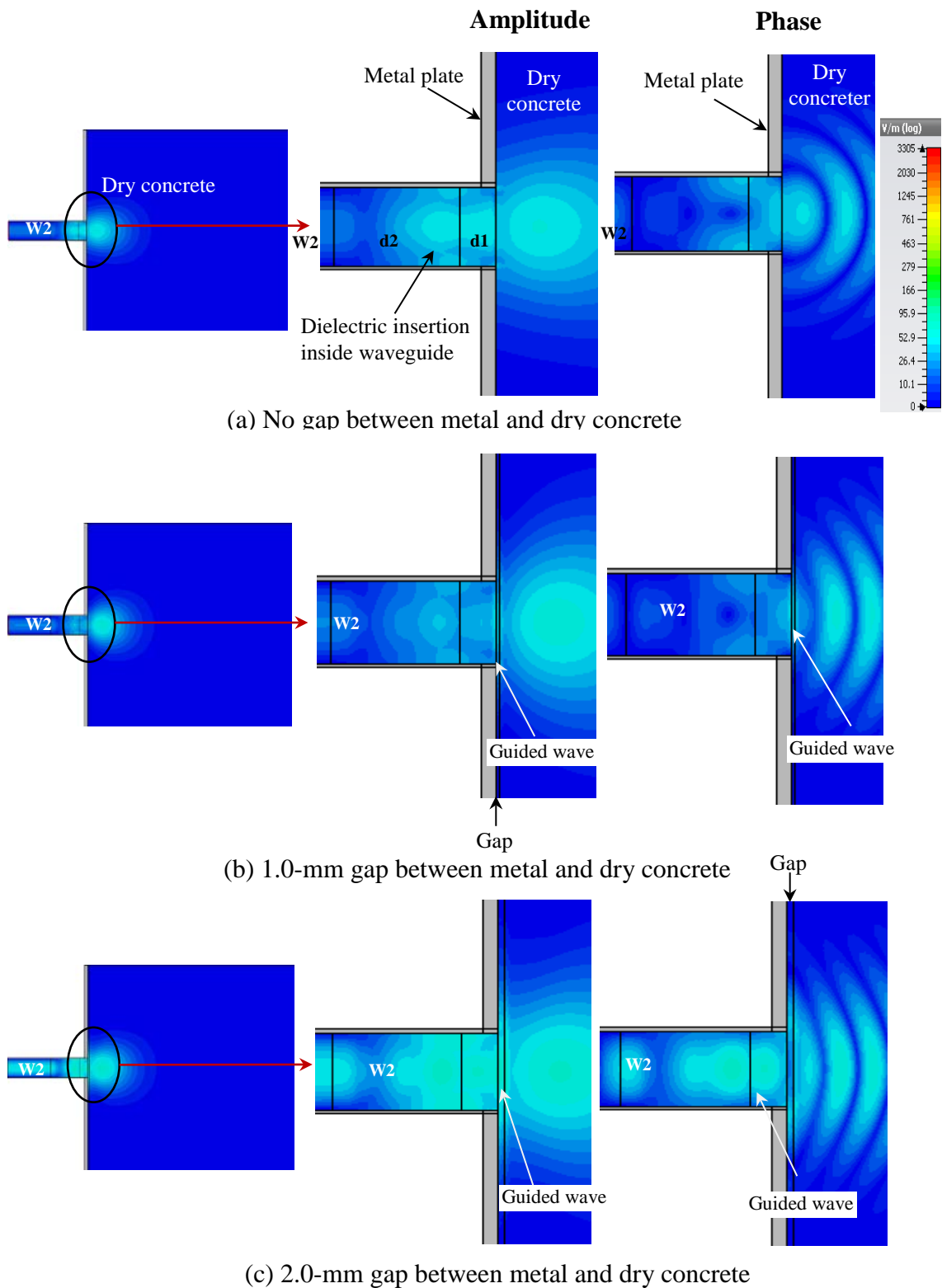
Figure 7.27: Cross-sectional top view of electric field intensity distribution inside waveguides of DWS with tapered dielectric insertions having $d_1 = 10$ mm and $d_2 = 35$ mm and dry concrete specimen ($\varepsilon_r = 4.1 - j\,0.82$) for different gap conditions between surfaces of metal and specimen at 10.3 GHz (without dielectric layer).

(a) No gap between metal and dielectric layer

(b) 1.0-mm gap between metal and dielectric layer

(c) 2.0-mm gap between metal and dielectric layer
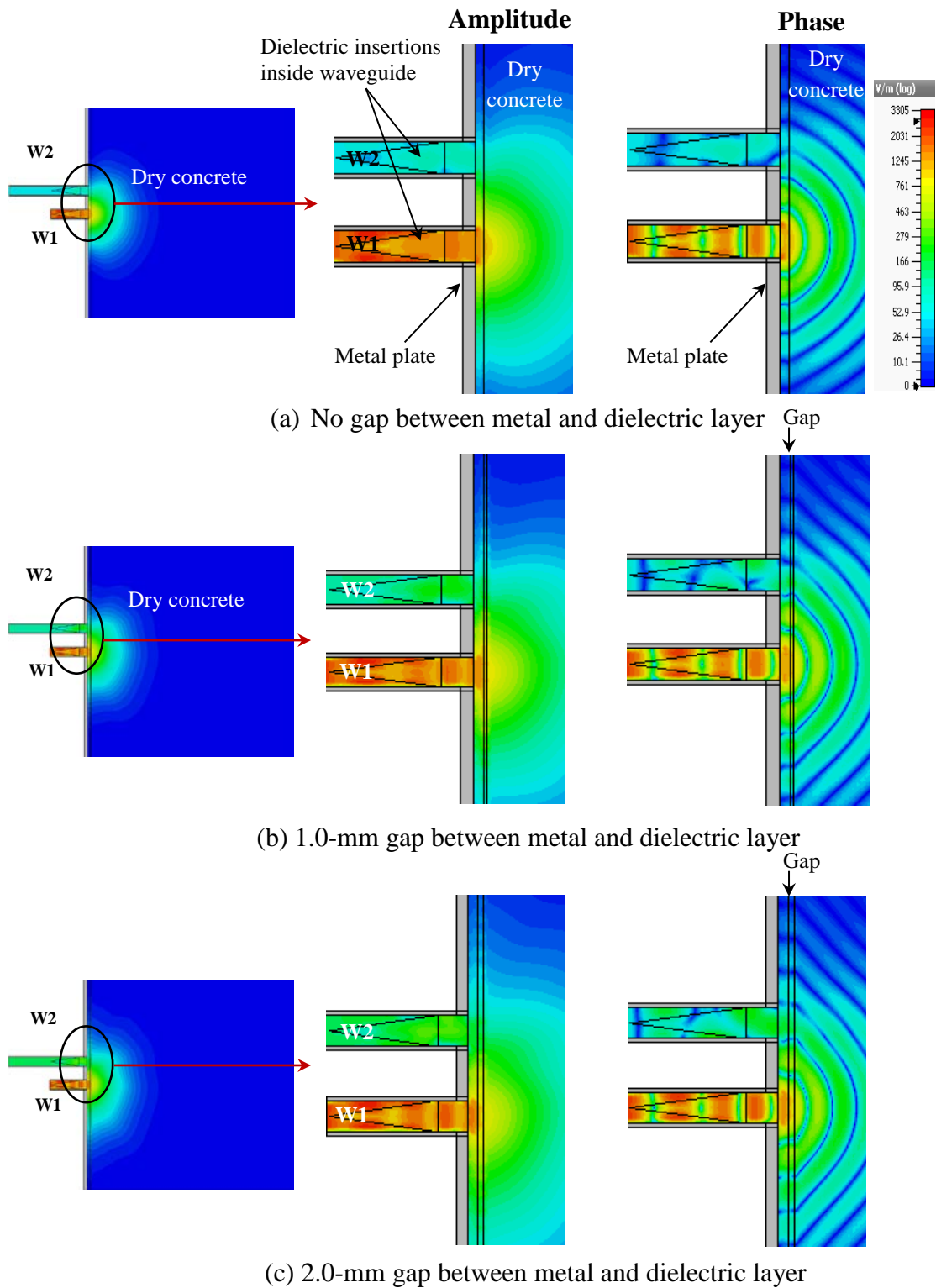
Figure 7.28: Cross-sectional side view of electric field intensity distribution inside the waveguides (W1 and W2), 3-mm thick dielectric layer attached with tapered dielectric-loaded DWS having $d_1 = 10$ mm and $d_2 = 35$ mm, and dry concrete ($\varepsilon_{rc} = 4.1 - j0.82$) specimen for three gap values at a frequency of 10.3 GHz (with dielectric layer).

(b) No gap between metal and dielectric layer

(b) 1.0-mm gap between metal and dielectric layer

(c) 2.0-mm gap between metal and dielectric layer
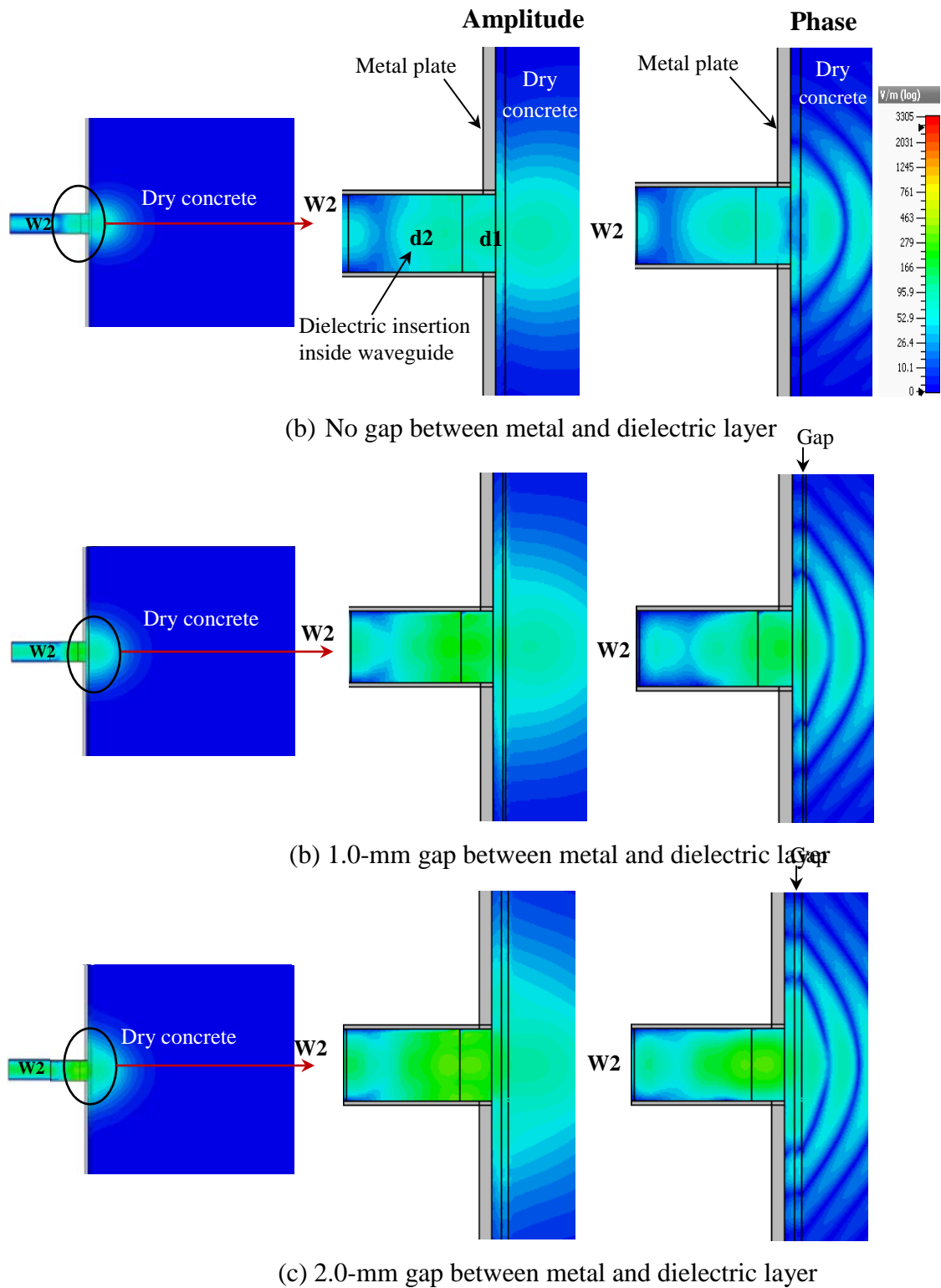
Figure 7.29: Cross-sectional top view of electric field intensity distribution inside waveguides of DWS with tapered dielectric insertions having $d_1 = 10$ mm and $d_2 = 35$ mm and dry concrete specimen ($\varepsilon_r = 4.1 - j\,0.82$) for different gap conditions between surfaces of metal and specimen at 10.3 GHz (with dielectric layer).

7.9 Summary

In this chapter, the design and modification of DWS with tapered dielectric insertions are proposed to reduce wave reflection from the insertions. Firstly, the proposed DWS was modelled with the concrete specimens, and parametric studies were performed with variable lengths of rectangular and taper part of the insertions. The DWS with optimized dimensions of the insertions made of acrylic was built and tested. Simulation and measurement results showed that that the resonant responses occurred at the magnitude of reflection coefficient curves. These resonant responses can be attributed to quarter-wavelength resonators formed in the dielectric-filled area by an open end at the tapered part and shorted part at the interface between the aperture and concrete. It was observed that the changes of gap value changed the values of magnitude of reflection coefficient as well as the resonant frequencies. In general, magnitude of reflection coefficient is < -10 dB that is significantly lower than in the DWS with rectangular dielectric insertions, i.e. a good matching between an empty part and a dielectric-filled part of the DWS with the tapered dielectric inserts is achieved. Furthermore, no resonant responses in the magnitude of transmission coefficient curves at all gap values and it did not depend on the dimensions of insertions. However, the magnitude of transmission coefficient non-monotonically increases when gap value increases from 0.5 mm to 2.0 mm over the entire operating frequency band. Compared to the results with the DWS with rectangular dielectric insertions the increase of 1dB - 2 dB was observed in the DWS with the tapered dielectric inserts. This increase is less than expected from the increase of the magnitude of reflection coefficient. These results showed that efficiency of transmission of waves from waveguide 1 to waveguide 2 mostly depends of the transformation of waveguide waves (the guided wave) into the guided wave (waveguide waves).

Secondly, a dielectric layer was inserted between the metal plate and concrete in the proposed DWS to increase wave transmission (i.e., coupling) between waveguide 1 and waveguide 2 of the DWS. It was shown that the insertion of the layer significantly increased the magnitude of transmission coefficient over an entire frequency band the highest magnitude is achieved at the layer thickness of 6 mm.

Moreover, the magnitude increased when gap value increased and the highest increase was achieved at the layer thickness of 2 mm. It was also shown that the magnitude of reflection coefficient at non-resonant frequencies was slightly higher than it was without layer. However, at the resonant frequency the relatively thin (2 mm and 3 mm) dielectric layer decreased significantly the magnitude of reflection coefficient at all gap values.

The results showed that the DWS with a dielectric layer can be used for the evaluation of gap value between the dielectric layer and concrete.

Chapter 8

Conclusions and Recommendations

8.1   Conclusions

Infrastructure health monitoring is becoming compulsory for all civil engineering structures mainly for safety and economic reasons, and therefore, there are high demands of advanced sensory techniques. Microwave sensory techniques have great advantages and potential for material characterization and quality assessment of concrete-metal composite materials, and monitoring of critical parts of infrastructure such as concrete-filled steel tubes. However, several practical drawbacks still exist in those techniques and need to be solved. One of them is the detection and monitoring of disbonding gap between concrete and metal surfaces. Another drawback is characterization of fresh and early-age concrete, which is very essential for initial quality assessment of concrete. In particular, lack of such data in the vicinity of the sensing area is very critical and it is required for modelling and simulation which are needed for the development and optimization of microwave sensors.

In this thesis, methodology for the determination of the complex dielectric permittivity of concrete at different stages of its life and four advanced microwave sensors for the detection and monitoring of small gaps in concrete-based composites were proposed. They were explicitly elaborated in Chapters 3-7, and the major investigations and outcomes can be summarised as follows:

In chapter 3, the methodology for the determination of the complex dielectric permittivity of concrete specimens from the measured and simulated magnitude of reflection coefficient using a single flanged open-ended waveguide sensor was developed and applied for early-age concrete specimens. The main challenging and limitation of this method were related to electromagnetic waves radiation by the sensor in free space and reflection and scattering of electromagnetic waves from boundaries and edges of the specimen under test. Therefore, the sensitivity of the magnitude of the reflection coefficient to the gap between the sensor aperture and the

specimen, changes in the sensor aperture position on the specimen surface, non-uniform dielectric permittivity distribution, and the effect of the size of the concrete specimen was numerically investigated. It was shown that small gaps between sensor and specimen up to 1.5 mm for R-band and 0.3 mm for X-band SWS did not have significant effects on the measured magnitude of the reflection coefficients. However, significant changes were observed for gaps larger than those, attributable to the influence of higher-order modes at the aperture. It was found that the magnitude of the reflection coefficient varied significantly when the sensor aperture locations approached and passed the edge of the concrete specimen. It was also shown that the influence of the non-uniform dielectric permittivity distributions in early-age concrete specimens was negligible.

The design, development and application of a novel microwave dual waveguide sensor for concrete-metal composite structures are presented **in chapter 4**. A parametric study of the proposed DWS with fresh concrete specimens performed in single waveguide mode and in dual waveguide mode showed that the dual waveguide mode of the proposed DWS may provide more measurement data than the single waveguide mode for characterising concrete-metal structures such as: (1) transmission properties of guided waves along the gap between the metal and concrete surfaces, (2) reflection properties of the metal–concrete interface at two different places at the same stage of concrete; and (3) data for a larger area of the interface under inspection. The DWS was fabricated and applied to measure small gaps between concrete specimens of different ages and a steel plate. The measured magnitude of reflection and transmission coefficients and simulation with CST were used to determine the dielectric permittivity of the fresh concrete specimen in the area of measurement using the modified algorithm. Comparisons between measured and simulated results showed a good agreement and clearly indicated capability of the proposed sensor for detection of a small debonding gap with improved accuracy. It was also shown that cracks in concrete filling can be detected using the magnitude and/or phase of transmission coefficient. Finally, the sensitivity of the magnitude of the reflection coefficient and transmission coefficient of the proposed DWS to variations in dielectric constant and loss tangent of concrete specimens, and the effects of surface roughness and were studied numerically. It was found that the

magnitude of the reflection (transmission) coefficient was most sensitive to changes of dielectric constant (loss tangent) of concrete specimens. These results showed that the measurement and analysis of both the reflection coefficient and the transmission coefficient can distinguish the effect of changes of gap size and dielectric properties of concrete. Application of this sensor in practice can be limited by possible penetration of water and/or concrete obstacles in the waveguide sections.

In chapter 5, the design and application of a dual waveguide sensor with rectangular dielectric insertions were presented. The main goal of this work was to improve the dual waveguide sensor for characterisation of concrete–metal structures at different stages of the concrete life, including its fresh stage. The sensor was designed, numerically investigated with concrete specimens, fabricated, and tested. It was shown that the dielectric insertions prevented water and concrete entering the waveguides, created the resonant responses, and allowed long-term monitoring of the concrete hydration, including the detection of the transition from fresh to hardened concrete (settling of concrete) on its first day. The proposed sensor was used for the determination of the complex dielectric permittivity of fresh and dry concrete specimens using measured data and extensive simulations with an improved algorithm. The measurement and simulation of the reflection and transmission properties of the sensor with concrete specimens for different gaps between concrete and metal plate were performed and it was clearly shown that the DWS measured 0.5 to 2.0 mm gaps. Comparison between measured and simulated results clearly showed that they were in good agreement. Furthermore, numerical investigation into the sensitivity of the reflection and transmission properties of the dielectric-loaded DWS to changes in the geometry and dielectric properties of the rectangular insertions showed that the magnitude of reflection coefficient at the resonant frequency and the resonant frequency itself are sensitive to changes in physical (geometrical) and electrical length of the insertions, whereas changes of magnitude of the transmission coefficient are relatively small.

In chapter 6 two modifications of the DWSs were made to increase matching between the waveguide section waves and the guided waves. They consisted of empty DWS and dielectric-loaded DWS with the attached dielectric layers. The

proposed DWSs with the dielectric layer of different thicknesses were designed, numerically investigated, built and applied for the determination of the complex dielectric permittivity of fresh and dry concrete as well as for the detection and monitoring of debonding gaps in concrete-metal composite structures of different ages. It was found that it can detect and measure the gap using the reflection and transmission coefficient data independently in the range of 0.5–2.0 mm with moderate accuracy. To detect gaps between dry concrete and the dielectric layer, the proposed empty DWS with a 6 mm-thick dielectric layer produced the best results, especially for gap values in the range of 0.0–0.5 mm over the entire X-band frequency range. The parametric studies were performed and measurements were conducted for the DWS with the rectangular insertions and the attached dielectric layer. It was shown that the measurement of the transmission coefficient using the proposed sensor with 2-mm or 3 mm-thick attached dielectric layer detect and monitor gaps between the dielectric layer and dry concrete very effectively, with good agreement between simulated and measured results. The modified DWSs can be applied to characterise fresh concrete in a mould with a plastic wall or on-line, and to investigate the shrinkage of different categories of concrete.

In chapter 7, the design and modifications of DWS with tapered dielectric insertions were proposed to reduce wave reflection from the insertions. After modelling and extensive simulations the proposed DWS with optimized dimensions of the insertions was built and tested. Simulation and measurement results showed that that the resonant responses occurred at the magnitude of reflection coefficient curves can be attributed to quarter-wavelength resonators formed in the dielectric-filled area by an open end at the tapered part and shorted part at the interface between the aperture and concrete. It was observed that the changes of gap value changed the values of magnitude of reflection coefficient as well as the resonant frequencies. In general, magnitude of reflection coefficient is less than -10 dB that is significantly lower than in the DWS with rectangular dielectric insertions, i.e. a good matching between an empty part and a dielectric-filled part of the DWS with the tapered dielectric inserts is achieved. Furthermore, no resonant responses in the magnitude of transmission coefficient curves were observed and the magnitude of transmission coefficient increased non-monotonically when gap value increases from

0.5 mm to 2.0 mm over the entire operating frequency band. Compared to the results with the DWS with rectangular dielectric insertions the increase of 1dB - 2 dB was observed in the DWS with the tapered dielectric inserts. These results showed that efficiency of transmission of waves from waveguide 1 to waveguide 2 mostly depends of the transformation of waveguide waves (the guided wave) into the guided wave (waveguide waves). Therefore, a dielectric layer was inserted between the metal plate and concrete in the proposed DWS to increase wave transmission (i.e., coupling) between waveguide 1 and waveguide 2 of the DWS. It was shown that the insertion of the layer significantly increased the magnitude of transmission coefficient over an entire frequency band and the highest magnitude is achieved at the layer thickness of 6 mm. The results showed that the DWS with a dielectric layer can be used for the evaluation of gap value between the dielectric layer and concrete.

8.2   Recommendations for Future Research

In this thesis, methodology for characterization of concrete and four novel microwave dual waveguide sensors were proposed to solve problems of a single microwave waveguide sensor for infrastructure health monitoring application. Although the results are promising, several remaining issues can still be addressed in the future research plan as follows:

- In this thesis the developed methodology for the determination of the complex dielectric permittivity of concrete was developed and applied for a flanged open-ended waveguide sensor and the proposed dual waveguide sensors. Simulated data were obtained with a computational tool CST Microwave studio, which provided a full electromagnetic formulation of the problem. However, in spite of relative simplicity of the sensors, some limitation may occur due to limited accuracy of mesh setting, boundary conditions, etc. It would be interesting and useful to perform a strict analytical consideration and numerical investigation into the proposed sensors with concrete specimens, and compare the results with the results of this thesis.

- In chapters 5-7 the DWSs with dielectric insertions and dielectric layers were presented. To provide experimental verification of the simulation results only acrylic was used as a dielectric material. However, there are numerous suitable materials with different dielectric and physical properties which can increase coupling between the waveguide through the guided waves (i.e., gaps) and as a result, the sensitivity to disbonding gap will be increased. Therefore, it is important to investigate the proposed sensors with other materials.

- In this thesis, for all the proposed microwave sensors, measurements were conducted using the performance network analyser which is bulky and expensive device, and microwave cables. On the other hand, it was shown in the thesis that only magnitude of reflection or transmission coefficient can be used for desired measurements. It means that a relatively simple measurement unit as a transceiver can be designed and attached to the sensor. Furthermore, wireless link instead of the cables can be created between the transceiver and wireless node or base station.

- The proposed DWSs with attached dielectric layer showed improved performance. It could not be applied for characterization of concrete-metal structures such as concrete-filled steel tubes. However, a comprehensive research can be conducted to design and apply a measurement unit consisting of the proposed microwave DWS and a dielectric mould made of low loss materials such as acrylic or ceramic for the quick and high-accuracy characterization of the fresh concrete in construction sites.

References

[1] E. Ellobody and B. Young, "Design and behaviour of concrete-filled cold-formed stainless steel tube columns," *Engineering Structures,* vol. 28, no. 5, pp.716–728, Apr. 2006.

[2] B. Uy, "Stability and ductility of high performance steel sections with concrete infill," *Journal of Constructional Steel Research*, vol. 64, No. 7-8, pp. 748–754, Jul-Aug. 2008.

[3] Z. Tao, B. Uy, L. H. Han, and Z. B. Wang, "Analysis and design of concretefilled stiffened thin-walled steel tubular columns under axial compression," *Thin-Walled Structures*, vol. 47, no. 12, pp. 1544–1556, Jan. 2009.

[4] Z. Tao, B. Uy, and L.H. Han, "Nonlinear analysis of concrete-filled square stainless steel stub columns under axial compression," *Journal of Constructional Steel Research,* Vol. 67, no. 11, pp.1719-1732, Nov. 2011

[5] F. Y. Liao, L. H. Han, and S. H. He, "Behaviour of CFST short colunm and beam with initial concrete imperfection: Experiments," *Journal of Constructional Steel Research*, vol. 67, no. 12, pp. 1922–1935, Dec. 2011.

[6] J. Q. Xue, B. Briseghella, and B. C Chen, "Effects of debonding on circular CFST stub columns," *Journal of Constructional Steel Research,* vol. 69, no. 1, pp. 64–76, Feb. 2012.

[7] W.B. Na and T. Kundu, "EMAT-based Inspection of concrete-filled steel pipes for internal voids and inclusions," *ASME J. Pressure Vessel Technol.*, vol. 124, no. 3, pp. 265-272, Aug. 2002.

[8] B. Xu, T. Zhang, G. Song and H. Gu, "Active interface debonding detection of a concrete-filled steel tube with piezoelectric technologies using wavelet packet analysis," *Mechanical Systems and Signal Processing*, vol. 36, no. 1, pp. 7–17, March 2013.

[9] X.Q. Zhu, H. Hao, K.Q. Fan, "Detection of delamination between steel bars and concrete using embedded piezoelectric actuators/sensors," *Journal of Civil Structural Health Monitoring,* vol. 3, no. 2, pp. 105-115, May 2013.

[10] S. Kharkovsky and Z. Tao, "Measurement and monitoring of gap in concrete-metal structures using microwave sensor technologies," *in Proc IEEE Intern. Instrum.Meas. Technology Conference (I2MTC 2012)*, Graz, Austria, 13 –16 May, 2012, pp. 2440-2443.

[11] H.C Rhim and O. Büyüköztürk, "Electromagnetic properties of concrete at microwave frequency range," *ACI Materials Journal,* vol. 95, no. 3, pp. 262-271, May-June 1998.

[12] K.J. Bois, A.D. Benally and R. Zoughi, "Microwave near-field reflection property analysis of concrete for material content determination," *IEEE Trans. Instrum. Meas*, vol. 49, no. 1, pp. 49–55, Feb. 2000.

[13] S. N. Kharkovsky, M. F. Akay, U. C. Hasar, and C. D. Atis, "Measurement and monitoring of microwave reflection and transmission properties of cement-based specimens," *IEEE Trans. Instrum. Meas.,*vol. 51, no. 6, pp. 1210–1218, Dec. 2002.

[14] K. L. Chung, and S. Kharkovsky, "Monitoring of microwave properties of Early-age concrete and mortar specimens," *IEEE Trans. Instrum. Meas.*, vol. 64, no. 5, pp. 1196–1203, May 2015.

[15] A. Cataldo, E. D. Benedetto and G. Cannazza, "Hydration monitoring and moisture control of cement-based samples through embedded wire-like sensing elements," *IEEE Sensors J.,* vol. 15, no. 2, pp. 1208–1215, Feb. 2015.

[16] S. Kharkovsky, A. C. Ryley, V. Stephen, and R. Zoughi, "Dual-polarized near-field microwave reflectometer for noninvasive inspection of carbon fiber reinforced polymer-strengthened structures," *IEEE Trans. Instrum. Meas.*, vol. 57, no. 1, pp. 168–175, Jan. 2008.

[17] J. Nadakuduti, G. Chen, and R. Zoughi, "Semiempirical electromagnetic modeling of crack detection and sizing in cement-based materials using near-field microwave methods." *IEEE Trans. Instrum. Meas.*, vol. 55, no. 2, pp. 588–597, Apr. 2006.

[18] G. Roqueta, L. Jofre and M.Q Feng, "Analysis of the electromagnetic signature of reinforced concrete structures for nondestructive evaluation of corrosion damage," *IEEE Trans. Instrum. Meas.*, vol. 61, no. 4, pp. 1090–1098, Apr. 2012.

[19] S. Kharkovsky, P. Giri and B. Samali, "Non-contact inspection of construction materials using 3-axis multifunctional imaging system with microwave and laser sensing techniques," *IEEE Instrum. Meas. Mag.*, vol 19, no. 2, pp. 6 – 12, Apr 2016.

[20] B. Ozbey, H. V. Demir, O. Kurc, V. B. Ertürk and A. Altintas, "Wireless sensing in complex electromagnetic media: construction materials and structural monitoring," *IEEE Sensors J.,* vol. 15, no. 10, pp. 5545–5554, Oct. 2015.

[21] K. Y. Lee, B. K. Chung, K. Y. You, E. M. Cheng and Z. Abbas, "Study of dual open ended coaxial sensor system for calculation of phase using two magnitudes," *IEEE Sensors J.,* vol. 14, no. 1, pp. 129–134, Jan. 2014.

[22] M. W. Hyde, M. J. Havrilla, A. E. Bogle and E. J. Rothwell, "Nondestructive material characterization of a free-space-backed magnetic material using a dual-waveguide probe," *IEEE Trans. Antennas Propag.,* vol. 60, no. 2, pp. 1009–1019, Feb. 2012.

[23] M. A. Islam and S. Kharkovsky, "Advanced microwave sensors for the detection of gap in concrete-filled steel tubes," *in Proc. Third International Conference on Smart Monitoring, Assessment and Rehabilitation of Civil Structures (SMAR 2015)*, Sept 9-11, 2015, Antalya, Turkey, 8 pages.

[24] M. A. Islam, S. Kharkovsky and K. Chung, "Microwave reflection properties of early-age concrete specimens: Sensitivity analysis," *in Proc. IEEE Intern. Instrum. Meas. Techn. Conf. (I2MTC 2015)*, pp. 920-924, May 11-14, 2015, Pisa, Italy.

[25] *CST Microwave Studio Software*, *Computer Simulation Technology*, accessed on Mar. 2014. [Online]. Available: http:// www.cst.com.

[26] M. A. Islam and S. Kharkovsky, "Microwave dual waveguide sensor system for the measurement of gap between concrete and metal surfaces", *in Proc.*

IEEE Intern. Instrum. Meas. Techn. Conf. (I2MTC 2016), pp. 557-562, May 23-26, 2016, Taipei, Taiwan.

[27]   L. H. Han, Y. Ye, and F. Y. Liao, "Effects of core concrete initial imperfection on performance of eccentrically loaded CFST columns," *Journal of Structural Engineering*, vol. 142, no. 12, pp. 04016132-1–13, Dec. 2016.

[28]   C. R. Farrar, and K. Worden, "An introduction to structural health monitoring," *Phil. Trans. R. Soc. A: Math. Phys. & Eng. Sci.,* vol. 365, pp. 303 – 315, Feb. 2007.

[29]   D. Balageas, C. P. Fritzen, and A. Güemes, *Structural health monitoring,* 1st ed. London: ISTE Ltd, 2006.

[30]   D. Huston, *Structural sensing, health monitoring, and performance evaluation,* 1st ed. New York: Taylor & Francis Inc, 2010.

[31]   Brownjohn, J. M. (2007). Structural health monitoring of civil infrastructure. *Phil. Trans. R. Soc. A: Math. Phys. & Eng. Sci.,* vol. 365, pp. 589 – 622, Feb. 2007.

[32]   M. M. Ettouney, and S.Alampalli, *Infrastructure health in civil engineering: theory and components,* Bosa Roca: Taylor & Francis Inc, 2011.

[33]   Y. Liu, and S. Nayak, "Structural health monitoring: state of the art and perspectives,", *J. of The Minerals, Metals & Materials Society,* vol. 64, no. 7, pp. 789 – 792, Jul.2012.

[34]   V. M. Karbhari, and F. Ansari, *Structural health monitoring of civil infrastructure systems,* 1st ed. Woodhead Publishing, 2009.

[35]   H. T. Chan, and D. P. Thambiratnam, *Structural Health Monitoring in Australia*, New York: Nova Science Publishers, 2011.

[36]   P. C. Chang, A. Flatau, and S. C. Liu, "Review paper: health monitoring of civil infrastructure," *Structural Health Monitoring,* vol. 2, no. 3, pp. 257 – 266, Sep. 2003.

[37]   A. Raghavan, and C. E. S. Cesnik, "Review of guided-wave structural health monitoring," *The Shock and Vibration Digest*, vol. 39, no. 2, pp. 91 – 114, Mar. 2007.

[38] H. A. Sodano, "Development of an Automated Eddy Current Structural Health Monitoring Technique with an Extended Sensing Region for Corrosion Detection," *Structural Health Monitoring,* vol. 6, no. 2, pp. 111 – 119, Jun. 2007.

[39] S. C. Mukhopadhyay, *New developments in sensing technology for structural health monitoring.* Berlin:Springer, 2011.

[40] M. L. Wang, J. P. Lynch, and H. Sohn, *Sensor technologies for civil infrastructures: sensing hardware and data collection methods for performance assessment.* Cambridge:Woodhead publishing, 2014.

[41] J. H. Thomsen IV, and J. W. Wallace, "Displacement-based design of slender reinforced concrete structural walls – experimental verification," *Journal of Structural Engineering,* vol. 130, no. 4, pp. 618 – 630, Apr. 2004.

[42] J. Li, H. Hao, K. Fan, and J. Brownjohn, "Development and application of a relative displacement sensor for structural health monitoring of composite bridges," *Struct. Control Health Monit.* vol. 22, no. 4, pp. 726 – 742, Apr. 2015.

[43] D. Feng, M. Q. Feng, E. Ozer, and Y. Fukuda, "A vision-based sensor for noncontact structural displacement measurement," *Sensors* vol. 15, pp. 16557– 16575, 2015.

[44] P. Kohut, K. Holak, T. Uhl, Ł. Ortyl, T. Owerko, P. Kuras, and R. Kocierz, "Monitoring of a civil structure's state based on noncontact measurement," *Structural Health Monitoring,* vol. 12, no. 5-6, pp. 411 – 429, May. 2013.

[45] T. Yi, H. Li, and M. Gu, "Recent research and applications of GPS-based monitoring technology for high-rise structures," *Structural Control and Health Monitoring* vol. 20, no. 5, pp. 649 – 670, May. 2013.

[46] Y. Fukuda, M. Q. Feng, M. Shinozuka, "Cost-Effective vision-based system for monitoring dynamic response of civil engineering structures," *Struct. Control Health Monit.* vol. 17, no. 8, pp. 918 – 936, Dec. 2010.

[47] H. H. Nassif, M. Gindy, and J. Davis, "Comparison of laser Doppler vibrometer with contact sensors for monitoring bridge deflection and vibration," *NDT & E international* vol. 38, no. 3, pp. 213 – 218, Apr. 2005.

[48] D. Ribeiro, R. Calçada, J. Ferreira, T. Martins, "Non-contact measurement of the dynamic displacement of railway bridges using an advanced video-based system," *Eng. Struct.* vol. 75, pp. 164 – 180, 2014.

[49] C. Gentile, and G. Bernardini, "An interferometric radar for non-contact measurement of deflections on civil engineering structures: Laboratory and full-scale tests," *Struct. Infrastruct. Eng.* vol. 6, no. 5, pp. 521 – 534, 2010.

[50] G. Bartoli, L. Facchini, M. Pieraccini, M. Fratini, and C. Atzeni, "Experimental utilization of interferometric radar techniques for structural monitoring," *Structural Control and Health Monitoring,* vol. 15, no. 3, pp. 283 – 298, Apr. 2008.

[51] L. H. Han, Y. Ye, and F. Y. Liao, "Effects of Core Concrete Initial Imperfection on Performance of Eccentrically Loaded CFST Columns," *Journal of Structural Engineering,* vol. 142, no. 12, Dec. 2016.

[52] J. Fraden, *Handbook of modern sensors: physics, designs, and applications,* 4th ed. London: Springer, 2010.

[53] W. Boyes, *Instrumentation reference book,* Boston: Elsevier Science, 2010.

[54] H. M. Lee, J. M. Kim, K. Sho, and H. S. Park, "A wireless vibrating wire sensor node for continuous structural health monitoring", *Smart Mater. Struct.,* vol. 19, no. 5, Mar. 2010.

[55] S. A. Neild, M. s. Williams, and P. D. McFadden, "Development of a vibrating wire strain gauge for measuring small strains in concrete Beams," *Strain,* vol. 41, no. 1, pp. 3 – 9, Feb. 2005.

[56] H. S. Park, H. Y. Lee, S. W. Choi, and Y. Kim, "A practical monitoring system for the structural safety of mega-trusses using wireless vibrating wire strain gauges," *Sensors,* vol. 13, no. 12, pp. 17346 – 17361, Dec. 2013.

[57] E. Udd, *Fiber optic smart structures*, New York: John Wiley & Sons Inc., 1995.

[58] K. T. V. Grattan, and T. Sun, "Fiber optic sensor technology: an overview," *Sensors and Actuators, A: Physical*, vol. 82, no. 1, pp. 40–61, 2000.

[59] L. Deng, and C. S. Cai, "Applications of fiber optic sensors in civil engineering," *Structural Engineering and Mechanics*, vol. 25, no. 5, pp. 577–596, 2007.

[60] F. Ansari, "State-of-the-art in the applications of fiber-optic sensors to cementitious composites," *Cement and Concrete Composites*, vol. 19, no. 1, pp. 3–19, 1997.

[61] F. Ansari, "Practical Implementation of Optical Fiber Sensors in Civil Structural Health Monitoring," *Journal of Intelligent Material Systems and Structures,* vol. 18, no. 8, pp. 879 – 889, Aug. 2007.

[62] H. N. Li, D. S. Li, and G. B. Song, "Recent applications of fiber optic sensors to health monitoring in civil engineering," *Engineering Structures,* vol. 26, no. 11, pp. 1647–1657, Sep. 2004.

[63] X. W. Ye, Y. H. Su, and J. P. Han, "Structural health monitoring of civil infrastructure using optical fiber sensing technology: a comprehensive review," *The Scientific World Journal,* vol. 2014, Article ID 652329, 11 pages, 2014.

[64] M. Sun, W. J. Staszewski, and R. N. Swamy, "Smart sensing technologies for structural health monitoring of civil engineering structures," *Advances in Civil Engineering,* vol. 2010, Article ID 724962, 13 pages, 2010.

[65] J. M. L´opez-Higuera, L. R. Cobo, A. Q. Incera, and A. Cobo "Fiber optic sensors in structural health monitoring," *Journal of Lightwave Technology*, vol. 29, no. 4, pp. 587–608, 2011.

[66] C. I. Merzbacher, A. D. Kersey, and E. J. Friebele, "Fiber optic sensors in concrete structures: a review," *Smart Materials and Structures*, vol. 5, no. 2, pp. 196–208, 1996.

[67] H. Murayama, K. Kageyama, K. Uzawa, K. Ohara, and H. Igawa, "Strain monitoring of a single-lap joint with embedded fiber optic distributed sensors," *Structural Health Monitoring*, vol. 11, no. 3, pp. 325–344, 2011.

[68] C. Rodrigues, F. Cavadas, C. F´elix, and J. Figueiras, "FBG based strain monitoring in the rehabilitation of a centenary metallic bridge," *Engineering Structures*, vol. 44, pp. 281–290, 2012.

[69] C. Barbosa, N. Costa, L. A. Ferreira et al., "Weldable fibre Bragg grating sensors for steel bridge monitoring," *Measurement Science and Technology*, vol. 19, no. 12, Article ID 125305, 2008.

[70] F. Bastianini, M. Corradi, A. Borri, and A. D. Tommaso, "Retrofit and monitoring of an historical building using "smart" CFRP with embedded fibre optic Brillouin sensors," *Construction and Building Materials*, vol. 19, no. 7, pp. 525–535, 2005.

[71] D. S. Li, L. Ren, H. N. Li, and G. B. Song, "Structural health monitoring of a tall building during construction with fiber Bragg grating sensors," *International Journal of Distributed Sensor Networks*, vol. 2012, Article ID 272190, 10 pages, 2012.

[72] B. Glisic and Y. Yao, "Fiber optic method for health assessment of pipelines subjected to earthquake-induced ground movement," *Structural Health Monitoring*, vol. 11, no. 6, pp. 696–711, 2012.

[73] X. W. Ye, Y. Q. Ni, and J. H. Yin, "Safety monitoring of railway tunnel construction using FBG sensing technology," *Advances in Structural Engineering*, vol. 16, no. 8, pp. 1401–1409, 2013.

[74] G. Song, H. Gu, and Y. L. Mo, "Smart aggregates: multi-functional sensors for concrete structures—a tutorial and a review," *Smart Mater. Struct.,* vol. 17, no. 3, Article ID 033001, pp. 17, Mar. 2008.

[75] Q. Kong, Q. Feng, and G. Song, "Water presence detection in a concrete crack using smart aggregates," *International Journal of Smart and Nano Materials,* vol. 6, no. 3, pp. 149 - 161, Sep. 2015.

[76] R. Ahmad, S. Banerjee, and T. Kundu, "Pipe wall damage detection in buried pipes using guided waves," *Journal of Pressure Vessel Technology,* vol. 131, no. 1, Article ID 011501, 2009.

[77] S. Yan, W. Sun, G. Song, H. Gu, L. S. Huo, B. Liu, and Y. G. Zhang, "Health monitoring of reinforced concrete shear walls using smart aggregates," *Smart Mater. Struct.,* vol. 18, no. 4, Article ID 047001, pp. 7, Mar. 2009.

[78] H. Gu, Y. Moslehy, D. Sanders, G. Song, and Y. L. Mo, "Multi-functional smart aggregate-based structural health monitoring of circular reinforced

concrete columns subjected to seismic excitations," *Smart Mater. Struct.,* vol. 19, no. 6, Article ID 065026, pp. 7, May. 2010.

[79] W. I. Liao, J. X. Wang, G. Song, H. Gu, C. Olmi, Y. L. Mo, K. C. Chang, and C. H. Lo, "Structural health monitoring of concrete columns subjected to seismic excitations using piezoceramic-based sensors," *Smart Mater. Struct.,* vol. 20, no. 12, Article ID 125015, pp. 10, Nov. 2011.

[80] J. Zhao, T. Bao, S. Chen, and T. Kundu, "Smart Aggregate-Piezoceramic Patch Combination for Health Monitoring of Concrete Structures," *Journal of Sensors,* vol. 2016, Article ID 3270916, 7 pages, 2016.

[81] J. Korvink, and O. Paul, "*MEMS: Micro-electro-mechanical systems; a practical guide to design, analysis, and applications.* Norwich: Andrew William Publishing Inc., 2006.

[82] E. Gaura, and R. Newman, *Smart MEMS and sensor systems*, London: Imperial College Press, 2006.

[83] A. Norris, M. Saafi, and P. Romine, "Temperature and moisture monitoring in concrete structures using embedded nanotechnology/microelectromechanical systems (MEMS) sensors," *Construction and Building Materials,* vol. 22, no. 2, pp. 111 – 120, Feb. 2008.

[84] D. J. Bell, T. J. Lu, N. A. Fleck, and S. M. Spearing, "MEMS actuators and sensors: observations on their performance and selection for purpose," *Journal of Micromechanics and Micro engineering*, vol. 15, no. 7, pp. S153 – S164, Jun. 2005.

[85] H. Ceylan, k. Gopalakrishnan, S. Kim, S., P. C. Taylor, M. Prokudin, and A. F. Buss, "Highway infrastructure health monitoring using micro-electromechanical sensors and systems (MEMS)," *Journal of Civil Engineering & Management,* vol. 19, no. Sup-1, pp. 188-201, Jan. 2014.

[86] Attoh-Okine, Transportation Research Circular No. E-C056: The future of MEMS in transportation infrastructure systems. *Washington DC: Transportation Research Board, National Research Council,* 2003.

[87] D. M. Pozar, *Microwave engineering.* Fourth ed. New York: John Wiley &

Sons, Inc., 2013.

[88]   F. T. Ulaby, E. Michielssen, and U. Ravaioli, *Fundamentals of applied electromagnetics*, 6th ed., Prentice Hall, 2010.

[89]   C. A. Balanis, *Advanced engineering electromagnetics*, 2nd ed., USA: Wiley, 2012.

[90]   S. R. Saunders, and A. Aragon-Zavala, *Antennas and Propagation for Wireless Communication Systems*, 2nd ed. London: John Willey & Sons, Ltd., 2007.

[91]   U. S Inan, and A. S Inan, *Electromagnetic waves*, 1st ed. Prentice Hall, 2000.

[92]   S. Kharkovsky and R. Zoughi, "Response of microwave dielectric-slab-loaded rectangular waveguide resonators to wall displacements," in *Proceedings of the Asia-Pacific Microwave Conference,* Melbourne, Victoria, 2011, pp. 155-158.

[93]   D. J. Thomson, D. Card, and G. E. Bridges, "RF cavity passive wireless sensors with time-domain gating-based interrogation for SHM of civil structures," *IEEE Sensors Journal*, vol. 9, no. 11, pp. 1430-1438, Nov. 2009.

[94]   S. Fericean, A. Hiller-Brod, A. D. Dorneich, and M. Fritton, "Microwave displacement sensor for hydraulic devices," *IEEE Sensors Journal*, vol. 13, no. 12, pp. 4682-4689, Dec. 2013.

[95]   J. Chuang, D. J. Thomson, and G. E. Bridges, "Embeddable wireless strain sensor based on resonant rf cavities," *Review of Scientific Instruments,* vol. 76, pp. 094703.1-7, July 2005.

[96]   U. Tata, H. Huang, R. L. Carter, and J. C. Chiao, "Exploiting a patch antenna for strain measurements," *Measurement Science and Technology,* vol. 20, Aricle ID 015201, 7 pp. Nov. 2009.

[97]   A. Daliri, A. Galehdar, W. S. T. Rowe, K. Ghorbani, and S. John, "Utilising micro strip patch antenna strain sensors for structural health monitoring," *Journal of Intelligent Material Systems and Structures*, vol.23, no. 2, pp. 169-182, Dec. 2011.

[98]   S. Popovics, *Concrete materials: properties, specifications, and testing,* 2nd ed. New Jersey: Noyes Publications, 1992.

[99] A. M. Neville, *Properties of concrete*, 5th ed., Harlow, United Kingdom: Pearson Education, 2012.

[100] M. Grantham, C. Majorana, and V. Salomoni, *Proceedings of the international Conference on Concrete solutions,* Padua, Italy, June 2009.

[101] D. Breysse, G. Klysz, X. Dérobert, C. Sirieix, and J. F. Lataste, "How to combine several non-destructive techniques for a better assessment of concrete structures," *Cement and Concrete Research,* vol.38, no. 6, pp. 783-793, June 2008.

[102] Q. Kong, S. Hou, Q. Ji, Y. L. Mo, and G. Song, "Very early age concrete hydration characterization monitoring using piezo ceramic based smart aggregates," *Smart Mater. Struct.,* vol. 22, no. 8, Article ID 085025, pp. 7, Jul. 2013.

[103] H. Gu, G. Song, H .Dhonde, Y. L. Mo, and S. Yan, "Concrete early-age strength monitoring using embedded piezoelectric transducers," *Smart Mater. Struct.,* vo. 15, no. 6, pp. 1837-1845, Nov. 2006.

[104] K. Chung, S. Kharkovsky, Q. Kong, and G. Song "Cure-state monitoring of concrete and mortar specimens using smart aggregates," in *Proceed. of Instrum. and Measur. Technology Conference (I2MTC),* Montevideo, Uruguay, 2014, 5 pages.

[105] K. J. Bois, A. D. Benally, P. S. Nowak, and R. Zoughi, "Cure-state monitoring and water-to-cement ratio determination of fresh Portland cement-based materials using near-field microwave techniques," *IEEE Trans. Instrum. Meas.,* vol. 47. no. 3, pp. 628-637, Jun.1998.

[106] H. M. A. Al-Mattarneh, D. K. Ghodgaonkar, W. M. B. W. A Majid, "Microwave sensing of moisture content in concrete using open-ended rectangular waveguide," *Subsurface Sensing Technologies and Applications,* vol. 2, no. 4, pp. 377-390, Oct. 2001.

[107] K. Chung, and S. Kharkovsky, "Measurements of microwave reflection properties of early-age concrete and mortar specimens," in *Proceed. of Instrum. and Measur. Technology Conference (I2MTC),* Montevideo, Uruguay, 2014, 6 pages.

[108] K. L. Chung, and S. Kharkovsky, "Monitoring of microwave properties of Early-age concrete and mortar specimens," *IEEE Trans. Instrum. Meas.*, vol. 64, no. 5, pp. 1196–1203, May 2015.

[109] S. Kharkovsky, M. F. Akay, U. C. Hasar, U. C., and C. D. Atis, "Measurement and monitoring of microwave reflection and transmission properties of cement-based specimens," *IEEE Trans. Instrum. Meas.,* vol. 51. no. 6, pp. 1210-1218, Dec. 2002.

[110] K. J. Bois, A. Benally, P. S. Nowak, and R. Zoughi, "Microwave nondestructive determination of sand-to-cement ratio in mortar," *Research in Nondestructive Evaluation,* vol. 9, no. 4, pp. 227-238, 1997.

[111] K. J. Bois, and R. Zoughi, "A decision process implementation for microwave near-field characterization of concrete constituent makeup," *Subsurface Sensing Technologies and Applications,* vol. 2, no. 4, pp. 363-376, Oct. 2001.

[112] K. J. Bois, A. Benally, and R. Zoughi, "Near-field microwave noninvasive determination of NaCl in mortar," *IEE Proc. Science, Measurement Technol. (Special Issue on Non-destructive Testing and Evaluation)*, vol. 148, no. 4, pp. 178–182, July 2001.

[113] R. H. Haddad, and I. L. Al-Qadi, "Characterization of portland cement concrete using electromagnetic waves over the microwave frequencies," *Cement and Concrete Research,* vol. 28, no. 10, pp. 1379-1391, Oct. 1998.

[114] R. Zoughi, S. D. Gray, and P. S. Nowak, "Microwave nondestructive estimation of cement paste compressive strength," *ACI Mater. J.*, vol. 92, no. 1, pp. 64–70, Jan. 1995.

[115] W. Shalaby, and R. Zoughi, "Microwave compressive strength estimation of cement paste using monopole probes," *Research in Nondestructive Evaluation,* vol. 7, no. 2-3, pp. 101-115, 1995.

[116] S. Peer, J. T. Case, E. Gallaher, K. E. Kurtis, and R. Zoughi, "Microwave reflection and dielectric properties of mortar subjected to compression force and cyclically exposed to water and sodium chloride solution," *IEEE Transactions on Instrumentation and Measurement,* vol. 52, no. 1, pp. 111-

118, Feb. 2003.

[117] S. Kwon, M. Q. Feng, T. Park, and U. Na, "An experimental study on evaluation of compressive strength in cement mortar using averaged electromagnetic properties," *International Journal of Concrete Structures and Materials,* vol.3, No.1, pp. 25-32, June 2009.

[118] S. Kwon, M. Q. Feng, and S. S. Park, "Characterization of electromagnetic properties for durability performance and saturation in hardened cement mortar," *NDT & E International,* vol. 43, no. 2, pp. 86-95, March. 2010.

[119] J. Baker-Jarvis, M. D. Janezic, P. D. Domich, and R. G. Geyer, "Analysis of an open-ended coaxial probe with lift-off for nondestructive testing," *IEEE Transactions on Instrumentation and Measurement,* vol. 43, no. 5, pp. 711-718, May. 1994.

[120] A. J. Bahr, *Microwave Nondestructive Testing Methods*, New York: Gordon and Breach Science Publishers, 1982.

[121] R. Zoughi, *Microwave Non-Destructive Testing and Evaluation.* The Netherlands: Kluwer, 2000.

[122] S. Kharkovsky and R. Zoughi, "Microwave and millimetre wave non-destructive testing and evaluation – overview and recent advances," *IEEE Instrumentation & Measurement Magazine,* vol. 10, no. 2, pp. 26-38, Apr. 2007.

[123] K. L. Rens, T. J. Wipf, and F. W. Klaiber, "Review of nondestructive evaluation techniques of civil infrastructure," *Journal of Performance of Constructed Facilities*, vol. 11, no. 4, pp. 152–160, 1997.

[124] N. Han, "Role of NDE in quality control during construction of concrete infrastructures on the basis of service life design," *Construction and Building Materials,* vol. 18, no. 3, pp. 163-172, April 2004.

[125] A. Jain, A. Kathuria, A. Kumar, K. Murari, "Combined use of non-destructive tests for assessment of strength of concrete in structure," *Procedia Engineering*, vol. 54, pp. 241-251, 2013.

[126] K. Arunachalam, V. R. Melapudi, L. Udpa, and S. S. Udpa, "Microwave NDT of cement-based materials using far-field reflection coefficients," *NDT & E International,* vol. 39, no. 7, pp. 585-593, Oct. 2006.

[127] J. M. Catalá-Civera, A. J. Canós, F. L, Peñaranda-Foix, and E. R. Davó, "Accurate determination of the complex permittivity of materials with transmission reflection measurements in partially filled rectangular waveguides," *IEEE Transactions on Microwave Theory and Techniques,* vol. 51, no. 1, pp. 16-24, Jan. 2003.

[128] C. A. Grosvenor, R. T. Johnk, J. Baker-Jarvis, M. D. Janezic, and B. Riddle, "Time-domain free-field measurements of the relative permittivity of building materials," *IEEE Transactions on Instrumentation and Measurement,* vol. 58 no. 7, pp. 2275-2282, July 2009.

[129] I. L. Al-Qadi, O. A. Hazim, W. Su, and S. Riad, "Dielectric properties of portland cement concrete at low radio frequencies," *Journal of Materials in Civil Engineering,* vol. 7, no. 3, pp. 192-198, 1995.

[130] J. Baker-Jarvis, R. G. Geyer, J. H. Grosvenor, Jr., M. D. Janezic, C. A. Jones, B. Riddle, and J. Krupka, "Dielectric characterization of low-loss materials a comparison of techniques," *IEEE Transactions on Dielectrics and Electrical Insulation,* vol. 5, no. 4, pp. 571-577, Aug. 1998.

[131] C. Lee, and C. Yang, "Thickness and permittivity measurement in multi-layered dielectric structures using complementary split-ring resonators," *IEEE Sensors J.,* vol. 14, no. 3, pp. 695-700, March. 2014.

[132] J. Baker-Jarvis, E. J. Vanzura, and W. A. Kissick, "Improved technique for determining complex permittivity with the transmission/reflection method," *IEEE Transactions on Microwave Theory and Techniques,* vol. 38, no. 8, pp. 1096-1103, Aug. 1990.

[133] M. D. Deshpande, C. J. Reddy, P. I. Tiemsin, and R. Cravey, "A new approach to estimate complex permittivity of dielectric materials at microwave frequencies using waveguide measurements," *IEEE Transactions on Microwave Theory and Techniques,* vol. 45, no. 3, pp. 359-366, March 1997.

[134] N. Jebbor, S. Bri, A. Nakheli, L. Bejjit, M. Haddad, and A. Mamouni, "Complex permittivity determination with the transmission/reflection method," *International Journal of Emerging Sciences,* vol. 1, no. 4, pp. 682-695, Dec. 2011.

[135] M. D. Belrhiti, S. Bri, A. Nakheli, and A. Mamouni, "Dielectric properties by rectangular waveguide," *International Journal of Emerging Sciences,* vol. 3, no. 2, pp. 163-171, Jun. 2013.

[136] B. Daout, M. Sallin and H. Wipf, "Measurment of complex permittivity of large concrete samples with an open-ended coaxial line," *Measurement Notes*; 10 January 2014.

[137] Z. Ma, and S. Okamura, "Permittivity determination using amplitudes of transmission and reflection coefficients at microwave frequency," *IEEE Transactions on Instrumentation and Measurement,* vol. 47, no. 5, pp. 546-550, May. 1999.

[138] O. Büyüköztürk, T. Y. Yu and J. A. Ortega, "A methodology for determining complex permittivity of construction materials based on transmission-only coherent, wide-bandwidth free-space measurements," *Cement and Concrete Composites*, vol. 28, pp. 349–359, 2006.

[139] X. Hui, L. Bangyu, X. Shaobo, and F. Hongzhuan, "The measurement of dielectric constant of the concrete using single-frequency cw radar," in *Procee. of First International Conference on Intelligent Networks and Intelligent Systems,* Whhan, China, pp. 588-591, Nov. 2008.

[140] M. Olkkonen, V. Mikhnev, E. Huuskonen-Snicker, "Complex Permittivity of Concrete in the Frequency Range 0.8 to 12 GHz," in *Proceed. Of 7th European Conference on Antennas and Propagation (EuCAP),* Sweden, 2013, pp. 3319-3321.

[141] M. Jamil, M. K. Hassan, H. M. A. Al-Mattarneh, M. F. M. Zain, "Concrete dielectric properties investigation using microwave nondestructive techniques," *Materials and Structures,* 46(1-2), 77-87, 2013.

[142] A. Robert, "Dielectric permittivity of concrete between 50 Mhz and 1 Ghz and GPR measurements for building materials evaluation," *Journal of Applied Geophysics,* vol. 40, no. 1–3, pp. 89-94, Oct. 1998.

[143] K. Y. You, and Y. L. Then, "Simple calibration and dielectric measurement technique for thin material using coaxial probe," *IEEE Sensors J.,*vol. 15, no. 10, pp. 5393-5397, Oct. 2015.

[144] M. C. Decreton, and F. E. Gardiol, "Simple nondestructive method for the measurement of complex permittivity," *IEEE Transactions on Instrumentation and Measurement,* vol. IM-23, no. 4, pp. 434-438, Dec. 1974.

[145] C. Chang, K. Chen, and J. Qian, "Nondestructive determination of electromagnetic parameters of dielectric materials at X-band frequencies using a waveguide probe system," *IEEE Trans. Instrum. Meas.*, vol. 46, no. 5, pp. 1084–1092, Oct. 1997.

[146] U. C. Hasar, "Permittivity determinatation of fresh cement-based materials by an open-ended waveguide probe using amplitude-only measurements,'' *Progress Electromag. Res.*, PIER 97, pp. 27--43, 2009.

[147] S. I. Ganchev, S. Bakhtiari, and R. Zoughi, "A novel numerical technique for dielectric measurement of generally lossy dielectrics," *IEEE Transactions on Instrumentation and Measurement,* vol. 41, no. 3, pp. 361-365, June. 1992.

[148] K. J. Bois, A. D. Benally, and R. Zoughi, "Multimode solution for the reflection properties of an open-ended rectangular waveguide radiating into a dielectric half-space: the forward and inverse Problems," *IEEE Transactions on Instrumentation and Measurement,* vol. 48, no. 6, pp. 1131-1140, Dec. 1999.

[149] D. Hughes, and R. Zoughi, "A method for evaluating the dielectric properties of composites using a combined embedded modulated scattering and near-field microwave nondestructive testing technique ", *in Proc. IEEE Intern. Instrum. Meas. Techn. Conf.*, pp. 1882-1886, May 21-23, 2001, Budapest, Hungary.

[150] D. Hughes and R. Zoughi, "A novel method for determination of dielectric properties of materials using a combined embedded modulated scattering and

near-field microwave techniques. Part I—Forward model," *IEEE Trans. Instrum. Meas* ., vol. 54, no. 6, pp. 2389–2397, Dec. 2005.

[151] D. Hughes and R. Zoughi, "A novel method for determination of dielectric properties of materials using a combined embedded modulated scattering and near-field microwave techniques. Part II—Dielectric property recalculation," *IEEE Trans. Instrum. Meas* ., vol. 54, no. 6, pp. 2398–2401, Dec. 2005.

[152] P. Juan-García and J. M. Torrents, "Measurement of mortar permittivity during setting using a coplanar waveguide," *Meas. Sci. Technol.*, vol. 21, no. 4, pp. 045702-1–045702-6, Mar. 2010.

[153] M. A. H. Ansari, A. k. Jha, and M. J. Akhtar, "Design and application of the CSRR-based planar sensor for noninvasive measurement of complex permittivity," *IEEE Sensors J.,* vol. 15, no. 12, pp. 7181-7189, Dec. 2015.

[154] M. T. Ghasr, D. Simms, and R. Zoughi, "Multimodal solution for a waveguide radiating into multilayered structures-dielectric property and thickness evaluation," *IEEE Trans. Instrum. Meas.*, vol. 58, no. 5, pp. 1505–1513, May. 2009.

[155] M. S. B. A. Karim, Y. Konishi, K. Harafuji and T. Kitazawa, "Determination of complex permittivities of layered materials using waveguide measurements," *IEEE Trans. Microw. Theory Techn.,* vol. 62, no. 9, pp. 2140–2148, Sep. 2014.

[156] M. Kempin, M. T. Ghasr, J. T. Case, and R. Zoughi, "Modified waveguide flange for evaluation of stratified composites," *IEEE Transactions on Instrumentation and Measurement,* vol. 63, no. 6, pp. 1524-1534, June. 2014.

[157] O. Tantot, M. Chatard_Moulin, and P. Guillon, "Measurement of complex permittivity and permeability and thickness of multilayered medium by an open-ended waveguide method," *IEEE Transactions on Instrumentation and Measurement,* vol. 46, no. 2, pp. 519-522, Apr. 1997.

[158] S. Panda, N. K. Tiwari, and M. J. Akhtar, "Computationally intellegent sensor system for microwave characterization of dielectric sheet," *IEEE Sensors J.,* vol. 16, no. 20, pp. 7483–7493, Oct. 2016.

[159] S. Sun, D. J. Pommerenke, J. L. Drewniak, G. Chen, L. Xue, M. A. Brower, and M. Y. Koledintseva, "A novel TDR-based coaxial cable sensor for crack/strain sensing in reinforced concrete structures," *IEEE Transactions on Instrumentation and Measurement,* vol. 58, no. 8, pp. 2714-2725, Aug. 2009.

[160] S. Kim, J. Surek, and J. Baker-Jarvis, "Electromagnetic metrology on concrete and corrosion" *J. Res. Natl. Inst. Stand. Technol.,*vol. 116, no. 3, pp. 655-669, June. 2011.

[161] N. Qaddoumi, A. Shroyer, and R. Zoughi, "Microwave detection of rust under paint and composite laminates," *Res. Nondestruct. Eval.*, vol. 9, no. 4, pp. 201–212, 1997.

[162] M. T. Ghasr, S. Kharkovsky, R. Zoughi, and R. Austin, "Comparison of near-field millimeter-wave probes for detecting corrosion precursor pitting under paint," *IEEE Transactions on Instrumentation and Measurement,* vol. 54, no. 4, pp. 1497-1504, Aug. 2005.

[163] S. Kharkovsky, A. McClanahan, R. Zoughi, and D. D. Plamer, "Microwave-dielectric-loaded rectangular waveguide resonator for depth evaluation of shallow flaws in metals," *IEEE Transactions on Instrumentation and Measurement,* vol. 60, no. 12, pp. 3923-3930, Dec. 2011.

[164] Y. J. Kim, L. Jofre, F. D. Flaviis, and Maria Q. Feng, "Microwave reflection tomographic array for damage detection of civil structures," *IEEE transaction on antennas and propagation*, vol. 51, no. 11, Nov. 2003.

[165] S. Aman, A. Aman, S. Majcherek, S. Hirsch, and B. Schmidt, "Microwave based method of monitoring crack formation," *Measurement Science and Technology,* vol. 25, no. 2, Article ID 025014, pp. 5, Jan. 2014.

[166] M. Q. Feng, F. D. Flaviis, and Y. J. Kim, "Use of microwaves for damage detection of fiber reinforced polymer-wrapped concrete structures," *Journal of Engineering Mechanics,* vol. 128, pp. 172-183, Feb. 2002.

[167] S. Kharkovsky, A. C. Ryley, V. Stephen, and R. Zoughi, "Dual-polarized near-field microwave reflectometer for noninvasive inspection of carbon fiber reinforced polymer-strengthened structures," *IEEE Trans. Instrum. Meas.*, vol. 57, no. 1, pp. 168–175, Jan. 2008.

[168] D. A. Sack, and L. D. Olson, "Advanced NDT method for evaluating concrete bridges and other structures," *NDT & E International,* vol. 28, no. 6, pp. 349-357, Dec. 1995.

[169] A. A. Shah, and Y. Ribakov, "Non-destructive measurements of crack assessment and defect detection in concrete structures," *Materials & Design,* vol. 29, no. 1, pp. 61-69, 2008.

[170] F. Y. Liao, L. H. Han, and S. H. He, "Behaviour of CFST short colunm and beam with initial concrete imperfection: Experiments," *Journal of Constructional Steel Research*, vol. 67, no. 12, pp. 1922–1935, Dec. 2011.

[171] J. Q. Xue, B. Briseghella, and B. C Chen, "Effects of debonding on circular CFST stub columns," *Journal of Constructional Steel Research,* vol. 69, no. 1, pp. 64–76, Feb. 2012.

[172] W.B. Na and T. Kundu, "EMAT-based Inspection of concrete-filled steel pipes for internal voids and inclusions," *ASME J. Pressure Vessel Technol.*, vol. 124, no. 3, pp. 265-272, Aug. 2002.

[173] B. Xu, T. Zhang, G. Song and H. Gu, "Active interface debonding detection of a concrete-filled steel tube with piezoelectric technologies using wavelet packet analysis," *Mechanical Systems and Signal Processing*, vol. 36, no. 1, pp. 7–17, March 2013.

[174] G. Ou, Y. Wang, H. Hao, and X. Q. Zhu, "Identification of de-bonding between steel bars and concrete using wavelet techniques: Comparative Study," *Australian Journal of Structural Engineering,* vol. 14 no. 1, pp. 43-56, Nov. 2013.

[175] S. Bakhtiari, N. Qaddoumi, S. I. Ganchev and R. Zoughi, "Microwave noncontact examination of disbond and thickness variations in stratified composite media," *IEEE Transactions on Microwave Theory and Techniques,* vol. 42, no. 3, pp. 389-395, March 1994.

[176] N. Qaddoumi, R. Zoughi, and G. W. Carriveau, "Microwave detection and depth determination of disbonds in low-permittivity and low-loss thick

sandwich composites," *Research in Nondestructive Evaluation,* vol. 8, no. 1, pp. 51-63, March 1996.

[177] B. Akuthota, D. Hughes, R. Zoughi, J. Myers, and A. Nanni, "Near-field microwave detection of disbond in carbon fiber reinforced polymer composites used for strengthening cement-based structures and disbond repair verification," *Journal of Materials in Civil Engineering,* vol. 16, no. 6, pp. 540-546, Dec. 2004.

[178] A. Khanfar, M. Abu-Khousa, and N. Qaddoumi, "Microwave near-field nondestructive detection and characterization of disbonds in concrete structures using fuzzy logic techniques," *Composite Structures, 62*(3–4), 335-339, 2003.

[179] S. Kharkovsky and Z. Tao, "Measurement and monitoring of gap in concrete-metal structures using microwave sensor technologies," *in Proc IEEE Intern. Instrum.Meas. Technology Conference (I2MTC 2012)*, Graz, Austria, 13 –16 May, 2012, pp. 2440-2443.

[180] L. Sandrolini, U. Reggiani, and A. Ogunsola, "Modelling the electrical properties of concrete for shielding effectiveness prediction," *J. Phys. D, Appl. Phys.*, vol. 40, pp. 5366-5372, 2007.

[181] T. Bourdi, J. E. Rhazi, F. Boone, and G. Ballivy, "Modelling dielectric constant values of concrete: An aid to shielding effectiveness prediction and ground-penetrating radar wave technique interpretation," *J. Phys. D, Appl. Phys.*, vol. 45,   pp. 405401-1–405401-12, 2012.

[182] T. Bird, "Analysis of mutual coupling in finite arrays of different-sized rectangular waveguides," *IEEE Transactions on Antennas and Propagation,* vol. 38, no. 2, pp. 166-172, Feb. 1990.

[183] T. S. Bird, *Fundamentals of Aperture Antennas and Arrays: From Theory to Design, Fabrication and Testing*, 1st Ed., John Wiley & Sons., Chichester, United Kingdom, 2016.